

~~CONFIDENTIAL~~

NASA SP-148

CONFERENCE ON HYPERSONIC AIRCRAFT TECHNOLOGY

*Ames Research Center
Moffett Field, California
May 16-18, 1967*

NOFORN

~~CLASSIFIED DOCUMENT—
TITLE UNCLASSIFIED •~~

~~This material contains information affecting the national defense of the United States within the meaning of the espionage laws, Title 18, U.S.C., Secs. 793 and 794, the transmission or revelation of which in any manner to an unauthorized person is prohibited by law.~~

~~GROUP 1
Downgraded at 3-yr
intervals; declassified
after 12 years.~~

NOTICE • This document should not be returned after it has satisfied your requirements. It may be disposed of in accordance with your local security regulations or the appropriate provisions of the Industrial Security Manual for Safeguarding Classified Information.

~~CLASSIFIED BY _____
SUBJECT TO GENERAL DECLASSIFICATION
SCHEDULE OF EXECUTIVE ORDER 11652.
AUTOMATICALLY DECLASSIFIED AT
TWO-YEAR INTERVALS.
DECLASSIFIED ON DECEMBER 31, 1974~~



Scientific and Technical Information Division
OFFICE OF TECHNOLOGY UTILIZATION
NATIONAL AERONAUTICS AND SPACE ADMINISTRATION
Washington, D.C.

1967

~~CONFIDENTIAL~~

NOTICE

THIS DOCUMENT HAS BEEN REPRODUCED FROM THE BEST COPY FURNISHED US BY THE SPONSORING AGENCY. ALTHOUGH IT IS RECOGNIZED THAT CERTAIN PORTIONS ARE ILLEGIBLE, IT IS BEING RELEASED IN THE INTEREST OF MAKING AVAILABLE AS MUCH INFORMATION AS POSSIBLE.

~~CONFIDENTIAL~~

PREFACE

This compilation consists of papers presented at a Conference on Hypersonic Aircraft Technology sponsored by the National Aeronautics and Space Administration at its Ames Research Center, May 16-18, 1967. The presentations were made in sessions subdivided according to subject matter as follows: (1) Mission Studies, (2) Configuration Aerodynamics, (3) Hypersonic Viscous Flow, (4) Propulsion, and (5) Structures and Materials.

Contributors include representatives from the Ames Research Center, the Flight Research Center, the Langley Research Center, the Lewis Research Center, and the NASA Headquarters Mission Analysis Division.

~~CONFIDENTIAL~~

CONTENTS

PREFACE	iii
-------------------	-----

SUMMARY OF MISSION STUDIES

Hubert M. Drake, Chairman

1. HYPERSONIC TECHNOLOGY PROBLEMS IDENTIFIED IN MISSION STUDIES	1
Hubert M. Drake, Thomas J. Gregory, and Richard H. Petersen	

CONFIGURATION AERODYNAMICS

J. Lloyd Jones, Chairman

2. INTRODUCTORY REMARKS ON CONFIGURATION AERODYNAMICS	21
J. Lloyd Jones	
3. EXPERIMENTAL AND THEORETICAL AERODYNAMIC CHARACTERISTICS OF REPRESENTATIVE HYPERSONIC CRUISE CONFIGURATIONS	27
Part I. Lift and Drag - W. P. Nelms	
Part II. Stability and Trim - J. A. Axelson	
4. COMPARATIVE AERODYNAMIC STUDY OF TWO HYPERSONIC CRUISE AIRCRAFT CONFIGURATIONS DERIVED FROM TRADE-OFF STUDIES	45
Jim A. Penland, Clyde L. W. Edwards, Robert D. Witcofski, and Don C. Marcum, Jr.	
5. EXPERIMENTAL AERODYNAMICS AND ANALYSIS OF THE STAGE SEPARATION OF REUSABLE LAUNCH VEHICLES	63
John P. Decker	
6. THE PROSPECTS OF AERODYNAMIC PERFORMANCE GAINS FROM WING CAMBER AND TWIST AT LOW HYPERSONIC MACH NUMBERS	79
Ralph L. Carmichael	
7. STUDIES OF OPTIMUM BODY SHAPES	87
Louis S. Stivers, Jr., and Bernard Spencer, Jr.	

8. A STUDY OF NUMERICAL METHODS FOR PREDICTING FLOW ABOUT BODIES AT ANGLE OF ATTACK	103
William F. Gallo, John V. Rakich, and Joseph W. Cleary	
9. STUDIES OF AIRFRAME—PROPULSION-SYSTEM INTEGRATION FOR MACH 6 CRUISE VEHICLES	115
Frank S. Kirkham, James M. Cabbage, Jr., Walter A. Vahl, and William J. Small	
10. SCRAMJET VEHICLE ENGINE-AIRFRAME INTEGRATION EFFECTS	137
Louis J. Williams and Darrell E. Wilcox	
11. HANDLING QUALITIES OF HYPERSONIC CRUISE AIRCRAFT	155
Harold J. Walker and Milton O. Thompson	
12. SOME EFFECTS OF MACH NUMBER AND GEOMETRY ON SONIC BOOM	171
Raymond M. Hicks, Joel P. Mendoza, and Lynn W. Hunton	
13. DETERMINATION OF THE INTERNAL DRAG OF SMALL-SCALE SIMULATED AIRBREATHING ENGINES AT $M_\infty = 4.1$	181
Lawrence A. Graham	

HYPERSONIC VISCOUS FLOW

John V. Becker, Chairman

14. BOUNDARY-LAYER TRANSITION ON HYPERSONIC-CRUISE AIRCRAFT	189
K. R. Czarnecki, Jerry M. Allen, and Mary W. Jackson	
15. TRANSITION FIXING FOR HYPERSONIC FLOW	203
James R. Sterrett, E. Leon Morrisette, Allen H. Whitehead, Jr., and Raymond M. Hicks	
16. SOME TOPICS IN HYPERSONIC TURBULENT BOUNDARY LAYER, HEAT TRANSFER, AND SKIN FRICTION	223
Mitchel H. Bertram and Aubrey M. Cary, Jr.	
17. CORNER FLOW AT HYPERSONIC SPEEDS	245
P. Calvin Stainback and Leonard M. Weinstein	
18. EFFECTS OF SHOCK IMPINGEMENT AND OTHER FACTORS ON LEADING-EDGE HEAT TRANSFER	263
Dennis M. Bushnell	

~~CONFIDENTIAL~~

PROPULSION

Edward W. Perkins, Chairman

19. INTRODUCTORY REMARKS ON PROPULSION	279
Edward W. Perkins	
20. A STUDY OF HYPERSONIC INLET TECHNOLOGY	283
Norman E. Sorensen, Shelby J. Morris, Jr., and Frank A. Pfyl	
21. TWO-DIMENSIONAL BOUNDARY LAYERS AND FLOW FIELDS OF HYPERSONIC INLETS	299
A. Vernon Gnos, William F. Gallo, and Eldon A. Latham	
22. SHOCK-WAVE—BOUNDARY-LAYER INTERACTIONS IN HYPERSONIC INLETS	315
Earl C. Watson, John D. Murphy, and William C. Rose	
23. FUEL INJECTION AND MIXING IN SCRAMJET COMBUSTORS	345
John R. Henry	
24. IGNITION AND CHEMICAL KINETICS IN HYPERSONIC RAMJETS	371
E. A. Lezberg	
25. THE VARIABLE-PITCH SUPERSONIC INFLOW COMPRESSOR AND ITS APPLICATION IN A HYPERSONIC ENGINE	401
Emanuel Boxer	
26. MEASUREMENT TECHNIQUES FOR HYPERSONIC PROPULSION	417
L. N. Krause, D. R. Buchele, and I. Warshawsky	

STRUCTURES AND MATERIALS

R. R. Heldenfels, Chairman

27. INTRODUCTORY REMARKS ON STRUCTURES AND MATERIALS FOR HYPERSONIC AIRCRAFT	471
R. R. Heldenfels	
28. STRUCTURAL MATERIALS FOR HYPERSONIC AIRCRAFT	485
Bland A. Stein, Walter Illg, and John D. Buckley	
29. A CARBON DIOXIDE PURGE AND THERMAL PROTECTION SYSTEM FOR LIQUID HYDROGEN TANKS	501
L. Robert Jackson and Ellsworth L. Sharpe	
30. FUSELAGE AND TANK STRUCTURES FOR HYPERSONIC AIRCRAFT	515
John L. Shideler and L. Robert Jackson	

~~CONFIDENTIAL~~

31. ANALYSIS OF WING STRUCTURES FOR HYPERSONIC AIRCRAFT	527
Melvin S. Anderson, James C. Robinson, and George F. Klich	
32. REGENERATIVELY COOLED STRUCTURES FOR HYPERSONIC AIRCRAFT	541
H. Neale Kelly and John L. Shideler	
33. DYNAMIC AND AEROELASTIC CONSIDERATIONS OF HYPERSONIC AIRCRAFT	555
A. Gerald Rainey and Dennis J. Martin	
34. FLUTTER DESIGN OF STIFFENED-SKIN PANELS FOR HYPERSONIC AIRCRAFT . . .	569
Herman L. Bohon, Melvin S. Anderson, and Walter L. Heard, Jr.	

~~CONFIDENTIAL~~

1. HYPERSONIC TECHNOLOGY PROBLEMS IDENTIFIED IN MISSION STUDIES

By Hubert M. Drake, Thomas J. Gregory,
and Richard H. Petersen

NASA Headquarters
Mission Analysis Division
Moffett Field, California

The primary purpose of this paper is to present some of the technological problems encountered in mission studies of hypersonic aircraft. Since the Air Force Aerospaceplane work in 1958, many agencies have studied a number of missions all of which fall into the two general classes of cruise or launch missions. Examples of the performance obtained in some of these early mission studies (refs. 1 and 2) are used here to indicate some of the reasons for interest in hypersonic aircraft. The aircraft assumed for these example studies (fig. 1) has features more or less characteristic of these aircraft such as: large volume resulting from the use of liquid hydrogen, highly swept surfaces, and a large propulsion system installed in the wing-body compression field. This particular aircraft is tailless, with an aft mounted wing, and, therefore, a large vertical fin is required for directional stability. The aircraft shown is generalized and could represent either a transport or a launch aircraft, with the second stage indicated by the dotted outline.

The somewhat optimistic performance of such a transport aircraft obtained in this early study is shown in figure 2 in which the payload plus reserves fraction is plotted as a function of range for various cruise Mach numbers. It is apparent that ranges greater than 5000 n. mi. can be attained for conventional values (15 percent) of payload plus reserves, and that the maximum range is obtained at Mach numbers near 6. The large decrease in range at a Mach number of 8 resulted from the necessity to use more fuel for cooling than was required by the assumed engines.

The performance of a two-stage launch system, consisting of a Mach 7 turboramjet-powered launch aircraft and a liquid hydrogen-oxygen rocket second stage (ref. 2) is shown in figure 3. In this case about 22,000 lb could be orbited if the landing were made downrange (no flyback). Flyback to a landing at the take-off site reduced this to about 20,000 lb. If the launch aircraft were designed for launch at 2000 n. mi. lateral offset, the payload would be reduced further as shown. If the Mach 6 cruise vehicle discussed previously were modified for the launch mission it would have somewhat reduced capabilities compared with the launch vehicle.

The mission studies reviewed above were preliminary, being based on generalized, and in some cases, optimistic assumptions. Studies in greater depth have been made, and are in progress now, by NASA, the Air Force, and many contractors, to establish promising approaches and to identify fruitful research areas. Figure 4 lists the investigations referred to in the paper and covered by references 3 through 7. It should be emphasized that these mission studies are only a few of those available and are used because of their familiarity to the authors. Other studies have obtained similar results. It should be pointed out that such studies are very sensitive to

~~CONFIDENTIAL~~

~~CONFIDENTIAL~~

the assumptions and in most areas technological verification of the assumptions is required. It is not possible in the brief time available to cover in detail all of the technological problems developed in each study, but a few will be covered and then the general problems areas for both the cruise and launch missions will be listed.

For the commercial cruise mission, initially five configurations were considered in a cursory fashion (ref. 3) and then the two configurations shown in figures 5 and 6 were studied in detail. Both configurations were designed to take off at 160 knots, to land at 135 knots, and to have a subsonic loiter/hold capability of 1000 seconds and 100 n. mi. at 40,000 ft altitude. One configuration is a relatively conventional delta wing-body aircraft while the other is a double delta, blended wing-body configuration. The largest portion of both fuselages contains the liquid hydrogen tanks. Separate tanks, as shown, allow sequencing for center-of-gravity control. The passenger compartment is above the fuel tanks. Both aircraft are about the same size but the blended wing-body configuration is slightly shorter and has a greater wing area. Both aircraft are powered by four turboramjet engines. The gross weights given in figure 7 indicate how the weights varied as the study progressed. The delta wing-body configuration increased in weight with the detailed performance estimates because it was found necessary to increase the wing size for take-off. As shown, the blended wing-body configuration appears to be lighter at each stage of the study. The final column indicates the effects of what were estimated to be reasonable projections of technology advancements for the probable time period of such aircraft. Examples of the magnitude of these improvements are as follows:

The lift-drag ratio was increased throughout the speed range; the hypersonic value of the blended wing body was increased from 5.05 to 5.7 by assumed fin area reduction and improvements in body camber and body shape to reduce wave drag, drag due to lift, and friction drag.

Specific fuel consumption was improved, with the hypersonic level being reduced from 1.355 to 1.17.

Structural weight was reduced about 13 percent by improvements in materials, reduction of thermal stresses, and improvements in insulation and joining technology.

The first general technology area to be considered is that of propulsion system airframe integration. As indicated in figures 5 and 6, the propulsion packages are installed so that the two-dimensional variable-geometry inlets are in the wing pressure field and the engines are near the center of gravity. Relatively small changes in this installation (fig. 8) result in substantial performance changes. Because the engine diameter was about twice the depth of the inlet cowl, the drag of the cowl and nacelle of this configuration was significant. Eliminating this drag by burying the engines as shown by the lower sketch improved cruise fuel consumption sufficiently to reduce take-off weight by about 25 percent. This, of course, complicates the engine and nozzle installation, as well as the fuselage structure. As is discussed in several of the following papers, careful design of the inlet and nozzle are necessary, particularly at the highest Mach numbers in order to attain

~~CONFIDENTIAL~~

acceptable flight efficiency. Another critically important aspect of the propulsion system installation is the inlet and engine cooling requirements during cruise. Fuel required for cooling in excess of that required for propulsion will, of course, directly reduce the overall performance of the aircraft. In the aircraft considered here, up to 19-percent excess fuel was required to maintain the assumed metal temperature of 1500° F. In order to avoid this, the cruise Mach number would have to be reduced from 6 to about 5.3, or the engine cooling requirements reduced, or eliminated, for example, by improved design or materials. A later paper considers the problems of regeneratively cooled structures.

Major structural problems result from the aerodynamic heating environment and from the use of liquid hydrogen as fuel. Both the high and low temperature structural and material problems are covered in this conference; only some of the hydrogen tankage problems will be discussed here.

The problems of the fuel tanks may be illustrated by the representative fuel tank shown in figure 9. Tank configurations may be integral or non-integral. Basically, the integral tank carries flight loads in the tank structure while the nonintegral tank is isolated from these loads. The choice between these approaches is not clear cut; for example, although integral tanks are usually lighter, in the study of reference 3 there was found to be little difference between integral and nonintegral tanks because the lighter weight of the integral tanks was offset by the weight of structure required by their greater thermal stresses. These stresses are a result of normal fuel usage and are aggravated by tank sequencing for center-of-gravity control. The various tanks may have to accommodate temperatures from -423° F (liquid hydrogen) to 800° F, with differentials as great as 1000° F between the top and bottom of the tank. These temperature extremes introduce problems of material selection, boiloff control (particularly that resulting from fuel sloshing on hot tank walls), and tradeoff between structure, boiloff, and insulation. Problems of inspection and maintenance procedures will undoubtedly have a strong influence on which structural approach is chosen.

Probably the most difficult considerations involved with the liquid hydrogen tankage are prevention of cryopumping and provision of safety from LH₂ leaks. Cryopumping occurs because, at some depth in the insulation, the temperature is sufficiently low to condense air. Due to the volume change associated with this phase change, the insulation will act as a vacuum pump and continue to liquefy air which will ultimately freeze on the tank wall increasing its heat flux. The liquid run-off will be primarily oxygen and, thus, will introduce additional hazards. In order to prevent cryopumping, air must be excluded from the insulation. Several ways of doing this were investigated, one of which is shown in figure 9. In this concept helium gas is diffused, by means of a distribution system, throughout the insulation from the time fueling starts until the tanks have warmed up after emptying. This helium gas is also recycled and checked in order to detect leaking hydrogen. The use of helium in this manner, however, introduces additional problems primarily resulting from the high cost of helium. Present technology would allow sufficient helium to leak away as to make the transport completely uneconomic; however, such a system might be acceptable for a launch aircraft.

~~CONFIDENTIAL~~

~~CONFIDENTIAL~~

Other approaches such as vacuum wall tanks, sealed insulation, and CO₂ frost systems are being explored and are discussed in several papers in this conference.

There is also a sonic boom problem for this cruise aircraft. Figure 10 shows the area development of the delta wing airplane (fig. 5) as originally designed and as modified to reduce sonic boom. The variation in overpressure for both shapes over the 5000 n. mi. mission indicates that, owing to the high cruise altitude, sonic boom will not be a major problem except for a couple of hundred miles at each end of the flight where the overpressure is comparable to that of the SST for this size aircraft. These overpressures were calculated; a later paper in this conference examines experimental results on the sonic boom for this and several other configurations.

Several mission studies of wing-body shapes have resulted in cruise aircraft in which the wing is minimized by being faired into the body and the fuselage no longer retains a circular cross section. A comparative mission study is currently being performed by the Mission Analysis Division to determine if such configurations offer improved performance over conventional wing-body shapes. Figure 11 shows the somewhat idealized aircraft used in this study. The wing-body configuration consists of a Sears-Haack fuselage and a delta wing; the all-body, or wingless, configuration consists of an elliptical cone with front and rear stabilizing and controlling surfaces. All of the geometric characteristics of these aircraft are being varied in the study. Gross weight and volume are held constant.

One characteristic of the all-body shape is that it provides a forebody-afterbody surface which is well suited for use as a propulsion stream-tube compression and expansion surface. While this characteristic is generally useful at all hypersonic speeds, it is particularly beneficial in the case of scramjet powered aircraft. However, integrating the airframe and propulsion system to realize these benefits presents a problem of attaining a compromise between low-speed and hypersonic performance. Configurations which have sufficient base area for maximum hypersonic performance can have transonic drag levels three or four times that of a wing-body aircraft of the same volume and weight. This characteristic suggests that the propulsion system for such aircraft may have to incorporate special features for transonic acceleration, possibly even some form of rocket augmentation.

In assessing the effects on performance of wide variations in the shape of the all-body configuration it was found that one parameter, the aircraft leading-edge sweep, showed a pronounced effect on mission performance. Figure 12 indicates that, for a typical hypersonic transport mission of 5500 n. mi. range, payload increased with increasing sweep angle up to a maximum at 82.5° for all Mach numbers considered. These results represent the idealized case in which no take-off or landing constraints are applied; therefore, they may be used to indicate the level of penalties which can result from the imposition of constraints that reduce the usable sweep angle. Figure 13 shows an aircraft of 82.5° sweep, which is the highest sweep able to accommodate the required propulsion systems. Consideration of handling qualities and take-off and landing characteristics of such an extreme configuration would probably result in still further modifications.

~~CONFIDENTIAL~~

~~CONFIDENTIAL~~

The preliminary findings of the comparative studies of wing-body and all-body shapes are tabulated on figure 14. These results suggest that for the ramjet-powered hypersonic transport mission, the performance of the two configurations is comparable even though the major aircraft weight items show significant differences. Further study and refinement may materially change these values; for example, one aspect yet to be explored is the provision of propulsion for transonic acceleration for the all-body aircraft. These preliminary results indicate the all-body configuration with scramjets to be slightly superior; but, again, before a clear advantage can be identified, further analysis and technology verification is necessary. A paper in this conference discusses some of the propulsion system airframe integration considerations of such all-body aircraft.

In considering the hypersonic launch aircraft mission it is apparent that many of the technology requirements of cruise and launch aircraft are common; however, there are important differences. The cruise vehicle, in order to be attractive economically, must have a useful life of 20,000-30,000 flight hours with only routine maintenance while a life of 2,000 hours, or less, with more extensive between-flight maintenance would be acceptable for the launch vehicle. Generally, in order to be at all attractive economically, the transport must be extremely efficient aerodynamically, propulsively, and structurally. The launch vehicle, however, is much less sensitive to the level of efficiency but, because of its relatively few flights, requires low development costs in order to compete with existing launch systems.

The launch mission poses some technology problems that differ considerably from the transport mission. The choice of propulsion system, for example, is potentially much wider and is determined to an extreme degree by mission specification. For example, the amount of offset, and flyback, required can vary from zero, where rockets might be adequate, to thousands of miles which could require engines similar to those of the transport. A study of propulsion systems for a launch mission has been performed (ref. 5), in order to determine the relative performance of a wide range of propulsion systems. The specific mission considered required no offset but did require the first stage to flyback to the launch site, and perform a 5-minute power-on loiter and landing. The two-stage vehicles were considered to have a gross weight of one million pounds, and were required to place the payload in a 262 n. mi. orbit. The majority of these systems were of the "composite" type involving air augmented rockets or ejectors, ramjets, scramjets, LACE, and recycled slush hydrogen, but with no mechanical air compression more complex than a single-stage tip-driven fan. Rockets and turboramjets were compared with these composite cycles. LACE, as utilized in this study, describes a system in which air, liquefied by liquid hydrogen, is burned immediately in the ejector rockets (no storage or enrichment). Because this cycle must run fuel rich, due to insufficient heat sink in stoichiometric hydrogen, the use of recycled slush hydrogen was investigated.

Figure 15 shows the performance of several of the 38 propulsion systems considered in the initial part of this study. The "advanced rocket," of course, does poorly both because it is reusable and because it has to carry turbojet engines to satisfy the mission requirements for flyback and loiter. It is apparent from these data that the more complex systems promise better

~~CONFIDENTIAL~~

~~CONFIDENTIAL~~

performance and that some of the more complex composite systems perform as well as the turboramjet or better. The effect of recycled slush hydrogen on the payload is shown to be small by the open extensions of the ramplate and scramplate bars. Four of the systems were studied in greater depth and the results are shown in figure 16. Again, all of the airbreathers offer better performance than the rocket, with the more advanced and complex systems promising the highest performance. It is also apparent that staging Mach numbers near 8, for subsonic combustion, and 10, for supersonic combustion, offer maximum performance. It should be pointed out that it is not meant to infer that scramplate has the best performance possible, only that it was one of the best considered in this study. It is probable that a turbojet convertible scramjet would have still better performance.

Another study, reference 4, obtained similar results but also investigated the effect of payload size. Some of these results are given in figure 17 which shows the payload fraction in terms of payload size. The important points on this figure are that the ranking of the propulsion systems is unchanged by payload size and, as might be expected, the larger payload weights are more efficient. All estimates of the performance for hypersonic propulsion systems, of course, are critically dependent upon the engine characteristics used. Experimental verification is sorely needed in this area. Several of the later papers will discuss various aspects of the propulsion systems.

A problem area inherent in the launch vehicle is, of course, the launch maneuver which involves questions of navigation and guidance, performance, propulsion initiation, separation, and stability and control. In a study of the navigation and guidance problem (ref. 6), it was found that the current state of the art was adequate for the performance of this mission with little penalty. Performance studies have indicated little effect of staging dynamic pressure on orbital payload between 100 and 800 psf; therefore the choice of staging condition will be determined more by separation, interference, and stability and control considerations. These effects are extremely complex; they depend on the configuration and necessitate experimental investigation. A paper in this conference discusses some current investigations in this area.

Configuration considerations for the launch mission introduce the problem of second-stage integration. In a current study of the matrix of configurations shown on figure 18 many of these interactions are being investigated. As may be seen, the payloads being considered range from ballistic shapes to high L/D entry vehicles and the first stages range from the relatively conventional wing-body aircraft to axisymmetric shapes. The variety and unusual nature of these configurations reflect the early state of hypersonic aircraft development. The session of this conference on aerodynamic configurations will have early information on some of these shapes while the Air Force has sponsored a study of the wing-body shape in the second column.

An example of the penalties that can result from poor integration of the upper stage is illustrated on figure 19. In this case, a lifting body upper stage is considered on a blended-body launch vehicle. When the second stage is completely submerged the payload fraction is 2-1/2 percent. If the second stage is exposed, the payload is reduced until at 70-percent exposure the performance has deteriorated to the point that no orbital payload remains.

~~CONFIDENTIAL~~

~~CONFIDENTIAL~~

The magnitude of the integration problem is illustrated by the mismatch of the upper and lower stage in figure 20. This problem of stage integration affects configuration, propulsion system choice, and integration and operational mode.

The sonic boom considerations for the launch mission differ considerably from those for the cruise mission. The launch vehicle, because of the necessity of integrating the upper stage, which adversely affects its cross-sectional area development, and because it tends to be heavier than the cruise vehicle, may produce a substantially higher overpressure. A current study has considered the effect that shaping the trajectory to minimize the overpressure would have on the orbital payload. Some of the results are shown on figure 21. In this case, a turboramjet powered all-body, launch aircraft could orbit a payload of 50,000 pounds in the absence of sonic boom constraints. The maximum overpressure in this case was about 7 psf. Shaping the trajectory to reduce the overpressure to 4 psf decreased payload by only 3 percent; however, further shaping to attain 3 psf overpressure produced a loss of 30 percent of the payload capability. The level of acceptable overpressure for the relatively restricted operations of a launch vehicle may be substantially different from those for the cruise vehicle. It is apparent that unless substantially higher overpressures are acceptable, serious payload penalties may result.

This paper has attempted to discuss in general fashion a few of the technological problems encountered during mission studies of hypersonic aircraft. Figure 22 indicates the wide range of problems that are discussed, except for costs, in this conference. Serious technological problems exist, as indicated, in each of the major research disciplines.

REFERENCES

1. Gregory, Thomas J.; Petersen, Richard H.; and Wyss, John A.: Performance Tradeoffs and Research Problems for Hypersonic Transports. J. Aircraft, vol. 2, no. 4, 1965, pp. 266-271.
2. Petersen, Richard H.; Gregory, Thomas J.; and Smith, Cynthia L.: Some Comparisons of Turboramjet-Powered Hypersonic Aircraft for Cruise and Boost Missions. J. Aircraft, vol. 3, no. 5, 1966, pp. 398-405.
3. General Dynamics/Convair Division: Performance Potential Hydrogen Fueled, Airbreathing Cruise Aircraft. Rept. Nos. GDC-DCB-66-004/1 - 66-004/4 (Contract NAS 2-3180), May and Sept. 1966.
4. Douglas Aircraft Company, Inc.: Design Considerations of Reusable Launch Vehicles. Vol. IV - Maneuverable Class Vehicles. Rept. No. DAC-57915 (Contract NAS 2-3191), Oct. 1966.

~~CONFIDENTIAL~~

~~CONFIDENTIAL~~

5. The Marquardt Corporation: A Study of Composite Propulsion Systems for Advanced Launch Vehicle Applications. Rept. No. 25,194 (Contract NAS 7-377).
6. The Boeing Company: Study of Navigation and Guidance of Launch Vehicles Having Cruise Capability. Contract NAS 2-3691.
7. Lockheed-California Company: Reusable Aerospace Passenger Transport System. In Rept. No. LR 20066, Study of Incremental Systems Development Approaches and Applications; Rept. No. LR20099, Advanced Air-breathing First Stage Booster Operational Analysis (Contract NAS 8-20294).

~~CONFIDENTIAL~~

TYPICAL CONFIGURATION

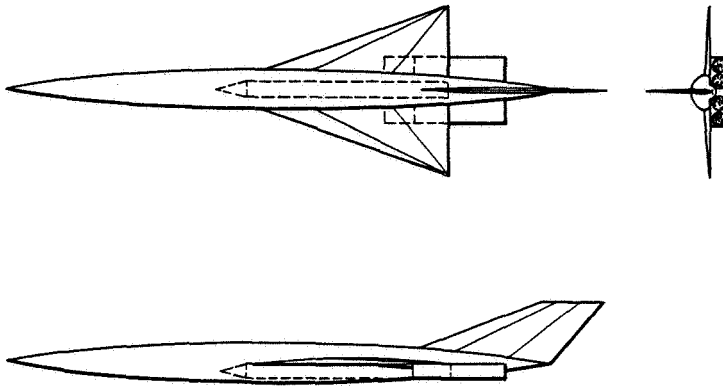


Figure 1

HYPERSONIC TRANSPORT RANGE-PAYLOAD CAPABILITY

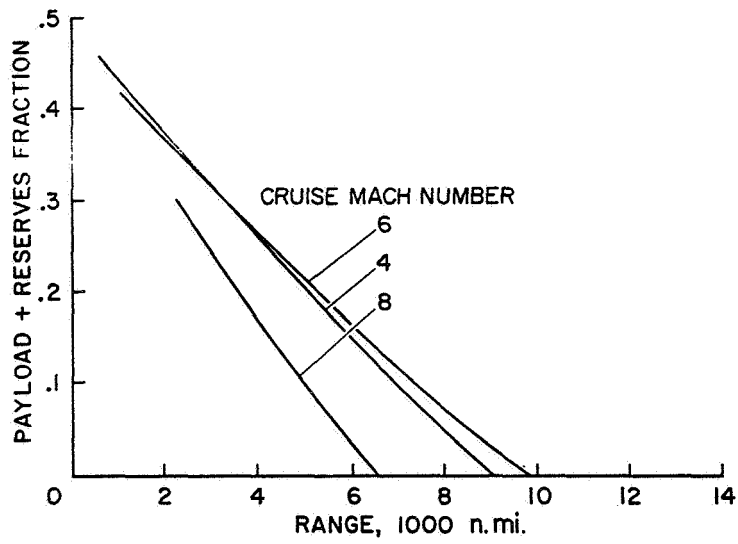


Figure 2

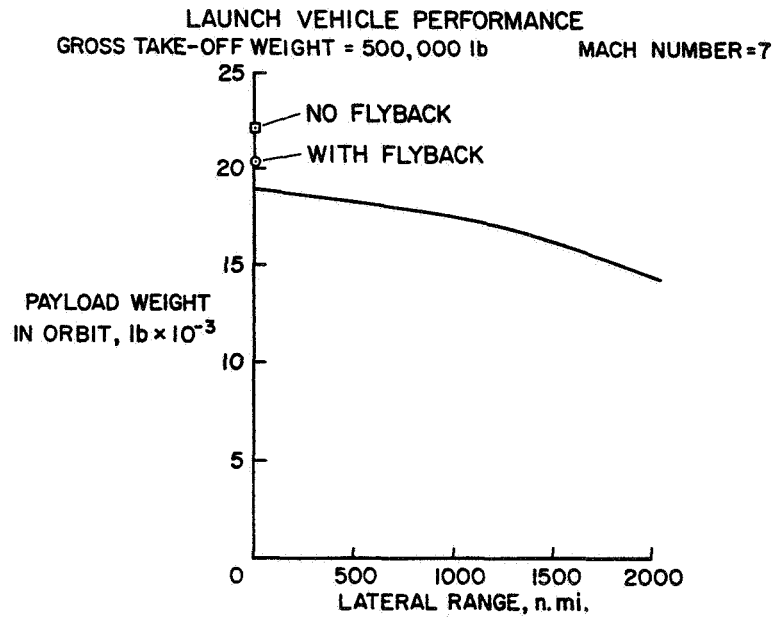


Figure 3

RECENT STUDIES

MISSION	INVESTIGATOR	REFERENCE
CRUISE	NASA GENERAL DYNAMICS CONVAIR	NAS 2-3180
LAUNCH	NASA DOUGLAS MARQUARDT, LOCKHEED, ROCKETDYNE LOCKHEED BOEING LOCKHEED	NAS 2-3191 NAS 7-377 NAS 8-20294 NAS 2-3691 NAS 2-4084

Figure 4

~~CONFIDENTIAL~~

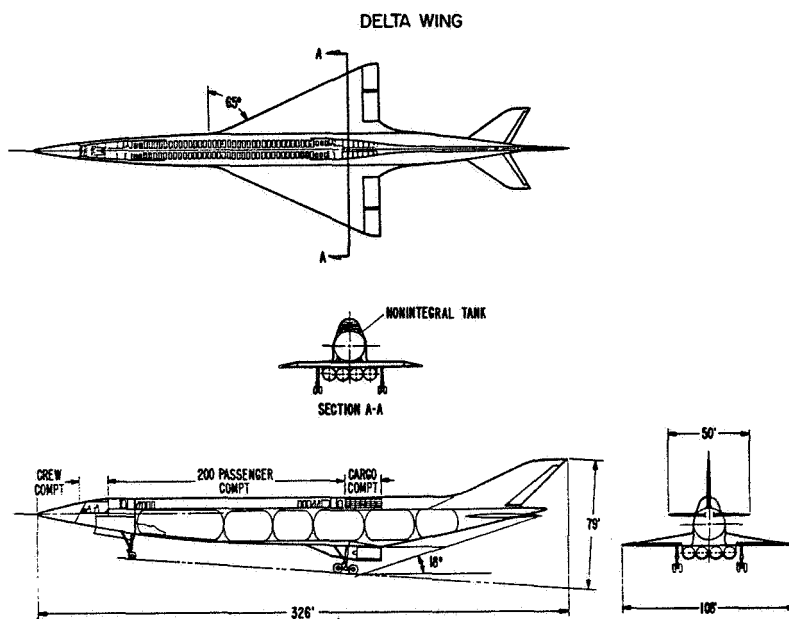


Figure 5

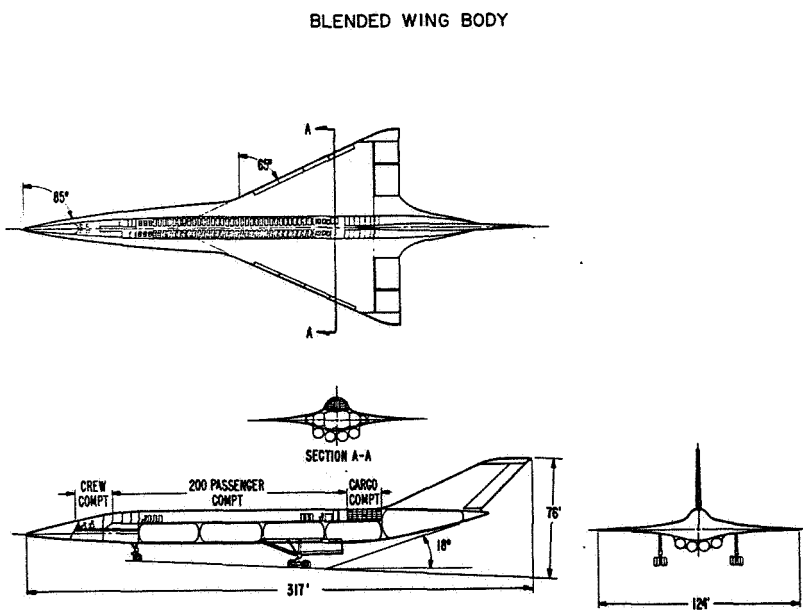


Figure 6

~~CONFIDENTIAL~~

CRUISE AIRCRAFT STUDY
200 PASSENGERS 5000 n. mi. RANGE

CONFIGURATION	GROSS WEIGHT, 10 ³ lb		
	SIMPLIFIED PERFORMANCE ESTIMATES	DETAILED PERFORMANCE ESTIMATES	PROJECTED PERFORMANCE ESTIMATES
DELTA-WING BODY	585	750	521
BLENDED WING BODY	555	512	401

Figure 7

INLET/ENGINE INSTALLATION

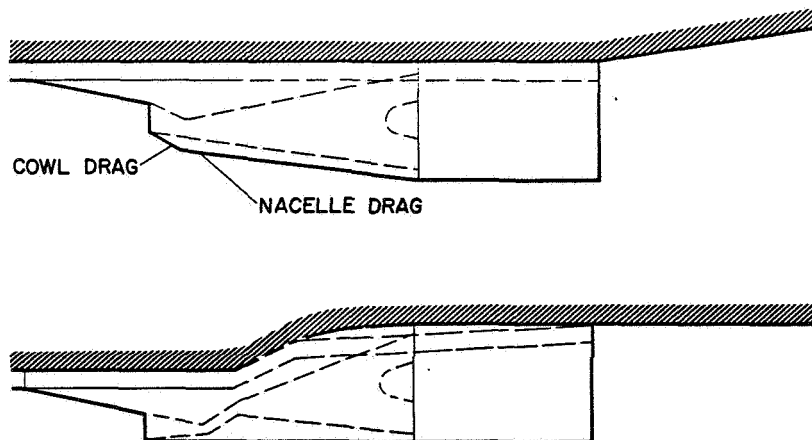


Figure 8

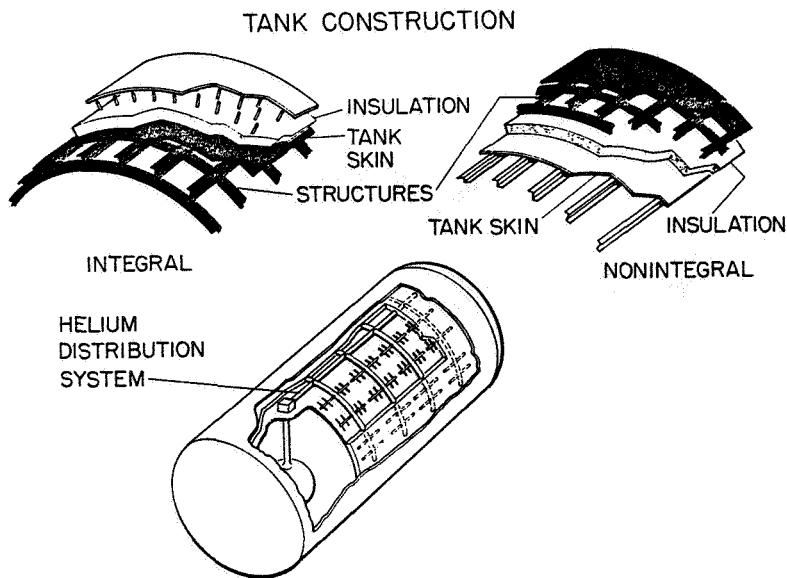


Figure 9

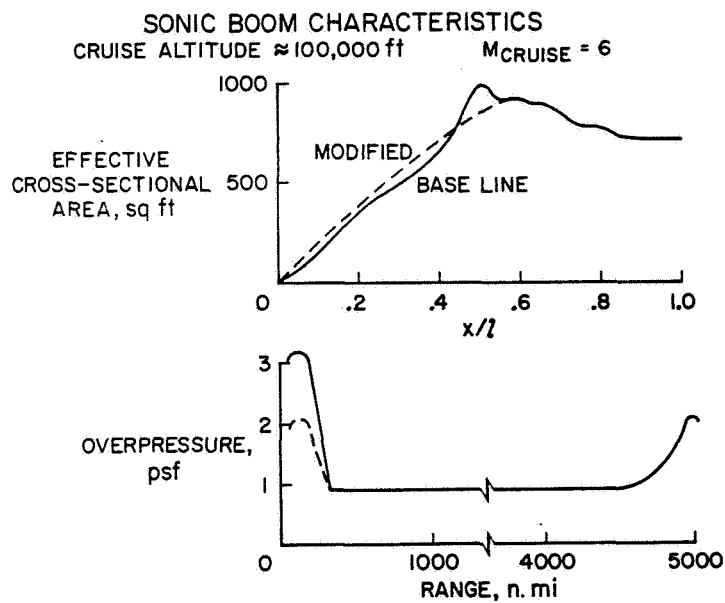
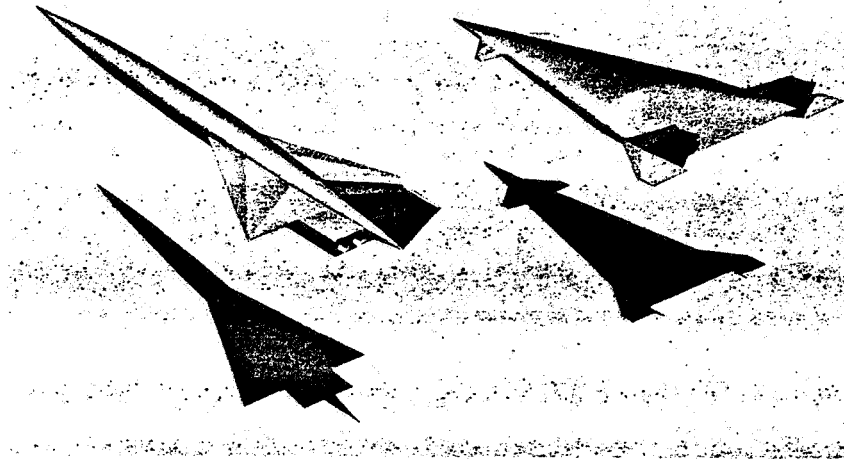


Figure 10

CONFIGURATIONS



AAA360-11

Figure 11

EFFECT OF VEHICLE LEADING-EDGE SWEEP

ALL-BODY SCRAMJET

RANGE = 5500 n. mi.

GROSS TAKE-OFF WEIGHT = 500,000 lb

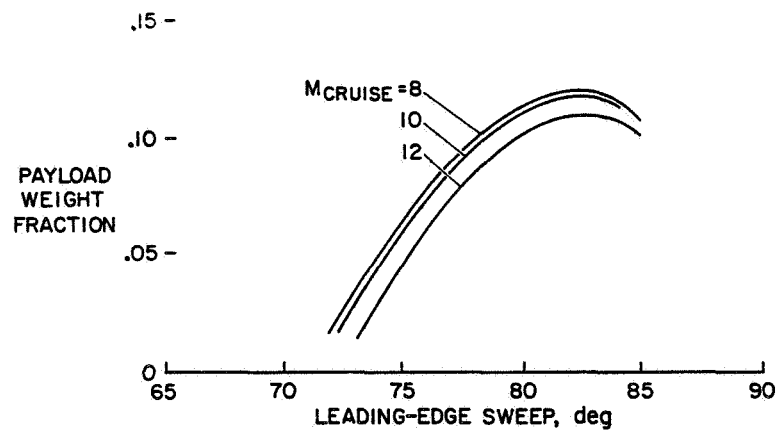


Figure 12

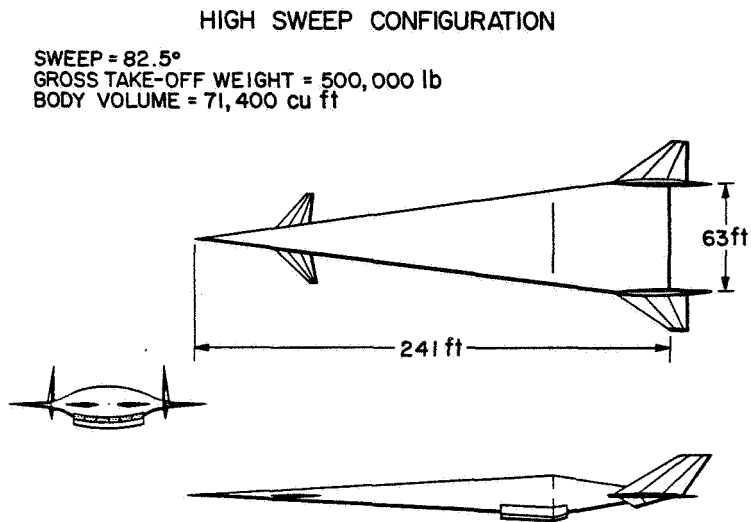


Figure 13

VEHICLE PERFORMANCE COMPARISON

VEHICLE	WEIGHT (PERCENT OF GROSS TAKE-OFF WEIGHT)				
	STRUCTURE	EQUIP	PROPULSION	FUEL	PAYLOAD
WING BODY M=6 (TURBORAMJET)	38	7	11	35	9
ALL BODY M=6 (TURBORAMJET)	28	5	22	40	5
ALL BODY M=10 (TURBOJET + SCRAMJET)	29	9	18	33	11

Figure 14

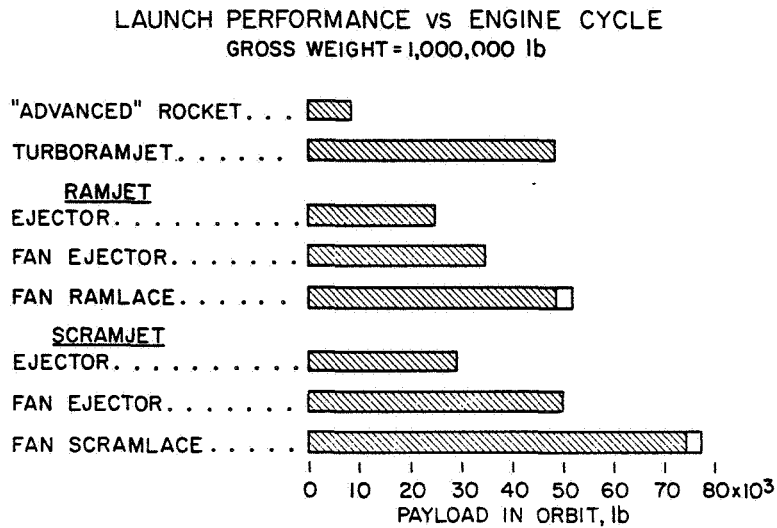


Figure 15

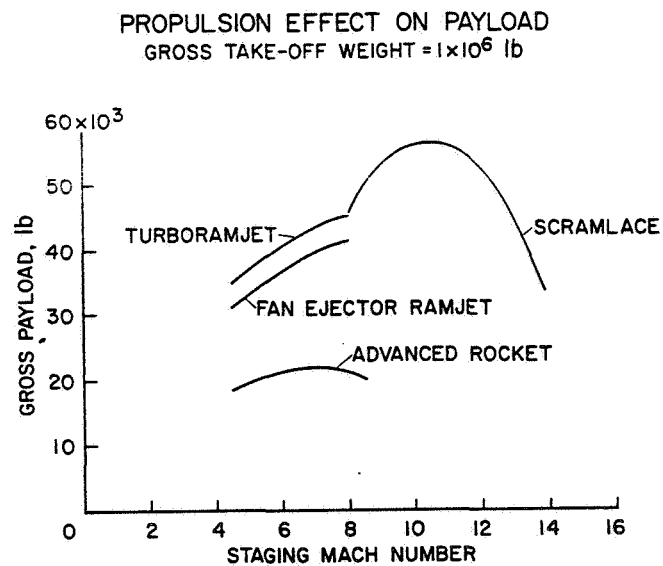


Figure 16

REUSABLE LAUNCH VEHICLE PAYLOAD RATIO COMPARISON

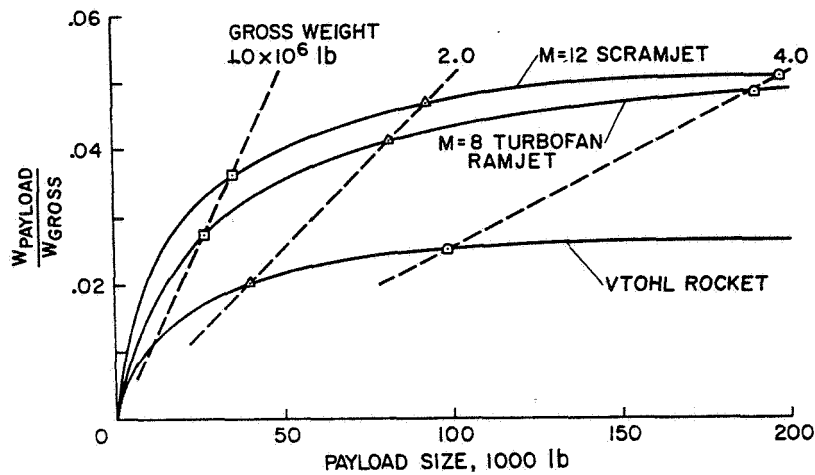


Figure 17

CONFIGURATION MATRIX

		WINGED BODIES		BLENDED BODIES	
1st STAGE	2nd STAGE				

Figure 18

LAUNCH AIRCRAFT INTEGRATION PROBLEM

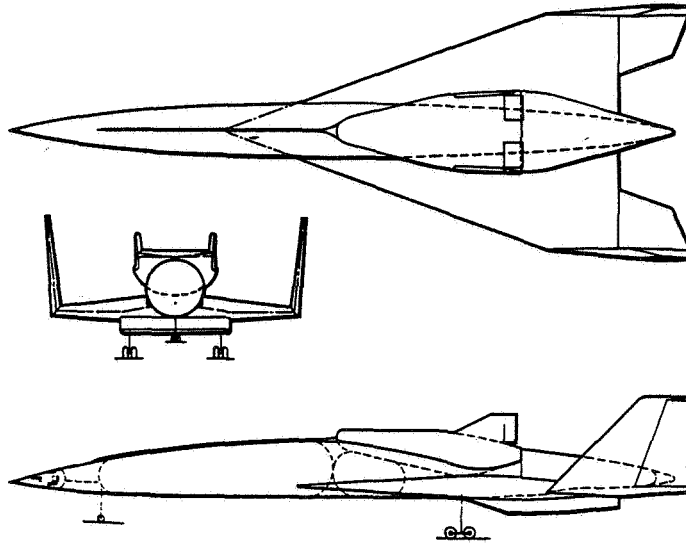


Figure 19

EFFECT OF UPPER STAGE EXPOSURE ON ORBITAL PAYLOAD LIFTING BODY UPPER STAGE

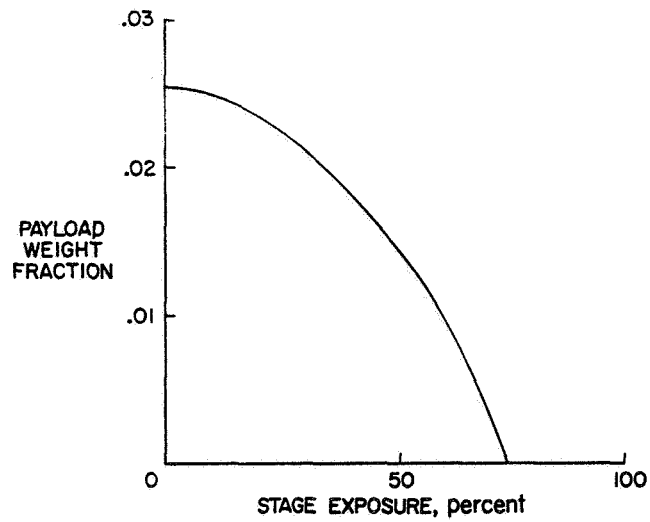


Figure 20

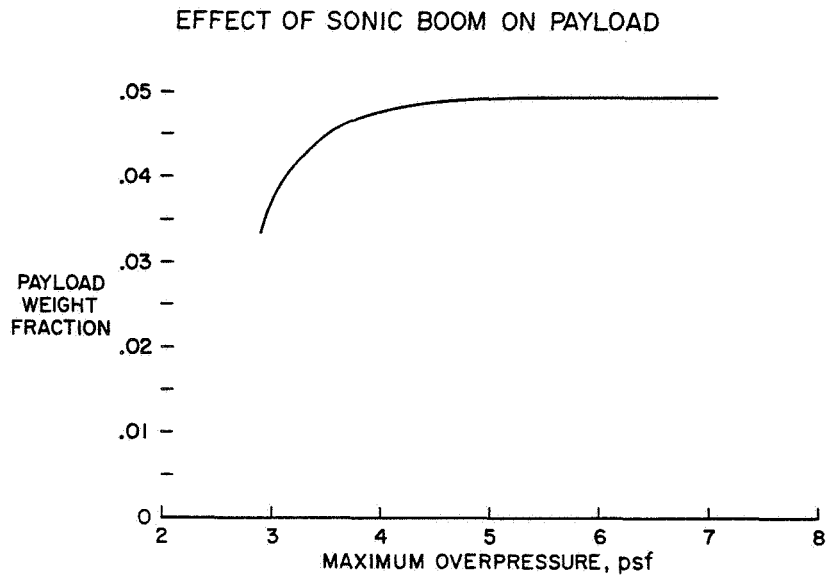


Figure 21

PROBLEM AREAS

CONFIGURATION AERODYNAMICS	PROPULSION (CONTINUED)
PERFORMANCE	ENGINE
HYPERSONIC L/D	CYCLE
TRANSONIC DRAG	SFC (HYPERSONIC, SUBSONIC)
STABILITY AND CONTROL	COOLING LOAD
SONIC BOOM	NOZZLE
TAKE-OFF AND LANDING	EFFICIENCY
SECOND STAGE INTEGRATION/SEPARATION	COOLING LOAD
	INTEGRATION WITH AIRFRAME
HYPERSONIC VISCOUS FLOW	STRUCTURES CONCEPTS
TRANSITION	HOT STRUCTURES
INTERFERENCE	TANKAGE
HEATING	REGENERATIVE COOLING
PROPULSION	MATERIALS
INLET	AEROELASTICITY
PRESSURE RECOVERY	OPERATIONS
FLOW DISTORTION	SAFETY
SIMPLIFICATION	INSPECTION
COOLING LOAD	COST
	DEVELOPMENT
	OPERATING

Figure 22

~~CONFIDENTIAL~~

2. INTRODUCTORY REMARKS ON CONFIGURATION AERODYNAMICS

By J. Lloyd Jones
Ames Research Center

2

Mr. Drake has reviewed in some detail systems studies of hydrogen fueled aircraft with airbreathing propulsion systems for long range cruise and space vehicle launch mission applications. Because of the indicated potential performance of these aircraft systems, NASA has been exploring the state of the art in the area of configuration aerodynamics with two objectives. The first is the identification of those areas where deficiencies exist (a) in our understanding of the physical phenomena involved and (b) in our ability to predict by theoretical and experimental means the aerodynamic characteristics of hypersonic aircraft. The second is the initiation of research programs to improve these deficiencies to the point initially that aerodynamic characteristics can be defined with sufficient accuracy for realistic assessment of performance potentials. We are currently in only the early phases of this program. Improvements in the levels of aerodynamic efficiency can be expected over the values measured for early conceptual configurations to be reported at this meeting. To illustrate this point I would like to draw an analogy to the development of supersonic cruise aircraft as depicted in figure 1 by the increase in maximum lift-to-drag ratio achieved in wind-tunnel tests over the past 10-year period. The total increase amounts to about 30 percent. At the left of the figure is shown the gradual improvement realized during the development of the XB-70. Continued configuration studies at a low level of effort indicated that further gains could be achieved as illustrated in the time period from 1960 to 1962. Greater emphasis led to the SCAT studies in 1963, followed by the initiation of the SST program late in 1963. The improvement achieved during this period reflects the influence of applying the knowledge gained in research programs. This improvement was largely a result of a more thorough understanding of interfering flow fields and the development of improved theoretical concepts and computational techniques for configuration optimization. To complete the analogy, in our consideration of hypersonic aircraft configuration development we are relatively somewhat behind the supersonic cruise aircraft developmental status of 1958. Much remains to be done. It should be recognized, however, that the potential aerodynamic improvements indicated by theory are not as large for the hypersonic cruise aircraft as were those for supersonic cruise aircraft at the same relative time period in the development cycle.

In reviewing the developments in hypersonic theory over the past 10 years, it is immediately apparent that the emphasis has been almost entirely on the flow fields about atmosphere entry vehicles (e.g., the blunt body and conical flow fields). These flow fields generally can be characterized as simple single shock systems, as contrasted to the complex interfering flow fields about the types of aircraft to be considered at this conference. Attention is required in developing methods for the prediction of pressures, forces, and moments acting on these more complex shapes at hypersonic speeds.

~~CONFIDENTIAL~~

~~CONFIDENTIAL~~

Experimental studies in hypersonic wind tunnels over this same time period likewise have been predominately of atmosphere entry configurations. Whether the configurations were ballistic, lifting body, or winged body, they have been high drag configurations relative to the aircraft concepts we are considering here. Emphasis has gradually turned to configurations with higher lift-to-drag ratios, but the flight regime of greatest concern has been at high altitude and low Reynolds numbers. Existing wind-tunnel facilities have satisfactory test characteristics for experimental investigations of this class of vehicle.

Hypersonic cruise aircraft will be very large and will fly at altitudes where the boundary-layer flow will be essentially all turbulent. The precise knowledge of the drag of cruise aircraft is extremely important in determining the efficiency of flight. As indicated in figure 2, friction drag, while reduced in importance relative to the supersonic cruise aircraft, is still a significant fraction of the total drag. A major problem in experimental studies of the aerodynamic characteristics of hypersonic cruise aircraft is that of establishing and verifying turbulent boundary-layer flows on wind-tunnel models.

Figure 3 illustrates the problem. Presented in the figure are the lift, drag, and pitching-moment characteristics for an eighteen-inch-long delta-wing body model tested in the Ames 3.5-foot hypersonic wind tunnel at Mach numbers of 7.4 and 10.4 at several unit Reynolds numbers. At the lower Mach number an increase in unit Reynolds number from 1.6×10^6 to 3.5×10^6 per foot resulted in a considerable decrease in the drag level. A further increase to a unit Reynolds number of 6.3×10^6 per foot resulted in further, though smaller, decrease. From all indications, the flow was nearly all laminar even at the highest Reynolds number. At a Mach number of 10.4 and a unit Reynolds number of 0.8×10^6 per foot the measured characteristics were highly irregular. At 2×10^6 per foot the variations were more nearly what would be expected, but one would certainly question the values obtained. This, incidentally, is the highest test Reynolds number attainable in the facility at this Mach number. Methods for tripping the boundary layer on models will certainly have to be developed. This subject will be discussed in detail in a paper in the session on viscous flows. The point to be made here is that experimental techniques will have to be improved to provide the same degree of confidence in the measurement of aerodynamic characteristics of hypersonic cruise aircraft models and their extrapolation to flight conditions that has been developed in the SST studies.

This session on configuration aerodynamics will not attempt to cover the entire field in a state-of-the-art assessment. This session, as are the others in this conference, is more in the nature of a status report and is outlined in figure 4. The first three papers present the results of wind-tunnel studies of cruise configurations and of the stage separation problem for launch vehicles. The general geometric characteristics of the cruise configurations considered are based upon the results of performance studies and systems analyses described by Mr. Drake.

~~CONFIDENTIAL~~

~~CONFIDENTIAL~~

The next five papers summarize some phases of configuration optimization and synthesis techniques where studies have been conducted.

Finally, a review of two operational problem areas of particular concern will be included.

Also included in the compilation of papers for the conference, although not presented orally at the conference, is a paper which summarizes the results obtained to date in an experimental investigation of the internal drag of several different propulsion system pod configurations representative of those that would be employed on wind-tunnel models of hypersonic cruise configurations.

~~CONFIDENTIAL~~

~~CONFIDENTIAL~~ SUPERSONIC CRUISE AIRCRAFT $(L/D)_{MAX}$

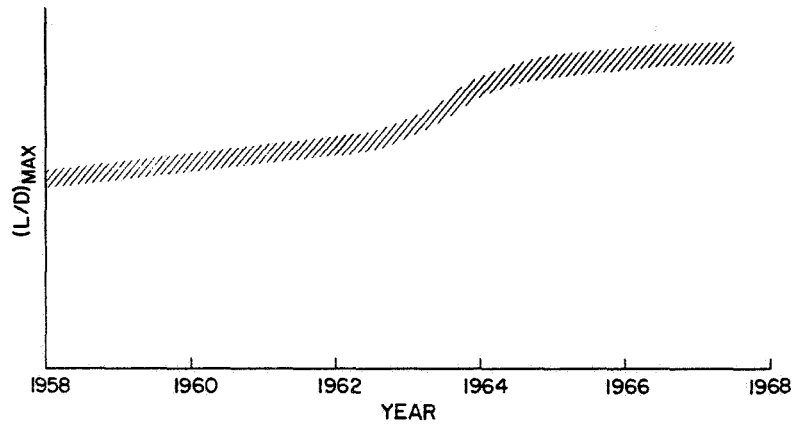


Figure 1

DRAG COMPONENTS AT $(L/D)_{MAX}$

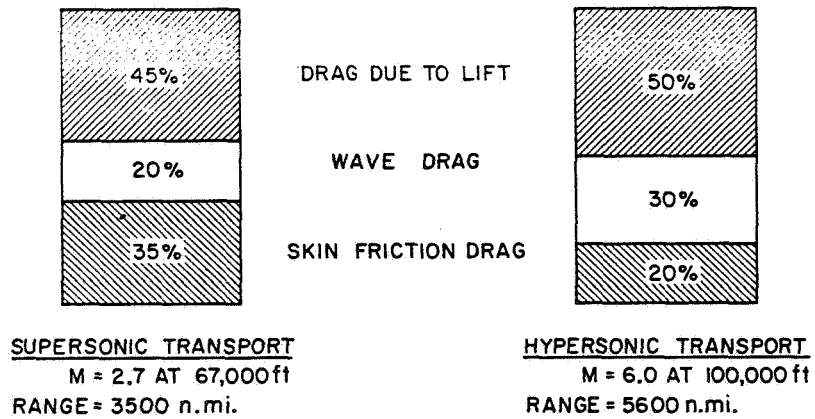


Figure 2

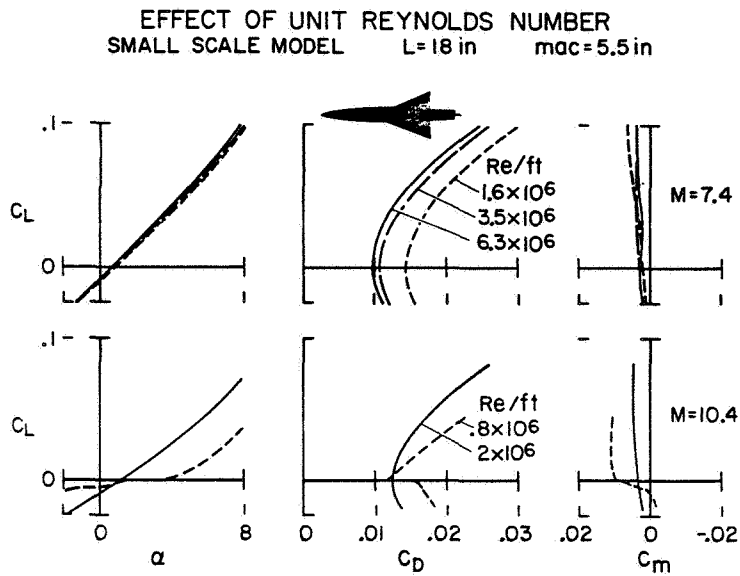


Figure 3

CONFIGURATION AERODYNAMICS

EXPERIMENTAL EVALUATION

- CRUISE AIRCRAFT
- LAUNCH VEHICLES

OPTIMIZATION AND SYNTHESIS

- WINGS
- BODIES
- AIRFRAME-PROPULSION SYSTEM INTEGRATION

OPERATIONAL PROBLEMS

- HANDLING QUALITIES
- SONIC BOOM

Figure 4

~~CONFIDENTIAL~~

3. EXPERIMENTAL AND THEORETICAL AERODYNAMIC CHARACTERISTICS OF REPRESENTATIVE HYPERSONIC CRUISE CONFIGURATIONS

PART I. LIFT AND DRAG
By W. P. Nelms

PART II. STABILITY AND TRIM
By J. A. Axelson

Ames Research Center

SUMMARY

Experimental results for three models representative of hypersonic cruise aircraft have been measured over a Mach number range from 0.65 to 7.4 and compared with various theoretical estimates for the supersonic and hypersonic speed ranges. The three different models were designed to the same general specifications for an air-breathing, liquid-hydrogen fueled, hypersonic cruise aircraft having a gross weight of approximately a half-million pounds and a wing area of 6250 square feet.

The basic models comprised of wing, body, and vertical tail, with nacelles removed, developed untrimmed hypersonic maximum lift-drag ratios near 4.2. Theoretical estimates of the lift characteristics generally agreed well with the experimental results. Less satisfactory agreement between theory and experiment resulted for the drag characteristics, however, primarily because of the underprediction of zero-lift drag at hypersonic speeds.

The longitudinal and directional aerodynamic centers and the aerodynamic performance are presented for the configuration buildups and for various degrees of stability and trim. Inviscid theoretical estimates of aerodynamic center were in fair agreement with experiment around a Mach number of 5 but inadequately accounted for the effects of increasing hypersonic Mach number where viscous interaction effects became dominant. The trimmed maximum lift-drag ratio at hypersonic Mach numbers for the models with rudders flared for directional stability and control was approximately 3.5.

INTRODUCTION

Recent studies of the potential of hydrogen-fueled hypersonic aircraft for both cruise and boost missions, as typified by reference 1, have indicated a need for research in the areas of theoretical prediction techniques and experimental testing procedures for these types of configurations. Theories are available for predicting hypersonic aerodynamic characteristics of relatively simple shapes, but it is not known if these same theories can be combined to predict the characteristics of complex multiple-shock systems such as those associated with aircraft-type configurations.

~~CONFIDENTIAL~~

CONFIDENTIAL

The objectives of this paper are to present experimental aerodynamic characteristics for three representative hypersonic cruise configurations and to compare the results with theoretical estimates.

SYMBOLS

\bar{c}	mean aerodynamic chord
C_D	drag coefficient
C_{D_0}	drag at zero lift
C_L	lift coefficient
C_{L_0}	lift at zero angle of attack
C_{L_α}	lift-curve slope
C_{m_0}	pitching-moment coefficient at zero lift
$(L/D)_{\max}$	maximum lift-drag ratio
M	Mach number
S_{ref}	reference wing area
S_v	exposed vertical-tail area
α	angle of attack

EXPERIMENT

Models

The three models used in the present investigations are shown in figure 1. They were designed to the same specifications, namely, an air-breathing, liquid-hydrogen fueled, hypersonic aircraft having a gross weight of approximately a half-million pounds, a cruise Mach number near 6, and a wing area of 6250 square feet. The wings, with an aspect ratio of 1.46, had flat under-surfaces for minimizing local flow acceleration and hypersonic boundary-layer expansion ahead of the inlets. The engines were placed on the three configurations so as to avoid jet impingement on the structure downstream of the nacelle exits. The plane containing the wing lower surface passed through the fuselage center line on the three models.

Reference model. - The model at the top of figure 1 was derived from the analytical studies of reference 1. The fuselage had a circular cross section,

~~CONFIDENTIAL~~

a fineness ratio of 12, and a Sears-Haack area distribution. The model scale was 1 inch equals 16 feet full scale. The flat-bottomed wing had a 70° swept-back leading edge and a 4-percent-thick wedge-slab-wedge airfoil section with ridge lines on the upper surface at 30 and 70 percent of the local chords. This model could be fitted with either of two vertical tails, both of which had the same planform (i.e., 60° sweptback leading edges and exposed areas equal to one-fourth of the reference wing area) but different airfoil sections. One vertical tail had a 4-percent-thick symmetrical diamond section; the other had an 8-percent-thick wedge section. The latter vertical tail in effect represents the former tail incorporating flare of the surface aft of the ridge line. The external contours of the two-dimensional nacelles, with the inlets located in the wing compression field, simulated a design containing two turbojet engines per nacelle. For the reference model, constant-area internal ducts were used, but not inlet precompression ramps nor a boundary-layer bypass.

Flat-bottomed model.- The model at the lower left in figure 1 is designated the flat-bottom model because of the flat undersurfaces on all model components. The forebody of the flat-bottomed fuselage was longitudinally curved upward to the nose but was laterally flat. The 70° sweptback delta wing was tested with 4- and 3-percent-thick airfoil sections which had rounded ridge lines at 35- and 70-percent chord on the upper surface. The nacelle and horizontal stabilizer combination was designed to bypass the boundary layers from the adjacent wing and body surfaces and to draw air from the compression field under the wing in flight. This model also incorporated a pair of wing-mounted flaps conceived to deflect downward in front of the inlets and to afford protection from debris ingestion during powered ground operations. Under these conditions, the inlets would draw air from the upper surface of the wing. The exit areas of the nacelles were twice the inlet areas.

Blended model.- The blended model at lower right in figure 1 had a flattened body of elliptical cross section merged to a 3-percent-thick, 80° - 65° double delta wing with clipped tips. The elliptical cross sections had a ratio of major to minor axes of 16/9. The nacelles, like those on the flat-bottomed model, provided for boundary-layer bypass. By comparison the nacelles on the blended model were mounted farther forward under the wing, with the ramps above rather than below the inlets. The wing had a double-wedge section with inboard and outboard rounded ridge lines at 64-percent chord on the upper surface. The wing extended relatively far aft on this short body for balance between the weight and aerodynamic forces.

Vertical tails and rudders.- The afterbodies of the flat-bottomed and blended models were fitted on the center line with similar vertical tails that had symmetrical wedge-slab-wedge sections, 70° sweptback leading edges, and exposed areas equal to one-tenth the wing reference area. These models were also equipped with identical pairs of wing-mounted 70° sweptback fins with wedges simulating deflected rudders. The combined areas of the three vertical surfaces totaled to the same one-fourth of the wing reference area as that of the single large vertical tail on the reference model.

~~CONFIDENTIAL~~

Tests

Experimental data were obtained in the Ames 6- by 6-foot transonic, 1- by 3-foot supersonic, and 3.5-foot hypersonic wind tunnels over a Mach number range from 0.65 to 7.4. In the 6- by 6-foot tunnel, the Mach number was varied from 0.65 to 2.0 (a few measurements were also made at 0.25), and in the 1- by 3-foot facility, from 2.0 to 4.8. Mach numbers of 5.3 and 7.4 were obtained in the 3.5-foot hypersonic tunnel, where the stagnation temperature was maintained at 800° F to prevent liquefaction of air in the test section. Data were taken at a constant Reynolds number of 3.5 million per foot at all Mach numbers, except 2.0 in the 6- by 6-foot tunnel, where the Reynolds number was held at 2.5 million per foot because of pressure limitations.

The models were sting-mounted through the rear of the fuselages. Force and moment measurements were made with an internally mounted six-component strain-gage balance over a nominal angle-of-attack range from -4° to $+12^{\circ}$ and angle-of-sideslip range from -2° to $+10^{\circ}$. The angles of attack and sideslip were corrected for balance and sting deflections due to the aerodynamic loads, and the measured forces were adjusted to a condition of free-stream static pressure over the model bases.

At several points throughout the test Mach number range, pressure surveys were made of the flow through the nacelles, and the computed results were used to correct for internal drag. Also, the pressure on the base of the reference model nacelles was measured and the axial force adjusted to a condition corresponding to free-stream static pressure.

Generally transition was not fixed on the models, but grit studies were conducted at several of the lower Mach numbers in order to provide an all-turbulent boundary layer as a basis for data evaluation. At the hypersonic speeds, no effective method was found for fixing transition near the leading edges of the model components to achieve fully turbulent flow. Studies utilizing flow visualization and Reynolds number variation indicated the hypersonic boundary layers to be nearly all laminar with possible small areas of transitional flow.

DISCUSSION

Part I. Lift and Drag

This part of the discussion concerns the lift and drag characteristics of the three representative hypersonic cruise configurations. Experimental data obtained for the three models during the wind-tunnel tests are compared over the test Mach number range. The results of several theoretical prediction techniques are correlated with the experimental data for the reference configuration.

Experimental lift and drag.- In order to compare experimental lift and drag characteristics of the three models, it was desired to have the configurations on as nearly an equal basis as possible. Therefore, the comparisons

~~CONFIDENTIAL~~

are made for the wing-body configurations with the vertical tail at the center line and the nacelles removed. Also, the data as presented are for mixed-flow boundary-layer conditions. The experimental results, indicating very little difference in the lift and drag characteristics of these three configurations throughout the test Mach number range, are presented in figure 2. This figure shows zero-lift drag (C_{D_0}), lift-curve slope at zero lift (CL_α), and untrimmed, maximum lift-drag ratio ($(L/D)_{max}$) versus Mach number for the three models. As can be seen, the nearly identical values of maximum lift-drag ratio decrease from about 9 at 0.9 Mach number to about 4.2 at $M = 6$. Because the experimental results for the three configurations are very similar over the Mach number range, the reference configuration is considered representative for the theoretical comparisons.

Theoretical methods.- Several theoretical prediction methods were employed in a comparison with the foregoing experimental data. A brief summary of these techniques is presented in figure 3. This figure shows the procedures for calculating both pressure and skin friction forces and each has been assigned an identifying number to be used in the figures that follow. Because most of the methods are adequately discussed in the literature, only a brief comment on each will be given here.

In the pressure-force calculation technique number 1, identified as linearized method, the wave drag was computed by a computer program (ref. 2) which applied the supersonic area rule to an "equivalent" body of revolution. The lift characteristics, including wing-body interference effects, and the drag due to wing camber were determined in an aerodynamic influence coefficient program discussed in reference 3. The drag due to lift was set equal to the relation $C_L \tan \alpha$, which assumes no leading-edge suction or thrust. In the pressure-force calculation procedure number 2, tangent-cone theory was used for the body and tangent-wedge theory for the wing and vertical tail (ref. 4). Pressure-force prediction technique number 3 consisted of Newtonian theory applied to the windward surfaces of the configuration. These latter two theoretical methods employed a Prandtl-Meyer expansion on the leeward or expansion surfaces. Pressure-force prediction methods 2 and 3 did not include the effects of wing-body interference.

The friction drag computation that was combined with the pressure force estimates utilized the reference temperature method of reference 5; in all cases, both an all-turbulent and an all-laminar boundary layer were assumed.

Experimental theory correlations.- The lift and drag characteristics as computed by the foregoing theoretical methods are compared with the experimental results in the remaining figures. These comparisons will be made for the reference model with the nacelles removed.

Zero-lift drag.- The results of correlating the experimental and theoretical zero-lift drag values throughout the test Mach number range are presented in figure 4. This figure is a plot of zero-lift drag (C_{D_0}) versus Mach number. The open symbols denote experimental data for which the boundary-layer flow over the model was mixed, varying from a combination of laminar and turbulent flow at the lower Mach numbers to essentially all-laminar flow at the higher

~~CONFIDENTIAL~~

speeds. The solid symbols represent experimental points for all-turbulent boundary-layer flow. These all-turbulent values were obtained from a detailed wind-tunnel drag study in which six sizes of carborundum particles were used and the grit-free all-turbulent drag level was determined by the methods of reference 6. The linearized method shows excellent agreement with the experimental data for all-turbulent flow at the lower Mach numbers with an error at $M = 1.3$ on the order of 3 percent. However, at Mach numbers above about 4, the drag predictions are too low, since the all-laminar theoretical curve should be approaching the mostly laminar-flow experimental data in this area. Likewise, the drag level predicted by the tangent-cone tangent-wedge theories is low, since, as before, the results of laminar theory should agree closer with the experimental results. Nevertheless, the laminar curve for this theory generally predicts the variation of drag level with Mach number. Hypersonic drag predicted by this theoretical method is too low for several reasons, such as model component interference effects, underestimation of the viscous interaction effects, and underestimated contributions of the leeward or "shadow" surfaces. As the figure shows, the Newtonian theoretical estimates are also low in comparison to the data, but this is not unexpected, since, in addition to the aforementioned reasons, the most general application of this theory is for blunt shapes at high hypersonic speeds.

Lift. - In general, the lift characteristics of this type of configuration can be predicted with more certainty than the drag level. This fact is demonstrated in figure 5 which presents a correlation of the theoretical and experimental lift results. The figure is a plot of lift at zero angle of attack (C_{L_0}) and lift-curve slope at zero lift (C_{L_α}) as a function of Mach number. The experimental data indicate that the positive values of lift at zero angle of attack, begin to decrease with increasing Mach number until at Mach numbers above about 3 (where the wing leading edge becomes supersonic), the values become slightly negative. As shown on the figure, the C_{L_0} level is overestimated by the linearized method at Mach numbers below 3, but all methods provide good correlation at the higher Mach numbers. The linearized method gives good estimates of lift-curve slope around $M = 2$, but tends to overestimate this value at a Mach number of 3 and above. Tangent-cone and tangent-wedge theories show good agreement with the experimental values of lift-curve slope; but as would be expected at these Mach numbers, Newtonian theory underestimates this parameter. The value of $4/\beta$ is shown on the figure, and when the wing leading edge is supersonic, it gives surprisingly good results for the lift-curve slope of this configuration despite the presence of the large-volume fuselage. With the exception of the Newtonian method, the generally good agreement of the various theories with the experimental data throughout the test Mach number range is evident.

Maximum lift-drag ratio. - The aerodynamic characteristics can now be summarized into a lift-drag ratio by including the drag-due-to-lift term and, at the higher Mach numbers, by accounting for the increase in lift-curve slope with angle of attack. Figure 6 presents a correlation of theoretical and experimental values of maximum, untrimmed, lift-drag ratio $((L/D)_{\max})$ as a function of Mach number. As in the case of the drag comparison, the all-turbulent theoretical results of the linearized theoretical method exhibit excellent agreement at the lower Mach numbers with the corresponding

~~CONFIDENTIAL~~

~~CONFIDENTIAL~~

all-turbulent experimental data, differing only about 5 percent at $M = 1.3$. However, above about $M = 3$, the linearized method is predicting too high a value of L/D since the laminar, and not the turbulent, curve should be approaching the data in this area. This is a consequence of the low value of drag and high value of lift-curve slope that was predicted in this region as discussed earlier. These same comments apply to the results of tangent-cone and tangent-wedge theories, since, because of the low drag estimates, the predicted L/D values are also too high. It is only fortuitous that the Newtonian method gives good results in the vicinity of $M = 5$, because, as previously shown, it underestimates both the drag and the lift-curve slope. At around $M = 7$, however, the Newtonian method also overestimates the maximum L/D values, since the theory is for turbulent and the data are for mostly laminar flow.

DISCUSSION

Part II. Stability and Trim

This part of the discussion examines the aerodynamic stability and trim requirements and the related aerodynamic performance penalties of the present models. The effects on stability of variations in Mach number and in model geometry are shown in the figures in the form of longitudinal and directional aerodynamic center locations. The effects on aerodynamic performance of adding the model components and of achieving longitudinal trim and directional stability appear in the form of maximum lift-drag ratios. All aerodynamic centers were evaluated near maximum lift-drag ratio which occurred at angles of attack between 6° and 9° . Aerodynamic characteristics in each case are given both for the basic wing-body models with a vertical tail on the center line and for the complete models.

Longitudinal aerodynamic center.- The longitudinal aerodynamic centers shown in figure 7 for the models with nacelles and wing fins removed indicate that the most rearward locations occurred around $M = 1.1$, and the most forward locations resulted at or above $M = 4.8$. The forward placement of the aerodynamic centers for the blended model relative to those of the other two models is not particularly significant here, but rather is a consequence of the more aft location of the wing on this model and the use of percent mean aerodynamic chord rather than percent body length as the ordinate. For perspective, it may be noted that the 5-percent \bar{c} of the blended model and the 35-percent \bar{c} of the flat-bottomed model both correspond to 61 percent of the respective fuselage lengths. A significant point to observe in figure 7 is the large 35-percent \bar{c} travel of the aerodynamic center for the blended model, as indicated by the arrow at the right of the figure. The corresponding travel was 16-percent \bar{c} for the flat-bottomed model and 21-percent \bar{c} for the reference model. The large travel for the blended model is believed to result from the increased loadings on the forward strakes of the double delta wing and on the wider forebody at hypersonic Mach numbers.

Longitudinal aerodynamic centers - complete models.- The longitudinal aerodynamic centers for the complete models are shown in figure 8. The

~~CONFIDENTIAL~~

additions of the nacelles to the reference model and of the nacelles and wing fins to the flat-bottomed and blended models moved the longitudinal aerodynamic centers aft. The overall excursions of aerodynamic center over the Mach number range for the reference and flat-bottomed models differed by only a few percent \bar{c} from those shown in figure 7. Adding the nacelles and wing fins to the blended model, on the other hand, significantly reduced the overall excursion of aerodynamic center from the previous 35-percent \bar{c} (fig. 7) to 22-percent \bar{c} . This improvement resulted almost entirely from the shift in hypersonic aerodynamic center from -4-percent (fig. 7) to 10-percent \bar{c} for the complete model.

One approach for dealing with the aerodynamic center travel and the associated stability and control problems is fuel-distribution management, which shifts the aircraft center of gravity to maintain acceptable static margins throughout the speed range. Relying on this recourse through the acceleration phase, the present configurations would operate hypersonically with centers of gravity around 35-percent \bar{c} for the flat-bottomed vehicle and around 5-percent \bar{c} for the blended configuration.

Directional aerodynamic center.- Another significant problem during acceleration through the supersonic speed range is the deterioration in directional stability. The directional aerodynamic centers of the models with nacelles and wing fins off are shown in figure 9. The larger vertical tail of the reference model resulted in the directional aerodynamic centers being 20-percent \bar{c} aft of those of the flat-bottomed model with the smaller center line vertical tail. The differences in tail size, however, had little influence on the overall travel of the directional aerodynamic centers, which was in the vicinity of 60-percent \bar{c} for both models. A somewhat smaller travel of 47-percent \bar{c} resulted for the blended model. Because of the reductions in static directional stability at the highest Mach number, the hypersonic directional aerodynamic centers shown in figure 9 were generally forward of the longitudinal aerodynamic centers for the complete models (fig. 8).

Directional aerodynamic centers - complete models.- One of the objectives of the present study was to find means for maintaining hypersonic directional stability. One effort consisted of flaring the large vertical tail of the reference model by means of a cross section shape change from a diamond to a wedge. The total leading-edge wedge angle for both tails was 4.6° . The trailing edge of the wedge tail corresponded to a 4-foot thickness full scale. The results shown in figure 10 indicate that the directional aerodynamic center moved aft from 40 percent for the diamond tail to 50-percent \bar{c} for the wedge tail at 5.3 Mach number, but the aerodynamic centers for both tails shifted considerably forward as Mach number was increased to 7.4. Although not shown in figure 10, the directional stability of the reference model with either tail diminished seriously at angles of attack above 6° . Included on figure 10 are theoretical estimates of the hypersonic aerodynamic center locations derived from tangent-cone theory on the forebody, Prandtl-Meyer expansion on the afterbody, and shock expansion on the vertical tails. These inviscid theoretical estimates are in fair agreement with experiment but indicate less variation with Mach number. A possible explanation is that theory does not account for shielding of the tail by the body shock and boundary layers, thus overestimates tail effectiveness at the higher hypersonic Mach number.

~~CONFIDENTIAL~~

A more effective control over hypersonic directional stability is indicated by the results in figure 11 for the flat-bottomed and blended models with the small wing-mounted fins and with rudder flare angles up to 35° . The combined area of these fins was 15 percent of the wing reference area, but only 5.4 percent was flared as rudders. As indicated by the vertical spread of the symbols, rudder flare exercised an increasingly powerful control over directional stability and directional aerodynamic center location as hypersonic Mach number was increased. In addition, the directional stability and the rudder control effectiveness did not deteriorate as angle of attack was increased, because the flared rudders extended below the wings and remained in windward exposure with high local dynamic pressure.

Included on figure 11 are theoretical estimates of the incremental changes in aerodynamic center due to inviscid oblique-shock loadings on the flared rudder surfaces only. The inadequacy of inviscid theory in predicting the effects of increasing hypersonic Mach number results from its not accounting for the additional loading induced on the fin surfaces upstream of the rudder hinge lines, where local separated flows developed and spread chordwise. A theoretical basis is not yet available for estimating these added fin loadings and the locations of the lines of separation on the fin and of reattachment on the rudder; both lines were partially submerged in the wing boundary layers and interacted with them. The effects of rudder flare on a full-scale vehicle might differ from these model results because of the change in boundary-layer characteristics.

The results in figure 11 indicate that the models were directionally stable for the previously cited center-of-gravity locations (i.e., 35-percent \bar{c} for the flat-bottomed model with 25° rudder flare and of 5-percent \bar{c} for the blended model with 15° flare). Rudder flare was effective in offsetting the characteristic nonlinearity of the hypersonic lift curves of the vertical tails wherein reduced slopes prevail at small surface inclination angles. The stabilizer inclination angle, then, is as important at hypersonic speed as is surface area at lower speeds.

Maximum lift-drag ratio. - Flared rudders provided hypersonic directional stability, but the associated drag penalized aerodynamic performance. The maximum lift-drag ratios for the configuration buildup and for various degrees of stability and trim for the flat-bottomed and blended models are shown in figures 12 and 13, respectively. The upper curves show the maximum untrimmed lift-drag ratios for the wing-body models with a vertical tail only on the center line. The next curve down in each figure shows the maximum lift-drag ratios for the complete models, untrimmed, with controls neutral. The lowest curves (right triangles) on the left of figures 12 and 13 are the maximum lift-drag ratios for the models longitudinally trimmed and stable for Mach numbers into the supersonic range. The penalty in lift-drag ratio due to longitudinal trimming was directly related to the negative pitching-moment coefficient at zero lift which characterized the effectively cambered, flat-bottomed wings used on the present models. Longitudinal trimming at hypersonic speeds caused no significant penalty in lift-drag ratio, because the pitching moment at zero lift was near zero or positive there. Finally, the lowest curves on the right of each figure (diamonds) show the maximum hypersonic lift-drag ratios for completely stable, trimmed models utilizing rudder

~~CONFIDENTIAL~~

~~CONFIDENTIAL~~

flare to achieve directional stability, with centers of gravity at 35-percent \bar{c} for the flat-bottomed model and at 5-percent \bar{c} for the blended model. It is likely that the penalty in lift-drag ratio from flaring the rudders on the flat-bottomed model could be halved if the flared rudders were moved from the wing trailing edge to the sides of the aft-mounted nacelle-stabilizer, which would more than double the tail length and would allow a smaller rudder flare angle. The hypersonic maximum lift-drag ratios for both models, trimmed and stable, would be near 3.5.

CONCLUDING REMARKS

An analysis of the experimental aerodynamic characteristics for three models representative of hypersonic cruise aircraft and comparisons with theory have indicated the areas of validity and of inadequacy of various theoretical methods, the prominent stability and trim problems, and the factors affecting aerodynamic performance.

Lift and drag characteristics for the reference model were estimated from linear theories, tangent-cone and tangent-wedge approximations, and Newtonian theory, each combined with estimates of all-laminar and all-turbulent skin friction using the reference temperature method, and were compared with experimental results at supersonic and hypersonic Mach numbers up to 7.4. Lift and drag estimates from the linear method agreed well with experiment for supersonic Mach numbers up to 3. Lift characteristics estimated by the tangent-cone tangent-wedge approach and simple supersonic linear airfoil theory agreed well with experiment at supersonic and hypersonic Mach numbers. Newtonian theory underestimated both the lift and the drag. At Mach numbers above 3, all of the theories underestimated the drag and, therefore, overestimated the lift-drag ratios.

The overall travels of the longitudinal aerodynamic centers were about 11 percent of the wing mean aerodynamic chords, with the hypersonic locations being fairly close to those prevailing at subsonic speeds. Adequate directional stability and control at hypersonic speeds was demonstrated by the use of a pair of wing-mounted fins supporting flared rudders which extended above and below the wing plane. The rudders became increasingly effective in controlling directional stability and directional aerodynamic center location as hypersonic Mach number was increased. Theoretical predictions of stability and control characteristics require further refinement to account for viscous interaction effects which become predominant at the higher hypersonic Mach numbers. The hypersonic maximum lift-drag ratios were above 4.0 untrimmed, decreasing to about 3.5 for the trimmed and stable models that incorporated optimum rudder flare for directional stability.

~~CONFIDENTIAL~~

~~CONFIDENTIAL~~

REFERENCES

1. Gregory, Thomas J.; Petersen, Richard H.; and Wyss, John A.: Performance Trade-Offs and Research Problems for Hypersonic Transports. J. Aircraft, vol. 2, no. 4, 1965, pp. 266-271.
2. Harris, Roy V., Jr.: An Analysis and Correlation of Aircraft Wave Drag. NASA TM X-947, 1964.
3. Woodward, F. A.; and Larson, J. W.: Staff of the Aerodynamic Research Unit. A Method of Optimizing Camber Surfaces for Wing-Body Combinations at Supersonic Speeds. Part I. Theory and Application. DOC. D6-10741, Pt. I (prepared for NASA under contract No. NAS2-2282), The Boeing Co., 1965.
4. Ames Research Staff: Equations, Tables, and Charts for Compressible Flow. NACA Rep. 1135, 1953.
5. Eckert, E. R. G.: Survey on Heat Transfer at High Speeds. WADC TR 54-70, 1954.
6. Braslow, Albert L.; Hicks, Raymond M.; and Harris, Roy V., Jr.: Use of Grit-Type Boundary-Layer-Transition Trips on Wind-Tunnel Models. NASA TN D-3579, 1966.

~~CONFIDENTIAL~~

CONFIGURATIONS

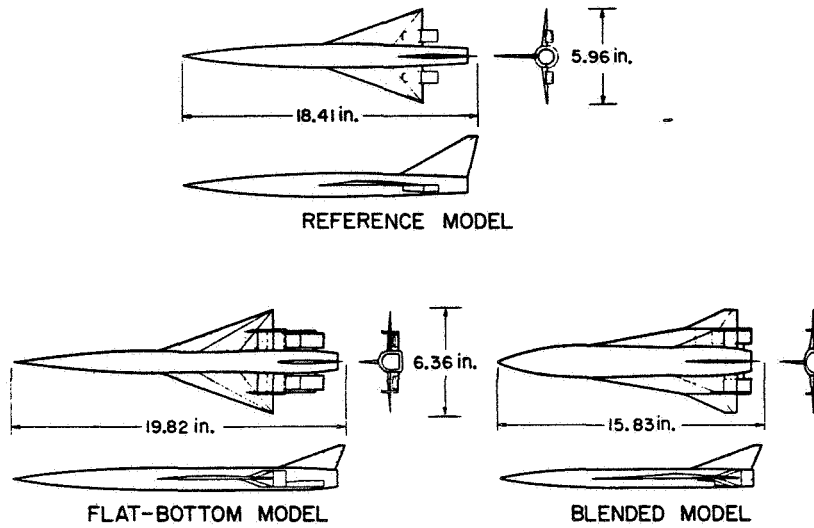


Figure 1

EXPERIMENTAL CHARACTERISTICS

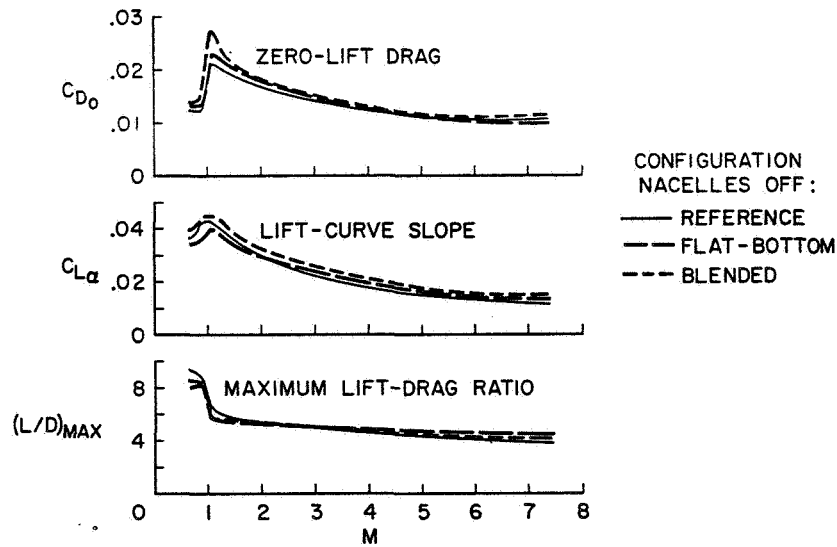


Figure 2

THEORETICAL PREDICTION TECHNIQUES

PRESSURE FORCES	+	SKIN FRICTION
① LINEARIZED METHOD	+	REFERENCE TEMPERATURE
② TANGENT CONE AND WEDGE	+	REFERENCE TEMPERATURE
③ NEWTONIAN	+	REFERENCE TEMPERATURE

Figure 3

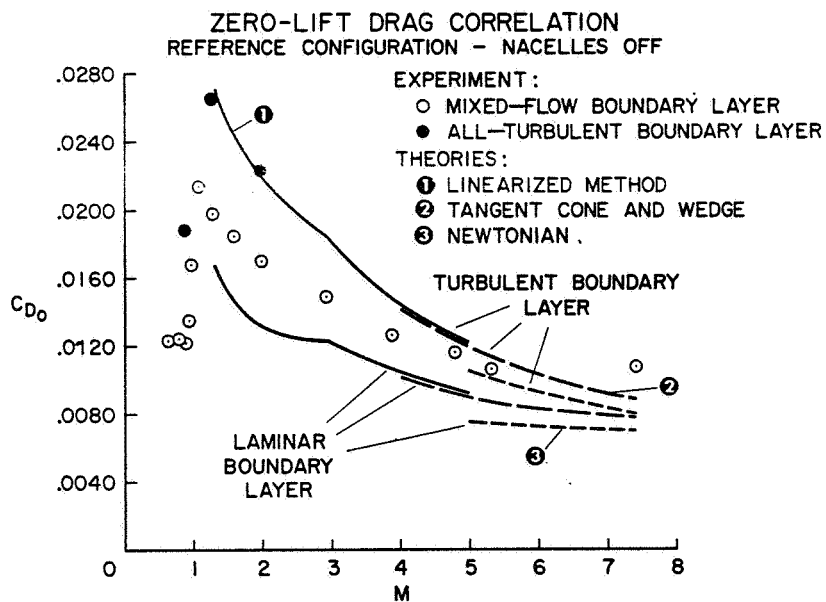


Figure 4

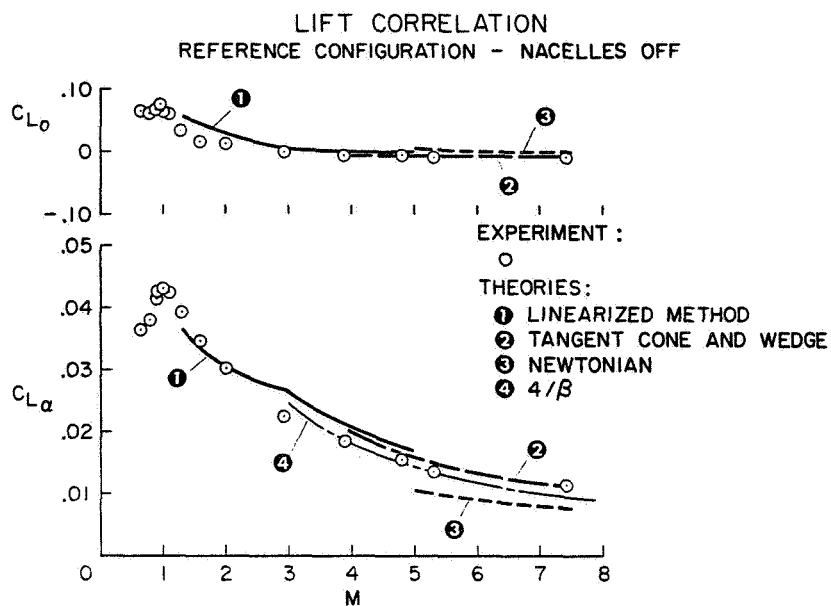


Figure 5

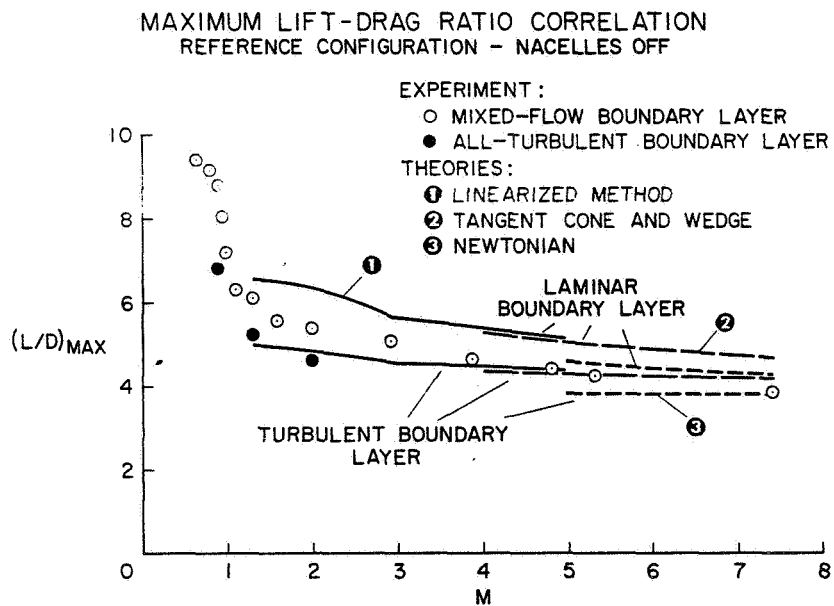


Figure 6

LONGITUDINAL AERODYNAMIC CENTER
NACELLES AND WING FINS OFF

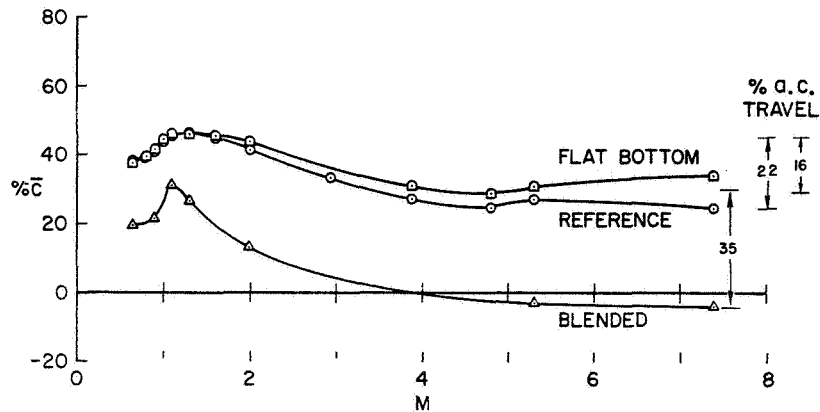


Figure 7

LONGITUDINAL AERODYNAMIC CENTER
COMPLETE MODELS

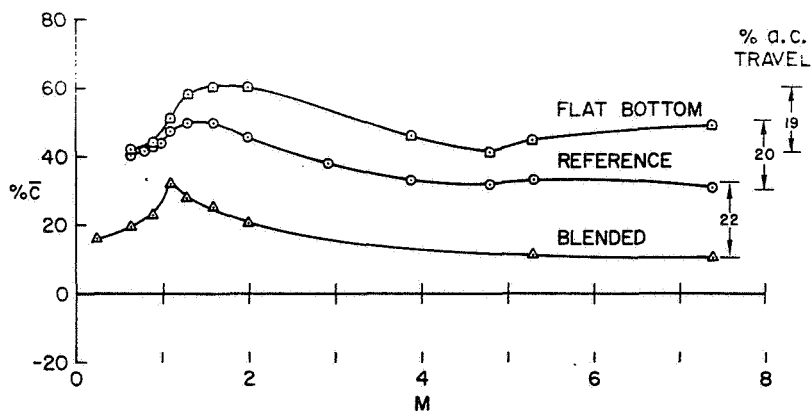


Figure 8

DIRECTIONAL AERODYNAMIC CENTER
NACELLES AND WING FINS OFF

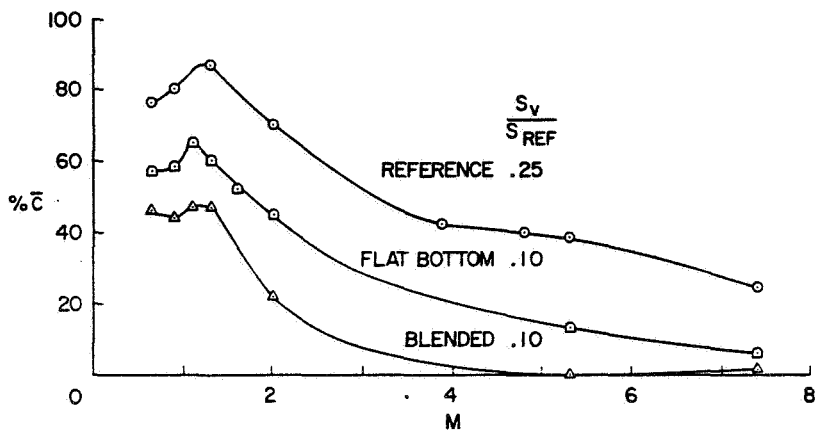


Figure 9

DIRECTIONAL AERODYNAMIC CENTER
REFERENCE MODEL

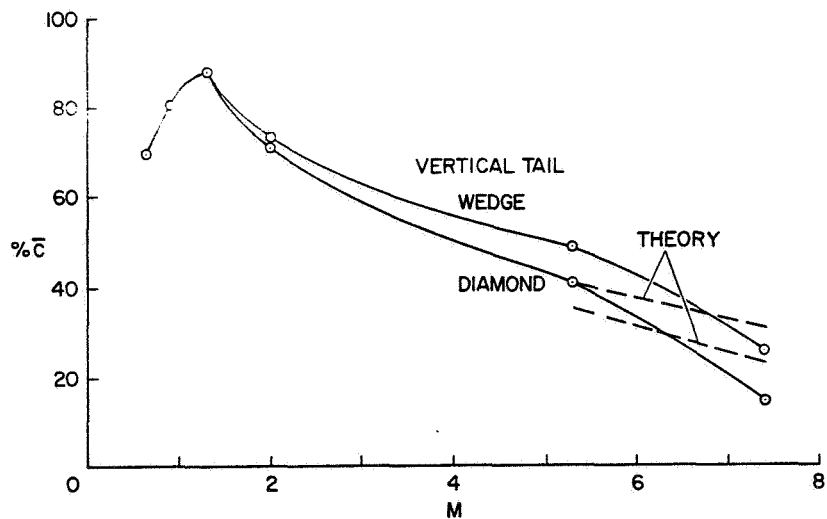


Figure 10

CONFIDENTIAL

DIRECTIONAL AERODYNAMIC CENTER
COMPLETE MODELS

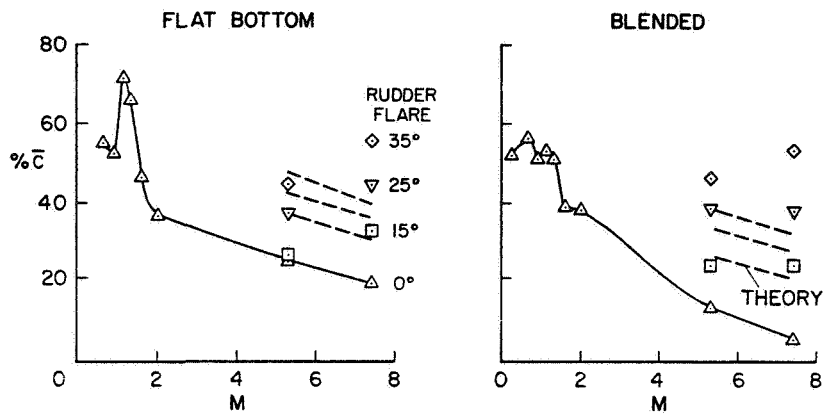


Figure 11

MAXIMUM LIFT-DRAG RATIO
FLAT-BOTTOM MODEL

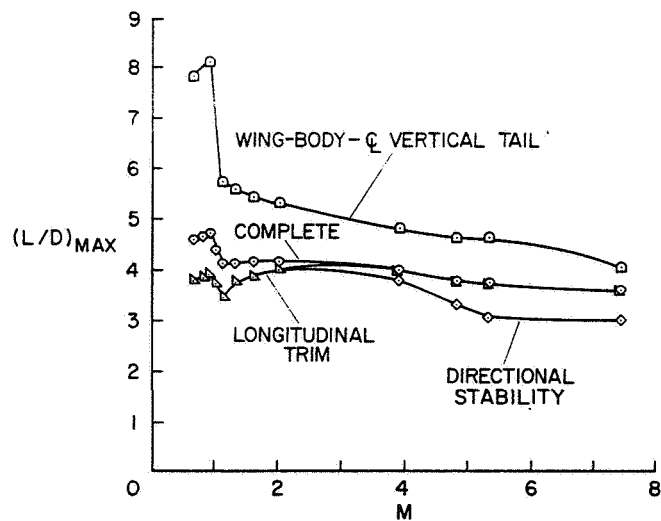


Figure 12

CONFIDENTIAL

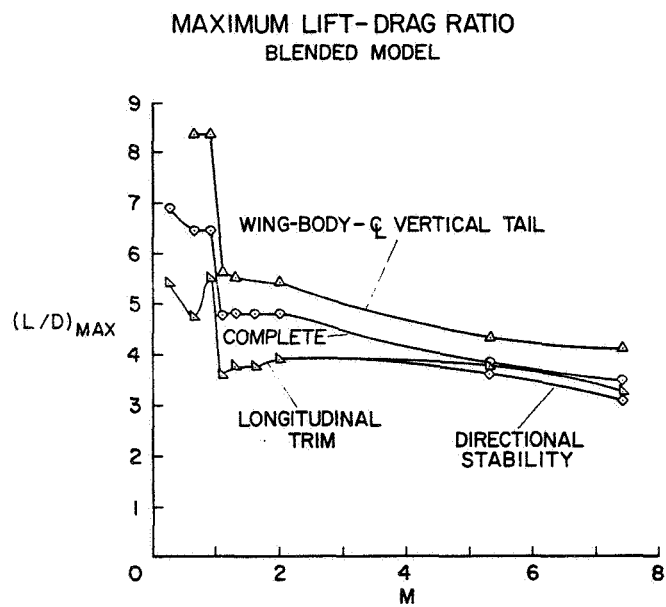


Figure 13

4. COMPARATIVE AERODYNAMIC STUDY OF
TWO HYPERSONIC CRUISE AIRCRAFT CONFIGURATIONS
DERIVED FROM TRADE-OFF STUDIES

By Jim A. Penland, Clyde L. W. Edwards, Robert D. Witcofski,
and Don C. Marcum, Jr.
Langley Research Center

SUMMARY

Analytic and experimental evaluations are made of two hypersonic cruise configurations designed to common ground rules. The ground rules were established to represent commercial-transport vehicles with a payload of 200 passengers, a range of 5000 nautical miles, and a cruise speed of Mach 6. Liquid hydrogen fuel was necessary to meet the range requirement. The two evolving configuration concepts were a delta-wing vehicle with a distinct body and wing having elevators for longitudinal control and a blended wing body with double delta planform and elevons for pitch control. Both configurations were tested at Mach numbers from 0.1 to 1.2 and at 6.0. Tests of modifications to the delta-wing configuration were also made at Mach 6.8.

Experimental and calculated results are presented for assessing longitudinal stability and control, directional stability, aerodynamic performance characteristics, and the effect of configuration modifications on maximum lift-drag ratio. The results of preliminary calculations are also included to show first-order effects of the nozzle exhaust on longitudinal trim.

INTRODUCTION

Until recently, aerodynamic investigations pertaining to hypersonic cruise vehicles have been limited to simple body-wing arrangements which did not account for the important interplay between structures, propulsion, and aerodynamics. Consequently, the aerodynamicist has been unable to compare different configuration concepts having the same mission capability because the design influences of structures and propulsion could not be accounted for in sufficient detail. Some insight into the large influences of structures and propulsion has recently been obtained from the Convair study discussed in reference 1.

The ground rules for this comparative configuration study are as follows:

Mission	Commercial transport
Payload, lb	50000 (200 passengers)
Range, n. mi.	5000
Cruise speed	Mach 6

Propulsion	Turboramjet
Fuel	Liquid hydrogen
Speed, knots:	
Take-off	160
Landing	135

The two comparable configuration concepts designed to these ground rules are shown in figure 1. One is a delta-wing vehicle with a distinct body and wing having elevators for longitudinal control. The other is a blended wing body with double delta planform and elevons for pitch control. For this aircraft, high lift devices could not be used and a lower wing loading was required to meet take-off requirements. The wing loadings shown in figure 1 are based on the area of the main delta wing including the body intercept. This area was taken to be the reference area for the aerodynamic coefficients presented herein. Both configurations were optimized through systematic variation of their primary design features, and the relatively blunt high-volume designs obtained represent the lightest weight vehicles for the commercial transport mission.

Reference 1 gave the striking result that the Mach 6 transport mission could be much more effectively accomplished by the blended wing body which had about two-thirds of the gross weight of the delta-wing configuration. Blending the wing and body apparently produced a significant saving in structural weight, which was the basic reason for the superiority of this arrangement. Note that this occurred even though the blended configuration had a much lower wing loading.

Because of the preliminary nature of the Convair study, the analyses were limited to simplified analytic techniques with no experimental verification. To assess the aerodynamics of these vehicles in a more detailed manner, analytic and experimental studies are in progress at the Langley Research Center. This report presents the latest results obtained from this investigation.

SYMBOLS

The longitudinal forces and moments are referenced to the stability-axis system, whereas the lateral forces and moments are referenced to the body-axis system.

b wing span, in.

\bar{c} mean aerodynamic chord of wing, in.

C_D drag coefficient, $\frac{\text{Drag}}{q_\infty S}$

C_L lift coefficient, $\frac{\text{Lift}}{q_\infty S}$

C_m	pitching-moment coefficient, $\frac{\text{Pitching moment}}{q_\infty S \bar{c}}$
C_{m_0}	pitching-moment coefficient at zero lift
C_n	yawing-moment coefficient, $\frac{\text{Yawing moment}}{q_\infty S b}$
$C_{n\beta}$	directional-stability parameter at $\beta = 0^\circ$, $\frac{\partial \bar{C}_n}{\partial \beta}$, per deg
F.R.	fineness ratio
l	fuselage length, in.
L/D	lift-drag ratio
$(L/D)_{\max}$	maximum lift-drag ratio
M_∞	free-stream Mach number
q_∞	free-stream dynamic pressure, psi
R_l	Reynolds number, based on fuselage length
S	planform area of basic delta wing, in ²
x_{cg}	distance from leading edge of \bar{c} to center of gravity, in.
α	angle of attack, deg
β	angle of sideslip, deg
δ_r	horizontal-tail or elevon deflection angle (positive when trailing edge is deflected down, deg)

WIND-TUNNEL TEST PROGRAM

The scope of the experimental program is shown in figure 2. The two basic aircraft configurations were tested through the Mach number range from subsonic through transonic speeds to a hypersonic Mach number of 6.0. The Reynolds number based on body length varied from 2.2×10^6 at subsonic speed to 13.4×10^6 at $M_\infty = 6.0$. In addition, tests of several modifications to the basic delta-wing aircraft were made at $M_\infty = 6.8$. The Mach 6 tests were made in the Langley 20-inch Mach 6 tunnel at the highest operating pressure and the 18-inch-long model is the maximum length model that can be tested at present in this facility. The resulting test Reynolds number (13.4×10^6) is

~~CONFIDENTIAL~~

representative of the Reynolds number available from larger facilities throughout the country at this time. This Reynolds number, however, is considerably below full-scale condition where the Reynolds number approaches 200×10^6 .

The aft end of each model was altered to the extent shown to accept the sting-mounted force balances. The inlets on all test models had their outer shape designed to duplicate the external nacelle drag. Constant-area internal ducts passed the design engine air, and corrections for the internal drag were made by skin-friction calculations. Model base pressures were measured, and the drag components were corrected to a pressure coefficient of $-\frac{1}{M_\infty^2}$.

LONGITUDINAL STABILITY

In figure 3 the pitching-moment coefficient for the blended wing body is shown as a function of lift coefficient for two control deflections at $M_\infty = 0.1, 1.2$, and 6.0 . Notice that the design center-of-gravity (c.g.) positions vary with Mach number. Management of the large fuel supply distributed along the body of these vehicles makes these c.g. adjustments possible. Throughout this report, these c.g. positions are used for presentation of data for the respective configurations and Mach numbers.

At hypersonic speed the configuration is stable and the control effectiveness is predictable. The hypersonic theories used consisted of tangent-cone theory in compression regions on that portion of the configuration inboard of the elevons which includes the forward strake-like wings and Prandtl-Meyer coefficients in expansion regions. Shock-expansion theory was used on the outboard wing sections and control surfaces. These theories were applied by using a modification of the computerized method of reference 2.

The blended-wing-body configuration is also stable at $M_\infty = 1.2$ but becomes unstable at $M_\infty = 0.1$. The c.g. at this low Mach number is determined by the full fuel load and cannot be adjusted by fuel management. Design changes, therefore, would be required to improve this low speed stability.

The characteristics of these off-design speeds are again predictable. The theories used consisted of a modification of the Multhopp lifting-surface theory (ref. 3) at subsonic speeds and Campbell's method (ref. 4) for determining the wing downwash field and the local dynamic pressure. At $M_\infty = 1.2$ linearized supersonic theory was applied by numerical methods (ref. 5). Use was made of references 6 and 7 in determining effects of the wing-body combination and the body alone.

The longitudinal stability for the delta-wing configuration is shown in figure 4. At hypersonic speed the configuration is stable and the horizontal tail is effective but the pitching-moment predictions are grossly in error. The method used to obtain these theoretical results was similar to that discussed previously, and the wing interference effects on the tail pitching-moment inputs were taken into account by the method described in reference 8,

which assumes a two-dimensional wing flow field. Improved predictions will require a more realistic description of this wing flow field and also the perturbing effects of the large fuselage.

At $M_\infty = 1.2$ the delta-wing configuration is stable at low lift coefficients where it would be expected to operate. The prediction based on linearized supersonic theory, however, is unrealistic; this might be expected since the large body departs considerably from slender body assumptions on which this theory is based. At $M_\infty = 0.1$, this configuration is also unstable and the behavior is significantly underestimated by theory. To investigate this subsonic instability in more detail, component breakdown tests were performed. These results are shown in figure 5.

Component Effects

The pitching-moment variations with angle of attack are shown for the body with and without the horizontal tail and for the complete configuration with and without the tail (fig. 5). The results for the body tests indicate a large tail effectiveness. The addition of the wing to the body and body-tail configurations, however, indicates that because of wing flow-field effects, the tail is not only less effective but actually produces a positive tail pitching-moment increment. These results imply the existence of an abnormally large wing downwash field. In an effort to determine whether a more favorable tail location would improve the tail effectiveness, additional tests were performed and these results are presented in figure 6. Pitching-moment data are shown for the tail off and various tail positions. None of the tail positions provide satisfactory stability characteristics. Of importance are the results shown for the T-tail configuration. At low angles of attack where the elevator is located above and out of the wing downwash field, the delta-wing aircraft exhibits a small region of longitudinal stability. Although the Reynolds number for these tests is low compared with the flight value, because of the sharp wing leading edges it is not anticipated that Reynolds number would have major effects on these characteristics. It is clear that these low speed aerodynamic characteristics require further study.

The power-off longitudinal results having been discussed, the additional complexities imposed by thrust and underexpanded nozzle exhaust effects are now considered. The simple engine nacelles used on these models preclude at this time any experimental determination of these effects. However, preliminary analyses at hypersonic speeds have been performed on the exhaust effects and possible benefits on $(L/D)_{\max}$ are shown in reference 9.

Thrust and Jet-Exhaust Effects

Some insight into the power-on trim problems at hypersonic speeds is provided in figure 7. The low mounting position of the engines can produce a sizable positive pitching-moment increment due to the thrust vector, which would require a positive control deflection to trim. The nozzle exhaust can have an additional effect of producing a lifting force on the aft end of the

~~CONFIDENTIAL~~

airplane which gives a negative C_m . The delta-wing configuration, however, does not develop appreciable lift due to the trailing-edge location of the engine exit and to the small body area affected and, thus, little or no counter effects to the thrust moment are produced by the nozzle exhaust.

For the blended wing body, the engine exit is forward of the wing trailing edge. The underexpanded nozzle exhaust, therefore, affects a significant portion of the wing area and first-order calculations indicate that the moment produced by the additional lift is sufficient to balance out the thrust moment. Although this result is based on an overly simplified analysis and requires experimental verification, it does indicate that by proper design the adverse thrust moment can be neutralized. Any L/D benefits, therefore, may be obtained with little or no trim penalty.

DIRECTIONAL STABILITY

Of equal importance to longitudinal trim are the directional stability characteristics which are considered in figure 8 where the directional stability derivative $C_{n\beta}$ is shown for three Mach numbers. At low and transonic speeds the blended wing body exhibits good directional stability characteristics through the angle-of-attack range. This stable variation with angle of attack is typical for double-delta-planform configurations having strake-like forward delta wings (ref. 10). At hypersonic speeds, however, the configuration becomes unstable at angles of attack above about 5° .

At low speeds the delta-wing aircraft shows a rapid decay of directional stability with angle of attack and is unstable at the landing attitude of about 15° . This directional instability is due to the large fuselage and to wing vortex flow. At transonic speeds the configuration is stable; however, at hypersonic speeds the vertical tail is obviously too small since the model is only marginally stable at zero angle of attack and is unstable at all higher angles of attack.

This decay in directional stability at hypersonic speeds for both configurations results from the decreasing local dynamic pressure which causes the vertical tail to become ineffective. By taking the local-dynamic-pressure decrease into account, body flow-field analysis shows this angle-of-attack effect to be predictable; however, the theory is still unsatisfactory since it predicts instability at all angles of attack.

Theoretical results are also shown for the other speeds near zero angle of attack. Although the theory predicts stable values of $C_{n\beta}$, the predictions are not in good agreement with the experimental values.

HYPERSONIC PERFORMANCE CHARACTERISTICS

The performance characteristics at the cruise Mach number are of prime importance in the study of these hypersonic aircraft. The variation of lift-drag ratio, lift coefficient, and drag coefficient with angle of attack for both configurations is presented in figure 9. The blended wing body shows a higher $(L/D)_{\max}$ than the delta-wing configuration even though some loss occurred due to trim. The negative C_{m_0} produced by the forward fuselage and the relatively short control-surface moment arm resulted in relatively large control deflections which are responsible for this loss. Negative camber in the forward portion of the configuration would tend to decrease this trim penalty. The delta-wing configuration, however, had negative camber in the forward fuselage and, consequently, suffered no trim penalty.

The theory underestimated $(L/D)_{\max}$ for the blended configuration more than for the delta-wing design primarily because of underestimation of the lift. The lift-curve slope for both configurations, however, is underpredicted. As mentioned previously, tangent-cone theory was used on the body and shock-expansion theory on the outboard wing sections. One of the problems in applying these methods to complex shapes involves the proper selection of the portion of the configuration represented by body flows and the portion represented by wing flows. The arbitrarily assumed extent of wing and body flows for these complex shapes, therefore, is one reason for these unrealistic lift predictions. Furthermore, wing-body interference effects, which were neglected in the theory, are another reason. Improved predictions can result only after detailed local investigations have been made to better define the appropriate region over which these basic theories can be applied and determine the significance of component interference effects.

The theory for the drag coefficients included turbulent-skin-friction calculations (ref. 11). However, heat-transfer measurements using phase-change-paint techniques showed that the boundary layer was largely transitional. The agreement of theory with experiment, therefore, is not as good as implied by figure 9. At the present time no satisfactory method exists for predicting the skin friction with these transitional flows. Consequently, evaluation of the adequacy of the pressure drag or drag due to lift predictions from these tests is not possible.

EFFECTS OF CONFIGURATION MODIFICATIONS ON $(L/D)_{\max}$

Since these configurations are only an early stage of hypersonic-cruise-vehicle development, many additional configurations will require investigation. It is of interest, therefore, to determine the ability to predict changes in configuration aerodynamics as affected by component modifications such as body fineness ratio and cross-sectional shape. Accordingly, simple body modifications were made to the delta-wing configuration and tests were made at $M_\infty = 6.8$. Results of these tests are given in figure 10(a).

A comparison of the basic delta-wing configuration having a body fineness ratio of 13 with one having a fineness ratio of 16 indicates that the predicted increase in $(L/D)_{\max}$ was obtained. Changing the body cross-sectional shape to increase its lifting surface, however, gave a greater increase in $(L/D)_{\max}$ than expected from examination of the theoretical trends.

Both of these modifications improved the directional stability over that of the basic configuration. However, the increased forward planform area of the body cross-sectional change decreased the longitudinal stability and this particular configuration could not be trimmed at the design c.g.

As already shown in figure 9, the blended wing body has a substantially higher $(L/D)_{\max}$ than the delta-wing configuration. To determine how much of this improvement results from the relatively larger wing planform, the delta-wing configuration was modified as shown in figure 10(b). The basic delta-wing configuration is shown on the left for reference. The wing was modified to have the same planform as the blended wing body including the elimination of the horizontal tails. In addition, the forward part of the wing was given incidence to offset the trim penalty in $(L/D)_{\max}$ shown for the blended wing body.

The double delta results indicate an improvement in $(L/D)_{\max}$ over that of the basic delta configuration with no trim penalty. When compared with the trimmed values for the blended wing body, this improved $(L/D)_{\max}$ is largely due to the larger wing area; however, some secondary benefits appear to result from the wing-body blending. These benefits could result from the relief of interference effects of the body on the lee side of the wing. Theory overpredicts the $(L/D)_{\max}$ for this double-delta-configuration modification, in part because of neglect of these component interference effects.

PARAMETERS AFFECTING FLIGHT EXTRAPOLATIONS OF $(L/D)_{\max}$

Although considerable insight into the comparative aerodynamics of these hypersonic cruise configurations has been provided by the wind-tunnel studies, extrapolation of the hypersonic characteristics, especially $(L/D)_{\max}$, to full-scale flight conditions remains a major problem. Flight Reynolds numbers, based on vehicle length, will be in the range of 200×10^6 and a turbulent boundary layer will cover all except a few feet of the vehicle near the wing leading edge and the body apex. The parameters affecting flight extrapolations of $(L/D)_{\max}$ are as follows:

Pressure drag, $C_{D,p}$
Drag due to lift, $C_{D,L}$
Control effectiveness, ΔC_m , ΔC_L , ΔC_D
Friction drag, $C_{D,F}$

These parameters should be determined in tests of models over which the boundary layer is predominately turbulent.

The basic goal of wind-tunnel tests of complete configurations, of course, is to determine precisely the value of the first three parameters by subtracting the calculated wind-tunnel friction drag from the total measured drag. Full-scale $(L/D)_{\max}$ extrapolations are then obtained by adding back the turbulent-skin-friction drag calculated for high Reynolds number flight conditions. This approach, however, is not reliable at hypersonic speeds because limited Reynolds number capability of available facilities allows model boundary layers which are largely transitional with very little fully developed turbulent flow. Because of these transitional flows the wind-tunnel friction drag is all but impossible to calculate accurately and important turbulent flow effects which may exist on the other parameters are presently unknown.

Large regions of transitional flow, of course, are not unique to hypersonic testing. At lower speeds, more precise values of these parameters can be obtained because large regions of turbulent flow can be artificially produced by small boundary-layer trips which require only small corrections. The trips required at hypersonic speeds, however, become very large; for example, the boundary-layer trips on an SST model scaled to a full-size vehicle are about the size of golf balls, whereas those required on a hypersonic cruise vehicle would scale to the size of volley balls. It is now too early to say whether these larger trips can be used to advantage in complete configuration testing since corrections for the trip drag and other possible extraneous effects produced by the trips are unknown. A more detailed discussion of these hypersonic trips is given in reference 12. It is clear that this area of flight extrapolation will require much additional study, and facilities capable of higher Reynolds numbers will be an essential ingredient in these studies. Several of the Langley facilities are now being modified to provide this capability.

In spite of the fact that the full-scale $(L/D)_{\max}$ cannot yet be determined with the desired precision, it can be surmised from the magnitude of the wind-tunnel results presented herein that the desired flight values of $(L/D)_{\max}$ approaching 5 can probably be achieved at $M_{\infty} = 6.0$ for these high-volume hypersonic cruise configurations.

CONCLUDING REMARKS

The investigation of these preliminary hypersonic cruise configurations indicates significant problems in low speed longitudinal stability and in directional stability at both landing and hypersonic speeds. Of the two configurations investigated, the blended-wing-body concept showed clear aerodynamic advantages in both of these areas over the distinct wing-body concept. Furthermore, the blended wing body primarily because of its large wing planform area confirmed the expected additional advantage in the hypersonic maximum lift-drag ratio. These important aerodynamic advantages of the blended configuration in combination with the structural weight advantage indicated in the preliminary studies suggest that this concept is a promising approach which merits further research and refinement.

~~CONFIDENTIAL~~

Because of limitations in both the present theoretical and experimental techniques, the aerodynamic characteristics of these complete hypersonic configurations cannot be determined with the same degree of precision and confidence enjoyed at lower supersonic speeds. One reason for this lies in the important component interference effects which exist on hypersonic aircraft and which are not adequately accounted for by present theoretical predictions. Wind-tunnel results are also subject to doubt due to the presence of laminar and transitional boundary-layer flows or, alternatively, due to the large flow disturbances of tripping devices.

~~CONFIDENTIAL~~

~~CONFIDENTIAL~~

REFERENCES

1. Drake, Hubert M.; Gregory, Thomas J.; and Petersen, Richard H.: Hypersonic Technology Problems Identified in Mission Studies. Conference on Hypersonic Aircraft Technology, NASA SP-148, 1967. (Paper No. 1 herein.)
2. Gellert, George O.: Geometric Computing - Electronic Geometry for Semi-automated Design. Machine Design, vol. 37.
Part 1: The Method and Its Application, no. 7, Mar. 18, 1965, pp. 152-159.
Part 2: Fields of Application, no. 8, Apr. 1, 1965, pp. 94-100.
3. Multhopp, H.: Methods for Calculating the Lift Distribution of Wings (Subsonic Lifting-Surface Theory). R. & M. No. 2884, Brit. A.R.C., Jan. 1950.
4. Campbell, George S.: A Finite-Step Method for the Calculation of Span Loadings of Unusual Plan Forms. NACA RM L50L13, 1951.
5. Middleton, Wilbur D.; and Carlson, Harry W.: A Numerical Method for Calculating the Flat-Plate Pressure Distributions on Supersonic Wings of Arbitrary Planform. NASA TN D-2570, 1965.
6. Pitts, William C.; Nielsen, Jack N.; and Kaattari, George E.: Lift and Center of Pressure of Wing-Body-Tail Combinations at Subsonic, Transonic, and Supersonic Speeds. NACA Rept. 1307, 1957.
7. Allen, H. Julian; and Perkins, Edward W.: A Study of Effects of Viscosity on Flow Over Slender Inclined Bodies of Revolution. NACA Rept. 1048, 1951. (Supersedes NACA TN 2044.)
8. Dugan, Duane W.: Estimation of Static Longitudinal Stability of Aircraft Configurations at High Mach Numbers and at Angles of Attack Between 0° and $\pm 180^\circ$. NASA MEMO 1-17-59A, 1959.
9. Kirkham, Frank S.; Cabbage, James M., Jr.; Vahl, Walter A.; and Small, William J.: Studies of Airframe-Propulsion-System Integration for Mach 6 Cruise Vehicles. Conference on Hypersonic Aircraft Technology, NASA SP-148, 1967. (Paper No. 9 herein.)
10. Polhamus, Edward C.; and Spreeman, Kenneth P.: Effect at High Subsonic Speeds of Fuselage Forebody Strakes on the Static Stability and Vertical-Tail-Load Characteristics of a Complete Model Having a Delta Wing. NASA TN D-903, 1961. (Supersedes NACA RM L57K15a.)
11. Spalding, D. B.; and Chi, S. W.: The Drag of a Compressible Turbulent Boundary Layer on a Smooth Flat Plate With and Without Heat Transfer. J. Fluid Mech., vol. 18, pt. 1, Jan. 1964, pp. 117-143.

~~CONFIDENTIAL~~

~~CONFIDENTIAL~~

12. Sterrett, James R.; Morrisette, E. Leon; Whitehead, Allen H., Jr.; and Hicks, Raymond M.: Transition Fixing for Hypersonic Flow. Conference on Hypersonic Aircraft Technology, NASA SP-148, 1967. (Paper No. 15 herein.)

~~CONFIDENTIAL~~

~~CONFIDENTIAL~~

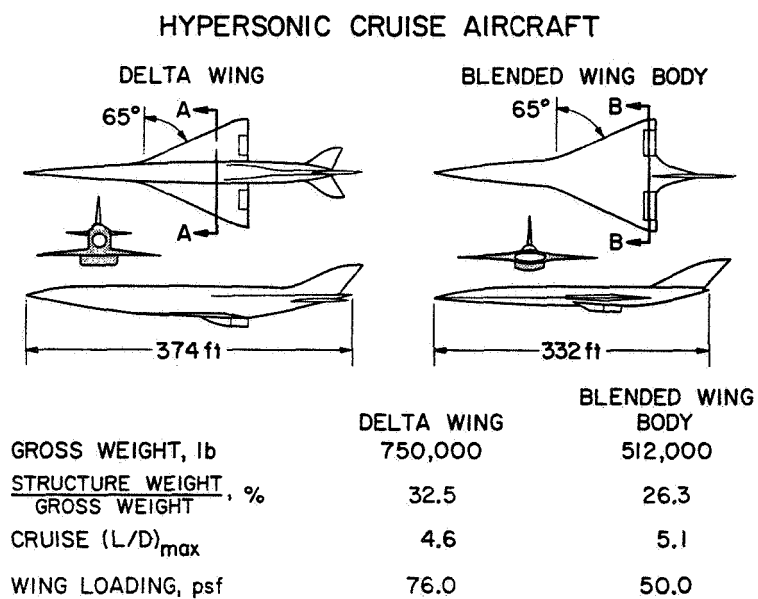


Figure 1

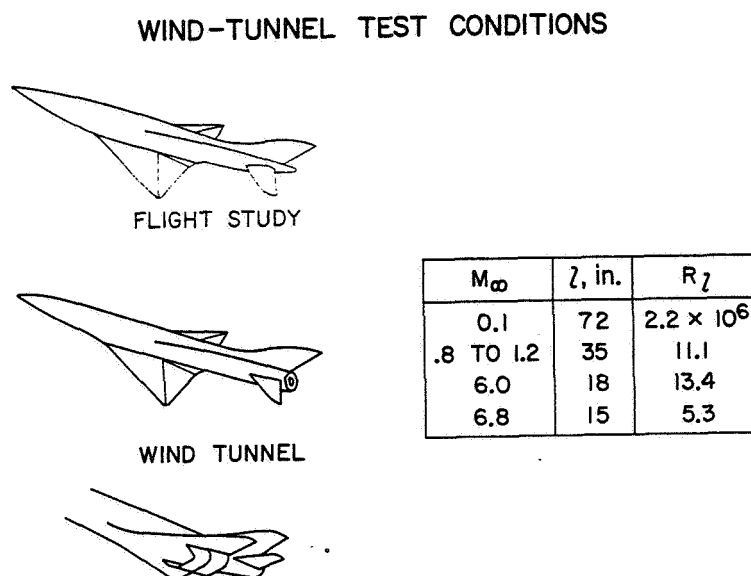


Figure 2

~~CONFIDENTIAL~~

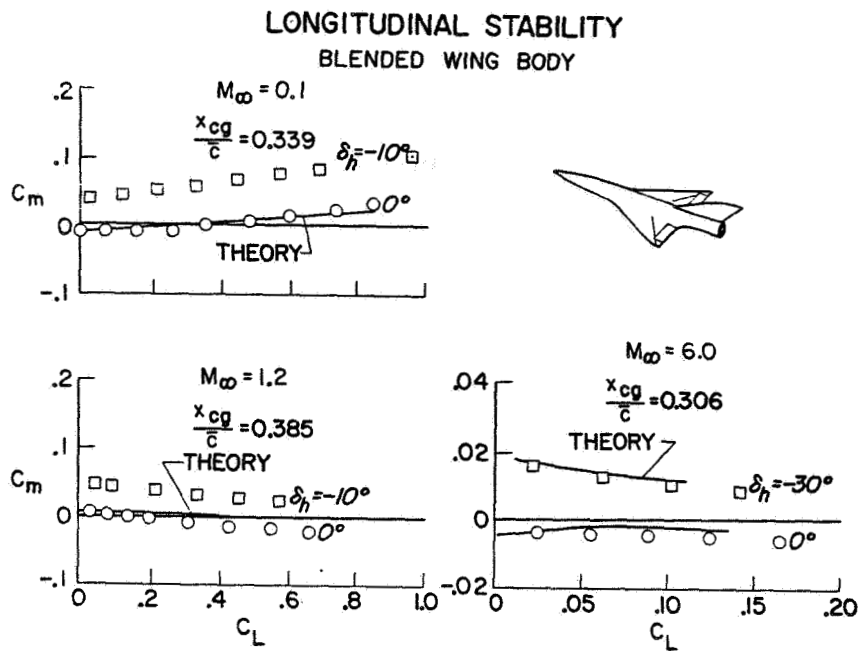


Figure 3

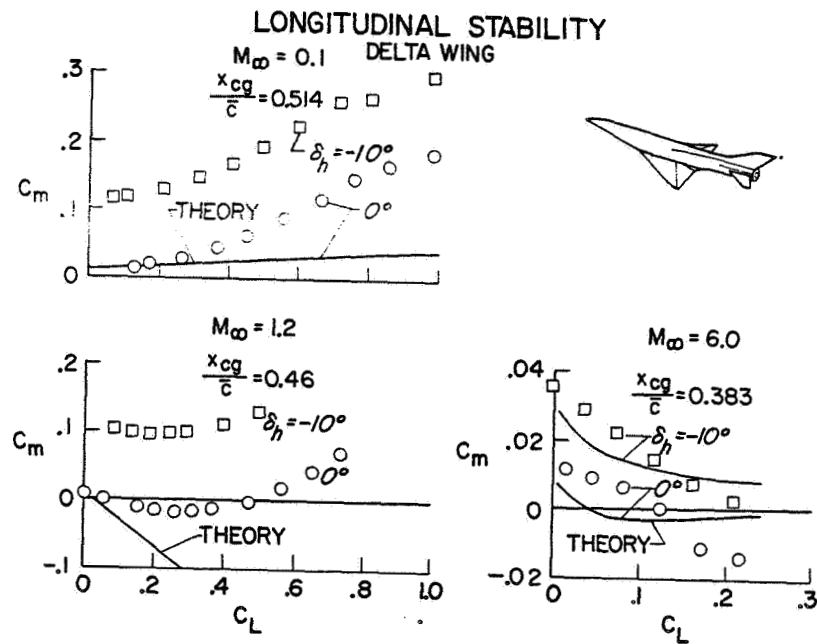


Figure 4

COMPONENT EFFECTS ON LONGITUDINAL STABILITY

$M_\infty = 0.1$; $R_L = 2.2 \times 10^6$; $\delta_h = 0^\circ$

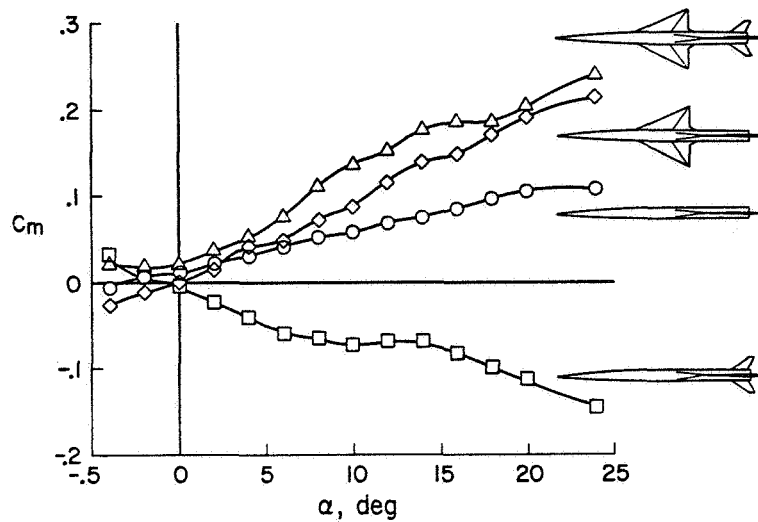


Figure 5

DELTA-WING LONGITUDINAL STABILITY EFFECT OF HORIZONTAL-TAIL LOCATION; $\delta_h = 0^\circ$; $M_\infty = 0.1$; $R_L = 2.2 \times 10^6$

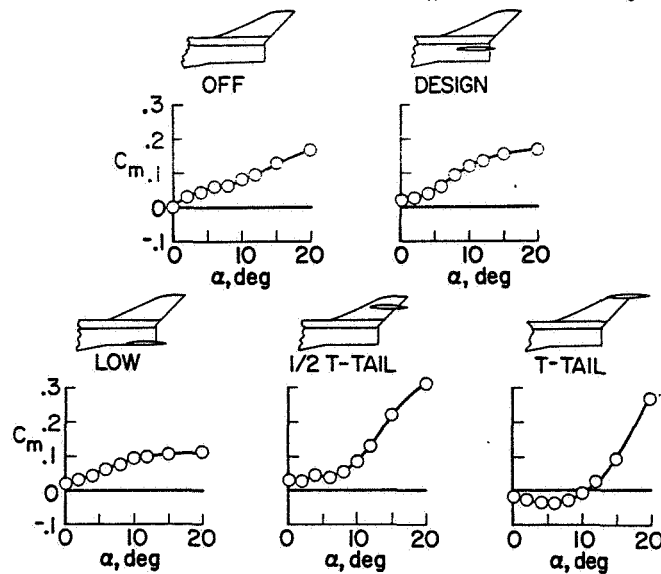


Figure 6

~~CONFIDENTIAL~~

THRUST AND JET-EXHAUST EFFECTS

$M_\infty = 6.0$

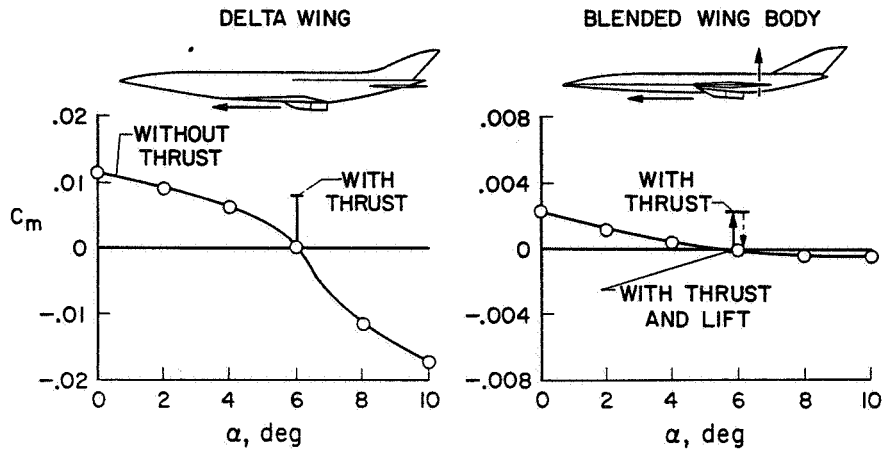


Figure 7

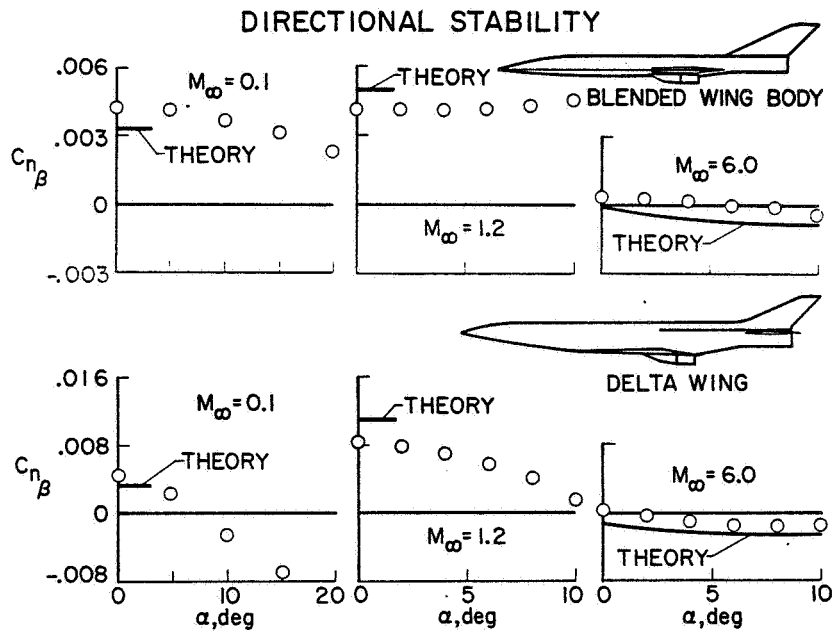
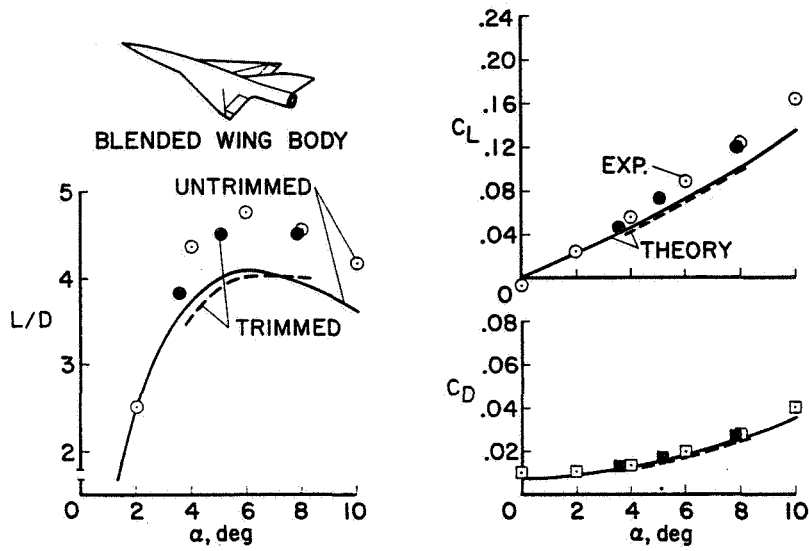


Figure 8

~~CONFIDENTIAL~~

HYPERSONIC PERFORMANCE CHARACTERISTICS

$M_\infty = 6.0$; $R_L = 13.3 \times 10^6$



$M_\infty = 6.0$; $R_L = 13.4 \times 10^6$

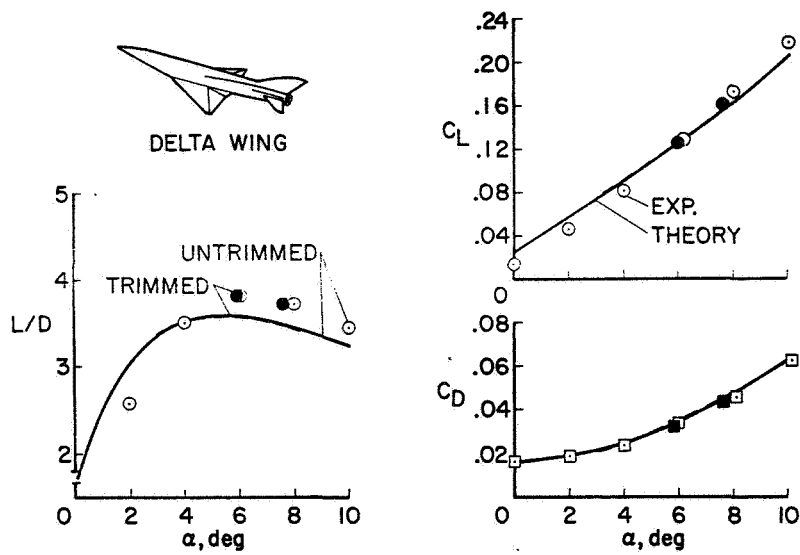
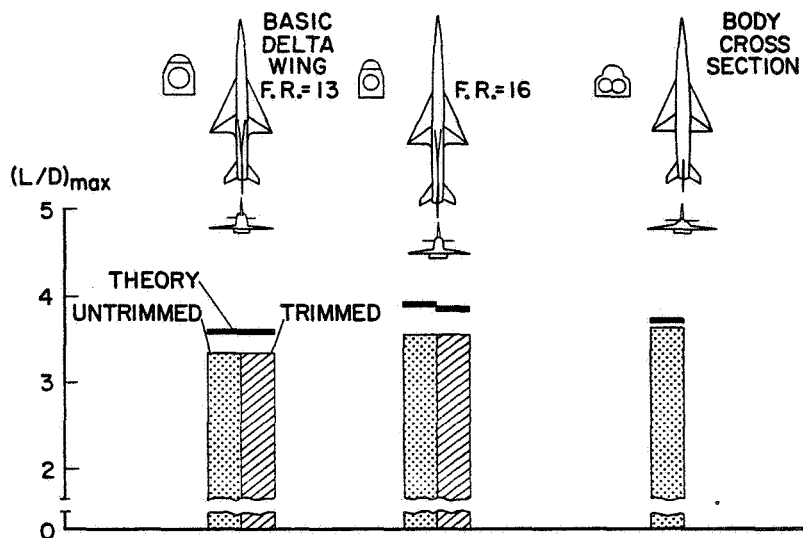


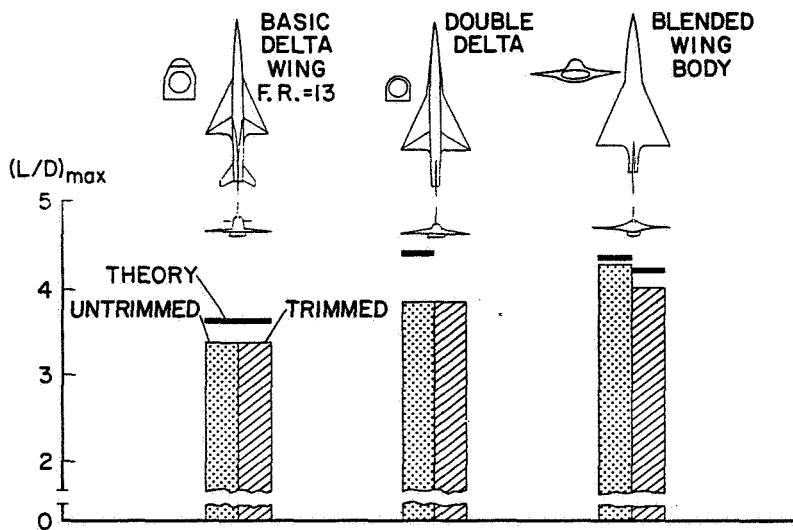
Figure 9

~~CONFIDENTIAL~~

CONFIGURATION MODIFICATION EFFECTS ON $(L/D)_{\max}$ $M_w=6.8; R_L=5 \times 10^6$



(a)

 $M_w=6.8; R_L=5 \times 10^6$


(b)

Figure 10

~~CONFIDENTIAL~~

5. EXPERIMENTAL AERODYNAMICS AND ANALYSIS OF THE STAGE

SEPARATION OF REUSABLE LAUNCH VEHICLES

By John P. Decker
Langley Research Center

SUMMARY

Preliminary studies have been made of the stage separation of parallel-staged reusable launch vehicles. Effects of vertical spacing, incidence angle, configuration, and Mach number on the longitudinal stability of two airplane-type vehicles in close proximity are discussed. The aerodynamic data obtained for the two vehicles in proximity were used as input to a two-body trajectory-simulation computer program to evaluate the potential effects on the vehicle behavior of the aerodynamic interference. The results indicate that an evaluation of the potential of any given vehicle system will require appreciable aerodynamic data and critical trajectory analysis to determine the constraints under which safe separation may be achieved.

INTRODUCTION

During the past several years a number of feasibility studies have been made to investigate the recovery and reuse of launch vehicles. The spectrum of concepts has varied from reusable ballistic to reusable airbreathing winged vehicles. This paper will be restricted to a discussion of winged vehicle systems for which parallel staging will be required.

Figure 1 shows an airplane type of launch vehicle as the two stages separate during the early phase of a staging maneuver. The types of interference that can be anticipated if staging is required within the sensible atmosphere and at supersonic or hypersonic speeds are illustrated in the schlieren photograph shown as figure 2. These interferences are potential stability and control problems for both vehicle stages and consequently this paper has two primary objectives:

- (1) To discuss the effect that these interferences have on the stability characteristics of two airplane-type vehicles in close proximity and
- (2) To discuss the potential effects on the vehicle behavior of the aerodynamic interference as obtained by using a two-body trajectory-simulation computer program. The data presented should be considered only as illustrative of potential problems.

~~CONFIDENTIAL~~

~~CONFIDENTIAL~~

SYMBOLS

C_m	pitching-moment coefficient
$C_{m\dot{\alpha}}$	pitching moment due to rate of change of angle of attack
C_{mq}	pitching moment due to pitch rate
C_Z	normal-force coefficient
$C_{Z\dot{\alpha}}$	normal-force coefficient due to rate of change of angle of attack
C_{Zq}	normal-force coefficient due to pitch rate
i	relative incidence angle between first and second stage or upper stages
l	length of first stage
M_∞	free-stream Mach number
q	pitch rate
Δx	longitudinal spacing between centers of gravity of first and second stage
Δz	vertical spacing between centers of gravity of first and second stage
α	angle of attack
$\dot{\alpha}$	time rate of change of angle of attack
Subscripts:	
1	first stage
2	second stage or upper stages

STAGING CONDITIONS

A typical trajectory of altitude plotted as a function of Mach number is illustrated in figure 3, shown only out to a Mach number of 8, and indicates some of the conditions at which staging may be required. Typical reusable launch vehicles using airbreathing engines would probably separate at the lower altitudes and consequently the higher dynamic pressures; whereas rocket-powered vehicles would probably separate at the higher altitudes and lower dynamic pressures. Normal mission staging could occur, depending on the vehicle concept,

~~CONFIDENTIAL~~

anywhere above a Mach number of about 3; whereas abort staging could occur at any Mach number below mission staging. Abort separation for either rocket or airbreathing-type vehicles would likely occur at the higher dynamic pressures.

Potential problems that could occur at staging are indicated schematically in figure 4. The second stage, at release, would be at an initial spacing distance and attitude with respect to the first stage. A trapeze or similar mechanism could be employed to achieve the desired initial release conditions. The problem is not only to examine the divergence of the centers of gravity of the two stages but also to insure that the two vehicles do not collide as a result of subsequent vehicle rotation, for example in case the second stage rotates into the first stage as illustrated by the lower two sketches.

EXPERIMENTAL RESULTS

Wind-tunnel models for which experimental aerodynamic interference data have been obtained are shown in figure 5. The lower one is a three-stage-vehicle system consisting of three fully reusable stages which are essentially wing-body configurations. (See refs. 1 and 2.) The other vehicle is a two-stage launch-vehicle system which has a first stage similar to that of the three-stage vehicle but an integrated lifting body as the upper stage. Both these vehicle concepts are representative of rocket-powered vehicles. Airbreathing-type vehicles would probably have similar first stages but smaller upper stages.

Static longitudinal aerodynamic data were obtained for each stage with strain-gage balances mounted on separate stings. (See fig. 6.) Position variables Δz and Δx , as well as the relative incidence angle i , could be varied for a range of angle of attack and Mach number. These variables were systematically varied in the wind tunnel to obtain the aerodynamic data needed for the trajectory computations. A small portion of the experimental test results at a constant longitudinal relative position, that is, $\Delta x = \text{Constant}$, is used to illustrate the effect of vertical spacing Δz , incidence angle i , configuration, and Mach number on the longitudinal stability of the two vehicles during separation.

Figure 7 shows the effect of spacing for the two-stage launch-vehicle system for a Mach number of 3 and an incidence angle of 0° . Pitching-moment coefficients for the first ($C_{m,1}$) and second ($C_{m,2}$) stage have been plotted against angle of attack for various spacing distances (nondimensionalized with respect to the first-stage length l) from a value of 0.10 to 0.20. For reference, the interference-free curve or the pitching-moment curve at very large separation distance is shown for both the first and the second stage.

For the second-stage vehicle, the stability level changed and the magnitude of the pitching moment varied with spacing. For the first-stage vehicle, the stability did not change appreciably; however, there is a large positive increment in the magnitude of the pitching moment due to the interference. Also, for the maximum spacing tested, large interference is still present

~~CONFIDENTIAL~~

because the curve is not yet approaching the interference-free curve. From control effectiveness data, not shown here, there appears to be no aerodynamic control surface of reasonable dimensions which could overcome such large pitching-moment increments.

Figure 8 shows the same type of data at a hypersonic Mach number of 6 for the two-stage launch-vehicle system. Comparison of these data with the data in figure 7 indicates that there is a hypersonic Mach number effect. Data for other configurations have shown different Mach number effects and indicate that the results are strongly dependent on configuration. Because the results presented herein are only illustrative and since complete data at a Mach number of 6 are not available, the remaining discussion is principally concerned with the data at a Mach number of 3, which illustrate other important aerodynamic effects.

The effect of varying the incidence angle at a Mach number of 3 (fig. 7) for a selected nondimensional spacing of 0.13 for both the first and second stage is shown in figure 9. The solid curves in this figure are from figure 7 at zero incidence angle. For the second stage, increasing the incidence angle caused a large negative increment in the pitching-moment coefficient which would cause the second stage to tend to nose down. For the first stage, however, the exact opposite occurred, that is, increasing the incidence angle caused a large positive increment in the pitching moment which would tend to cause the first stage to nose up.

Examination of results at other supersonic and hypersonic Mach numbers along with schlieren data has led to two major conclusions as to the source of the behavior of the pitching-moment coefficients as compared with the interference-free values. These results are illustrated in figure 10. Test conditions correspond to a Mach number of 3, angle of attack and incidence angle of 0° , and an intermediate spacing. The first conclusion is that the effects on the first stage are caused by the impingement on the first stage of the principal disturbance generated by the second stage. Consequently, the changes in pitching moment, previously shown for the first stage, are proportional to the strength of this disturbance and the area affected. The second conclusion is that the effects on the second stage are caused by the flow field from the first stage to which must be added the effects of the first reflection of this principal disturbance.

The data presented so far have been for the two-stage launch vehicle with a lifting-body second stage. The effects of configuration are illustrated in figures 11 and 12, which compare the pitching-moment curves for only the upper-stage configurations of the two wind-tunnel models shown in figure 5. Figure 11 shows the data presented in figure 7 for the lifting-body second stage with the addition of one extra spacing curve; whereas figure 12 presents data for the complete wing-body upper stage of the other wind-tunnel configuration. The pitching-moment curves for these two vehicle shapes are markedly different. Also, for the complete wing-body upper-stage vehicle (fig. 12), not only is the stability during separation changing rapidly (that is, the curves are not parallel to each other) but also the magnitude of the pitching-moment coefficient is inconsistent (that is, the curves are not in sequential order).

~~CONFIDENTIAL~~

One final aerodynamic effect is illustrated in figure 13. Again, data are for only the complete wing-body upper-stage vehicle, and the pitching-moment coefficient is plotted against angle of attack for the same nondimensional spacings but at a subsonic Mach number ($M_\infty = 0.60$). The data in figure 12 are at a Mach number of 3 and the interferences are the result of shock-wave impingement; whereas the data in figure 13 are at a subsonic Mach number for which no shock waves would be anticipated. Separation at this low Mach number might arise in case of a low-speed abort situation. Not only are the curves very different from those at supersonic speeds, but the interference is so large that it is difficult even to discuss stability. The significance of these changes, which depend largely on the dynamic pressures at which separation is required, must be evaluated.

TRAJECTORY RESULTS

Wind-tunnel data of the type that has been illustrated can be used in a two-body trajectory-simulation computer program (recently developed at the Langley Research Center) for evaluating the effects of the interferences. The computer program integrates the longitudinal equations of motion for each of the vehicle stages and calculates their relative position and attitude.

The aerodynamic inputs into the program consist of the normal-force, axial-force, and pitching-moment coefficients for two vehicle stages at different relative positions and attitudes when they are in proximity to each other. The other important aerodynamic inputs consist of the dynamic derivatives, C_{m_q} , $C_{m_{\dot{\alpha}}}$, C_{Z_q} , and $C_{Z_{\dot{\alpha}}}$. These quantities were estimated for each vehicle and assumed constant since these derivatives are not presently available for two vehicles in proximity. However, the program allows investigation of their effects by varying the magnitude of these quantities.

The vehicle input data consist of the fixed quantities, the mass, and the pitch moment of inertia for each of the vehicle stages. The quantities characteristic of the trajectory that the launch vehicle is flying are also used as input and consist of the altitude, pitch velocity, flight-path angle, Mach number, and angle of attack. These quantities can also be varied. Other vehicle input data consist of the initial geometric quantities which give the initial position and attitude of the second stage with respect to the first stage, namely, i , Δz , and Δx . It is also possible to give the first or second stage a separation thrust, which can be varied from a longitudinal thrust to a vertical thrust.

Initial attempts to obtain safe separation trajectories by using this program for the three-stage launch vehicle system met with frequent failure because the vehicles actually collided. The calculations showed the stages rotating into each other in a time period as little as 0.30 second. Application of initial pitch velocities to the launch vehicle did not lessen the possibility of collision, although such techniques have often been successful in separating stores from aircraft. Some other possibilities were therefore examined. Some of the results from the computer program are used to illustrate the effect of

~~CONFIDENTIAL~~

~~CONFIDENTIAL~~

the dynamic derivatives, the initial attitude, and the dynamic pressure as they influence safe separation or collision. The vehicle employed for these calculations was the two-stage launch vehicle with the lifting-body second stage on which most of the experimental data presented was concentrated.

Figure 14 shows the effect of the dynamic derivatives for the two-stage vehicle system where C_{mq} , the pitching moment due to pitch rate for the second stage, is plotted against C_{mq} for the first stage. Indicated in this figure are the regions where the two vehicles collided, an approximate region where they safely separated, and a region of uncertainty as to whether the two vehicles would collide or separate. Also indicated in this figure are the best current estimates of the interference-free values of C_{mq} for both the first and second stage. These values for this particular vehicle concept are one or more orders of magnitude smaller than the values needed to achieve safe separation at these conditions. For the purpose of illustrating some of the other important variables that need to be considered to achieve safe separation, figure 15 shows the type of results that can be generated by selecting a value of C_{mq} which lies in the safe separation region for both the first and second stage (square symbol, fig. 14) and varying the incidence angle and angle of attack. Again, the regions of collision and the approximate regions of safe separation are shown.

The problem can now be further narrowed by taking a suitable safe separation value for both the incidence angle and angle of attack (circular symbol, fig. 15) and illustrating the effect of dynamic pressure, as shown in figure 16. The separation distance (or the distance between the centers of gravity of the two stages) in 2 seconds after release has been plotted against dynamic pressure. Two curves are presented; one is for the condition in which no thrust was used in the calculations and the other is for the condition in which a constant vertical downward thrust corresponding to a ratio of thrust to weight of 0.1 has been applied to the first stage. For the no-thrust condition, at zero dynamic pressure, the position and attitude of the vehicles do not change; and separation does not occur. For this case, safe separation can be expected only at relatively high dynamic pressures. For the vertical-thrust condition, safe separation could result at low dynamic pressures but as the dynamic pressure increases there is a region of collision. At the higher dynamic pressures safe separation would also be predicted.

CONCLUDING REMARKS

Preliminary studies have been made of stage separation of reusable launch vehicles for which large aerodynamic interferences as well as a strong dependency on the separation maneuver of the dynamic derivatives, the initial attitude, and the dynamic pressure were evident. The results indicate that an evaluation of the potential of any given system will require appreciable aerodynamic data and critical trajectory analysis to determine the constraints under which safe separation may be achieved. It thus appears that other avenues of approach such as trajectory shaping, vehicle shaping, various thrusting maneuvers including attitude control thrust, and other auxiliary devices need to be considered.

~~CONFIDENTIAL~~

~~CONFIDENTIAL~~

REFERENCES

1. Decker, John P.; and Pierpont, P. K.: Aerodynamic Separation Characteristics of Conceptual Parallel-Staged Reusable Launch Vehicle at Mach 3 To 6. NASA TM X-1051, 1964.
2. Decker, John P.: Aerodynamic Abort-Separation Characteristics of a Parallel-Staged Reusable Launch Vehicle From Mach 0.60 To 1.20. NASA TM X-1174, 1965.

~~CONFIDENTIAL~~

REUSABLE LAUNCH VEHICLE

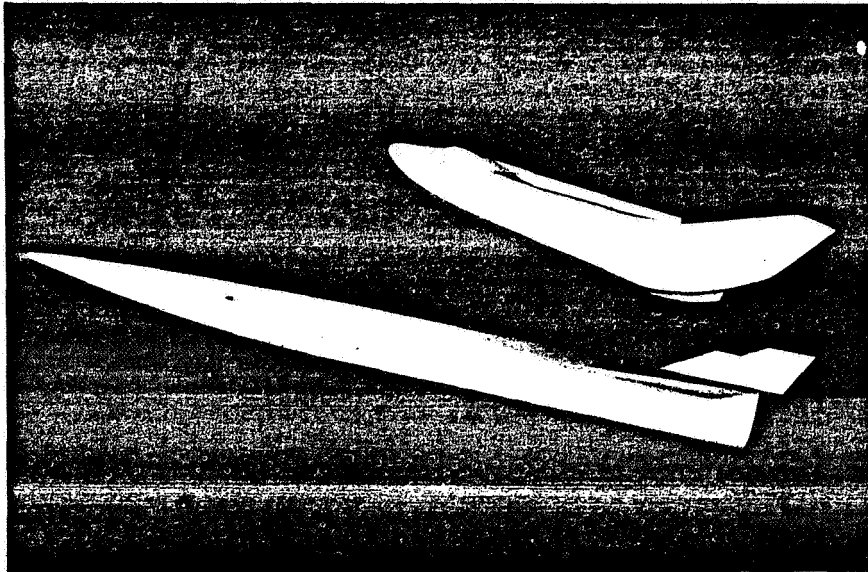


Figure 1

L-2866-1

AERODYNAMIC INTERFERENCE

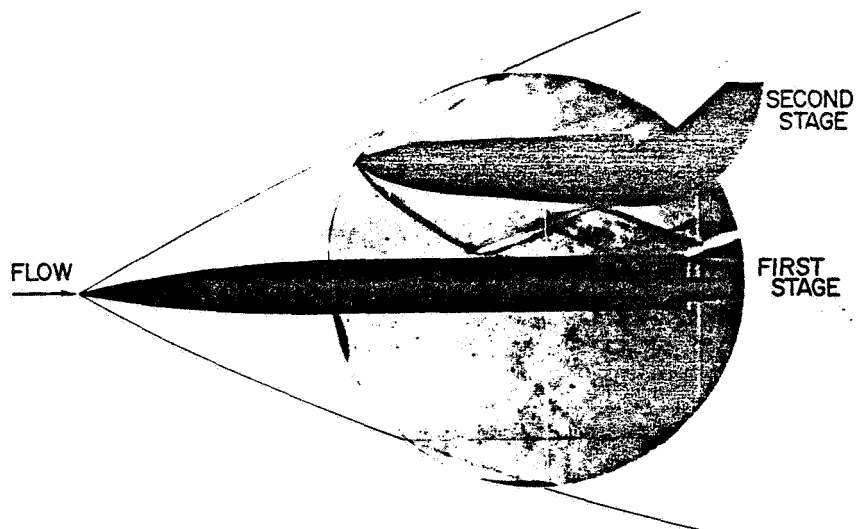


Figure 2

L-2866-2

~~CONFIDENTIAL~~

STAGING CONDITIONS

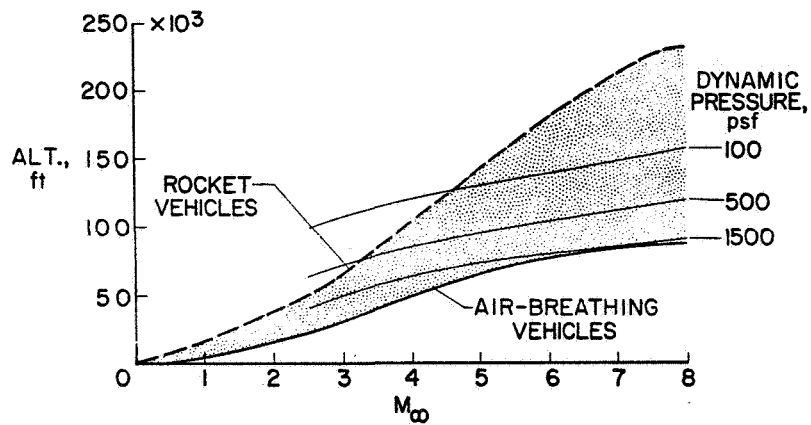


Figure 3

STAGING SEQUENCE

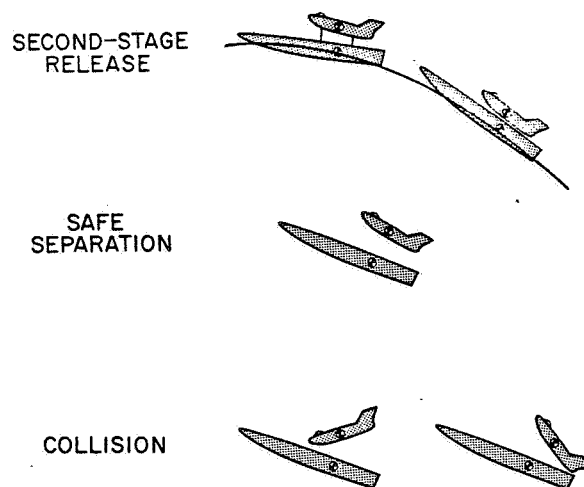
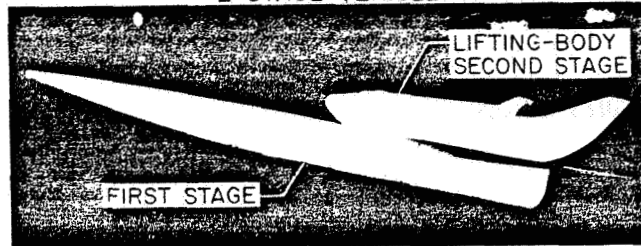


Figure 4

WIND-TUNNEL MODELS

2-STAGE VEHICLE



3-STAGE VEHICLE

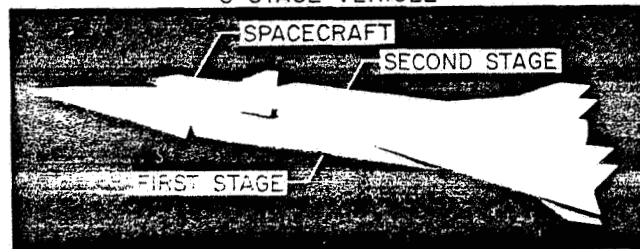


Figure 5

L-2866-5

STAGING VARIABLES

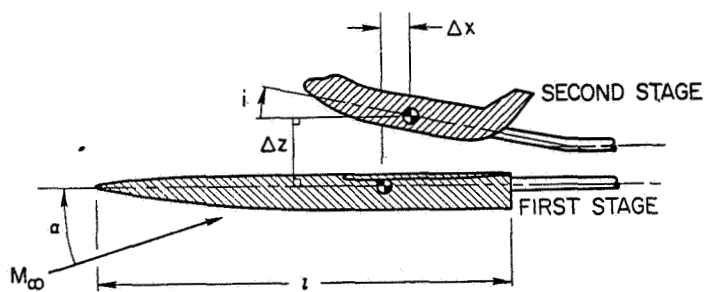


Figure 6

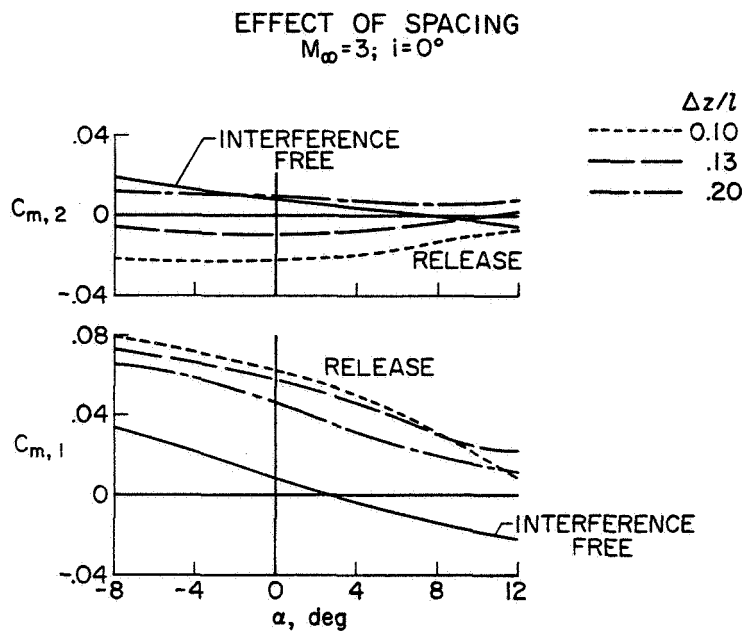


Figure 7

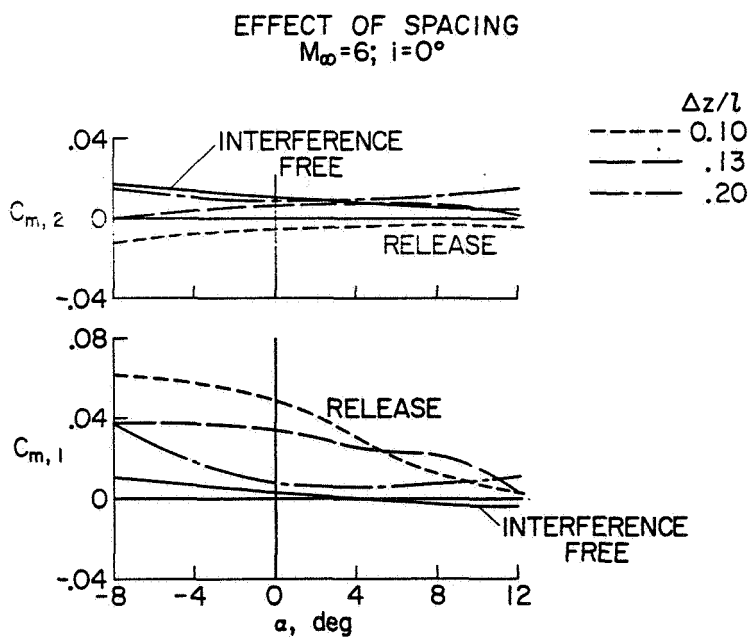


Figure 8

~~CONFIDENTIAL~~

EFFECT OF INCIDENCE ANGLE

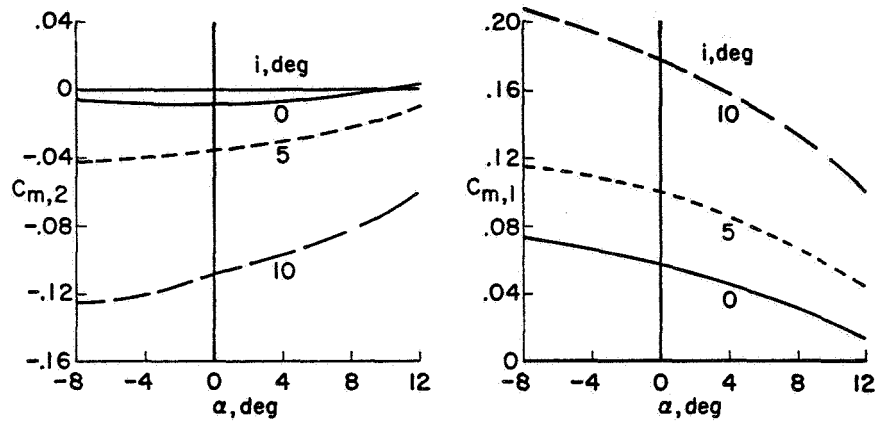
 $M_\infty=3$; $\Delta z/l=0.13$ 

Figure 9

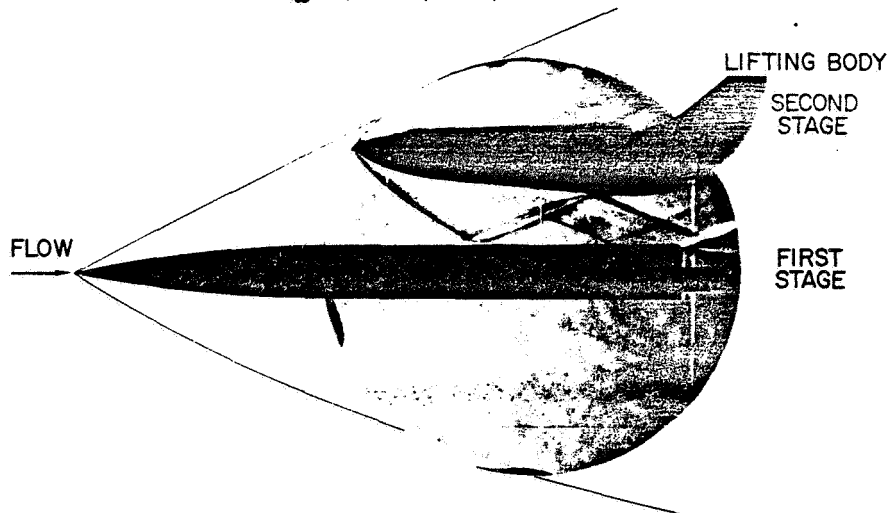
SCHLIEREN DATA
 $M_\infty=3$; $\alpha=0^\circ$; $i=0^\circ$; $\Delta z/l=0.15$ 

Figure 10

L-2866-7

~~CONFIDENTIAL~~

EFFECT OF SPACING ON LIFTING BODY
 $M_\infty = 3; i = 0^\circ$

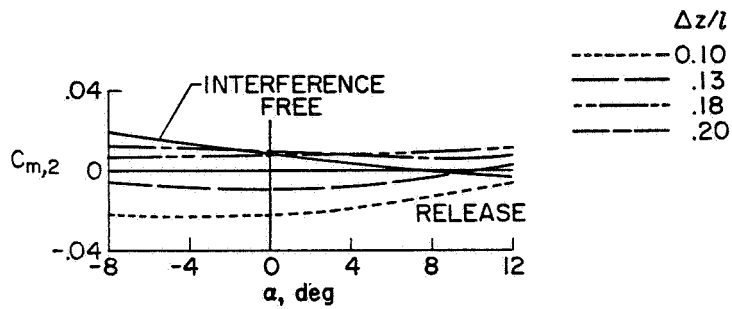


Figure 11

EFFECT OF SPACING ON 3-STAGE VEHICLE
 $M_\infty = 3; i = 0^\circ$

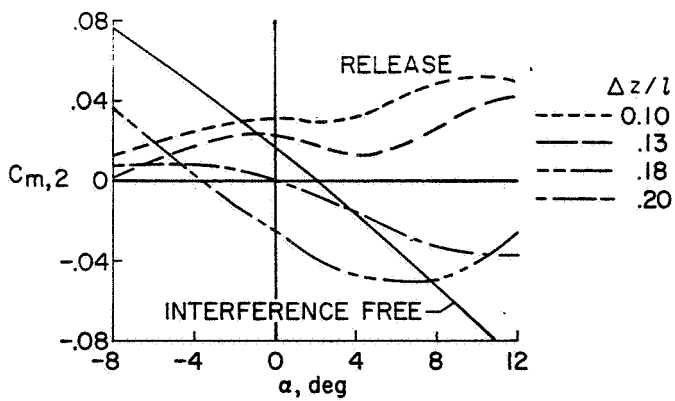


Figure 12

~~CONFIDENTIAL~~

EFFECT OF SPACING ON 3-STAGE VEHICLE

$M_\infty = 0.60; i = 0^\circ$

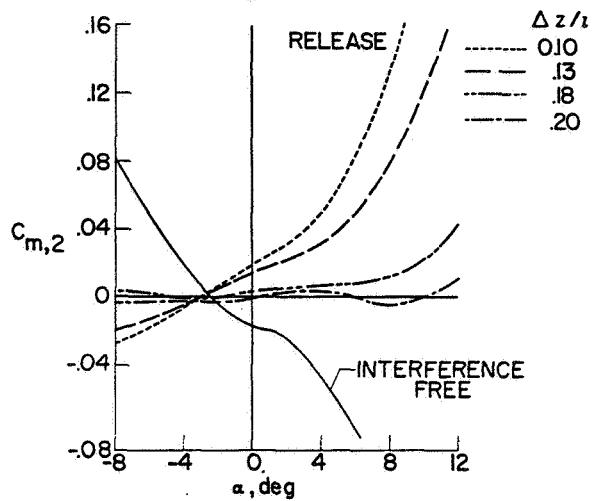


Figure 13

EFFECT OF DYNAMIC DERIVATIVES

$M_\infty = 3; \text{ALT.} = 70,000 \text{ ft}; \alpha = 6^\circ; i = 5^\circ$

$(C_{m\dot{\alpha}})_1 = -4 \text{ rad}^{-1}; (C_{m\dot{\alpha}})_2 = -1 \text{ rad}^{-1}$

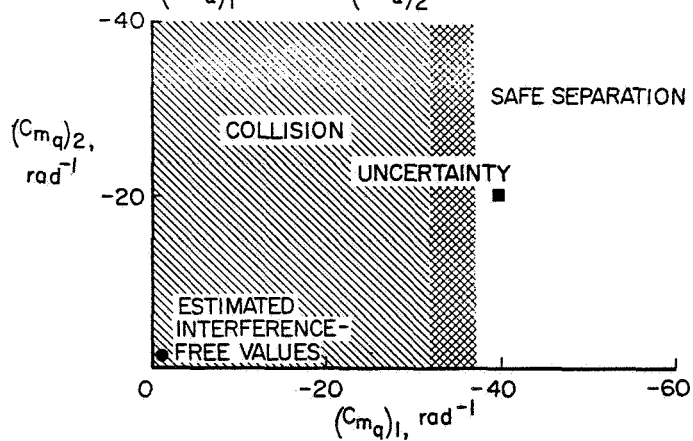


Figure 14

EFFECT OF INITIAL ATTITUDE

$M_\omega = 3$; ALT. = 70 000 ft; $(C_{m_q})_1 = -40 \text{ rad}^{-1}$;

$(C_{m_q})_2 = -20 \text{ rad}^{-1}$; $(C_{m_a})_1 = -4 \text{ rad}^{-1}$; $(C_{m_a})_2 = -1 \text{ rad}^{-1}$

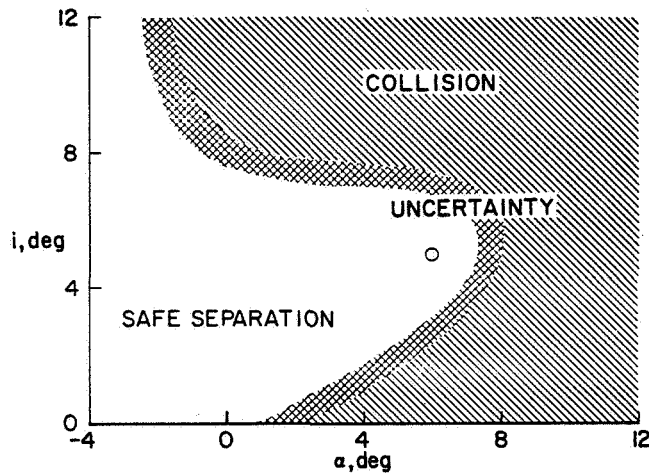


Figure 15

EFFECT OF DYNAMIC PRESSURE

$M_\omega = 3$; $\alpha = 6^\circ$; $i = 5^\circ$; $(C_{m_q})_1 = -40 \text{ rad}^{-1}$; $(C_{m_q})_2 = -20 \text{ rad}^{-1}$

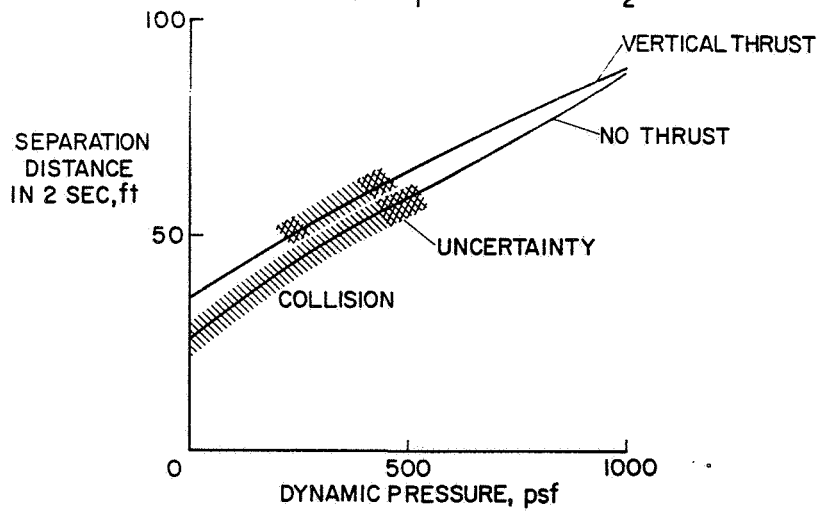


Figure 16

CONFIDENTIAL

6. THE PROSPECTS OF AERODYNAMIC PERFORMANCE GAINS FROM WING CAMBER AND TWIST AT LOW HYPERSONIC MACH NUMBERS

By Ralph L. Carmichael
Ames Research Center

SUMMARY

The optimum camber surface for the wing of wing-body combinations in which the leading edge of the wing is supersonic is very nearly uncambered. Consequently, wing warp cannot significantly improve untrimmed lift-to-drag ratio. However, for wings with cranked leading edges in which a portion of the leading edge is still subsonic, a significant increase in lift-to-drag ratio is theoretically available, even for Mach numbers of 5 to 6.

For configurations with thin wings operating at low hypersonic Mach numbers, a symmetrical section is aerodynamically superior to one with a flat-bottomed section.

INTRODUCTION

At moderate supersonic speeds, the performance of a thin wing may be improved by the use of camber and twist. In the development of the supersonic transport, considerable effort has been expended in the proper choice of wing warp for the reduction of drag due to lift. This effort has been justified by the performance improvements which have resulted from this use of wing warp. As the development of a hypersonic cruise vehicle is considered, it is appropriate to ask whether a similar effort is justified in the design of such airplanes.



SYMBOLS

b	span
C_D	drag coefficient
C_{D_0}	drag coefficient at zero lift
C_L	lift coefficient
C_m	pitching-moment coefficient
c	chord

CONFIDENTIAL

d body diameter
 h altitude
 L/D lift-drag ratio
 $(L/D)_{MAX}$ maximum lift-drag ratio
 M Mach number
 t thickness
 U_{∞} free-stream velocity
 x, y, z Cartesian coordinates
 α angle of attack
 $\beta = \sqrt{M^2 - 1}$
 Λ leading-edge sweep angle

WING THEORY

The computation of the wing surface with minimum drag for a given plan-form, lift, and Mach number has been treated by various investigators. The results of these calculations (refs. 1 and 2) are shown in figure 1 for a delta wing with 70° of sweep. The drag due to lift parameter $C_D/\beta C_L^2$ is plotted against Mach number for a flat delta wing and for the envelope of drag polars of wings having optimum warp. For flat wings with supersonic leading edges, this parameter is equal to 0.25, while flat wings with subsonic leading edges have higher values of $C_D/\beta C_L^2$ because of their lower lift-curve slope. When the Mach number is sufficiently high that the leading edge is supersonic, the polar envelope of the minimum drag wings is only slightly different from the polar of the flat wing. However, at lower Mach numbers, where the leading edge is subsonic, the polar envelope of minimum drag wings is significantly lower in drag due to lift than the corresponding flat wing.

WING-BODY THEORY

Recently, a new computational procedure (ref. 3) has been developed which enables one to compute the shape of the wing with least drag in the flow field of a body which may be at angle of attack. A typical configuration which may be analyzed is illustrated in figure 2. Figure 3, which is taken from reference 3, illustrates the application of the method to the computation of configurations with warped wings and bodies.

~~CONFIDENTIAL~~

This procedure has been used to determine whether the delta wing with supersonic leading edge in combination with a large fuselage could benefit from wing warp. This study was made on a 70° delta wing on a cylindrical fuselage with a parabolic nose. The diameter-to-span ratio of 0.25 was chosen as an appropriate value for a hydrogen fueled hypersonic transport. The results of these calculations (fig. 4) indicate very little theoretical potential for improvement. The mean camber surface for minimum drag due to lift is essentially planar.

In a study of planforms of interest for supersonic transport design, Hopkins (ref. 4) has noted that one of the principal advantages of the double delta planform is the greatly increased potential for improvement by use of wing warp. In order to investigate the possibilities of drag reduction at hypersonic speeds on these cranked leading-edge wings, a leading-edge extension was added to the delta wing-body configuration previously shown. This extension has a sweep angle of 81° which is subsonic up to a Mach number of 6.4. This new configuration was studied in the same manner as the delta configuration, and the results are summarized in figure 5. The results indicate that a significant amount of drag reduction is available even at a Mach number of 5.

In order to make these results more meaningful, estimates have been made of the zero lift drag of the delta and double delta configurations considered as typical Mach 5 vehicles cruising at an appropriate altitude. These estimates, coupled with the drag-due-to-lift data already computed, enable one to compute maximum lift-drag ratios for the flat and warped versions of these planforms. The L/D improvement for the delta is negligible, but the double delta does have a potential for improvement of about 0.13 in lift-drag ratio, as shown in figure 6. This represents an improvement of about 3 percent in lift-drag ratio.

CHOICE OF WING SECTION

In the study of the delta wing-body configuration, the mean camber surface was found to be nearly planar. This result is apparently in conflict with a well-known result of hypersonic wing theory (refs. 5 and 6) which holds that the best wing is flat on the lower surface, thereby having positive camber. The resolution of this apparent paradox may be accomplished by consideration of figure 7, which is adapted from reference 5. Here a symmetrical double wedge airfoil 4 percent thick is compared with a section that has the same thickness distribution but cambered so as to have a flat lower surface. Shock-expansion theory was used to calculate drag polars at several Mach numbers. At Mach numbers of 2 and 5, the symmetrical section is superior, while at Mach numbers of 10 and 20, the flat-bottomed section is superior. The significant result indicated here is that for a Mach number of 5 and a thickness ratio of 0.04, the symmetrical section is indeed superior.

~~CONFIDENTIAL~~

REFERENCES

1. Yoshihara, H.; Kainer, J.; and Strand, T.: On Optimum Thin Lifting Surfaces at Supersonic Speed. J. Aero/Space Sci., vol. 25, no. 8, Aug. 1958, pp. 473-479, 496.
2. Heaslet, Max. A.; and Fuller, Franklyn B.: Drag Minimization for Wings and Bodies in Supersonic Flow. NACA Rep. 1385, 1958.
3. Carmichael, Ralph L.; and Woodward, Frank A.: An Integrated Approach to the Analysis and Design of Wings and Wing-Body Combinations in Supersonic Flow. NASA TN D-3685, 1966.
4. Hopkins, Edward J.; Hicks, Raymond M.; and Carmichael, Ralph L.: Effects of Planform Variations on the Aerodynamic Characteristics of Low-Aspect-Ratio Wings With Cranked Leading Edges. Conference on Aircraft Aerodynamics, NASA SP-124, 1966, pp. 469-483.
5. Linnell, R. D.: Two-Dimensional Airfoils in Hypersonic Flows. J. Aero. Sci., vol. 16, no. 1, Jan. 1949, pp. 22-30.
6. Truitt, R. W.: Hypersonic Aerodynamics. Ronald Press, New York, 1959, p. 54.

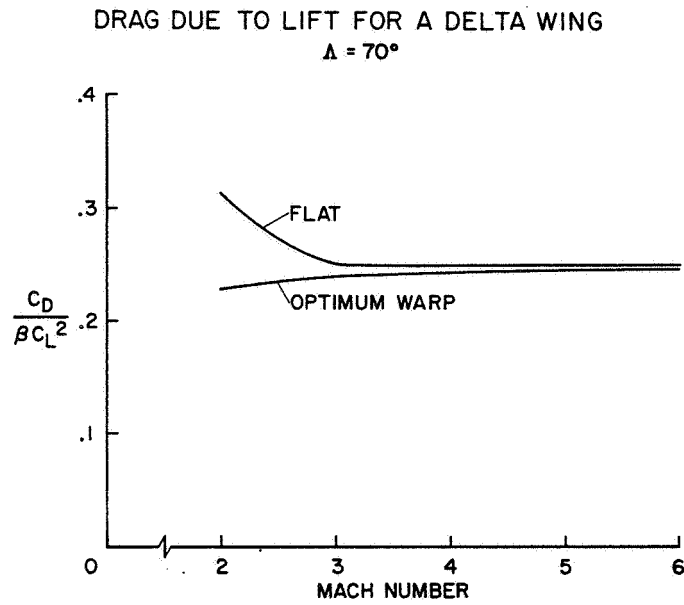


Figure 1

TYPICAL PANEL LAYOUT FOR WING-BODY COMBINATION

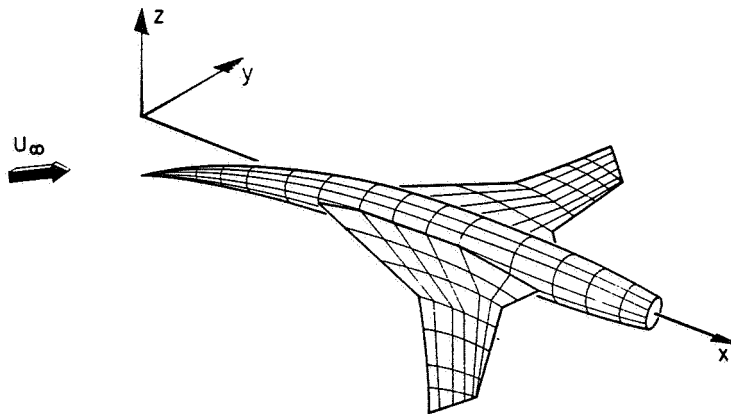


Figure 2

EFFECT OF WING AND BODY CAMBER AT M=2

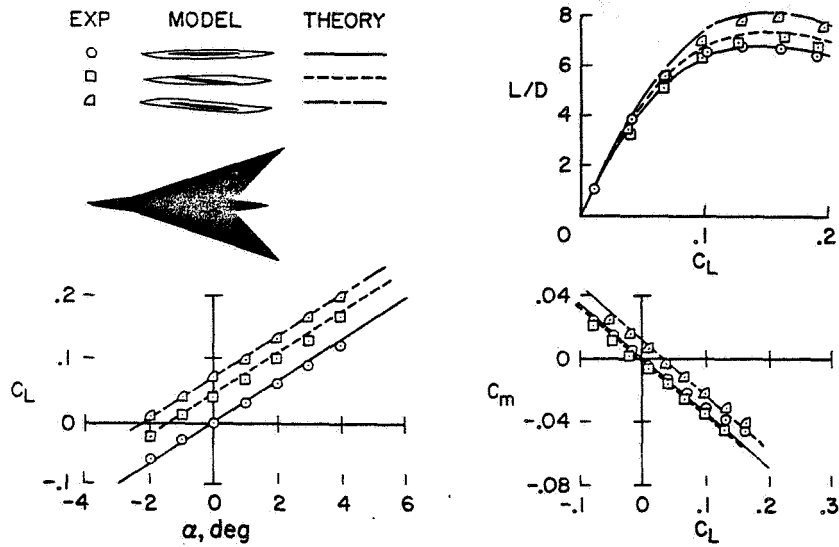


Figure 3

DRAG DUE TO LIFT DELTA WING-BODY

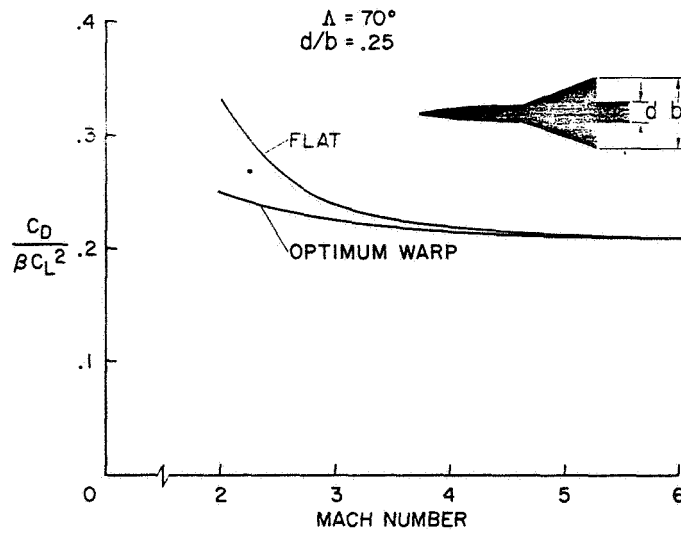


Figure 4

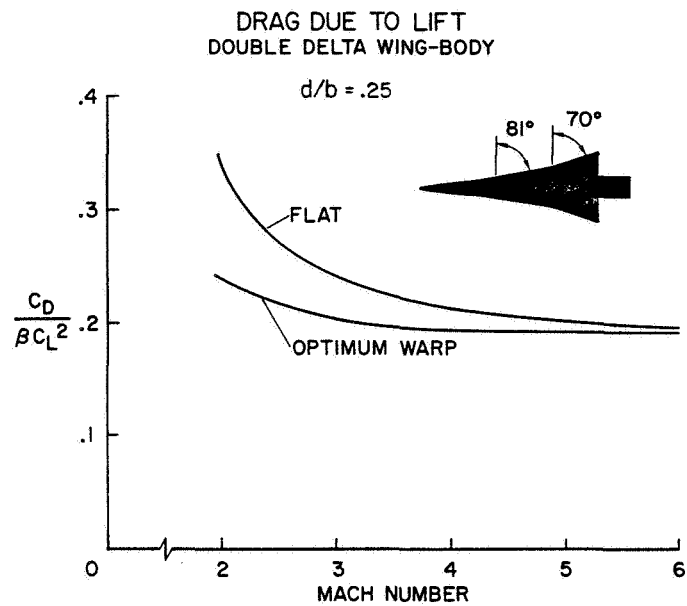


Figure 5

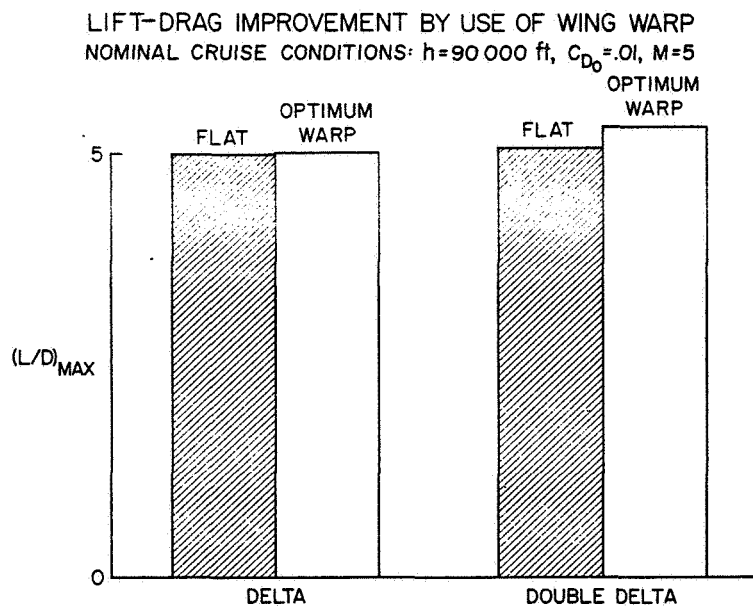


Figure 6

~~CONFIDENTIAL~~

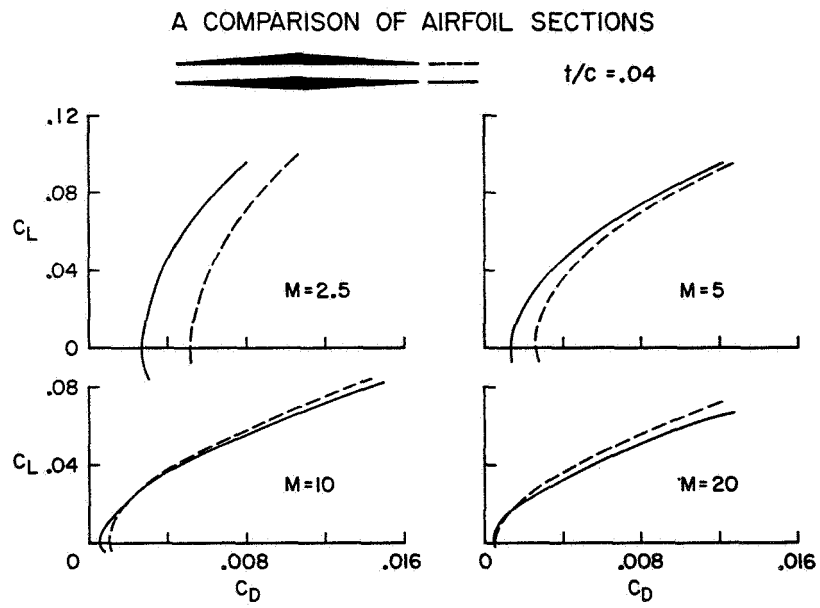


Figure 7

~~CONFIDENTIAL~~

7. STUDIES OF OPTIMUM BODY SHAPES

By Louis S. Stivers, Jr.
Ames Research Center

and

Bernard Spencer, Jr.
Langley Research Center

SUMMARY

The present study was directed toward the questions that arise in the application of optimum bodies to the design of hypersonic-cruise aircraft. The considerations were divided into two parts. The first involved the calculated minimum-drag characteristics of four families of slender bodies for Mach numbers from 2 to 12. The second concerned the experimental evaluation of the effects of body cross-sectional shape on the aerodynamic performance of bodies at a Mach number of 10. The constraints in each study were body length and volume, although the constant values are different in each part of the study.

INTRODUCTION

Hydrogen-fueled hypersonic-cruise aircraft require very large volume bodies, mainly to accommodate the low-density liquid fuel. Such bodies because of their size are especially unattractive from the standpoint of drag, but can be useful in providing significant contributions to the lift of the aircraft. Body profiles that provide minimum drag or maximum lift, or both, are of particular interest to the designer. Attention is generally given to the theoretical minimum wave-drag body profiles. Such profiles have been derived for use at low-supersonic, hypersonic, and low-hypersonic Mach numbers. (See refs. 1 to 5.) The application of these profiles, however, introduces many questions that must be answered. Some of these are: What profile should be used? Should it be one derived for low-supersonic Mach numbers or one derived for hypersonic Mach numbers? Can some base area be permitted, since by this means the wave drag can be reduced for a body of given length and volume? What is the effect of cross-sectional shape? Can the cross-sectional shape be altered appreciably to provide improved lift characteristics of the body without seriously affecting the drag characteristics?

It is the intent of this paper to provide a few answers to these questions. This will be done in two parts. The first part has been prepared at the Ames Research Center and deals with the calculated minimum-drag characteristics of four families of slender bodies. The second has been prepared at

~~CONFIDENTIAL~~

the Langley Research Center and is concerned with the experimental effects of body cross-sectional shape on the aerodynamic performance of bodies.

NOTATIONS

b	span of body base
C_D	drag coefficient
$C_{D_{min}}$	minimum-drag coefficient
C_{D_0}	drag coefficient at zero lift
C_L	lift coefficient
$C_{L_{(L/D)_{max}}}$	lift coefficient for maximum lift-drag ratio
C_{L_α}	lift-curve slope, $\frac{dC_L}{d\alpha}$
C_m	pitching-moment coefficient
h	height of body base
k	body cutoff, $1 - \frac{l}{l_0}$, amount of afterbody portion of fully closed body cutoff to provide a body with a base; 0 for a fully closed body and 0.5 for a body with maximum diameter at the base
$\frac{L}{D}$	lift-drag ratio, $\frac{C_L}{C_D}$
$\left(\frac{L}{D}\right)_{max}$	maximum lift-drag ratio, $\left(\frac{C_L}{C_D}\right)_{max}$
l	actual body length
l_0	length of fully closed body, virtual length
M	Mach number
n	exponent of power body equation, $\eta = \xi^n$
R_l	Reynolds number based on body length
r	body radius
r_0	maximum body radius

~~CONFIDENTIAL~~

V	volume of body
x	longitudinal distance along body axis
z	geometric altitude
α	angle of attack, deg
η	dimensionless radial coordinate of body, $\frac{r}{r_0}$
ξ	dimensionless longitudinal coordinate of body, $\frac{x}{l_0}$

RESULTS AND DISCUSSION

Calculated Minimum Drags of Slender Bodies

The total drag characteristics of four families of slender bodies at zero incidence were calculated for Mach numbers from 2 to 12. The length and volume of each of the bodies were held constant such that $V = 0.002655l^3$. Fineness ratios of the bodies ranged from about 12.5 to 14. The study of reference 6 has shown that fineness ratios within this range are the most favorable for hypersonic transport aircraft.

Body families.— Each family is composed of a series of bodies having various base areas formed by cutting off given amounts of the afterbody of a fully closed body. This is illustrated in figure 1. The fully closed body at the top of the figure has no cutoff and is designated $k = 0$. To form the other bodies, the same closed profile was adjusted in diameter and was stretched to such an extent that when 0.1, 0.3, and 0.5 of the virtual lengths were cut off, each remaining body had the same length and volume as the original closed body with no cutoff, but each had different amounts of base area. Four particular profiles were selected to make up the different families under this arrangement of body cutoffs.

1. The Sears-Haack profile optimized for a given length and volume (refs. 2 and 3) and defined by the equation:

$$\eta = [1 - (1 - 2\xi)^2]^{3/4}$$

2. A parabolic-arc profile defined by the equation:

$$\eta = 4\xi(1 - \xi)$$

3. One of Miele's profiles optimized for a given surface area and volume (ref. 7) and defined by the equation:

$$\eta = 1 - (1 - 2\xi)^{3/2} \quad [\text{Forebody only, } 0 \leq \xi \leq 0.5]$$

4. The von Kármán profile optimized for a given length and diameter (ref. 1) and defined by either of the equations:

$$\left. \begin{aligned} \eta &= \left[\cos^{-1}(1 - 4\xi) - 2(1 - 4\xi)\sqrt{2\xi(1 - 2\xi)} \right]^{1/2} \\ \text{or} \\ \eta &= \pi^{-(1/2)} \sqrt{\theta - \frac{1}{2} \sin 2\theta} \\ \text{where} \\ \xi &= \frac{1}{4} (1 - \cos \theta) \end{aligned} \right\} \begin{aligned} &\text{Forebody only,} \\ &0 \leq \xi \leq 0.5 \end{aligned}$$

The afterbodies of the last two profiles are undefined by the equations (i.e., for $0.5 < \xi \leq 1.0$), but each has zero profile slope at $\xi = 0.5$. Therefore, each profile was placed back-to-back in order to form a closed basic body.

The contours for the $k = 0.5$ bodies of each family are shown in figure 2. In this figure r/l is plotted to an expanded scale versus x/l . The Sears-Haack contour is the fullest for the smaller values of x/l and has the smallest radius at the base (i.e., at $x/l = 1.0$). A straight-line contour is also shown in this figure for a cone having the same length and volume as the $k = 0.5$ bodies. This cone has the least radii for the lower values of x/l of any of the bodies, and the greatest radius at the base. The contours for the other bodies are generally distributed between the limits of the Sears-Haack and cone profiles. For comparison with the data for the $k = 0.5$ bodies of each family, calculations were also made for a $3/4$ -power body ($\eta = \xi^{3/4}$) and a cone ($\eta = \xi$) both of which were restricted to the same length and volume as the other bodies.

Minimum-drag coefficients.- The calculated minimum-drag coefficients for all the bodies are based on a fictitious wing area equal to $0.07695l^2$ or $4.013V^{2/3}$, and have three components: wave drag, base drag, and skin-friction drag. The wave-drag component was computed by integrating the pressure distribution over the body which was machine calculated by the method of characteristics according to the procedure of reference 8. This procedure, however, was modified to accommodate pointed bodies. The base-drag component was computed by the procedure of Love, as reported in reference 9, extended to hypersonic Mach numbers. The computations of skin friction were made

CONFIDENTIAL

according to the Spalding-Chi procedure (see ref. 10) and flat-plate skin-friction coefficients corrected to a body of revolution, using Reynolds numbers determined by an assumed length of 300 feet and for the altitudes from the flight profile for hypersonic aircraft given in the following table.

M	2	4	6	8	10	12
Z, ft $\times 10^{-3}$	57.5	70	88	101	111.5	119

The effect of body cutoff for each family of bodies is shown in figure 3 for Mach numbers of 2, 4, and 12. In this figure calculated total-drag coefficient is plotted versus body cutoff, k . Drag coefficients for the $3/4$ -power and cone bodies are plotted along the $k = 0.5$ line. As the Mach number is increased the minimum-drag coefficient corresponds to increasing values of body cutoff. For each Mach number the minimum-drag coefficient is associated with the Sears-Haack profile. There is little difference in the drag coefficients for any of the bodies, however, at a Mach number of 12.

Drag coefficients for the Sears-Haack bodies are plotted in figure 4 versus Mach number for constant values of k . The drag coefficients for the cone are also presented for comparison. At Mach numbers from 2 to 5 the drag coefficients for the $k = 0.3$ and 0.5 bodies are undesirably large. Low drag coefficients over the range of Mach numbers from 2 to 12 are provided by the smaller values of body cutoff. At transonic Mach numbers, however, it is likely that no body cutoff would be desirable.

A breakdown of the total-drag coefficients for the $k = 0.1$ Sears-Haack body into the three components is shown in figure 5, where drag coefficient is plotted versus Mach number. The vertical height of each shaded band corresponds to the magnitude of that component. The skin-friction and wave-drag components are of the same order of magnitude over the range of Mach numbers shown. At a Mach number of 12 the base-drag component is particularly small because of the relatively small base area of this body. For the cone at this Mach number, the base-drag component is greater than the corresponding wave-drag component. This wave-drag component for the cone is only slightly less than the wave-drag component for the $k = 0.1$ Sears-Haack body shown in this figure.

In summary, the calculations show that for Mach numbers from 2 to 12 the Sears-Haack profile provides the lowest total-drag coefficients at zero incidence. Further, it appears that a body with a small base area would provide low total-drag coefficients over this range of Mach numbers. Drag considerations at transonic Mach numbers, however, would dictate to a great extent the allowable base area for an aircraft body.

Effects of Body Cross-Sectional Shape

In this portion of the paper, methods are examined for improving the lift and drag-due-to-lift characteristics at hypersonic speeds of various $k = 0.5$ bodies, that is, bodies having maximum cross-sectional areas at the base. In this study of body cross-sectional shape the geometric constraints of a given length and volume have also been imposed on each body such that $V = 0.0161^3$. Fineness ratios of these bodies ranged from about 5 to 7. Because the fineness ratios are low and the bases of the bodies are large, such bodies are primarily applicable as lifting reentry bodies. In the present paper, however, the experimental results are used to illustrate the aerodynamic trends that may result from changes in the cross-sectional shape of the forward portion of the fuselage of hypersonic-cruise aircraft.

Elliptic cross section.— Most analyses to determine optimum profiles of minimum wave-drag bodies at hypersonic speeds have been limited to bodies of circular cross section (see ref. 4). Experimental studies reported in references 11 and 12, however, have shown that bodies of elliptic cross section provide better performance at high supersonic speeds because of improved drag-due-to-lift characteristics. For this reason, Suddath and Oehman investigated profiles of minimum wave drag having elliptic cross section. The results of this investigation, reported in reference 13, indicated that the normalized distribution of cross-sectional area of an optimum body is relatively insensitive to variations in ellipticity, and further, that the wave drag does not change for moderate values of ellipticity. In an effort to explain this insensitivity Miele analyzed the problem using a slender body approximation to the Newtonian pressure relation (ref. 14), and found that a similarity law exists for optimum hypersonic bodies. It was found that the function which describes the optimum longitudinal contour of a body of arbitrary cross section is identical to the function which describes the optimum longitudinal contour of a body of circular cross section.

Experimental studies at a Mach number of 10 have been made both to verify these analytical results and to examine the effects of elliptical cross sections on the performance of power-law bodies and optimum hypersonic body profiles determined under the constraints of a given length and volume. (See ref. 15.) Sears-Haack profiles were not included in these experiments.

A summary of the experimental zero-lift drag characteristics of a series of power-law bodies of circular and elliptic cross section are shown in figure 6 for a Mach number of 10. Also shown are corresponding experimental drag coefficients for the optimum bodies, as determined for a circular cross section in reference 4, and for an elliptic cross section in reference 13. The elliptic bodies shown had major-to-minor axis ratios of 2.0. The zero-lift drag coefficients are only the measured foredrag coefficients; that is, the base-drag component is not included. Such drag coefficients have been normalized with respect to the corresponding data for a circular cone. The data for the power-law bodies are indicated by the symbols and are plotted against power-body exponent. The levels of the experimental data for the optimum bodies are indicated by the arrows since these bodies do not correspond to any power-body exponent.

~~CONFIDENTIAL~~

The minimum-drag coefficients for the power-law bodies correspond to an exponent of $n = 2/3$. This is the theoretical value for an optimum profile when the analysis is restricted to power-law bodies. (See ref. 16.) Since these minimum drags correspond to an exponent of $2/3$ for both the circular and elliptic cross sections, Miele's similarity law is verified. The values of the zero-lift drag associated with the optimum circular and elliptic body shapes are slightly lower than the minimum values for the power-law bodies. The greater drag for the elliptic bodies is apparently due to the increased skin friction associated with the greater wetted area.

Lift and maximum lift-drag ratio characteristics for the same power-law and optimum bodies are shown in figure 7, also for a Mach number of 10. The greatest maximum lift-drag ratios occur for the same power-law bodies having the lowest zero-lift drag coefficients. A change in cross section from circular to elliptic results in an almost constant incremental increase in maximum lift-drag ratio for any of the bodies. This results from the improved lift characteristics of the elliptic bodies which more than compensate for the increased drag. The maximum lift-drag ratios for the optimum bodies are essentially the same as the corresponding ratios for the $2/3$ -power bodies.

Other cross sections.- In an attempt to improve further the performance of bodies at hypersonic speeds, additional experimental studies have been made on a series of flat-bottomed bodies which have longitudinal distribution of cross-sectional areas identical with that of the optimum body derived by Eggers, Resnikoff, and Dennis (ref. 4). The results of these recent studies are presented in figure 8. The flat-bottomed body profile is illustrated at the top right of figure 8. Directly below are the cross sections at the base of the rectangular, trapezoidal, and triangular bodies. For each body including a reference body with elliptic cross sections having a major-to-minor axis ratio of 2, the span of the base, the base area, the length, and the volume have all been held constant, the only variables being body height and cross-sectional shape. Strictly, the significant variable is the angle that the lateral faces make with respect to the flat bottom. It is apparent, however, that this angle varies with body height.

A summary of the results of the experimental studies is shown on the left side of figure 8 for a Mach number of 10. The data have been normalized with respect to the corresponding data for the reference body with elliptic cross sections. Values of $C_{L(L/D)_{\max}}$, $C_{D_{\min}}$, and $(L/D)_{\max}$ are shown as a function of dimensionless base height. It is obvious that $(L/D)_{\max}$ increases as the base height is increased. This results from the large increases in lift occurring at $(L/D)_{\max}$. There was essentially no change in the measured drag coefficient.

An examination of the pitching-moment characteristics of each of the flat-bottomed configurations indicates unfavorable (that is, negative) pitching moments at zero lift, as would be expected for the camber of these bodies. In order to examine the possibility of providing a favorable C_{m_0} without incurring large penalties in performance, one of the trapezoidal configurations was modified by a reversal in camber by shearing the cross sections.

~~CONFIDENTIAL~~

CONFIDENTIAL

This resulted in a flat topped body with maximum width retained on the lower surface, as illustrated in figure 9. The results of this modification are presented in this figure where pitching-moment coefficient and lift-drag ratio are plotted as a function of lift coefficient. A favorable C_{m_0} and variation of pitching-moment with lift were obtained by the camber reversal. There was little or no corresponding change in $(L/D)_{\max}$ or lift at $(L/D)_{\max}$, and, in addition, no measurable effect on $C_{D_{\min}}$.

In summary, a prudent selection of cross-sectional shape and camber of the forward portion of the fuselage of hypersonic-cruise aircraft may significantly improve the aerodynamic performance of such bodies at hypersonic speeds.

CONCLUDING REMARKS

The present study was concerned with providing some of the answers to questions that arise in the application of optimum bodies to the design of hypersonic-cruise aircraft. This study involved the calculated minimum-drag characteristics of four families of slender bodies, and the experimental effects of body cross-sectional shape on the aerodynamic performance of bodies. In both parts of this study the restriction of a constant length and volume has been imposed on the bodies involved, but the constant values are different in each part.

The calculations of the drag characteristics of the families of slender bodies have shown that for Mach numbers from 2 to 12, the Sears-Haack profile provides the lowest total-drag coefficients at zero incidence. It appeared, also, that this profile with a small base area would provide low total-drag coefficients over this range of Mach numbers. The allowable base area for an aircraft body, however, would be dictated largely by drag considerations at transonic Mach numbers.

The experimental results for a Mach number of 10 concern bodies having various cross-sectional shapes. These results indicated that the careful choice of cross-sectional shape and camber for the forward portion of the fuselage of hypersonic-cruise aircraft may significantly improve the aerodynamic performance of such bodies at hypersonic speeds.

It remains to be determined whether or not the results of both parts of this paper will be significantly altered when the body is combined with a wing.

~~CONFIDENTIAL~~

REFERENCES

1. von Kármán, Th.: The Problem of Resistance in Compressible Fluids. GALCIT Pub. No. 75, 1936 (From Roma Reale Acad. D'Italia, vol. XIV, Roma, 1936).
2. Haack, W.: Geschossformen kleinsten Wellenwiderstandes. Lilienthal-Gesellschaft für Luftfahrtforschung, Bericht 139, Teil 1, October 9-10, 1941, pp. 14-28. (Translations: Douglas Aircraft Co., Inc., Rep. 288, 1946; also Brown University Graduate Division of Applied Mathematics, Translation No. A9-T-3, 1948.)
3. Sears, William R.: On Projectiles of Minimum Wave Drag. Quart. Appl. Math., vol. IV, no. 4, Jan. 1947, pp. 361-366.
4. Eggers, A. J., Jr.; Resnikoff, Meyer M.; and Dennis, David H.: Bodies of Revolution Having Minimum Drag at High Supersonic Airspeeds. NACA Rep. 1306, 1957.
5. Fink, Martin R.: Hypersonic Minimum-Drag Slender Bodies of Revolution. AIAA J., vol. 4, no. 10, Oct. 1966, pp. 1717-1724.
6. Gregory, Thomas J.; Petersen, Richard H.; and Wyss, John A.: Performance Trade-Offs and Research Problems for Hypersonic Transports. AIAA Paper 64-605, Aug. 1964. Also: J. Aircraft, vol. 2, no. 4, July-Aug. 1965, pp. 266-271.
7. Miele, Angelo: Slender Shapes of Minimum Pressure Drag. Theory of Optimum Aerodynamic Shapes, Ch. 13, A. Miele, ed., Academic Press, 1965.
8. Inouye, Mamoru; Rakich, John V.; and Lomax, Harvard: A Description of Numerical Methods and Computer Programs for Two-Dimensional and Axisymmetric Supersonic Flow Over Blunt-Nosed and Flared Bodies. NASA TN D-2970, 1965.
9. Love, Eugene S.: Base Pressure at Supersonic Speeds on Two-Dimensional Airfoils and on Bodies of Revolution With and Without Fins Having Turbulent Boundary Layers. NACA TN 3819, 1957.
10. Neal, Luther, Jr.; and Bertram, Michel H.: Turbulent-Skin-Friction and Heat-Transfer Charts Adapted From the Spalding and Chi Method. NASA TN D-3969, 1967.
11. Jorgensen, Leland H.: Elliptic Cones Alone and With Wings at Supersonic Speeds. NACA Rep. 1376, 1958.
12. Spencer, Bernard, Jr.; Phillips, W. Pelham; and Fournier, Roger H.: Supersonic Aerodynamic Characteristics of a Series of Bodies Having Variations in Fineness Ratio and Cross-Section Ellipticity. NASA TN D-2389, 1964.

~~CONFIDENTIAL~~

CONFIDENTIAL

13. Suddath, Jerrold H.; and Oehman, Waldo I.: Minimum Drag Bodies With Cross-Sectional Ellipticity. NASA TN D-2432, 1964.
14. Miele, Angelo: Similarity Laws for Optimum Hypersonic Bodies. Astronautica Acta, vol. II, no. 3, 1965, pp. 202-206.
15. Spencer, Bernard, Jr.; and Fox, Charles E., Jr.: Hypersonic Aerodynamic Performance of Minimum-Wave-Drag Bodies. NASA TR R-250, 1966.
16. Lusty, A. H., Jr.: Slender, Axisymmetric Power Bodies Having Minimum Zero-Lift Drag in Hypersonic Flow. Boeing Scientific Research Laboratories, Flight Science Laboratory, TR no. 77, 1963.

ILLUSTRATION OF BODY CUTOFFS

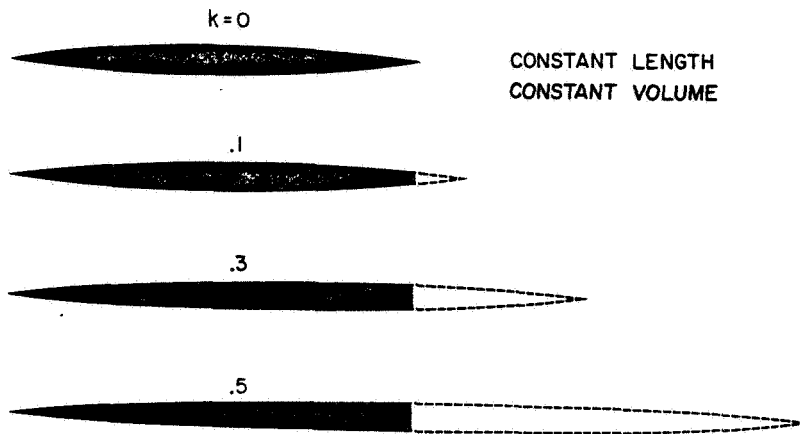


Figure 1

COMPARISON OF $k=.5$ BODY PROFILES

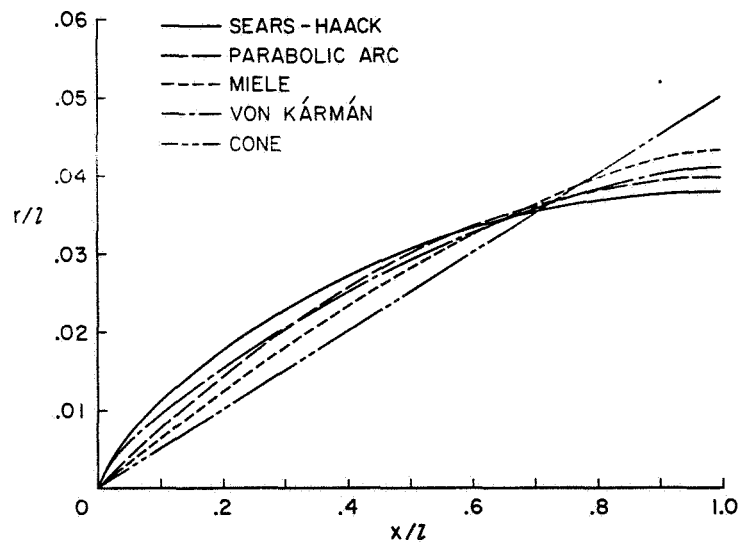


Figure 2

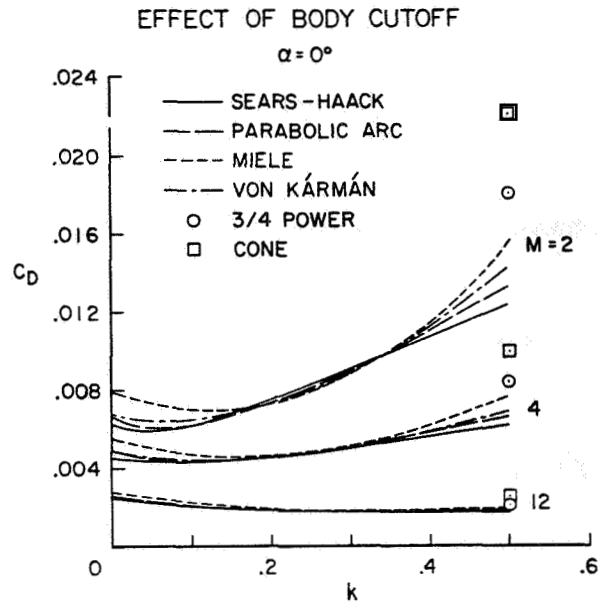


Figure 3

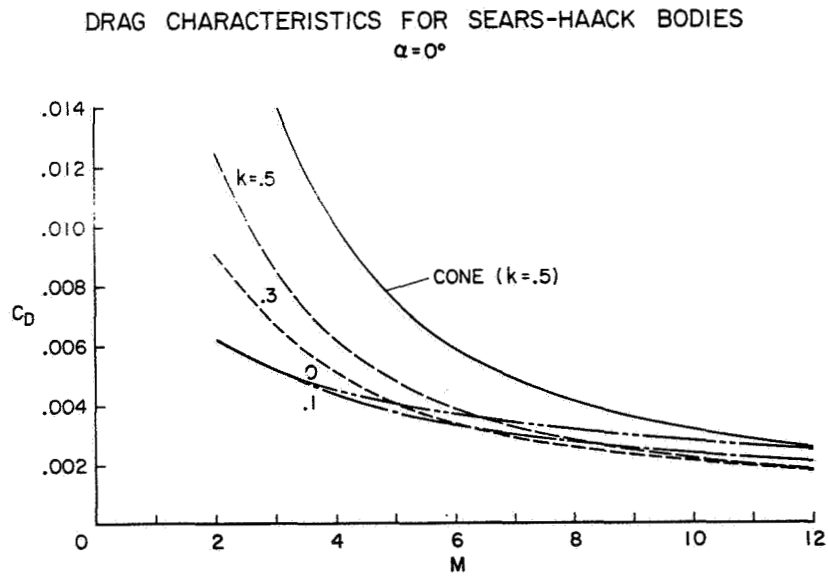


Figure 4

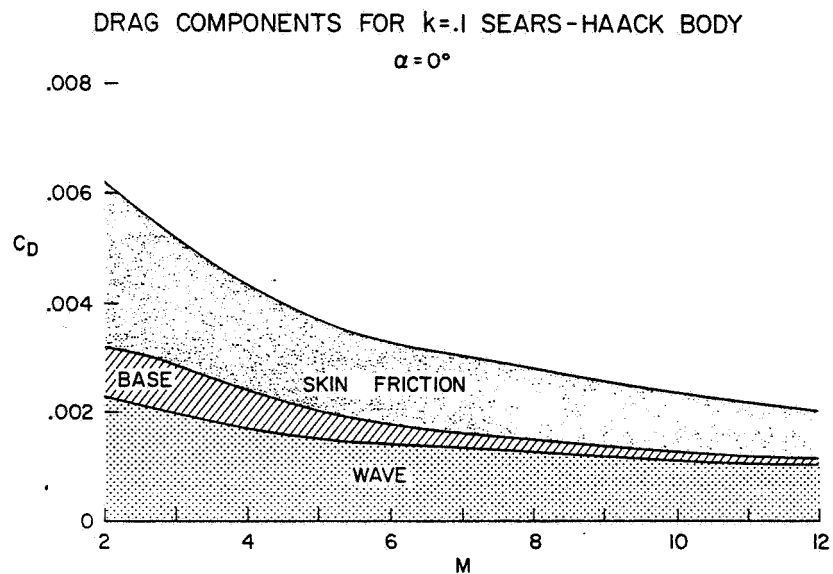


Figure 5

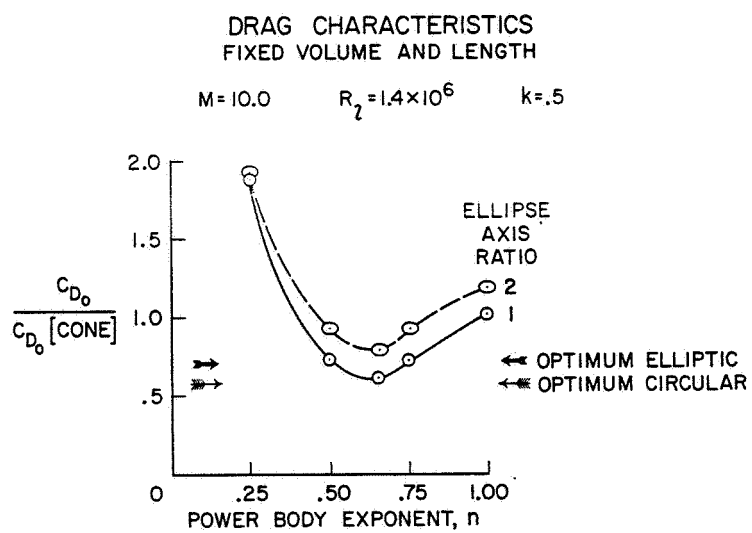


Figure 6

LIFT AND PERFORMANCE CHARACTERISTICS FIXED VOLUME AND LENGTH

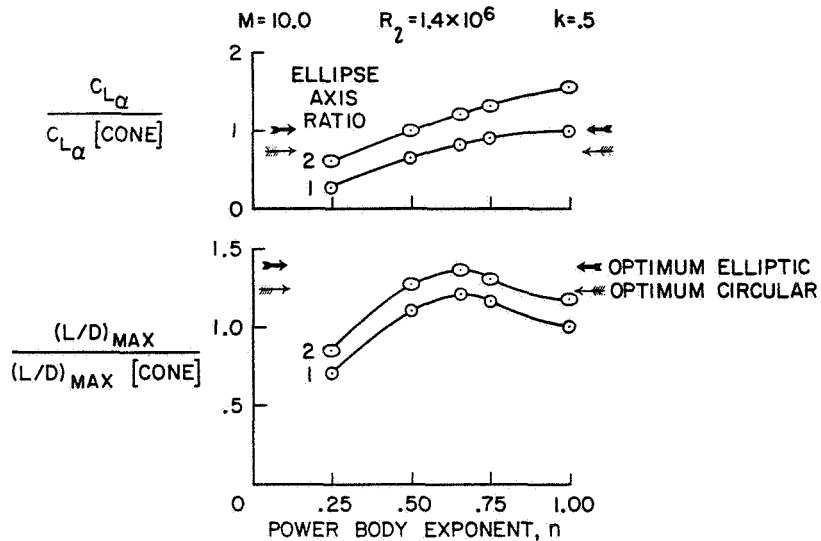


Figure 7

MINIMUM WAVE-DRAG BODIES FIXED VOLUME AND LENGTH CROSS-SECTION EFFECT

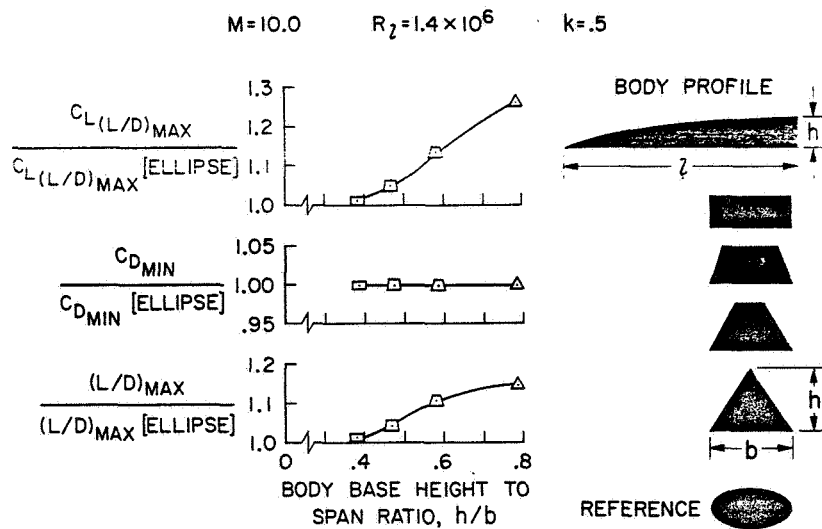


Figure 8

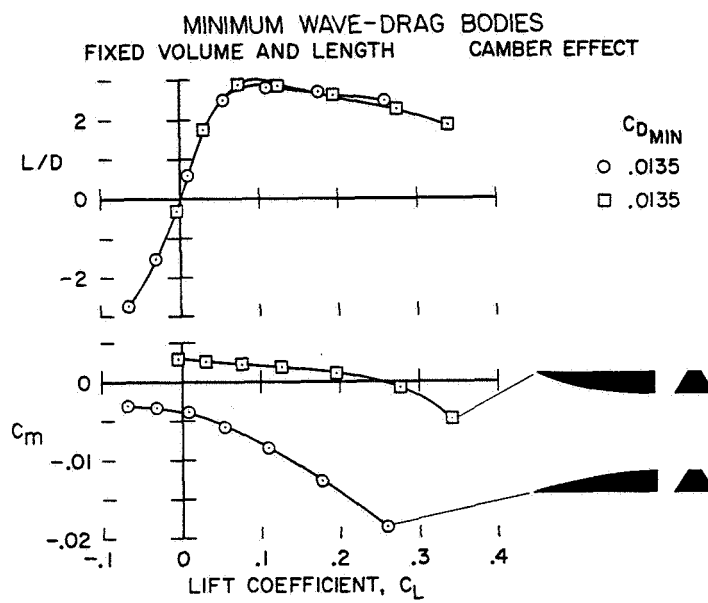


Figure 9

~~CONFIDENTIAL~~

8. A STUDY OF NUMERICAL METHODS FOR PREDICTING FLOW

ABOUT BODIES AT ANGLE OF ATTACK

By William F. Gallo, John V. Rakich,
and Joseph W. Cleary
Ames Research Center

SUMMARY

Four separate theoretical methods have been used to calculate the shock layer of sharp and blunt-nosed 15° cones at small angles of attack: (1) a fully three-dimensional method of characteristics developed at Ames Research Center (as yet unpublished); (2) the linearized method of characteristics, similar to that used in Kopal's tables; (3) an exact numerical solution for cones by K. I. Babenko; and (4) a so-called equivalent body method.

Predictions from the four methods are compared with data and regions of applicability are suggested. The equivalent body method appears to be most applicable in blunt-nose regions, whereas the linearized characteristics method gave good results on moderate fineness ratio bodies well downstream of the nose.

INTRODUCTION

Knowledge of the effects of angle of attack on the flow field over hypersonic vehicles is of fundamental importance to designers in predicting aerodynamic performance. Before these effects on more complex vehicles are understood it is essential to study the flows over basic shapes. Although many comparisons between theory and experiment have been made of surface properties, little has been said of the flow in the shock layer, especially at angle of attack. Accordingly, the present study applies four separate theoretical methods to determine some of the effects of angle of attack on the flow field within the shock layer of 15° cones. The methods are all inviscid; therefore, boundary-layer effects are neglected. An attempt is also made to point out some of the advantages and disadvantages of the methods. Some aspects of this study are more fully covered in references 1 and 2.

SYMBOLS

C_{p_p} pitot pressure coefficient, $\frac{p - p_\infty}{q_\infty}$

L length

~~CONFIDENTIAL~~

~~CONFIDENTIAL~~

M	Mach number
p	pressure
q	dynamic pressure
R	nose radius
V	velocity
w	crossflow velocity
x,y,z	rectangular coordinates
α	angle of attack
η	distance normal from the body surface
ϕ	azimuth coordinate

Subscripts

0	zero order variable from solution of axisymmetric flow
1	first-order perturbation variable
∞	free stream

NUMERICAL METHODS

Four separate theoretical methods which yield flow-field results for axisymmetric bodies at angle of attack are investigated. The first theoretical method considered is a fully three-dimensional method of characteristics developed at Ames by John Rakich and as yet unpublished (fig. 1). It may be considered a standard upon which the other theoretical methods are compared. The second method is the linearized method of characteristics, an approximate method which has been used previously to obtain the first-order effects of angle of attack in the supersonic portion of flow over bodies of revolution. This method is similar to that used by Kopal and Sims (refs. 3 and 4) for the special case of pointed cones. In essence, the linear term of a power series in angle of attack α is added to the zero-angle-of-attack solution. The present results improve upon this by including second-order terms in the velocity relation in figure 1. The third method is an exact numerical solution for cones (ref. 5). This method fully accounts for the three-dimensional effects in contrast to the linearized method. The present results are an extrapolation of published tabulated values from $M = 7$ to 10.6. The fourth method is termed here, for purposes of discussion, the equivalent body method, which is similar in concept to the tangent-cone approximation. It applies the

~~CONFIDENTIAL~~

~~CONFIDENTIAL~~

method of characteristics to an axisymmetric body at zero angle of attack to simulate the flow in a plane about a similar shaped body at angle of attack. That is, the flow on the windward surface of a 15° cone at 5° angle of attack is approximated by the flow on a 20° cone at 0° angle of attack. Of course, this approximation neglects crossflow effects and is generally limited to the plane of flow symmetry.

EXPERIMENTAL COMPARISONS

Figure 2 shows a comparison between experimental pitot pressure data taken on the windward side of a 15° half-angle sharp cone at 10° angle of attack and the four theories discussed. Distance η is normalized by the x distance from the nose to the probing station. Data are shown normal to the body from the surface to the shock and were taken at two stations, $x/L = 0.27$ and 0.78 . The Mach number considered is 10.6 . Three of the theories, the three-dimensional (3-D) characteristics theory, the equivalent body method, and the Babenko method, agree well with data except very close to the body where there is a boundary layer. The linearized characteristics method provides a reasonable estimate but is about 15 percent high. The data from the two x/L stations are in agreement, confirming the essentially conical nature of the flow.

For the same conditions (fig. 3), the data for the leeward side of the cone appear to indicate a viscous separated region usually associated with vortex formation. Agreement, of course, cannot be expected here. However, away from this region limited comparisons between data and theories may be made. The exact 3-D characteristics method appears to give the correct level of pitot pressure; the Babenko method is a little high and the equivalent body method somewhat low. The linearized characteristics method did not give applicable results here.

Figure 4 shows the same comparisons again but at $\Phi = 90^\circ$. None of the theories agree exactly although two appear to give the correct shape with fair levels of pressure correlation. The exact 3-D characteristics method provides the best correlation, with the Babenko method a little high in magnitude. These two methods should give identical results since they both utilize exact equations; however, different numerical techniques are employed to produce the results. Possible differences with experiment may be accounted for by the boundary-layer displacement thickness. If theory were displaced by the height indicated by the data, correlation would be much improved. Neither the equivalent body nor the linearized characteristics method agrees except near the shock.

Now, consider a more complex flow field; data for the windward plane of a blunted 15° half-angle cone are compared in figure 5 with the theories. As in the previous figures, pitot pressure data are shown normal to the body from surface to shock. Data are shown at only one station, $x/R = 3.6$. The 3-D characteristics and the equivalent body methods both appear to give quite acceptable comparisons. The linearized characteristics method, although correct in shape, is inaccurate in pressure level. A modification to the

~~CONFIDENTIAL~~

linear characteristics method improves the level to an acceptable value. The modification was suggested by the observation that near a spherical nose the flow changes at angle of attack are due entirely to the rotation of the body within an axisymmetric shock. A linearized rotation is used in the standard method, and an exact rotation is used in the modified method. The modified method is limited primarily to regions near the nose where the body does not move a large distance compared to the shock layer.

The comparison is also shown on the leeward side of the blunt cone (fig. 6). Again, the 3-D characteristics and the equivalent body method agree well with data along with the modified linear characteristics. The basic linearized characteristics method does not correlate well here.

Figure 7 shows comparison for the plane at $\phi = 90^\circ$. All theories shown agree quite well here. It should be mentioned that the equivalent body method applied was the zero-angle-of-attack solution for the 15° cone. Although this method neglects crossflow, the agreement with data indicates that the contribution to pitot pressure from crossflow is small in this region near the nose. Again, since the agreement is quite good at the 90° plane where the crossflow velocity is maximum, it might be expected that the method would be applicable at any plane in this region. Farther downstream, however, the flow would approach the velocity over a pointed cone, the crossflow would become a larger component of velocity, and agreement would probably not be good, as for the pointed cone data in the previous figures. The linearized method shown here is, in effect, the same as the equivalent body method but the crossflow velocity is included. Again, this contribution to pitot pressure is negligible.

Initially, we set out to compare methods for predicting properties of the shock layer around hypersonic vehicles at angle of attack and have looked thus far at some basic shapes where exact theories and adequate experiments were available. The two approximate methods studied gave reasonable estimates in the windward plane of symmetry and, in some cases, for other planes.

As a final example we will compare these two approximate methods to data from wind-tunnel tests of the X-15 airplane. At present, exact calculations are not available. For the numerical calculations, the X-15 body was approximated by a sphere-ogive-cylinder. Its fineness ratio is about 10 compared to a fineness ratio of less than 4 for the conical bodies studied. The blunt nose created strong gradients which were difficult to resolve numerically, and special methods to handle entropy histories were necessary to perform the desired calculations. These numerical methods were also included in the equivalent body and linearized characteristics results previously shown on the blunted cone.

Figure 8 shows the pitot pressure distribution in the aft underside region of the X-15 at a station 145 nose radii from the tip. This is the region of interest for mounting a research scramjet propulsion system. The sketch shows the rather complex X-15 shape and the elements neglected when a body of revolution is used as an approximation for the shape. Although the approximation neglects many asymmetric protuberances, it was felt that their effect would be small in the aft windward region studied.

~~CONFIDENTIAL~~

The results from the equivalent body and linearized characteristics methods are shown in the figure, as well as wind-tunnel data for a 0.0667-scale model of the complete configuration. Comparisons are good for the linearized method of characteristics although not quite so good for the equivalent body method. It may be mentioned that at $\alpha = 0^\circ$ both methods reduce to the method of characteristics.

Figure 9 shows, for a particular application, the Mach number variation as predicted by the linearized characteristics method. It demonstrates that as angle of attack is increased from -3° to $+10^\circ$, the Mach number near the proposed research engine inlet face can be expected to decrease about two full Mach numbers.

CONCLUSIONS

For the sharp 15° cone, as figure 10 indicates, there is generally good agreement for the Babenko, the 3-D characteristics, and the equivalent body methods. This agreement breaks down on the leeward side because large viscous effects predominate. For the blunt 15° cone, the Babenko results are unavailable. The 3-D, the equivalent body, and the modified linearized characteristics methods all gave good correlation; the basic linearized characteristics method did not.

For the X-15 case the linearized characteristics agreed well, even at $\alpha = 10^\circ$. The equivalent body agreement was fair.

If one were to recommend regions where the various theories might be used, several conclusions might be drawn. First, in blunt-nose regions, with the associated large variations in entropy, the equivalent body and the modified linear characteristics methods appear quite attractive. The basic linearized characteristics method, because it is a linear method, does not account for the large nonlinear entropy gradients well. Second, for regions where there is a large shock layer and the body translates a small percentage of this shock layer height to angle of attack from its zero angle-of-attack position, the linearized characteristics method gave quite useful results. This condition is usually encountered with moderate fineness ratio bodies. There are tabulated results for the Babenko method only for pointed cones, and for this shape it gives generally good results. The 3-D method of characteristics should be generally applicable and, although more difficult to use, should give the best results.

~~CONFIDENTIAL~~

~~CONFIDENTIAL~~

REFERENCES

1. Gallo, William F.; and Rakich, John V.: Investigation of Methods for Predicting Flow in the Shock Layer Over Bodies at Small Angles of Attack. NASA TN D-3946, 1967.
2. Cleary, Joseph W.: Effects of Angle of Attack and Nose Bluntness on the Hypersonic Flow Over Cones. AIAA paper 66-414, 1966.
3. Sims, Joseph L.: Tables for Supersonic Flow Around Right Circular Cones at Zero Angle of Attack. NASA SP-3004, 1964.
4. Staff of the Computing Section, Center of Analysis (Under direction of Zdeněk Kopal): Tables of Supersonic Flow Around Yawing Cones. Tech. Rep. 3, M.I.T., Cambridge, Mass., 1947.
5. Babenko, K. I.; Voskresenskiy, G. P.; Lyabimov, A. N.; and Rusanov, V. V.: Three-Dimensional Flow of Ideal Gas Past Smooth Bodies. NASA TT F-380, 1966.

~~CONFIDENTIAL~~

CONFIDENTIAL

THEORETICAL METHODS

1. EXACT THREE-DIMENSIONAL METHOD OF CHARACTERISTICS
2. LINEARIZED METHOD OF CHARACTERISTICS
3. BABENKO TABULATED CONE SOLUTIONS
4. EQUIVALENT BODY

$$v^2 = (v_0 + \alpha v_1 \cos \phi)^2 + (\alpha w_1 \sin \phi)^2$$

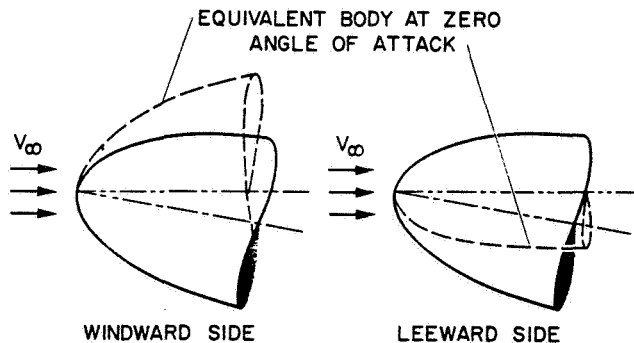


Figure 1

PITOT PRESSURE PROFILE 15° SHARP CONE $M_\infty = 10.6$ WINDWARD SIDE

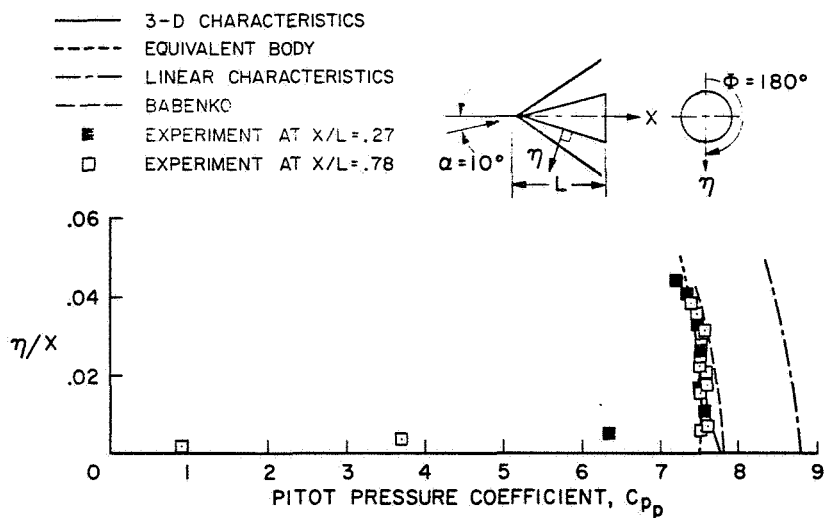


Figure 2

CONFIDENTIAL

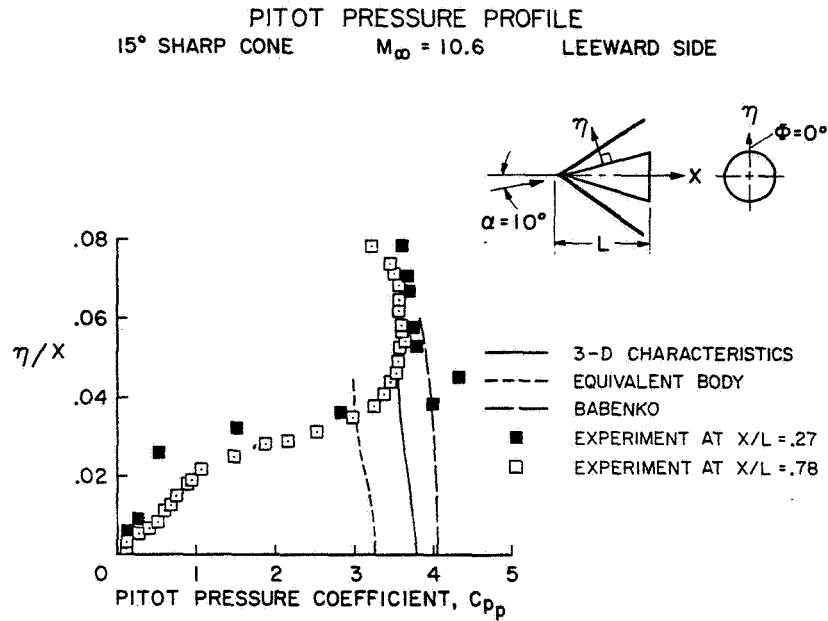


Figure 3

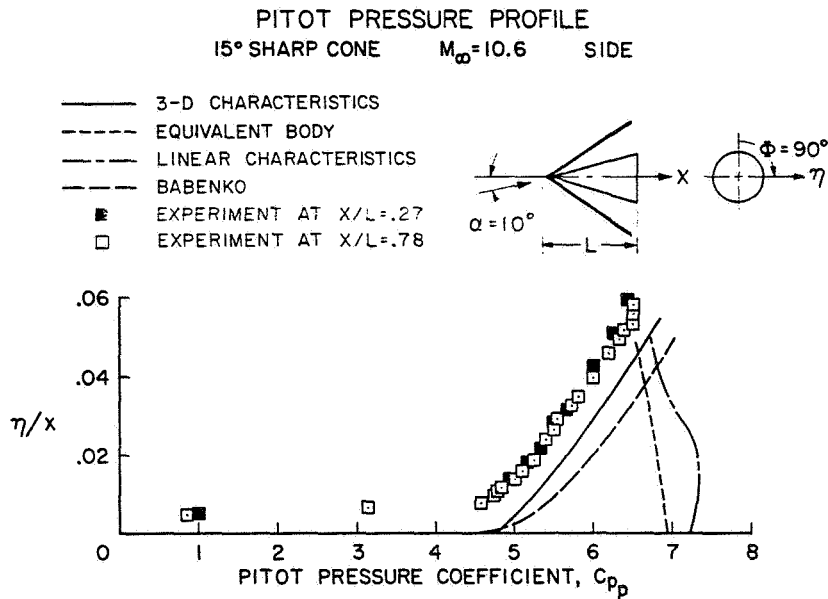


Figure 4

CONFIDENTIAL

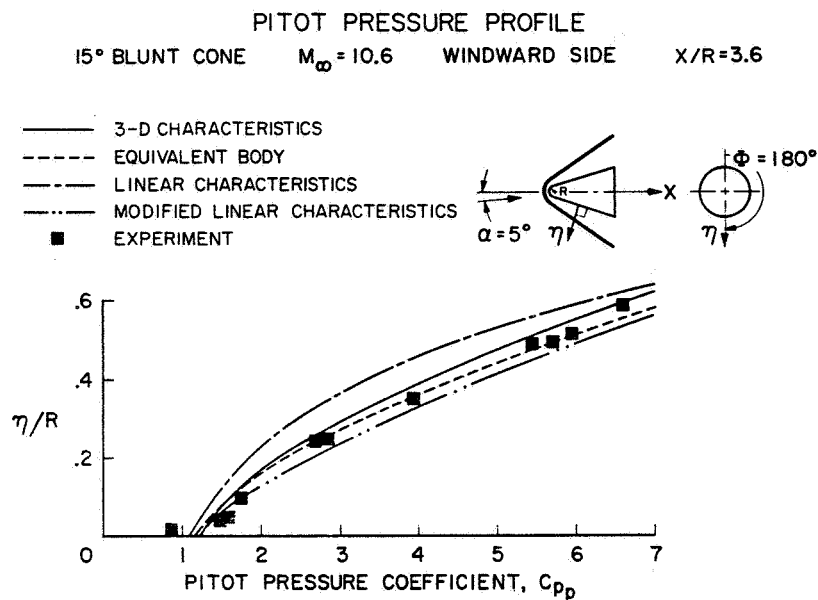


Figure 5

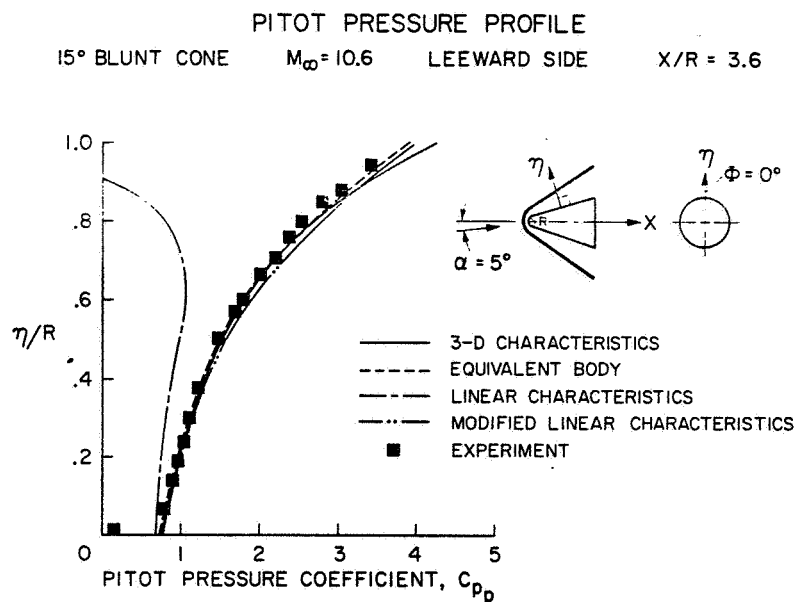
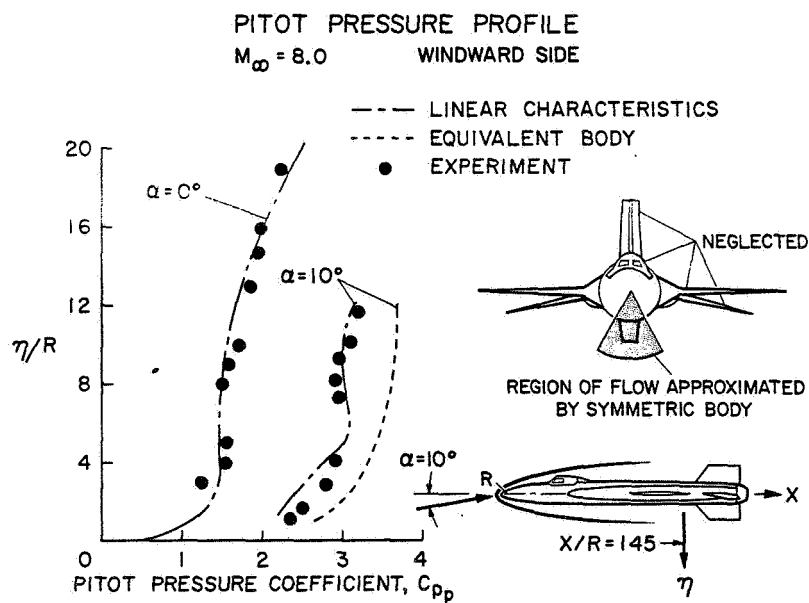
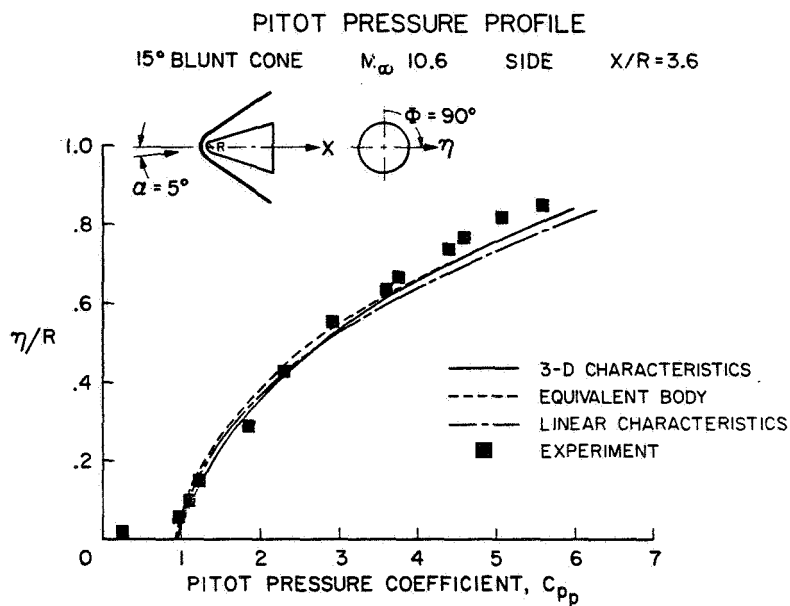


Figure 6

CONFIDENTIAL



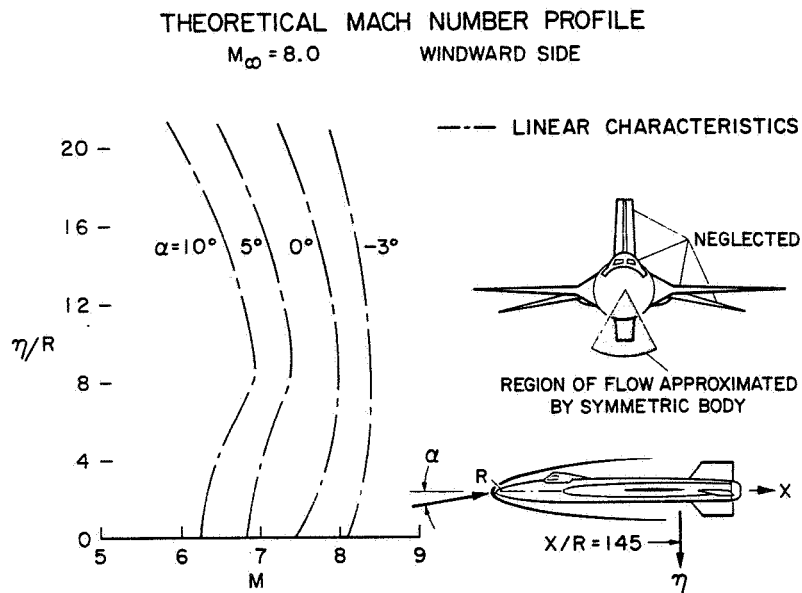


Figure 9

APPLICABILITY OF THEORIES

	BABENKO CONICAL	3 DIMENSIONAL CHARACTERISTICS	EQUIVALENT BODY	LINEARIZED CHARACTERISTICS	MODIFIED LINEAR
SHARP 15° CONE	GENERALLY GOOD	GENERALLY GOOD	FAIR	FAIR TO POOR	---
BLUNT 15° CONE $X/R \leq 4$	---	GOOD	GOOD	POOR	GOOD
SLENDER X-15 FINENESS RATIO ≈ 10	---	---	FAIR	GOOD	---

Figure 10

~~CONFIDENTIAL~~

9. STUDIES OF AIRFRAME—PROPULSION-SYSTEM INTEGRATION FOR MACH 6 CRUISE VEHICLES

By Frank S. Kirkham, James M. Cabbage, Jr., Walter A. Vahl,
and William J. Small
Langley Research Center

SUMMARY

An exploratory, experimental, and analytic investigation of airframe—propulsion-system integration has been conducted at a Mach number of 6. A two-pod nacelle configuration, a four-pod nacelle configuration, and a two-dimensional nacelle configuration with and without boundary-layer diverters were tested at a Reynolds number sufficient to produce a turbulent boundary layer on the wing ahead of the nacelles.

These preliminary results indicate no particular advantage of pod-type nacelles over two-dimensional designs and that the best over-all performance is obtained when the nacelle expansion area is no larger than the minimum required to enclose the turboramjet engines. A potential for significantly improving the lift-drag ratio of a configuration by utilizing the exhaust from underexpanded nozzles is also shown.

INTRODUCTION

One of the principal problems involved in the design of the hypersonic air-breathing aircraft is the efficient integration of the airframe and propulsion system. The engine airflow requirements for cruise-type aircraft designed to operate in the Mach 6 to 8 speed range are such that the inlet can be placed between the wing surface and wing-leading-edge shocks to take advantage of the high pressure airflow beneath the wing (fig. 1). At this speed, the area between the wing and shock system is large enough to permit considerable latitude in the shaping and placement of the engine nacelles (ref. 1). Some of the basic questions pertinent to this problem for Mach 6 cruise configurations are as follows:

What is the most effective exit-to-inlet area ratio for an engine housing?

Is a two-dimensional engine housing more efficient than pod-type nacelles?

Can any jet effects present be used to advantage?

The present exploratory study attempts to provide first answers to these questions, using simplified analytic and experimental models.

9

~~CONFIDENTIAL~~

SYMBOLS

A_e	nacelle exit area
A_i	nacelle inlet area
$A_{i,t}$	total inlet area of a specific configuration
ΔC_D	incremental drag coefficient, Drag of wing with nacelles minus Drag of wing without nacelles
ΔC_L	incremental lift coefficient, Lift of wing with nacelles minus Lift of wing without nacelles
C_f	local skin-friction coefficient
\bar{d}_i	inlet diameter (fig. 10)
h_c	height of boundary-layer diverter for two-dimensional nacelle (fig. 13)
h_i	height of inlet of two-dimensional nacelle (fig. 13)
I_{sp}	internal specific impulse, seconds
$(L/D)_{max}$	maximum lift-drag ratio
$(L/D)_o$	lift-drag ratio without jet effects
$(L/D)/(L/D)_o$	ratio of lift-drag ratio with jet effects to lift-drag ratio without jet effects
l_{strut}	length of pod support strut (fig. 10)
M_∞	free-stream Mach number
p_e	nozzle exit static pressure
p_l	static pressure under wing
R_l	local Reynolds number
S_w	wing planform area
α	angle of attack, degrees
ϵ	wing reflex angle, degrees (fig. 18)
θ	diverter wedge angle, degrees (fig. 13)

RESULTS AND DISCUSSION

Engine Nacelle Sizing Requirements

As a starting point, consider the size engine and inlet required for cruising flight at Mach 6. A representative thrust-drag schedule for the acceleration trajectory of a Mach 6 cruise vehicle is presented in figure 2. In-line subsonic combustion turboramjets are used with the transition from turbojet to ramjet operation occurring at approximately Mach 3. In determining the size of the propulsion system required, the turbojet thrust must be adequate to provide the minimum acceleration desired in the pinch regions occurring either during the subsonic climb which may be imposed due to sonic-boom consideration or during the transonic acceleration. The ramjet thrust and the inlet area required are usually tailored to the cruise conditions, provided that satisfactory performance can be obtained over the complete acceleration trajectory. Once the thrust requirements and hence the engine size have been determined, the minimum propulsion pod dimensions are established - that is, the pod inlet area and engine exhaust nozzle exit area.

A parametric variation of the ratio of nozzle-exit static pressure p_e to underwing static pressure p_1 is given as a function of nacelle expansion ratio A_e/A_1 in figure 3. These curves are generally applicable for subsonic combustion ramjets and are constant over a range of altitude provided that the maximum duct internal pressure limit is not exceeded. Also shown are the results from an in-house mission-analysis computer program which sizes the engine for a particular set of vehicle aerodynamics. The aerodynamics used herein were obtained from the study results of the distinct delta wing and blended wing-body cruise configurations described in reference 2. The sizes of both in-line and wrap-around turboramjet engines required are indicated by bars in the figure for an altitude of approximately 100 000 ft. The lengths of these bars indicate the variation obtained as the aircraft configuration was changed from the distinct wing-body concept with a wing loading of 76 lb/ft² ($\alpha \approx 7^\circ$) to a blended wing-body concept with a wing loading of 42 lb/ft² ($\alpha \approx 5^\circ$). The minimum nacelle expansion ratio required for the in-line engine is about 1.3. The wrap-around engine is somewhat larger and requires a nacelle expansion ratio of about 1.7. The nozzle exhausts are underexpanded ($p_e/p_1 > 1$) for both engine types and nacelle expansion ratios on the order of 2.5 would be required to achieve full expansion.

As shown in figure 4, about a 5-percent increase in internal specific impulse can be obtained by fully expanding the nozzle exhausts. If the nozzle flow can be expanded into the wing surface, this increased engine performance might be obtained with no penalty in aerodynamic drag. If, however, the frontal area of the nacelle must be enlarged to achieve full expansion, the increase in engine performance with increasing nacelle exit-to-inlet area ratio must be traded off against the attendant drag penalty of an enlarged nacelle.

Aerodynamic Characteristics

A wind-tunnel program to examine the aerodynamic characteristics of various nacelle configurations was initiated. The types of nacelles considered are shown in figure 5. Tests were conducted in the Langley 20-inch Mach 6 tunnel with a sharp leading-edge 70° sweep delta wing. (A description of the wind tunnel is given in ref. 3.) Flow-through nacelles with constant internal duct areas were used to simulate a two-pod nacelle configuration, a four-pod nacelle configuration, and a two-dimensional nacelle configuration. The total inlet area was 1.8 percent of the wing planform area for all configurations. Neither the inlet compression surfaces nor the correct nozzle exhaust flow were simulated in this investigation. The pod external contour was parabolic with a 14° initial angle at the lip. The distance between adjacent pod center lines was 2 inlet diameters and the pods were 5 diameters long for all pod configurations tested. The pods were placed longitudinally so that the outboard pods would be behind the wing shocks throughout the angle-of-attack range ($0^\circ \leq \alpha \leq 8^\circ$).

It was determined experimentally (ref. 4) that the boundary layer on the wing is fully turbulent in the hatched region shown in the sketches. The nacelles were tested in this region of fully turbulent wing boundary layer. The boundary layer on the two-dimensional and four-pod engine nacelles is believed to be transitional while a region of fully turbulent flow probably existed on the rearmost portion of the two-pod engine nacelles.

The importance of testing with turbulent boundary layers is illustrated in figure 6. The relative drag penalties of two-dimensional nacelles and pod nacelles are shown for both laminar and turbulent wing boundary layers. Tests conducted in the Langley 11-inch hypersonic tunnel at Mach 6.8 where the wing boundary layer was laminar indicate that the pod-nacelle installation has 50 percent more drag than the two-dimensional nacelle. Earlier results of this kind were interpreted as virtually ruling out the use of pods on hypersonic vehicles (ref. 1). However, tests at Mach 6 with turbulent wing boundary layers show the pods to have only a 20-percent drag penalty relative to the two-dimensional installation and this can probably be further reduced with refinements in design. Thus, by testing with the correct type of boundary layer, the pod nacelle is restored to a more competitive position relative to the two-dimensional design. The Reynolds number for the Mach 6 tests is still only 5 percent of the full-scale flight Reynolds number and, thus, additional scale effects may be expected.

The results obtained in the wind-tunnel program are presented in figures 7 to 16. For two-pod nacelles, the effect of increasing the nacelle expansion ratio is shown in figure 7. The oil-flow photograph shows that a strong interaction occurs between the nacelle shocks and the wing surface which produces significant interference forces on the wing and nacelles.

The increments in lift and drag obtained when the nacelles are added to the basic wing are shown as a function of α in figure 7. These data were obtained with a six-component strain-gage balance. All data are corrected for nacelle internal drag and for nacelle base drag. The internal drag correction was obtained by calculating the internal skin friction with the assumption of

a laminar boundary layer. The base pressure was corrected to free-stream static pressure by assuming that the base pressure coefficient in the wind-tunnel tests was equal to $1/M_\infty^2$.

The theoretical predictions, shown as dashed curves, consisted of an estimate of the external pressure and friction drag on the nacelles and their support struts plus an estimate of the forces on the wing in the interference region. The pressure forces on the pod nacelles were calculated by the method of characteristics for axisymmetric rotational flow. Shock-expansion theory was used on the support struts. The drag of all leading edges was obtained from Newtonian theory with a maximum pressure coefficient of 1.2. The interference pressures on the wing were obtained from the pressure distribution in the axisymmetric flow field in the plane of the wing. Skin friction on the nacelles was assumed laminar for calculation purposes and to follow the equation $C_f \sqrt{R_L} = 0.625$. The theory predicts the trends but not the magnitude of the experimental data.

The increments in lift and drag were used with the drag polar obtained from wind-tunnel tests of the delta-wing hypersonic cruise vehicle configuration described in reference 5 to obtain the effects of engine nacelle modifications on the maximum untrimmed lift-drag ratio for a practical cruise vehicle design. The results are shown in figure 8. Addition of two pods with an expansion ratio of 1.5 decreased the maximum L/D from about 4 to 3.8 while increasing the nacelle expansion ratio to 2 decreased maximum L/D to about 3.6.

The effect of changing the length of the pod support strut is shown in figure 9. At low angles of attack, the incremental lift ΔC_L is increased as pods are pulled closer to the wing surface but the incremental drag is unchanged. The drag is affected at the higher angles because the contribution of normal force to drag becomes significant. When these increments are applied to the delta-wing cruise configuration (fig. 10) only a slight benefit in $(L/D)_{\max}$ is obtained by decreasing the strut length because $(L/D)_{\max}$ occurs at about $\alpha = 8^\circ$. A higher performance configuration with $(L/D)_{\max}$ occurring at lower angles of attack ($\alpha \leq 4^\circ$) would benefit more from short pod support struts because additional lift could be obtained with no increase in drag. Thus, pod nacelles should be placed as close to the wing surface as is practical and perhaps merged into the wing surface.

A four-pod nacelle configuration is compared with the two-pod nacelle configuration in figure 11. The theory, contrary to the data, predicts a larger ΔC_L for the four-pod configuration than for the two-pod configuration. This discrepancy is possibly a result of the nacelles being placed farther forward from the wing trailing edge (relative to the length of the nacelle) for the four-pod configuration than the nacelles of the two-pod configuration. Both force and pressure tests to determine the effects of varying longitudinal placement of pod-type nacelles are needed to see whether significant changes in the aerodynamic forces occur. The theory does, however, predict an increase in drag as the number of pods is increased as would be expected since the wetted

area and leading-edge area increase as the number of pods increases. The effects of these increments on $(L/D)_{\max}$ are shown in figure 12.

The results of the investigation of a two-dimensional nacelle with an exit-to-inlet area ratio of 1.5 are shown in figures 13 to 15. The nacelle was tested with and without boundary-layer diverters. Without diverters, the nacelle was mounted flush with the wing surface and the wing boundary layer was allowed to flow through the nacelle. The lower surface of the nacelle was a circular-arc profile with an initial angle of 8.4° . The side plates were swept 75° with sharp leading edges and a 5° wedge angle.

Boundary-layer diverters may be used to avoid degrading engine performance due to ingesting the wing boundary layer. To simulate boundary-layer diverters, the two-dimensional nacelle was supported on two struts (fig. 13). The upper surface of the nacelle had a 5° wedge angle which diverted the wing boundary layer toward the wing surface. The center portion of the boundary layer flowed through a constant area duct between the wing and nacelle, whereas the outer portion was diverted toward the sides of the nacelles by the wedges on the diverters. The diverter height was sized such that the entire wing boundary layer in the wind-tunnel model would be diverted away from the inlet. On a flight vehicle the wing boundary layer would be relatively 60 percent as thick as in the wind tunnel and the diverter height could be correspondingly reduced. The curved shocks produced by the diverters (shown in the photograph) indicate that there is a complicated interaction between the wing, the diverter, and the nacelle which may be in part caused by choking in the diverter duct and boundary-layer separation.

The lift and drag increments for this configuration are shown in figure 14. The theoretical prediction of the forces on the lower surface of the nacelle was obtained by using two-dimensional shock-expansion theory with a correction for edge effects by the method of reference 6. The theoretical predictions of the effects of adding boundary-layer diverters were done by first finding the equivalent Mach number in the turbulent wing boundary layer at the forward face of the two-dimensional inlet (ref. 7). The flow was assumed inviscid aft of this point and the pressures were calculated by shock-expansion theory using the equivalent boundary-layer Mach number as a starting point. The skin friction in the diverter ducts was assumed turbulent and calculated by the T' method described in reference 8. The seemingly accurate predictions of lift and drag given in figure 14 are fortuitous since the axial force was underpredicted and the normal force overpredicted which tended to compensate each other when lift and drag were calculated.

The effect of these increments on $(L/D)_{\max}$ is shown in figure 15. The two-dimensional nacelle without boundary-layer diverters caused only a small loss in $(L/D)_{\max}$ in spite of the fact that the lower surface of the nacelle was contoured to give an exit-to-inlet area ratio of 1.5. When diverters are added, however, a significant penalty in $(L/D)_{\max}$ is incurred. This penalty is unchanged by reducing the diverter height by about 30 percent. Increasing the diverter wedge angle from 5° to 10° reduced $(L/D)_{\max}$ as expected.

A comparison of the various nacelle concepts is shown in figure 16. The best aerodynamic performance was obtained with the two-dimensional nacelle without boundary-layer diverters. The addition of boundary-layer diverters, however, decreased the performance of the two-dimensional nacelle to below that of the two-pod nacelle configuration. More carefully designed diverters would undoubtedly increase this performance level but the drag penalty for pod nacelle installations can also probably be reduced by proper integration of the pods and aircraft. Some of the pertinent variables for integrating pod nacelles with the aircraft at lower speeds ($M \approx 3$) are described in references 9 to 12. Since additional work to optimize both nacelle types is needed, no clear-cut choice between two-dimensional nacelles and pod nacelles can be made at this time.

The trade-off between the increase in engine performance against the decrease in aerodynamic performance as the nacelle expansion ratio is increased can now be examined. The pertinent parameter $(L/D)_{\max}(I_{sp})$ is shown on the right of figure 16. Assuming expansion of the nozzle flow into the wing surface and no increase in external drag, the two-dimensional nacelle without boundary-layer diverters can obtain a $2\frac{1}{2}$ percent gain in performance as A_e/A_1 is increased from 1.5 to 2. This increase is due solely to increasing I_{sp} and the degradation in engine performance due to boundary-layer ingestion has not been included for this configuration. This performance level would be reduced if boundary-layer ingestion effects were included. For the two-pod configuration, the increase in drag with increasing expansion ratio more than counterbalances the improvement in engine performance, and the best over-all performance is obtained with the low area ratio nacelle. Considering the small performance gains obtainable by additional nozzle expansion, it appears that the nozzle exits should not be enlarged beyond the minimum size required by the engine. If the nozzle exit areas are thus restricted, the nozzle exhaust flow will be underexpanded as was discussed in conjunction with figure 3. The flow from underexpanded nozzles may impinge on adjacent aircraft surfaces and produce jet interference forces on the aircraft. A preliminary estimate of the jet interference effects on the blended wing-body configuration has been made and is considered next.

Jet Interference Effects

The configuration shown in figure 17 is the blended wing-body concept. Further description of this configuration is given in reference 5. The nacelle housing the engines is 30 ft wide and the nozzle exits are 40 ft upstream of the wing trailing edge. If the nozzle exit pressure p_e is greater than the underwing static pressure p_1 the nozzle flow continues to expand along the surface of the wing creating an interference pressure field and a resulting force on the wing. In the flow model used to obtain a preliminary estimate of these forces, the flow was assumed to be two dimensional, the wing to be flat, and the pressure p_e to be constant along the wing surface to the point where the trailing expansion wave strikes the wing.

~~CONFIDENTIAL~~

An example jet effect calculation utilizing these assumptions is illustrated in figure 18 where the ratio L/D with jet effects to L/D without jet effects is plotted as a function of the wing reflex angle ϵ . Significant improvements in L/D can be achieved throughout the range of static-pressure ratios considered without reflexing the wing. Wing reflex has a small beneficial effect at the higher pressures but is detrimental at lower pressures. A discussion of the utilization of underexpanded exhausts from asymmetric nozzles is given in reference 13.

The effect of jet interference on L/D that might be obtained with realistic engines was determined through a range of cruise Mach numbers from 5 to 8, as shown in figures 19 and 20. In figure 19, the static-pressure ratios for both in-line and wrap-around turboramjet engines, as obtained by the methods discussed in conjunction with figure 3, are shown as a function of cruise Mach number. Both engine types have underexpanded nozzle exhausts throughout this Mach number range. The L/D improvements obtained by utilizing these exhaust overpressures range from 5 to 15 percent for the in-line engines and from 3 to 10 percent for the wrap-around engines (fig. 20). Some of the implications of these interference forces on aircraft stability are discussed in reference 5.

Although these L/D improvements were obtained from an idealized analytical flow model, it is apparent that significant improvement in L/D can probably be realized by proper utilization of the exhausts of underexpanded nozzles. Because of the extreme complexity of the exhaust flow field, a more realistic assessment of these effects must be obtained through experimental tests.

CONCLUDING REMARKS

These exploratory studies of airframe—propulsion-system integration at Mach 6 have revealed that underexpanded nozzles, whose exit areas are no larger than the maximum area required by the engine, appear to produce better over-all performance than fully expanded nozzles. Preliminary calculations indicate that underexpanded nozzles exhausting well ahead of the wing trailing edge have a significant potential for increasing the lift-drag ratio. These jet exhaust effects, however, require detailed experimental verification.

In regard to nacelle type, these preliminary results indicated no particular advantage of two-dimensional designs over individual pods.

The important interference effects of the nacelles on both lift and drag at hypersonic speeds were in general not predicted accurately by the simple analytic techniques currently in use.

CONFIDENTIAL

REFERENCES

1. Fetterman, David E.; McLellan, Charles H.; Jackson, L. Robert; Henry, Beverly Z., Jr.; and Henry, John R.: A Review of Hypersonic Cruise Vehicles. NASA TM X-1276, 1966.
2. Drake, Hubert M.; Gregory, Thomas J.; and Petersen, Richard H.: Hypersonic Technology Problems Identified in Mission Studies. Conference on Hypersonic Aircraft Technology, NASA SP-148, 1967. (Paper No. 1 herein.)
3. Sterrett, James R.; and Emery, James C.: Extension of Boundary-Layer-Separation Criteria to a Mach Number of 6.5 by Utilizing Flat Plates With Forward-Facing Steps. NASA TN D-618, 1960.
4. Sterrett, James R.; Morrisette, E. Leon; Whitehead, Allen H., Jr.; and Hicks, Raymond M.: Transition Fixing for Hypersonic Flow. Conference on Hypersonic Aircraft Technology, NASA SP-148, 1967. (Paper No. 15 herein.)
5. Penland, Jim A.; Edwards, Clyde L. W.; Witcofski, Robert D.; and Marcum, Don C., Jr.: Comparative Aerodynamic Study of Two Hypersonic Cruise Aircraft Configurations Derived From Trade-Off Studies. Conference on Hypersonic Aircraft Technology, NASA SP-148, 1967. (Paper No. 4 herein.)
6. Liepmann, H. W.; and Roshko, A.: Elements of Gasdynamics. John Wiley & Sons, Inc., c.1957.
7. Pinckney, S. Z.: Semiempirical Method for Predicting Effects of Incident-Reflecting Shocks on the Turbulent Boundary Layer. NASA TN D-3029, 1965.
8. Peterson, John B., Jr.: A Comparison of Experimental and Theoretical Results for the Compressible Turbulent-Boundary-Layer Skin Friction With Zero Pressure Gradient. NASA TN D-1795, 1963.
9. Nichols, Mark R.: Aerodynamics of Airframe-Engine Integration of Supersonic Aircraft. NASA TN D-3390, 1966.
10. Swan, Walter C.: A Discussion of Selected Aerodynamic Problems on Integration of Propulsion Systems With Airframe on Transport Aircraft. Aerodynamics of Power Plant Installation, Part 1, AGARDograph 103, Oct. 1965, pp. 23-68.
11. Robins, A. Warner; Morris, Odell A.; and Harris, Roy V., Jr.: Recent Research Results in the Aerodynamics of Supersonic Vehicles. J. Aircraft, vol. 3, no. 6, Nov.-Dec. 1966, pp. 573-577.
12. Landrum, Emma Jean: Effect of Nacelle Orientation on the Aerodynamic Characteristics of an Arrow Wing-Body Configuration at Mach Number 2.03. NASA TN D-3284, 1966.

CONFIDENTIAL

- ~~CONFIDENTIAL~~
13. Lewis, W. G. E.; Herd, R. J.; and Herbert, M. V.: Lift Characteristics of Asymmetric Exhaust Nozzles at High Flight Speeds. J. Roy. Aeron. Soc. (Tech. Notes), vol. 70, no. 671, Nov. 1966, pp. 1036-1040.

MACH 6 CRUISE CONFIGURATION

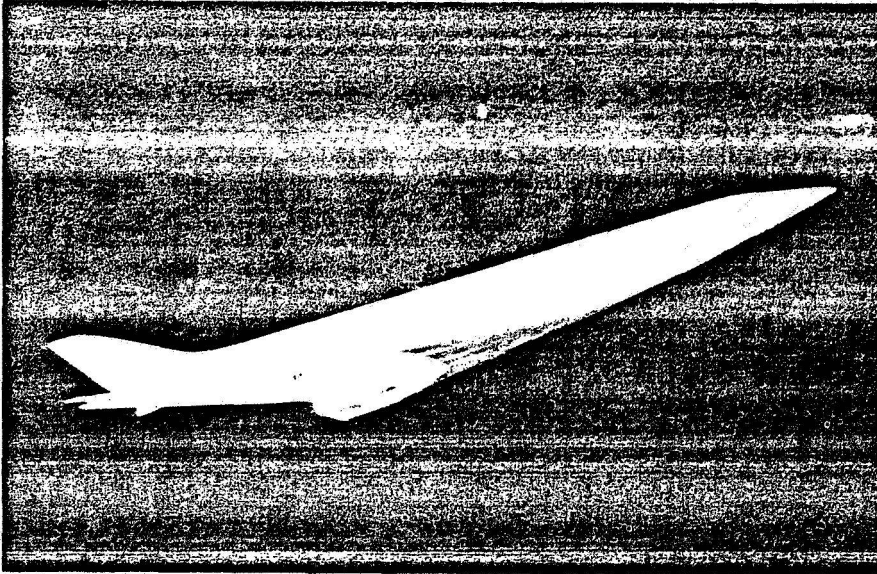


Figure 1

L-2871-19

TYPICAL THRUST-DRAG SCHEDULE IN-LINE TURBORAMJET

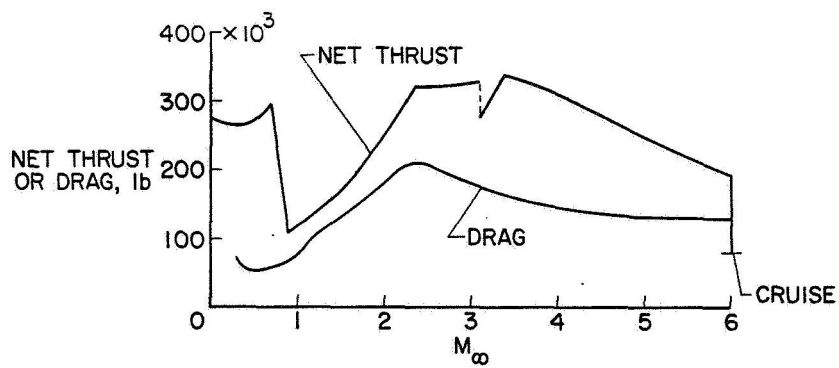


Figure 2

~~CONFIDENTIAL~~

NOZZLE-EXIT STATIC-PRESSURE RATIOS AT $M_\infty=6$

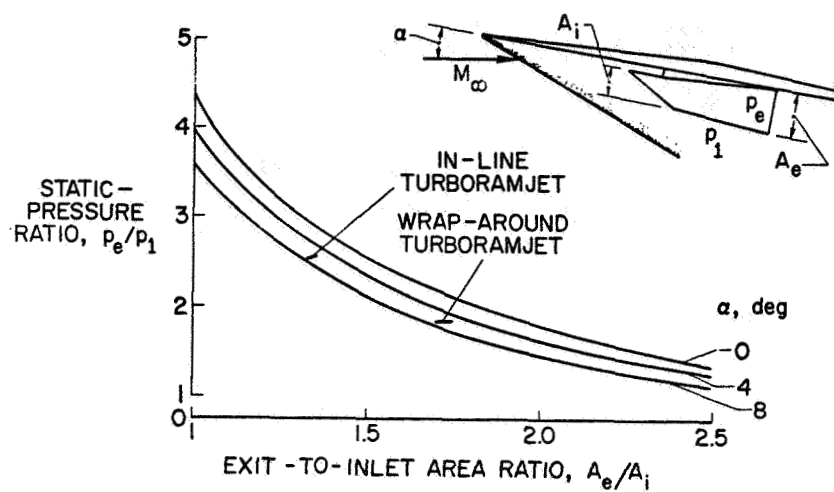


Figure 3

RAMJET SPECIFIC IMPULSE $M_\infty=6$

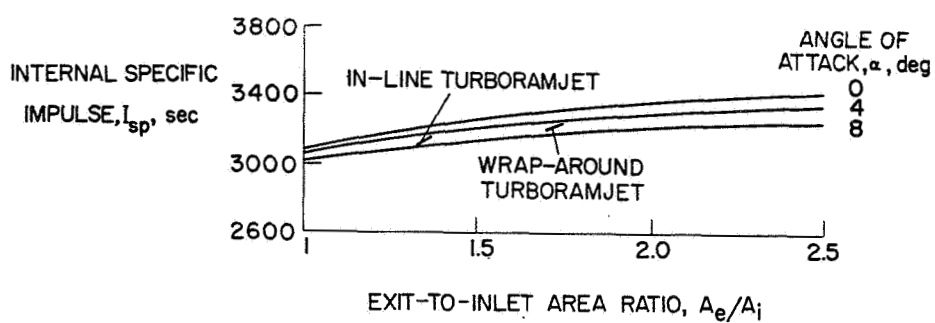


Figure 4

NACELLE CONFIGURATIONS INVESTIGATED

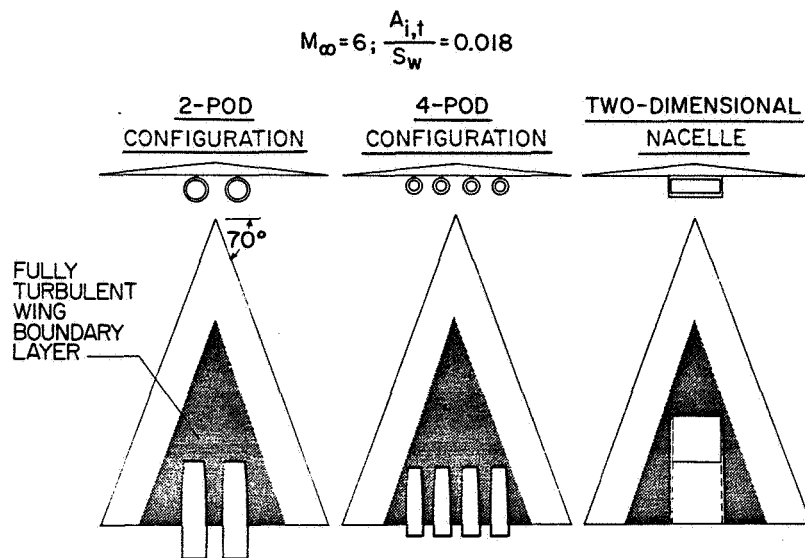


Figure 5

COMPARISON OF NACELLE DRAG IN LAMINAR AND TURBULENT FLOW

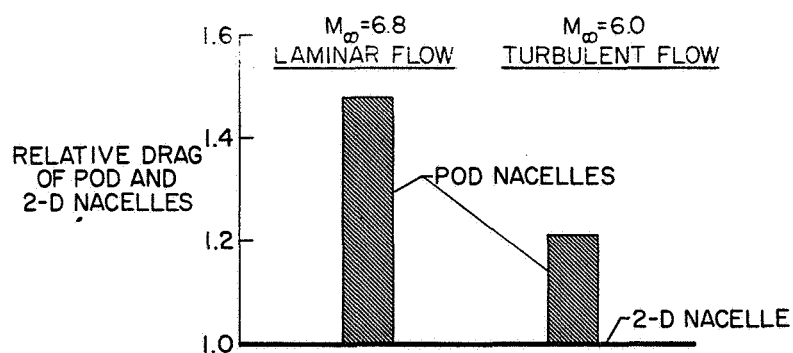


Figure 6

EFFECT OF A_e/A_i
2-POD NACELLES ; $M_\infty = 6$; $l_{\text{strut}}/d_i = 0.250$

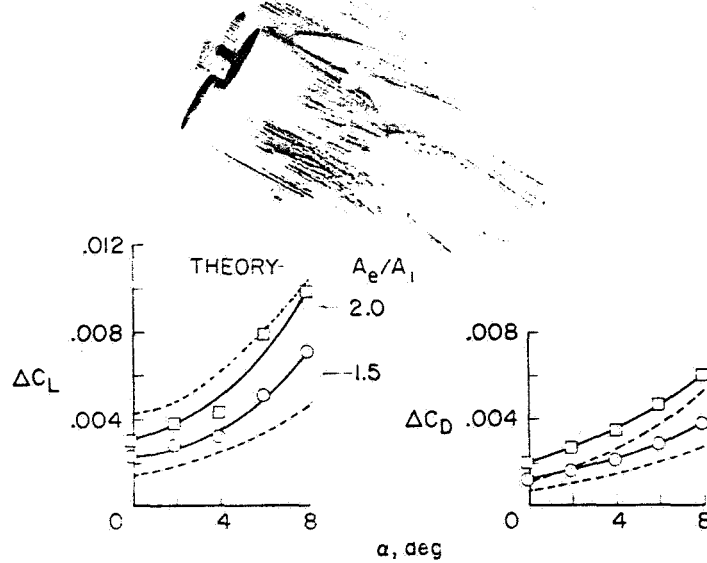


Figure 7

L-2871-4

EFFECT OF A_e/A_i ON UNTRIMMED $(\frac{L}{D})_{\text{max}}$
2-POD NACELLES; $M_\infty = 6$; $\frac{l_{\text{strut}}}{d_i} = 0.250$

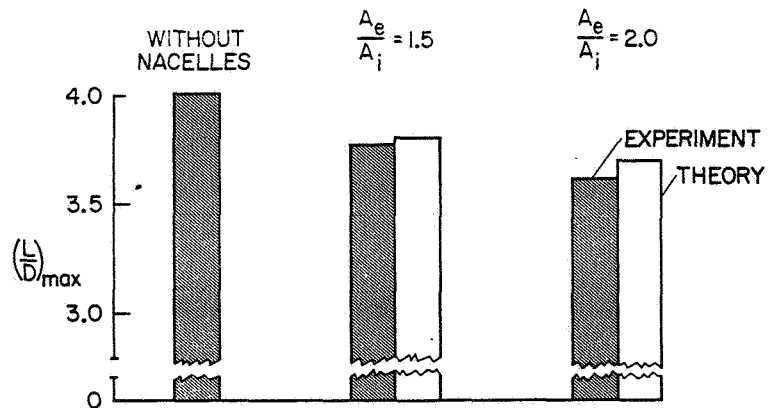


Figure 8

EFFECT OF STRUT LENGTH 2-POD NACELLES; $M_\infty=6$; $A_e/A_i=1.5$

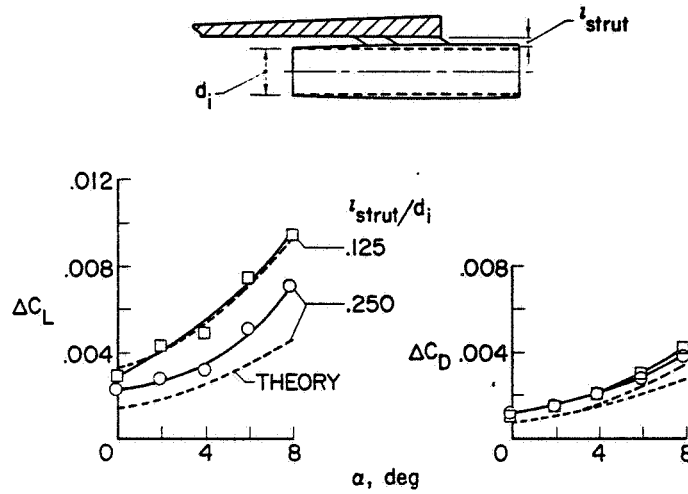


Figure 9

EFFECT OF STRUT LENGTH ON UNTRIMMED $(\frac{L}{D})_{max}$ 2-POD NACELLES; $M_\infty=6$; $A_e/A_i=1.5$

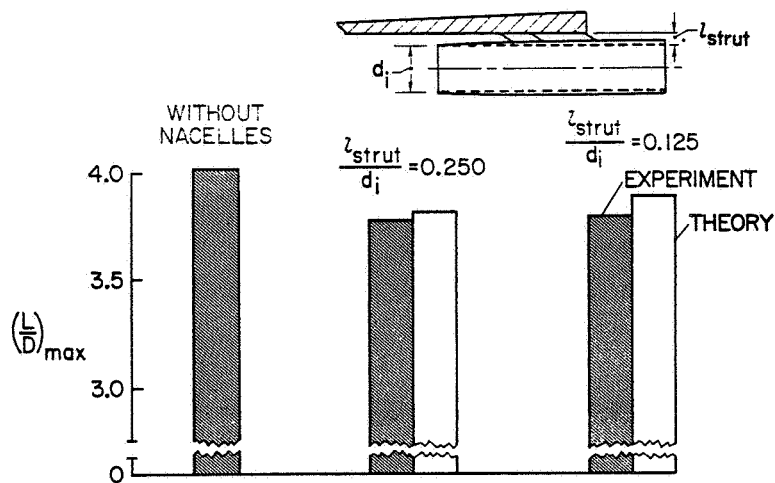


Figure 10

EFFECT OF NUMBER OF PODS

$M_\infty = 6$; $A_e/A_i = 1.5$; $l_{\text{strut}}/d_i = 0.250$

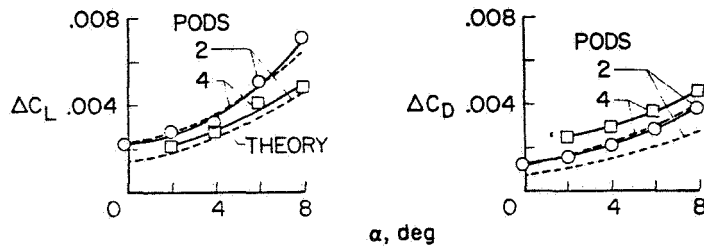


Figure 11

L-2871-8

EFFECT OF NUMBER OF PODS ON UNTRIMMED $(\frac{L}{D})_{\text{max}}$

$M_\infty = 6$; $A_e/A_i = 1.5$; $\frac{l_{\text{strut}}}{d_i} = 0.250$

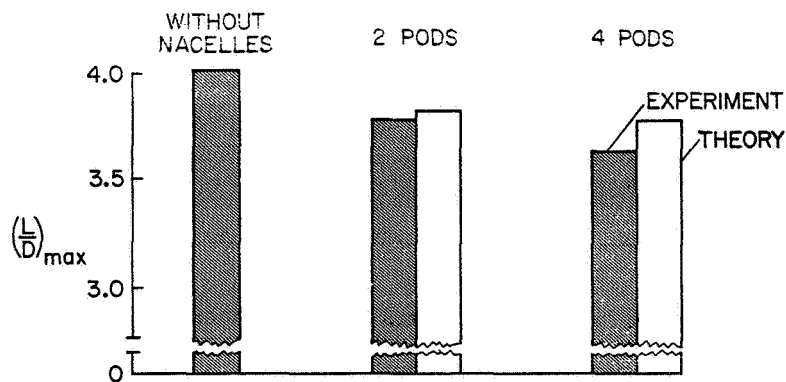


Figure 12

~~CONFIDENTIAL~~

TWO-DIMENSIONAL NACELLE WITH
FLOW-THROUGH DIVERTER

$$A_e/A_i = 1.5$$

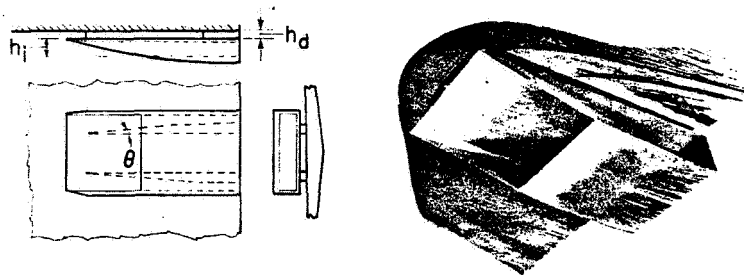


Figure 13

L-2871-10

~~CONFIDENTIAL~~

EFFECT OF 2-DIMENSIONAL NACELLE ON LIFT AND DRAG

 $M_\infty = 6$ $A_e/A_i = 1.5$

DATA	THEORY	TYPE DIVERter
○	---	WITHOUT DIVERter
□	---	$\theta = 5^\circ$ $h_d/h_i = 0.29$
◇	---	$\theta = 5^\circ$ $h_d/h_i = 0.17$
△	---	$\theta = 10^\circ$ $h_d/h_i = 0.29$

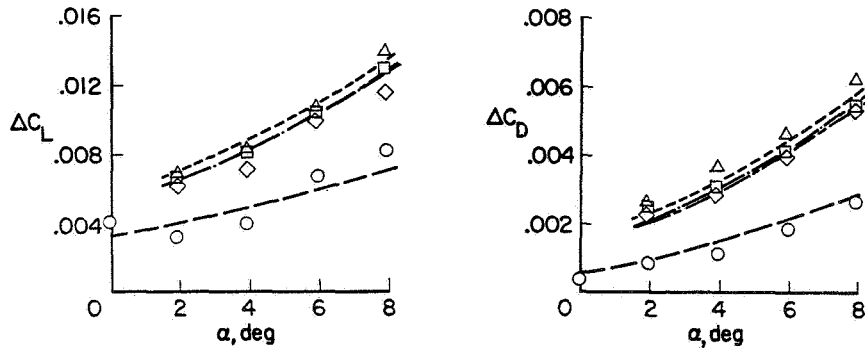


Figure 14

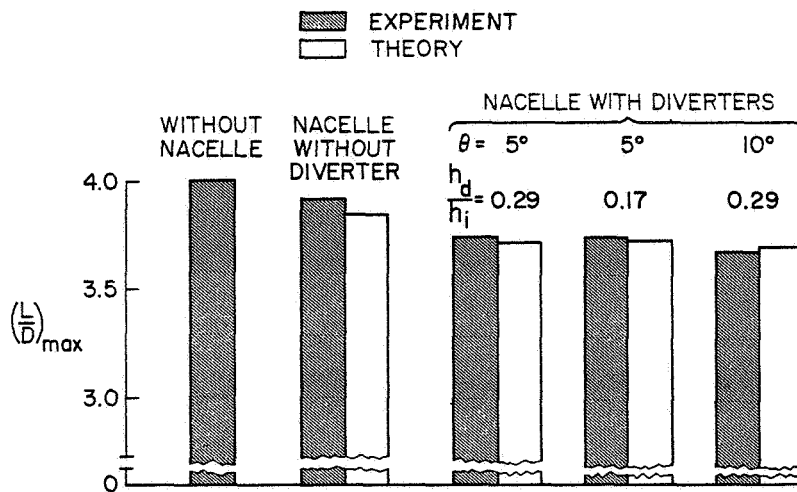
EFFECT OF 2-DIMENSIONAL NACELLES ON UNTRIMMED $(\frac{L}{D})_{\max}$ $M_\infty = 6$; $A_e/A_i = 1.5$ 

Figure 15

SUMMARY OF 2-DIMENSIONAL AND POD NACELLE PERFORMANCE

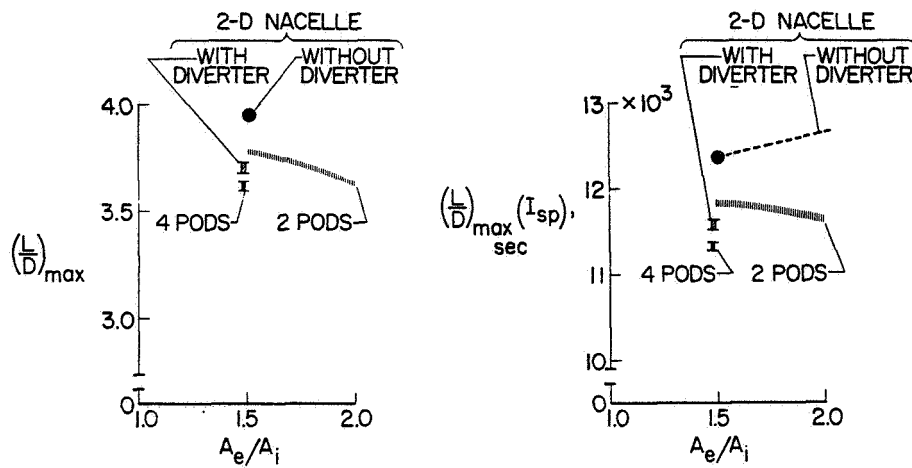


Figure 16

JET-INTERFERENCE FLOW MODEL

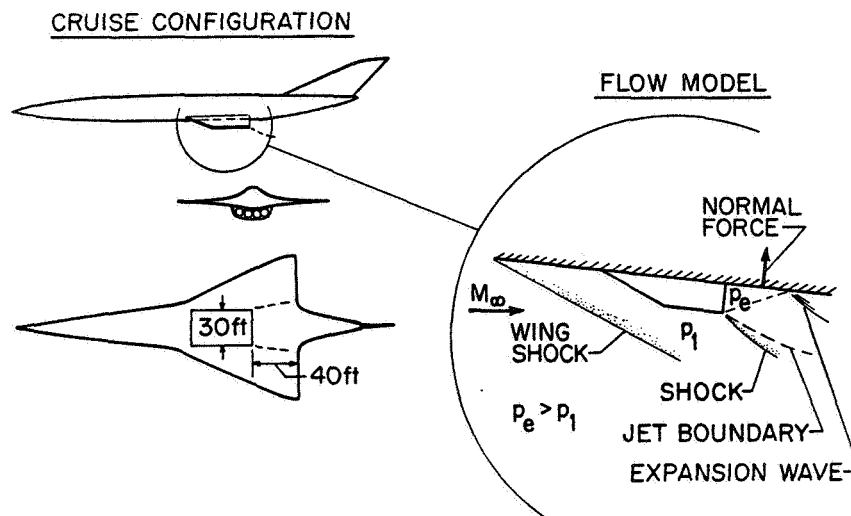


Figure 17

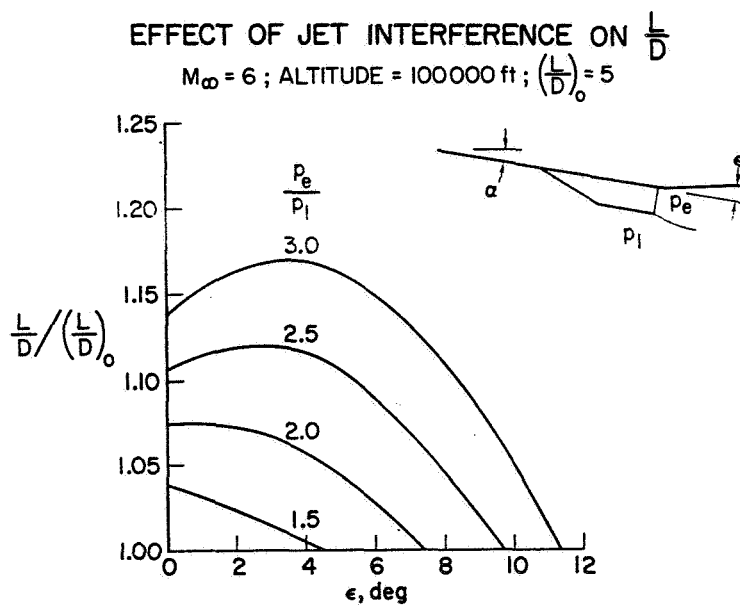


Figure 18

NOZZLE-EXIT STATIC-PRESSURE RATIOS AT CRUISE

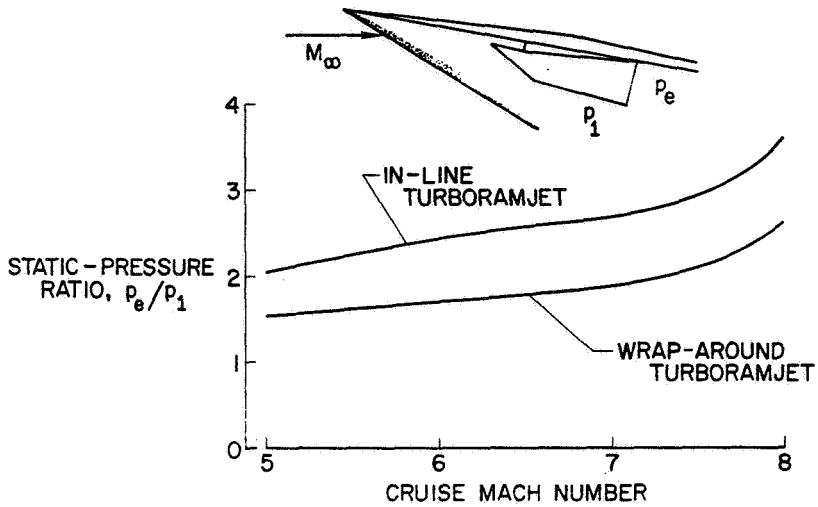


Figure 19

$\frac{L}{D}$ IMPROVEMENT DUE TO ENGINE-EXHAUST-WING INTERFERENCE

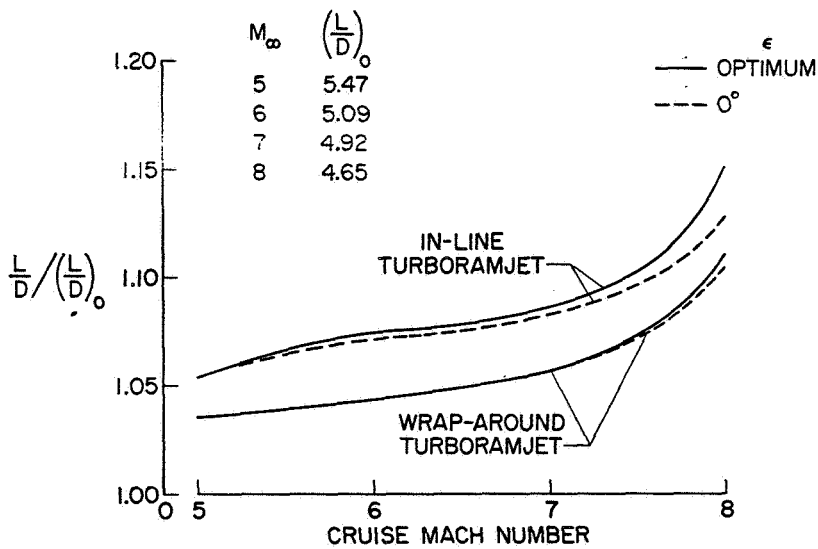


Figure 20

~~CONFIDENTIAL~~

10. SCRAMJET VEHICLE ENGINE-AIRFRAME INTEGRATION EFFECTS

By Louis J. Williams and Darrell E. Wilcox

NASA Headquarters
Mission Analysis Division
Moffett Field, Calif.

SUMMARY

A digital computer program was used to analyze the effects of engine-airframe integration on the cruise performance of a Mach 12 scramjet-powered aircraft. Parametric shape variations of an all-body configuration were made to determine the extent to which use of the vehicle afterbody as a nozzle expansion surface may lead to increased vehicle performance. Results are presented in the form of the cruise Breguet factor and a coefficient of integration. The term "coefficient of integration" is introduced to illustrate the effectiveness of integration. Also presented are the effects of engine-airframe integration on the vehicle stability characteristics and on vehicle surface temperatures.

INTRODUCTION

Hypersonic aircraft powered by hydrogen fueled scramjet propulsion systems have shown potentially high performance for both cruise and boost missions. A characteristic of these aircraft is a large-volume fuselage required for the low-density hydrogen fuel. Attempts to optimize these configurations have resulted in various degrees of wing and fuselage blending. Resulting configurations range from the distinct wing-body vehicle to the all-body vehicle shown in figure 1. An important characteristic of the all-body configuration is the possibility of using the underside of the airframe as inlet compression and nozzle expansion surfaces for the scramjet propulsion system. Such extensive integration of airframe and propulsion system results in vehicle performance in which the engine and airframe performance are no longer separable. The objective of the present study was to determine the extent to which this engine-airframe integration may improve vehicle performance in the cruise mode. To accomplish this objective two performance parameters were used. The actual cruise performance of the integrated vehicle was measured by the Breguet factor (BF) which includes all the effects of integration, such as underexpanded nozzle flow and propulsive lift due to thrust deflection.

To measure the efficiency of the engine-airframe integration for a given configuration, this paper introduces the term "coefficient of integration (C_I).". The term relates the integrated vehicle performance as measured by the actual cruise Breguet factor to an ideal Breguet factor obtained from the separate performance of the engine and airframe as defined by uninstalled I_{sp} and L/D .

~~CONFIDENTIAL~~

Data presented in this paper show the effect on the Breguet factor and coefficient of integration of changes in vehicle shape, angle of attack, and engine efficiency for a cruise Mach number of 12. The factors influencing the effectiveness of engine-airframe integration are briefly discussed. Also included is the effect of integration on the vehicle longitudinal stability characteristics and vehicle surface temperatures.

METHOD OF ANALYSIS

The basic approach used in this study was to select a simply defined all-body configuration and vary its major shape parameters to determine their effect on component and vehicle performance. The nominal configuration studied is shown in figure 2. The body has a delta planform with an elliptical cone forebody and an elliptical cross-section afterbody making a smooth transition from the break-point cross section to a straight-line trailing edge. The shape of this body can be varied by specifying three independent parameters: (1) the position of the break point between the forebody and afterbody, specified as a ratio of the forebody length to the total body length, l_{π}/l , (2) the sweepback of the leading edge, Λ , and (3) the fatness ratio, specified as the ratio of the maximum cross-sectional area to the total planform area, S_{π}/S . For l_{π}/l greater than 0.5 the position of maximum cross-sectional area and break point coincide. The parameter fatness ratio was chosen so that the effect of changing sweep and break-point length ratio would not be dominated by a change in the frontal area. Hence, for constant fatness ratio the forebody ellipse ratio will vary with the break-point length ratio and sweep. The nominal values of these parameters are also shown in figure 2.

All parametric studies were done at a cruise Mach number of 12 with a fixed gross take-off weight and body volume. The control surfaces shown in figure 2 were sized for hypersonic stability. The scramjet propulsion system is shown in this figure and was allowed to extend over 80 percent of the body span at the break point.

The results of this study were calculated by an integrated computer program which computes the vehicle geometry, aerodynamic characteristics, propulsion system performance and sizing, fuel consumption, cruise altitude, and angle of attack. This program properly accounted for all effects of parametric changes in a variable. A typical Mach 12 cruise force diagram calculated by this program is shown in figure 3. The importance of proper airframe-engine integration is evidenced by the relatively small lift and drag vectors of the airframe compared to the large ram drag and gross thrust vectors. The ram drag shown is the combined momentum and pressure force of the flow at the inlet entrance. The gross thrust is the combined momentum and pressure force of the flow at the nozzle exit. A small deflection of the gross thrust angle, θ_T , as shown in the figure can cause large changes in vehicle performance.

~~CONFIDENTIAL~~

Aerodynamics

Estimates of the basic vehicle aerodynamics for the all-body configuration were based on nonlinear lift and induced drag relations similar to those for a delta wing (ref. 1). These relations were checked with experimental data (ref. 2) for elliptic cones and found to agree well. The zero-lift drag was calculated from a pressure and skin-friction-coefficient distribution on the body. The pressure distribution on the forebody was obtained from the second-order elliptic cone expressions of Van Dyke (ref. 3) where applicable, and Newtonian theory for the lower sweep angles. The afterbody pressure distributions were estimated by assuming a Prandtl-Meyer expansion of the flow field at the body break point. From these pressure distributions the turbulent skin friction was calculated using the reference enthalpy technique (ref. 4) for the local skin-friction coefficients. The bluntness drag resulting from the necessary rounding of the nose and the fin leading edges was also included in the zero-lift drag. The radii used were calculated for a specified radiation equilibrium temperature at a design Mach number and altitude.

Body temperature profiles were obtained from the same reference enthalpy technique used in the skin-friction calculations. The variation in temperature with gross thrust deflection angle was estimated on the forebody lower surface from calculations based on a wedge with the same included body angle and lift loading.

The fin sizes were estimated for hypersonic stability and a canard was felt necessary for trim and landing. No penalty was assessed for trim drag, but the skin friction and minimum wave drag of the fin surfaces have been included in the drag estimation.

Propulsion

The scramjet performance was based on a one-dimensional cycle analysis of the inlet and combustor, and a two-dimensional analysis of a nozzle integrated with the vehicle afterbody. The nominal inlet characteristics included a process efficiency of 0.90 and a geometric contraction ratio of 8.3. The inlet diffusion and vehicle flow field effects were computed separately, so that the indicated contraction ratio specifies compression of the airstream in addition to that due to the vehicle bow shock. The process efficiency used corresponds to an η_{KE} value of 0.98 at Mach 12.

The combustor calculation was based on a real-gas analysis of the working fluid thermodynamic properties. The effects of added momentum of the injected fuel stream were included in the analysis, and a constant pressure combustion process was assumed. The engine flow was considered to be adiabatic, so the total temperature of the injected fuel was zero. The fuel-to-air ratio was variable, and a combustor efficiency of 0.95 was input to specify the fraction of the fuel which was effectively burned.

~~CONFIDENTIAL~~

~~CONFIDENTIAL~~

The nozzle performance was computed for the configuration shown in figure 4. This nozzle utilizes two-dimensional Prandtl-Meyer expansions with an internal expansion turning the flow up against the afterbody and an external expansion over the afterbody. The cowl and afterbody are shaped so that there are no wave reflections. The amount of internal and external expansion is uniquely determined for a given afterbody length and depth. The resulting gross thrust is measured by combining the momentum and pressure forces across the final expansion ray extending from the end of the cowl to the vehicle trailing edge. Using this nozzle configuration may result in higher or lower performance than that of a one-dimensional complete expansion nozzle. This is demonstrated in figure 5 which compares an underexpanded two-dimensional nozzle to a complete expansion nozzle. The momentum force of the two-dimensional nozzle is reduced by the underexpansion. However, the deflection of the pressure force may yield a gross thrust vector which is longer in scalar magnitude than that of the complete expansion momentum force. This is denoted by λ_{ND} which is the ratio of the gross thrust (two-dimensionally) to the gross thrust of the completely expanded one-dimensional nozzle. Figure 5 demonstrates a particular case when λ_{ND} can be greater than 1. A variable nozzle efficiency, defined as the ratio of actual-to-ideal gross thrust, introduces viscous and divergence losses into the thrust equations. A nominal nozzle efficiency of 1.0, based on chemically frozen flow, was used throughout this study.

Because of the uncertainty associated with scramjet efficiency, parametric variations of component performance were made to obtain sensitivity data. The effects of inlet efficiency, combustor efficiency, nozzle efficiency, and inlet contraction ratio were determined for the nominal Mach 12 cruise vehicle.

Coefficient of Integration

To measure the degree to which a configuration represents an efficient integration of the airframe and engine, the term coefficient of integration is introduced. The definition of this parameter is outlined in figure 6. Coefficient of integration is defined as the ratio of the actual cruise Breguet factor of the completely integrated vehicle to an ideal Breguet factor. The ideal Breguet factor is defined by the conventional Breguet factor equation derived when the engine and airframe performance were considered separately and there was no thrust deflection. The component performances used in this equation are the lift-drag ratio of the clean airframe without the engine attached and the specific impulse of the uninstalled scramjet propulsion system. This I_{sp} is calculated for a nozzle which is fully expanded to cruise ambient pressure.

The actual Breguet factor is calculated by a computer program which balances the vehicle forces in cruise and determines the fuel flow required. The meaning of Breguet factor as a measure of cruise efficiency can best be understood as representing the weight carried times the distance carried divided by the fuel expended in the process. Instantaneously, this Breguet factor can be calculated as the vehicle weight times the velocity divided by the fuel flow rate.

CONFIDENTIAL

The coefficient of integration is of interest because it allows the actual Breguet factor to be estimated from the uninstalled component performances. The actual Breguet factor can be obtained by combining the separate engine and airframe performances in the ideal Breguet factor and multiplying by the appropriate coefficient of integration. The coefficient of integration embodies all the interactions and geometric constraints that occur in the integration of the scramjet engine and all-body configuration. For example, a low value of C_I may reflect underexpanded nozzle flow when the underside of the afterbody does not lend itself to an efficient nozzle configuration. Similarly, a high value of C_I may represent the benefit of thrust deflection in obtaining high cruise performance.

RESULTS

Performance

Figure 7 shows the effect of the break-point length ratio on the vehicle performance parameters. The ticks denote the nominal configuration value and the sketches serve as reference to the vehicle profile. Increasing break-point length ratio, which corresponds to increasing forebody length relative to the overall body length, causes the lift-to-drag ratio to increase as a result of decreasing forebody wave drag. At the higher Mach numbers, such as the $M = 12$ cruise condition, the forebody wave drag is the dominant part of the vehicle zero-lift drag with the afterbody base drag becoming more important at the lower Mach numbers. The Breguet factor shows a trade-off at the higher values of break-point length ratio between increasing lift-drag ratio and decreasing coefficient of integration. This change in coefficient of integration with break-point length ratios is the result of changing nozzle performance.

The relationship between nozzle performance and break-point length ratio is shown in figure 8. Because the flow is underexpanded, the key parameter influencing the nozzle performance is the expansion area ratio. The expansion area ratio of the nozzle is denoted by A_E/A_C which is the ratio of the stream area at the nozzle exit to the combustor exit area. This exit area is determined by θ_V , the velocity deflection at the exit of the nozzle with respect to the horizontal reference line of the fuselage. It can be seen from the sketch of the vehicle afterbody that for upward velocity deflection, the exit area is decreased since it is measured perpendicular to the exit velocity vector. Hence, the expansion area ratio is reduced for the large upward velocity deflections occurring at the higher break-point length ratios where the shorter afterbody length limits the amount of expansion.

The effect of the vehicle sweep is shown in figure 9. The lift-to-drag ratio increases with increasing sweep because of the decreasing forebody wave drag, while the coefficient of integration increases because of higher nozzle expansion area ratios. This higher nozzle performance is primarily due to increased afterbody length which allows more turning of the flow and, hence, more expansion. The increased afterbody length with increasing sweep is due to the constant vehicle volume constraint.

CONFIDENTIAL

Figure 10 shows the effect of vehicle fatness ratio (the ratio of the vehicle cross-sectional area at the break point to the total vehicle planform area). For the higher values of fatness ratio the vehicle has more frontal area for the same planform area and, consequently, a lower L/D . Although the fatter vehicles have a greater base area available for expansion, the use of this area is limited by the reduced afterbody length. The result is a slight reduction in C_I which, in combination with the reduced L/D , results in lower Breguet factors at the higher values of fatness ratio.

Although figure 10 indicates that Breguet factors as high as 25,000 n.mi. may be possible with slender vehicles, the actual gains for lower values of fatness ratio are limited by increased structural weight. For this reason a nominal value for fatness ratio of 0.0935 was used in this study.

Figure 11 illustrates the effect of vehicle angle of attack, presented as the ratio to the angle for maximum L/D . The Breguet factor shows the trade-off between the decreasing lift-to-drag ratio and the increasing coefficient of integration with decreasing angle of attack. At reduced angles of attack the coefficient of integration is based on a lift-to-drag ratio reduced from $(L/D)_{max}$ in the computation of both ideal and actual Breguet factor. For the preselected nominal vehicle, this figure shows that the maximum engine performance and airframe performance are not properly matched at the angle for $(L/D)_{max}$. Better engine-airframe matching would be expected to yield a higher Breguet factor than shown here.

The sensitivity of Breguet factor to engine efficiencies is shown in figure 12 for the nominal vehicle. The inlet process efficiency (η_{KD}) and combustion efficiency (η_c) change the Breguet factor very slightly as compared to the extreme sensitivity to nozzle efficiency. The dashed line on figure 12 indicates the improvement to be gained with equilibrium nozzle flow over chemically frozen flow (represented by the solid line). Examination of figure 12 reveals that the assumption of frozen flow with a nozzle efficiency of 1.0 is roughly equivalent to a value of 0.965 for equilibrium flow, a reasonably conservative nominal value.

The sensitivity of Breguet factor to inlet diffusion at $M = 12$ is illustrated in figure 13. The geometric contraction ratio, or ratio of capture area to the minimum inlet area, is A_c/A_1 . The diffusion indicated here does not include the compression due to the vehicle flow-field effect, which adds a substantial pressure rise at the $M = 12$ cruise condition. This figure indicates that cruise performance is not unduly sensitive to the contraction ratio selected, except that below an A_c/A_1 of about 7:1, the Breguet factor and integration coefficient fall off because the combustor exit Mach number is too high to achieve the required amount of expansion along the available surface. Other considerations are as important to the selection of contraction ratio as performance, however, and the nominal A_c/A_1 of 8.25 at $M = 12$ was selected to minimize the internal wetted area and the duct pressure. Both of these factors lead to lower engine weight and reduced cooling flow.

--CONFIDENTIAL--

Stability

The vehicle stability analysis was concerned with longitudinal static stability and was performed to investigate the effects of the large gross thrust and ram drag vectors. The results of this longitudinal stability study are shown in figure 14 for the nominal configuration trimmed at $(L/D)_{\max}$ with a floating canard at 9° angle of attack with respect to the free stream. The solid line shows the normal power-on stability of the nominal configuration. The dashed line is the same configuration with no fuel flow to the scramjet engine and shows that the configuration maintains stability and would balance at a slightly higher angle of attack. The solid-dashed line shows the effect of the canard remaining fixed at the trim condition and shows a slight decrease in stability with a fixed canard. All curves show a pitch-up at the higher angles of attack.

Figure 15 shows the components in the pitching-moment curve. The solid line is the component in pitching moment due to the ram drag vector, the solid-dashed line is the pitching moment due to the basic body, and the dashed line is the pitching moment due to the gross thrust vector. The gross thrust vector is responsible for the pitch-up at the higher angles of attack. At an angle of attack of approximately $12-1/2^\circ$ the gross thrust vector is acting directly through the center of gravity. But, at the higher angles of attack the gross thrust is acting at an angle which produces a positive pitching moment about the vehicle center of gravity.

Temperatures

Besides being very important in the stability analysis, the thrust deflection angle can play an important role in reducing the vehicle surface temperatures due to aerodynamic heating.

Figure 16 shows the vehicle temperature on the lower surface versus the thrust deflection angle. It can be seen that this temperature can be reduced substantially if the cruise altitude is increased for the same thrust deflection angle and can be reduced still further if thrust deflection is increased. Increased thrust deflection allows the vehicle to balance at a lower lift loading because the thrust is contributing to the required vehicle lift. The decrease in temperature with increased altitude is due to the change in the environment even though the required angle of attack for the same lift loading is increased. The change in temperature with thrust deflection is due to the change in angle of attack which is more pronounced at the higher altitudes.

CONCLUSIONS

In conclusion, it is important to see where this study has led in regard to hypersonic configurations possessing high cruise performance. One such configuration is shown in figure 17. This configuration shows the trend toward high sweep vehicle shapes for efficient cruise. It has a high

CONFIDENTIAL

~~CONFIDENTIAL~~

coefficient of integration and a high Breguet factor, and is longitudinally stable in cruise. However, this configuration was unconstrained by take-off, acceleration, transonic drag, or landing performance considerations. The optimization of a hypersonic vehicle design requires a complete mission study where vehicle performance including structural weight can be evaluated over a given mission.

REFERENCES

1. Gregory, Thomas J.; Petersen, Richard H.; and Wyss, John A.: Performance Tradeoffs and Research Problems for Hypersonic Transports. J. Aircraft, vol. 2, 1965, pp. 266-271.
2. Jorgensen, Leland H.: Elliptic Cones Alone and With Wings at Supersonic Speeds. NACA Rep. 1376, 1958.
3. Van Dyke, Milton D.: The Slender Elliptic Cone as a Model for Nonlinear Supersonic Flow Theory. J. Fluid Mech., vol. 1, May 1956, pp. 1-15.
4. Eckert, Ernst R. G.: Survey on Heat Transfer at High Speeds. ARL 189, Aeronautical Research Laboratory, Office of Aerospace Research, Wright-Patterson Air Force Base, Ohio (Dec. 1961).

~~CONFIDENTIAL~~

CONFIGURATIONS

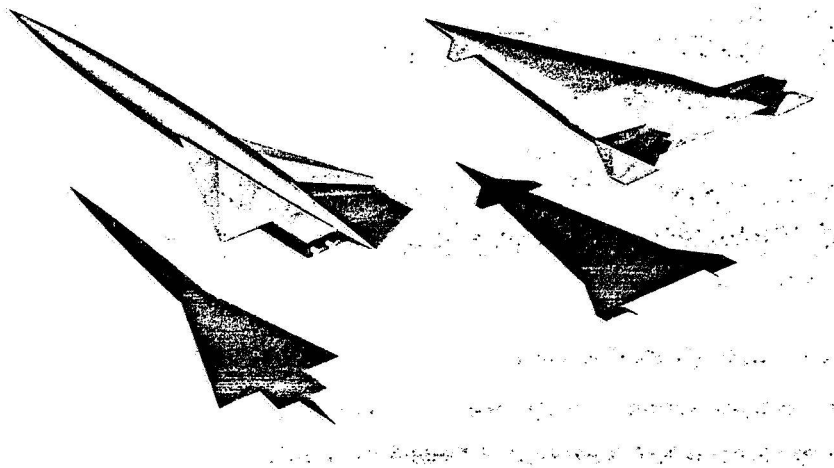
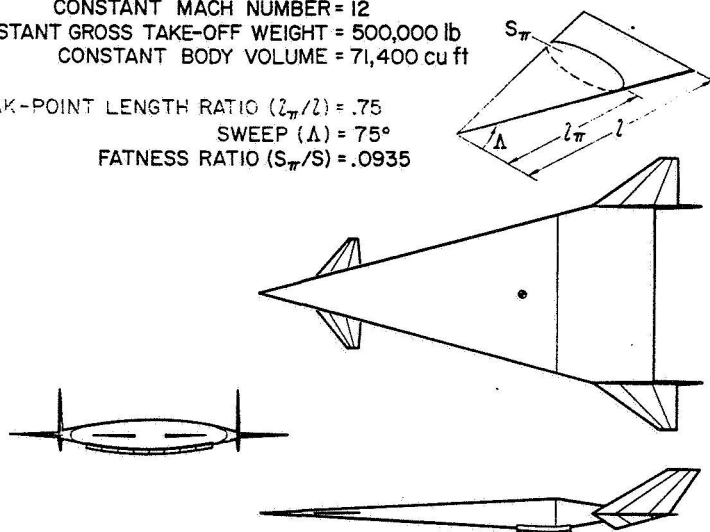


Figure 1

NOMINAL CONFIGURATION

CONSTANT MACH NUMBER = 12
CONSTANT GROSS TAKE-OFF WEIGHT = 500,000 lb
CONSTANT BODY VOLUME = 71,400 cu ft
BREAK-POINT LENGTH RATIO (l_π/l) = .75
SWEEP (Λ) = 75°
FATNESS RATIO (S_π/S) = .0935



~~CONFIDENTIAL~~

CRUISE FORCE DIAGRAM

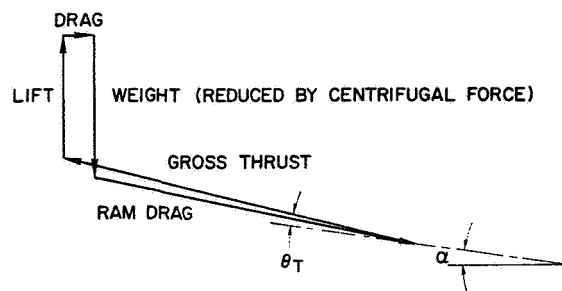


Figure 3

NOMINAL NOZZLE CONFIGURATION

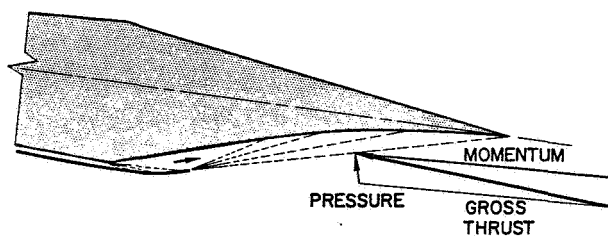


Figure 4

CONFIDENTIAL

NOZZLE SCHEMATIC

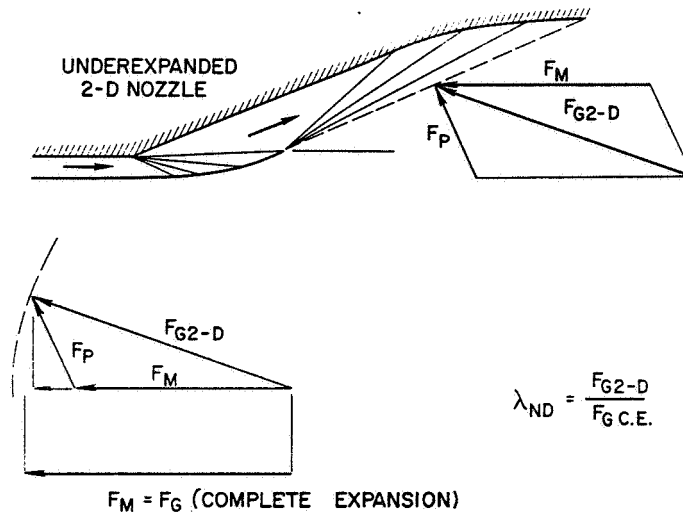
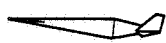


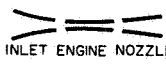
Figure 5

ENGINE - AIRFRAME INTEGRATION

$$C_I = \frac{(BF)_{ACTUAL}}{(BF)_{IDEAL}}$$

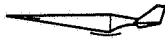
$$(BF)_{IDEAL} = \frac{V(L/D)_{AIRFRAME} (ISP)_{ENGINE}}{1 - (V/V_S)^2}$$

$(L/D)_{AIRFRAME}$ 

$(ISP)_{ENGINE}$ 

INLET ENGINE NOZZLE

$$(BF)_{ACTUAL} = \frac{WV}{W}$$



$$(BF)_{ACTUAL} = C_I (BF)_{IDEAL}$$

Figure 6

CONFIDENTIAL

EFFECT OF BREAK-POINT LENGTH RATIO

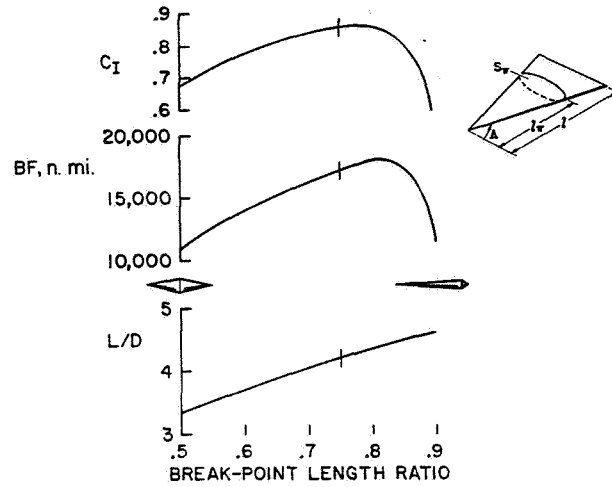


Figure 7

NOZZLE PERFORMANCE PARAMETERS

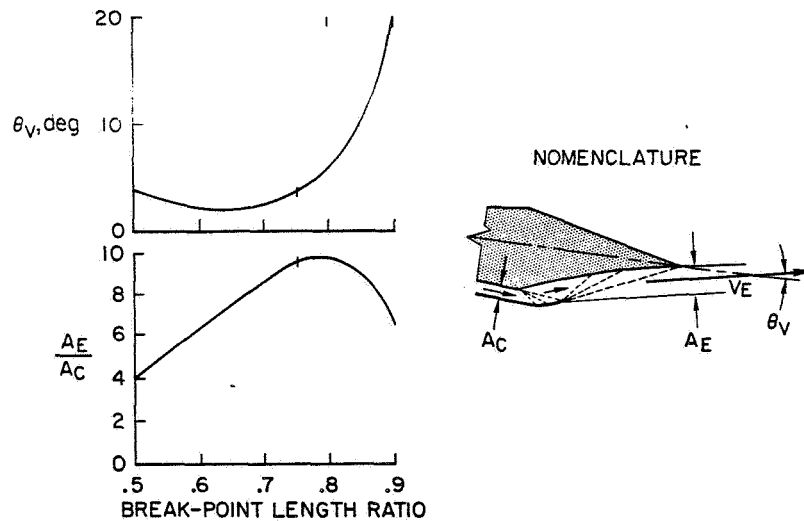


Figure 8

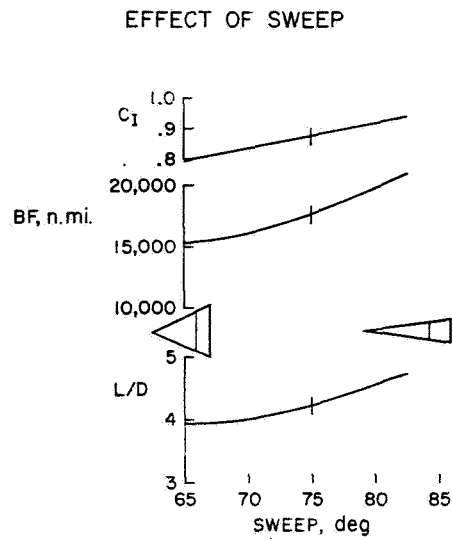


Figure 9

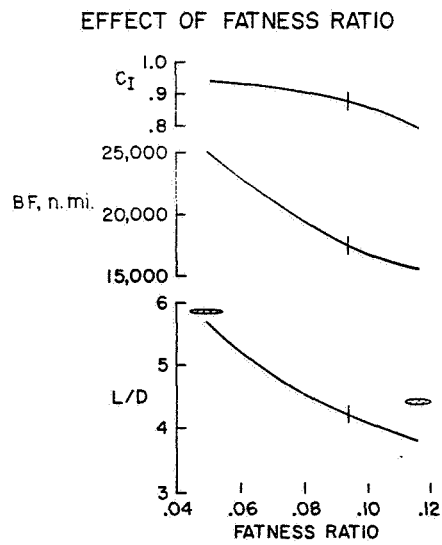


Figure 10

EFFECT OF ANGLE OF ATTACK

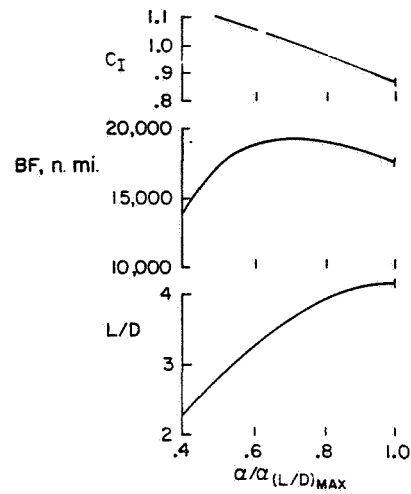


Figure 11

SENSITIVITY TO ENGINE EFFICIENCIES

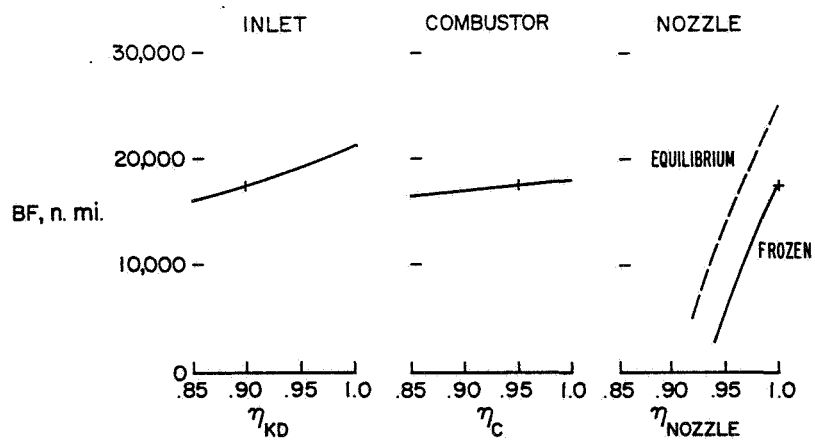


Figure 12

CONFIDENTIAL

EFFECT OF INLET CONTRACTION RATIO

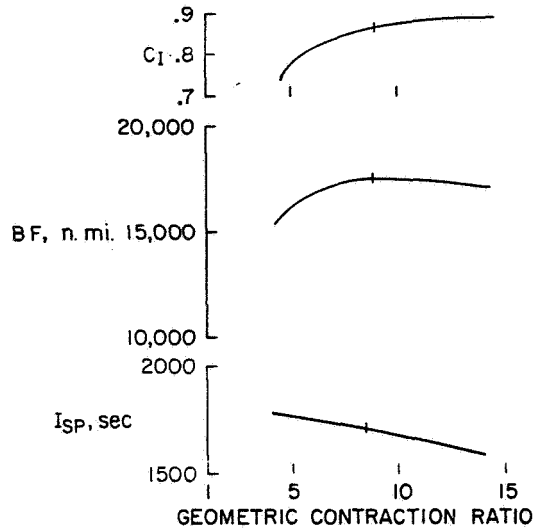


Figure 13

LONGITUDINAL STABILITY

M=12

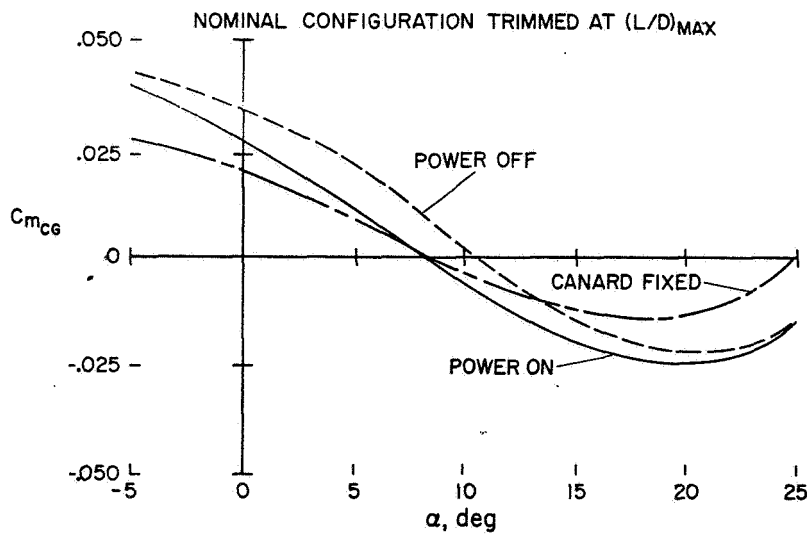


Figure 14

CONFIDENTIAL

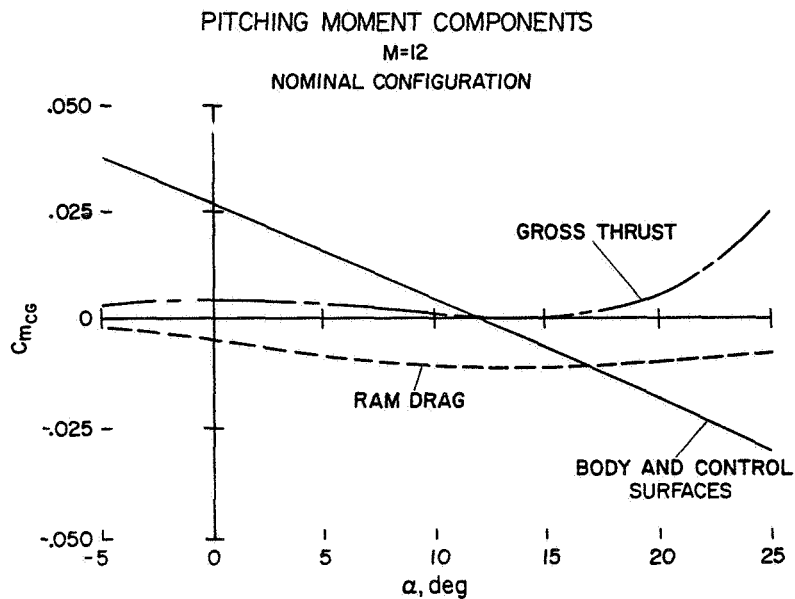


Figure 15

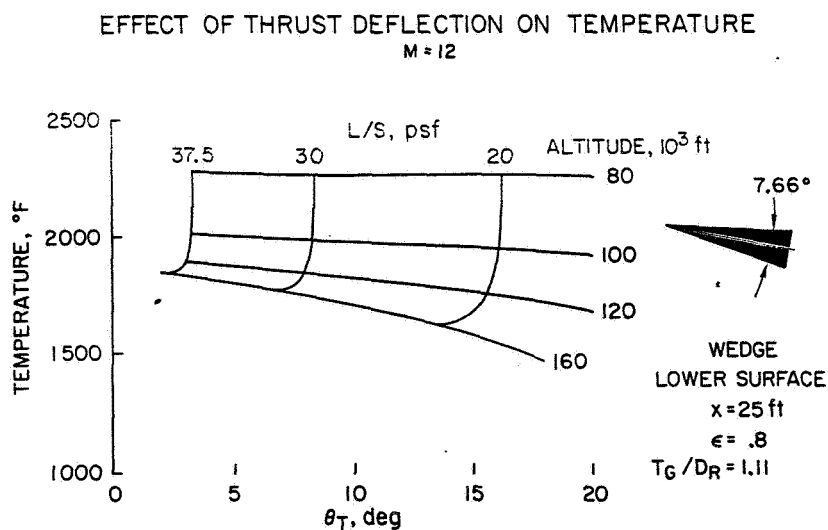


Figure 16

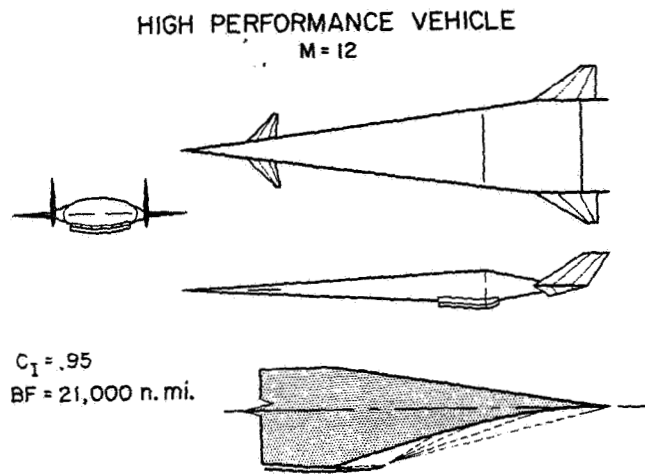


Figure 17

11. HANDLING QUALITIES OF HYPERSONIC CRUISE AIRCRAFT

By Harold J. Walker and Milton O. Thompson
Flight Research Center

SUMMARY

The apparent trends in the handling characteristics of transport aircraft as cruise speeds are extended to the hypersonic range are considered in more or less broad perspective. The piloting factors and aircraft response characteristics which appear to be most sensitive to a substantial advance in cruise velocity - such as projected for the hypersonic transport - are discussed in light of recent flight experience with the XB-70. In particular, possible piloting problems concerned with control of altitude, speed, and heading are assessed in relation to the aircraft response characteristics at high cruise speeds. A brief review is made of the possibility of employing full-authority augmentation systems to achieve an optimum handling aircraft and to allow greater stability-and-control design uncertainties in developing the highly complex hypersonic transport.

INTRODUCTION

This paper considers in somewhat broad perspective the foreseeable trends in the handling characteristics of large transport aircraft as cruise speeds are extended to the hypersonic range. Considerations are limited in general to the cruise regime.

SYMBOLS

b	span
$C_{L\alpha}$	lift-curve slope
$C_{l\beta}$	rolling moment due to sideslip
$C_{l\delta_a}$	rolling moment due to aileron deflection
$C_{m\alpha}$	pitching-moment-curve slope
$C_{n\beta}$	yawing moment due to sideslip
$C_{n\delta_a}$	yawing moment due to aileron deflection
f_n	frequency of short-period longitudinal oscillation

g	acceleration due to gravity
h	altitude
Δh	incremental change in altitude
$\dot{\Delta h}$	incremental rate of change of altitude
I_z	moment of inertia about vertical axis
M	Mach number
m	mass
n_z	normal acceleration
P	period of phugoid oscillation
q	dynamic pressure
S	wing planform area
Δt	incremental time
V	velocity
ΔV	incremental velocity
β	sideslip angle
$\Delta \gamma$	incremental flight-path angle
δ_a	aileron deflection angle
δ_e	elevator deflection angle
δ_r	rudder deflection angle
ζ	damping ratio
θ	pitch-attitude angle
ρ	air density
$\Delta \phi$	error in bank angle
$\Delta \psi$	error in heading angle
ω_d	Dutch roll frequency
ω_{ϕ}	term in the roll-rate-to-aileron transfer function which determines the amount and direction of sideslip produced in aileron rolls

~~CONFIDENTIAL~~

BACKGROUND

The first-generation hypersonic transport, as noted in the previous papers, is envisioned as a long slender vehicle of roughly the same size and weight as the SST, and capable of cruise speeds extending to, and possibly beyond, a Mach number of 6. Three of the proposed concepts are illustrated in figure 1, where their relative size and shape are compared with the recent SST designs and the XB-70. In general, there is a high degree of similarity between the supersonic and hypersonic configurations. The operational envelope of the hypersonic transport, however, will extend through a broader range of altitudes and dynamic pressures (fig. 2). The average level of dynamic pressure for these configurations at cruising speeds will be considerably higher than that for the present subsonic jets in order to achieve the best possible propulsive efficiency. A noteworthy effect of this upward trend in dynamic pressure is its tendency to compensate for the natural loss in lift effectiveness as both vehicle size and speed are increased. This effect is shown in figure 3 in terms of the ratio of lift effectiveness to mass for the three generations of transports. The curve on the left, for unit dynamic pressure, shows the usual rapid decline of this parameter beyond the transonic range. Inclusion of the average operating dynamic pressure, as shown on the right, raises the effectiveness at the higher Mach numbers and results in a near-level trend. This effect in conjunction with apparently similar trends in static margins, radii of gyration, relative control-surface areas, and so forth, suggests that the various transports may not differ significantly in many basic response and handling characteristics. The recent flight experience with the XB-70 should also provide a meaningful insight into possible future trends in the progression from subsonic to hypersonic cruise.

LONGITUDINAL CHARACTERISTICS

With regard to the longitudinal modes, the pilot's attention in cruise is mainly concerned with controlling altitude and speed within an allowed corridor. Occasional throttle and elevator adjustments would normally be required to establish and maintain the desired flight path. A significant effect of extending cruise speeds to the hypersonic range, however, is the large increase in time required to alter the flight path, as shown in figure 4. The time required to change the flight path 1° by using a steady normal acceleration of $1/10g$ is seen to be about 30 seconds at a Mach number of 6, nearly an order of magnitude greater than the time required at subsonic speeds. Long path-alteration times such as this will require greater anticipation by the pilot to prevent excessive altitude overshoot, as for example in terminating the climb at cruise altitude. This difficulty can, of course, be alleviated with the aid of a flight-director type of display to provide the pilot with the proper lead time for the leveling-off maneuver. Avoidance of collisions at these speeds also will require much greater lead times than are available from visual sightings of other aircraft.

Another important effect at high cruise speeds is the extreme sensitivity of rate of climb to small changes in flight-path angle. Climb or descent rates

~~CONFIDENTIAL~~

during cruise are not expected to differ significantly from those normally used in subsonic operations. The changes in aircraft attitude, therefore, will necessarily be very small, and the pilot will require greater precision in his attitude display. This requirement is illustrated in figure 5, which shows the required accuracy in flight-path angle with increasing Mach number for control of altitude rate within (for example) 500 feet per minute. The requirement for hypersonic cruise is seen to be an order of magnitude smaller than that for subsonic speeds and about half that for supersonic cruise. This inattention to attitude could result in large altitude errors and correspondingly long recovery times to regain the cruise altitude.

An interesting contrast in altitude hold performance experienced during the XB-70 program is seen in figure 6, which shows time histories of altitude, attitude, and elevon deflection for two flights of the XB-70. In one case the pilot used primarily the air data display (i.e., altitude and altitude rate), and in the other, the attitude display. The time history on the left represents conditions after the aircraft encountered a sudden change in atmospheric conditions. This caused apparent changes on the pilot's altimeter and rate-of-climb indicators, both of which are pressure-sensing instruments. The pilot then used these instruments in an attempt to hold the indicated altitude constant. The large lag in the pressure instruments at high altitudes and the slow response of the aircraft resulted in "instrument chasing" by the pilot, which caused large altitude excursions (as shown) and altitude rates which at times exceeded 6000 ft/min.

For the time history on the right, the pilot was asked to hold altitude constant for a sonic-boom run, and the pitch-attitude indicator was used as the primary reference. Also, the pilot was aided on this run by the absence of large atmospheric disturbances. This and other similar runs have demonstrated that altitude can be controlled fairly precisely at high speeds through use of the attitude indicator. The pilots have complained, however, that their task is made difficult by a lower-than-desired resolution of the attitude indicator. Recent flights of the XB-70 with the sensitivity of the attitude display increased by a factor of 2 indicate a definite improvement in the altitude hold task. In general, large altitude excursions have not occurred when pitch attitude was used to hold constant altitude.

In acquiring and holding a desired altitude or speed, the pilot is involved mainly with the short-period response of the aircraft. If any deviations from trim are left unattended, however, the long-period phugoid oscillation will develop. At high cruise speeds the character of the phugoid mode is totally different from that normally observed in subsonic flight (ref. 1). The period, as shown on the left in figure 7, increases with speed and, when density effects are taken into account, tends to level off in the neighborhood of 160 seconds at hypersonic speeds. The effect of density becomes significant above a Mach number of approximately 1.0. The figure on the right shows a linearly increasing ratio of altitude excursions to velocity excursions as speed is increased. Thus at high Mach numbers the phugoid will appear primarily as an oscillation in altitude. When cruising velocity is high, large altitude excursions may develop and the pilot's main concern will be maintaining altitude rather than speed. The period is relatively long, however, and the pilot would probably not sense the altitude and speed excursions as part of a phugoid oscillation.

~~CONFIDENTIAL~~

Rather, they would appear to him as relatively slow divergences which, if recognized in time, would be relatively easy to correct. In the XB-70 program, thus far, the pilots have not been aware of the phugoid oscillation, mainly because the excursions from trim have always been corrected at an early stage. Since occasional excitations do occur, however, the pilot must monitor rather closely the attitude, altitude, and rate-of-climb displays during cruise.

The normal-acceleration response and short-period characteristics of the hypersonic transport are essentially independent of speed and therefore should be similar to those of the SST's and XB-70. An estimate of the trends in the short-period mode is given in figure 8. Ranges of frequency and damping ratio are shown for the various transports in unaugmented flight and a comparison is made with approximate boundaries for acceptance in transport operations (ref. 2). These boundaries are based on a general assessment of available criteria for this class of aircraft. The subsonic jets are seen to exhibit a generally higher level of stability than either the supersonic or hypersonic transports, and are adequately damped without augmentation. The unaugmented damping levels for the SST and HST are, naturally, quite low but can, of course, be shifted to the satisfactory region with proper augmentation. The damping levels for the XB-70 barely fall within the unsatisfactory region; however, the consensus of the pilots thus far indicates that a lower level of damping than suggested by this criterion will probably be acceptable for emergency operations. A similar result is found in relation to the satisfactory region with augmented damping.

Rough estimates of the frequency range for the hypersonic transport show a generally lower trend as compared with the XB-70 and SST. Frequencies approaching the 0.1-cps level shown for the hypersonic transport have often been experienced in XB-70 flight tests at low speeds and were found to be satisfactory. It is believed that the lower stability level for the hypersonic transport may also be satisfactory at cruise speeds if adequate damping is provided.

LATERAL-DIRECTIONAL CHARACTERISTICS

The principal piloting task in the lateral-directional modes is one of establishing and maintaining prescribed headings primarily through control of bank angle. Turning rates for a given bank angle, however, will diminish with increasing speed in the same manner as flight-path angle in the vertical plane. On the other hand, heading holds will become less sensitive to errors in bank angle. Figure 9 shows the flight-track offset per 100 nautical miles for 1° errors in bank angle and heading. The offset due to an error in bank angle diminishes to an insignificant level at hypersonic speeds, and control of heading becomes the more critical factor. The offset due to heading error, although constant on a mileage basis, will develop very rapidly with time at hypersonic speeds, and more precise control of heading will be needed to maintain adequate lateral separations in future cruise corridors.

The roll response to the ailerons generally tends to couple with the Dutch roll mode, particularly if damping is low. As shown in figure 10, the terms

~~CONFIDENTIAL~~

~~CONFIDENTIAL~~

which best describe this tendency (refs. 3 and 4) are ω_d , the Dutch roll frequency, and ω_ϕ , which determines the amount and direction of sideslip produced in roll maneuvers. The extent of roll-yaw coupling is determined primarily by the relative magnitudes and signs of the dihedral effect and aileron-yaw term in the expression for ω_ϕ (at the top of the figure). For best aileron-roll response the ratio of ω_ϕ to ω_d should be near unity, that is, near the diagonal line for which $\omega_\phi = \omega_d$. The data points shown were obtained from XB-70 flight tests with augmentation off at various Mach numbers ranging from 0.4 to 2.9. At subsonic Mach numbers with the wing tips up, the ratio of ω_ϕ to ω_d falls considerably below the diagonal, and the airplane under these conditions exhibits an objectionable adverse yaw tendency. Although adequate roll power is available, the pilot cannot command even modest roll rates for fear of exceeding structural limitations in sideslip. Transition is made to supersonic cruise speeds by deflecting the wing tips downward 65°. In this configuration the dihedral effect changes sign and the ratio of ω_ϕ to ω_d moves to the upper side of the diagonal. Under these conditions there is a strong tendency for the pilot to induce an objectionable Dutch roll type of oscillation.

A typical time history of a pilot-induced oscillation is given in figure 11 for steady cruising flight at a Mach number of 2.5. Sideslip excursions are shown here in conjunction with the pilot's aileron and rudder control inputs. The roll and yaw dampers were disengaged, and the pilot initiated a divergent lateral-directional oscillation. The motion was finally suppressed by reengaging the damper system, although releasing the controls would have produced a similar effect. With the dampers engaged the pattern of the data points shown in figure 10 does not change significantly; rather, there is a greater tolerance for deviations from the diagonal. These results emphasize the importance of maintaining a level of ω_ϕ/ω_d near unity. Since turning rates are quite small at hypersonic speeds, a low level of control power may be preferred during cruise. If control power is low, then a level of ω_ϕ/ω_d slightly above unity is indicated to be more nearly optimum if the Dutch roll mode is adequately damped. A rudder-aileron interconnect is, of course, one of the devices available to the designer for establishing an optimum ratio.

As a final consideration of the lateral-directional handling characteristics, the unaugmented Dutch roll frequency and damping ratio are presented in figure 12, together with approximate boundaries (ref. 2) defining satisfactory, unsatisfactory, and unacceptable regions for transport aircraft. The frequency levels for the XB-70 and SST are generally lower than that for the subsonic jets, and the level for the hypersonic transport is likely to be still lower. Low frequencies, although appearing to be unsatisfactory even at modest levels of damping ratio, have not been found unacceptable in flight tests of the XB-70 at high cruise speeds. The presently available criteria thus are believed to be overly conservative in applications to large transport aircraft. Damping ratios for the hypersonic transport can, of course, be raised to a satisfactory level with suitable augmentation.

SYSTEMS APPROACH

In consideration of the many complex aerostructural and thermostructural problems that face the designer of the hypersonic transport, the achievement of fully satisfactory handling qualities in all flight regimes will truly be an impressive task. Indeed, after all possible precautions are taken in model tests and analytical studies, a number of unexpected and sometimes critical handling problems are likely to turn up in flight. The XB-70 adverse aileron yaw problem is a case in point. These circumstances suggest the adoption of at least a limited fail-operational systems approach in the development of a new concept, wherein the more critical design uncertainties may be accommodated without undue penalties in handling or performance characteristics. A further extension of this principle would of course provide for full optimization of the handling characteristics, and even allow tradeoffs of basic aircraft stability in favor of improved performance.

Figure 13 illustrates the apparent trend in systems development and acceptance through the three stages (subsonic, supersonic, and hypersonic) of transport development. The growing demand for greater systems authority in vehicle control as speed is increased is quite apparent, starting with the simple dampers in today's jet transports and evolving to the full-authority command augmentation systems that will most certainly be available in the hypersonic transport era. For supersonic cruise, limited-authority augmentation as well as some of the more advanced systems are already operationally qualified in recent fighter-type aircraft, and these systems will be strong contenders for adoption in the SST program. Model-following and variable (or adaptive) gain systems also have emerged from the experimental stage after rather extensive testing in research aircraft, and may offer attractive advantages in the design of future hypersonic cruise aircraft. The fly-by-wire system is still limited to space vehicle and booster applications. This approach, however, is also certain to become more widely accepted as reliability levels continue to rise.

Some appreciation of the potential margins that are available to the designer in adopting a full-authority augmentation system may be gained from the study presented in figure 14. This figure shows the effect on pilot rating of varying the magnitudes of two basic derivatives, $C_{m\alpha}$ and $C_{l\beta}$, through sufficiently wide ranges to render the aircraft unflyable without augmentation. The study covered a number of the principal derivatives and was performed on the X-15 simulator at a Mach number of 6 using a rate-command augmentation system. The derivative values are expressed in multiples of the basic X-15 values (shown on the figure). The lower line in each case represents the unaugmented aircraft, which for negative values of static margin and dihedral effect is impossible to handle. The augmentation system, it is seen, will absorb substantial deviations of these parameters from the design levels and still provide acceptable handling characteristics. The implication is, of course, that a system of this kind can be designed around a statically neutral or even unstable aircraft, and therefore offer a more versatile approach in the design of such a complex vehicle as the hypersonic transport.

CONCLUSIONS

To summarize this rather broad projection of trends in the handling characteristics of future transport aircraft, one might say that the steps now being taken to develop a safe easy-to-fly supersonic transport will bridge many of the gaps between the present-day subsonic jet and the hypersonic transport of tomorrow. In general, it would appear that the pilot's control of altitude, speed, and heading at hypersonic speeds will not differ substantially from that at lower speeds if suitable guidance and navigational aids are provided. An increase in flight-path alteration time will be largely offset by a lower requirement for changes in flight-path angle. The phugoid oscillation will be characterized by excursions in altitude rather than velocity, and will become a dominant factor in maintaining flight paths within prescribed corridors. Flight-path deviations will be more sensitive to small errors in attitude and heading, and are likely to place greater demands on the pilot and guidance system. New avenues need to be explored for optimizing the pilot's role in actively handling the aircraft and monitoring an increasing complexity of automatic control and guidance functions. Finally, greater emphasis, it is believed, will be given to the systems approach as a means for establishing favorable trades between stability and performance and for providing greater design margins in ultimately achieving an optimum handling airplane.

REFERENCES

1. Porter, Richard F.: The Linearized Long-Period Longitudinal Modes of Aerospace Vehicles in Equilibrium Flight. AFFTC-TN-61-2, U.S. Air Force, Jan. 1961. (Available from ASTIA as AD 251 998.)
2. Anon.: Design Objectives for Flying Qualities of Civil Transport Aircraft. ARP 842, Soc. Automotive Engrs., Aug. 1, 1964.
3. Ashkenas, I. L.: A Consolidation of Lateral-Directional Handling Qualities. AIAA Paper No. 65-314, July 1965.
4. Taylor, Lawrence W., Jr.; and Iliff, Kenneth W.: Recent Research Directed Toward the Prediction of Lateral-Directional Handling Qualities. Presented to Flight Mechanics Panel of AGARD (Paris, France), May 10-11, 1966.

CONFIDENTIAL

HIGH-SPEED CRUISE CONFIGURATIONS

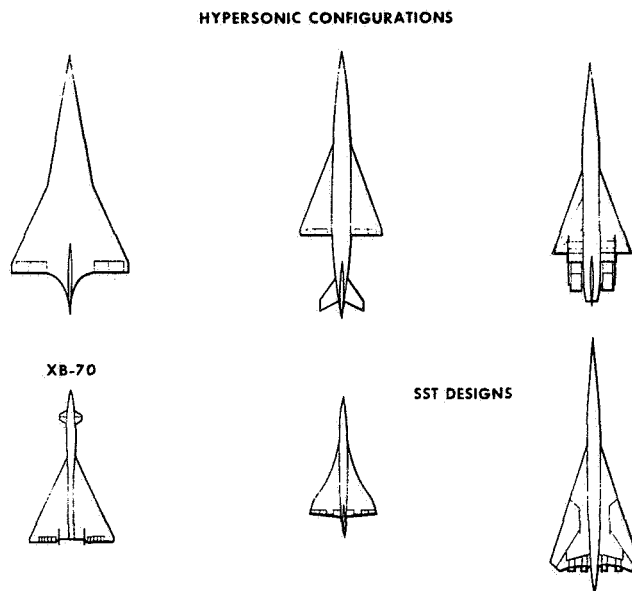


Figure 1

TRENDS IN FLIGHT PROFILES

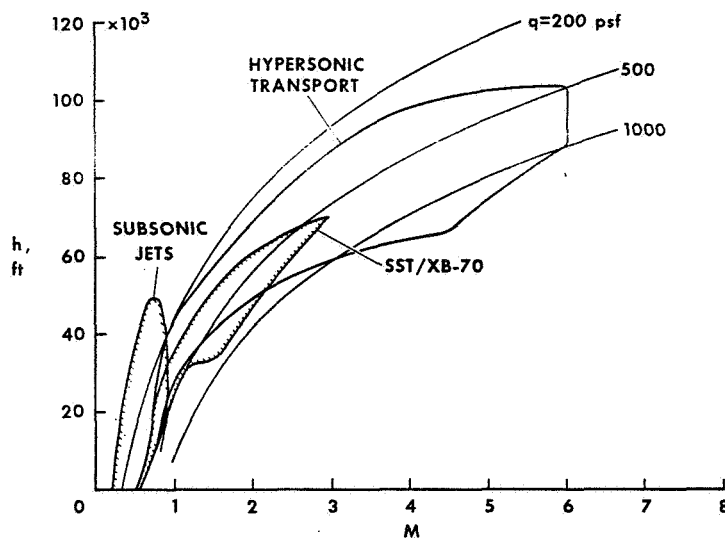


Figure 2

CONFIDENTIAL

TREND IN LIFT-TO-MASS RATIO

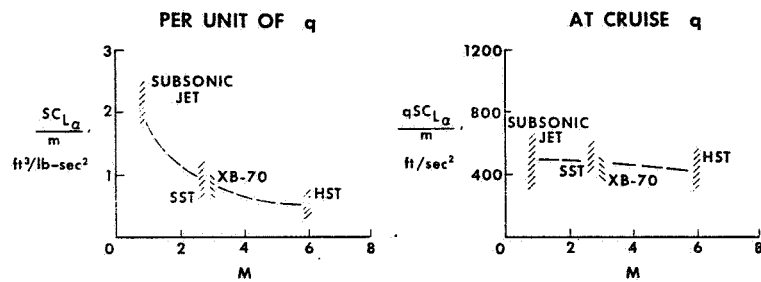


Figure 3

PATH ALTERATION TIME

$$\frac{\Delta t}{\Delta \gamma} \approx \frac{V}{g n_z}; \quad n_z = \frac{1}{10} g$$

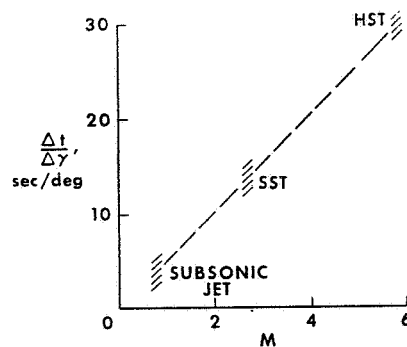


Figure 4

FLIGHT-PATH ACCURACY

$$\Delta\gamma \approx \frac{1}{V} \Delta h$$

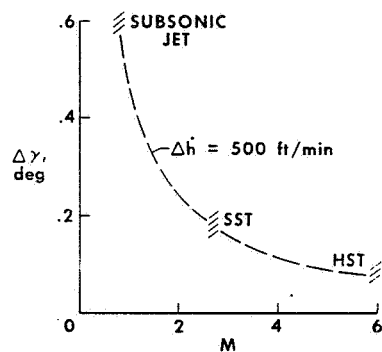


Figure 5

XB-70 ALTITUDE HOLD EXPERIENCE

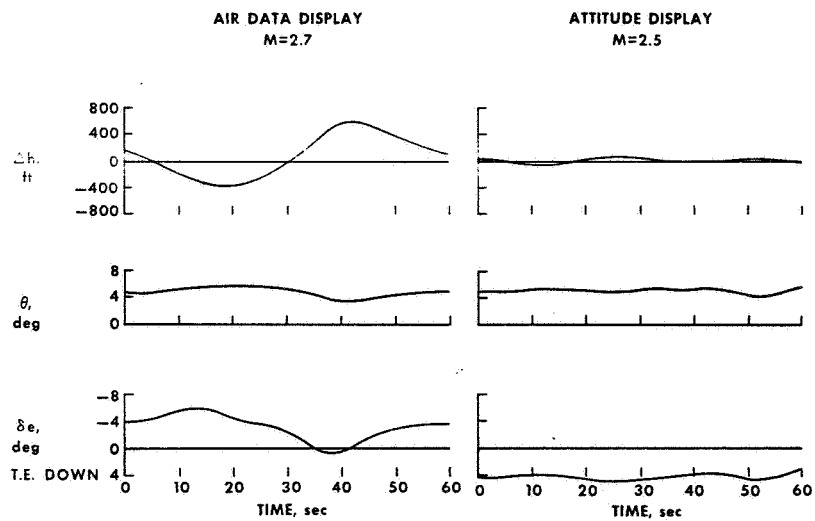


Figure 6

~~CONFIDENTIAL~~

PHUGOID CHARACTERISTICS

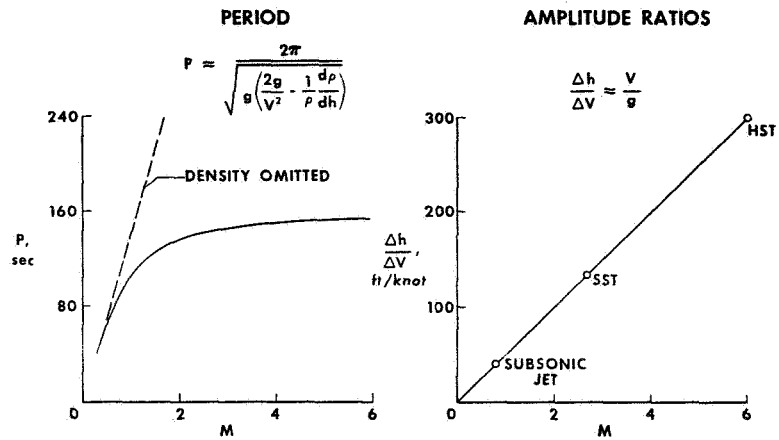


Figure 7

LONGITUDINAL SHORT-PERIOD TRENDS UNAUGMENTED

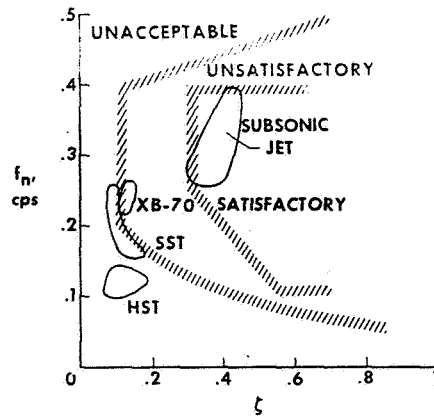


Figure 8

LATERAL FLIGHT-PATH OFFSET PER 100 NAUTICAL MILES

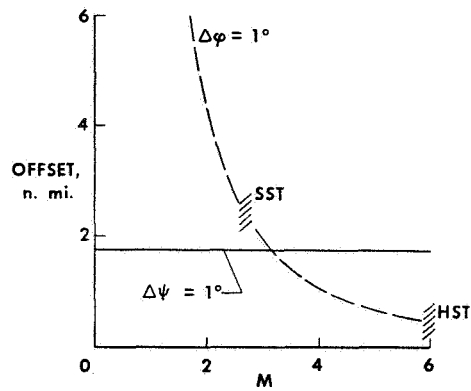


Figure 9

XB-70 ROLL-YAW COUPLING

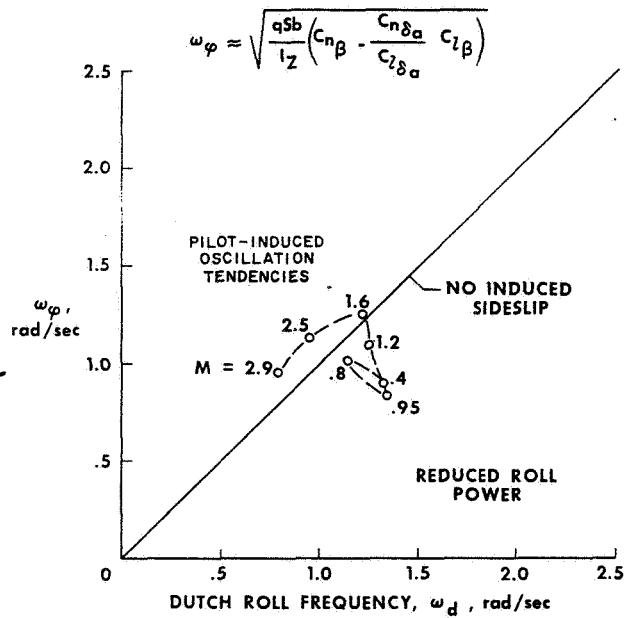


Figure 10

XB-70 PILOT-INDUCED OSCILLATION

$M = 2.5, h = 60,000 \text{ FT}$

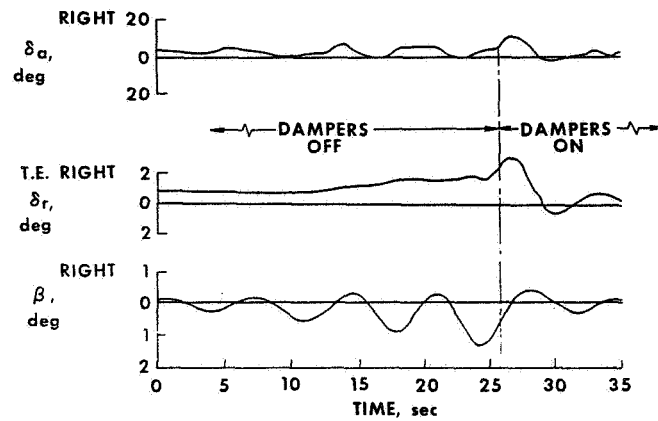


Figure 11

DUTCH ROLL TRENDS UNAUUGMENTED

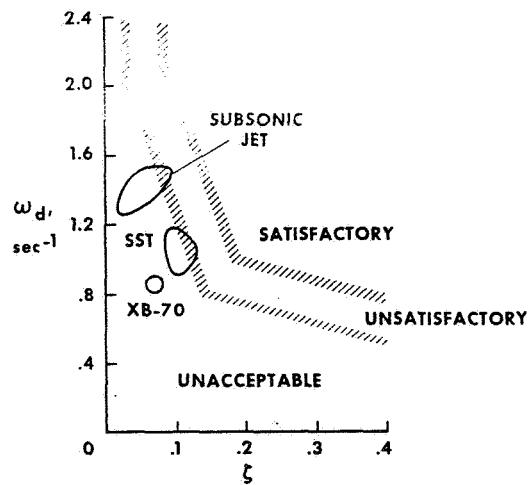


Figure 12

CONTROL SYSTEM TRENDS

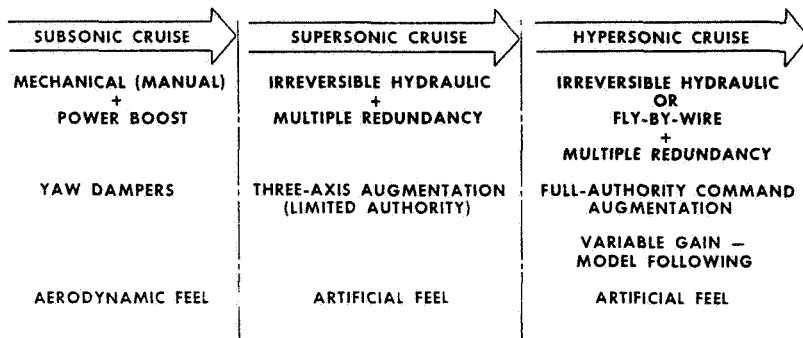


Figure 13

AUGMENTATION EFFECTIVENESS

X-15 SIMULATOR M=6

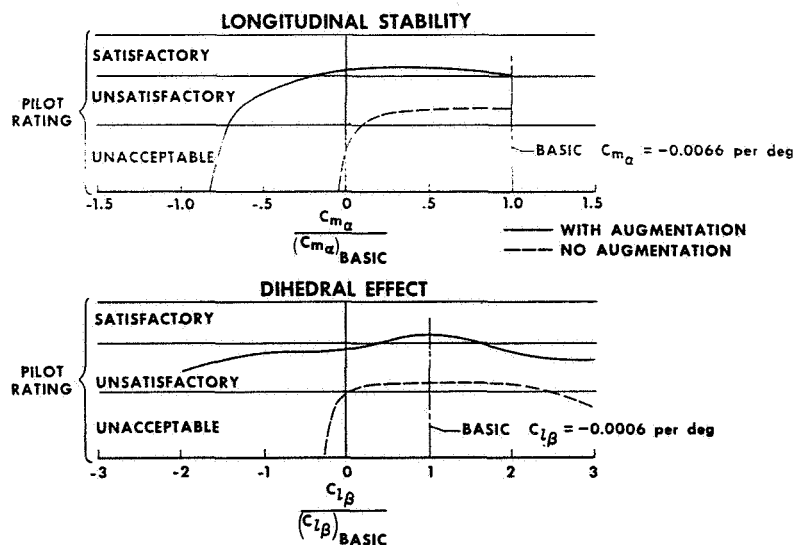


Figure 14

~~CONFIDENTIAL~~

~~CONFIDENTIAL~~

12. SOME EFFECTS OF MACH NUMBER AND GEOMETRY

ON SONIC BOOM

By Raymond M. Hicks, Joel P. Mendoza,
and Lynn W. Hunton
Ames Research Center

12

SUMMARY

A study has been conducted to determine the effects of Mach number and geometry on the level of sonic boom overpressure and on the applicability of the Whitham theory to the calculation of sonic boom. This study consisted of wind-tunnel tests and a theoretical analysis of the sonic boom characteristics of a 7.5° half-angle cone-cylinder and a model of the X-15 airplane over a Mach number range from 2 to 5.5 to compare experiment with theory. The geometric effect was examined in tests of three hypersonic transport configurations over the same Mach number range. This study shows the Whitham theory gives good predictions of sonic boom overpressure up to a Mach number of about 3, but deviates rapidly from experiment above a Mach number of 3. It also shows that configuration geometry can have a considerable influence on the level of sonic boom overpressure at low hypersonic Mach numbers.

INTRODUCTION

Experience gained in the development of the supersonic transport has shown that an important area of hypersonic transport research is the sonic boom. The problem at hypersonic Mach numbers may be somewhat different from the supersonic counterpart because of the different configuration geometry characteristic of cryogenic fueled hypersonic aircraft. This report will present some answers to two questions raised by the sonic boom problem at hypersonic Mach numbers: (1) Will the good correlation between experiment and the Whitham theory at moderate supersonic Mach numbers persist at hypersonic Mach numbers? (2) How will changing the geometry of hypersonic configurations change the level of sonic boom? The validity of the Whitham theory at hypersonic speeds will be considered by comparing experiment and theory for a body of revolution and a complete airplane configuration. The effect of geometry will be examined by presenting data for three different hypersonic transport aircraft.

NOMENCLATURE

C_L lift coefficient

h altitude

~~CONFIDENTIAL~~

CONFIDENTIAL

l body length
 M Mach number
 P reference pressure
 α angle of attack
 ΔP sonic boom overpressure
 η shock angle minus Mach angle

MODELS AND APPARATUS

The models in this study were a 7.5° half-angle cone-cylinder, a model of the X-15 airplane, and three hypersonic transport models - a blended-wing-body, a delta-wing-body, and an all-body configuration. The three hypersonic transport configurations and the cone-cylinder were manufactured from mild steel and the X-15 model was cast from beryllium copper. The three transport models and the cone-cylinder were 4 inches long, and the X-15 model was 4.8 inches long.

The tests were conducted at Mach numbers of 2 and 3 in the Ames 9- by 7-foot and 8- by 7-foot wind tunnels, respectively, and at Mach numbers of 4 and 5.5 in the 21-inch hypersonic wind tunnel of the Jet Propulsion Laboratory.

All models were mounted on a two-component internal strain-gage balance which was manufactured integral with the sting support. The static probe used to measure the pressures in the model shock system was manufactured from stainless steel in two sections. The front section was a 10-inch long, $1/2^\circ$ half-angle cone; the aft section, also 10 inches long, was a $1-1/4^\circ$ half-angle cone.

The pressure transducers used in the study were of the capacitance type and had a maximum load capability of 10 mm of mercury.

TEST TECHNIQUE

The comparison between experiment and theory was made for an altitude of 100 body lengths (an altitude for which the Whitham theory is known to predict sonic boom characteristics accurately at moderate supersonic Mach numbers). Since it was not practical to obtain wind-tunnel data at an altitude of 100 body lengths, an experimental technique developed at Ames for deriving sonic boom characteristics from near field data for any greater altitude was used.

CONFIDENTIAL

~~CONFIDENTIAL~~

An expeditious way to describe the experimental technique is to compare it with the standard theoretical procedure. This comparison is presented in figure 1. The theoretical procedure shown at the left requires a detailed calculation of the cross-sectional area distribution, lift distribution, and interference lift distribution before the F-function and the desired pressure signature can be calculated. One of the main difficulties with the theoretical procedure is the inability of existing theories to define the lift distribution accurately. (For a complete description of this procedure, see ref. 1.) The only requirement for applying the experimental procedure shown at the right is that a near field pressure signature be measured in a wind tunnel (or other suitable experimental facility). Once this has been done, an experimental F-function and then the pressure signature at any higher altitude can be calculated.

An evaluation of the validity of the experimental procedure used for deriving sonic boom characteristics from measurements of near field pressure signatures is presented in figure 2. The XB-70 at $M = 1.8$ and the X-15 at $M = 5.5$ were used as test cases. The two pressure signatures shown at the top of the figure were measured in a wind tunnel at a ratio of altitude to body length (h/l) of 1. The experimental F-functions calculated from these near field pressure signatures were used to calculate pressure signatures (hereafter called derived pressure signatures) for altitude-length ratios of 4.5 and 290 for the XB-70 and for an altitude-length ratio of 1770 for the X-15. These derived pressure signatures are compared with experimental data obtained at the same altitude-length ratios. As can be seen, the derived pressure signatures and the experimental data agree well, except for the location and strength of the rear shock for the X-15 at $h/l = 1770$. An analysis of schlieren photographs has indicated that this discrepancy is due to interference with the trailing shock on the X-15 model caused by a shock emanating from the model support system. This problem is particularly severe at high Mach numbers and, to obtain reliable data for the trailing shock, would require a longer sting than that employed in this test. This experimental procedure has been used to derive the experimental sonic boom characteristics shown for all configurations in the remainder of this report.

RESULTS AND DISCUSSION

The first question to be considered here concerns the validity of the modified linear theory of Whitham at hypersonic speeds. A comparison of experiment with the Whitham theory for a 7.5° half-angle cone-cylinder at $h/l = 100$ is shown in figure 3. The correlation between experiment and theory is good at Mach numbers of 2 and 3 while the Whitham theory is seen to underpredict the strength of the bow shock at Mach numbers of 4 and 5.5. This trend is not surprising since the assumptions used in the development of the Whitham theory place a definite Mach number limitation on the theory (see ref. 2). This underprediction of the bow shock strength at low hypersonic Mach numbers has been noted before (ref. 3) on a 7.5° half-angle cone at $M = 5.14$.

~~CONFIDENTIAL~~

CONFIDENTIAL

Figure 4 shows a comparison of experiment with theory for the X-15 at the lift coefficients indicated. Again, it is evident that the correlation between experiment and theory is fairly good at the low Mach numbers but not as good as for the slender, nonlifting configuration shown in figure 3. At Mach numbers of 4 and 5.5 the theory again underpredicts the strength of the bow shock. In the calculation of sonic boom, the theoretical overpressure signatures for the X-15 were based on experimental pressure distributions (see refs. 4-6). Hence, the lack of correlation between experiment and theory cannot be blamed on inaccurate loading distributions.

Another measure of the accuracy of a sonic boom theory is the degree of correlation between experimental and theoretical shock angle. This comparison is made in figure 5 by plotting shock angle minus free-stream Mach angle for a 7.5° half-angle cone. Two theories (the Whitham theory and the cone tables) are presented along with an experimental value at $M = 5.5$. It can be seen that the cone tables quite accurately predict the shock angle at $M = 5.5$. If the cone tables are accepted as a good estimate of shock angle throughout the Mach number range shown in this figure, it can be seen that the Whitham theory predicts the shock angle well to about $M = 3$ and then deviates rapidly from experiment above $M = 3$. It is interesting that the bow shock angle predicted by the Whitham method is greater than the experimental shock angle at high Mach numbers while the opposite is true for the pressure jump at the bow shock (see figs. 3 and 4). This anomaly has not yet been explained.

The second question to be considered here is the effect of geometry on the level of sonic boom. This question has been examined in tests of the three hypersonic transport configurations shown in figure 6 at Mach numbers of 2, 3, 4, and 5.5. The three configurations chosen were a blended wing body, a delta wing body, and an all body. All models, complete with empennage and simulated engine inlets, were 4 inches long. These models were not designed to minimize sonic boom, but were chosen as being typical of current thinking on hypersonic transports; hence, the level of sonic boom overpressure presented may be somewhat higher than could be achieved if the configuration geometry were reshaped. The results of this study are presented in figure 7, which is a plot of maximum overpressure divided by the reference pressure versus Mach number for the three hypersonic configurations flying at a constant altitude of 50,000 feet and a constant weight of 600,000 pounds. All aircraft had the same volume. As shown by the silhouettes of the configurations in figure 7, however, the lengths for constant volume were different for each aircraft. The results of this study indicate that for the Mach number range shown, the level of sonic boom generated by the blended wing body is about the same as that generated by the delta wing body, both being less than that for the all-body configuration. It should be pointed out that the assumption of constant weight may have penalized the all-body configuration since preliminary mission analysis studies indicate that the weight of the all body may be less than the weight of the other two configurations for the same mission. This would result in a somewhat lower sonic boom overpressure.

Now that the relative levels of sonic boom overpressure have been established for the three hypersonic transport configurations, it is of

~~CONFIDENTIAL~~

interest to see what level of sonic boom (in pounds per square foot) would be generated by the blended wing body flying a typical mission profile. In the plot at the left in figure 8, the solid curve defines the basic mission profile. The mission begins at $M = 2$ since tests were not conducted at Mach numbers below 2. The overpressures that would be generated on the ground by the blended wing body flying the basic mission are shown by the solid curve at the right in the figure. (The values for $M = 6$ were obtained by extrapolating the $M = 5.5$ values.) As can be seen, overpressures would be rather large between $M = 2$ and 3 but would drop rapidly to about 1 psf at the end of cruise. The 1 psf value is lower than that anticipated for the supersonic transport because of the higher cruise altitude for the hypersonic transport. If engines were available that would permit alteration of the climb leg of the mission profile to that shown by the dashed curve at the left, the level of sonic boom overpressure could be reduced during climb to the level shown by the dashed curve at the right.

CONCLUSIONS

The following conclusions can be drawn from this study:

1. The modified linear theory of Whitham predicts sonic boom characteristics fairly well for slender configurations up to a Mach number of about 3 but deviates rapidly from experiment above Mach 3.
2. The sonic boom overpressure generated by the delta-wing configuration is approximately the same as that generated by the blended-wing-body configuration, both being considerably below the overpressure level of the all-body configuration for the conditions and Mach number range of this study.
3. The use of near field data to derive sonic boom characteristics at any larger altitude appears to have application up to low hypersonic Mach numbers.

~~CONFIDENTIAL~~

~~CONFIDENTIAL~~

REFERENCES

1. Carlson, H. W.: Influence of Airplane Configuration on Sonic-Boom Characteristics. J. Aircraft, vol. 1, no. 2, 1964, pp. 82-86.
2. Whitham, G. B.: The Flow Pattern of a Supersonic Projectile. Communications on Pure and Applied Mathematics, vol. V, 1952, pp. 301-348.
3. Callaghan, J. G.: A Feasibility Investigation Concerning the Simulation of Sonic Boom by Ballistic Models. Rep. 52970A, Douglas Aircraft Co., 1966.
4. Keener, Earl R.; and Pembo, Chris: Aerodynamic Forces on Components of the X-15 Airplane. NASA TM X-712, 1962.
5. Pyle, Jon S.: Comparison of Flight Pressure Measurements With Wind-Tunnel Data and Theory for the Forward Fuselage of the X-15 Airplane at Mach Numbers From 0.8 to 6.0. NASA TN D-2241, 1964.
6. Pyle, Jon S.: Flight-Measured Wing Surface Pressures and Loads for the X-15 Airplane at Mach Numbers From 1.2 to 6.0. NASA TN D-2602, 1965.

~~CONFIDENTIAL~~

DESCRIPTION OF THEORETICAL AND EXPERIMENTAL PROCEDURE

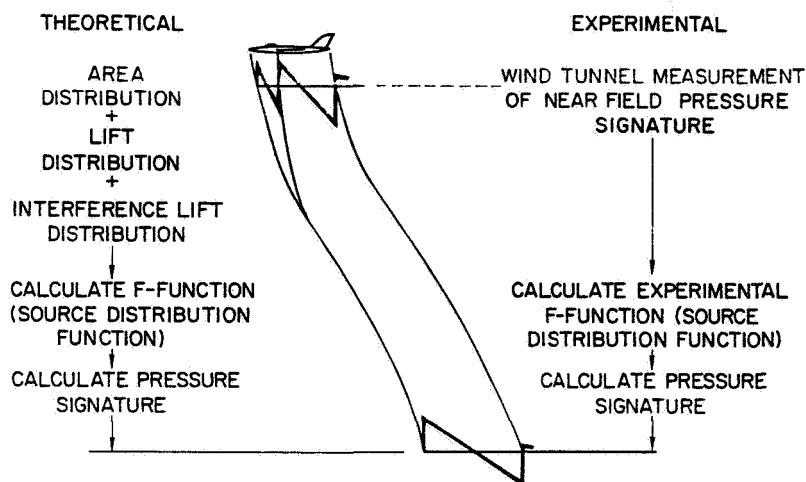


Figure 1

EVALUATION OF EXPERIMENTAL PROCEDURE

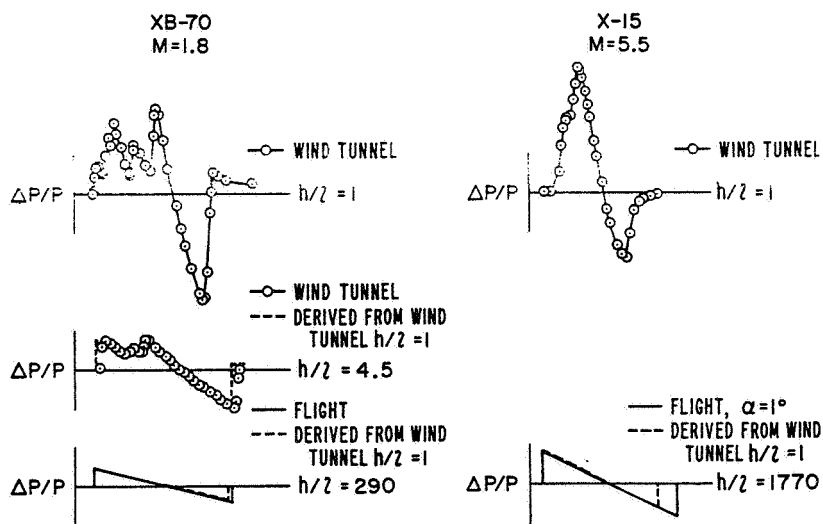


Figure 2

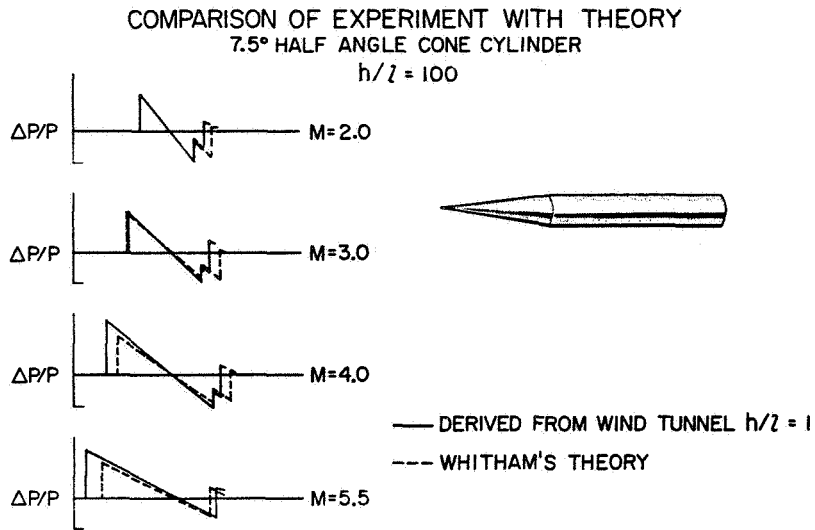


Figure 3

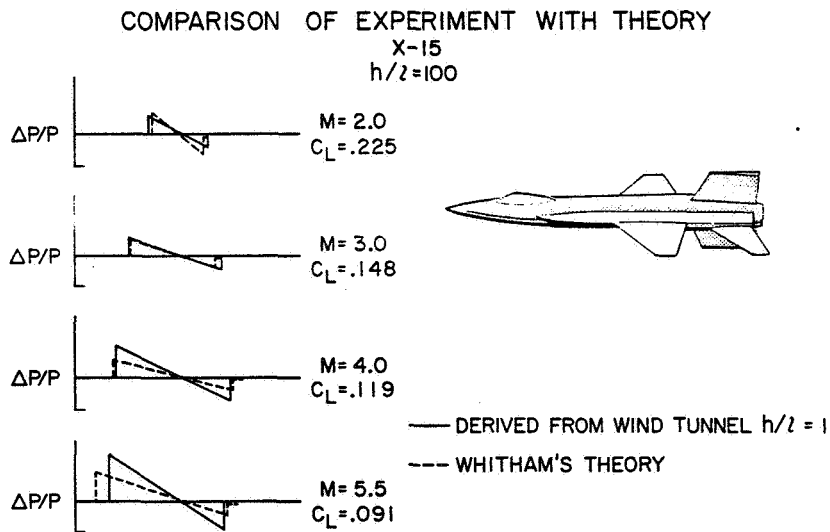


Figure 4

COMPARISON OF WHITHAM'S THEORY WITH THE CONE TABLES AND EXPERIMENT

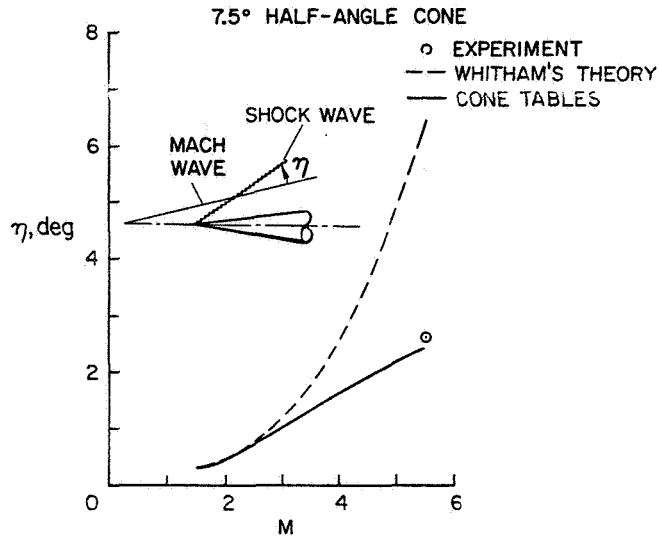


Figure 5

MODELS

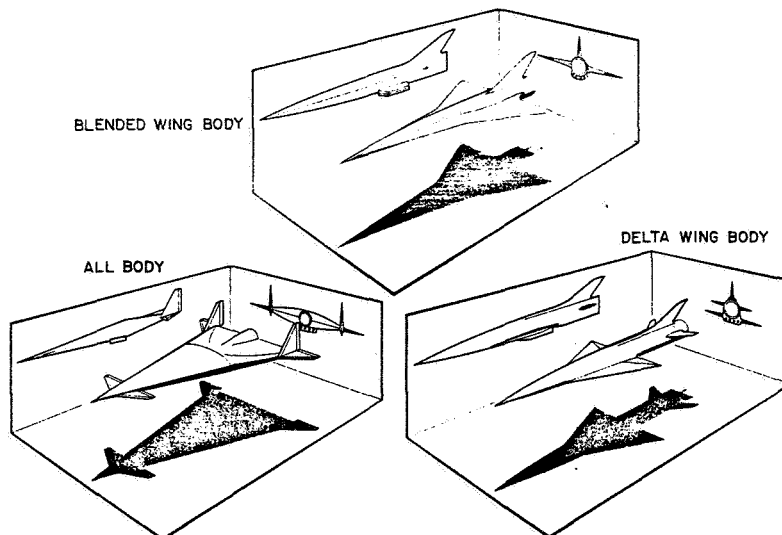


Figure 6

CONFIGURATION EFFECT
 ALTITUDE = 50,000 ft WEIGHT = 600,000 lb CONSTANT VOLUME
 DERIVED FROM WIND TUNNEL $h/z = 1$

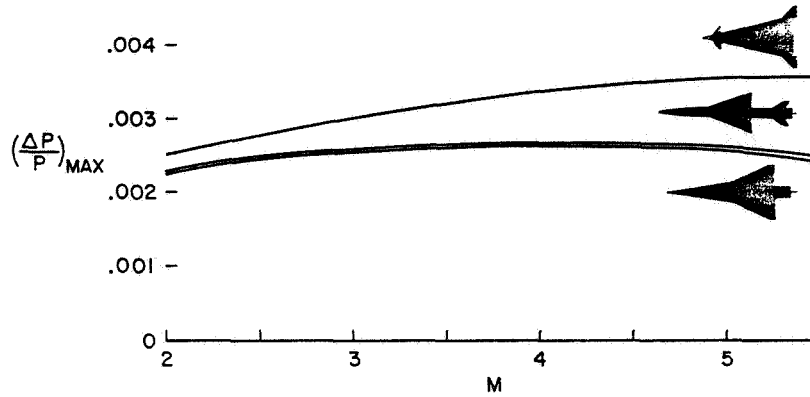


Figure 7

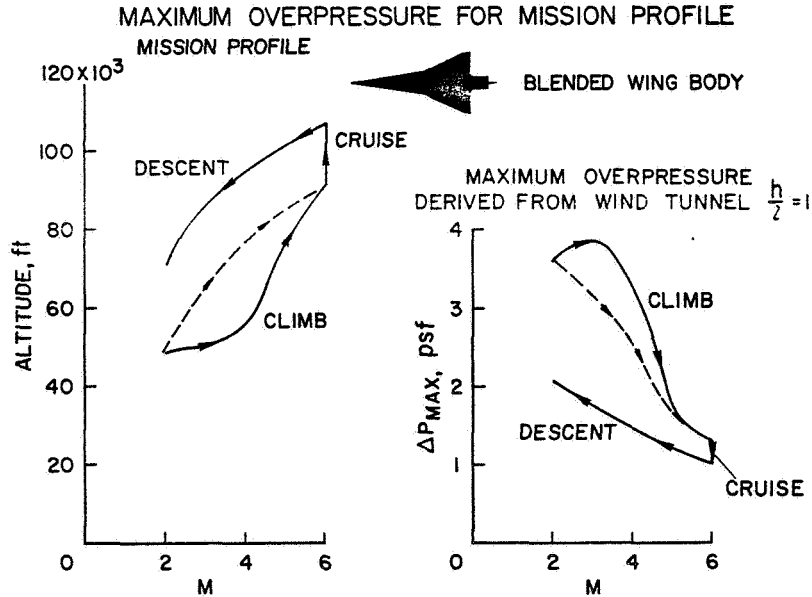


Figure 8

~~CONFIDENTIAL~~

13. DETERMINATION OF THE INTERNAL DRAG OF SMALL-SCALE
SIMULATED AIRBREATHING ENGINES AT $M_\infty = 4.1$

By Lawrence A. Graham
Ames Research Center

SUMMARY

The internal drag of a straight circular duct at zero angle of attack has been determined by force measurements, pressure surveys, and boundary-layer calculations; the results from these methods are compared, and a simplified experimental technique is described. Flow characteristics near the exit of several ducts with different geometries have been determined, and some of the difficulties encountered in assessing the momentum in ducts such as these are discussed. Tests were made at a free-stream Mach number of 4.1 and a Reynolds number of 4.3 million per foot. Angles of attack considered were 0° and 5° .

INTRODUCTION

At supersonic and hypersonic speeds, wind-tunnel models of aircraft with airbreathing engines must represent both the internal and the external details if the aerodynamics are to be properly assessed. This includes internal ducting of propulsion units to permit simulation of the external flow field. In such investigations, a major problem is the accurate determination of the internal drag of the ducting.

This problem of the accurate determination of the internal drag of small ducts is not new. The measurement of internal drag has always been difficult and large errors can result from the improper use of measurement techniques. At low speeds such errors did not seriously affect the final drag results since the internal drag of the duct was small compared to the total external drag of the airplane. However, for certain propulsion systems the size of the propulsion unit relative to the wing area increases as the airplane cruising speed increases. Consequently, for some configurations presently being studied the internal drag of the duct used to simulate the external aerodynamics of an airbreathing propulsion system on a small-scale model may be large in comparison to the total external drag of the model. The purposes of this paper are: (1) to compare several methods for obtaining the internal drag of a small circular duct; (2) to illustrate some of the difficulties encountered in assessing the momentum losses in small-scale ducts; and (3) to consider the feasibility of a simplified test procedure for determining internal drag.

~~CONFIDENTIAL~~

CONFIDENTIAL

SYMBOLS

d	diameter, in.
M_e	duct exit Mach number
M_∞	free-stream Mach number
p_e	duct exit static pressure, psia
p_{t_e}	duct exit total pressure, psia
p_∞	free-stream static pressure, psia
r	radius, in.
α	angle of attack, deg

DISCUSSION

Comparison of Methods

The flow in a straight circular duct with infinitesimal wall thickness perfectly aligned with the free stream is symmetrical about the duct longitudinal center line. This symmetry of flow simplifies the determination of the flow characteristics at the duct exit. Knowing the inlet and exit flow characteristics permits the calculation of the internal drag from momentum relationships. In addition, the internal forces on such a straight duct are solely skin friction on the inner surface which can be determined analytically or can be measured with a strain-gage balance. Under ideal conditions, the internal drag determined from methods such as these would be in perfect agreement.

Figure 1 shows an isometric sectional view of the model assembly used to obtain the internal drag of a circular duct by a force measuring technique. Inside the model is a sleeve which is supported, independently from the outer wall of the model, on flexures. The flexure cavity is open only to the duct inlet and to a pressure measuring tube at the rear of the flexure cavity. A thin flexible diaphragm at the base of the model prevents flow between the inner sleeve and wall of the model. Model base pressure and flexure cavity pressure were measured during each run and corrections were applied as necessary.

A movable rake shown in figure 1 was used to measure the flow characteristics near the duct exit. The rake could be moved in the vertical and horizontal planes and rotated $\pm 180^\circ$ separately or in any combination. It was thus possible to measure the exit static and total pressure at any point across the duct at the survey plane. Since the conditions at the inlet for

CONFIDENTIAL

this configuration are the same as free stream, the internal drag may be determined as the change in momentum between the inlet and the exit.

For the computation of the internal skin friction an all-turbulent boundary layer from inlet to exit was assumed and the method of reference 1, appendix A, was used. The internal surface of the duct was considered to be an adiabatic flat plate developed by unrolling the internal surface of the duct. The following table compares the internal drag coefficient obtained from the three methods just described for the circular duct at $\alpha = 0^\circ$. The internal drag coefficient is based upon the exit area of the duct which has a diameter of 1 inch. Results from the force measurement and from the detailed survey

Method	Internal drag coefficient
Force measurement	0.098
Detailed pressure survey	.098
Calculated skin friction	.087

agree surprisingly well. The values shown for the force and pressure survey methods are averages obtained from several runs. For any given run these two methods were found to agree within ± 1 percent. The skin-friction result is approximately 11 percent lower than the result from either of the other methods.

Flow Characteristics at $\alpha = 0^\circ$

In order to investigate nacelles with inlets other than circular, detailed pressure surveys were made near the exit of the ducts shown in figure 2 to determine the flow characteristics and to define some of the problems encountered in determining internal drag for such configurations. In addition to the circular duct previously discussed (fig. 2, upper left) there was a square duct (fig. 2, upper right), a two-dimensional inlet with a circular exit in a wing compression field (fig. 2, lower left), and a two-dimensional inlet with precompression ramps and circular exit in a wing compression field (fig. 2, lower right). Thus, all the models had circular exits except the square duct and all exit areas were equal.

Mach number and static-pressure ratio along the horizontal and vertical axes near the duct exit are shown in figure 3 for the models just described at 0° angle of attack. The data for the circular and square ducts indicate essentially symmetrical flow about the duct longitudinal center line which would make the determination of the momentum near the duct exit relatively straightforward. This was, in fact, the case for the circular duct. However, it should be kept in mind that the flow characteristics in the corners of the square duct are not defined in this figure and without this information the internal-drag results will be questionable. The circumferential flow distortion near the exit of the ducts with two-dimensional inlets is quite

CONFIDENTIAL

~~CONFIDENTIAL~~

pronounced as seen in the lower portion of figure 3. Such distortion greatly complicates the determination of the momentum at the survey station and points up the detail required in pressure measurements to define the flow characteristics properly near the exit of such ducts. The symbols in this figure illustrate the detail of the surveys made in this study.

Flow Characteristics at $\alpha = 5^\circ$

The determination of the momentum near the exit of ducts may be further complicated by changes in angle of attack. In figure 4 this effect is illustrated by the difference in flow characteristics for these models at $\alpha = 0^\circ$ and 5° . The flow distortion for the circular and square ducts is considerably greater at $\alpha = 5^\circ$ than at $\alpha = 0^\circ$ (upper portion of fig. 4) particularly along the vertical axis (upper right portion of fig. 4). Now the flow is no longer symmetrical about the duct longitudinal center line and the determination of the momentum at the survey station requires detailed surveys. Pronounced changes in pressure and Mach number are also found near the exit of the models with two-dimensional inlets when the angle of attack is changed from 0° to 5° (see lower part of fig. 4). For instance, at $\alpha = 0^\circ$ the static-pressure ratio across the duct in the survey plane is seen to be nearly constant for these models. But at $\alpha = 5^\circ$ the static-pressure-ratio distribution is considerably distorted along both the horizontal and vertical axes. Hence, identification of the flow characteristics in the survey plane of the models with two-dimensional inlets requires detailed pressure surveys at both $\alpha = 0^\circ$ and 5° . It can also be noted from these results that the presence of the wing as a flow straightener for the inlet does not eliminate the problem of exit flow distortion at angle of attack. It should be recognized that these comments are restricted to the specific configurations of this study and additional research is required to assess the effects of the individual parameters such as the distance from the leading edge of the wing to the duct inlet.

Internal Geometry Changes

The effects on flow distortion that can be generated by variations in the internal geometry, such as the transition from rectangular to circular section, are illustrated in figure 5. Shown in this figure is a two-dimensional inlet with precompression ramps and a circular exit. The length of the transition section (from the two-dimensional inlet to the circular exit) is different for each model. It can be seen that as the transition section length increases, the flow distortion near the exit decreases. This result was obtained despite the fact that the length of the constant-diameter section decreased as the length of the transition section increased. It would appear that great care must be exercised to properly proportion the lengths of the transition section and the constant cross-section parts of the duct if flow distortion is to be reduced.

Simplified Test Procedure

The final objective of this study was to examine the potential of short-cut test procedures that would permit the accurate determination of the internal drag of small-scale ducts. In view of the foregoing results it is clear that the assessment of internal drag of most of the ducts of this study requires complicated test techniques and instrumentation. Only the circular duct at zero incidence was found to offer sufficiently uniform flow conditions to encourage serious consideration of the indicated objective. The circular duct is also of particular interest here since it is representative of one of the more commonly used configurations for simulating the propulsion system on aircraft models. A simplified method illustrated in figure 6 requires a stationary rake with as few as three total-pressure probes and two static-pressure measurements. Experimental static- and total-pressure distributions obtained by detail pressure measurements across the duct are shown as solid lines. Static-pressure measurements are made at approximately $r/3$ and at the duct wall and total-pressure measurements at $r = 0$ and at approximately $r/3$ and $(2/3)r$. The two latter total-pressure probes can be seen to have been carefully placed to be inside and outside the wall boundary layer. With these pressure measurements the total- and static-pressure distributions across the duct can be approximated as indicated by the straight dashed lines. From these approximations the internal drag was determined within ± 1 percent of the force measurement. It should be noted, however, that the proper location for the probes depends to some extent on the thickness of the boundary layer at the survey station. Hence, some small adjustment in the positioning of the probes may be required for test conditions other than those used herein.

CONCLUDING REMARKS

Several methods have been demonstrated for determining the internal drag of a circular duct at a Mach number of 4.1 and $\alpha = 0^\circ$. Results from the experimental techniques agree well while the results from a boundary-layer estimate are approximately 11 percent lower than the measured results. The flow near the exit of several ducts with inlets other than circular was found to be quite distorted. Changing the angle of attack of any of the ducts of this study from 0° to 5° increased flow distortion considerably. Increasing the transition section length of a two-dimensional inlet having a circular exit decreased the flow distortion near the exit. A simplified experimental procedure that will provide accurate values of internal drag appears feasible for the circular duct at $\alpha = 0^\circ$.

REFERENCE

1. Hicks, Raymond M.; and Hopkins, Edward J.: Effects of Spanwise Variation of Leading-Edge Sweep on the Lift, Drag, and Pitching Moment of a Wing-Body Combination at Mach Numbers From 0.7 to 2.94. NASA TN D-2236, 1964.

FORCE-MODEL ASSEMBLY
ISOMETRIC SECTIONAL VIEW

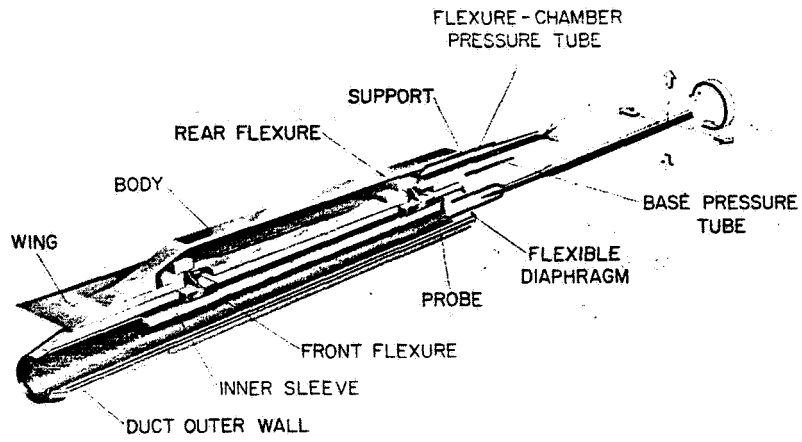


Figure 1

DUCT STUDY MODELS

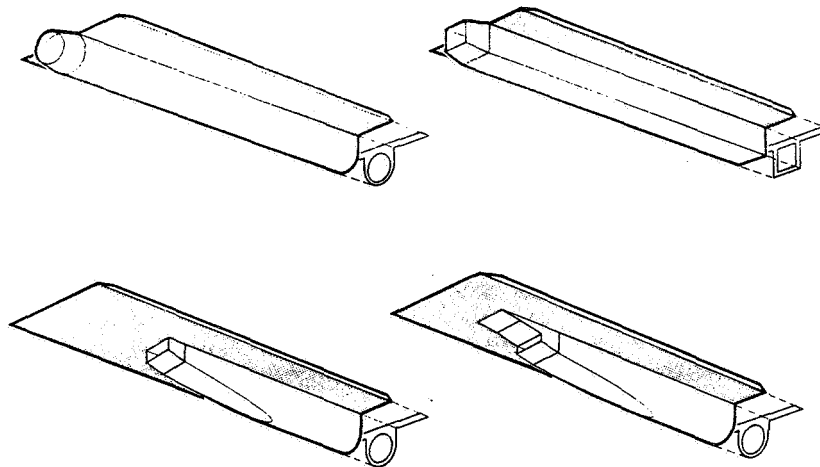


Figure 2

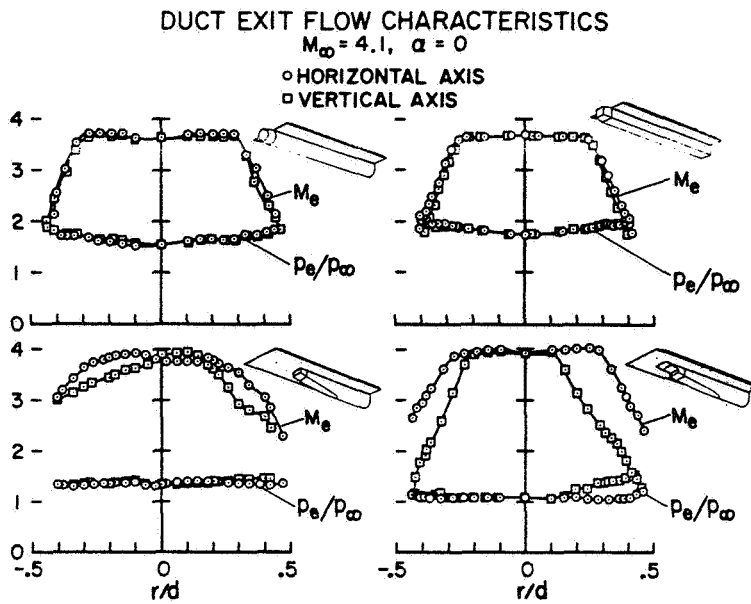


Figure 3

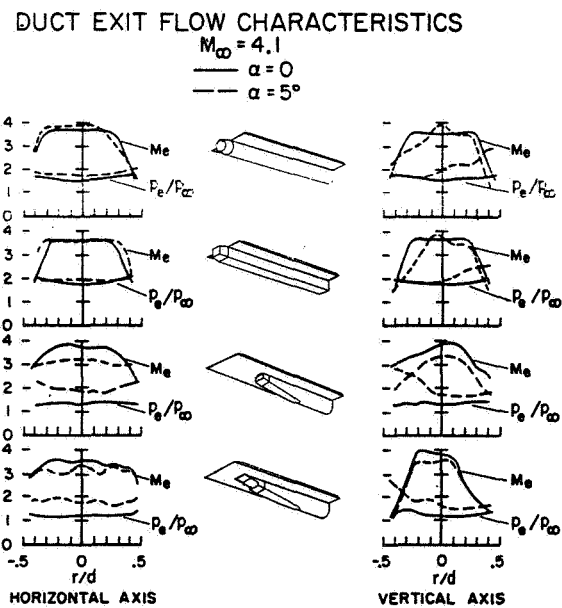


Figure 4

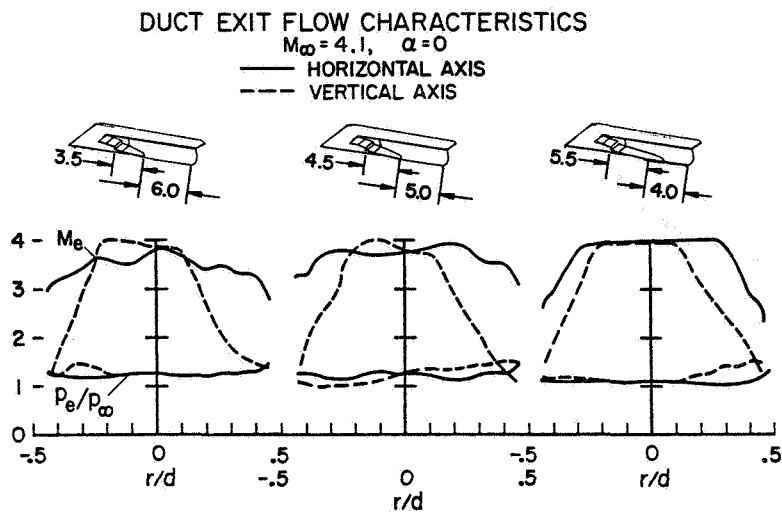


Figure 5

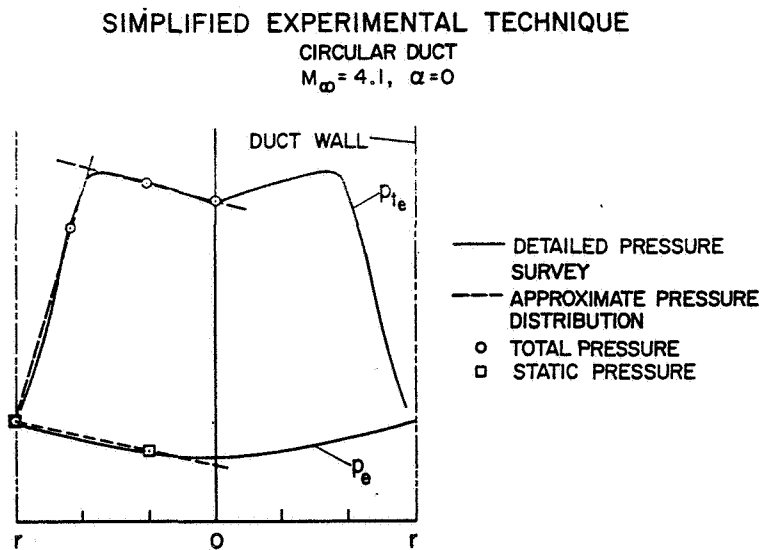


Figure 6

~~CONFIDENTIAL~~

14. BOUNDARY-LAYER TRANSITION ON HYPERSONIC-CRUISE AIRCRAFT

By K. R. Czarnecki, Jerry M. Allen,
and Mary W. Jackson
Langley Research Center

SUMMARY

An assessment has been made of the influence of boundary-layer transition on the component design of a hypersonic-cruise transport aircraft. The assessment indicates that more theoretical boundary-layer stability calculations are needed, more sophisticated analyses of presently available transition results are required, and additional experimental data obtained under highly controlled conditions are necessary. On the hypersonic-cruise transport, the detail design of the fuselage nose and engine air inlet will be strongly affected by transition characteristics, whereas the wing and tail leading edges will have to be designed for essentially turbulent flow. Surface-temperature effects on transition and effects of transition on airplane performance are expected to be small.

14

INTRODUCTION

Boundary-layer transition is a highly complex phenomena which can influence the performance and detail design of aircraft. With the possible extension of the flight speeds of transport aircraft to hypersonic speeds where ambient densities are low and significant boundary-layer cooling can be expected, it appears desirable to reassess the possibility of attaining long runs of laminar flow. The primary emphasis of the assessment will be on the influence of boundary-layer transition on component design. Although laminar flow may not be of great importance in terms of airplane performance, it is still significant in terms of detail design.

SYMBOLS

M_l	local Mach number
M_N	Mach number normal to wing leading edge
M_∞	free-stream Mach number
r_n	nose radius of cone, in.
R/ft	unit Reynolds number
R_D	Reynolds number based on nose diameter and sharp-cone local flow conditions

~~CONFIDENTIAL~~

CONFIDENTIAL

$R_{x,tr}$	transition Reynolds number based on axial distance from nose and on sharp-cone local flow conditions
T_{aw}	adiabatic wall temperature, °F abs
T_t	stagnation temperature, °F abs
T_w	wall temperature, °F abs
u	velocity within boundary layer, ft/sec
u_2	local velocity just outside the boundary layer, ft/sec
x_{tr}	transition distance from model nose, ft
z	distance normal to local surface, ft
α	angle of attack, deg
Λ	sweep angle, deg

TRANSITION PARAMETERS

The airplane components whose detail design may be affected by the characteristics of boundary-layer transition are depicted in figure 1. These components include the fuselage nose, the wing and tail leading edges, portions of the control leading edges, and the engine air inlet. There will probably be some items (not shown in the sketch), such as impact tubes, angle-of-attack indicators, and radio antennas, that may protrude through the airplane boundary layer and whose detail design will be affected by the type of boundary-layer flow that might be expected.

Some typical uncorrelated transition data are presented in figure 2. The data have been restricted to cones having nose radii on the order of 1/4 to 1/2 inch. The transition Reynolds number based on the distance from the cone nose and on local flow conditions is plotted against the local Mach number. In both parameters, local flow refers to sharp-nose body conditions. Three types of data are differentiated in the figure: wind tunnel, ballistic range, and free flight.

These samplings of data show a large scatter. Obviously, uncorrelated transition data of this type, which have been gathered for decades, are of little direct use to the designer. Methods must be found for differentiating the effects of the many parameters that influence transition.

The most common variables or parameters which affect boundary-layer transition are tabulated as follows:

CONFIDENTIAL

Mach number	Stagnation temperature
Unit Reynolds number	Two- or three-dimensional flow
Heat transfer	Pressure gradients
Nose blunting	Surface waviness
Wing sweep	Surface roughness
Angle of attack	Free-stream turbulence
	Noise and vibration

The problem is that the number of significant parameters is large and that the effects of changes in each parameter are affected by the level or by changes in all the other parameters. For this reason, it is extremely difficult to isolate the effects of a single parameter sufficiently well to enable the physical mechanism to be understood and to develop a procedure for estimating these effects for all conditions of the other variables. The basic objective of this paper is to discuss a few of the more recent developments or indications and their application to component design without going too deeply into the technical details. The discussion will be limited to the items listed in the left-hand column of the tabulation.

DISCUSSION OF TRANSITION CHARACTERISTICS

Effects of Mach Number and Unit Reynolds Number

Two of the most important parameters affecting boundary-layer transition are Mach number and unit Reynolds number. Some typical effects of these parameters are shown in figure 3, which is really a selective version of figure 2. The transition Reynolds number is plotted against the local Mach number. The data are restricted to relatively sharp cones in flight and in wind tunnels. Data are presented for a low unit Reynolds number range from 1×10^6 to 3×10^6 and for a high unit Reynolds number range from 10×10^6 to 30×10^6 . Below a local Mach number of 8, the data have been limited to a ratio of wall temperature to adiabatic wall temperature between 0.3 and 0.6, a range which encompasses the values of interest for a Mach 6 hypersonic transport. Above this Mach number, this temperature restriction was removed because the only available flight data have a wall-temperature ratio of about 0.1 and because, as will be shown subsequently, the effects of wall-temperature ratio at these higher Mach numbers are expected to be relatively small.

The first point to be made (see fig. 3) is that wind-tunnel transition Reynolds numbers appear to be lower than flight values. A part of this difference is ascribed to the higher stagnation temperatures encountered in flight. These higher stagnation temperatures should have a favorable effect on transition according to the theoretical stability calculations of Mack (ref. 1) and of Brown (ref. 2). There is a lack of flight data in the local Mach number range from 5 to 10. This region is of direct interest to the designer of hypersonic transports. The second point to be made is that at the lower unit Reynolds numbers, approaching those where the hypersonic transports will operate, there is a rapid increase in transition Reynolds number with Mach number. At the higher unit Reynolds numbers, the effect of Mach number is very small -

if it exists at all - although some evidence exists which indicates that there may be some favorable effect above $M_1 = 8$. The last point to be made is that at a Mach number of about 6, there is a powerful effect of unit Reynolds number in the wind-tunnel data. At higher Mach numbers, this unit Reynolds number effect appears to diminish; however, because this trend is based on meager data and because it may be a characteristic peculiar to the temperature range chosen, further investigation is needed.

The existence of a unit Reynolds number or apparent unit Reynolds number effect on transition is one of the key problems in the interpretation of transition data. There are several reasons for expecting the existence of a free-stream unit Reynolds number effect both in the wind tunnel and in flight. First, the cones were not sufficiently sharp to eliminate bluntness effects; second, there may be a hypersonic viscous interaction effect between the boundary layer and nose shock even on a sharp cone; and, third, tunnel-wall disturbances may be responsible for the effect. As discussed in reference 3, other reasons for expecting unit Reynolds number effect may exist.

The first three reasons for expecting a free-stream unit Reynolds number effect can be explained with the aid of figure 4, which shows a blunted cone mounted in a hypersonic wind tunnel. The coupling of the blunting effect with unit Reynolds number occurs because the free-stream flow close to the axis of the blunted cone, as exemplified by the streamline, passes through the strong portion of the detached nose shock and undergoes large effective reductions in density and velocity and increases in viscosity. These changes in flow characteristics cause changes in local unit Reynolds number, Mach number, and pressure gradient on the cone surface which vary with distance downstream from the nose. The effect is felt as far as 100 to 1000 nose diameters downstream. For the blunted-nose cone then, the ideal cone boundary layer of constant surface flow conditions usually does not exist. Consequently, as the free-stream unit Reynolds number is changed and transition moves over the cone surface, the transition location moves into areas of different local Mach number and local Reynolds number. Therefore, the local unit Reynolds number at transition does not change proportionately to the free-stream unit Reynolds number. The appearance of these local-surface effects derived from nose blunting should not be interpreted as implying that there is a unit Reynolds number effect in the case of the ideal cone boundary layer of constant surface flow conditions. On geometrically sharp-nose cones, similar changes in local flow conditions occur as a result of the shock generated by the growth in displacement thickness at the model nose; hence, free-stream unit Reynolds number effects exist.

In most wind tunnels, the boundary layer on the tunnel walls is turbulent. Disturbances from the outer edge of the wall boundary layer can impinge on the model and affect transition. If the relative magnitude of these disturbances should change with tunnel stagnation pressure, there will be an apparent free-stream unit Reynolds number effect on transition. Such an effect could also occur on an airplane in flight because of radiation of disturbances from the turbulent boundary layer on a fuselage or wing to the engine air inlet or vertical tail.

CONFIDENTIAL

Effects of Nose Blunting

In order to illustrate the nose-blunting effect in more detail, some typical effects of nose blunting on transition are presented in figure 5. These transition results are for cones and are plotted against the nose-bluntness Reynolds number R_D . Stainback's data (ref. 4) are limited to constant unit Reynolds number because of unit Reynolds number effects. For the data of Stetson and Rushton (ref. 5), where the unit Reynolds number effects were small, this restriction was not necessary, and a more extensive composite curve could be formed. The data (fig. 5) show a strong tendency for the bluntness effects to disappear at low bluntness Reynolds numbers at constant unit Reynolds number. At the higher bluntness Reynolds numbers, the transition Reynolds numbers reach a peak and then decrease as transition moves close to the blunted nose where the local static pressures and, hence, local unit Reynolds numbers are somewhat higher than they are farther downstream. When there is a unit Reynolds number effect for the sharp-nose cones, the location of the peak transition Reynolds number is dependent upon the unit Reynolds number and moves toward lower bluntness Reynolds numbers as the unit Reynolds number is decreased and toward higher values as the unit Reynolds number is increased.

Note that it appears feasible to design the fuselage nose for maximum transition Reynolds number. The nose diameter will be on the order of 1 foot. For the spike on a spike air inlet, the allowable diameters will be small and relatively low transition Reynolds numbers (on the order of 3×10^6 or less) will have to be accepted. For two-dimensional blunting, the optimum transition Reynolds numbers occur at very low bluntness Reynolds numbers ($R_D < 10^4$) and it again appears feasible to design for optimum transition Reynolds numbers for inlet lips or leading edges.

Effects of Angle of Attack

The significance of angle of attack on transition on a conical body is illustrated in figure 6 (from ref. 5). In order to simplify interpretation, the results are presented as the ratio of the transition distance for the various values of r_n and α to the transition distance for the sharp cone at $\alpha = 0^\circ$. Transition-distance ratios are shown for both the windward and leeward meridians. The rise in transition distance with nose bluntness at $\alpha = 0^\circ$ is a favorable effect of nose blunting, as mentioned in the discussion of the previous figure.

The transition results presented in figure 6 indicate a relatively small overall effect for a sharp cone; that is, the increases in transition on the windward meridian tend to counteract the decreases in transition on the leeward side. For the blunted cone, however, increasing angle of attack tends to negate rapidly the favorable effects of nose blunting on both sides of the model. At an angle of attack of about 8° , the angle at which the hypersonic transport will fly, practically no favorable effect of blunting remains. Thus, a relatively close alinement of the fuselage nose or inlet spike with the

CONFIDENTIAL

CONFIDENTIAL

direction of the ambient stream must be maintained if it is desired to exploit the favorable effects of nose blunting.

Effects of Heat Transfer

The hypersonic-cruise transport will fly under conditions of heat transfer. The effects of heat transfer on transition are depicted in figure 7. On the left-hand side of the figure are plotted the wall-temperature ratios T_w/T_t for infinite boundary-layer stability as a function of local Mach number as calculated by Dunn and Lin (ref. 6), the short-dashed curve, and by Reshotko (ref. 7), the solid curve. Within these loops the boundary layer should be theoretically stable for all Reynolds numbers. Dunn and Lin neglected temperature fluctuations whereas Reshotko included these effects; hence, Reshotko's theory can be expected to be more reliable, as is confirmed by experimental results. In order to illustrate what these stability implications mean in terms of transition Reynolds numbers as a function of wall-temperature ratio, three Mach numbers have been chosen as shown by the long-dashed vertical lines at $M_1 = 1.6, 3.5$, and 7.8 . Some typical transition curves are illustrated for these Mach numbers in the plot on the right-hand side of figure 7. These transition curves are based primarily on experiment. No ordinate scale has been provided for $R_{x,tr}$ because the following discussion is meant to be qualitative.

At a Mach number of 1.6, infinite stability (shown by the solid vertical lines) occurs at the relatively high wall-temperature ratio of 0.67. Consequently, because of the relatively short distance between this temperature ratio and that for adiabatic wall (or even stagnation temperature), the experimental transition Reynolds number tends to rise fairly rapidly with boundary-layer cooling toward tangency with the theoretical infinite-stability temperature ratio until surface roughness or other adverse effects such as the boundary-layer instability between loops become significant. Such adverse effects would actually cause a decrease in transition Reynolds number with further cooling. At a Mach number of 3.5, infinite stability occurs at a lower wall-temperature ratio, and the experimental rise in $R_{x,tr}$ with decrease in T_w/T_t becomes smaller over most of the temperature range. At a Mach number of 7.8, there is no infinite stability at any wall temperature, and the change in $R_{x,tr}$ with T_w/T_t is very small. This trend provides the justification for removing the temperature restrictions on the high Mach number data in figure 3.

If the surface roughness is fairly high, the favorable effects of boundary-layer cooling may be lost as indicated by the dashed line for $M_1 = 3.5$, based on the experimental results of Van Driest and Boison (ref. 8). Roughness effects become more critical with cooling because of the decreases in boundary-layer thicknesses and increases in local density. A similar loss in cooling effectiveness occurs if the tunnel turbulence level is too high (ref. 8).

~~CONFIDENTIAL~~

Effects of Wing Sweep

Because of the relatively large surface areas involved, probably the most important single parameter affecting transition on a hypersonic transport is wing sweep angle. Some typical effects of wing sweep on transition are shown in figure 8 for a free-stream Mach number of 4.0 (refs. 9 and 10). This value is about the highest Mach number for which sufficient data were available for a simplified discussion. Swept-wing results at lower Mach numbers, swept-cylinder results at $M_\infty = 7$ (ref. 11), and more recent flat-plate results at $M_\infty = 8$ (ref. 12) indicate that the basic trends will change little, if any at all, for swept wings at higher free-stream Mach numbers. In order to simplify the discussion, the data are presented as the ratio of transition distance x_{tr} for the wing with sweep to transition distance for the same wing section at zero sweep.

The transition results indicate a large decrease in transition distance with increasing sweep angle. Analysis indicates that three factors affect boundary-layer transition under conditions of wing sweep. The first factor, which normally dominates over most of the low and moderate sweep-angle range, is associated with decreasing favorable effects of nose blunting as sweep is increased. This fact is shown by the general agreement of the experimental trends with the theory (ref. 13). In the theory, the assumption is made that the favorable effects of nose blunting are dependent upon the component of Mach number normal to the wing leading edge and that there is a normal shock ahead of the unswept reference wing which reduces the wing local Reynolds number. Some of the differences in transition levels in the experimental data can be ascribed to the fact that, as was shown in the discussion of blunting effects on cones, the assumed optimum blunting is usually not attained. For hypersonic-cruise transports, the wing sweep will be on the order of 75° and the transition distances will obviously be small. For sweep angles on the order of 75° , two additional factors appear and tend to fix transition practically at the wing leading edge. The first of these additional effects is purely geometrical and results from the fact that the wing apex angle is approaching the angle for lateral spread of turbulence. Actually, Bushnell's results, discussed in reference 14, indicate that if a fuselage is present this effect may be more severe than indicated on the basis of the angles of the turbulent wedges if the bluntness Reynolds number is greater than 2×10^5 . The second additional effect derives from the fact that, as the wing is swept, a cross-flow component is set up in the boundary-layer flow (as shown in the insert sketch of fig. 8) in a plane normal to the external streamline near the wing leading edge (refs. 13 and 15). This cross-flow profile is unstable at relatively low Reynolds numbers and leads to the development of a vortex type of secondary flow which causes early transition. Thus, for the swept wings and tails of the hypersonic transports, these three factors appear to restrict these surfaces to essentially fully turbulent flow.

CONCLUDING REMARKS

An assessment has been made of the influence of boundary-layer transition on the component design of a hypersonic-cruise aircraft. The following

~~CONFIDENTIAL~~

~~CONFIDENTIAL~~

concluding remarks may be made: First, more boundary-layer stability calculations based on the full stability equations without approximations are needed; second, more sophisticated analyses of the presently available transition results are required; and, third, additional experimental results will have to be obtained wherein all variables are closely controlled while changes are being made in the variable under investigation. Some efforts in the last two fields are already underway at NASA. On the hypersonic-cruise transport, the detail design of the fuselage nose and engine air inlet will be strongly affected by transition characteristics, whereas the wing and tail leading edges will probably have to be designed for essentially turbulent flow. Surface-temperature effects on transition and effects of transition on airplane performance are expected to be relatively small, and, hence, little favorable effect with boundary-layer cooling should be expected. So long as the adverse effects of wing sweep on transition are not eliminated, the prospects for significantly improving hypersonic airplane performance by maintaining long runs of laminar flow appear to be poor.

~~CONFIDENTIAL~~

REFERENCES

1. Mack, L. M.: The Stability of the Compressible Laminar Boundary Layer According to a Direct Numerical Solution. Recent Developments in Boundary Layer Research, Pt. I, AGARDograph 97, May 1965, pp. 329-362.
2. Brown, W. Byron: Exact Numerical Solution of the Complete Linearized Equations for the Stability of Compressible Boundary Layers. Rept. No. NOR-62-15, Northrop Corp., Jan. 1962.
3. Whitfield, Jack D.; and Potter, J. Leith: The Unit Reynolds Number as a Parameter in Boundary Layer Stability. AEDC TN-58-77, ASTIA Doc. No. AD-202731, U.S. Air Force, Oct. 1958.
4. Stainback, P. Calvin: Some Effects of Roughness and Variable Entropy on Transition at a Mach Number of 8. AIAA Paper No. 67-132, Jan. 1967.
5. Stetson, Kenneth F.; and Rushton, George H.: A Shock Tunnel Investigation of the Effects of Nose Bluntness, Angle of Attack and Boundary Layer Cooling on Boundary Layer Transition at a Mach Number of 5.5. AIAA Paper No. 66-495, June 1966.
6. Dunn, D. W.; and Lin, C. C.: On the Stability of the Laminar Boundary Layer in a Compressible Fluid. J. Aeron. Sci., vol. 22, no. 7, July 1955, pp. 455-477.
7. Reshotko, Eli: Transition Reversal and Tollmien-Schlichting Instability. Phys. Fluids, vol. 6, no. 3, Mar. 1963, pp. 335-342.
8. Van Driest, E. R.; and Boison, J. Christopher: Experiments on Boundary-Layer Transition at Supersonic Speeds. J. Aeron. Sci., vol. 24, no. 12, Dec. 1957, pp. 885-899.
9. Jillie, Don W.; and Hopkins, Edward J.: Effects of Mach Number, Leading-Edge Bluntness, and Sweep on Boundary-Layer Transition on a Flat Plate. NASA TN D-1071, 1961.
10. Dunning, Robert W.; and Ulmann, Edward F.: Effect of Sweep and Angle of Attack on Boundary-Layer Transition on Wings at Mach Number 4.04. NACA TN 3473, 1955.
11. Feller, William V.: Investigation of Equilibrium Temperatures and Average Laminar Heat-Transfer Coefficients for the Front Half of Swept Circular Cylinders at a Mach Number of 6.9. NACA RM L55F08a, 1955.
12. Deem, Ralph E.; and Murphy, James S.: Flat Plate Boundary Layer Transition at Hypersonic Speeds. AIAA Paper No. 65-128, Jan. 1965.

- ~~CONFIDENTIAL~~
13. Chapman, Gary T.: Some Effects of Leading-Edge Sweep on Boundary-Layer Transition at Supersonic Speeds. NASA TN D-1075, 1961.
 14. Bushnell, Dennis M.: Effects of Shock Impingement and Other Factors on Leading-Edge Heat Transfer. Conference on Hypersonic Aircraft Technology, NASA SP-148, 1967. (Paper No. 18 herein.)
 15. Owen, P. R.; and Randall, D. G.: Boundary Layer Transition on a Sweptback Wing. Rept. No. Aero 277, Brit. R.A.E., May 1952.

AIRPLANE COMPONENTS AFFECTED BY TRANSITION

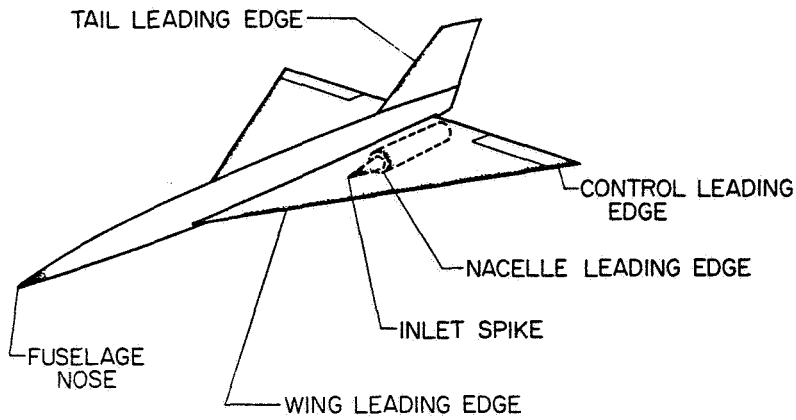


Figure 1

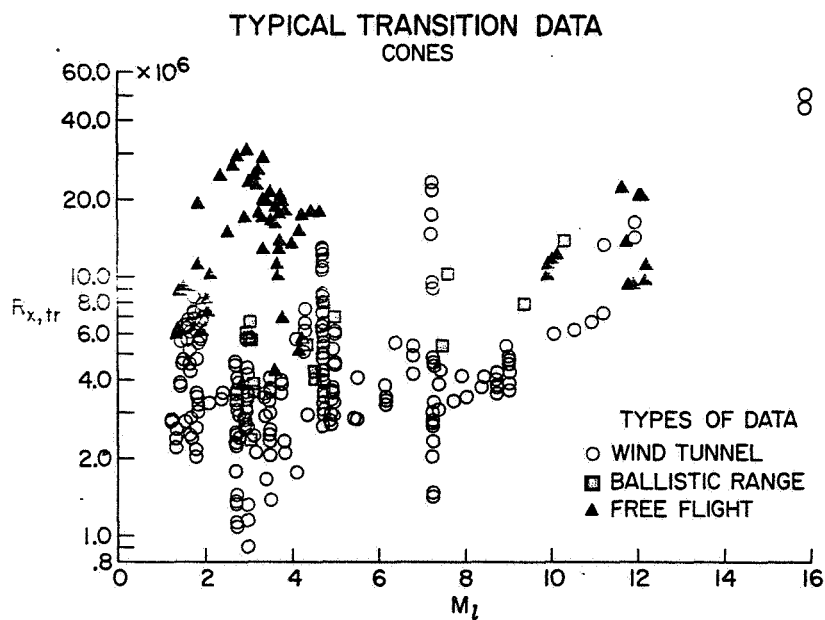


Figure 2

EFFECT OF M_i AND R/ft ON TRANSITION EXPERIMENTAL SHARP-CONE DATA

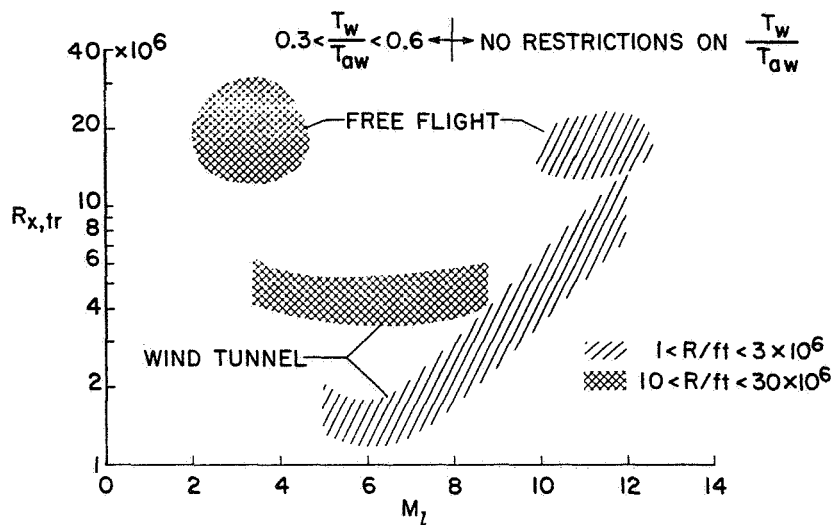


Figure 3

SOME FACTORS AFFECTING TRANSITION

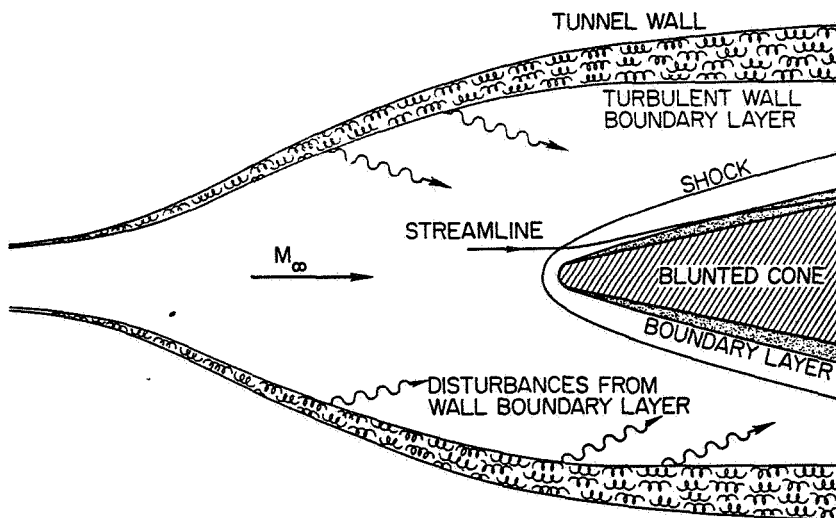


Figure 4

EFFECT OF BLUNTNES ON TRANSITION CONES

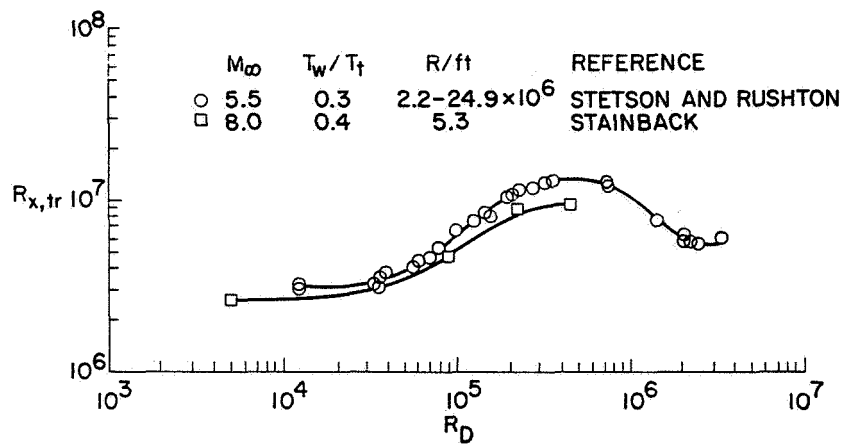


Figure 5

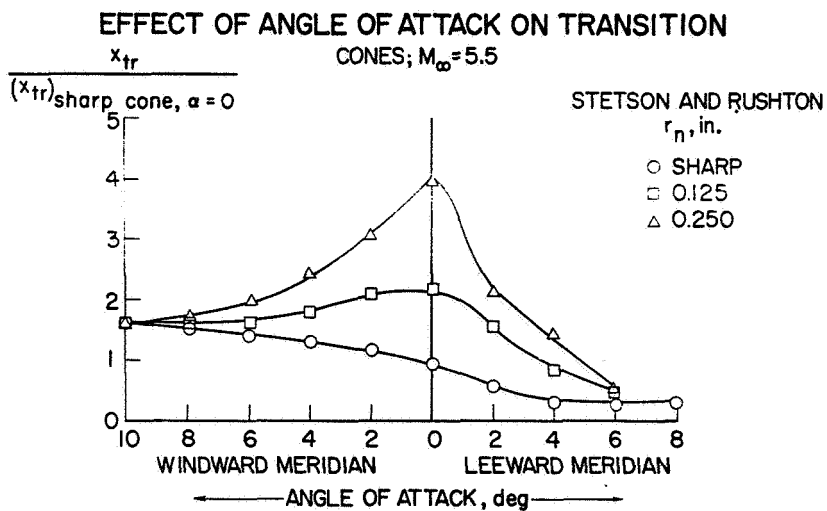


Figure 6

EFFECT OF HEAT TRANSFER

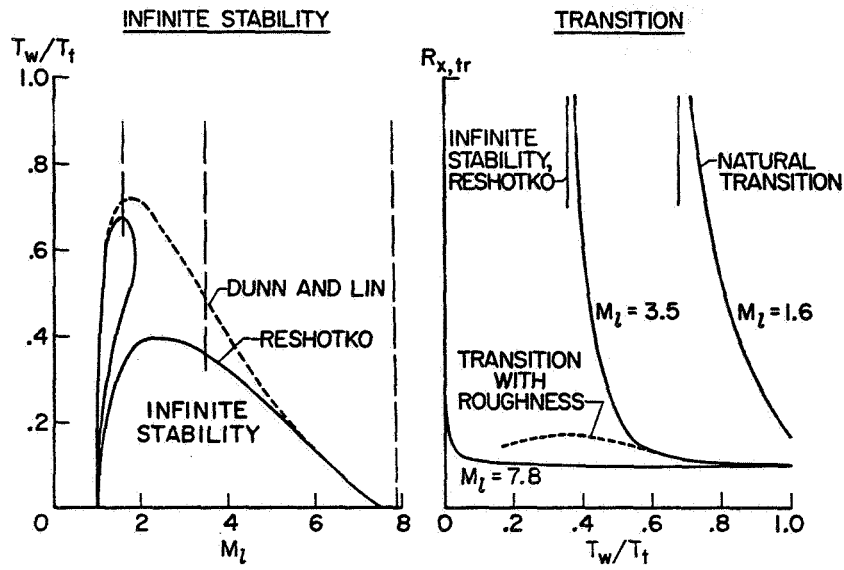


Figure 7

EFFECT OF SWEEP ON TRANSITION $M_\infty = 4; \alpha = 0^\circ$

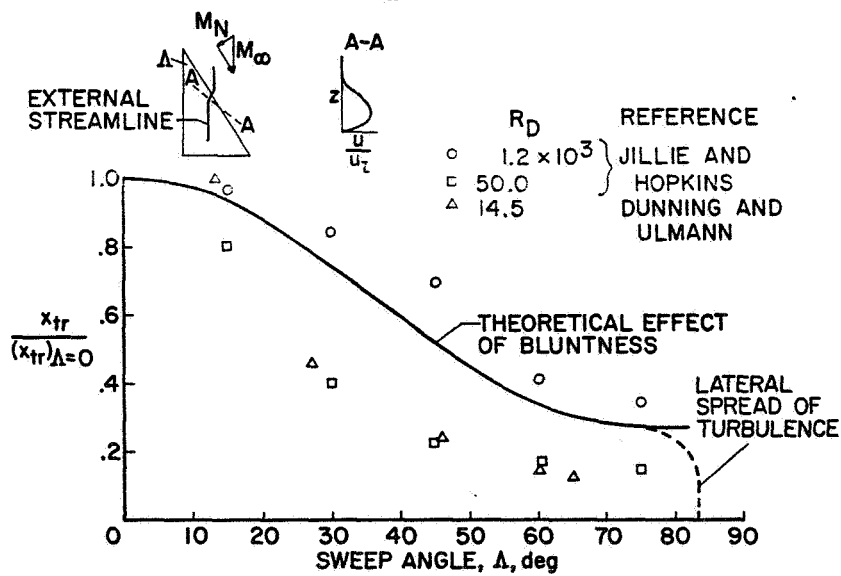


Figure 8

15. TRANSITION FIXING FOR HYPERSONIC FLOW

By James R. Sterrett, E. Leon Morrisette, Allen H. Whitehead, Jr.
Langley Research Center

and

Raymond M. Hicks
Ames Research Center

SUMMARY

Present wind-tunnel facilities lack the capability to duplicate the Reynolds number associated with the hypersonic-cruise vehicle. As a means of overcoming this problem, attention is being given to artificial promotion of transition by means of surface roughness. At lower speeds, boundary-layer roughness has been used successfully. However, at hypersonic speeds, the required roughness height is so large that the method raises many questions. This paper considers these questions and examines the overall problems associated with boundary-layer "trips" to produce turbulence at hypersonic conditions.

The data indicate that the required roughness heights are so large that whether trips should be used in hypersonic wind-tunnel tests depends upon the particular purpose of any experiment. For example, an engineer can successfully use trips to study the heat transfer associated with an aircraft component or to produce turbulent flow in front of an inlet or control that otherwise might be transitional or laminar. However, at the present time, trips cannot be used when an accurate value of the total drag of a configuration is required because of the large pressure drag associated with the roughness elements. With additional study, the drag associated with the roughness elements could probably be determined accurately. The vortex shedding that occurs in the lee side of delta wings at moderate angles of attack places further limitations on the use of trips for wind-tunnel simulations of hypersonic cruise vehicles. For any test, care must be taken to dimension the trips properly.

INTRODUCTION

Turbulent flow is known to exist over most aircraft configurations at hypersonic speeds, yet laminar flow exists over large parts of wind-tunnel models at these speeds. In order to provide proper simulation in the hypersonic range, methods of producing turbulent flow near the leading edge of wind-tunnel models are being studied. At lower speeds, boundary-layer roughness elements have been used successfully (for example, in ref. 1); however, the required roughness height is small as compared with the boundary-layer thickness. At hypersonic Mach numbers, the roughness elements (trips) must be approximately as high as the boundary layer before even the position of transition is

affected. Small trips can even delay transition. (See ref. 2.) Since the roughness heights required to promote transition at hypersonic speeds are so large, the method raises many questions, such as: "Does a tripped turbulent boundary layer behave in the same way as a natural turbulent boundary layer?" and "How large is the drag associated with the tripping element?" In this presentation these questions and the overall problems associated with boundary-layer trips at hypersonic conditions are discussed.

SYMBOLS

C_D	coefficient of drag, $\frac{\text{Drag}}{q_\infty S}$
ΔC_D	increase in coefficient of drag due to pressure drag of roughness elements
C_F	skin-friction coefficient
c	chord (see fig. 12)
d	diameter of roughness elements
k	vertical height of roughness above plate
L	length of configuration
M	Mach number
N_{St}	Stanton number
p	static pressure
q_∞	free-stream dynamic pressure
R_k	Reynolds number based on fluid conditions at top of roughness elements and height of roughness, $\frac{\rho_k u_k k}{\mu_k}$
$R_{k,c}$	Reynolds number based on fluid conditions at top of roughness necessary to move turbulent flow close to trip position
R_L	Reynolds number based on model length
$R_{x,k}$	Reynolds number based on conditions at outer edge of boundary layer and distance from leading edge to roughness position, $\frac{\rho_o u_o x_k}{\mu_o}$

$R_{x,tr}$	Reynolds number based on conditions at outer edge of boundary layer and position where boundary layer becomes turbulent, $\frac{\rho_o u_o x_t}{\mu_o}$ (see fig. 2)
R_v	Reynolds number based on distance from virtual origin, $\frac{\rho_o u_o (x - x_v)}{\mu_o}$
R_∞	free-stream Reynolds number
S	planform area of configuration
s	lateral spacing of center of roughness elements
u	velocity component of flow parallel to surface
t	average diameter (thickness) of leading edge
x	distance from leading edge or distance from junction of delta wing and flap
x_k	distance from leading edge to roughness position
x_t	distance from leading edge to position where flow becomes turbulent
y	vertical distance measured from plate surface
α	angle of attack
δ	boundary-layer thickness based on velocity
δ_f	flap angle (see fig. 10)
δ_k	boundary-layer thickness on smooth model at roughness position
δ^*	boundary-layer displacement thickness
ρ	density
μ	viscosity

Subscripts:

l	local
k	conditions at top of roughness
o	local conditions at outer edge of boundary layer

∞ free stream
 v virtual origin

DISCUSSION

Previous work on boundary-layer transition has indicated that the process by which trips (roughness) produce turbulent flow is for the trips to produce some type of vortex flow downstream of a tripping element. An example of this phenomenon is shown in figure 1. The lower part of the figure shows paint patterns taken downstream of a sphere and reported in reference 3. The sphere was one of many which were placed on a blunted cone as is illustrated in the top part of figure 1. This figure shows that at least two vortices are produced by each roughness sphere. Similar results were reported in references 4 and 5. The effects of these vortices are shown as dark patterns, where the flow scrubs the surface and produces a high temperature. Vortices dissipate and form turbulent flow very similar to wake flows. (See, for example, refs. 6 and 7.) How soon they form turbulent flow depends very strongly upon the local Reynolds number. In fact, if the Reynolds number associated with the trip is too low, these vortices will not be produced. (See ref. 7.) On the other hand, if the roughness sphere is too large, spanwise disturbances resulting from these vortices will persist very far downstream, as is shown in reference 3.

Two methods often used to determine when turbulent flow exists are illustrated in figure 2. One method is to examine velocity profiles obtained with a pressure probe. This method is very tedious to use and the probe apparently causes distortions in the boundary layer near the surface. Examples of this latter effect are seen by comparing the data shown for both natural and tripped conditions. To compare several profiles and to determine where transition occurred is difficult because of these probe distortions. However, the method of using the location of the maximum pressure from a total-pressure tube traversed longitudinally along the model surface to locate the beginning of turbulent flow, as illustrated in reference 8, has been used successfully. The method generally used to detect transition in the present investigation is by heat-transfer measurements. An example is shown on the left-hand side of figure 2 where the heat-transfer rate in terms of Stanton number is presented. The circles, which are for natural transition, show that turbulent flow occurs approximately at a Reynolds number of 3.5×10^6 . When roughness is placed on this model, the beginning of turbulent flow moves from a Reynolds number of approximately 3.5×10^6 to less than 0.7×10^6 .

The model used to detect spanwise distortions (fig. 3) had three chordwise rows of thermocouples placed at different spanwise positions behind one roughness element. The roughness elements on the plate are actually closer together than is indicated in the figure. Typical data taken with this model are presented in figure 3. The results show that when the roughness is of proper size, in this case $k/\delta_k \approx 1.9$, spanwise distortion of the flow is very slight. The beginning of turbulent flow is reasonably close to the roughness, and the

CONFIDENTIAL

experimental heat-transfer measurements are approximately those calculated by the Spalding-Chi method (ref. 9) when the virtual origin is assumed to be located at the trip. However, if k/δ_k is decreased to approximately 1.4, the spanwise variation behind the roughness element is considerably increased. The flow becomes uniform spanwise at approximately 8 inches from the leading edge. This position would be chosen as the beginning of turbulent flow and is the position identified as the virtual origin for the calculation shown. However, if the roughness is made too high, spanwise distortions appear for the entire length of the instrumentation as can be seen when $k/\delta_k \approx 5.4$. The trends of the data for this condition are no longer similar to those calculated for turbulent flow. These data are taken at conditions where the spanwise distortions can be minimized by properly sizing the trips. At higher Mach numbers, where the maximum Reynolds number of wind-tunnel facilities is limited, spanwise distortions may always exist.

Roughness-Transition Parameters

The more important roughness-transition parameters are as follows:

- (1) Pressure gradient
- (2) Wall temperature
- (3) Spacing
- (4) Local Mach number
- (5) Roughness-position Reynolds number $R_{x,k}$
- (6) Unit Reynolds number
- (7) Type of roughness
- (8) Roughness-height Reynolds number R_k
- (9) Model configuration

The pressure gradient and wall temperature are not included in the present discussion. In reference 5 the spacing of the roughness elements was not found to be critical at supersonic Mach numbers. (However, these elements should not be too closely spaced.) Similar trends have been noted at Mach 6. In this investigation the lateral spacing between the elements has generally been made 4 times the width of the element (or larger).

In figure 4, the effect of varying the last three parameters in the foregoing list while the other parameters are kept unchanged is examined. Bear in mind that the object is to find the most effective trip that has the smallest drag. The effect of using various types of roughness to trip the boundary layer on a flat plate is shown on the left side of figure 4, where the transition Reynolds number is plotted against the height of the roughness. The various types of roughness elements are indicated in the figure. The type of roughness element is not too important in producing transition; however, apparently an appreciable part of the area of the element must be located near the top. For example the data show that the pyramidal roughness does not trip the flow as well as the other types. On the other hand, a pinhead type of roughness which has its largest area near the top seems to be as good as (or better than) any trip tried. The pinhead is of interest as it would reduce the frontal area of the trip and thus probably reduce the pressure drag associated with the

CONFIDENTIAL

trip. However, the drag reduction is limited in that the area decrease takes place on that portion of the element which experiences the lowest pressures; furthermore, there is a strong possibility that the flow below the head of the pin would become choked, whereby some of the possible benefits would be negated.

On the right-hand side of figure 4 the effects of tripping the boundary layer on a delta wing and a flat plate are compared. The results indicate that the flow on a delta wing is easier to trip than that on a flat plate.

The effect of the roughness-position Reynolds number $R_{x,k}$ is now examined. This Reynolds number is based on conditions at the edge of the boundary layer and the distance from the leading edge to the roughness position. Another Reynolds number must be defined for this discussion. This Reynolds number $R_{k,c}$ is the Reynolds number based on conditions at the top of the roughness element necessary to move turbulent flow close to the trip position. (Turbulent flow is probably never moved completely to the roughness position.) Most previous data were taken at positions where $k/\delta_k < 1$ and have shown that the Reynolds number necessary to move turbulent flow close to the trip, $R_{k,c}$, is not a function of the roughness-position Reynolds number, $R_{x,k}$, if $R_{x,k} > 10^5$ (ref. 1). However, the present data show that at a Mach number of 6, $R_{k,c}$ is a function of the roughness-position Reynolds number $R_{x,k}$. It is true that k/δ_k must be greater than 1 for the Mach 6 data, whereas previously most of the available data were taken under conditions where $k/\delta_k < 1$. This difference in k/δ_k may explain why $R_{k,c}$ is a function of $R_{x,k}$. However, the important point is that when $k/\delta_k > 1$, a plot of the Reynolds number necessary to move transition close to the roughness position must consider $R_{x,k}$. At a Mach number of 6, $R_{x,k}$ has been varied by a factor of 10, and the values of $R_{k,c}$ for these conditions are shown in figure 5. This figure includes other data obtained on a flat plate or a cone. The data shown for $M_\infty < 4$ and $k/\delta_k < 1$ are from reference 10 which includes other sources. Also included are some data at supersonic conditions which have been taken at the Ames Research Center for $k/\delta_k > 1$. However, not enough data are available to determine the effect of $R_{x,k}$ for the Ames Center data.

Although data at Mach numbers greater than 6 are very limited, indications are that the values of $R_{k,c}$ required to move turbulent flow close to the roughness position become very large and increase rapidly above approximately Mach 6. This result is indicated by the correlation of Potter and Whitfield* from reference 11 which is plotted in figure 5 and also by some unpublished data taken on a flat plate at a local Mach number of 8 by P. Calvin Stainback at the Langley Research Center. Stainback's roughness had a value of R_k approximately equal to 1.7×10^4 ($R_{x,k} \approx 0.19 \times 10^6$) but the position of transition was not decreased at all. On the other hand, McCauley (ref. 12) presents data

*The correlation of Potter and Whitfield given in reference 11 is in a different form than that presented in figure 5.

at a local Mach number of approximately 8.5 where $R_k \approx 1.5 \times 10^4$ ($R_{x,k} \approx 10^6$) and the transition Reynolds number was decreased by a factor of approximately 2. (Note that the $R_{x,k}$ value of McCauley's data was larger than that for Stainback's data.) The main point to be noted is that at high Mach numbers, if turbulent flow can be moved to the roughness position at all, very high roughness elements must be used. However, the boundary-layer transition position can be moved forward by using smaller trips.

It should be emphasized that if $R_{x,k}$ is below some limiting value, it is extremely difficult to trip the boundary layer. (See, for example, ref. 1.) Therefore, it is not sufficient to speak of a transition parameter in terms of only boundary-layer thickness. Another way of saying the same thing is to note that if the trips are too close to the leading edge, the boundary layer may not become turbulent, even for relatively large values of k/δ_k . More information about the relationship between $R_{x,k}$ and $R_{k,c}$ when $k/\delta_k > 1$ would be helpful. This information might also be useful in predicting when spanwise distortions might be expected.

Pressure Drag of Roughness Trips

The model chosen to study the pressure drag of the trips was the wing-body configuration shown in figure 6. Sixty-nine cylindrical rods were placed on one side of the model as indicated by the figure. The drag coefficient C_D for the model with and without roughness elements as obtained from force tests is shown in figure 6. The difference between the drag coefficient for the models shown in figure 6 is due to the roughness elements. This difference can be divided into two parts: the additional skin friction due to the forward movement of transition caused by the roughness elements and the pressure drag associated with the tripping elements. The additional skin friction C_F is shown in figure 6 and was calculated by the Spalding-Chi method (ref. 9). The position of transition was determined from heat-transfer measurements on this model. The remaining C_D difference for the model with and without roughness is assumed to be the pressure drag of the elements. (This model is believed to have a detached shock and the element drag might be different for a model with an attached shock.)

On an actual wind-tunnel model, roughness trips would probably be placed on both sides of the model instead of on only one side as was done in this case. Therefore, the pressure drag associated with the roughness elements alone, for this body with trips on both sides would be approximately twice that shown in figure 6 and would be approximately 15 percent of the total drag of the body. The trip drag for a typical supersonic transport wind-tunnel model was generally less than 5 percent of the total (ref. 1).

The methods applied at supersonic speeds to determine roughness element drag (ref. 1) seem to be no longer applicable at hypersonic conditions. Work is presently being conducted in an attempt to determine experimentally the trip

drag directly at hypersonic speeds. At this time, however, trips cannot be used when an accurate value of the total drag of a configuration is required.

The size of the roughness necessary to move transition close to the trips for the higher Mach numbers becomes very large, as is indicated by the oversimplified results shown in figure 7. The large sizes can create very large spanwise effects in the boundary layer in addition to the large pressure drag ΔC_D associated with the trip elements. For this reason, at high Mach numbers, tripping of the flow will probably be limited to those conditions where the transition distance from the leading edge is decreased to approximately $1/2$ or $1/4$ of that occurring with natural transition.

It also desirable to decrease the pressure drag of the trips. One method suggested is to decrease the frontal area of the roughness element by using a pinhead type of roughness. The limitations of this method have been previously discussed. One promising method of minimizing the drag of the element is to use air jets as tripping elements, since it is difficult to transmit the force associated with the column of air to the model, but some inherent disadvantages are associated with using an air jet in model testing. Because this method does offer some promise, it appears to be worth further investigation. (Ref. 13 includes some examples of tripping by air jets.)

Comparison of the Heat Transfer With and Without Trips

For the purpose of investigating whether a natural turbulent boundary layer and a tripped turbulent boundary layer have the same heat transfer (and skin friction), measurements were made on a flat plate and a 20° wedge both with and without trips. The model is shown at the top of figure 8. The Reynolds number on the wedge can be varied both by moving the position of the wedge and by placing trips on the model. The results are given in figure 8 where the Stanton number is plotted against Reynolds number R_v (based on the distance from the virtual origin). Thus, the data can be compared on an equivalent Reynolds number basis. The virtual origin is taken as the experimentally determined beginning of turbulent flow. The data for both the smooth and the rough plate are approximately the same both on the plate and on the wedge. This comparison seems to indicate that if roughness of the proper size is used, a tripped turbulent boundary layer gives the same heat transfer as a natural turbulent boundary layer. One difference is indicated, however, by the oil patterns shown in figure 9 which were obtained on the same plate but with a 40° wedge. The position of the roughness elements and the wedge are indicated in the figure. Initially dots of oil were placed on this plate. Downstream of the roughness elements on the plate, no influence of the roughness elements is indicated except close to the elements; whereas, on the wedge there is a trace or a wake directly behind each of the roughness spheres. In order to determine the effect of these wakes, thermocouples were placed on the wedge as is indicated by the arrows. Only small spanwise differences in the heating rates along these various rows were found, and the wakes are consequently considered to be only a secondary influence that can be ignored as a design factor for most engineering studies. (These spanwise differences, however, might be important in fluid-mechanics

studies.) From these data, a tripped turbulent boundary layer is concluded to have the same heat transfer as a natural turbulent boundary layer if the roughness elements are of proper size.

Roughness on Delta Wings

Oil-flow studies on a delta wing with a natural turbulent boundary layer and separation are now examined. The delta wing with a trailing-edge flap is shown in figure 10. Also shown in the figure is the approximate position of the beginning of fully turbulent flow as determined by heat-transfer methods. Previous studies have shown that whether separation occurs depends strongly upon whether the flow is laminar, transitional, or turbulent (e.g., refs. 14, 15, and 16). This result is also found in the present studies. For example, it is observed in figure 10 that when the flap is at 30° , separation occurs along the edges of the model where transitional or laminar flow exists, whereas on the center of the wing where the flow is turbulent, the flow does not separate. When the flap angle is increased to 40° , separation occurs in front of the entire flap on the wing. This flow is very complex, and the oil patterns show that there are several vortices existing on the surface of the plate. The sketch in figure 10 indicates a simplified flow model constructed from a study of the oil patterns. Apparently, there is a vortex flow lifting off the surface in the separation region and reattaching onto the flap. It is believed that the vortex pattern results from the fact that at the chordwise location of the vortex, the flow is turbulent on the center of the wing and is transitional or laminar near the edge of the wing. The difference in the surface shear forces produces the vortex flow pattern, which is a different type of transitional separation than that observed in two-dimensional flow.

Examples of the effects of placing roughness elements near the leading edges of the wing are shown in figure 11. With the roughness elements on the wing an entirely different type of separated flow occurs than was previously observed without roughness. The explanation for this difference appears to be that the roughness trips the boundary layer ahead of the wing-flap junction and thereby provides a turbulent spanwise flow prior to separation. Supporting this conclusion is figure 11(c) in which the same configuration is placed at a 5° angle of attack. In this case, the local Reynolds number is increased and a spanwise turbulent boundary layer develops naturally prior to separation, so that a flow similar to that of figure 11(b) is produced.

A certain amount of outflow from the separated region occurs in the vicinity of the wing-flap juncture. This phenomenon indicates one of the problems of using roughness elements in separated flow for delta-wing configurations. For example, the roughness elements close to the edge of the wing in the separated region would probably change the amount of outflow from the value that would be obtained with natural turbulent-boundary-layer conditions. Figure 11 also suggests that difficulty would be encountered in making tip-control studies when turbulent flow is produced by trips, inasmuch as at least a short run of turbulent flow behind a trip is desirable before the flow encounters a control surface. It is concluded that trips can be useful in wind-tunnel tests of

delta wings if consideration is given to the local flow and the purpose of any particular investigation.

The two oil-flow photographs of the model at $\alpha = 0^\circ$ in figure 11 show a major difference in the flow patterns that develop for the turbulent separated condition (with roughness) when compared with the transitionally separated condition (no roughness). Although the data are not shown, the pressure and heat transfer for these two conditions show that forward of the flap junction, only minor variations occur. Over the flap portion of the transitionally separated model, a loss occurs in the integrated pressure level as compared with that of the model with roughness, with its more nearly two-dimensional separation. A comparison of the experimental data with the two-dimensional calculations presented in reference 15 shows that present prediction methods are useful in predicting pressure and heat-transfer magnitudes for delta wings with complete turbulent separated flow ahead of the flap-wing junction. However, more work is required on delta-wing configurations with transitional separation.

In figures 12 and 13 some results obtained on this wing at an angle of attack are given. The oil patterns show that the flow is again very complex. The flow is apparently attached to the surface near the leading edge of the wing but then separates and produces a vortex flow as indicated in the sketch of figure 13. (See ref. 17 for a somewhat similar type of vortex flow.) The vortex flow reattaches near the center line and then apparently reseparates to produce the feather like appearance shown in figure 12. This is a rather shallow type of separated flow, as can be seen by inspecting the oil flows with the flap at 30° , where the flow reattaches to the surface very close to the flap-wing junction. The pressure distributions of figure 13 also indicate this shallow type of separation. Another point to be noted is that the flow for these conditions is apparently very difficult to trip, and simulation of naturally turbulent conditions may be impossible. Both pressure and heat-transfer measurements have been made with various sizes of roughness elements near the leading edge. It has not been determined whether this flow was made turbulent by the use of trips. However, it appears to be extremely difficult, if not impossible, to obtain a simulation of flight behavior in a wind tunnel by using trips under conditions where the behavior on the lee side shown in figure 12 occurs. (Ref. 18 gives a more detailed discussion of this problem at supersonic speeds.) On the other hand, it may not be necessary to duplicate Reynolds number conditions with vortex shedding near the leading edge. (Nevertheless, it should be mentioned that research at lower Mach numbers (ref. 18) indicates that the Reynolds number does affect the flow associated with vortices.) This phenomenon needs additional study since hypersonic-cruise vehicles will probably encounter flow fields similar to this.

CONCLUDING REMARKS

Boundary layers have been made turbulent by roughness elements up to local Mach numbers of approximately 9 or higher. However, the size of the roughness necessary to move transition close to the trips for the higher Mach numbers becomes very large. The large size of the trips can create very large spanwise effects in the boundary layer and large pressure drags associated with the trip

~~CONFIDENTIAL~~

elements. For this reason, at high Mach numbers tripping will probably be limited to those conditions where the transition distance from the leading edge will be decreased to approximately $1/2$ or $1/4$ of that occurring with natural transition.

Whether roughness should be used to promote turbulent flow in hypersonic wind-tunnel tests depends upon the particular purpose of any experiment. For example, trips can be used successfully to study the heat transfer associated with an aircraft component or to produce turbulent flow in front of an inlet or control that might otherwise be transitional or laminar. However, at the present time, trips cannot be used when an accurate value of the total drag of a configuration is required because of the large pressure drag associated with the roughness elements. Additional work is necessary to determine the pressure drag of the elements with reasonable accuracy. Another problem for study is the use of trips for wind-tunnel simulations of hypersonic-cruise vehicles when vortex shedding occurs on the lee side of delta wings at moderate angles of attack. For any test, care must be taken to provide roughness elements of proper size.

~~CONFIDENTIAL~~

REFERENCES

1. Braslow, Albert L.; Hicks, Raymond M.; and Harris, Roy V., Jr.: Use of Grit-Type Boundary-Layer-Transition Trips on Wind-Tunnel Models. Conference on Aircraft Aerodynamics, NASA SP-124, 1966, pp. 19-36. (Also, available as NASA TN D-3579.)
2. Holloway, Paul F.; and Sterrett, James K.: Effect of Controlled Surface Roughness on Boundary-Layer Transition and Heat Transfer at Mach Number of 4.8 and 6.0. NASA TN D-2054, 1964.
3. Stainback, P. Calvin: Some Effects of Roughness and Variable Entropy on Transition at a Mach Number of 8. AIAA Paper No. 67-132, Jan. 1967.
4. Korkegi, Robert H.: Transition Studies and Skin-Friction Measurement on an Insulated Flat Plate at a Mach Number of 5.8. J. Aeron. Sci., vol. 23, no. 2, Feb. 1956, pp. 97-107, 192.
5. Van Driest, E. R.; and McCauley, W. D.: The Effect of Controlled Three-Dimensional Roughness on Boundary-Layer Transition at Supersonic Speeds. J. Aero/Space Sci., vol. 27, no. 4, Apr. 1960, pp. 261-271, 303.
6. Fay, J. A.; and Goldburg, A.: Vortex Shedding, Transition and Growth of Luminous Wakes Behind Spheres at Mach 15 to 25. Res. Note 295(BSD-TDR-62-105), Avco-Everett Res. Lab., Apr. 1962.
7. Hall, Gordon R.: Interaction of the Wake From Bluff Bodies With an Initially Laminar Boundary Layer. AIAA Paper No. 66-126, Jan. 1966.
8. Potter, J. Leith; and Whitfield, Jack D.: Effects of Unit Reynolds Number, Nose Bluntness, and Roughness on Boundary Layer Transition. AEDC-TR-60-5, U.S. Air Force, Mar. 1960.
9. Spalding, D. B.; and Chi, S. W.: The Drag of a Compressible Turbulent Boundary Layer on a Smooth Flat Plate With and Without Heat Transfer. J. Fluid Mech., vol. 18, pt. 1, Jan. 1964, pp. 117-143.
10. Braslow, Albert L.: Review of the Effect of Disturbed Surface Roughness on Boundary-Layer Transition. AGARD Rept. 254, Apr. 1960.
11. Potter, J. Leith; and Whitfield, Jack D.: Boundary-Layer Transition Under Hypersonic Conditions. Recent Developments in Boundary Layer Research, Pt. III, AGARDograph 97, May 1965, pp. 1-62.
12. McCauley, W. D.; Saydah, A.; and Bueche, J.: The Effect of Controlled Three Dimensional Roughness on Hypersonic Laminar Boundary Layer Transition. AIAA Paper No. 66-26, Jan. 1966.
13. Nagel, A. L.; Savage, R. T.; and Wanner, R. (With appendix by R. W. Blank): Investigation of Boundary Layer Transition in Hypersonic Flow at Angle of Attack. AFFDL-TR-66-122, U.S. Air Force, Aug. 1966. (Available from DDC as AD 803 781.)

14. Chapman, Dean R.; Kuehn, Donald M.; and Larson, Howard K.: Investigation of Separated Flows in Supersonic and Subsonic Streams With Emphasis on the Effect of Transition. NACA Rept. 1356, 1958. (Supersedes NACA TN 3869.)
15. Holloway, Paul F.; Sterrett, James R.; and Creekmore, Helen S.: An Investigation of Heat Transfer Within Regions of Separated Flow at a Mach Number of 6.0. NASA TN D-3074, 1965.
16. Arrington, James P.; Molloy, John K.; and Goldberg, Theodore J.: Flare-Stabilization Problems at Hypersonic Mach Numbers. AIAA Sounding Rocket Vehicle Technology Specialist Conference, Feb.-Mar. 1967, pp. 84-91.
17. Rainbird, W. J.; Crabbe, R. S.; Peake, D. J.; and Meyer, R. F.: Some Examples of Separation in Three-Dimensional Flows. Quart. Bull. No. 1, Div. Mech. Eng. & Natl. Aeron. Estab., Natl. Res. Council Can., 1966, pp. 1-52.
18. Rein, J. A.: Flow Over the Suction Surface of Sharp Edge Delta Wings With Detached Leading Edge Shock Waves. Tech. Note HSA 102, Weapons Res. Estab., Australian Defence Sci. Serv., Dec. 1964.

PAINT PATTERN DOWNSTREAM OF ROUGHNESS ELEMENT 5° BLUNTED CONE; $M_\infty \approx 8$; $k/\delta_k \approx 24$

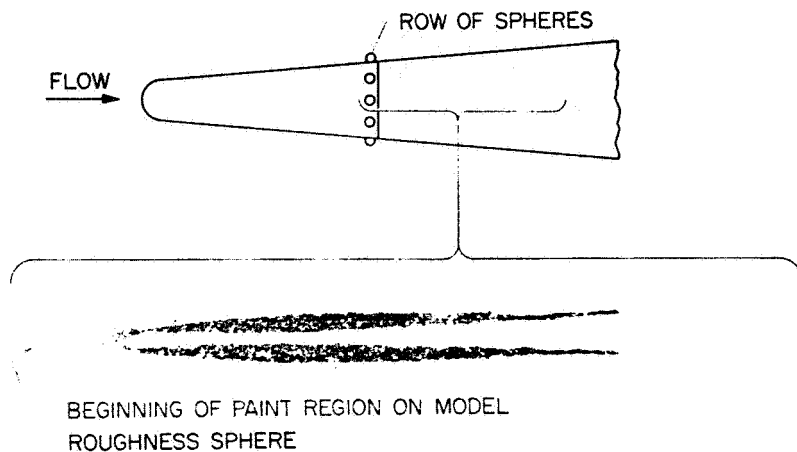


Figure 1

L-2865-10

METHODS FOR DETECTING TRANSITION FLAT PLATE; $M_\infty = 6$

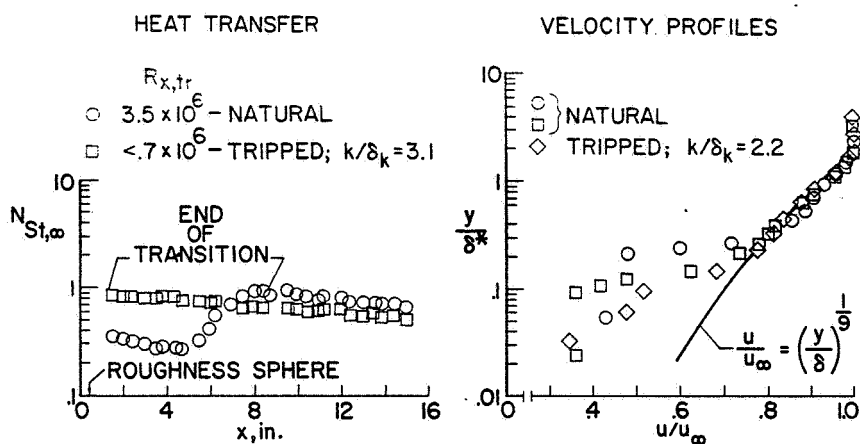


Figure 2

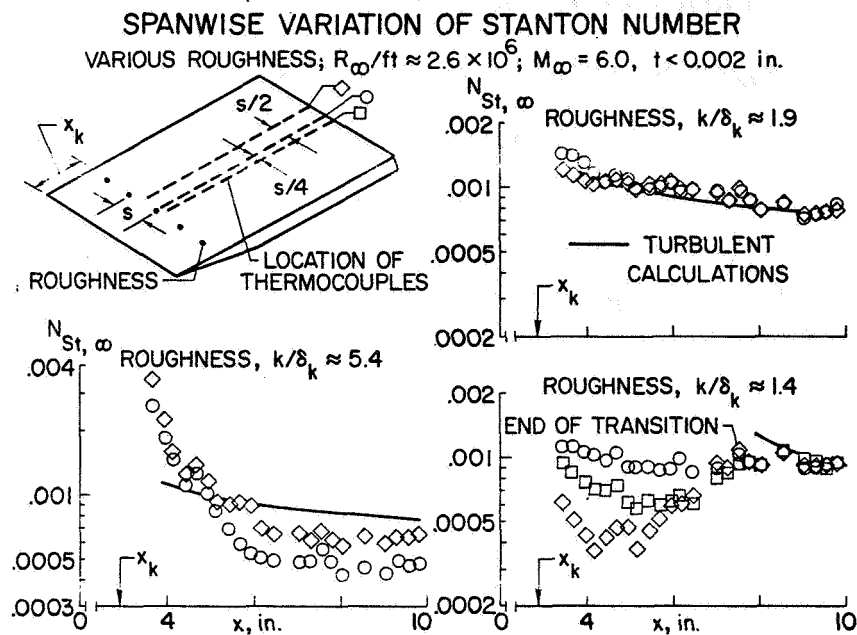


Figure 3

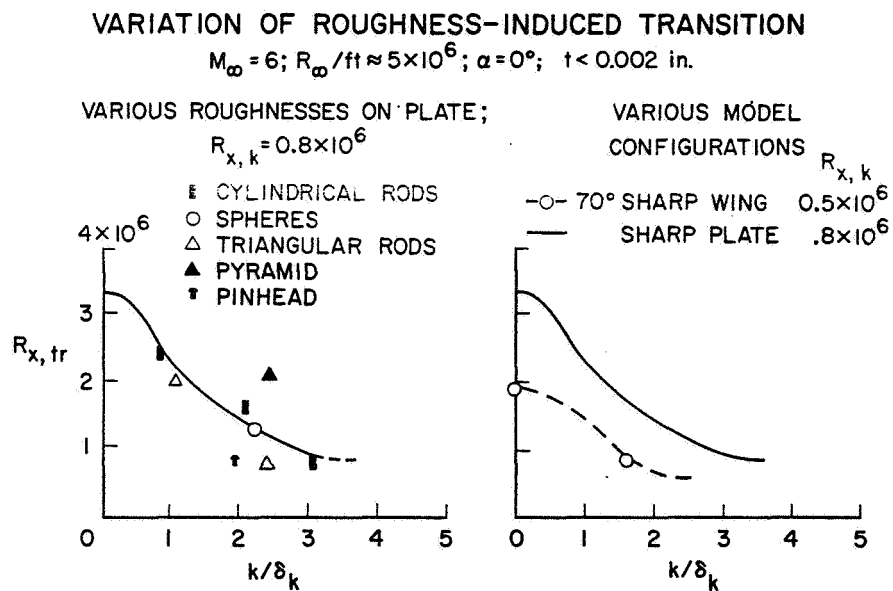


Figure 4

CONFIDENTIAL

CORRELATION OF $R_{k,c}$ AND M_z

$k/\delta_k < 1$; $R_{k,c} \neq f(R_{x,k})$ IF $R_{x,k} > 10^5$; $k/\delta_k > 1$; $R_{k,c} = f(R_{x,k})$

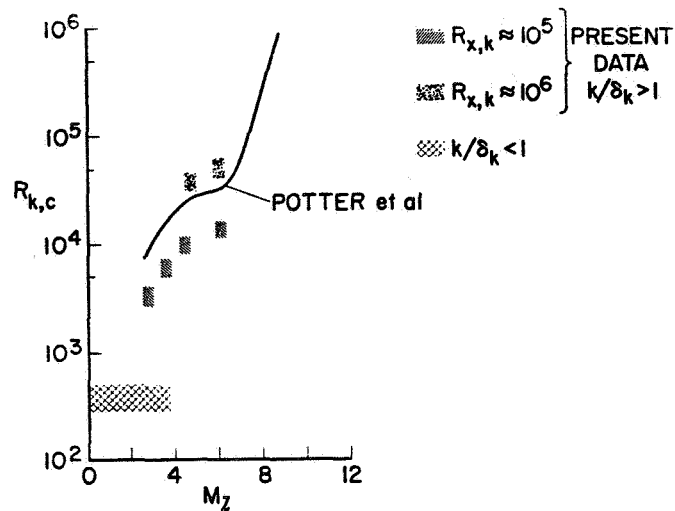


Figure 5

PRESSURE DRAG OF ROUGHNESS ELEMENTS

$M_\infty = 6$; $R_L = 17.7 \times 10^6$; $\alpha = 0^\circ$; $k/\delta_k \approx 1.5$; $d = 0.069$ in.; $k = 0.031$ in.; $t = 0.031$ in.

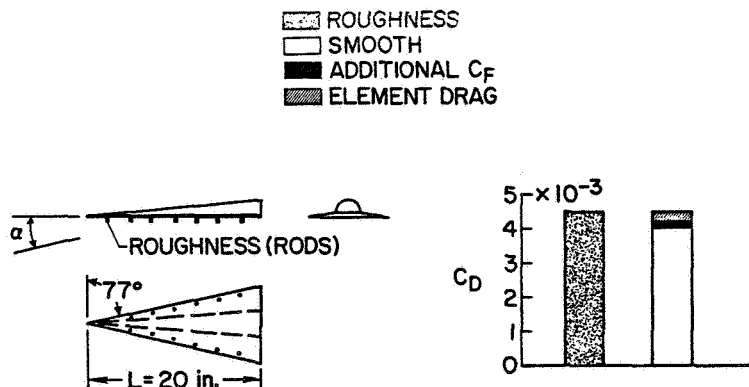


Figure 6

TRANSITION CLOSE TO ROUGHNESS TYPICAL TUNNEL CONDITIONS FOR A PLATE

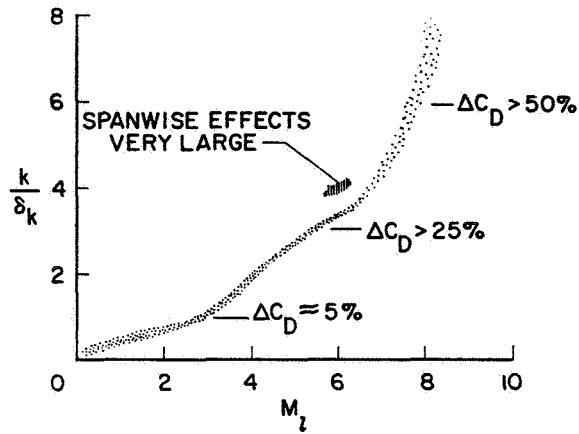


Figure 7

HEAT TRANSFER WITH AND WITHOUT ROUGHNESS

$M_\infty = 6$; $R_\infty / ft \approx 8.0 \times 10^6$; $t < 0.002$ in.; $s = 0.3$ in.; $\delta_f = -20^\circ$

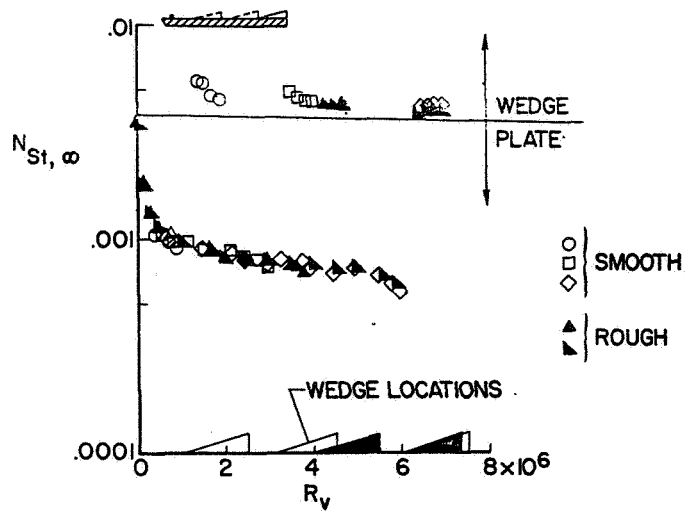


Figure 8

OIL PATTERNS DOWNSTREAM OF ROUGHNESS ELEMENTS

$k/\delta_k \approx 1.6$; $R_\omega/ft = 1.4 \times 10^6$; $M_\infty = 6$; $t < 0.002$ in.; $s = 0.62$ in.; $\delta_f = -40^\circ$

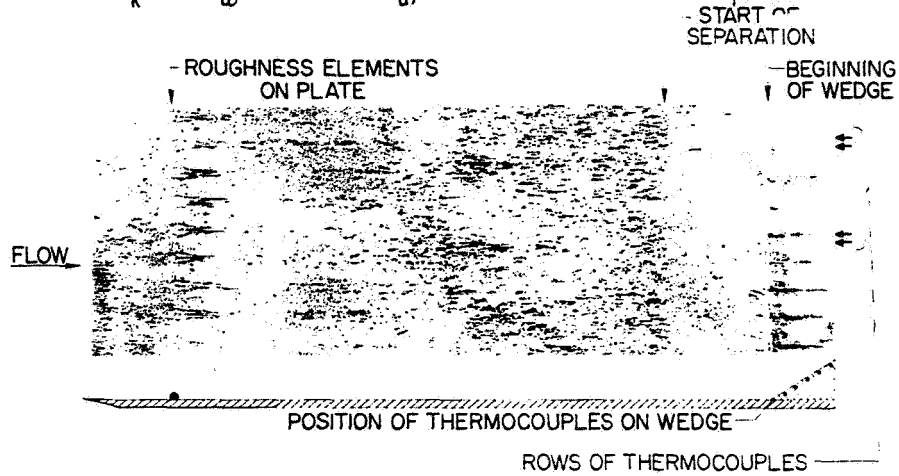


Figure 9

L-2865-3

TRANSITIONAL SEPARATION ON 70° DELTA WING

TRAILING-EDGE FLAP; NO ROUGHNESS; $M_\infty = 6.0$; $R_\omega/ft = 7 \times 10^6$; $\alpha = 0^\circ$; $t < 0.002$ in.

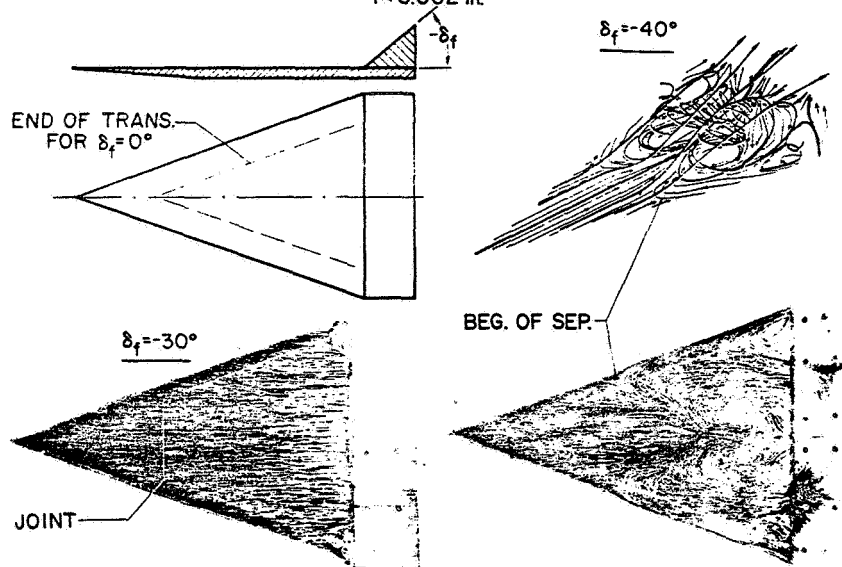


Figure 10

L-2865-6

~~CONFIDENTIAL~~

OIL PATTERNS ON 70° DELTA WING
TRAILING-EDGE FLAP; $M_\infty = 6.0$; $\delta_f = -40^\circ$; $R_\infty/ft = 7 \times 10^6$; $k = 0.047$ in.

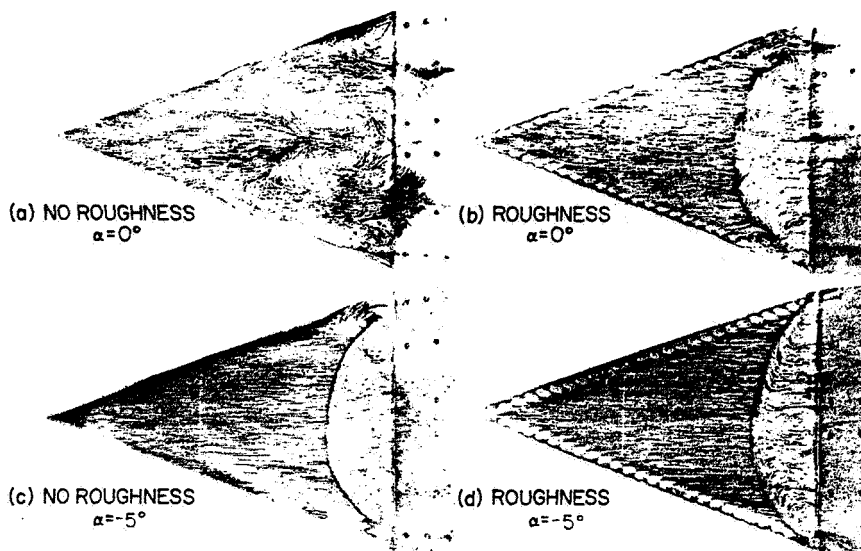


Figure 11

L-2865-1

LEE SIDE OF 70° DELTA WING
OIL PATTERNS; $M_\infty = 6.0$; $R_\infty/ft = 6.9 \times 10^6$; $\alpha = 10^\circ$

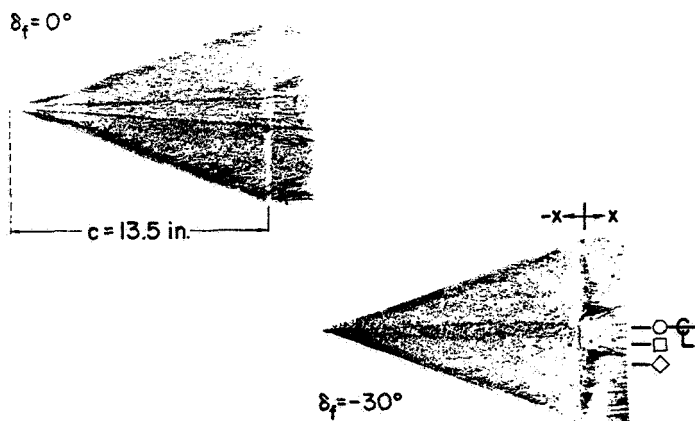


Figure 12

L-2865-11

~~CONFIDENTIAL~~

~~CONFIDENTIAL~~

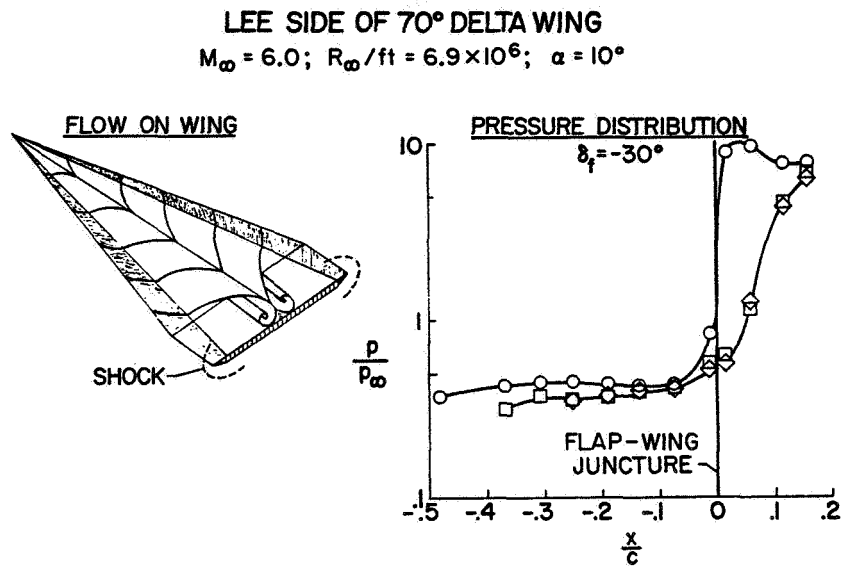


Figure 13

CONFIDENTIAL

16. SOME TOPICS IN HYPERSONIC TURBULENT BOUNDARY LAYER, HEAT TRANSFER, AND SKIN FRICTION

By Mitchel H. Bertram and Aubrey M. Cary, Jr.
Langley Research Center

SUMMARY

Recent hypersonic turbulent-boundary-layer experiments and proposed prediction methods pertinent to the problem of the effect of wall temperature, the transformation of the compressible boundary layer to the constant-density type, and the delta wing have been considered. Based on flat-plate experiments, the level of the heat-transfer coefficient is found to be little affected by significant changes in wall temperature as predicted by the Spalding-Chi method. The T' or reference temperature method overpredicts skin friction and heat transfer at low wall temperature ratios. The Coles transformation as modified by Baronti and Libby has been examined by utilizing boundary-layer profiles covering a wide range of Mach number and wall temperature ratio. Some success is found for the transformation up to the lower end of the hypersonic range and down to moderately low wall temperature ratios. However, at the lowest wall temperature ratios, the transformation gave high wall shears as compared with Spalding-Chi predictions and shears that were actually measured. Delta-wing heat transfer has been examined for several types of flow. At low angle of attack, in cases where the flow near the surface is essentially streamwise, strip application of successful flat-plate methods gives good predictions of the heat transfer if the pressures are known. This method applies whether the shock is attached to or detached from the leading edge. On the lee side of delta wings where vortices are indicated, the predictions are poor. Success in predicting the heat transfer to delta wings appears to be limited by the ability to predict the flow field.

16

INTRODUCTION

The study of the turbulent boundary layer still largely consists of qualitative theory combined with quantitative empiricism. In the present paper, emphasis will be on experimental results. Configurations are considered not for practicality in an engineering sense but to allow the assessment of the basic validity of various prediction methods for skin friction and heat transfer.

Data have been obtained on flat plates, cones, nozzle walls, and more or less planar delta wings so that such a problem as the effect of wall temperature on skin friction and heat transfer can be evaluated. In 1961 the report of heat transfer at low wall temperature ratios obtained in X-15 flight experiments, which were at variance with the prediction methods in use at that time, provoked considerable controversy (ref. 1). Later results from wind tunnels

CONFIDENTIAL

have tended to confirm the trend indicated by the X-15 flight data (ref. 2). Recent experiments bearing on this problem are examined.

Allied to this problem but with the possibility of wider application is the prospect of a transformation for compressible turbulent boundary layers. This approach, which has appealed to investigators for a number of years, is to determine a transformation, which when applied to boundary-layer profiles or other characteristics will precisely yield the incompressible result. After such a transformation has been obtained, the boundary-layer details are given in terms of the better known incompressible results. Coles has proposed one such transformation which has been modified by Baronti and Libby and examined by them in some detail (ref. 3). This transformation is intended to apply at arbitrary wall temperatures and pressure gradients and, if successful, would provide a tool for not only determining profiles but also skin friction and heat transfer over a wide range of high-speed flow conditions. Recently obtained boundary-layer profiles for extensive values of Mach numbers and wall temperatures, combined with those previously available, allow the determination of the overall validity of the proposed transformation.

Finally, the heat transfer to the more practically shaped delta wing is considered for the case of low angles of attack. Although this wing shape has been dealt with extensively for the laminar case, there is a paucity of data for the turbulent case. Notable exceptions are the results reported in references 4 to 6. In references 4 and 5 the configuration is complicated by considerable leading-edge bluntness.

Some general details pertinent to the results given in this paper are given in the appendix.

SYMBOLS

A	constant in law of the wall, taken here to be 2.43
b	constant in law of the wall (taken here to be 7.5) or wing span
C_f	local skin-friction coefficient
h	enthalpy
k	vertical height of roughness above plate
M	Mach number
N_{Pr}	Prandtl number
N_{St}	Stanton number
p	static pressure

r	body radius
R	Reynolds number
$R_{x,k}$	Reynolds number based on distance to roughness location
R_θ	Reynolds number based on boundary-layer edge conditions and momentum thickness
R_p	Reynolds number based on distance to peak heating
T	absolute temperature
u	velocity
x	distance from leading edge in streamwise direction
x_c	distance from apex of delta wing along root chord
y	distance normal to root chord of delta wing or distance normal to surface for boundary-layer profile measurements
α	angle of attack of instrumented surface
δ	boundary-layer thickness
Λ	leading-edge sweep angle
ν	kinematic viscosity
ρ	density
θ	ray angle from apex of delta wing and root chord
τ	shearing stress

Subscripts:

B-L	from Baronti-Libby method
i	incompressible
l	local conditions
meas	from direct measurement
S-C	from Spalding-Chi method
t	total
v	based on distance from virtual origin

w conditions at wall

∞ conditions in undisturbed free stream

A bar over a symbol denotes that the variable is in transformed (constant properties) flow.

DISCUSSION

Effect of Wall Temperature Ratio on Heat Transfer

and Skin Friction

Since the time of the X-15 flight data, discussed in the "Introduction," a significant body of wind-tunnel results has been obtained. A comprehensive review of available results up to 1965 was presented in reference 2. On combining results from a number of different facilities, general agreement was found with the trend from the X-15 experiments which indicated little effect of wall temperature on the heat-transfer coefficient.

Recently, data have been obtained by Cary on a sharp flat plate, at zero incidence to the stream, cooled by interior circulation of liquid nitrogen. The plate was precooled outside the nozzle and, upon attaining the desired temperature, was suddenly plunged into the Mach number 6 airstream of the Langley 20-inch hypersonic tunnel. The average Reynolds number based on distance from the virtual origin (location of peak heating) for these tests was about 3×10^6 . The results shown in figure 1 are typical of the latest findings on wall temperature effect in that there is found little effect on the Stanton number due to changing the level of the ratio of wall temperature to total temperature. The experimental trend agrees with that predicted by the Spalding-Chi method (ref. 7 as modified to heat transfer in appendix A of ref. 2) and Hank's $\rho_r \mu_r$ method (appendix B of ref. 5); however, the data are between the two predictions and a general choice based on these data alone cannot be made as to the best method. Clearly, the T' or reference temperature method (Monaghan, ref. 8) significantly overestimates the heat transfer at the low wall temperatures.

Further knowledge of the effect of low temperature ratios can be obtained from new work done in a shock tunnel at the Cornell Aeronautical Laboratory (refs. 9 and 10). In this investigation shots were made at relatively low temperatures and at the lower end of the hypersonic Mach number range to obtain high Reynolds number. Pressure, skin friction, and heat transfer were obtained and the sharp flat-plate model was tested in the range of surface incidence from 0° to 20° . Only data from the sharp flat-plate model are considered here and these data were re-reduced from the original tabulation (ref. 11) as follows:

(a) Coefficients and Reynolds numbers were based on local conditions;

(b) Local conditions were obtained by plotting the pressures and making a comparison with theory (Prandtl-Meyer expansion or oblique shock). If the

- CONFIDENTIAL

average experimental pressure essentially agreed with theory for the quoted angle of attack within 5 percent, the local conditions for this angle of attack were used. If the average experimental pressure deviated from theory for the quoted angle of attack by more than 5 percent, the local conditions corresponding to the indicated angle of attack were used.

(c) The enthalpy difference in the heat transfer was corrected to a recovery factor of 0.89.

Local Reynolds numbers based on distance from the assumed virtual origin (peak heating) varied from about 10^6 to 2×10^8 . Where peak heating occurred ahead of the first measuring station, a value for the Reynolds number at peak heating was assumed which was consistent with the data where the location of peak heating was known.

Average values of skin-friction and heat-transfer-coefficient ratios obtained from the Cornell Aeronautical Laboratory data are shown in figure 2 compared with theory as in figure 1. The Mach numbers cover the range from 4.5 to 11.7 and the ratio of wall enthalpy to total enthalpy varies from 0.09 to 0.30. Except for the highest Mach number data, the best agreement with experiment is given by the Spalding-Chi theory. As for the Mach 6 results, the Monaghan T' method is generally above the data and the $\rho_r \mu_r$ method generally below the data. Whereas the experimental values of the skin-friction and heat-transfer-coefficient ratios are about equal, the $\rho_r \mu_r$ method predicts the values for the skin-friction-coefficient ratio to be significantly less than those for the heat-transfer-coefficient ratio.

The highest Mach number data are anomalous in that the best agreement is with the T' method which appreciably overpredicts all the other data. In this case, the measured wall pressures were 70 to 80 percent of the stream value with the quoted zero plate incidence. If the measured pressures are ignored and the pressure ratio is taken as unity, as done by the authors themselves, there is good agreement of experiment and the Spalding-Chi prediction. These alternatives, of course, leave the problem unresolved.

The Transformation of Compressible Boundary-Layer Profiles

One approach to the compressible turbulent boundary-layer problem which has received considerable attention in recent years has been to seek a transformation, which when applied to the compressible turbulent boundary-layer equations will yield identically the better known incompressible turbulent boundary-layer equations. In this manner the more extensive knowledge for the incompressible turbulent boundary layer can, in theory, be extended to the compressible flow case of interest. Typical investigations (refs. 12 to 17, 3) have achieved some measure of success in defining transformations for the turbulent boundary layer. Coles (ref. 17) has proposed an approach to the transformation of the compressible turbulent boundary-layer equations in which the compressible and the constant-density flows are assumed to be related by three scaling parameters $\sigma(x)$, $\eta(x)$, and $\xi(x)$. The first parameter relates the stream functions of the two flows, the second is a multiplicative factor of the Dorodnitsyn-Howarth

CONFIDENTIAL

scaling of the normal coordinate, and the third relates the streamwise coordinates of the two flows. An additional assumption pertaining to the invariance of a Reynolds number characterizing the law of the wall region of the boundary layer is necessary to complete the transformation. This assumption, called the "substructure hypothesis" by Coles, provides a substitute for a reference state utilized with many theoretical approaches. Coles' transformation has been extended by Crocco (ref. 16) in the mathematical sense and modified as well as applied to practical cases by Baronti and Libby (ref. 3). It is with the analysis of Baronti and Libby that the remainder of this section is concerned.

Baronti and Libby modified Coles' substructure hypothesis (they introduced a sublayer hypothesis) and applied the transformation technique by point-by-point mapping of supersonic velocity profiles into the incompressible plane. It should be noted that the transformation theory is applicable only for two-dimensional or axisymmetric ($r \gg \delta$) flow with and without heat transfer or streamwise pressure gradient. This analysis does not define completely the constant-density flow corresponding to the compressible case since the velocity profiles once transformed correspond to some unknown \bar{x} -station in the constant-density flow. Determination of this \bar{x} -station would require full exploitation of the transformation theory.

Baronti and Libby employed the conventional incompressible universal velocity profile equations in their analysis such that the boundary-layer profile is composed of two distinct regions, a law-of-the-wall region near the wall and a wake or velocity defect region consisting of the major portion of the boundary layer. The equations governing each of these regions, respectively, are:

$$\text{Law of the wall, } \bar{u}/\bar{u}_\tau = f(\bar{\xi})$$

$$\text{Velocity defect law, } (\bar{u} - \bar{u}_e)/\bar{u}_\tau = F(\bar{y}/\bar{\delta}, \bar{x})$$

where $\bar{u}_\tau = (\bar{\tau}_w/\bar{\rho}_w)^{1/2}$ and $\bar{\xi} = \bar{y}\bar{u}_\tau/\bar{v}$. The law of the wall is conventionally expressed as:

$$\frac{\bar{u}}{\bar{u}_\tau} = \bar{\xi} \quad (0 \leq \bar{\xi} \leq \bar{\xi}_f \text{ (sublayer)})$$

and

$$\frac{\bar{u}}{\bar{u}_\tau} = A \ln b\bar{\xi} \quad (\bar{\xi}_f \leq \bar{\xi} \leq \bar{\xi}_1)$$

where $\bar{\xi}_f$ and $\bar{\xi}_1$ are the values of $\bar{\xi}$ at the edge of the laminar sublayer and the outer limit of the region of application of the law of the wall, respectively. The coefficients A and b are 2.43 and 7.5, respectively, as taken from Clauser (ref. 18) so that $\bar{\xi}_f = 10.6$. The outer limit for the application of the law of the wall is taken as the end of the logarithmic portion of the

boundary-layer profile on a scale of \bar{u}/\bar{u}_τ plotted against $\bar{\xi}$. Simplified equations for the direct application of the Baronti and Libby analysis to velocity profiles for compressible flow may be found in reference 19.

The process of applying the transformation theory through the law of the wall is actually an iterative one, since knowledge of the skin friction at the wall in the incompressible plane is necessary in order to transform the corresponding compressible velocity profile to the incompressible plane. In actual practice, the procedure is to assume values of the wall skin friction in an incompressible plane until correlation of the velocity profile with the constant-density results is achieved. The success of the transformation may then be judged by observing how well the transformed velocity profile correlates with the incompressible results and comparing the resulting skin friction estimate with that measured or predicted by a reliable theory. Once the incompressible skin friction has been determined from the law-of-the-wall analysis, a comparison with the velocity-defect law is directly obtainable.

Baronti and Libby applied the transformation to velocity profiles for compressible flows up to Mach 9 for adiabatic wall and moderate heat-transfer conditions. In general, their results indicated good correlation of the compressible velocity profiles for the law of the wall in the incompressible plane, and the values of skin friction resulting from the transformation compared well with those measured in most of the investigations cited. However, when a correlation was attempted with the velocity-defect law, the results indicated that a zero-pressure-gradient compressible velocity profile would transform into the compressible plane and show the characteristics of an incompressible velocity profile under the influence of a pressure gradient. In a recent article, Tennekes (ref. 20) has suggested that this discrepancy may be a result of distortion of the velocity-defect region of the boundary layer by the Dorodnitsyn-Howarth density scaling of the normal coordinate.

Here the same procedures were used to reduce the compressible velocity profiles to the incompressible form as were used by Baronti and Libby but the range of Mach number and heat transfer is extended. Illustrations of the correlation of the transformed compressible boundary-layer profiles according to the law of the wall with the classical incompressible results are shown in figure 3. Since C_f was not directly measured for most of the profiles presented, the skin-friction results obtained from the transformation for all the cases were normalized by the skin-friction coefficient predicted by the method of Spalding and Chi (ref. 7). In each case, the Spalding-Chi prediction was based on the measured Re and T_w/T_t .

The transformation of profiles obtained on tunnel walls in nominal zero-pressure-gradient flow as shown in figure 3(a) provides good correlation for Mach numbers from 2.5 to 8. The skin-friction results from these profiles compare favorably with the Spalding-Chi predictions. For still higher Mach numbers, in the range from 15 to 20, the profiles shown in figure 3(b) appear to correlate well with the incompressible results, but the extent of the logarithmic part of the law-of-the-wall region of the profile is small in comparison with the lower Mach number profiles. An inspection of the compressible velocity profiles

indicates that, in general, as Mach number increases, the laminar sublayer thickness as well as the extent of the wake or velocity-defect region becomes larger. As a result, there appears to be a corresponding decrease in the extent of the logarithmic law-of-the-wall region. Since the wall shear obtained from the transformation is dependent upon a curve fit in the logarithmic law-of-the-wall region, a physical limit of the application of the transformation in the present form may thus exist. However, for profiles with thick laminar sublayers for which sublayer velocity measurements are accurate, the transformation could be applied directly in conjunction with the sublayer part of the law of the wall. The skin-friction results from the transformation of the high Mach number profiles show more deviation than those for the lower Mach number profiles.

An illustration of the effect of previous history of the boundary layer on the results of the transformation is shown in figure 3(c). The transformed profiles correlate nicely, and the skin-friction results compare favorably with the predictions of Spalding and Chi even though each of the boundary layers developed under different conditions.

A compilation of the skin-friction results obtained from the transformation technique is presented in the upper part of figure 4. The skin-friction results from the transformation are referenced to the skin friction predicted by the Spalding-Chi method and presented as a function of the ratio of wall temperature to total temperature for each particular case. The data include all the experiments analyzed by Baronti and Libby as well as results obtained from references 2, 10, and 21 to 24 and unpublished results obtained by Feller at Mach 8 in the Langley Mach 8 variable-density hypersonic tunnel and Harvey and Clark at Mach 18.5 in the Langley hypersonic nitrogen tunnel. It has been shown in several investigations (for example, ref. 2 and in the first section of this paper) that the method of Spalding and Chi can be expected to give accurate skin-friction predictions on flat plates and cones up to Mach 9 and over the entire range of T_w/T_t for the data in figure 4.

In general, the skin-friction results from the transformation appear to be consistently higher than those predicted by the Spalding-Chi method. Although the overprediction is in the 10-percent range for adiabatic and moderately cooled walls, the error is large for extreme cooling conditions. Wallace (ref. 10) obtained direct skin-friction measurements on the nozzle wall at the same locations and for the same flow conditions as the profile data. The measured skin-friction results shown in the bottom part of figure 4 are in good agreement with the Spalding-Chi predictions, as are the results from other investigations in which direct measurements of skin friction were made. It thus appears that the transformation is not generally applicable even for the logarithmic portion of the law of the wall. Since in the application of the transformation theory it is necessary to define a temperature distribution through the boundary layer (see ref. 19), it may be suspected that the particular temperature distribution assumed would affect the skin friction obtained from the transformation. In those cases where temperatures through the boundary layer had not been measured, the Crocco temperature distribution ($N_{Pr} = 1$) had been assumed. In light of this assumption, the transformation was applied by using both the Crocco temperature profile and one, which was a better fit to experiment, which had the quadratic form

~~CONFIDENTIAL~~

$$\frac{T_t - T_w}{T_{t,\infty} - T_w} = \left(\frac{u}{u_\infty}\right)^2$$

In each case the velocity profiles were calculated by using both the linear (Crocco) and the quadratic temperature law, and the transformation was applied to the velocity profile by using the same temperature law. The differences were small between the skin-friction coefficients resulting from the consistent use of the particular temperature profile in the data reduction to velocity and in the transformation. Baronti and Libby obtained similar results when they used Crocco's temperature profile and a measured temperature profile to complete the transformation of experimental profiles in their paper. The discrepancy in wall shear at low wall-to-total-temperature ratios does not appear to be a function of Mach number or Reynolds number and is assumed to result from a deficiency in the transformation theory itself.

Heat Transfer to Delta Wings at Low Angles of Attack

The delta planform is of interest as a practical shape wing for hypersonic flight purposes. For efficient flight, the angle of attack will be low and for the large air-breathing vehicles the leading-edge size necessary from aerodynamic heating requirements is small compared with wing chord. Only wings with essentially sharp leading edges are treated here.

Consider the wing shown in figure 5 on which tests were made at zero angle of attack by Whitehead in the Mach 6 airstream of the Langley 20-inch hypersonic tunnel.* The cross section was actually half-diamond with the flat side instrumented and aligned with the flow. The shock was attached to the leading edge and the pressure ratio on the instrumented surface was essentially unity. Stanton number is shown as a function of Reynolds number and the boundary layer flow is indicated to be transitional at the most forward measuring stations. If the virtual origin of the turbulent boundary layer is taken to be at the location of peak heating, the assumption of strip-like flow which is successful in laminar boundary layers is found to give a good prediction in this case also. For this wing, in the same airstream, tilted so that the instrumented surface faces 5° to the windward, the shock remains attached and the pressures are within 5 to 10 percent of the two-dimensional shock value. The Stanton number is predicted within about 10 percent by strip theory.

The flow condition where the shock is detached from the leading edge of the delta wing but attached at the apex is also of interest. Examples of this type of flow are contained in the data reported in reference 6. The particular case of a 70° swept wing at zero angle of attack in a Mach 3 flow is shown in figure 6.** Leading-edge shock detachment is caused by a bevel on the underside

*Test conditions of $T_t = 960^\circ \text{ R}$, $T_w/T_t = 0.6$, $R_\infty/\text{in.} = 0.53$ and 0.60×10^6 ; model span 9.827 in.

**Test conditions of $T_t = 710^\circ \text{ R}$, $T_w/T_t = 0.83$, $R_\infty/\text{in.} = 0.50 \times 10^6$; tripped boundary layer with equivalent two-dimensional value of $k/\delta_k = 4.4$; model span, 24 inches.

~~CONFIDENTIAL~~

~~CONFIDENTIAL~~

of the wing. The pressures show a behavior typical of a subsonic cross flow where the stagnation point is on the beveled underside and there is a sharp drop in pressure as the flow expands around the sharp leading edge. The conical coordinate used gives good correlation of the pressures measured on the wing surface. The surface on which the pressures are measured is flat and aligned with the flow, but the pressures are as low as 50 percent of free-stream pressure at the most forward stations.

Oil flow on a 70° swept wing in the same stream, but which had a somewhat smaller leading-edge bevel angle, indicated surface flow lines essentially parallel to the root chord. The leading-edge shock was also detached on this latter wing. By using the modified Spalding-Chi method in stripwise fashion with local values of correlated experimental pressures, a good prediction of the heat-transfer results was obtained. However, if the pressures had not been available and the surface pressure had been taken as equal to free-stream pressure, a significant error would have been incurred in heat-transfer predictions over much of the wing, as shown in figure 6.

Again, consider the wing tested by Whitehead in the Mach 6 airstream. With the flat instrumented side of the wing facing leeward at an angle of 5° to the free stream, the shock is calculated to be attached. However, only a small deflection of the wing under load would suffice to cause leading-edge shock detachment. The pressures, shown in figure 7(a), do not vary much over the span and appear to correlate well in conical coordinates with no particular difference in the distribution between the case where the surface is smooth and the case where spherical boundary layer trips are placed on the surface near the leading edge.

Without boundary-layer trips, the heat transfer to this surface was only transitional at the rearmost stations of the near root chord region. With spherical trips, the level of aerodynamic heating was increased to a level expected with turbulent flow as shown in figure 7(b). In this case Stanton number is shown as a function of Reynolds number based on free-stream conditions and distance from the leading edge parallel to the root chord. For reference purposes, the modified Spalding-Chi method applied in stripwise fashion for a constant pressure on the wing equal to the two-dimensional value. (The virtual origin is taken as $R_{\infty, x} = 2 \times 10^6$ based on the indicated peak in heating along the root chord.) If the prediction method applied, then one would not expect more than about 20-percent difference between prediction and experiment based on the variation in the pressures. Clearly, there is no correlation of the data and there are large increases in heat transfer in the midportion of the wing where surface-oil-flow studies indicate a conical vortex system to be formed. (See ref. 25.) A similar trend can be found in the heat transfer reported in reference 6 from tests at lower Mach numbers.

CONCLUDING REMARKS

Recent hypersonic turbulent-boundary-layer experiments and proposed prediction methods pertinent to the problem of the effect of wall temperature, the

~~CONFIDENTIAL~~

transformation of the compressible boundary layer to a constant-density type, and the delta wing have been considered.

Up to a Mach number of at least 9, based on flat-plate experiments, the level of the heat-transfer coefficient is found to be little affected by significant changes in wall temperature as predicted by the Spalding-Chi method among several prediction methods. The T' or reference temperature method overpredicts skin friction and heat transfer at low wall-temperature ratios.

The Coles transformation as modified by Baronti and Libby has been examined by utilizing boundary-layer profiles covering a wide range of Mach number and wall-temperature ratio. Some success is found for the transformation up to the lower end of the hypersonic range and down to moderately low wall-temperature ratios. However, at the lowest wall-temperature ratios, the transformation gave high wall shears as compared with Spalding-Chi predictions and shears that were actually measured. At high Mach numbers, very little of the logarithmic portion of the transformed profile remains because of an apparent thickening of the sub-layer adjacent to the wall and the velocity-defect wake region comprising the outer part of the profile. It is the logarithmic portion of the profile from which the indicated shear is obtained.

Delta-wing heat transfer has been examined for several types of flow. At low angles of attack, in cases where the flow near the surface is essentially streamwise, strip application of successful flat-plate methods gives good predictions of the heat transfer if the pressures are known. This result applies whether the shock is attached to or detached from the leading edge. On the lee side of delta wings where vortices are indicated, the predictions are poor. Success in predicting the heat transfer to delta wings appears to be limited by the ability to predict the flow field.

~~CONFIDENTIAL~~

~~CONFIDENTIAL~~

APPENDIX

ANALYSIS METHODS

In reducing the data and applying the various prediction methods the approach was the same as that given in appendix A of reference 2. Although not explicitly mentioned in reference 2, the recovery factor used in reducing the heat-transfer data was as follows. Where the recovery factor in the original data reduction was between 0.88 and 0.90, no correction for recovery factor was made. For data where the recovery factor assumed was outside these limits, the data were re-reduced by using a recovery factor of 0.89 and all new heat-transfer data were reduced by assuming this recovery factor.

When the Spalding-Chi method was applied, the values from this method and its modified form were generally taken from the charts given in reference 26. In this case and the T' method (Monaghan), the Prandtl number was assumed to be 0.725 for use with the Karman-Reynolds analogy factor. This same Prandtl number was used with the laminar T' method of Monaghan (ref. 27) to obtain values of the laminar boundary-layer thickness (δ) for defining values of k/δ_k .

~~CONFIDENTIAL~~

~~CONFIDENTIAL~~

REFERENCES

1. Banner, Richard D.; Kuhl, Albert E.; and Quinn, Robert D.: Preliminary Results of Aerodynamic Heating Studies on the X-15 Airplane. NASA TM X-638, 1962.
2. Bertram, Mitchel H.; and Neal, Luther, Jr.: Recent Experiments in Hypersonic Turbulent Boundary Layers. Presented to the AGARD Specialists Meeting on Recent Developments in Boundary-Layer Research (Naples, Italy), May 10-14, 1965.
3. Baronti, Paolo O.; and Libby, Paul A.: Velocity Profiles in Turbulent Compressible Boundary Layers. AIAA J., vol. 4, no. 2, Feb. 1966, pp. 193-202.
4. Paulsen, James J.; and Schadt, Gail H.: A Study of the Pressure and Heat Transfer Distribution on Highly Swept Slab Delta Wings in Supersonic Flow. AIAA Paper No. 66-130, Am. Inst. Aeron. Astronaut., Jan. 1966.
5. Nagel, A. L.; Fitzsimmons, H. D.; and Doyle, L. B.: Analysis of Hypersonic Pressure and Heat Transfer Tests on Delta Wings With Laminar and Turbulent Boundary Layers. NASA CR-535, 1966.
6. Murray, William M., Jr.; and Stallings, Robert L., Jr.: Heat-Transfer and Pressure Distributions on 60° and 70° Swept Delta Wings Having Turbulent Boundary Layers. NASA TN D-3644, 1966.
7. Spalding, D. B.; and Chi, S. W.: The Drag of a Compressible Turbulent Boundary Layer on a Smooth Flat Plate With and Without Heat Transfer. J. Fluid Mech., vol. 18, pt. 1, Jan. 1964, pp. 117-143.
8. Monaghan, R. J.: On the Behavior of Boundary Layers at Supersonic Speeds. Fifth International Aeronautical Conference, Rita J. Turino and Caroline Taylor, eds., Inst. Aeron. Sci., Inc., June 1955, pp. 277-315.
9. Wallace, J. E.; and McLaughlin E. J.: Experimental Investigations of Hypersonic, Turbulent Flow and Laminar, Leeward-Side Flow on Flat Plates. Tech. Rept. AFFDL-TR-66-63, vol. 1, U.S. Air Force, July 1966.
10. Wallace, J. E.: Hypersonic Turbulent Boundary Layer Studies at Cold Wall Conditions. Paper to be presented at 1967 Heat Transfer and Fluid Mechanics Institute (San Diego, Calif.), June 19-21, 1967.
11. Hironimus, G. A.: Hypersonic Shock Tunnel Experiments on the W7 Flat Plate Model - Expansion Side, Turbulent Flow and Leading Edge Transpiration Data. Rept. No. AA-1952-Y-2 (Contract No. AF 33(615)-1847), Cornell Aeron. Lab., Inc., Feb. 1966.
12. Burggraf, O. R.: The Compressibility Transformation and Turbulent-Boundary-Layer Equations. J. Aerospace Sci., vol. 29, no. 4, Apr. 1962, pp. 434-439.

~~CONFIDENTIAL~~

~~CONFIDENTIAL~~

13. Mager, Artur: Transformation of the Compressible Turbulent Boundary Layer. J. Aeron. Sci., vol. 25, no. 5, May 1958, pp. 305-311.
14. Spence, D. A.: Velocity and Enthalpy Distributions in the Compressible Turbulent Boundary Layer on a Flat Plate. J. Fluid Mech., vol. 8, pt. 3, July 1960, pp. 368-387.
15. Coles, Donald E.: Measurements in the Boundary Layer on a Smooth Flat Plate in Supersonic Flow. III. Measurements in a Flat-Plate Boundary Layer at the Jet Propulsion Laboratory. Rept. No. 20-71 (Contract No. DA-04-495-Ord 18), Jet Propulsion Lab., California Inst. Technol., June 1, 1953.
16. Crocco, L.: Transformations of the Compressible Turbulent Boundary Layer With Heat Exchange. AIAA J., vol. 1, no. 12, Dec. 1963, pp. 2723-2731.
17. Coles, D. E.: The Turbulent Boundary Layer in a Compressible Fluid. U.S. Air Force Project RAND Rept. R-403-PR, the RAND Corp., Sept. 1962.
18. Clauser, Francis H.: Turbulent Boundary Layers in Adverse Pressure Gradients. J. Aeron. Sci., vol. 21, no. 2, Feb. 1954, pp. 91-108.
19. Watson, Ralph D.; and Cary, A. M., Jr.: The Transformation of Hypersonic Turbulent Boundary Layers to Incompressible Form. AIAA J. (Tech. Notes), vol. 6, no. 6, June 1967, pp. 1202-1203.
20. Tennekes, H.: Law of the Wall for Turbulent Boundary Layers in Compressible Flow. AIAA J., vol. 5, no. 3, Mar. 1967, pp. 489-492.
21. Samuels, Richard D.; Peterson, John P., Jr.; and Adcock, Jerry B.: Experimental Investigation of the Turbulent Boundary Layer at a Mach Number of 6 With Heat Transfer at High Reynolds Numbers. NASA TN D-3858, 1967.
22. Sterrett, James R.; and Barber, John B.: A Theoretical and Experimental Investigation of Secondary Jets in a Mach 6 Free Stream With Emphasis on the Structure of the Jet and Separation Ahead of the Jet. Presented at the Separated Flows Specialists Meeting, Fluid Dynamics Panel (Brussels, Belgium), AGARD, May 9-11, 1966.
23. Maddalon, D. V.; Rogallo, R. S.; and Henderson, A., Jr.: Transition Measurements at Hypersonic Mach Numbers. AIAA J., vol. 5, no. 3, Mar. 1967, pp. 590-591.
24. Henderson, A.; Rogallo, R. S.; Woods, W. C.; and Spitzer, C. R.: Exploratory Hypersonic Boundary-Layer Transition Studies. AIAA J. (Tech. Notes), vol. 3, no. 7, July 1965, pp. 1363-1364.
25. Sterrett, James R.; Morrisette, E. Leon; Whitehead, Allen H., Jr.; and Hicks, Raymond M.: Transition Fixing for Hypersonic Flow. Conference on Hypersonic Aircraft Technology, NASA SP-148, 1967. (Paper No. 15 herein.)

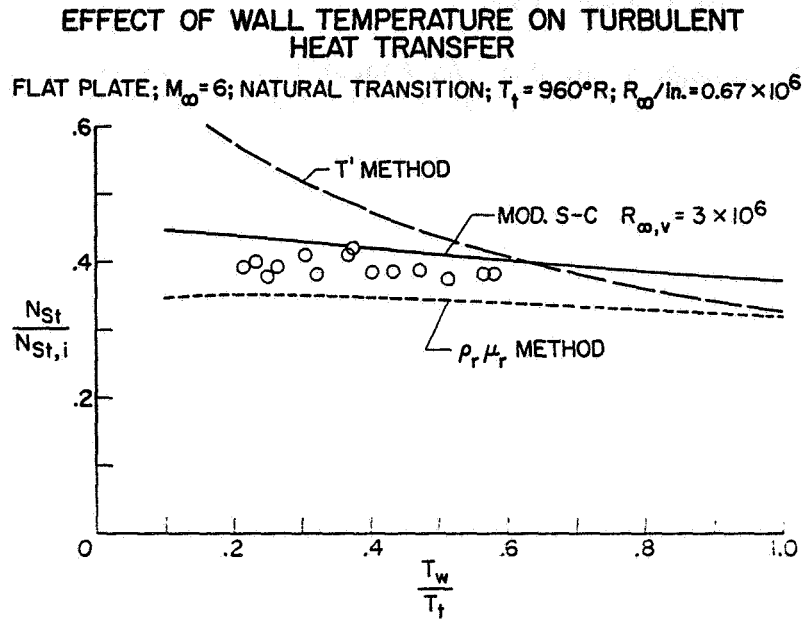
~~CONFIDENTIAL~~

~~CONFIDENTIAL~~

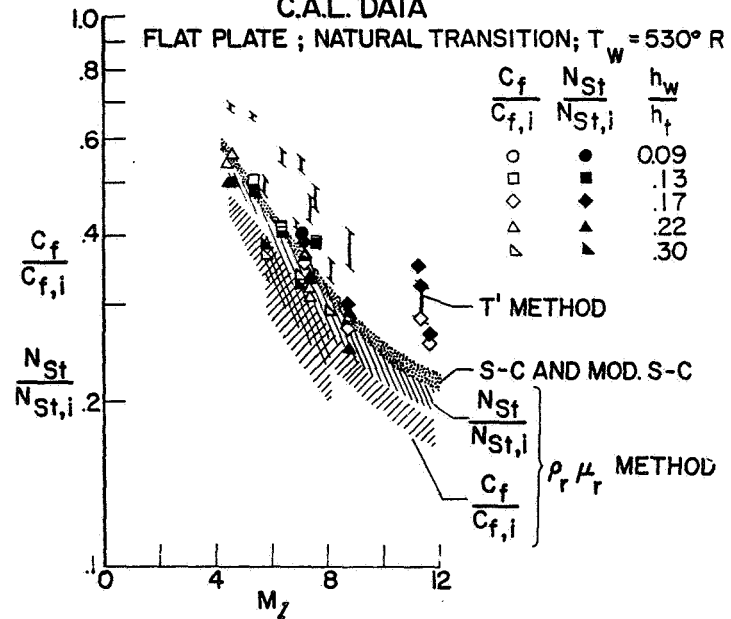
26. Neal, Luther, Jr.; and Bertram, Mitchel H.: Turbulent-Skin-Friction and Heat-Transfer Charts Adapted From the Spalding and Chi Method. NASA TN D-3969, 1967.
27. Monaghan, R. J.: An Approximate Solution of the Compressible Laminar Boundary Layer on a Flat Plate. R. & M. No. 2760, British A.R.C., 1953.

~~CONFIDENTIAL~~

CONFIDENTIAL



**COMPARISON OF TURBULENT PREDICTION METHODS WITH
C.A.L. DATA**



CONFIDENTIAL

CONFIDENTIAL

BARONTI-LIBBY TRANSFORMATION FOR VELOCITY PROFILES

TURBULENT FLOW; $M_t \approx 2.5$ TO 8

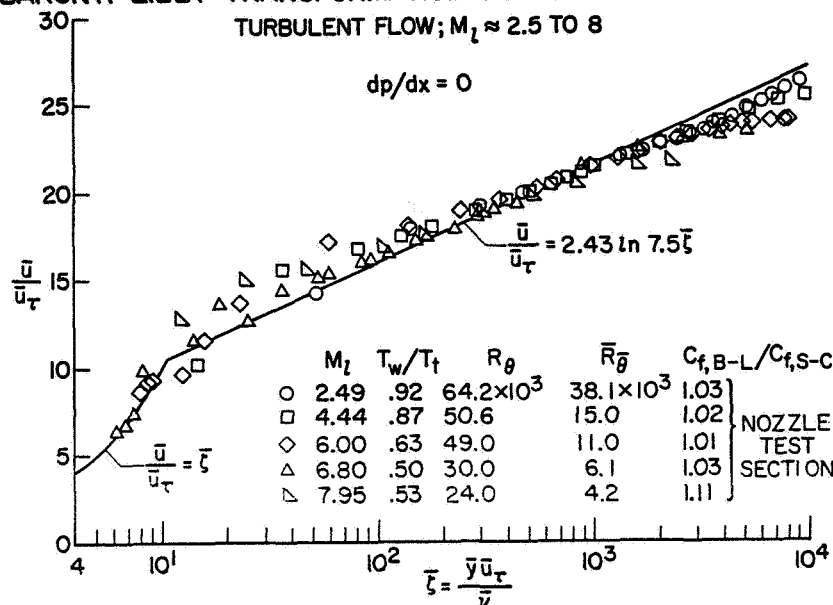


Figure 3(a)

BARONTI-LIBBY TRANSFORMATION FOR VELOCITY PROFILES

TURBULENT FLOW; $M_t \approx 15$ TO 20

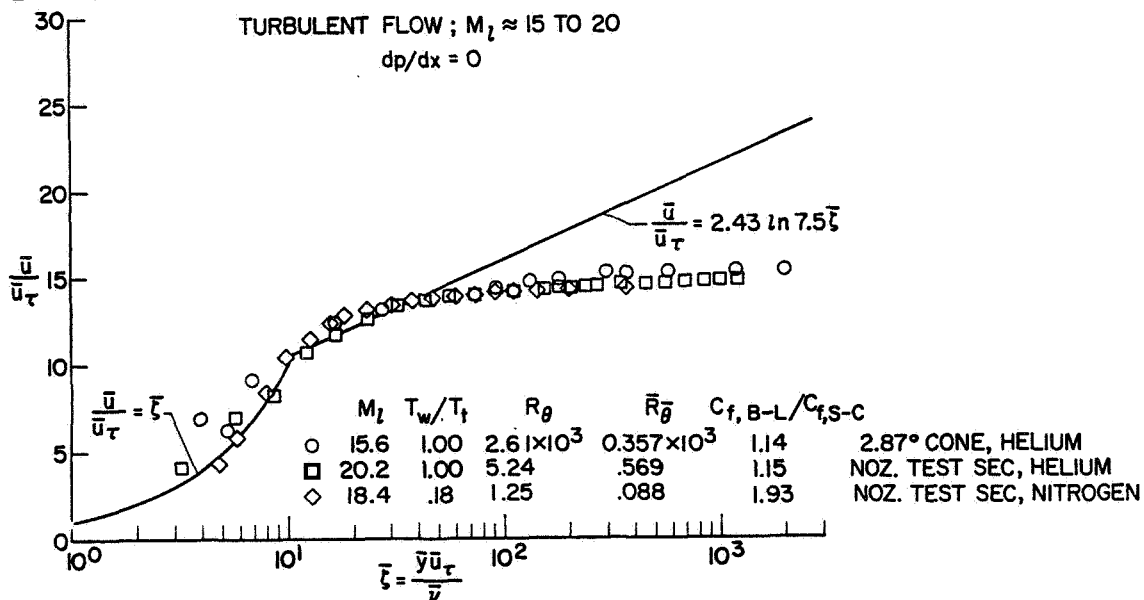


Figure 3(b)

CONFIDENTIAL

CONFIDENTIAL

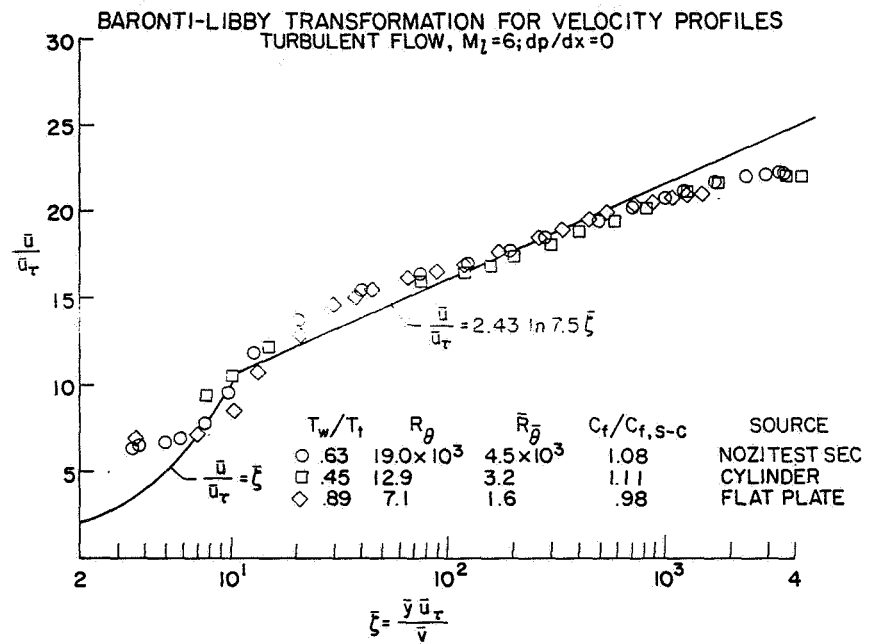


Figure 3(c)

CONFIDENTIAL

SKIN-FRICTION RESULTS BARONTI-LIBBY TRANSFORMATION

	M_t	R_θ	SOURCE
////	2-4.2	$2.2-702 \times 10^3$	BARONTI, LIBBY (REF. 3)
○	5-6.8	6.5-8.6	LOBB et al., NOZ. TEST SECT., AIR (REF. 3)
□	5.2	2.0-5.9	WINKLER, CHA, FLAT PLATE, AIR (REF. 3)
◇	6.0	19-49	BERTRAM, NEAL, NOZ. TEST SECT., AIR (REF. 2)
△	6.8	13-30	BERTRAM, NEAL, NOZ. TEST SECT., AIR (REF. 2)
▴	6.0	12.9	SAMUELS et al., CYLINDER, AIR (REF. 21)
▢	6.0	7.1	STERRETT, BARBER, FLAT PLATE, AIR (REF. 22)
▣	7.5	2.0	MADDALON et al., 10° CONE, HELIUM (REF. 23)
◇	15.6	2.6	HENDERSON et al., 2.87° CONE, HELIUM (REF. 24)
◇	20.2	5.2	BERTRAM, NEAL, NOZ. TEST SECT., HELIUM (REF. 2)
△	7.2-7.9	3.5-5.8	WALLACE, NOZ. TEST SEC.-AIR (REF. 10)
▽	18.4	1.25	HARVEY, CLARK, NOZ. TEST SECT., NITROGEN
□	7.9	11-24	FELLER, NOZ. TEST SECT., AIR

UNPUBLISHED

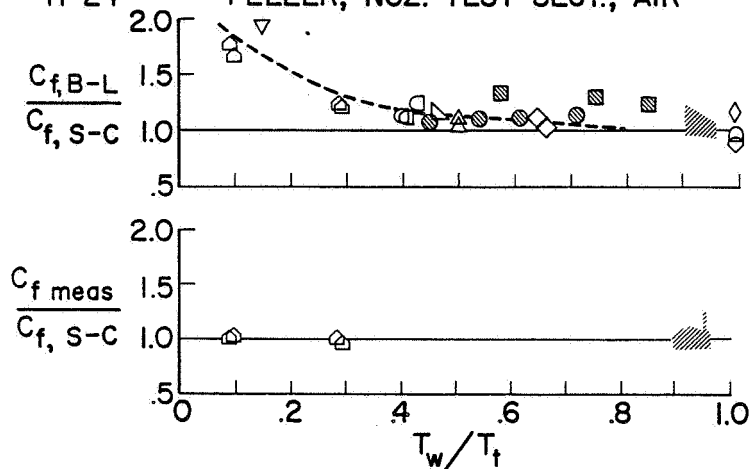


Figure 4

CONFIDENTIAL

HEAT TRANSFER TO FLAT DELTA WING WITH ATTACHED SHOCK $M_\infty = 6$; $\alpha = 0^\circ$; $\Delta = 70^\circ$; NATURAL TRANSITION

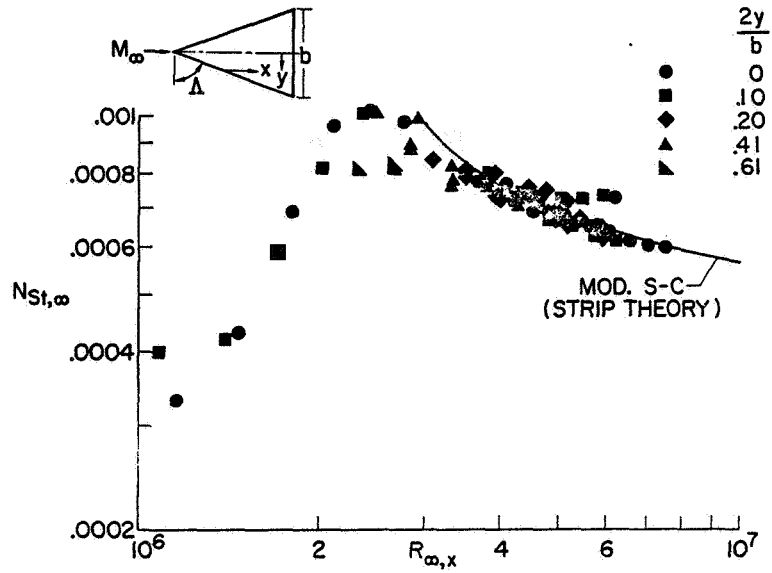


Figure 5

TURBULENT HEAT TRANSFER TO DELTA WING WITH DETACHED SHOCK

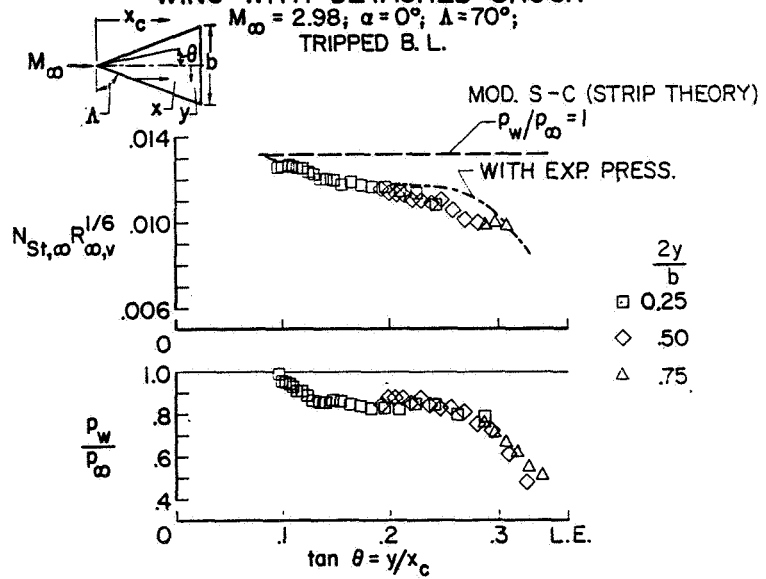


Figure 6

~~CONFIDENTIAL~~

PRESSURES ON FLAT DELTA WING, ATTACHED SHOCK (?)

$M_\infty = 6$; $\alpha = -5^\circ$; $\Delta = 70^\circ$

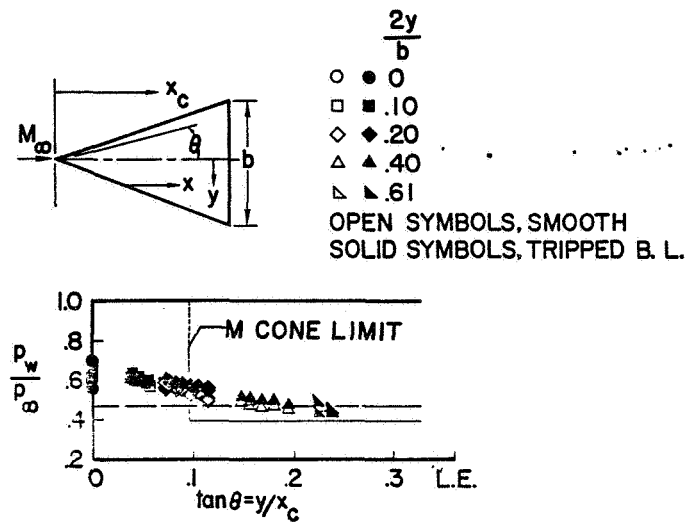


Figure 7(a)

HEAT TRANSFER TO FLAT DELTA WING, ATTACHED SHOCK (?)

$M_\infty = 6$; $\alpha = -5^\circ$; $\Delta = 70^\circ$

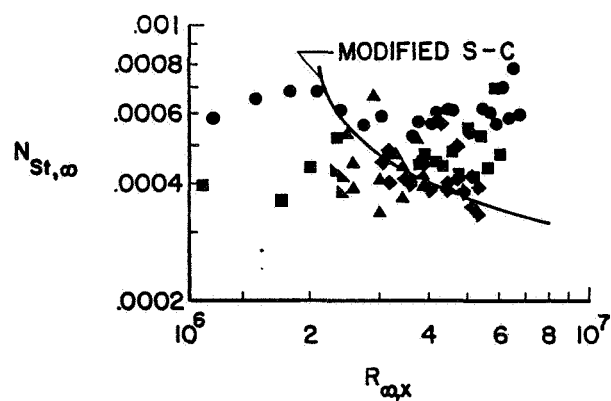


Figure 7(b)

~~CONFIDENTIAL~~

~~CONFIDENTIAL~~

17. CORNER FLOW AT HYPERSONIC SPEEDS

By P. Calvin Stainback and Leonard M. Weinstein
Langley Research Center

SUMMARY

A study of hypersonic flow in a corner based on past experimental and theoretical studies and recent experiments has revealed at least three flow phenomena which influence the skin friction and heat transfer in the vicinity of a corner. The mutual interaction of the boundary layers in the corner results in a decrease in the local skin friction and heat transfer very near the corner. A vortex system and reattachment of the boundary layer downstream of separation result in an increase in heating outboard of the mutual boundary interaction region. Attempts to correlate the peak laminar heating and the location of this peak in the vicinity of a corner for a simple model were partly successful. It was found from limited data that the effect of the corner on peak heating was less for a turbulent boundary layer than for a laminar boundary layer.

INTRODUCTION

The flow of a fluid in the vicinity of a corner formed by two intersecting plates is of interest since these intersections are often encountered in the design of high-performance hypersonic aircrafts. For example, they occur where the wing and control surfaces intersect the fuselage, where control surfaces intersect a wing, and in inlets. These corner flow fields can influence the local skin friction and heat transfer to aircraft components and possibly alter the effectiveness of control surfaces. Because of these possible influences, the characteristics of these corner flow regions should be investigated in order to determine their influence on overall vehicle performance.

Since most of the boundary layer over a high-performance hypersonic-cruise vehicle will probably be turbulent, it would be desirable to have data with fully developed turbulent flow in the corner region. Unfortunately, very few turbulent-flow data are available in corner regions at high Mach numbers since past interests were focused on high-altitude glide vehicles at conditions where laminar flow could be expected. Also, high Mach number facilities often have a limited maximum Reynolds number. Thus, present attempts must be made to infer turbulent trends from laminar data. Even though turbulent flow would be expected to have an effect on the level of heating in a corner, the basic corner-flow phenomena might not be changed to any great extent. Therefore, because of the lack of turbulent-flow data, laminar flow data will be reviewed to see whether the major flow phenomena occurring in the corner flow region can be defined. In addition, some laminar-flow data will be presented and an

~~CONFIDENTIAL~~

~~CONFIDENTIAL~~

attempt made to correlate these data. Some preliminary turbulent-flow data taken on simple shapes will also be presented. Most of the results will be limited to heat-transfer data; however, some surface-flow visualization and flow-field visualization data will be presented.

SYMBOLS

h	aerodynamic heat-transfer coefficient
$h_{\text{lam.th.}}$	aerodynamic heat-transfer coefficient based on laminar theory
$h_{\text{turb.th.}}$	aerodynamic heat-transfer coefficient based on turbulent theory
M_{∞}	free-stream Mach number
N_{St}	Stanton number based on inclined surface fluid properties
$N_{\text{St,max}}$	maximum Stanton number based on inclined surface fluid properties
R_x, R_y, R_z	Reynolds number based on inclined surface fluid properties and on x , y , and z , respectively
R_{∞}	free-stream Reynolds number
r_n	nose radius
V_{∞}	free-stream velocity
x, y, z	coordinates
x_0	initial length (see fig. 1)
α	angle of attack
Λ	leading-edge sweep angle
ϕ	cant or rollout angle
ψ	yaw angle

REVIEW OF CORNER-FLOW PROBLEM

Corner flow has been somewhat of a problem in aerodynamics since the days of subsonic aircrafts. However, at hypersonic speeds the corner-flow problem becomes much more complex as a result of the mutual intersection of shocks or

~~CONFIDENTIAL~~

the shock—boundary-layer interaction or a combination of these interactions. The corner-flow problem is not only complicated as a result of speed, but the many different geometries possible make the solution of the problem even more difficult. An example of some of the possible corner-flow configurations is shown in figure 1.

Several theoretical and experimental studies have been made by using one or a combination of the geometries shown in figure 1. These studies have revealed that at least three flow phenomena exist in and near corner regions. These phenomena are illustrated in figure 2.

From early theoretical studies by Loiziansky (ref. 1) and Loitsianskii and Bolshakov (ref. 2), a low-shear region was found to exist very close to the line of intersection between the two surfaces forming a corner. Later theoretical work by Bloom and Rubin (ref. 3) indicated that this low-shear region resulted in a low-heating region near the corner. Experimental pressure tests made by Bogdonoff and Vas (ref. 4) revealed a high-pressure region in the corner and a pressure distribution which they attributed to a vortex system generated by the leading edge of the corner. This high-pressure region was found to result in a high-heating region that was greater than could be attributed to the increase in pressure. (See ref. 5.) This increased heating tended to confirm the existence of the vortex system proposed by Bogdonoff and Vas. Flow surveys made by Cresci (ref. 6) using total-pressure and temperature probes probably give the best confirmation of the existence of a vortex system in the vicinity of the corner. Cresci states, however, that this vortex system exists within the boundary layer, a result which is in agreement with the theoretical results of Carrier (ref. 7). Further tests have been conducted to study vortex formations in the vicinity of a corner and these results will be presented subsequently.

Several investigators (Gulbran, et al. (ref. 8) and Thomas (ref. 9), for example) noted that a sufficiently strong shock produced by one side of the corner or a blunt leading edge can cause the boundary layer to separate on the adjacent surface in the vicinity of the shock. This separation phenomena could result in an increased heating at the point of reattachment. Therefore, it appears that there are two mechanisms which are responsible for increasing the heating in the vicinity of a corner: a vortex system or reattachment - or, perhaps, both.

The influence of several factors on the peak heating found in the vicinity of a corner has been investigated. (For example, see ref. 10.) The results have indicated that some of the factors which increase peak heating in a corner region are increased Mach number, angle of attack, and nose radius; those factors which decrease peak heating are increased leading-edge sweep, cant or roll-out angle, and fillets.

From this review, it appears that previous investigations have resulted in a reasonable understanding of the laminar-flow phenomena existing in a corner. Hopefully, for the present, this experience will be useful in predicting the phenomena that will be encountered in a corner when the flow is turbulent. However, the level and possibly the extent of influences of corner phenomena on

~~CONFIDENTIAL~~

~~CONFIDENTIAL~~

local surface conditions for the turbulent boundary layer would probably be different from those for the laminar boundary layer as a result of the greater mixing level encountered in the turbulent boundary layer.

RESULTS AND DISCUSSION

Corner-Flow Data and Correlation

Surface-flow visualization and heat-transfer data have been obtained on a simple corner model at a free-stream Mach number of 8 and a free-stream unit Reynolds number that ranged from 0.42×10^6 to 10×10^6 per foot. Flow-field visualization tests have also been conducted at a Mach number of 20 in helium with the use of the electron-beam technique.

Examples of the surface-flow visualization results are shown in figure 3. The model had an asymmetric angle of attack with one surface at an angle of attack of 5° and the other surface aligned with the free-stream velocity. The data presented are for the aligned surface. In the photograph showing the temperature-sensitive-paint results, the dark areas represent regions with higher heating rates than the light areas. The paint results indicate a series of low- and high-heating regions as the distance from the corner is increased. The low- and high-heating regions are seen to correspond to low- and high-shear regions as revealed by the oil-smear-technique results, also shown in the figure. The low- and high-shear regions revealed by the oil-flow results indicate the possible existence of separation (where oil accumulates) and reattachment (very light regions) in the regions of shock impingement. The large cross-flow component of some of the oil-flow lines revealed by the oil-dot technique also suggests the existence of a strong vortex system near the corner. Since it is difficult to distinguish between the influences of separation and reattachment and those of a vortex system by the use of surface-flow visualization techniques, an electron-beam technique has been used to visualize the flow field far from the surface. An example of the results is shown in figure 4 where both surfaces are inclined 10° with respect to the free-stream velocity. The sketch in the upper left-hand section of the figure indicates the general location of the model in the tunnel, and the schematic drawing in the upper right-hand section indicates a part of the resultant flow field.

The photographs in the lower portion of figure 4 illustrate some of the preliminary results obtained up to the present time. The left-hand photograph is a view from the rear of the model and below the level of the model surface; that is, flow appears to be flowing over the head of the observer. The electron beam reveals two types of structure in the flow. First, a tear-drop-shaped dark region indicates the existence of one branch of a vortex system. The other structure, indicated by a light area extending from the corner at about 45° from either surface, is believed to be the resultant shock formed by the intersection of the two undisturbed wedge shocks. This type of intersection has been suggested by the low Mach number results of Charwat and Redekopp (ref. 11). In the second photograph, the view is from the rear of the model and is directed parallel to the line of intersection of the two surfaces forming

~~CONFIDENTIAL~~

~~CONFIDENTIAL~~

the corner. Note the small dark region which is again interpreted as being the core of one branch of a vortex system. Therefore, this is additional evidence that a vortex system exists in the vicinity of a corner for the present geometry.

Some typical heat-transfer results obtained with a corner model at an asymmetric angle of attack of $\alpha = 10^\circ$ and an angle of yaw of $\psi = 0^\circ$ is shown in figure 5. The data for the inclined surface indicate that there is a relatively low heating region near the corner caused by the mutual interaction of the boundary layers from adjacent surfaces. The heating rate increases as the distance from the corner is increased, reaches a peak, and ultimately decreases to the theoretical flat-plate value. The peak values of $N_{St}\sqrt{R_x}$ for various distances from the leading edge do not appear to be a function of x ; therefore, the Stanton number for the peak heating would be expected to correlate as suggested by conventional flat-plate theory. Also, the peak values of $N_{St}\sqrt{R_x}$ are located at a given value of y/x . This fact indicates that the location of the peak heating is proportional to x .

The data for the alined surface (plotted on left-hand part of fig. 5) also indicate a low heating rate in the vicinity of the corner. The heating rate increases to a primary peak farther outboard and this location is nearer the corner than the projection of the shock from the inclined surface. Outboard of the primary peak, the heating decreases until a secondary increase in heating is formed outboard of the projected shock. Farther outboard of the secondary peak, the heating decreases to the theoretical flat-plate value. The Stanton and Reynolds numbers are based on properties for the inclined surface and result in the apparent low value of $N_{St}\sqrt{R_x}$ far from the corner on the alined surface.

It is interesting to note that for the alined surface the value of $N_{St}\sqrt{R_x}$ increases with increasing x ; therefore, the peak heating data will probably not correlate in terms of N_{St} as a function of Reynolds number as suggested by the results for the inclined surface. The location of the peaks, however, appears to be at about a constant value of z/x and this fact indicates that z is proportional to x .

Along the y/x and z/x coordinates of figure 5, the dark areas indicate regions in which oil remained on the model after the oil-flow tests, whereas the light areas indicate regions in which the oil was removed from the model by high shearing stresses. The peak heating rates are seen to occur where the shearing stresses were also high. The combined oil-flow and heat-transfer results indicate the existence of a vortex system as shown in figure 5.

Correlation of Laminar Peak Heating Data

Sample heat-transfer data have indicated the existence of peak heating rates on both of the surfaces that form a corner model. It would be desirable to correlate the magnitude of these peak heating rates and the location of their peaks. This information might be useful to design engineers if they encounter similar configurations in the design of practical high-performance hypersonic aircraft.

~~CONFIDENTIAL~~

~~CONFIDENTIAL~~

First, consider the data for the asymmetric corner where one surface is always alined with the free-stream velocity and the other surface has some inclination angle. The attempt to correlate these results for $\alpha = 0^\circ$, 5° , and 10° is shown in figure 6. Most of the data correlate fairly well with R_x , over a wide range of unit Reynolds numbers, until transition becomes apparent at high values of R_x . Some of the scatter present in the figure is due to the inability to define peak heating adequately as a result of the limited number of thermocouples near the leading edge of the model where peak heating is inboard of the thermocouples nearest the line of intersection. In general, the increase in heating ranges from about 50 to 65 percent above the laminar flat-plate theory of reference 12.

Since the data could be correlated in terms of the conventional viscous parameters, Stanton and Reynolds numbers, the peak heating rate on the inclined surface is apparently governed by viscous forces. This assumption appears reasonable since the shock produced by the alined surface is weak and probably would have negligible effect on the magnitude of the heating.

Although the present results for a Mach number of 8 and previous results from reference 5 for a Mach number of 5 indicate only a 50- to 65-percent increase in heating above theoretical flat-plate values for the $\alpha = 0^\circ$, $\psi = 0^\circ$ attitude, data taken at higher Mach numbers ($M = 12$ to 16 , refs. 6 and 13) indicate a greater increase in the value of the peak heating - about 300 percent above laminar flat-plate theory. Therefore, it appears that the present correlations will probably be limited in usefulness up to a Mach number of about 8. However, when data become available at higher Mach numbers, the types of correlation used herein might be applicable to the higher Mach number data.

The first attempt to correlate the data for the alined surface in terms of maximum Stanton number and Reynolds number is shown in figure 7. In this form, a satisfactory correlation was not obtained. Of course, this result was anticipated because of the results shown in figure 5 for the alined surface. It is interesting to note that the maximum Stanton number is almost constant with Reynolds number for the limitations of the present model. This result has been noted before in reference 14 and is also in agreement with the data of reference 8. This variation would not be expected to continue indefinitely, but rather to decrease after some value of Reynolds number is reached. The heating rate should ultimately become parallel to the laminar-flat-plate-theory line. This variation of the Stanton number, however, might not be reached as a result of the occurrence of transition, which ultimately must occur, at a sufficiently large Reynolds number.

It is not clear at the present time why the Stanton number is constant with increasing Reynolds number. However, the peak-heating result is probably due to a combination of vortex system and separation and reattachment. The invariance of the Stanton number with Reynolds number indicates that a strong inviscid phenomenon is probably controlling the peak heating on the alined surface.

Since the data did not correlate well with Stanton and Reynolds numbers, other parameters were tried in an attempt to obtain a better correlation. One

~~CONFIDENTIAL~~

such attempt is presented in figure 8. These parameters, $N_{St,max}/\sqrt{x}$ and R_x , appear to correlate the data fairly well, but unfortunately the data require a dimensional quantity in order to obtain their correlation.

Correlation of the Location of Peak Heating

The locations of the peak heating were correlated in the form of R_y or R_z as a function of R_x . These results are shown in figures 9 and 10. The correlations are fair for both surfaces of the model until transition occurs at high Reynolds numbers. The fact that the slope of these curves on log-log paper is about 1 indicates that y or z is almost proportional to x for most of the range of the data. This prediction was indicated from figure 5.

Effect of Cant Angle on Laminar Peak Heating

As pointed out in reference 10, several factors can reduce peak heating in the vicinity of a corner. Among these factors are increased leading-edge sweep, cant or rollout angle, and fillets. A second heat-transfer model was tested at a Mach number of 8 to investigate the effect of cant angle on peak heating in a corner. The instrumentation on this model was not as extensive as that on the model used to obtain the data previously discussed. The results of these tests for variation of the cant angle only are shown in figure 11. This figure reveals a substantial increase in peak heating resulting from reducing the angle between the plates from 90° to 60° . For example, the increase in peak heating for $\phi = 90^\circ$ is about 40 percent greater than that obtained from laminar flat-plate theory whereas the increase for $\phi = 60^\circ$ is about 80 percent greater. Of course, increasing the cant angle above 90° results in a decrease in peak heating until the angle reaches 270° (an exterior corner) where there is little or no increase in heating above laminar flat-plate theory. The increase in peak heating with increasing x seen in figure 11 is apparently due to the limited number of thermocouples in this model. This fact makes it difficult to define peak heating near the leading edge of the model.

If the data obtained with the second model, for all cant angles except 90° , are compared with those obtained with the more completely instrumented first model ($\phi = 90^\circ$), it can be seen (fig. 12) that there is little or no increase in peak heating for $\phi = 60^\circ$ when compared with the heating for $\phi = 90^\circ$. However, the two larger values of ϕ ($\phi = 120^\circ$ and 270°) indicate a decrease in the level of peak heating when compared with the 90° case.

Turbulent Heating in the Corner Region

There is very little fully developed turbulent-flow data at high Mach numbers available in the literature for corner flow. However, since most of the flow over a hypersonic-cruise vehicle will probably be turbulent, a program has been undertaken to obtain fully developed turbulent-corner-flow data at a Mach number of 8. The models were constructed of glass-fused mica, and preliminary

~~CONFIDENTIAL~~

~~CONFIDENTIAL~~

temperature-sensitive-paint data have been obtained with the model. An example of some of the results obtained with this model is presented in figures 13 and 14.

First consider only the data for the model with the sharp leading edges (fig. 13). The laminar-flow data (upper plot) reveal the characteristic low heating rate in the corner. The rate increases as the distance from the corner is increased, reaches a peak, and then subsequently approaches flat-plate-theory values. The temperature-sensitive-paint results at a Mach number of 8 indicate that for the same type of model with turbulent flow in the corner, there is no increase in heating in the corner above turbulent theory. (See lower plot of fig. 13.) This was also true for the Mach number 5 data of reference 5.

When one of the surfaces has a blunt leading edge of 0.25 inch and data are recorded on the adjacent surface, the results shown in figure 14 are obtained. For the laminar-flow data (upper plot), the shock produced by the blunt leading edge results in a very large increase in heating on the adjacent surface. This increase can be about 12 to 13 times the laminar-flat-plate-theory value. (This increase is a function of x/r_n .) However, if the flow is turbulent outboard of the shock, the results shown in the lower portion of figure 14 are obtained. An increase in heating is noted above the turbulent-flat-plate-theory value in the turbulent-flow region as a result of shock impingement; however, this increase is only about 2.5 to 3 times the theoretical value.

From these preliminary results, it appears that the factors which resulted in an increased peak heating in the vicinity of a corner for a laminar boundary layer are absent or greatly reduced in severity when the boundary layer is turbulent. This result is probably due to the greater heating associated with a turbulent boundary layer and to its greater mixing level which might tend to damp out extraneous influences generated by the corner and its shock system.

SUMMARY OF RESULTS

The results of the present study of flow in a corner at hypersonic Mach numbers can be summarized as follows:

1. A review of the literature has revealed at least three flow phenomena existing in a corner which influence laminar skin friction and heat transfer to adjacent surfaces. The first of these phenomena is the mutual interaction between the two boundary layers on the surfaces forming the corner and the accompanying reduction of skin friction and heat transfer as a result of the interaction. The second is a vortex generated by the corner flow field and the increase in heating caused by the vortex system. The third is the advent of separation and reattachment on one surface caused by strong shocks generated by the adjacent surface with an increase in heating at reattachment.

2. Some success has been achieved in correlating laminar peak heating and the location of the peak for a limited range of corner geometries.

~~CONFIDENTIAL~~

3. The limited amount of turbulent-flow data available indicates that the influence of the corner to increase peak heating in the corner will be less when the boundary layer is turbulent than when the boundary layer is laminar. This result is probably due to the higher heating rates accompanying a turbulent boundary layer and to its greater mixing level which might tend to reduce the influence of extraneous phenomena generated by the corner flow field.

~~CONFIDENTIAL~~

~~CONFIDENTIAL~~

REFERENCES

1. Loiziansky, L. G.: Interference of Boundary Layers. No. 249, Trans. Central Aero-Hydrodynamical Inst. (Moscow), 1936.
2. Loitsianskii, L. G.: and Bolshakov, V. P.: On Motion of Fluid in Boundary Layer Near Line of Intersection of Two Planes. NACA TM 1308, 1951.
3. Bloom, Martin H.; and Rubin, Stanley: High-Speed Viscous Corner Flow. J. Aerospace Sci., vol. 28, no. 2, Feb. 1961, pp. 145-157.
4. Bogdonoff, S. M.; and Vas, I. E.: A Preliminary Investigation of the Flow in a 90° Corner at Hypersonic Speeds. Part I - Flat Plate With Thin Leading Edges at Zero Angle of Attack. D143-978-013 (ARDC TR-59-202, AD 150 023), Bell Aircraft Corp., Dec. 20, 1957.
5. Stainback, P. Calvin: An Experimental Investigation at a Mach Number of 4.95 of Flow in the Vicinity of a 90° Interior Corner Aligned With the Free-Stream Velocity. NASA TN D-184, 1960.
6. Cresci, Robert J.: Hypersonic Flow Along Two Intersecting Planes. PIBAL Rept. No. 895 (AFOSR 66-0500), Polytech. Inst. Brooklyn, Mar. 1966.
7. Carrier, G. F.: The Boundary Layer in a Corner. Quart. Appl. Math., vol. IV, no. 4, Jan. 1947, pp. 367-370.
8. Gulbran, C. E.; Redeker, E.; Miller, D. S.; and Strack, S. L.: Heating in Regions of Interfering Flow Fields - Part I. Two- and Three-Dimensional Laminar Interactions at Mach 8. Tech. Rept. AFFDL-TR-65-49, Pt. I, U.S. Air Force, July 23, 1965.
9. Thomas, John P.: Investigation of the Pressure Distribution on a Blunt-Fin Blunt-Plate Combination at a Mach Number of 11.26. ARL 66-0142, U.S. Air Force, July 1966.
10. Caldwell, A. L.; Haugseth, E. G.; and Miller, D. S.: The Influence of Aerodynamic Interference Heating on Directional Stability Problems of Hypersonic Vehicles. Paper 63-6, Inst. Aerospace Sci., Jan. 1963.
11. Charwat, A. F.; and Redekopp, L. G.: Supersonic Interference Flow Along the Corner of Intersecting Wedges. AIAA J., vol. 5, no. 3, Mar. 1967, pp. 480-488.
12. Cohen, Nathaniel B.: Boundary-Layer Similar Solutions and Correlation Equations for Laminar Heat-Transfer Distribution in Equilibrium Air at Velocities up to 41,000 Feet Per Second. NASA TR R-118, 1961.

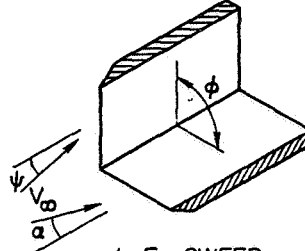
~~CONFIDENTIAL~~

13. Miller, D. S.; Hijman, R.; Redeker, E.; Janssen, W. C.; and Mullen, C. R.: A Study of Shock Impingements on Boundary Layers at Mach 16. Proc. 1962 Heat Transfer and Fluid Mech. Inst., F. Edward Ehlers, James J. Kauzlarich, Charles A. Sleicher, Jr., and Robert E. Street, eds., Stanford Univ. Press, 1962, pp. 255-278.
14. Bertram, Mitchel H.; Fetterman, David E., Jr.; and Henry, John R.: The Aerodynamics of Hypersonic Cruising and Boost Vehicles. Proceedings of the NASA-University Conference on the Science and Technology of Space Exploration, Vol. 2, NASA SP-11, 1962, pp. 215-234. (Also available as NASA SP-23.)

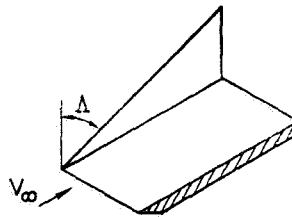
~~CONFIDENTIAL~~

CORNER-FLOW CONFIGURATION

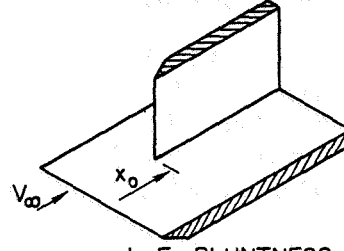
CANT ANGLE AND α
ONE OR BOTH SURFACES



L. E. SWEEP
ONE OR BOTH SURFACES



INITIAL BOUNDARY LAYER
ONE SURFACE



L. E. BLUNTNESS
ONE OR BOTH SURFACES

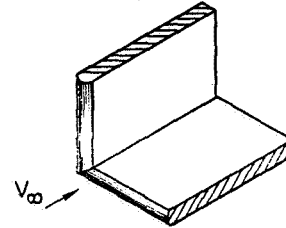


Figure 1

FLOW PHENOMENA IN A CORNER

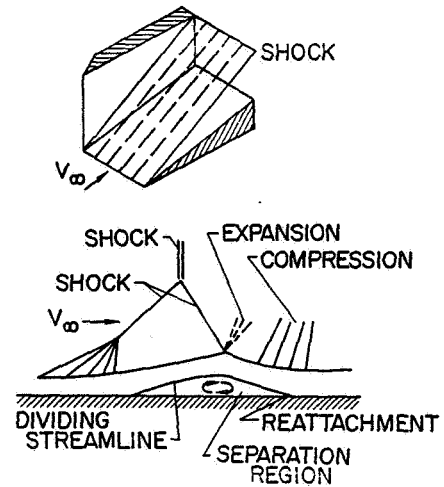
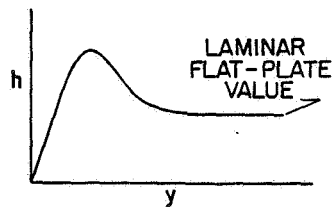
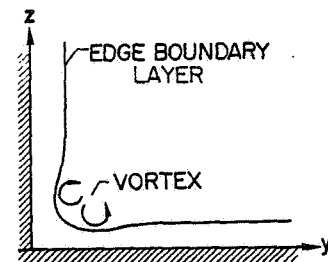


Figure 2

~~CONFIDENTIAL~~

SURFACE-FLOW VISUALIZATION IN A CORNER

$$M_\infty = 8; R_\infty / ft = 3.15 \times 10^6$$

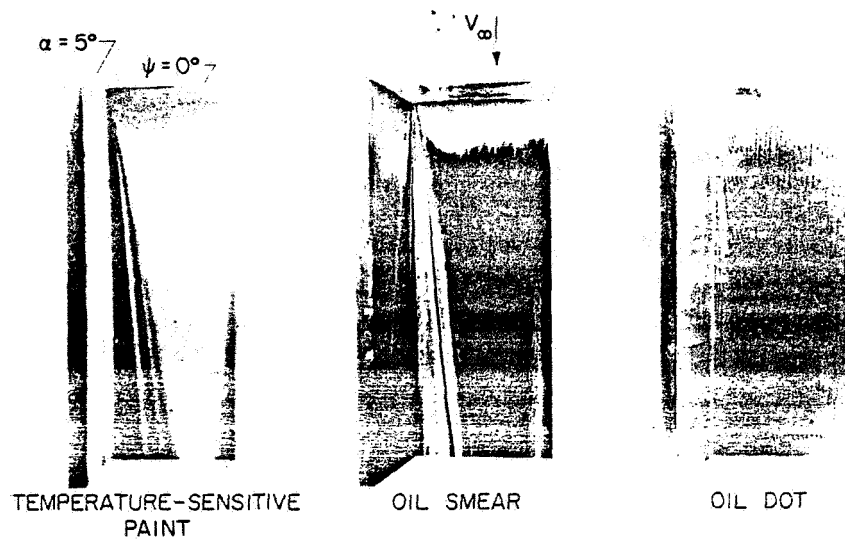


Figure 3

L-2872-1

ELECTRON-BEAM CORNER-FLOW VISUALIZATION

$$M_\infty = 20 \text{ IN HELIUM}; R_\infty / ft = 4.56 \times 10^6; \alpha = 10^\circ; \psi = 10^\circ; \phi = 90^\circ$$

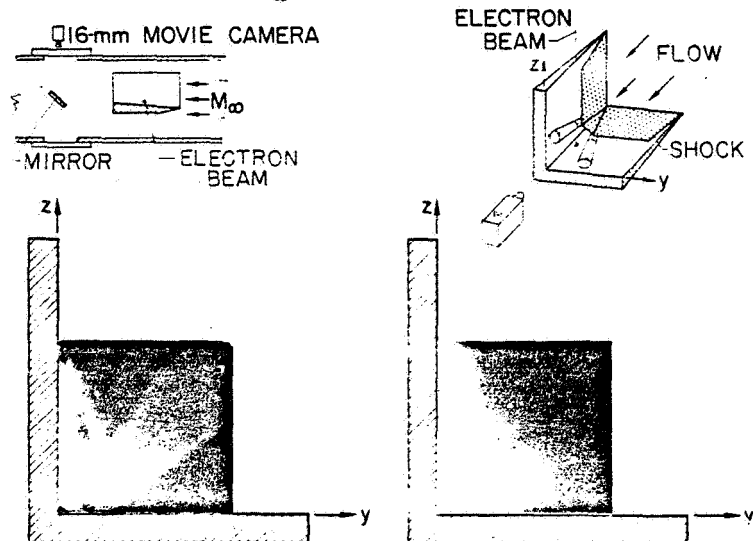


Figure 4

~~CONFIDENTIAL~~

CONFIDENTIAL

HEAT TRANSFER IN A CORNER

$M_\infty = 8$; $R_\infty/ft = 0.42 \times 10^6$

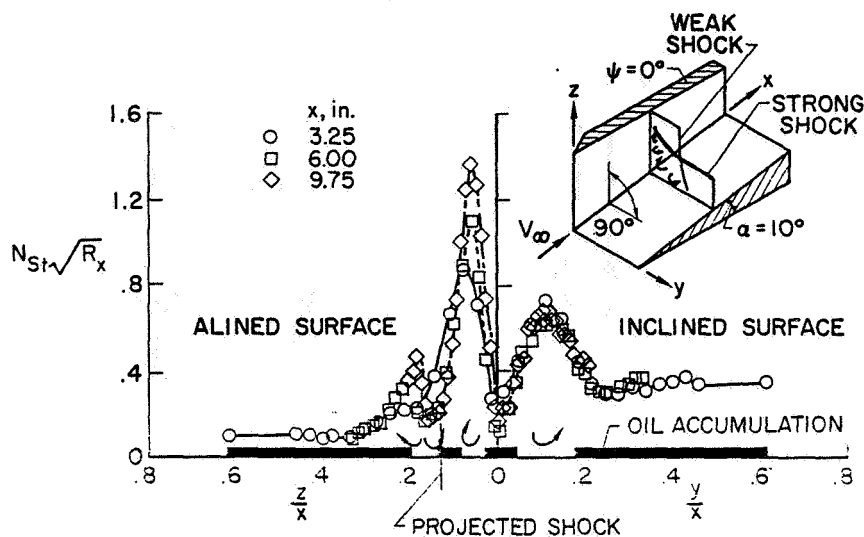


Figure 5

LAMINAR PEAK HEATING IN CORNER-FLOW REGION

INCLINED SURFACE; $M_\infty = 8$; $0.42 \times 10^6 \leq R_\infty/ft \leq 10 \times 10^6$

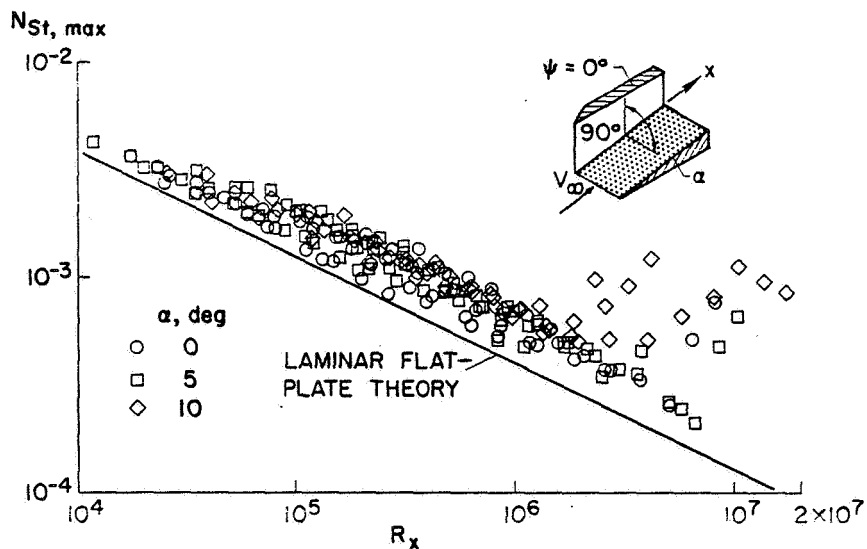


Figure 6

CONFIDENTIAL

LAMINAR PEAK HEATING IN CORNER-FLOW REGION ALINED SURFACE; $M_\infty = 8$

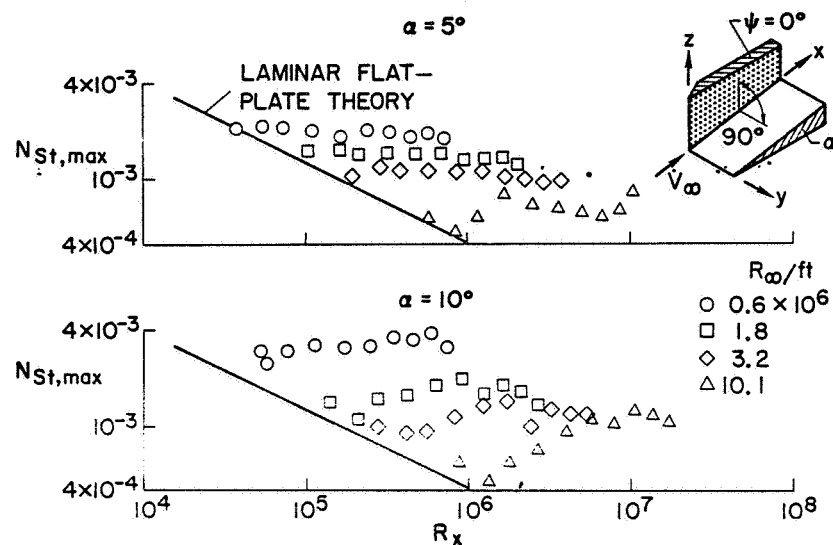


Figure 7

PEAK LAMINAR HEATING IN CORNER-FLOW REGION ALINED SURFACE; $M_\infty = 8$; $0.42 \times 10^6 \leq R_\infty/ft \leq 10 \times 10^6$

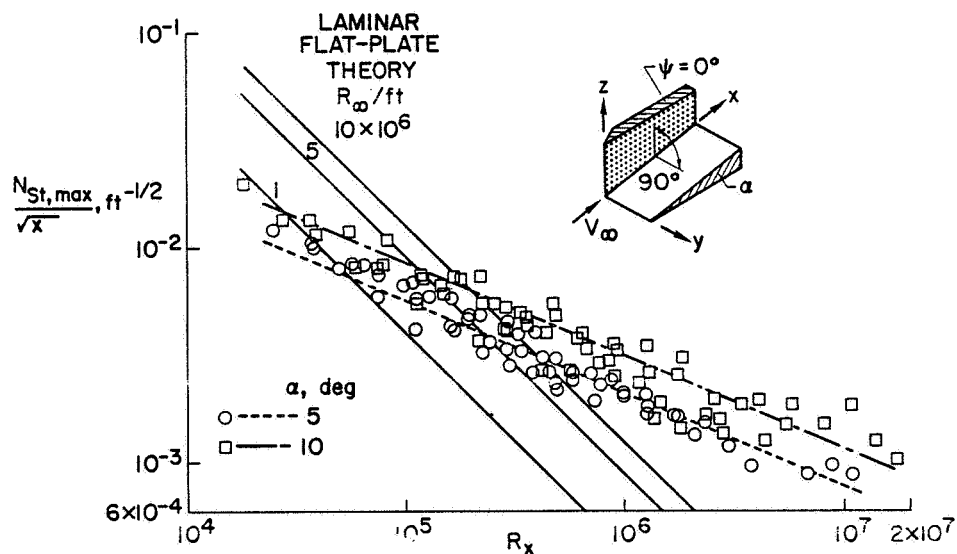


Figure 8

CONFIDENTIAL

~~CONFIDENTIAL~~

LOCATION OF LAMINAR PEAK HEATING INCLINED SURFACE; $M_\infty = 8$; $0.42 \times 10^6 \leq R_\infty/ft \leq 10 \times 10^6$

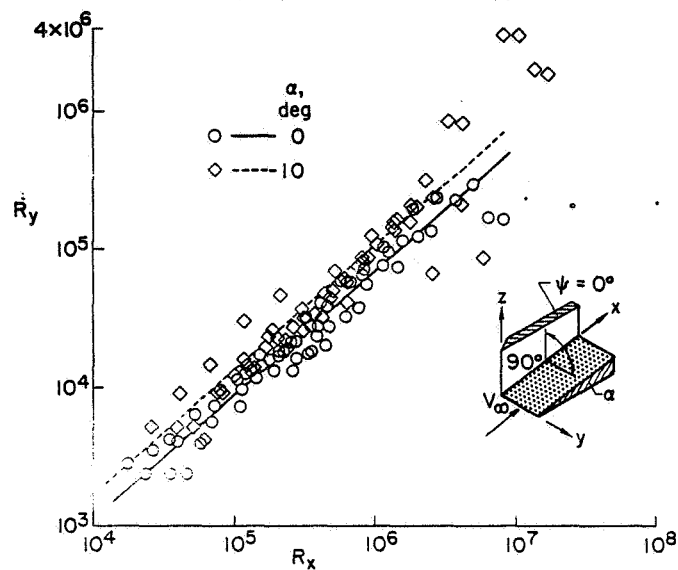


Figure 9

LOCATION OF LAMINAR PEAK HEATING ALINED SURFACE; $M_\infty = 8$; $0.42 \times 10^6 \leq R_\infty/ft \leq 10 \times 10^6$

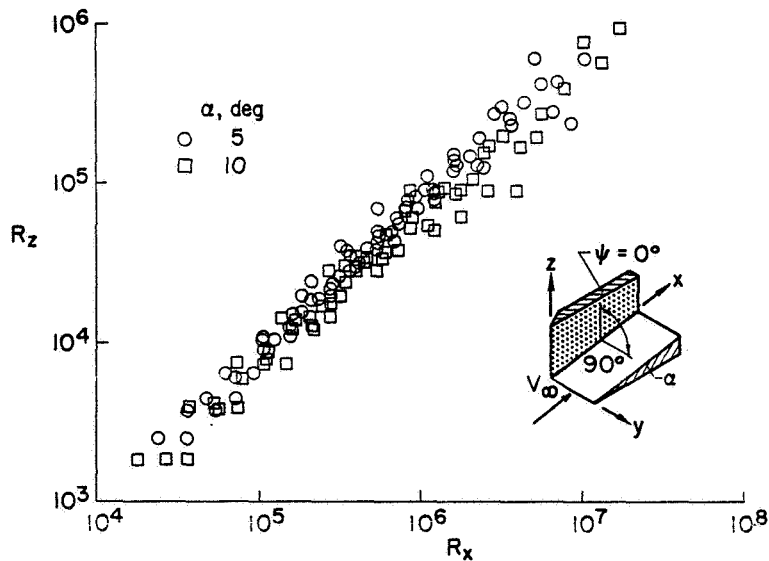


Figure 10

~~CONFIDENTIAL~~

EFFECT OF CANT ANGLE ON LAMINAR PEAK HEATING

$$M_\infty = 8; R_\infty / ft = 0.56 \times 10^6$$

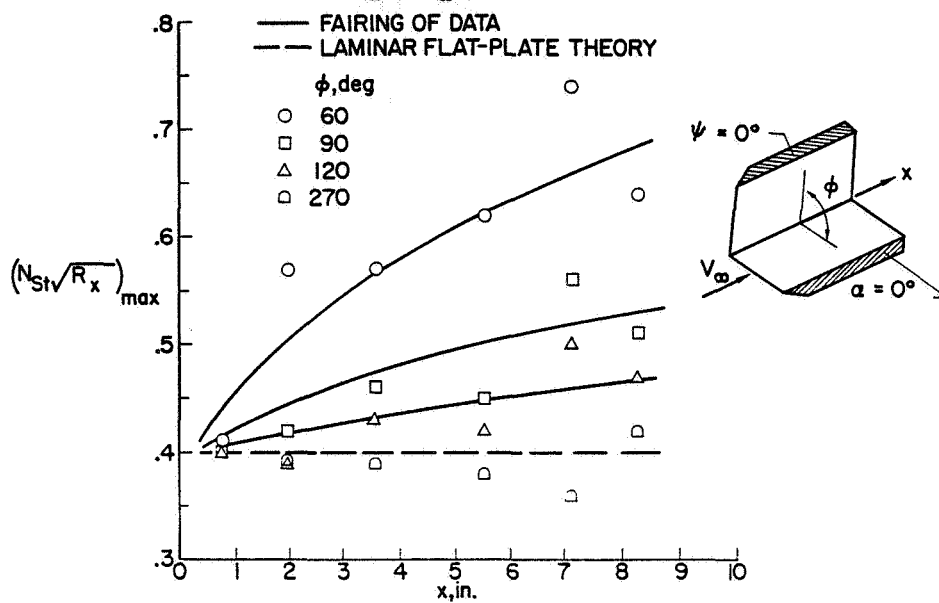


Figure 11

EFFECT OF CANT ANGLE ON LAMINAR PEAK HEATING

$$M_\infty = 8$$

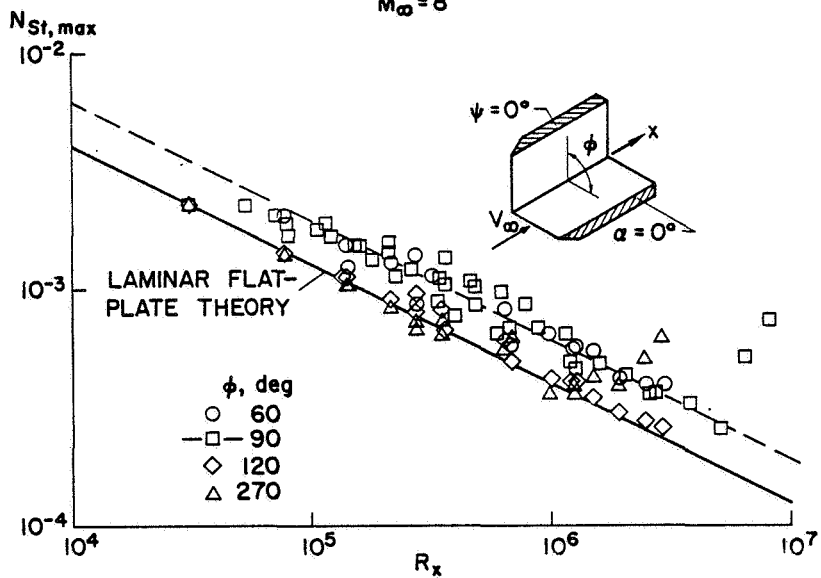


Figure 12

TURBULENT HEATING IN A CORNER

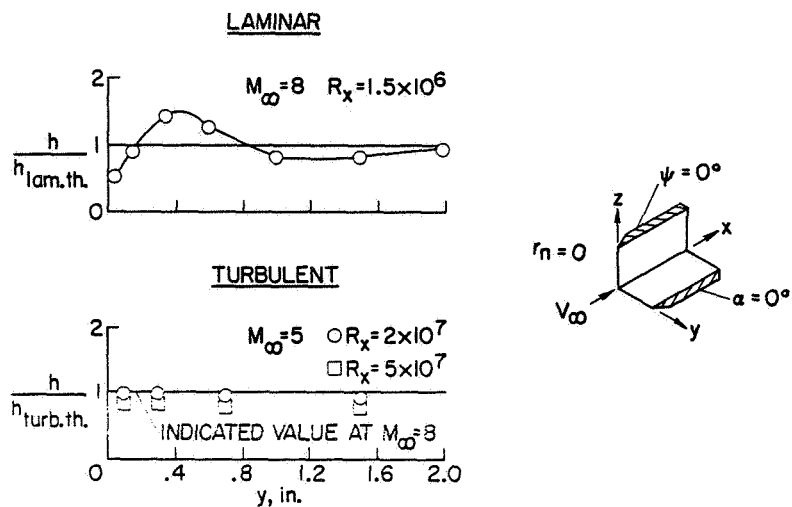


Figure 13

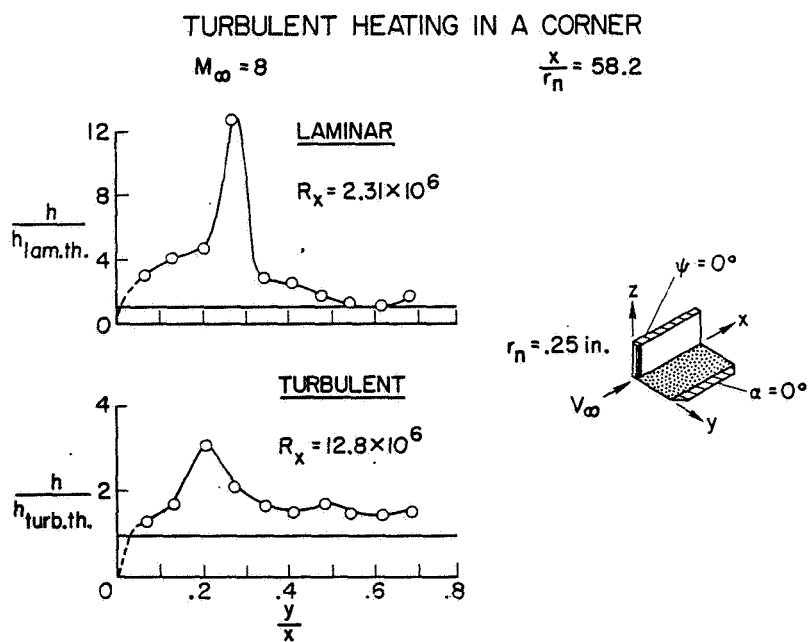


Figure 14

~~CONFIDENTIAL~~

18. EFFECTS OF SHOCK IMPINGEMENT AND OTHER FACTORS
ON LEADING-EDGE HEAT TRANSFER

By Dennis M. Bushnell
Langley Research Center

SUMMARY

An investigation was conducted at a Mach number of 8 to determine the effects on stagnation-line heat transfer of shock impingement, chordwise grooves in the leading edge, and end contamination of the leading-edge boundary layer from an adjoining surface.

The shock-impingement tests were conducted with an unswept cylinder. A flat plate inclined at an angle of 12° to the flow was used as the shock generator. The cylinder was separated from the shock generator to eliminate the effects of flow separation in the root region. A local peak in heating that was about twice the undisturbed heating level was observed in the stagnation region of the cylinder where a vortex sheet impinged on the leading edge. The vortex sheet originated at the intersection of the plate and cylinder shocks. Comparison of these data with previous measurements on similar configurations indicates that the magnitude of the peak in heating depends on the proximity of the shock impingement to the tip or root region in which the attached leading-edge boundary layer first develops. On the basis of this comparison and additional tests in which the shock impingement occurred closer to the tip of the cylinder, it is concluded that for leading edges at small sweep angles, shock impingement occurring far from the root of the leading edge causes only moderate increases in heating. If impingement occurs near the root of the leading edge, factors of the order of 5 to 10 times the undisturbed heating level are possible. Previous investigations have already shown that shock impingement on a leading edge which is at a large sweep angle causes no local increase in heating.

Heat-transfer measurements were made along the leading edge of a 76° swept fin mounted on a flat plate. Tests were made with and without a series of small chordwise grooves cut into the leading edge to simulate construction details. Analysis of the observed heating distribution on the leading edge with the grooves indicates that some fraction of the stagnation-line boundary layer is bled off by the grooves, so that a new viscous sublayer grows downstream of each groove. The general level of heating was about the same as or less than the leading-edge heating data obtained on the same configurations without the grooves.

The present heat-transfer data from the smooth 76° swept fin indicated that transition of the leading-edge boundary layer occurred at a Reynolds number, based on free-stream conditions and leading-edge diameter, of approximately 2×10^5 . A survey of heat-transfer data for swept leading edges

CONFIDENTIAL

~~CONFIDENTIAL~~

indicates that for leading edges having adjoining surfaces such as the flat plate in the present investigation, a transition Reynolds number of 2×10^5 is generally applicable for Mach numbers from 2 to 8 and sweep angles greater than 40° . On the other hand, the transition Reynolds number for leading-edge configurations without adjoining surfaces was generally found to be greater than 8×10^5 .

INTRODUCTION

The flow in the vicinity of leading edges is often complicated by the presence of phenomena associated either with adjoining surfaces or with departures from smooth-leading-edge geometry which are necessitated by structural considerations.

The present investigation is a study of the effects on leading-edge heat transfer of three types of these "interfering" flow fields. These interfering flows, depicted in figure 1, are leading-edge shock impingement, the effect of chordwise (normal to leading edge) grooves, and end contamination of the leading-edge boundary layer from an adjoining surface.

Several investigations of the leading-edge shock-impingement problem have been previously conducted (refs. 1 to 10), and for highly swept leading edges, it has been shown that no local increases in heating occur at shock impingement and that the leading-edge heat transfer can be predicted by using local conditions in simple theories.

The available data for leading edges at small sweep angles (refs. 4 to 10) indicate that a local peak in leading-edge heating occurs in the vicinity of shock impingement. Measurements of the magnitude of this peak have indicated factors from about 2 to 10 times the undisturbed level. These peaks have been generally measured in the region of the impingement of a vortex sheet which emanates from the vicinity of the intersection of the impinging shock and the leading-edge bow shock as shown in figure 2. This apparent discrepancy of a factor of 5 in the available data may in some cases be due to an insufficient density of instrumentation such that the exact local peak was not observed. Also, some of the available data are for situations in which shock impingement occurred in the vicinity of a separated-flow region near the root of the leading edge and the effects of the separated-flow reattachment and shock impingement could not be separated. The purpose of the present investigation was to obtain the effect of shock impingement on stagnation-line heat transfer for an unswept cylinder without these sources of uncertainty. A temperature-sensitive-paint technique was used to provide the magnitude and location of any local peaks in heating with greater accuracy than conventional thermocouple models. Also, the cylinder was separated from the shock generator so that the effects of flow separation in the juncture region could be eliminated and data could be obtained for a situation analogous to that of shock impingement occurring far out on a leading edge as well as close to the tip. Shock impingement occurring far out on the leading edge is generally of greater practical interest.

~~CONFIDENTIAL~~

Typical delta-wing configurations may have small chordwise grooves in the leading edge. (These grooves would be present because of the lapped, sliding joints used in the fabrication of the leading edge to allow for thermal expansion.) Previous investigations have been conducted to determine the effect of grooves on leading-edge heat transfer (refs. 11 and 12), but either the number of grooves was not sufficient or the Reynolds number range was not large enough to allow application of these results to current problems of interest. Therefore, an investigation was conducted to determine the effect of a large number of small chordwise grooves on the leading-edge heat transfer of a 76° swept fin over a Reynolds number range sufficient to provide both laminar and turbulent stagnation-line boundary-layer flow for a similar leading edge without the grooves.

As shown in reference 13 for low speeds, the effect of the flow over a surface adjoining a leading edge is to cause premature transition of the entire leading-edge boundary layer. To ascertain if an adjoining surface can cause premature transition for hypersonic flow and for large sweep angles, a smooth 76° swept leading-edge fin mounted on a flat plate was tested, and the transition Reynolds number was compared with previous transition data for similar configurations (fin-plate or cylinder-plate models) and "undisturbed" or "delta wing" configurations without any adjoining surface.

SYMBOLS

D	leading-edge diameter
h	heat-transfer coefficient
k	thermal conductivity
M	Mach number
N_{Nu}	Nusselt number, hD/k_∞
p	pressure
R	Reynolds number
x	distance along leading edge (fig. 8)
α	angle of attack
Δ	distance along leading edge from effective root to vortex-sheet impingement
Λ	sweep angle

~~CONFIDENTIAL~~

Subscripts:

∞ free stream
D leading-edge diameter
1,2 regions of flow (fig. 2)
max maximum
transition boundary-layer transition

RESULTS AND DISCUSSION

Maximum Heat Transfer Due to Shock Impingement
on an Unswept Leading Edge

The present shock-impingement investigation was conducted in the Langley Mach 8 variable-density hypersonic tunnel at a free-stream Reynolds number $R_{\infty, D}$ based on the model diameter of 1.8×10^5 . The models consisted of a sharp flat plate inclined at an angle of 12° to the test-section flow and a right circular cylinder 1 inch in diameter mounted normal to the test-section flow. The cylinder was constructed of a mica and glass composite material having a low thermal conductivity and, thus, data could be obtained by using the phase-change-coating technique outlined in reference 14. With this method it is possible to obtain the location and peak value of any local increases in heating with better accuracy than can be obtained on conventional thin-skin heat-transfer models.

The tunnel flow was started with the wedge in place and then the cylinder was injected into the wedge flow field. The end of the cylinder was kept far enough from the surface of the wedge so that no flow separation occurred on the wedge surface ahead of the cylinder. To provide reference heat-transfer-coefficient values for an unswept leading edge without shock impingement, the cylinder was also tested without the wedge.

A schlieren photograph and accompanying explanatory sketch of the flow in the vicinity of the leading-edge model is shown in figure 3. From this figure it is evident that no root separation occurred and comparison of this schlieren with the one shown in figure 4 for the cylinder alone indicates that shock impingement occurred far enough from the tip so that the leading-edge flow was almost fully developed before impingement occurred. The general features of the flow field are similar to those shown in figure 2. The vortex sheet which originates at the intersection of the plate shock and cylinder bow shock can be seen in figure 3.

From previous investigations it was expected that a peak in heating would occur in the vicinity of vortex impingement. In the present investigation a

~~CONFIDENTIAL~~

peak of this type was measured; however, the magnitude of this peak was only 1.8 times the undisturbed level, corresponding to that on an unswept leading edge without shock impingement, rather than the factors of 5 to 10 which have been previously measured (refs. 4 and 6). A plot of the maximum measured heat transfer due to shock impingement for the present and previous investigations at $\Lambda = 0^\circ$ is given in figure 5. The maximum value has been divided by the "undisturbed" value obtained far from the shock-impingement region where the leading edge is subjected to the free-stream flow. All data have been plotted as a function of the log of p_2/p_1 , which is a slightly modified form of the parameter used in reference 7 to correlate their data with those of reference 5. The pressure p_2 was calculated for all data by assuming that the free-stream flow was influenced by the impinging shock and a cylinder bow shock which was assumed parallel to the cylinder. This assumption was made because schlieren data or pressure data were not available for all cases, and therefore, additional shocks due to separation could not be properly accounted for. (Those investigations for which pressure data were available indicated that when separation shocks were present, the actual value of p_2 was as much as 50 percent higher than the value used.) The theoretical curve shown in figure 5 is therefore the approximate increase in heating which would be expected because p_2 is greater than p_1 (flow separation effects were not considered). The circular data points, which include the present $M = 8$ data and also data from reference 4, are results for the case of negligible root separation and shock impingement occurring after the leading-edge flow was fairly well developed. For these data, only moderate increases in heating above expected levels seem to occur. The actual increases are up to 50 percent above the values predicted by taking into account the nominal increases in pressure. Also, unpublished data obtained at the Langley Research Center seem to agree with these results. These data were obtained at a Mach number of 8 by Davis H. Crawford for an unswept leading edge under similar conditions (that is, no root separation and shock impingement occurring after the attached flow was fairly well developed).

The hatched areas in figure 5 indicate data obtained when some root separation was generally present and shock impingement may have occurred inboard of a region of fully developed leading-edge flow. As stated, if proper account could be taken of additional separation shocks for these data, they would be shifted to the right by varying amounts because the value of p_2 would be increased, but this shift would generally not be sufficiently large to bring these data into the same relative agreement with the theoretical curve as that exhibited by the circular data points. Therefore, there seems to be an additional increase in heating for the data designated by the hatched area above that which is observed when impingement occurs fairly far out on a leading edge, as was the case for the circular data points. An interesting feature of these data is that where actual values of p_2/p_1 are known, h_{\max}/h_1 is equal to p_2/p_1 , within approximately a 30-percent spread in the data. This correspondence was first pointed out in reference 9 but the reason for this apparent equivalence between the heat transfer and pressure ratios is not known at the present time.

~~CONFIDENTIAL~~

The cross-hatched areas indicate data (reported in ref. 6) obtained when shock impingement occurred in close proximity to a separated-flow region at the root and, therefore, when attached leading-edge flow was just starting to form. For these data, the magnitude of the peak was 10 times the undisturbed level. It is concluded by comparison of the data for the three conditions that the magnitude of the increase in leading-edge heating due to shock impingement depends on the proximity of the impingement to the region in which the attached leading-edge flow begins. (That is, when this flow is just beginning to form, the larger flow gradients that would be present there seem to increase the increment in heating caused by the vortex impingement.) For the usual practical case in which impingement occurs fairly far out on a leading edge, only moderate increases in heating would be indicated according to the present interpretation of the results shown in figure 5.

To further validate the conclusion that h_{\max}/h_1 increases as the shock-impingement location approaches the tip or root of the leading edge, additional data were obtained by increasing the distance from the plate to the end of the cylinder. This increased distance caused the shock impingement to occur closer to the end of the cylinder. The results of these tests are shown in figure 6 in which Δ is defined to be the distance from the point at which the leading-edge shock begins to form (for the present tests, the end of the cylinder) to the location of the vortex impingement (fig. 2). Previous data for which schlieren photographs are available (for determination of Δ) are also shown.

From figure 6 it is evident that the increment in heating due to shock impingement does increase as the tip is approached. The previous data at Mach numbers of 10 and 19 agree with the present results. Evidently, for these previous data, any increase in heating due to reattachment of the separated flow was not as large as the increase due to vortex impingement, although identification and separation of the two effects, even in these data, is not absolutely certain. Nevertheless, it can be speculated that shock impingement in the root region rather than phenomenon associated with flow separation is the dominant mechanism causing the large increases in heating. This tip effect is probably, at least in part, due to the occurrence of shock impingement closer to the tip where the bow-shock-layer thickness decreases, and therefore the distance from the origin of the vortex sheet to the impingement region on the leading edge is reduced. Hence the distance over which the vortex sheet grows and diffuses into a mixing layer is smaller. As a consequence, the vortex causes larger increases in heating when it impinges on the leading edge because of the larger gradients in velocity and temperature. If such a mechanism is actually the dominant cause of the increases in heating associated with the tip effect noted in the present investigation, large increases might also occur in the region of developed leading-edge flow if a very small leading-edge radius, which results in a very small shock standoff distance, were used. For the data shown in figure 5 the leading-edge radius was always of the same order of magnitude.

The results of a recent investigation of a different but analogous configuration conducted at the Langley Research Center by Robert A. Jones are apparently in agreement with the present conclusions concerning shock impingement. The configuration tested was a forward-facing probe projecting from the

~~CONFIDENTIAL~~

windward region of an Apollo command module in the reentry attitude. (The probe has been proposed as a possible reentry communication antenna.) A schlieren photograph of the flow over the configuration is shown in figure 7. From this figure it is seen that the probe tip was ahead of the main-body bow shock and, therefore, impingement of this shock occurred along the lower portion of the probe. The resultant flow within the main-body flow field is almost normal to the probe so that this portion of the probe can be treated as a cylinder at some small effective sweep angle to the local flow. The measured peak in heating occurred just downstream of shock impingement on the lower side of the probe. This measured peak was approximately a factor of 2 above the value calculated for an unswept cylinder exposed to the internal flow near the probe and, hence, is in agreement with the present leading-edge data in which root separation or tip effects were not large.

Effect of Chordwise Grooves on Leading-Edge Heat Transfer

The investigation of leading-edge heating in the presence of chordwise grooves was also conducted in the Langley Mach 8 variable-density hypersonic tunnel over a nominal Reynolds number range $R_{\infty,D}$, based on the 0.75-inch leading-edge diameter, of from 3×10^4 to 3×10^5 .

The model tested was a 76° swept slab fin with a semicylindrical leading edge. The fin was mounted on a flat plate 10 inches from the plate leading edge. The fin was constructed of high-temperature plastic and the phase-change-coating technique of reference 14 was also used to obtain heating data on this model. The fin was cast with grooves aligned normal to the leading edge and spaced 0.5 inch apart along the entire length of the model. The grooves were square in cross section, 0.030 inch on a side, and extended around to the sides of the fin. The leading edge of the model was 14.4 inches in length.

During the tests a weak shock that gave a 2° turning angle to the approaching flow was observed to originate near the plate leading edge, and this shock altered slightly the effective free-stream conditions for the leading edge. The Reynolds number range quoted for these tests includes this correction.

The measured Nusselt number variation along the fin leading edge at $R_{\infty,D} = 1.74 \times 10^5$ is shown in figure 8. The spanwise locations of the grooves are indicated in the figure. The variation of N_{Nu} with x/D downstream of a given groove is similar to that near the leading edge of a flat plate or near the tip of a cylinder. This variation can be explained by noting that the grooves provide a channel for removal or bleedoff of a portion of the stagnation-region boundary layer because of the large decrease in pressure from the stagnation region to the sides of the fin. Thus, if each groove bleeds off a portion of the leading-edge boundary layer, a new sublayer forms downstream of each groove. The subsequent growth of this sublayer would then result in a heating distribution analogous to that near the sharp tip of a cylinder. The general level of heating for this value of $R_{\infty,D}$ is not very different from that predicted by the application of swept-cylinder theories (ref. 15) as indicated on the right-hand side of figure 8.

~~CONFIDENTIAL~~

The variations with $R_{\infty,D}$ of the maximum and minimum values of N_{Nu} measured downstream of a typical groove at $x/D \approx 12$ is shown in figure 9. Also shown for reference are the predictions of the theories of reference 15 and leading-edge data obtained on the same model without grooves. The data for the fin with grooves is seen to be below or about the same as the data for the smooth or plain leading edge, depending on the Reynolds number. The gradual increase with $R_{\infty,D}$ of the grooved-fin data is believed to be due to more of the upstream boundary layer being bled off by the groove at higher $R_{\infty,D}$ values and the consequent increase in external velocity for the sublayer downstream of a given groove with increasing Reynolds number. This postulated mechanism is currently under further evaluation at Langley Research Center by the author.

The present results are for a particular groove size, leading-edge diameter, and Reynolds number range. On the basis of the postulated mechanism for the observed increases in heating with increasing Reynolds number (see fig. 9), it can be expected that a larger groove would presumably cause more bleed and, hence, could cause higher heating levels than those measured in the present tests.

Effect of End Contamination on Leading-Edge Heat Transfer

The data for the 76° swept fin with smooth leading edge shown in figure 9 indicate that transition of the leading-edge boundary layer for this configuration occurred at a Reynolds number $R_{\infty,D}$ of from 1.5×10^5 to 2×10^5 . To compare this transition Reynolds number with results from other investigations, a survey of the available heat-transfer data for swept leading edges was made. A portion of the results of this survey are summarized in figure 10. For configurations having end plates or adjoining surfaces (that is, configurations similar to the fin-plate combination of the present investigation), the value of $(R_{\infty,D})_{\text{transition}} \approx 2 \times 10^5$ adequately (within 30 percent) represents the available data for $\Lambda > 40^\circ$ and $2.5 \leq M_\infty \leq 8$. This Mach number limitation is imposed because transitional or turbulent leading-edge data evidently have not yet been obtained at Mach numbers higher than 8.

For the "delta wing" leading-edge models for which possible end contamination from an adjoining surface would not be present, most of the available data with the exception of two or three cases indicate that for Reynolds numbers up to 8×10^5 the leading-edge flow remains laminar. A Reynolds number of 8×10^5 is evidently the highest Reynolds number for which leading-edge data on these configurations are currently available.

It can be concluded that some type of end contamination of the leading-edge boundary layer, evidently emanating from the boundary layer of the adjoining surface, causes premature transition of the leading-edge boundary layer at $R_{\infty,D} \approx 2 \times 10^5$ for $\Lambda > 40^\circ$.

~~CONFIDENTIAL~~

CONCLUSIONS

An investigation was conducted to determine the effect on leading-edge heat transfer of shock impingement, chordwise grooves, and end contamination of the leading-edge boundary layer from an adjoining surface. The tests were conducted at a Mach number of 8. The following can be concluded:

1. The present results and comparisons with results of other investigations indicate that the magnitude of the increase in leading-edge heat transfer due to shock impingement for small sweep angles is a function of the proximity of the shock impingement to the tip or root region in which attached leading-edge flow begins. In the usual practical situation impingement would generally occur fairly far out on a leading edge and for this case the present results indicate that only moderate increases in heating of the order of 50 percent over the level predicted by simple theory can be expected.

2. A large number of small chordwise grooves in the leading edge of a 76° swept fin resulted in a heat-transfer distribution downstream of each groove that was similar to the type of distribution which occurs near the leading edge of a flat plate or in a region of developing flow near the tip of a swept cylinder. This distribution was repeated for each groove and was probably caused by removal or bleedoff of a portion of the stagnation-region boundary layer by the grooves. For the Reynolds number range and groove size of the present tests, the general level of heating along the leading edge with grooves was similar to or below that obtained on the same configuration without the grooves.

3. The results of the present tests and a survey of the available heat-transfer data for swept leading edges indicate that for leading edges having an adjoining surface such as an end plate, transition of the leading-edge boundary layer occurs at a free-stream Reynolds number, based on leading-edge diameter, of approximately 2×10^5 for sweep angles greater than 40° and Mach numbers up to 8. This premature transition is evidently caused by end contamination of the leading-edge flow associated with the presence of the adjoining surface because leading-edge transition has not been generally observed up to Reynolds numbers of 8×10^5 on "delta wing" configurations where this type of adjoining surface is absent.

~~CONFIDENTIAL~~

~~CONFIDENTIAL~~

REFERENCES

1. Beckwith, Ivan E.: Experimental Investigation of Heat Transfer and Pressures on a Swept Cylinder in the Vicinity of Its Intersection With a Wedge and Flat Plate at Mach Number 4.15 and High Reynolds Numbers. NASA TN D-2020, 1964.
2. Jones, Robert A.: Heat-Transfer and Pressure Investigation of a Fin-Plate Interference Model at a Mach Number of 6. NASA TN D-2028, 1964.
3. Bushnell, Dennis M.: Interference Heating on a Swept Cylinder in Region of Intersection With a Wedge at Mach Number 8. NASA TN D-3094, 1965.
4. Gulbran, C. E.; Redeker, E.; Miller, D. S.; and Strack, S. L.: Heating in Regions of Interfering Flow Fields. Part II: Leading Edge Shock Impingement. AFFDL-TR-65-49, Pt. II, U.S. Air Force, Jan. 1967.
5. Newlander, Robert A.: Effect of Shock Impingement on the Distribution of Heat-Transfer Coefficients on a Right Circular Cylinder at Mach Numbers of 2.65, 3.51, and 4.44. NASA TN D-642, 1961.
6. Hiers, Robert S.; and Loubsky, William J.: Effects of Shock-Wave Impingement on the Heat Transfer on a Cylindrical Leading Edge. NASA TN D-3859, 1967.
7. Francis, W. Leon: Experimental Heat-Transfer Study of Shock Impingement on Fins in Hypersonic Flow. J. Spacecraft Rockets, vol. 2, no. 4, July-Aug. 1965, pp. 630-632.
8. Siler, L. G.; and Deskins, H. E.: Effect of Shock Impingement on the Heat-Transfer and Pressure Distributions on a Cylindrical-Leading-Edge Model at Mach Number 19. AEDC-TDR-64-228, U.S. Air Force, Nov. 1964.
9. Knox, E. C.: Measurements of Shock-Impingement Effects on the Heat-Transfer and Pressure Distributions on a Hemicylinder Model at Mach Number 19. AEDC-TR-65-245, U.S. Air Force, Nov. 1965.
10. Ray, A. D.; and Palko, R. L.: An Investigation of the Effects of Shock Impingement on a Blunt Leading Edge. AEDC-TR-65-153, U.S. Air Force, July 1965.
11. Burchfield, C. G.; and Bontrager, P. J.: Pressure and Heat-Transfer Measurements on a Slotted Leading Edge in Hypersonic Flow. AEDC-TR-66-100, U.S. Air Force, May 1966.
12. Jaek, C. L.: Analysis of Pressures and Heat Transfer Tests on Surface Roughness Elements With Laminar and Turbulent Boundary Layers. NASA CR-537, 1966.
13. Gaster, M.: On the Flow Along Swept Leading Edges. CoA-AERO-167, College of Aeron., Cranfield (Engl.), Oct. 1965.

~~CONFIDENTIAL~~

~~CONFIDENTIAL~~

14. Jones, Robert A.; and Hunt, James L.: Use of Fusible Temperature Indicators for Obtaining Quantitative Aerodynamic Heat-Transfer Data. NASA TR R-230, 1966.
15. Beckwith, Ivan E.; and Gallagher, James J.: Local Heat Transfer and Recovery Temperatures on a Yawed Cylinder at a Mach Number of 4.15 and High Reynolds Numbers. NASA TR R-104, 1961. (Supersedes NASA MEMO 2-27-59L.)

~~CONFIDENTIAL~~

CONFIDENTIAL

INTERFERING FLOW FIELDS

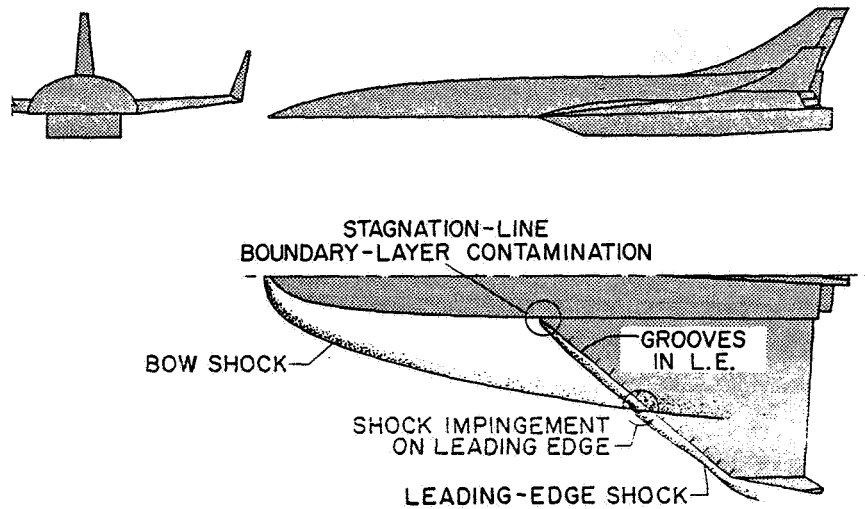


Figure 1

FLOW FIELD ASSOCIATED WITH LEADING-EDGE SHOCK IMPINGEMENT

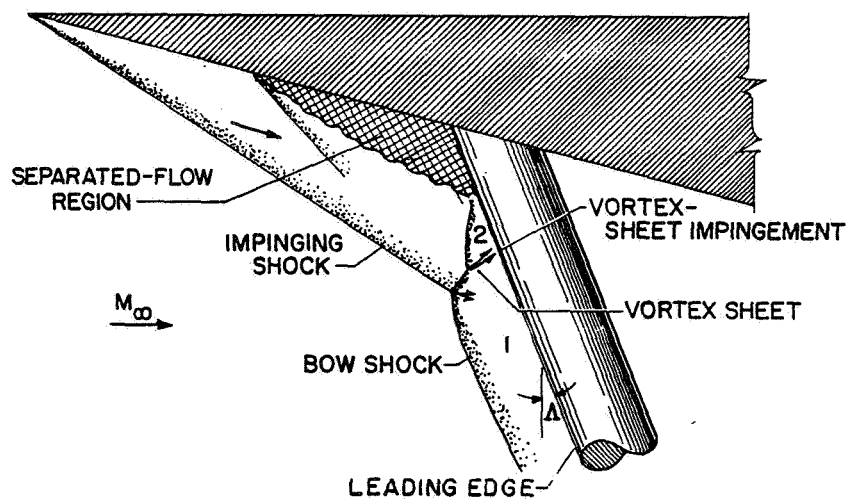


Figure 2

CONFIDENTIAL

~~CONFIDENTIAL~~

LEADING-EDGE SHOCK IMPINGEMENT

$\Lambda = 0^\circ$; $M_\infty = 8$

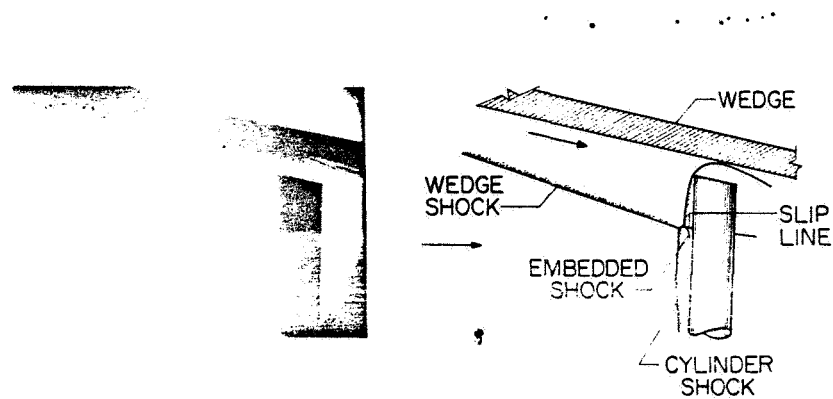


Figure 3

SCHLIEREN OF FLOW OVER UNSWEPT CYLINDER

$M_\infty = 8$



L-2864-8

Figure 4

~~CONFIDENTIAL~~

10/15

EFFECT OF SHOCK IMPINGEMENT ON MAXIMUM HEATING CYLINDRICAL LEADING EDGE ; $\Delta = 0^\circ$

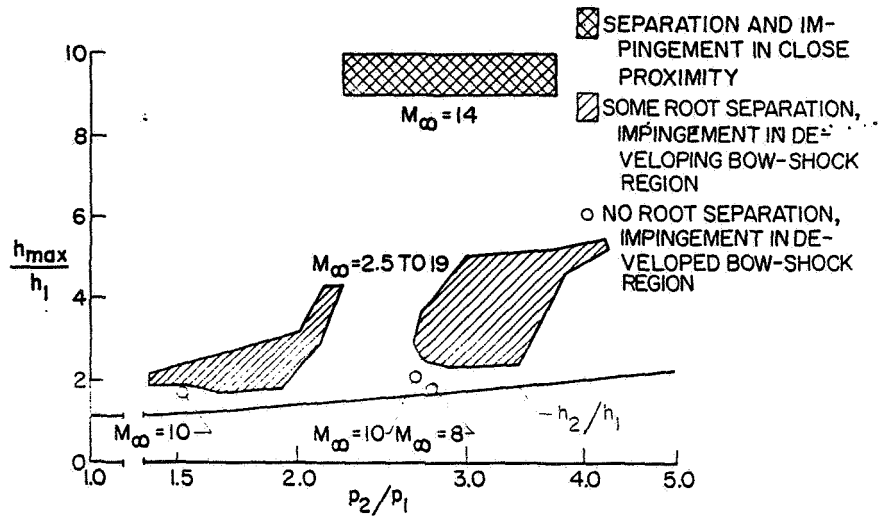


Figure 5

MAXIMUM HEATING AS A FUNCTION OF DISTANCE FROM TIP OF CYLINDER

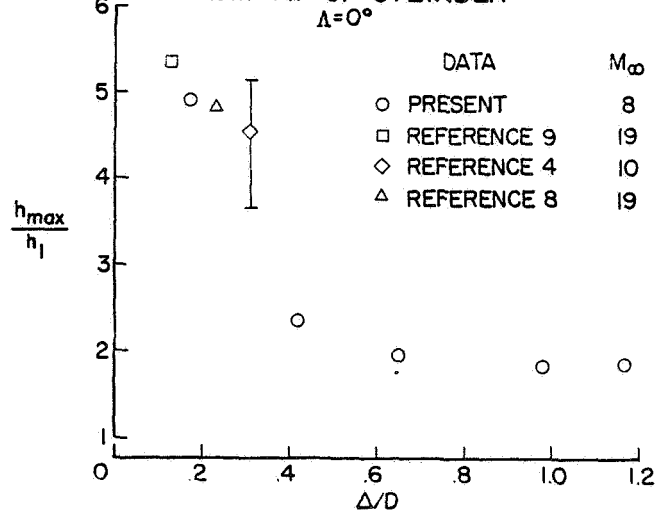
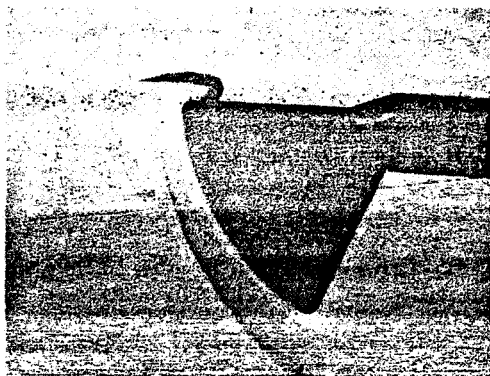


Figure 6

~~CONFIDENTIAL~~

SCHLIEREN OF FLOW OVER APOLLO MODEL
FORWARD-PROJECTING ANTENNA; $M_\infty = 8$; $\alpha = 25^\circ$



L-2864-9

Figure 7

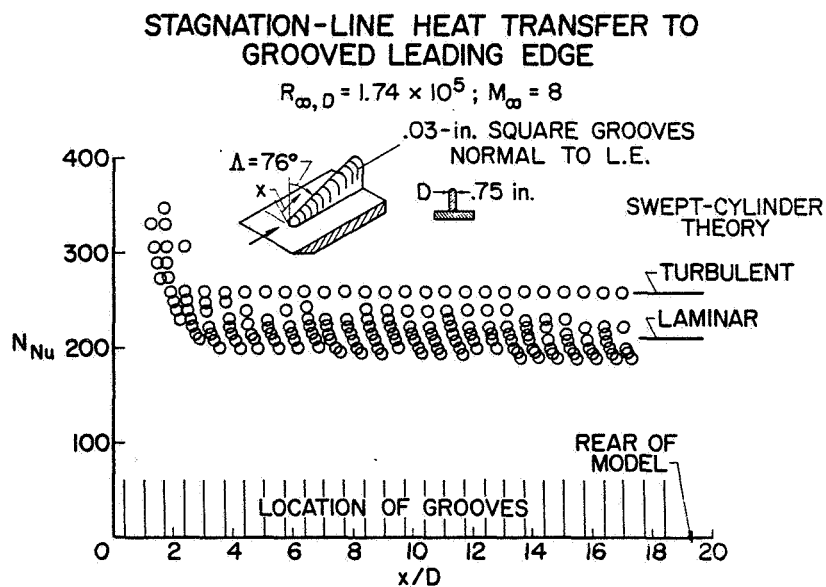


Figure 8

~~CONFIDENTIAL~~

HEAT TRANSFER TO LEADING EDGE WITH AND WITHOUT GROOVES

$M_\infty = 8$; $x/D \approx 12$

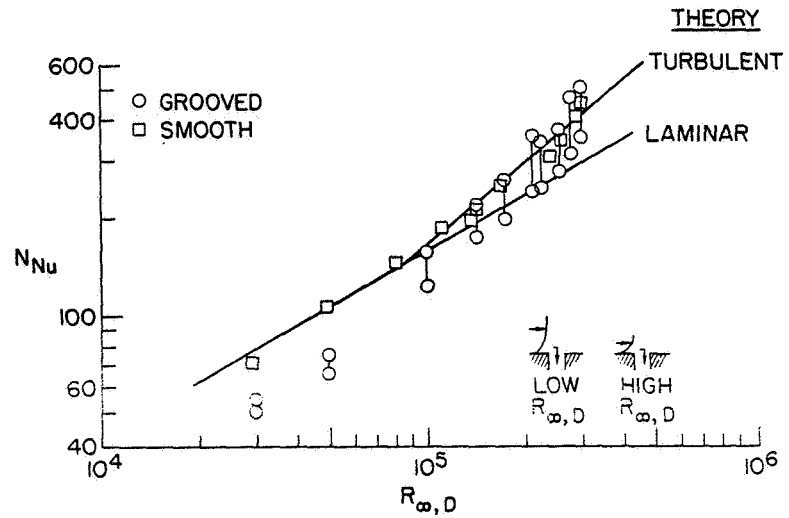


Figure 9

RESULTS OF SURVEY OF TRANSITION DATA ON SWEEPED LEADING EDGES

$2.5 \leq M_\infty \leq 8$; $\Lambda > 40^\circ$

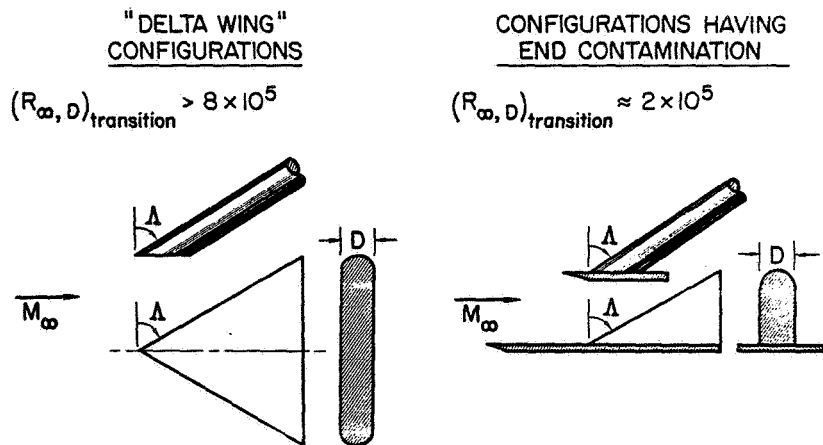


Figure 10

~~CONFIDENTIAL~~

19. INTRODUCTORY REMARKS ON PROPULSION

By Edward W. Perkins
Ames Research Center

The NASA effort in the hypersonic propulsion area has been rather small for the past several years. As a natural consequence, the papers in this session draw heavily on the results of other investigators, including those participating in the Air Force sponsored SCRAMJET technology development program. With the stimulus provided by the recent establishment of the NASA Hypersonic Research Engine Project, both the in-house and NASA sponsored contractor activities in the area have increased.

There is a substantial background of component research in relation to hypersonic airbreathing engines which indicates theoretically attractive performance to Mach numbers near 6 with subsonic burning and to much higher speeds with supersonic burning systems. The research information developed during the early phase of the Hypersonic Research Engine Project and under the Air Force technology program has done much to increase the confidence in these performance estimates. However, this work has not yet been crystallized in the development of an actual engine to produce the desired performance and flexibility of operation. The Hypersonic Research Engine Project provides a focal point for integration of much of these component research results. The immediate objectives of the project are shown in figure 1.

Some enlargement on the second objective may well be in order. We expect, under this project, to develop reliable numbers for both the component performance and the overall engine performance so as to provide a basis for a realistic assessment of the potential of this type of propulsion system. Further, results from tests conducted in ground based facilities, where only limited simulation of the flight environment is possible, will be compared with flight test results to aid in the evaluation of requirements for future ground and flight research facilities.

The project has been organized into three phases and as a joint effort between the Langley, Ames, Lewis, and Flight Research Centers with Langley responsible for overall project management. Phase I, the project definition phase, has been completed, and work on phase II, the component development and engine test phase, is being conducted by the AiResearch part of the Garrett Corporation, the contractor selected following the phase I competition.

Figure 2 is a schematic drawing of the engine under development. The engine is approximately 86 inches in overall length, has an inlet capture diameter of 18 inches, and an exit diameter of about 26 inches. The artist's concept in figure 3 shows the engine mounted on the stub ventral fin of the X-15 airplane.

Phase III, which is the flight test portion of the program, is tentatively scheduled to start in the fall of 1970.

CONFIDENTIAL

270

19

~~CONFIDENTIAL~~

Much of the research which will be discussed in this session bears on problems related to the engine being developed on the HRE project.

~~CONFIDENTIAL~~

~~CONFIDENTIAL~~

HRE PROJECT OBJECTIVES

1. Develop a hydrogen fueled research ramjet engine for operation between Mach 3 and 8 with subsonic and supersonic combustion capability
2. Conduct ground based and flight research experiments to provide a basis for appraisal of analytic and experimental ramjet engine design techniques

Figure 1

SCHEMATIC OF HYPERSONONIC RESEARCH ENGINE

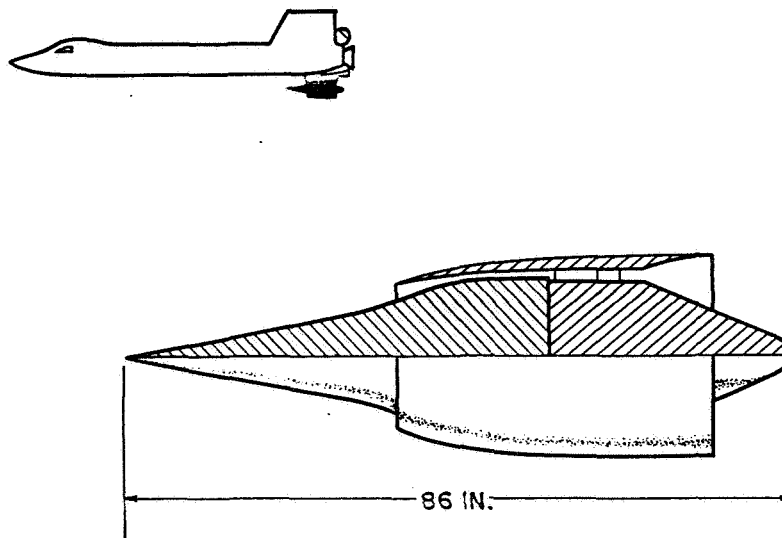


Figure 2

~~CONFIDENTIAL~~

~~CONFIDENTIAL~~

ARTIST'S CONCEPT OF HYPERSONIC RESEARCH ENGINE

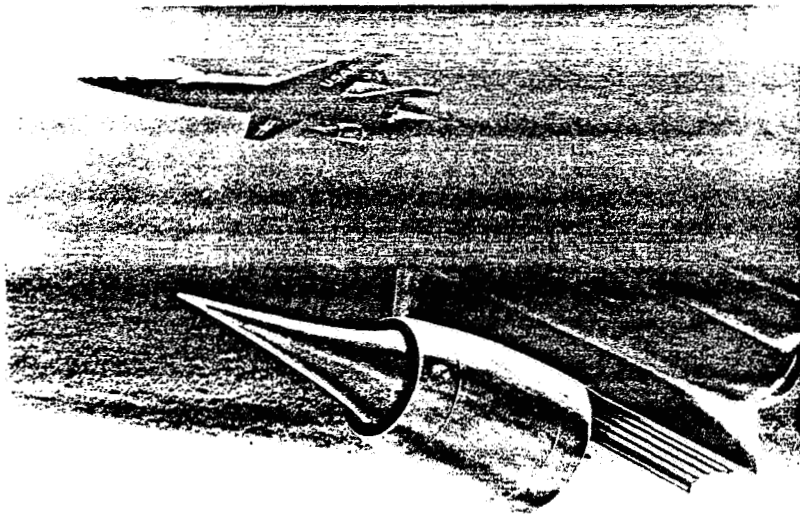


Figure 3

~~CONFIDENTIAL~~

20. A STUDY OF HYPERSONIC INLET TECHNOLOGY

By Norman E. Sorensen, Shelby J. Morris, Jr.,
and Frank A. Pfyl
Ames Research Center

SUMMARY

The present state of hypersonic inlet technology is summarized briefly to indicate the need to use a computer program as a design tool. Program usage is described, evaluated, and extended to the design of an inlet for efficient operation between Mach numbers 0 to 5.2. The study shows that the present state of the art does not provide adequate system performance for propulsion systems designed for Mach numbers greater than 3.0 that burn fuel in a subsonic stream. For propulsion systems that burn fuel in a supersonic stream, good progress has been made in attaining adequate inlet performance. It is believed that the performance achieved for most hypersonic inlet systems can be improved by advanced computer programs.

INTRODUCTION

An important objective of hypersonic inlet research has been to understand and predict hypersonic inlet compression flow field phenomena. Available data suggest that accurate analytical means are required to predict inlet performance. The present study uses a recently developed inlet computer program and shows the need for accurately predicting the compression phenomena in developing a feasible inlet design.

The main objectives of this paper are shown in figure 1. The first is to summarize the present state of the art of representative inlet systems up to a Mach number of 8.0 for propulsion systems employing engines that burn fuel in a subsonic stream. A summary is also presented for inlets from Mach numbers of about 4.0 to 15.5 for propulsion systems employing engines that burn fuel in a supersonic stream. The inlets for the former propulsion systems will be termed subsonic burning inlet systems, and the latter, supersonic burning inlet systems. Because the state of the art does not provide adequate system performance, a better approach to the prediction of inlet flow fields is required. The second objective, therefore, is to describe and evaluate a recently developed computer program for viscous inlet flow. Finally, the need for accurately predicting the inlet flow field is demonstrated by using the program to investigate analytically a short axisymmetric inlet system designed for high performance for Mach numbers from 0 to 5.2.

~~CONFIDENTIAL~~

~~CONFIDENTIAL~~

~~SYMBOLS~~

$\frac{A_o}{A_c}$	ratio of free-stream tube area to capture area
C_{D_a}	additive drag coefficient
D	capture diameter
$\frac{h}{H}$	ratio of local to total throat height
M	free-stream Mach number
M_e	boundary-layer-edge Mach number
$\frac{p_d}{p_u}$	ratio of downstream to upstream static pressure
Pr	Prandtl number
T_t	total temperature
T_w	wall static temperature
$\frac{u}{u^*}$	ratio of local to throat center-line velocity
δ	boundary-layer thickness
δ^*	boundary-layer displacement thickness
η_{KE}	kinetic energy efficiency

STATE OF THE ART

A number of different types of inlet systems have been proposed for hypersonic vehicles, and wind-tunnel testing of some of these systems has been completed. The three main types for subsonic burning engines along with the advantages and disadvantages of each are shown in figure 2.

The longest inlet, and consequently the heaviest and the one requiring the most cooling, is the internal compression type. It is the most difficult to start. In addition, it requires very high bleed to attain the high potential internal performance theoretically possible at its design Mach number. It does, however, have some advantages as listed in the figure, but overall considerations would not make it as attractive as the two inlets below.

~~CONFIDENTIAL~~

The external compression inlet has several serious faults. Four distinct disadvantages are listed in the figure which may eliminate this type of inlet from consideration for a hypersonic transport. On the positive side, it is the shortest of all inlets and has no starting requirements; that is, no geometry change is required to start the inlet because the terminal shock wave is external to the cowl lip. Inadequate off-design mass flow, however, creates the need for a contracting centerbody as indicated by the dashed lines.

The mixed compression inlet has high potential internal performance but the full potential of this type of inlet apparently has not yet been achieved. For a wraparound turboramjet engine the off-design mass flow required can be achieved with this type of inlet through a contracting centerbody system, but translation of the centerbody provides only a marginal or unacceptable mass flow. As can be seen by comparison with the external compression inlet above, the mixed compression inlet is somewhat longer, therefore heavier, and requires more cooling at hypersonic speeds. Accurate analytical tools should allow design of a minimum length mixed compression system which will have adequate performance.

Experimental performance of the three systems is indicated in figure 3. Engine-face pressure recovery is plotted as a function of inlet Mach number. The dashed line shows for comparison a reasonable goal for the pressure recovery and was derived from recent hypersonic transport studies (ref. 1). Up to $M = 4.0$ adequate performance appears to be possible. Beyond $M = 4.0$ (ref. 2) the performance is marginal when compared to the transport goal. Recent work with axisymmetric inlet systems is shown by the light line up to $M = 3.0$ (ref. 3). Extrapolation of this work to higher Mach numbers (ref. 4) indicates what might be attained with more research. The external compression system (ref. 5), indicated by the heavy line, appears competitive in the higher Mach number range. The single point shown for the all internal contraction inlet system (ref. 6) indicates high recovery, but at the expense of about 19-percent boundary-layer bleed. It should be emphasized that the performance data shown are composites of only the best performance attained for each of the inlet types, and no single inlet has achieved the hypersonic transport goal over the complete Mach number range. From the foregoing discussion it appears that for subsonic burning most of the advantages lie with the mixed compression inlet if the potential performance can be achieved experimentally over the complete Mach number range.

For supersonic burning inlet systems there appears to be more freedom in design. Figure 4 shows several inlets that have been or are being tested. The first inlet is one currently being readied for the NASA Hypersonic Research Engine for Mach numbers up to 8.0. It is an axisymmetric inlet designed so that forward translation of the centerbody will close off the inlet flow to reduce the cooling load during nonoperating conditions on the X-15. The second inlet is an axisymmetric design currently being tested up to $M = 10.0$ and is being considered for use in a self-accelerating vehicle. The three remaining designs appear less conventional having fixed geometry with self-starting capabilities down to lower Mach numbers. The difficulty of analyzing the flow fields is considerably greater than for the axisymmetric inlets. The third inlet is derived from an axisymmetric nozzle design.

~~CONFIDENTIAL~~

~~CONFIDENTIAL~~

Conventional means can be used to analyze this inlet although they do not predict the exact flow field. The inlet is currently considered for missile applications. The fourth and fifth inlets have more complicated three-dimensional flow fields requiring analytical means which are not fully developed as yet. The fifth inlet differs from the others in that combustion is initiated in the throat causing thermal compression of the flow. This allows self-starting to lower Mach numbers than the third or fourth inlets and it may be shorter entailing savings in weight and cooling requirements.

Inlets for supersonic burning must be compared on a different basis from that for subsonic burning. For supersonic burning, measurements of performance are usually made in the throat region of the inlet, and the kinetic energy efficiency is generally used to describe the performance. Figure 5 shows a band of experimental performance (refs. 7-16) for inlets such as just described. Pressure recovery at the throat is plotted as a function of Mach number. The dashed lines are for constant kinetic energy efficiencies of 98 and 96 percent. Performance falling above or between these lines is considered adequate. It is evident that good progress has been made in attaining adequate performance. The broader problem lies in combining the inlets with combustors and exit nozzles so as to achieve adequate system performance over the flight profile.

COMPUTER PROGRAMS

Turning now to the second objective, sophisticated tools in the form of computer programs will be described and evaluated. Two computer programs have been used in the present study which employ the method of characteristics. One program computes only the inviscid portion of the flow and will be termed the inviscid program (ref. 17). This program requires only about 2 minutes of computer time on an IBM 7094. The other program couples simultaneously the inviscid real gas solution with a boundary-layer solution and will be termed the viscous program. The program requires one-half to one hour per solution; hence, much computer time is saved when the inviscid program is used for preliminary designs. The viscous program was developed under NASA contract with Lockheed-California Company and is described and evaluated in reference 18. The capability of the viscous computer program is as follows (see fig. 6): From a known blunt-body solution at the nose, the program will compute the boundary layer under the blunt nose shock layer followed by computation of the real gas inviscid flow field simultaneously with the boundary layer. It will calculate a blunt cowl lip solution using the local upstream conditions. The program then calculates the internal flow field including shock-wave—boundary-layer interactions. If the bow shock wave falls inside the cowl lip as shown in figure 6, the program calculates the crossed shock waves and the associated vortex sheets. The theoretical approaches used in the program are believed to be valid, but further work, which will be described in the succeeding papers, may yield improved theories for flow details such as boundary-layer—shock-wave interactions. Such improvements are expected to be incorporated in the viscous program eventually.

~~CONFIDENTIAL~~

~~CONFIDENTIAL~~

The usefulness of the viscous program has been established by comparison with wind-tunnel results. Figure 7 is a comparison of computed and experimental velocity profiles across the throats of two different inlets. The Mach number 4.0 and 3.0 mixed compression designs shown have sharp noses and lips. Since the experimental profiles for both of these inlets were measured while some of the boundary layer was removed, one might expect an experimental profile with a thinner boundary layer than that predicted. However, a thicker boundary layer was observed on the centerbody for both inlets. Even though the comparisons may not agree well, the theories used are believed to be as good as is currently available. Better agreement should be achieved in the future with the development of more accurate theories.

PROGRAM USAGE

Proceeding to the final objective, the program usage will be extended to the design of an inlet. In the hypersonic Mach number range from 5.0 to 8.0, wraparound turbofan or turboramjet engines appear attractive and require inlet systems with subsonic as well as supersonic diffusion. Figure 8 shows such a system designed for Mach number 5.2 mated to a wraparound turbofan-ramjet. The axisymmetric inlet system has a mixed compression supersonic diffuser and a rather short subsonic diffuser. The propulsion system is about 3.0 capture diameters long from the cowl lip to the nozzle exit. The inlet system is 1.25 capture diameters from the cowl lip to the engine face. The dashed lines represent sectional views of two off-design modes of varying the geometry. The upper sectional view shows the centerbody translated to the Mach number 1.0 position while the lower view shows the centerbody in a contracted position for Mach number 1.0. The mass flow is only 20 percent of the capture area mass flow for the translating centerbody version, but is 50 percent for the contracting centerbody. Since for best performance candidate wraparound turbofan or turboramjet engines require on the order of 50 percent or more capture mass flow at $M = 1.0$, the contracting centerbody is an attractive mode of off-design operation for a mixed compression axisymmetric inlet system.

At $M = 5.2$ the subsonic diffuser can be rather short, mainly because the supersonic diffuser contraction ratio is high. That is, because the Mach number in the throat region after the terminal shock-wave system is about 0.5 to 0.7 and the throat height is small, the area ratio to diffuse the flow to $M = 0.2$ or less can be achieved in a relatively short axial distance with low diffusion efficiency losses. Beyond this point the sudden expansion losses are quite small since the Mach number is low. Turning the flow into the wraparound ramjet should also cause only small flow diffusion losses since the Mach number is only about 0.15 into the ramjet. The shapes of the subsonic diffusers for both the translating and contracting centerbody versions at Mach number 1.0 do not appear to offer a diffusion loss problem since tests of similar shapes have indicated that the losses are small.

Figure 9 shows the details of the internal supersonic flow field of one proposed design as predicted by the computer programs. Only the contours in the region of the cowl lip and throat are shown for clarity. The internal shock-wave system predicted by the viscous program is shown by the wavy lines.

~~CONFIDENTIAL~~

~~CONFIDENTIAL~~

For comparison, the system predicted by the inviscid program is shown by the solid lines. It is evident that the inviscid program predicted a shock-wave system which extended over a greater length than that predicted with the viscous program. This is mainly because boundary-layer displacement thickness shown by the dashed lines was not taken into account. The pressure ratios across each impingement predicted with the inviscid and viscous programs are indicated in the table at the bottom of the figure. It is evident that pressure ratios predicted with the inviscid program are considerably lower than those predicted with the viscous program again mainly because boundary-layer displacement thickness was not taken into account. The accuracy of the values shown for the viscous program depends to a considerable extent on the accuracy of the boundary-layer and boundary-layer-shock-wave interaction theories used in the program. These problem areas are discussed in this conference by Mr. Gnos and by Mr. Watson.

It is believed that separation of the boundary layer must be avoided both for on and off design if high performance is to be achieved. The hypersonic program has predicted the approaching boundary-layer thickness and Reynolds number for each shock-wave impingement shown in figure 9. Knowing these quantities the incipient pressure rise for separation can be estimated. Figure 10 is a plot of pressure ratio as a function of local boundary-layer edge Mach number ahead of the impingements. The dark band is an envelope of experimental data for incipient separation of a turbulent boundary layer caused by a shock wave impinging on a flat plate (ref. 19) corresponding to the range of Reynolds numbers based on the boundary-layer heights ahead of each impingement. Computed pressure ratios that fall above the band should separate; those that fall below should not separate. The inlet, however, has curved surfaces with high local pressure gradients in the region of the impingements. What part this may play in the accuracy of predicting separation is not known. The pressure ratios listed in the table of figure 9 are plotted in this figure. Those ratios predicted by the inviscid program shown by the filled symbols do not indicate separation, but these values, as previously indicated, are overly optimistic. It appears that more refinement in the design of the inlet contours is required since the pressure rise predicted with the viscous program for the second impingement falls in the region of separation.

The effect of cooling the boundary layer can also be predicted by the viscous program. Figure 11 shows the effect of varying the wall temperature ratio. The ratio of boundary-layer displacement thickness to the thickness at the near average adiabatic temperature of 904°R is plotted as a function of the ratio of wall temperature to 904°R for each impingement at $M = 5.2$. As expected, the boundary layer becomes thinner with increased cooling. In addition, cooling has more effect on thinning the boundary layer in the throat than forward on the centerbody as evidenced by comparison of the curves for the first and third impingements. The calculations shown here are for a suitable wind-tunnel total temperature of 1200°R . Actual flight conditions will demand that the walls be cooled to about 0.4 of the near adiabatic wall temperature ratio. Reducing the wall temperature ratio to 0.4 for the 1200°R case reduces the boundary-layer displacement thickness ahead of the first impingement about 20 percent while the thickness is reduced about 30 percent on the succeeding impingements. Cooling is expected to be favorable to the

~~CONFIDENTIAL~~

~~CONFIDENTIAL~~

performance by increasing the incipient pressure rise for separation and increasing the relative area of inviscid core flow in the throat. This assumes, however, that the heat removed by cooling is accomplished with the fuel and can be recovered in the propulsion system when the fuel is injected in the combustor.

CONCLUDING REMARKS

The foregoing study of hypersonic inlet technology has shown that the present state of the art does not provide what is considered adequate system performance over the complete Mach number range for subsonic burning inlet systems. Mixed compression inlet systems appear more promising than either the external or internal compression types for self-accelerating vehicles such as the hypersonic transport. For supersonic burning systems good progress has been made in attaining adequate inlet performance. The broader problem lies with attaining adequate performance over the flight profile when an inlet, a combustor, and exit nozzle are combined. It is believed that improved performance can be achieved for most hypersonic inlet systems through use of advanced computer programs which can accurately predict hypersonic inlet flow fields.

REFERENCES

1. Gregory, Thomas J.; Petersen, Richard H.; and Wyss, John A.: Performance Tradeoffs and Research Problems for Hypersonic Transports. AIAA paper 64-605, 1964.
2. Karanian, A. J.; and Kepler, C. E.: Experimental Hypersonic Inlet Investigation With Application to Dual-Mode Scramjet. AIAA paper 65-588, 1965.
3. Sorensen, Norman E.; Anderson, Warren E.; Wong, Norman D.; and Smeltzer, Donald B.: Performance Summary of a Two-Dimensional and an Axisymmetric Supersonic-Inlet System. NASA TM X-1302, 1966.
4. Kepler, C. Edward: Performance of a Mach 4.0 Variable-Geometry Axisymmetric Inlet Having External-Plus-Internal Compression. Report R-1285-12 (Contract NOa(s) 55-133-C, Lot III of Amendment 7), Propulsion Section of the Research Department, United Aircraft Corp., Sept. 1959.
5. Stitt, Leonard E.; and Flaherty, Richard J.: Experimental Investigation of Mach 5 Isentropic Spike Inlet at and Below Design Speed. NASA TM X-4, 1959.
6. Stitt, Leonard E.; and Obery, Leonard J.: Performance of an All-Internal Conical Compression Inlet With Annular Throat Bleed at Mach Number 5.0. NACA RM E58E14, 1958.

~~CONFIDENTIAL~~

~~CONFIDENTIAL~~

7. Hartill, W. R.: Analytical and Experimental Investigation of a Scramjet Inlet of Quadriform Shape. Tech. Rep. AF-APL-TR-65-74 (Contract AF33(657-8491 S/A 9), The Marquardt Corporation, Aug. 1965.
8. General Electric Staff: Advanced Air-Breathing Engines, Vol. II, Experimental Investigation. Tech. Rep. APL-TDR-64-21 (Contract AF33(657-9361), Advanced Engineering and Technical Department, G.E., Evendale, Ohio, May 7, 1964.
9. General Electric Staff: Quarterly Review of: Analytical and Experimental Evaluations of the Supersonic Combustion Ramjet Engine. Presentation to AF at Wright-Patterson (Contract AF33(615)-1586, BPSN 4(6399-615E)) Advanced Engineering and Technical Department, G.E., Evendale, Ohio, Feb. 10, 1965.
10. General Electric Staff: Analytical and Experimental Evaluation of the Supersonic Combustion Ramjet Engine - Vol. III, Component Evaluation. Tech. Rep. AF-APL-TR-65-103 (Contract AF33(615)-1586, BPSN 4(6399-651E)) Advanced Engineering and Technical Department, G.E., Evendale, Ohio, Dec. 1, 1965.
11. Keirsey, J. L.: A Study of the Aerodynamics of Scramjet Engine Inlets. Presented at the University of Tennessee Space Institute, Rep. TG-732, Johns Hopkins University, Applied Physics Lab., Aug. 1965.
12. Keirsey, J. L.; and Snow, M. L.: Modular Inlet Investigation. Quarterly Report AQR/66-1 Aeronautics Division, Research and Development, Johns Hopkins University, Applied Physics Lab., Jan.-March 1966.
13. Kutschenreuter, P. H.: Hypersonic Ramjet Research Engine - Inlets and Nozzles. Rep. R66FPD55 (Prepared for Phase I NASA Hypersonic Ramjet Experiment Project), Applied Research and Aerodynamic Design of Flight Propulsion Division, G.E., Evendale, Ohio, Feb. 23, 1966.
14. Garrett Staff: Preliminary Design, Vol. I, Rep. AF-66-0168-1 (Prepared for Phase I NASA Hypersonic Ramjet Experiment Project), AiResearch Division of the Garrett Corporation, Feb. 23, 1966.
15. Garrett Staff: Preliminary Design, Vol. III, AP-66-0168-3 (Prepared for Phase I NASA Hypersonic Ramjet Experiment Project), AiResearch Division of the Garrett Corporation, Feb. 23, 1966.
16. Heins, A. E.; and Hartill, W. R.: Shock Tunnel Testing of Scramjet Inlets. Report 5991 (Contract AF33(657)-8491), The Marquardt Corp., Van Nuys, Calif., May 24, 1963.
17. Sorensen, Virginia L.: Computer Program for Calculating Flow Fields in Supersonic Inlets. NASA TN D-2897, 1965.

~~CONFIDENTIAL~~

18. Benson, J. L.; and Maslowe, S. A.: Bluntness and Boundary-Layer Displacement Effects on Hypersonic Inlet Flow Fields. AIAA paper 65-617, 1965.
19. Kuehn, Donald M.: Experimental Investigation of the Pressure Rise Required for the Incipient Separation of Turbulent Boundary Layers in Two-Dimensional Supersonic Flow. NASA MEMO 1-21-59A, 1959.

~~CONFIDENTIAL~~

474

STUDY OF HYPERSONIC INLET TECHNOLOGY OBJECTIVES

- SUMMARIZE PRESENT STATE OF THE ART
- DESCRIBE AND EVALUATE COMPUTER PROGRAM
- EXTEND PROGRAM USAGE TO INLET DESIGN

Figure 1



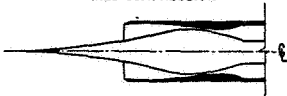
INLET TYPES SUBSONIC BURNING		
ADVANTAGES	TYPES	DISADVANTAGES
1. HIGH P.R. POTENTIAL 2. LOW COWL DRAG 3. LOW C_{D0} 4. HIGH MASS FLOW	INTERNAL COMPRESSION 	1. LONGEST INLET 2. DIFFICULT TO START 3. HIGH B.L. BLEED
1. SHORT INLET 2. NO STARTING REQUIREMENT	EXTERNAL COMPRESSION 	1. HIGH COWL DRAG 2. HIGH C_{D0} 3. MARGINAL P.R. 4. INADEQUATE TRANSONIC MASS FLOW
1. HIGH P.R. POTENTIAL 2. LOW COWL DRAG 3. LOW C_{D0}	MIXED COMPRESSION 	1. POTENTIAL UNREALIZED 2. MARGINAL TRANSONIC MASS FLOW 3. LONGER THAN EXTERNAL COMPRESSION INLET

Figure 2

~~CONFIDENTIAL~~

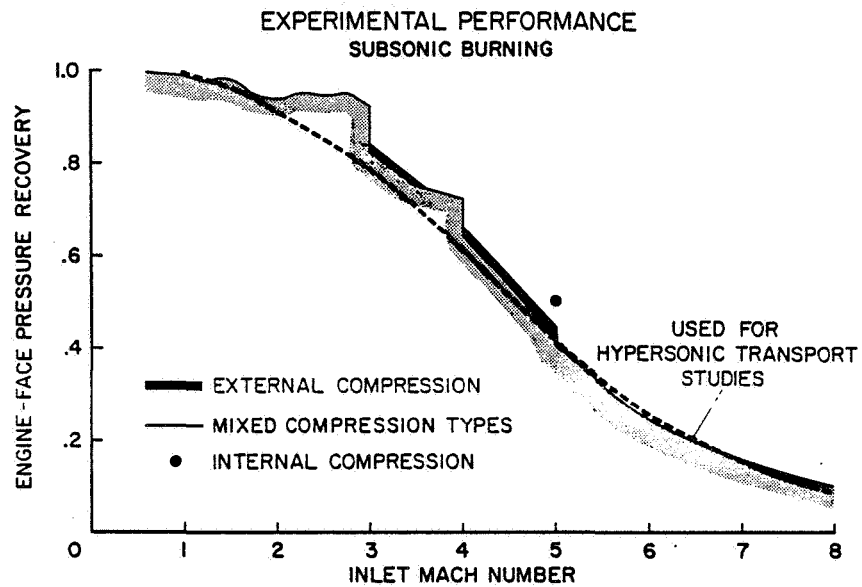


Figure 3

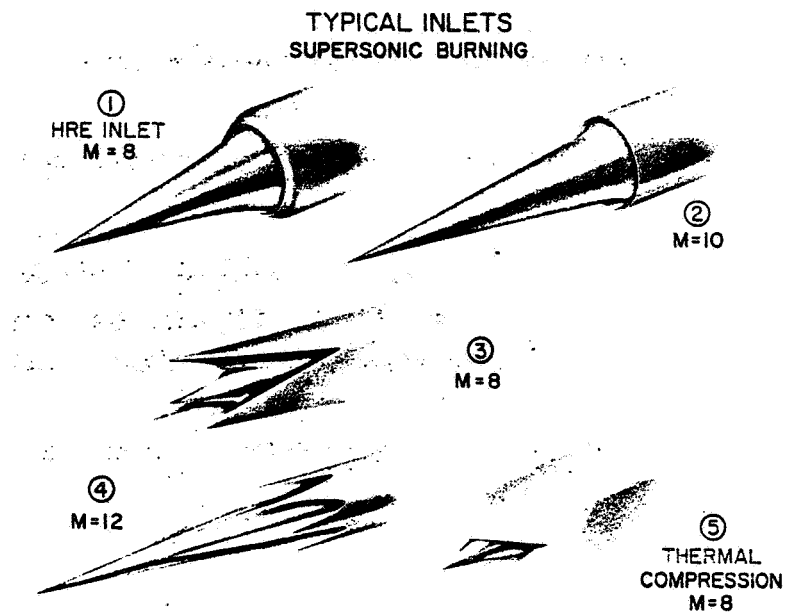


Figure 4

AAA375-4

~~CONFIDENTIAL~~

~~CONFIDENTIAL~~

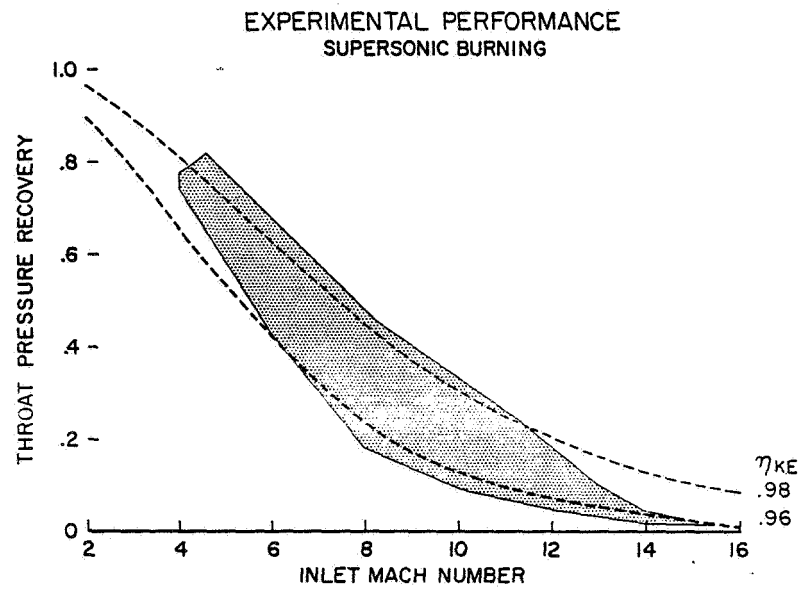


Figure 5

VISCOUS PROGRAM DESCRIPTION

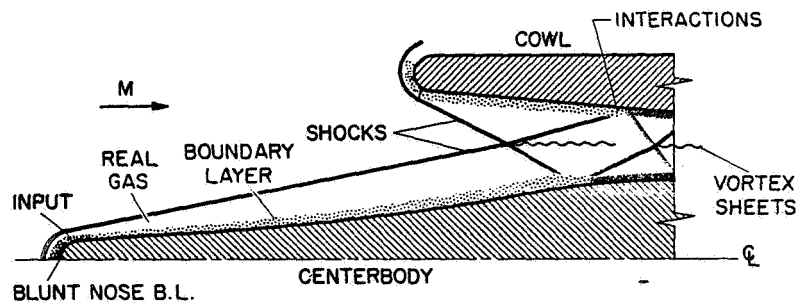


Figure 6

~~CONFIDENTIAL~~

~~CONFIDENTIAL~~

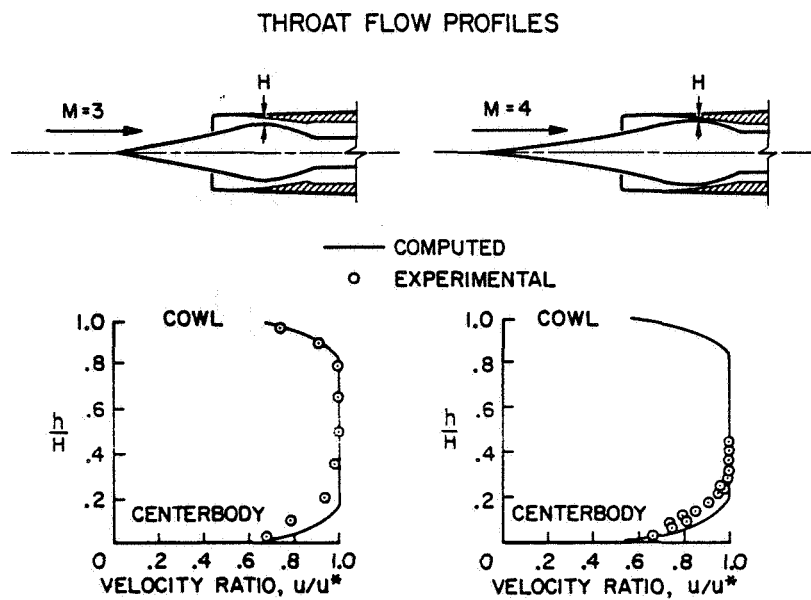


Figure 7

MACH 5.2 AXISYMMETRIC INLET SYSTEM

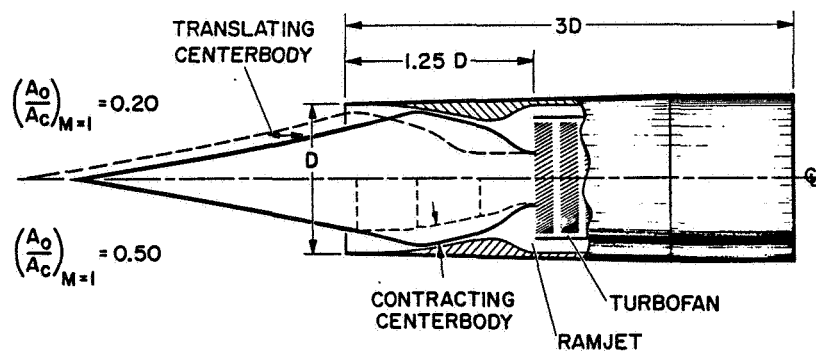


Figure 8

~~CONFIDENTIAL~~

~~CONFIDENTIAL~~

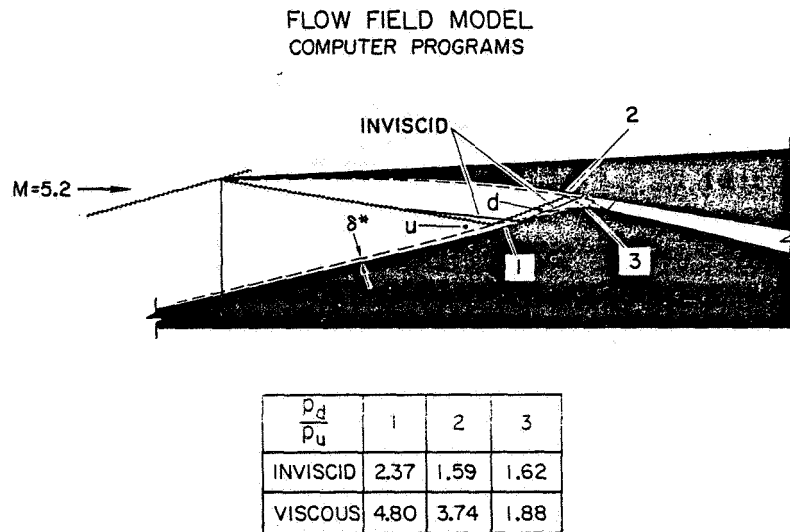


Figure 9

BOUNDARY-LAYER SEPARATION CRITERIA
M=5.2

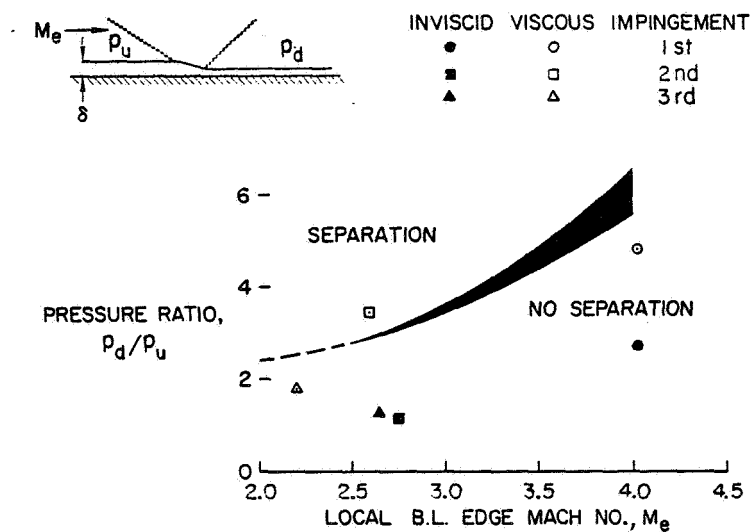


Figure 10

~~CONFIDENTIAL~~

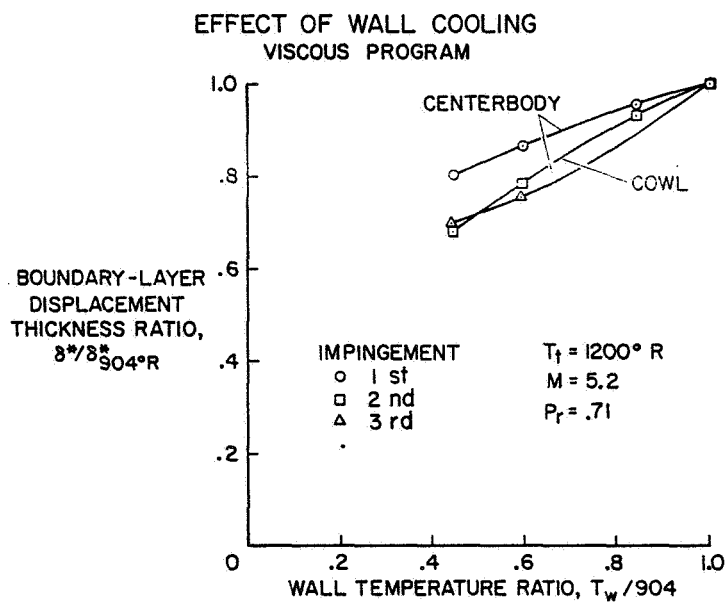


Figure 11

~~CONFIDENTIAL~~

21. TWO-DIMENSIONAL BOUNDARY LAYERS AND FLOW FIELDS OF HYPERSONIC INLETS

By A. Vernon Gnos, William F. Gallo,
and Eldon A. Latham
Ames Research Center

SUMMARY

An assessment is made of the adequacy of several available theoretical methods to predict typical two-dimensional inlet flow fields including the boundary layers up to but not including shock interaction regions. Results are presented of experimental and analytical investigations at Mach number 10.5 for a two-dimensional compression surface with sharp and blunt leading edges. Comparisons of data and theory are shown for (1) the bow-shock-wave location, (2) the surface-pressure distribution, (3) the boundary-layer growth along the compression surface, and (4) the flow-field and boundary-layer profiles normal to the surface. Bow-shock-wave shape and surface-pressure distributions are well predicted by existing theoretical methods. Laminar boundary-layer growth is shown to be adequately described by theory; however, theory underestimates turbulent boundary-layer growth. An excellent theoretical representation of velocity profiles in the inviscid flow field and laminar boundary layer far downstream of a blunt leading edge is indicated.

INTRODUCTION

For the design of an efficient hypersonic inlet it is essential to have analytical methods which are capable of predicting the many complicated flow phenomena involved. A typical hypersonic two-dimensional inlet shown in figure 1 indicates the following areas where representations must be accurate: (1) the blunt-body region including the bow shock, the subsonic flow field, and the stagnation region boundary layer; (2) the boundary-layer growth in an adverse pressure gradient including the laminar, turbulent, and transition regions; (3) the hypersonic inviscid flow field and shock-wave location; (4) the many shock intersections and shock-wave boundary-layer interactions. These individual phenomena must then be correctly predicted so that an inlet can be designed to give the desired performance.

The purpose of this paper is to assess the adequacy of several available theoretical methods for predicting the inviscid flow field and boundary layer for hypersonic inlet systems. The present paper will be concerned with the flow regions up to but not including the shock interactions. Interactions of the cowl shock wave with a two-dimensional ramp boundary layer are discussed in reference 1. Comparisons between two-dimensional experimental data and theory will be shown for (1) the bow-shock-wave shape and location,

~~CONFIDENTIAL~~

200

~~CONFIDENTIAL~~

(2) surface-pressure distribution along the compression surface, (3) boundary-layer growth along the compression surface, and (4) inviscid flow-field and boundary-layer profiles normal to the surface. These comparisons test the adequacy of theories which may be used for inlet design. Correct predictions of the several phenomena compared are important for the following reasons. The shock-wave location must be accurate so that a cowl lip may be located for a design condition. Pressure distributions, in addition to providing edge conditions for theoretical boundary-layer calculations, indicate whether the desired isentropic compression has been achieved. A prediction of the growth of boundary-layer thickness is uniquely important in hypersonic inlets since a large percentage of the exit flow may consist of boundary layer. A large part of the performance will, therefore, be determined by boundary layer at the exit. Therefore, in order to predict actual inlet performance, both the viscous and inviscid flow phenomena must be accurately determined.

SYMBOLS

L	model length in free-stream direction
M	Mach number (free stream)
$\frac{p}{p_{\infty}}$	static pressure ratio, $\frac{\text{local static pressure}}{\text{free-stream static pressure}}$
$\frac{p_t}{p_{t\infty}}$	pitot pressure ratio, $\frac{\text{local pitot pressure}}{\text{free-stream total pressure}}$
$\frac{Re}{ft}$	Reynolds number per foot (free stream)
$\frac{u}{U_{\infty}}$	velocity ratio, $\frac{\text{local velocity}}{\text{free-stream velocity}}$
$\frac{u}{U_{\delta}}$	velocity ratio, $\frac{\text{local velocity}}{\text{velocity at boundary-layer edge}}$
X	length from leading edge in stream direction
Y	distance normal to model surface
Z	ordinate of compression surface
δ	boundary-layer thickness
δ^*	boundary-layer displacement thickness $\delta \int_0^1 \left(1 - \frac{pu}{\rho_{\delta} U_{\delta}}\right) d \frac{u}{U_{\delta}}$

~~CONFIDENTIAL~~

θ boundary-layer momentum thickness $\delta \int_0^1 \frac{\rho u}{\rho_\delta U_\delta} \left(1 - \frac{u}{U_\delta}\right) d \frac{y}{\delta}$

$\frac{\rho}{\rho_\delta}$ density ratio, $\frac{\text{local density}}{\text{density at boundary-layer edge}}$

TEST FACILITY AND MODELS

An experimental investigation (ref. 2) was conducted in the Ames 3.5-foot hypersonic wind tunnel (ref. 3) to obtain boundary-layer, flow-field, and shock-wave data for comparison with results of analytical studies. Figure 2 is a sketch of the two-dimensional wind-tunnel model employed in the tests. The model was tested with a sharp leading edge and with two different blunt leading edges. The 0.062- and 0.188-inch radii of the blunt leading edges were considered to be representative of those required by regeneratively and radiatively cooled structures. Surface coordinates of the test model, which had an isentropic compression surface, are given in table I. The flat surface of the model was initially aligned at a 3° angle to the free stream to prevent flow separation and to simulate an inlet ramp. Small probes were used to measure temperature, pitot pressure, and static pressure in the boundary layer and flow field. Boundary-layer transition was induced with various trip configurations. Nominal test Mach numbers were 7.3 and 10.5; free-stream total temperature varied from 1500 to 2000° R; and free-stream Reynolds number per foot varied from 0.25 to 2.0 million. The ratio of wall temperature to free-stream total temperature was about 0.3, which is representative of a highly cooled surface condition. Mach number 10.5 data will be presented in this paper.

RESULTS AND DISCUSSION

Bow-shock-wave location and surface-pressure distribution are considered first. Theoretical and measured bow-shock-wave shape and surface-pressure distributions are compared in figure 3 for the sharp leading-edge model. The curves which represent results of viscous theory were obtained with the program described in references 4, 5, and 6.

The program utilized a semiempirical technique to determine shock shape for the sharp leading-edge case which required prior knowledge of the initial shock location. Such techniques are necessary since there is no existing exact theoretical treatment of the viscous interaction phenomenon near the leading edge. The technique uses an effective body to determine a starting line for the method of characteristics. This effective body is a combination of a wedge, to simulate the leading edge viscous effects, and the computed boundary-layer displacement thickness. The two are joined at a point along the body, by iteration, to provide agreement with the calculated and measured shock shape. This method predicts a surface-pressure distribution near the

~~CONFIDENTIAL~~

~~CONFIDENTIAL~~

leading edge that agrees with the method of reference 7. Also, good agreement with the experimental surface-pressure distribution is obtained over the entire model (fig. 3). The inviscid theory, calculated from the method of reference 8, for pressure distributions and shock shape is also shown in figure 3. It is seen that surface pressures are well represented over the downstream half of the model by the method of characteristics solution even without a correction for boundary-layer displacement thickness.

The bow-shock-wave shape and surface-pressure distributions for blunt leading edges are considered next. Data for the model with the 0.062-inch-radius leading edge are shown in figure 4, and those for the 0.188-inch-radius leading edge in figure 5. The theoretical method used (ref. 5) consists of a blunt-body solution (ref. 9), and a method of characteristics combined with a boundary-layer solution. The inviscid theoretical method employs the same blunt-body solution and the method of characteristics of reference 10, but without boundary-layer displacement effects. Generally, either theory gives a reasonably good prediction of surface pressures. Further, it is observed that the theory utilizing boundary-layer displacement effects more accurately predicts the shock-wave location than does the inviscid theory. It should be noted that in the downstream region where an inlet cowl may be placed the theoretical results diverge and the inviscid theory is not sufficiently accurate for locating a cowl lip. For example, at $X = 48$ inches with the 0.188-inch-radius leading-edge model and the test conditions of figure 5, viscous theory predicts a shock position 11.4 inches above the reference axis as compared to 11.0 inches indicated by inviscid theory. This would result in a difference of about 4 percent in inlet capture mass flow.

A comparison of experimental and theoretical laminar boundary-layer growth δ , and integral properties δ^* and θ , for the sharp leading-edge model is presented in figure 6. The experimental data were derived from boundary-layer velocity profile measurements at the several survey stations indicated in figure 2. Boundary-layer thicknesses at intermediate stations were obtained from schlieren photographs. Theoretical results were calculated with the laminar theory of reference 11. Good agreement is shown. The adverse pressure gradient is seen to thin the boundary layer over the downstream half of the model, as predicted by theory.

Figure 7 compares theoretical and experimental laminar boundary-layer growth and integral properties for the model with a 0.188-inch leading-edge radius. The experimental data were derived from boundary-layer velocity profiles. Only data derived from the velocity profiles are shown because the density gradients were so small that the boundary-layer edge could not be detected in schlieren photographs. The data generally agree with both the laminar boundary-layer solutions of Cohen (ref. 12), and of Kemp, Rose, and Detra (ref. 13). Again the thinning effect of the compression surface upon the boundary layer is illustrated.

Data for the model with the 0.062-inch leading-edge radius are not presented since analysis of the data has not yet been completed. For the two-dimensional compression surface of this investigation, it appears that available theoretical methods are adequate for predicting the laminar boundary growth for both sharp and blunt leading edges.

~~CONFIDENTIAL~~

Boundary-layer growth and integral properties of turbulent boundary layers were obtained with trips for the sharp leading-edged model (fig. 8). Experimental data and theoretical results are compared. Experimental data were derived from boundary-layer velocity profiles at the probe locations. At other stations boundary-layer thickness was obtained from schlieren photographs. The theoretical results were obtained from an integral method developed for the program of reference 5. The laminar boundary-layer growth was calculated to station $X/L = 0.22$, where schlieren data indicate the beginning of transition. The calculation of the turbulent boundary layer was begun at that station. The integral method describes the boundary layer in terms of a power-law velocity profile. In order to obtain correct integral properties from this theory, a correct boundary-layer thickness and power profile are necessary. Both the rate of growth and the absolute thickness of the boundary layer shown in figure 8 are underestimated by the theory in the region of the adverse pressure gradient. Although the integral properties appear to be fairly well predicted by theory, this agreement is fortuitous in view of the lack of agreement of boundary-layer thickness. It should be noted that the laminar boundary-layer theory used in this program (ref. 12) is not the same as that used for the lower Reynolds number case presented in figure 6. It is evident that the theory of reference 12 does not predict the growth in the high Reynolds number case. It is believed that the difference may be due to the effect of the boundary-layer trips.

For the blunt leading edge (0.188-inch radius), the data of figure 9 show a similar lack of agreement between experimental results and the integral-method theory. The experimental boundary-layer thicknesses were derived from boundary-layer velocity profiles since schlieren photographs did not reveal the boundary-layer edge with sufficient clarity. A calculation of turbulent boundary layer was started at the first probe station as indicated on the figure. The theory severely underestimates boundary-layer thickness. Thus, as in the case with the sharp leading edge, any agreement between data and theory for δ^* and θ is fortuitous.

The turbulent boundary-layer model considered in this comparison with data at $M = 10.5$ does not appear to be adequate for predicting boundary-layer growth and integral properties for the sharp and blunt leading-edge surfaces with a mild adverse pressure gradient.

Figure 10 presents profiles of the inviscid flow field normal to the body from body to shock, at the far downstream location ($X/L = 0.81$) for the 0.188-inch-radius compression surface. Comparisons of velocity (left figure) and pitot-pressure (right figure) profiles are made between data and the method of characteristics (ref. 10) using a blunt-body solution (ref. 9) for starting condition. The agreement is excellent even though the comparison is made at a location approximately 200 radii downstream of the blunt nose, where numerical errors might be expected to become significant. The edge of the boundary layer is indicated by departure of the pitot pressure and velocity profile data from inviscid theory. The departure, although fairly evident in the left-hand figure, is not always so clear. When the inviscid and the boundary-layer velocity profiles do not diverge sharply, additional indications of edge conditions are inferred from the temperature and Mach number

~~CONFIDENTIAL~~

~~CONFIDENTIAL~~

profiles. This difficulty does not occur, of course, when there is no velocity gradient, for example, for a sharp leading-edged flat plate.

Figure 11 portrays the laminar boundary-layer velocity profiles for the sharp leading-edge surface. Comparing the laminar theory (ref. 11) with data shows that at the longitudinal station of $X/L = 0.54$, the boundary-layer data indicate essentially a flat-plate velocity profile that agrees with theory. Further downstream ($X/L = 0.73$), however, the boundary-layer profile becomes distorted by the additional compression, and agreement with theory is poor. A reason for this lack of agreement may be the failure of the theory to account for effects of mild adverse pressure gradients. Also, transition near this station may account for some of the disparity. Other data from this model at Mach 7.3 indicate a less distorted profile at this station.

A comparison between data and laminar theory of reference 13 for the velocity profile downstream of a blunt leading edge is shown in figure 12. It is to be noted that this comparison is made at some 200 radii downstream of a 0.188-inch-radius leading edge in a region of a mild adverse pressure gradient. The profile is quite different from a flat-plate profile and normally might not be judged a laminar profile. The excellent agreement between the laminar theory and the data, however, indicates that it is indeed laminar. The theoretical turbulent boundary-layer profile on the right side of figure 12 does not agree as closely with data as the laminar profile. Near the wall the experimental velocity profile appears much fuller than the 4.1 power profile predicted by the theory of reference 5. In fact, no single power profile would fit the experimental data which has a power of about 4 at the outer edge and a power of nearly 12 in the lower one-third portion. Very near the wall the difficulty in obtaining precise temperature measurements may account for a small part of the spread between data and theory.

CONCLUSIONS

This study has shown that for a Mach number of 10.5, the inviscid flow field, shock-wave shapes, and surface-pressure distributions are well predicted for the 0.188-inch-radius leading-edge model by available theoretical methods. The noteworthy ability of theory to indicate accurate inviscid profiles in a mild adverse pressure gradient region has been demonstrated.

Laminar boundary-layer growth and integral properties are well described by several theoretical methods indicated.

Laminar boundary-layer properties, particularly velocity profiles, have been shown to be closely predicted by theory far downstream of a blunt leading edge in the adverse pressure gradient region considered. The agreement between the boundary layer and flow-field results gives confidence both in the theories used and in the experimental results.

~~CONFIDENTIAL~~

~~CONFIDENTIAL~~

The turbulent boundary-layer properties are more difficult to predict, however, and lack of agreement between theory and experiment indicates a need for further work with turbulent boundary layers.

REFERENCES

1. Watson, Earl C.; Murphy, John D.; and Rose, William C.: Shock-Wave—Boundary-Layer Interactions in Hypersonic Inlets. Conference on Hypersonic Aircraft Technology, NASA SP-148, 1967. (Paper No. 22 herein.)
2. Watson, Earl C.; Gnos, A. Vernon; Gallo, William F.; and Latham, Eldon A.: Boundary Layers and Hypersonic Inlet Flow Fields. AIAA paper 66-606, 1966.
3. Holdaway, George H.; Polek, Thomas E.; and Kemp, Joseph H., Jr.: Aerodynamic Characteristics of a Blunt Half-Cone Entry Configuration at Mach Numbers 5.2, 7.4, and 10.4. NASA TM X-782, 1963.
4. Sorensen, Norman E.; Morris, Shelby J., Jr.; and Pfyl, Frank A.: A Study of Hypersonic Inlet Technology. Conference on Hypersonic Aircraft Technology, NASA SP-148, 1967. (Paper No. 20 herein.)
5. Maslowe, S. A.; and Benson, J. L.: Computer Program for the Design and Analysis of Hypersonic Inlets, Final Report. Rep. No. 18079, Lockheed-California Company, Aug. 31, 1964.
6. Benson, J. L.; and Maslowe, S. A.: Bluntness and Boundary-Layer Displacement Effects on Hypersonic Inlet Flowfields. J. Spacecraft Rockets, vol. 3, no. 9, Sept. 1966, pp. 1394-1401.
7. Bertram, Mitchel H.; and Blackstock, Thomas A.: Some Simple Solutions to the Problem of Predicting Boundary-Layer Self-Induced Pressures. NASA TN D-798, 1961.
8. Sorensen, Virginia L.: Computer Program for Calculating Flow Fields in Supersonic Inlets. NASA TN D-2897, 1965.
9. Lomax, Harvard; and Inouye, Mamoru: Numerical Analysis of Flow Properties About Blunt Bodies Moving at Supersonic Speeds in an Equilibrium Gas. NASA TR R-204, 1964.
10. Inouye, Mamoru; Rakich, John V.; and Lomax, Harvard: A Description of Numerical Methods and Computer Programs for Two-Dimensional and Axisymmetric Supersonic Flow Over Blunt-Nosed and Flared Bodies. NASA TN D-2970, 1965.

~~CONFIDENTIAL~~

~~CONFIDENTIAL~~

11. Kendall, R. M.; and Bartlett, E. P.: Nonsimilar Solution of the Multicomponent Laminar Boundary Layer by an Integral Matrix Method. AIAA preprint 67-218, 1967.
12. Cohen, Nathaniel B.: Boundary-Layer Similar Solutions and Correlation Equations for Laminar Heat-Transfer Distribution in Equilibrium Air at Velocities up to 41,100 Feet Per Second. NASA TR R-118, 1961.
13. Kemp, Nelson H.; Rose, Peter H.; and Detra, Ralph W.: Laminar Heat Transfer Around Blunt Bodies in Dissociated Air. J. Aero/Space Sci., vol. 26, no. 7, July 1959, pp. 421-430.

~~CONFIDENTIAL~~

TABLE I

SURFACE COORDINATES
COMPRESSION SURFACE MODEL



X	Z	X	Z	X	Z	X	Z
0	0	19.000	1.066	29.000	1.926	39.000	3.260
10.000	.524	20.000	1.136	30.000	2.038	40.000	3.414
11.000	.578	21.000	1.210	31.000	2.156	41.000	3.572
12.000	.634	22.000	1.286	32.000	2.280	42.000	3.734
13.000	.692	23.000	1.366	33.000	2.408	43.000	3.900
14.000	.752	24.000	1.450	34.000	2.540	44.000	4.070
15.000	.813	25.000	1.536	35.000	2.676	45.000	4.244
16.000	.874	26.000	1.626	36.000	2.816	46.000	4.422
17.000	.936	27.000	1.720	37.000	2.960	47.000	4.604
18.000	1.000	28.000	1.820	38.000	3.108	48.000	4.790

~~CONFIDENTIAL~~

TYPICAL HYPERSONIC INLET

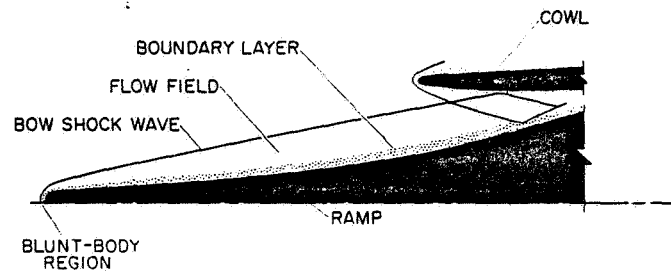


Figure 1

SCHEMATIC OF TEST MODEL

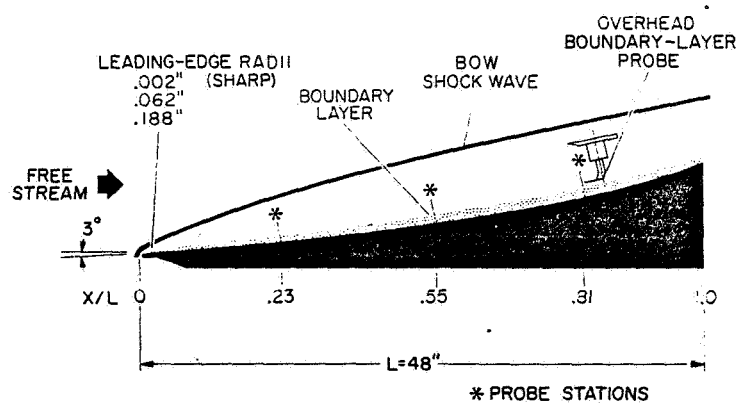


Figure 2

~~CONFIDENTIAL~~

SHOCK-WAVE LOCATION AND SURFACE-PRESSURE DISTRIBUTION

SHARP LEADING EDGE

$M=10.5$ $Re/ft = 2.0 \times 10^6$

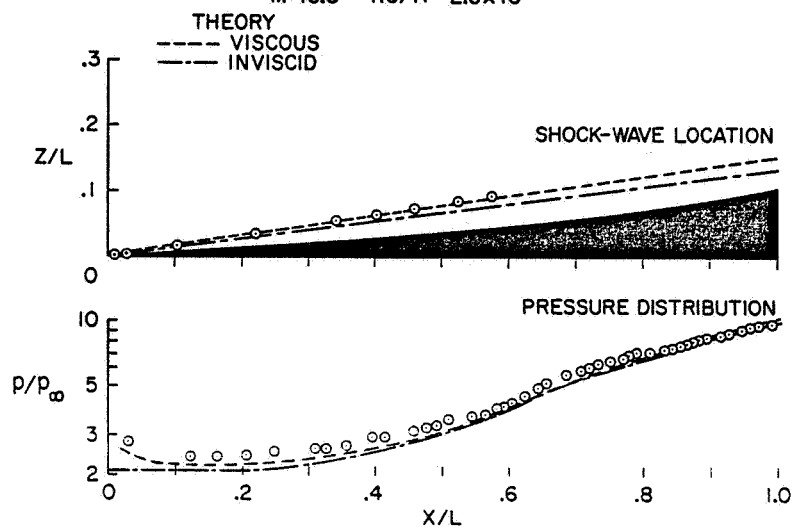


Figure 3

SHOCK-WAVE LOCATION AND SURFACE-PRESSURE DISTRIBUTION

.062" LEADING-EDGE RADIUS

$M=10.5$ $Re/ft = 2.0 \times 10^6$

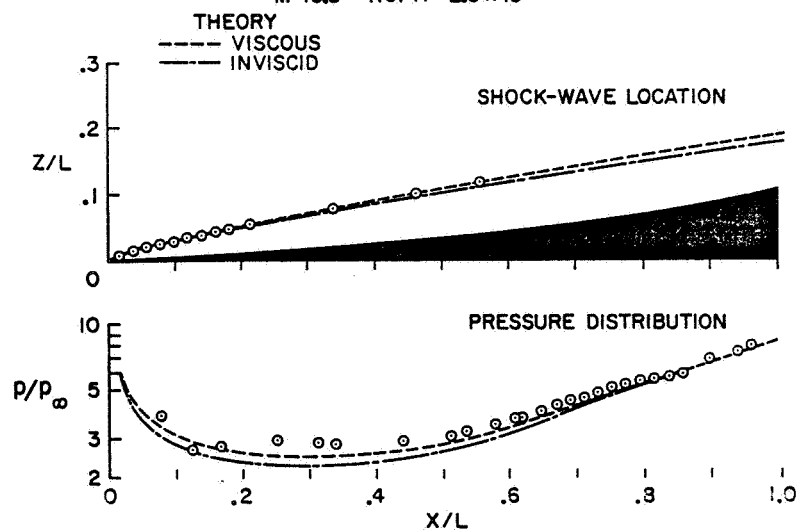


Figure 4

~~CONFIDENTIAL~~

~~CONFIDENTIAL~~

SHOCK-WAVE LOCATION AND SURFACE-PRESSURE DISTRIBUTION
.188" LEADING-EDGE RADIUS
 $M=10.5$ $Re/ft=2.0 \times 10^6$

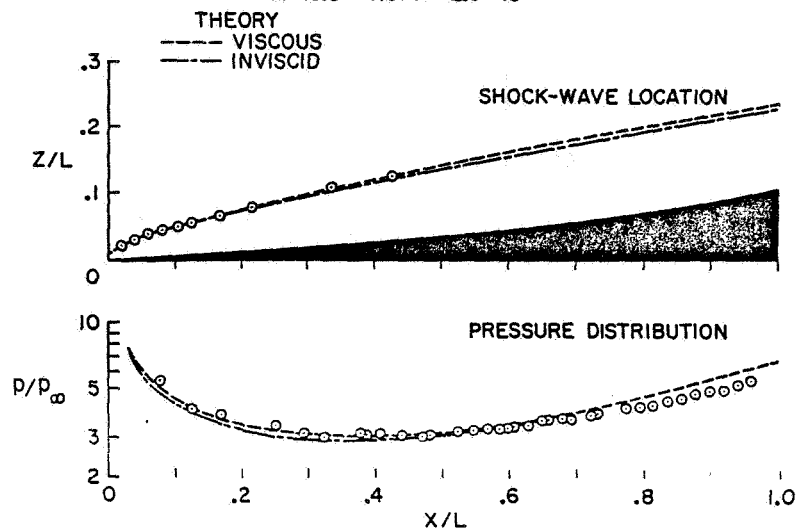


Figure 5

LAMINAR BOUNDARY-LAYER GROWTH
SHARP LEADING EDGE
 $M=10.4$ $Re/ft=0.7 \times 10^6$

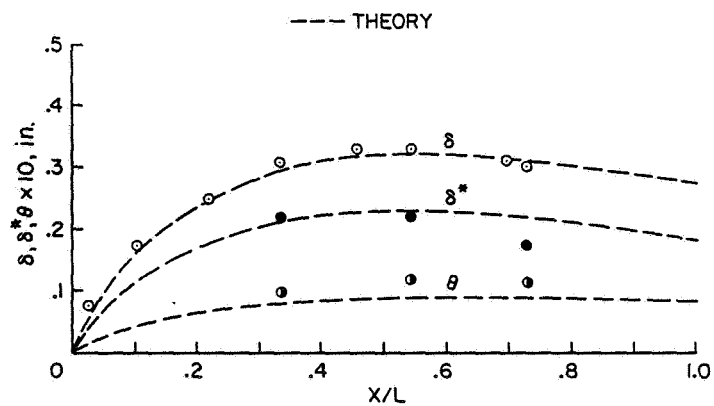


Figure 6

~~CONFIDENTIAL~~

~~CONFIDENTIAL~~

LAMINAR BOUNDARY-LAYER GROWTH
.188" LEADING-EDGE RADIUS
 $M=10.5$ $Re/ft=2.0 \times 10^6$

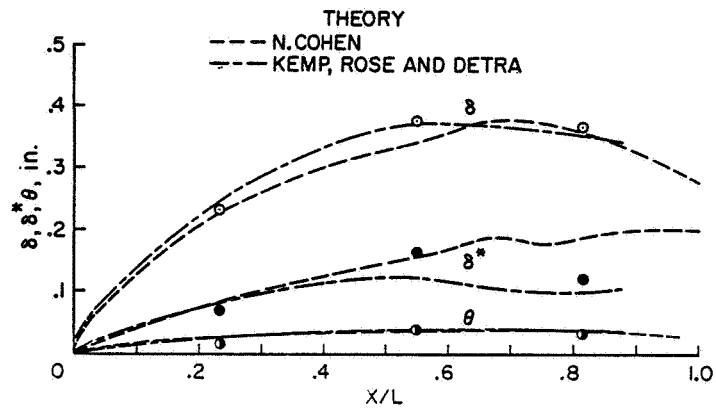


Figure 7

TURBULENT BOUNDARY-LAYER GROWTH
SHARP LEADING EDGE
 $M=10.5$ $Re/ft=2.0 \times 10^6$

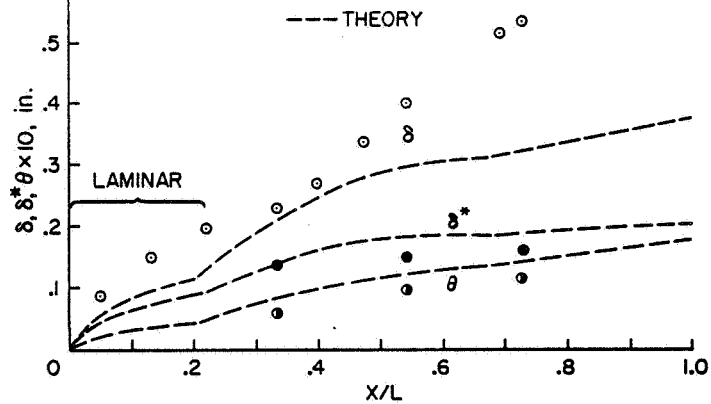


Figure 8

~~CONFIDENTIAL~~

~~CONFIDENTIAL~~

TURBULENT BOUNDARY-LAYER GROWTH
.188" LEADING-EDGE RADIUS
 $M=10.5$ $Re/ft=2.0 \times 10^6$

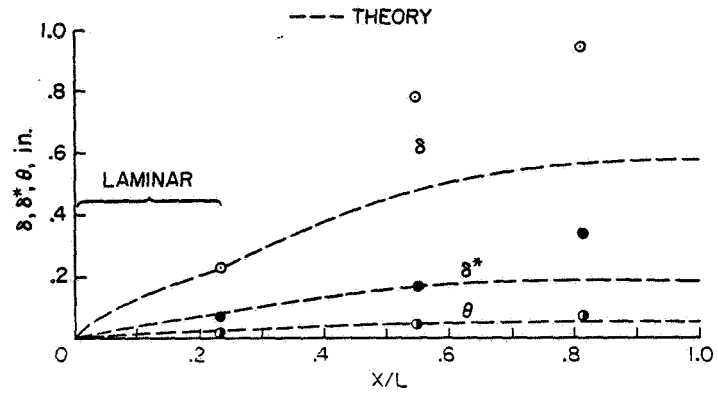


Figure 9

FLOW-FIELD PROFILES
.188" LEADING-EDGE RADIUS
 $M=10.5$ $Re/ft=2.0 \times 10^6$ $X/L=.81$

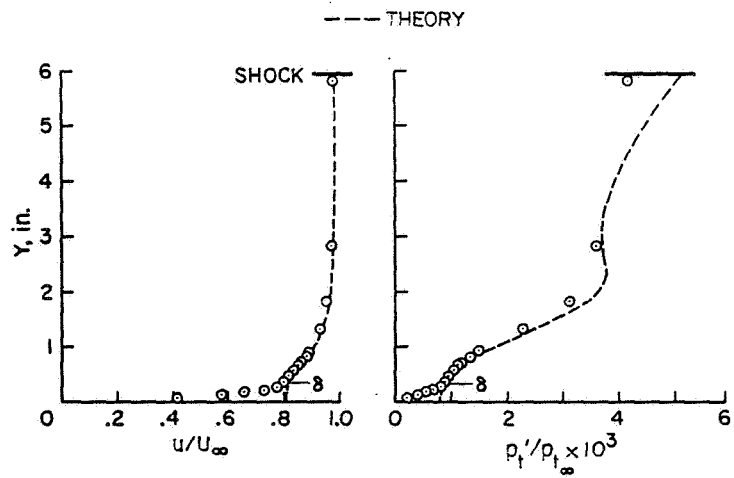


Figure 10

~~CONFIDENTIAL~~

~~CONFIDENTIAL~~

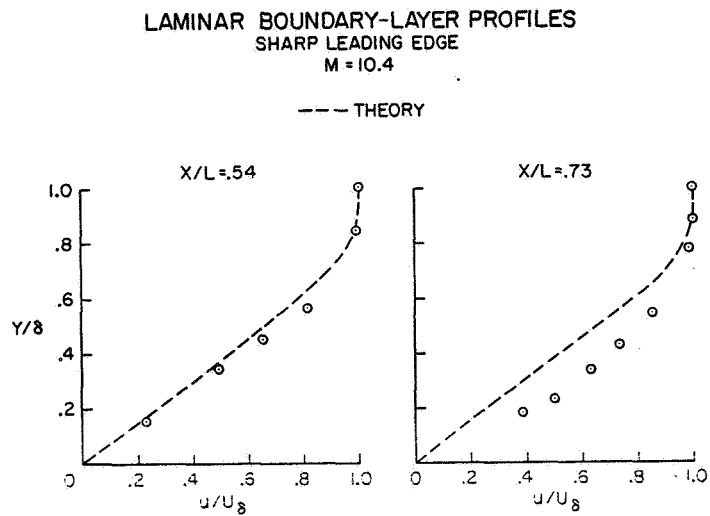


Figure 11

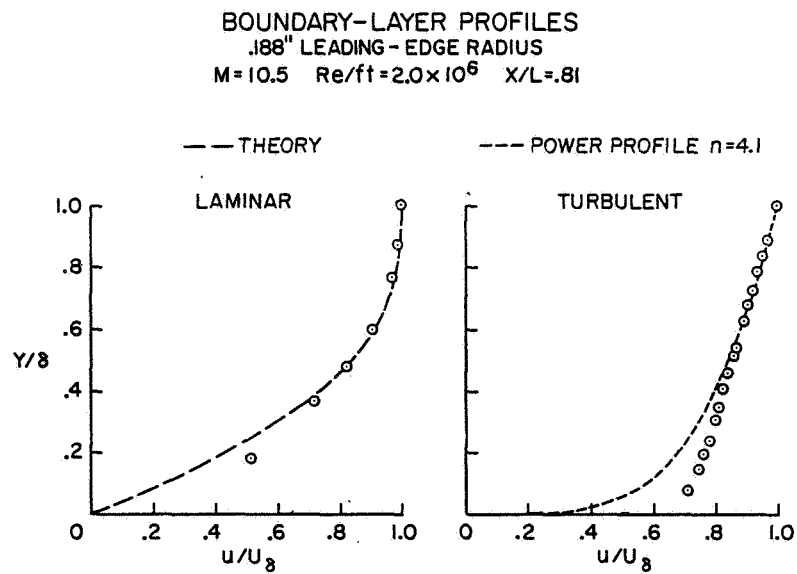


Figure 12

~~CONFIDENTIAL~~

~~CONFIDENTIAL~~

22. SHOCK-WAVE—BOUNDARY-LAYER INTERACTIONS

IN HYPERSONIC INLETS

By Earl C. Watson, John D. Murphy,
and William C. Rose
Ames Research Center

SUMMARY

The interactions of shock waves with laminar and turbulent boundary layers have been investigated from the viewpoint of their occurrence and importance in hypersonic inlets. The investigation included experimental studies and a review of previous related works. Experimental studies were made of interactions occurring on a flat plate and a representative isentropic compression surface for a hypersonic inlet. The tests were conducted at free-stream Mach numbers of 7.3 and 10.5. Data from the present and previous studies were examined to determine parameters which correlate significant pressure and length characteristics. These included incipient separation and plateau pressures, as well as free-interaction, plateau, and total-interaction lengths. The data considered were measured at free-stream Mach numbers from 2 to 15 and at free-stream Reynolds numbers per foot from 2×10^5 to 1×10^7 .

The results of the study indicated that some features of an interaction can be predicted with semiempirical correlation parameters, while others cannot. A technique is presented for describing some characteristics of the shock structure in an interaction of a shock wave with a turbulent boundary layer.

It is concluded that, from the viewpoint of inlet application, further study of the interaction phenomena is required. Analytical or semiempirical methods are needed for predicting total-interaction length, and, for separated flows, the lengths of the plateau and reattachment regions. In addition, further work is needed to define the shock structure within an interaction, as well as the changes in the boundary layer and flow field across an interaction, so that the downstream flow can be predicted.

INTRODUCTION

Some of the problems associated with the flow phenomena encountered in hypersonic inlets have been discussed by Sorensen et al. (ref. 1), and a more detailed study of the interaction of the boundary layer with the inviscid flow field on a representative inlet compression surface is presented by Gnos et al. (ref. 2). Both papers demonstrated that sophisticated analytic techniques which properly account for flow phenomena in hypersonic inlets are

~~CONFIDENTIAL~~

~~CONFIDENTIAL~~

needed for the design of inlet contours which provide high performance. Present machine computing methods for defining the inlet flow field employ simple unverified techniques for treating shock-wave—boundary-layer interactions because analytical models for these interactions are not well developed. This may seem paradoxical because many studies of separated flows and shock-wave—boundary-layer interactions have been conducted in the past (refs. 3-10 are examples).

In those studies a wide variety of separated flows were considered, including those for which the boundary layer is laminar and those for which it is turbulent, with interactions induced by steps, wedges, flares, and shock impingement. The range of speeds considered was from low supersonic to hypersonic. However, most of the studies have concerned aspects of the interactions that are important to external flow over control surfaces or flared afterbodies. Consequently, some details of the interactions which are important to internal flows have not been carefully studied.

Schematic diagrams of external and internal types of flow are shown in figure 1. In studies of control surfaces or flares, the major interest is directed toward the measurement of surface pressure, temperature, heat transfer, and skin friction. This information is also important for inlet applications. However, for inlet design purposes, changes which occur in the boundary layer and shock structure at their first interaction must be well defined. Then the impinging shock at the interactions downstream can be located, and the influence of the interactions accounted for.

The present report describes an investigation of shock-wave—boundary-layer interactions conducted with the primary interest focused on inlet application. Further, the study was conducted on a broad enough basis to have other applications and included experimental studies and a review of previous related work. The interaction types considered include those in which the boundary layer is laminar or turbulent, both with and without separation. Interactions on a compression surface and on flat plates were examined to determine parameters which correlate significant pressures and lengths. These include incipient separation and plateau pressures, as well as free-interaction, plateau, and total-interaction lengths. Some details of the flow field and boundary layer, in the absence of an interaction, are presented in reference 2, for the compression surface used in this study. Boundary-layer velocity and total-temperature profiles across representative interactions on the flat plate used in the present study are presented in reference 11.

NOTATION

C	Chapman-Rubesin constant
C_f	skin-friction coefficient
C_p	pressure coefficient

~~CONFIDENTIAL~~

$\left. \begin{matrix} l_P, l_R \\ l_T, l_U \end{matrix} \right\}$	lengths identified in figure 2
l_1	length identified in table IV
M	Mach number
N	profile index
P	local pressure
P_O, P_P, P_F	pressures identified in figure 2
q	dynamic pressure
r	recovery factor
Re_{x_0}	Reynolds number based on x_0
Re_{x_1}	Reynolds number based on x_1
Re_δ	Reynolds number based on δ
T	temperature
u	velocity
U_1	boundary-layer-edge velocity immediately upstream of impinging shock
U_2	boundary-layer-edge velocity immediately downstream of impinging shock
x	distance measured from leading edge in direction of free-stream flow
x_{eff}	distance measured from effective origin of turbulent boundary layer in direction of free-stream flow
Y	normal distance from wall to shock intercept (fig. 13)
α_L	local flow angle downstream of impinging shock
β	$\sqrt{M_O^2 - 1}$
δ	boundary-layer thickness

CONFIDENTIAL

δ^*	boundary-layer displacement thickness, $\delta \int_0^1 \left(1 - \frac{\rho u}{\rho_\delta u_\delta}\right) d \frac{y}{\delta}$
$\bar{\chi}$	viscous interaction parameter, $\frac{M^3 \sqrt{C}}{(Re_x)^{1/2}}$
ρ	density

Subscripts

i	intercept of linear projection of incident shock and wall
INC	incipient
O	onset of pressure rise at beginning of interaction
P	beginning of plateau
P_e	end of plateau
t	total conditions
δ	boundary-layer edge
1	intercept of impinging shock and edge of turbulent boundary layer or conditions upstream of impinging shock
∞	free stream

APPARATUS

The present study was conducted under a joint contract involving Ames Research Center, the Air Force Flight Dynamics Laboratory, and the General Electric Company, Evandale, Ohio. In the experimental part of the study, large-scale two-dimensional models were tested in the Ames 3.5-foot hypersonic wind tunnel (ref. 12). Representative wind-tunnel test conditions showing the range of test variables are presented in table I. Two models were employed for the flow studies: one was a flat plate 18 inches wide by 48 inches long, and the other was a curved isentropic compression surface. (Coordinates of the compression surface are presented in table II.) The models were aligned at 3° with respect to the free stream. Neither model had side plates to restrict the spanwise flow. For the studies reported herein, both models had sharp (0.002-inch radius) leading edges. The leading-edge section and the area directly behind it were water cooled. The remaining

~~CONFIDENTIAL~~

portion of the model did not have wall-temperature control, but the mass of the model was such that the wall-temperature distribution remained nearly constant during the test runs. For a free-stream Mach number of 10.4 the ratio of the wall to stagnation temperature was 0.28, and for Mach number 7.3 it varied from 0.37 to 0.41, depending on the stagnation temperature.

RESULTS AND DISCUSSION

Definitions

In order to facilitate the following discussion, it is necessary to establish some pertinent definitions. Figure 2 is a schematic diagram of the interaction between an incident shock and a laminar boundary layer. The sketch represents an interaction occurring on a compression surface where the shock strength is sufficient to cause local flow separation. The model alignment and flow direction and a typical surface pressure distribution are as shown. The impinging shock, which was formed by a generating surface (not shown), interacts with the laminar boundary layer and reflects back into the flow field. The quantity, α_L , indicates the strength of the impinging shock. It is the local flow-deflection angle which would produce the impinging shock wave. The location of the interaction is identified by the intercept at the wall of the linear projection of the impinging shock before it encounters any influence from the interaction. The pressures and lengths of interest are determined from the surface pressure distribution and shock structure. The pressures of interest are the upstream pressure, P_0 , the plateau pressure, P_p , and final pressure, P_F . The incremental lengths l_U , l_p , and l_R define the free interaction, plateau, and reattachment regions, respectively, while l_T defines the overall interaction length.

Pressure Distributions

The features of the surface pressure distribution depend on the local conditions in the interaction region. Similarities as well as differences are evident in the features of an interaction on a flat plate and a compression surface. A schlieren photograph and surface-pressure distributions for the flat plate for a free-stream Mach number of 7.3 are shown in figure 3. The local flow-deflection angle for the schlieren photograph and sketch is 10° . The shock structure and boundary layer in the schlieren photograph are identified in the sketch of the interaction. The variation of the local pressure ratio with distance along the surface from the onset of the interaction is shown below the sketch. The distributions are shown for a series of nominal, local flow-deflection angles ranging from 0.5° to 10° . When plotted in this manner, the pressure distributions show the similarity of the profile in the free-interaction region. This result supports the free-interaction hypothesis of Chapman et al. (ref. 3). It can be seen that with the onset of separation, an increase in shock strength lengthens the pressure plateau and changes the pressure distribution in the reattachment region. The plateau

CONFIDENTIAL

~~CONFIDENTIAL~~

pressure is less than that for incipient separation, in accordance with the findings of Chapman et al. (ref. 3) for supersonic speeds, and Needham (ref. 7) for hypersonic speeds. The incipient separation pressure can be obtained by cross plotting the plateau length, l_p , against the local flow-deflection angle, α_L , and extrapolating to zero plateau length. This process yields a pressure for incipient separation slightly higher than that shown for $\alpha_L = 2^\circ$.

The schlieren photograph and surface-pressure distributions in figure 4 were obtained for the compression surface. The photograph and tracing are shown for a local flow angle of 7° . Again, it can be seen that the pressure distributions in the free-interaction region are coincident, and a pressure higher than the plateau pressure was obtained without separation for the 3° flow-deflection angle. These pressure distributions differ from those on the flat plate in the length of the plateau region, and in the shape in the reattachment region. For local flow angles of 3° and 7° , the final pressure agrees with that obtained from inviscid theory for the incident and reflected shock system. For stronger interactions, however, the final pressure is low compared with that predicted by inviscid theory. It is believed this discrepancy is associated, in part, with the expansion fan emanating from the generating surface employed to form the impinging shock wave. In addition, the loss of two-dimensionality from lateral spillage in these strong interactions contributes to the reduction in overall pressure rise across the interaction.

Data obtained with a turbulent boundary layer for a free-stream Mach number of 7.3 are presented in figure 5. The schlieren photograph, for $\alpha_L = 8^\circ$, shows the penetration of the impinging shock. The two emerging compression waves form a reflected compression fan that coalesces into the emerging shock. The pressure distributions have been aligned so that the point of intercept of the shock and wall is coincident. When plotted in this manner, the data show the increase in the extent of the upstream influence with increasing shock strength. The subscript 1 denotes the beginning of the interaction associated with the intercept of the shock and the edge of the boundary layer. In the laminar case, the beginning is associated with the rise in surface pressure somewhat upstream of shock impingement. For the shock strengths shown in figure 5, there is no evidence of a pressure plateau. However, it is believed that the orifice spacing was not small enough to detect the small plateau which is believed to have occurred for the strongest shock.

The formation of a plateau was observed on the compression surface for somewhat stronger shocks. Figure 6 presents the pressure data for the compression surface. The pressure plateau is obvious in this figure and indicates the presence of separation. The shock structure shows that the first emerging shock originates upstream of the impinging shock. It is believed that the first emerging shock is associated with the free-interaction behavior of the sublayer flow. This will be discussed further in connection with an analytical model of the interaction.

~~CONFIDENTIAL~~

Correlations

Pressure distributions and schlieren photographs similar to those presented in the preceding section have been analyzed to determine significant pressure and length quantities characteristic of an interaction. These and similar quantities from other investigations have been incorporated into parameters which correlate significant features of an interaction. Data were considered for free-stream Mach numbers ranging from 2 to 14.8, and free-stream Reynolds numbers per foot from 2×10^5 to 1×10^7 . An analysis of the data over this wide range of conditions was made to provide a broad basis for determining empirical relations for predicting specific features of an interaction. The features for which correlation parameters were sought are presented in tables III and IV for the pressures and lengths, respectively. The comments in the tables are made on the basis of an analysis of data presented and discussed in the following sections.

Pressure correlations.- Correlation of the pressure ratio for incipient separation of laminar boundary layers is presented in figure 7(a). The data of references 4, 7, and 13 and the present study are correlated in this figure by the pressure ratio and viscous interaction parameter, \bar{X}_0 . It is believed that more data are needed to substantiate the validity of these parameters for the correlation of incipient separation. Therefore, caution should be exercised in applying these results for design purposes. In addition, it should be remembered that all available data are for single interactions. If two or more interactions occur in tandem, such as in hypersonic inlets, incipient separation may occur at different pressure ratios for interactions downstream of the first. Further investigation is needed to determine the mutual interference of tandem interactions.

Figure 7(b) presents a correlation of the pressure rise for incipient separation of turbulent boundary layers. In this figure the data of Kuehn (ref. 14) as given by Popinski and Ehrlich (ref. 9) and the data of the present study are compared. The line represents the relation proposed by Popinski. Fairly good correlation is obtained with both flat plate and compression surface data. Again, due to the paucity of experimental data, caution should be exercised in employing these results for design purposes.

In figure 8(a) a correlation of plateau pressure for interactions with laminar boundary layers is presented. The parameters proposed by Needham (ref. 7) are used to compare the data of references 4, 7, and 15 with those of the present study. Excellent correlation is obtained for both flat plate and compression surface data. In addition, the data also represent interactions occurring for a wide range of wall conditions, varying from adiabatic for the data of reference 4 to cold wall for the data of reference 7 and the present study.

In figure 8(b) a correlation of plateau pressure for turbulent boundary layers is presented. These parameters (from ref. 9) are used to compare the data of references 5, 10, and 14 with those of the present study. Again, the correlation is fairly good. It should be noted that the data are not sufficiently precise to provide complete support for the relation represented by

the line (ref. 9), since this relation results in only a slightly better correlation than a relation proposed by Erdos and Pallone (ref. 6). In this figure the results of the present study are shown with an uncertainty band because, for turbulent flow, the pressure plateau is not flat. A substantial amount of subjectivity enters into the choice of plateau pressure; in the present case, the band represents the pressure limits associated with the beginning and end of the plateau.

.... Figure 9(a) presents the dimensionless pressure distribution in the free-interaction region of a laminar boundary-layer—shock-wave interaction. Erdos and Pallone (ref. 6) hypothesized that this profile was universal. As can be seen, the "universal" profile presented in reference 6, which was derived from the data of reference 3 for an adiabatic wall, departs quite markedly from the profiles obtained on a cold wall in the present study. In addition, profiles obtained at free-stream Mach numbers of 7.3 and 10.4 show significant differences. It is concluded that there probably is no universal pressure profile in the free-interaction region.

Figure 9(b) presents dimensionless pressure profiles for the reattachment region of a laminar boundary-layer—shock-wave interaction. These profiles appear to be highly sensitive to Mach number and less sensitive to shock strength. Also, it is evident from examination of the difference between profiles on the compression surface and flat plate, for approximately the same range of local flow angles, that local pressure gradient affects the shape of these profiles.

Adequate definition of dimensionless pressure profiles for the free-interaction and reattachment regions of the turbulent boundary-layer—shock-wave interactions could not be made in the present study.

The dimensionless pressure distributions for unseparated interactions are given for the laminar boundary layer in figure 10(a) and for the turbulent boundary layer in figure 10(b). Again, the pronounced Mach number dependence is demonstrated for both the laminar and turbulent boundary layers. The importance of local pressure gradient is also evident for these unseparated interactions.

The foregoing discussion of the dimensionless pressure distributions has shown that they are affected by wall cooling, Mach number, and local pressure gradient. Further studies of these effects are needed before relations for design purposes can be obtained.

Length correlations.—Parameters used for correlating the free-interaction length are presented in figures 11(a) and 11(b) for interactions with laminar and turbulent boundary layers, respectively. The parameters used for the laminar boundary layer were developed during the present study, whereas those for the turbulent boundary layer were proposed by Popinski and Ehrlich (ref. 9). The lines presented in these figures represent the recommended relation for defining the free-interaction length as a function of the incremental pressure rise to the beginning of the plateau. For the laminar interactions the reference data used were obtained from references 3, 4, and 7;

~~CONFIDENTIAL~~

for the turbulent interactions the data from references 14, 16, and 17 are shown as presented by Popinski and Ehrlich (ref. 9).

No simple parameters are available for describing the length of the plateau region for interactions with separation. Hakkinen et al. (ref. 4) applied a momentum analysis to a separated region to determine the parameters involved in a laminar separation for adiabatic wall conditions. The expressions evolved in that analysis were used in the present study for comparing the data for plateau length presented in figure 12. Although these parameters correlate the length for weak interactions on a flat plate for a wide range of Mach numbers (2.0 to 8.4) and for cold wall and adiabatic wall conditions, the parameters do not correlate the data for the strong interactions, nor any of the data for the compression surface. The laminar data from the present test have been analyzed also by Kutschenreuter et al. (ref. 18) with respect to the separation length parameters proposed by Erdos and Pallone (ref. 6). No correlating relation was found; however, there was evidence of a strong Mach number dependence. No correlations are available for predicting the plateau length for interactions involving a turbulent boundary layer. During that part of the present study which involved a review of past work, it became evident that the flow in the reattachment region had not been investigated adequately. Consequently, there are no empirical methods for predicting the length of the reattachment region. It is concluded that the present understanding of the factors which affect the lengths of the plateau and reattachment regions is inadequate. Further study is needed in these areas to obtain useful analytical or semiempirical methods for predicting these lengths.

For turbulent interactions, the height, Y , to the intercept of the first emerging shock and the impinging shock is a quantity required in the semiempirical method of interaction analysis proposed by Pinckney (ref. 10). The shock structure of the turbulent interactions of the present study has been examined to determine the intercept and total-length parameters used in that semiempirical method. Figure 13 presents the variation of the intercept of the impinging and first emerging shocks with the pressure coefficient across the interaction; figure 14 presents the variation of the total-interaction length with the strength of the impinging shock, α_L . It can be seen from these figures that the variation of both the shock intercept and total-length parameters with increasing shock strength differs in each case from the respective variation indicated by Pinckney. Whereas the Pinckney results were obtained for adiabatic wall conditions and for Mach numbers up to 5, the present results are for cold wall conditions and a local Mach number of 6.5. An approximate analysis of the effect of the ratio of wall temperature to total temperature at the edge of the boundary layer for a turbulent interaction is presented by Kutschenreuter et al. in reference 18. It is concluded that further investigation of the effect of wall cooling is needed, and that care should be exercised in extrapolating the Pinckney results.

For laminar interactions, correlation parameters obtained in the present study for the total-interaction length are shown in figure 15. In view of the lack of success in obtaining correlations for plateau and reattachment lengths, it is somewhat unexpected to find such good correlation for the total-interaction length. Whereas the data for the flat plate from the referenced and present studies agree reasonably well for the wide range of conditions

~~CONFIDENTIAL~~

~~CONFIDENTIAL~~

represented, the data for the compression surface and the stronger interactions are different. This indicates a sensitivity of total-interaction length to local pressure gradient.

Interaction models.- The preceding sections have been concerned for the most part with those features of the interaction that can be determined from surface measurements and the location and strength of the impinging shock. It is also of interest to observe the actual shock structure in an interaction region and to compare it with the structure assumed in analytical methods that are employed to represent the interaction. Figure 16(a) is a schlieren photograph of the interaction between a shock wave and a laminar boundary layer. A tracing of the photograph is presented in figure 16(b), and superimposed on it are dashed lines representing the shock structure as it might be assumed in two analytical methods. In one method, the incident shock reflects from the wall, and in the other it reflects from the boundary-layer displacement thickness. It is evident that neither of these models represents the actual interaction.

When the boundary layer is turbulent, a somewhat similar situation exists, as indicated in figure 17. In this case also, it is evident that the inviscid shock structures, represented by the dashed lines in figure 17(b), poorly represent the actual interaction. Examination of the schlieren photograph (fig. 17(a)) shows two emerging shocks. One explanation for the presence of the first emerging shock is that it is formed by the coalescence of weak compression waves which are associated with a free interaction. It is believed that this free interaction occurs between the sublayer and the actual impinging shock which has penetrated the boundary layer, and, in this respect, the shock is evidence of the presence of a flow process that is similar to that involved in a free interaction with laminar flow.

It is obvious that simplified representations of the interactions are inadequate when applied to internal flows, and that more sophisticated methods must be sought. Further studies are needed to ascertain what effects might ensue within an inlet if an entering shock were mislocated by several boundary-layer thicknesses. For laminar interactions efforts are currently in progress to improve the analytical methods of Lees and Reeves (ref. 19) and Nielsen et al. (ref. 20), so that better overall definition of the interaction can be realized. In addition, an effort is also being made to obtain a more exact analytical method for interactions with a turbulent boundary layer. In this method the shock structure was analyzed by a method of characteristics technique. A schlieren photograph and a tracing of an interaction are presented in figures 18(a) and 18(b), respectively. It is assumed that the boundary layer consists of two layers, an inviscid constant total-temperature outer layer and a viscous sublayer. The inviscid layer, which has a given Mach number and entropy profile, provides the starting mesh in a method of characteristics computing program. A shock wave of appropriate strength, generated by a wedge, impinges on the inviscid layer and reflects from the sublayer. A similar technique was proposed by Tucker (ref. 21), who employed only Mach lines, as a method for accounting for boundary-layer effects in supersonic nozzles. The shock structure obtained from the computer program using the present technique is shown by the dashed lines. Except for the presence of

~~CONFIDENTIAL~~

the first emerging shock associated with the precompression process discussed previously, there is good agreement in the shock structure.

On the basis of these preliminary results, it appears that a representation of a turbulent interaction might be obtained if a viscous solution for the sublayer flow, subject to the influence of the local shock impingement, were coupled with a characteristics solution of the flow for the outer layer.

CONCLUDING REMARKS

Plateau or incipient separation pressures have been used as criteria for allowable shock strength for inlet design purposes, with simple shock reflections from the displacement thickness. For hypersonic speeds these criteria must be reexamined in view of the changes that occur in shock structure across an interaction. With a turbulent boundary layer, changes in shock structure begin at shock strengths relatively weak in comparison with those required for incipient separation.

Shock-wave—boundary-layer interactions have been discussed from the inlet viewpoint. It has been shown that present analytical models of the interactions do not adequately represent the shock structure. Expressions are given for correlating such features as incipient separation and plateau pressures, and free-interaction lengths. No correlating expressions are available for such features as plateau and reattachment lengths. Some new thoughts for an analytical model of the interaction of a turbulent boundary layer and shock wave have been presented. It is evident that continued study of shock-wave--boundary-layer interaction problems is needed.

REFERENCES

1. Sorensen, Norman E.; Morris, Shelby J., Jr.; and Pfyl, Frank A.: A Study of Hypersonic Inlet Technology. Conference on Hypersonic Aircraft Technology, NASA SP-148, 1967. (Paper No. 20 herein.)
2. Gnos, A. Vernon; Gallo, William F.; and Latham, Eldon A.: Two-Dimensional Boundary Layers and Flow Fields of Hypersonic Inlets. Conference on Hypersonic Aircraft Technology, NASA SP-148, 1967. (Paper No. 21 herein.)
3. Chapman, Dean R.; Kuehn, Donald M.; and Larson, Howard K.: Investigation of Separated Flows in Supersonic and Subsonic Streams With Emphasis on the Effect of Transition. NACA Rep. 1356, 1958.

~~CONFIDENTIAL~~

~~CONFIDENTIAL~~

4. Hakkinen, R. J.; Greber, I.; Trilling, L.; and Abarbanel, S. S.: The Interaction of an Oblique Shock Wave With a Laminar Boundary Layer. NASA MEMO 2-18-59W, 1959.
5. Kuehn, Donald M.: Turbulent Boundary-Layer Separation Induced by Flares on Cylinders at Zero Angle of Attack. NASA TR R-117, 1961.
6. Erdos, John; and Pallone, Adrian: Shock-Boundary-Layer Interaction and Flow Separation. Proceedings of the 1962 Heat Transfer and Fluid Mechanics Institute, F. E. Ehlers, J. J. Kauzlarich, C. A. Sleicher, Jr., R. E. Street, eds., Stanford University Press, 1962, pp. 239-254.
7. Needham, D. A.: Laminar Separation in Hypersonic Flow. Ph.D. Thesis, University of London, 1965.
8. Popinski, Z.: Shock-Wave Boundary-Layer Interaction. Rep. LR 18307, Lockheed-California Company, 29 June 1965.
9. Popinski, Z.; and Ehrlich, C. F.: Development Design Methods for Predicting Hypersonic Aerodynamic Control Characteristics. (AFFDL-TR-66-85), Lockheed-California Company, Sept. 1966.
10. Pinckney, S. Z.: Semiempirical Method for Predicting Effects of Incident-Reflecting Shocks on the Turbulent Boundary Layer. NASA TN D-3029, 1965.
11. Watson, Earl C.; Ghos, A. Vernon; Gallo, William F.; and Latham, Eldon A.: Boundary Layers and Hypersonic Inlet Flow Fields. AIAA paper 66-606, 1966.
12. Holdaway, George H.; Polek, Thomas E.; and Kemp, Joseph H., Jr.: Aerodynamic Characteristics of a Blunt Half-Cone Entry Configuration at Mach Numbers of 5.2, 7.4, and 10.4. NASA TM X-782, 1963.
13. Holden, M. S.: Separated Flow Studies at Hypersonic Speeds. Part II. Two-Dimensional Wedge Separated Flow Studies. CAL-AF-1285-A-13(2), Cornell Aero. Labs., Dec. 1964.
14. Kuehn, Donald M.: Experimental Investigation of the Pressure Rise Required for the Incipient Separation of Turbulent Boundary Layers in Two-Dimensional Supersonic Flow. NASA MEMO 1-21-59A, 1959.
15. Sterrett, James R.; and Emery, James C.: Extension of Boundary-Layer-Separation Criteria to a Mach Number of 6.5 by Utilizing Flat Plates With Forward-Facing Steps. NASA TN D-618, 1960.
16. Levin, V.; and Fabish, T. J.: Thermal Effect of Shockwave Turbulent Boundary Layer Interaction at Mach Numbers 3 and 5. Rep. NA-62H-795, North American Aviation, Inc., Nov. 1962.

~~CONFIDENTIAL~~

17. Sayano, S.; Bauch, H. P.; and Donnelly, R. J.: Aerodynamic Heating Due to Shock Impingement on a Flat Plate, Model IM-20. Rep. SM 41331, Missile and Space Systems Division, Douglas Aircraft Company, Aug. 1962.
18. Kutschenreuter, Paul H., Jr.; Brown, David L.; and Hoelmer, Werner: Investigation of Hypersonic Inlet Shock-Wave Boundary Layer Interaction. Part II. Continuous Flow Test and Analyses. Rep. AFFDL TR-65-36 (Contract AF33(657)-11747), General Electric Co., Evendale, Ohio.
19. Lees, Lester; and Reeves, Barry L.: Supersonic Separated and Reattaching Laminar Flows: I. General Theory and Application to Adiabatic Boundary-Layer/Shock-Wave Interactions. AIAA J., vol. 2, no. 11, Nov. 1964, pp. 1907-1920.
20. Nielsen, Jack N.; Lynes, Larry L.; and Goodwin, Frederick K.: Calculation of Laminar Separation with Free Interaction by the Method of Integral Relations. Part II. Two-Dimensional Supersonic Nonadiabatic Flow and Axisymmetric Supersonic Adiabatic and Nonadiabatic Flows. Rep. 203, Vidya Corp., Palo Alto, Calif., AFFDL-TR-65-107-Pt-2, Jan. 1966.
21. Tucker, Maurice: Approximate Turbulent Boundary-Layer Development in Plane Compressible Flow Along Thermally Insulated Surfaces With Application to Supersonic-Tunnel Contour Correction. NACA TN 2045, 1950.

~~CONFIDENTIAL~~

~~CONFIDENTIAL~~

TABLE I

REPRESENTATIVE TEST CONDITIONS

M_∞	$P_{t\infty}$, psia	$T_{t\infty}$, °R	$(Re/ft)_\infty$ $\times 10^{-6}$	EQUIVALENT PRESSURE ALTITUDE, ft
10.5	1810	1930	2.00	140,000
	430	1750	.63	180,000
7.3	630	1320	3.50	100,000
	60	1700	.22	167,000

TABLE II

SURFACE COORDINATES
COMPRESSION SURFACE MODEL

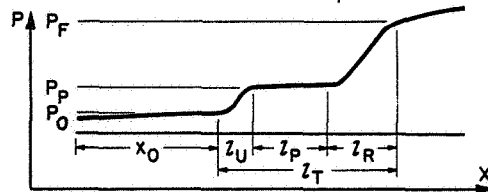


X	Z	X	Z	X	Z	X	Z
0	0	19.000	1.066	29.000	1.926	39.000	3.260
10.000	.524	20.000	1.136	30.000	2.038	40.000	3.414
11.000	.578	21.000	1.210	31.000	2.156	41.000	3.572
12.000	.634	22.000	1.286	32.000	2.280	42.000	3.734
13.000	.692	23.000	1.366	33.000	2.408	43.000	3.900
14.000	.752	24.000	1.450	34.000	2.540	44.000	4.070
15.000	.813	25.000	1.536	35.000	2.676	45.000	4.244
16.000	.874	26.000	1.626	36.000	2.816	46.000	4.422
17.000	.936	27.000	1.720	37.000	2.960	47.000	4.604
18.000	1.000	28.000	1.820	38.000	3.108	48.000	4.790

~~CONFIDENTIAL~~

TABLE III

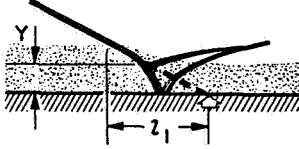
PRESSURE CORRELATION SUMMARY



ITEM	LAMINAR	TURBULENT
1. C_p INCIPIENT	PRESENT STUDY	POPINSKI (1966)
2. C_p PLATEAU	NEEDHAM	POPINSKI (1966)
3. FREE INTERACTION	NO UNIVERSAL PROFILE	NONE FROM PRESENT TEST
4. REATTACHMENT	NO UNIVERSAL PROFILE	NONE FROM PRESENT TEST
5. UNSEPARATED	NO UNIVERSAL PROFILE	NO UNIVERSAL PROFILE

TABLE IV

LENGTH CORRELATION SUMMARY

ITEM	LAMINAR	TURBULENT
1. FREE INTERACTION LENGTH, z_U	PRESENT STUDY	POPINSKI (1965)
2. PLATEAU LENGTH, z_P	IMPROVEMENT NEEDED	NONE
3. REATTACHMENT LENGTH, z_R	NONE	NONE
4. SHOCK INTERCEPT 	(NOT APPLICABLE)	PRESENT TEST RESULTS DIFFER FROM THOSE OF PINCKNEY
5. TOTAL LENGTH, z_T	IMPROVEMENT NEEDED	

CONFIDENTIAL

INTERACTIONS OF BOUNDARY LAYERS AND SHOCK WAVES AT HYPERSONIC SPEEDS

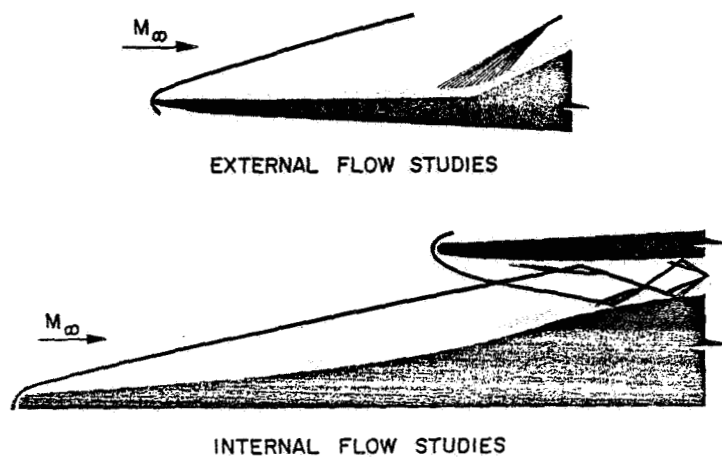


Figure 1

INTERACTION OF SHOCK WAVE WITH LAMINAR BOUNDARY LAYER SCHEMATIC

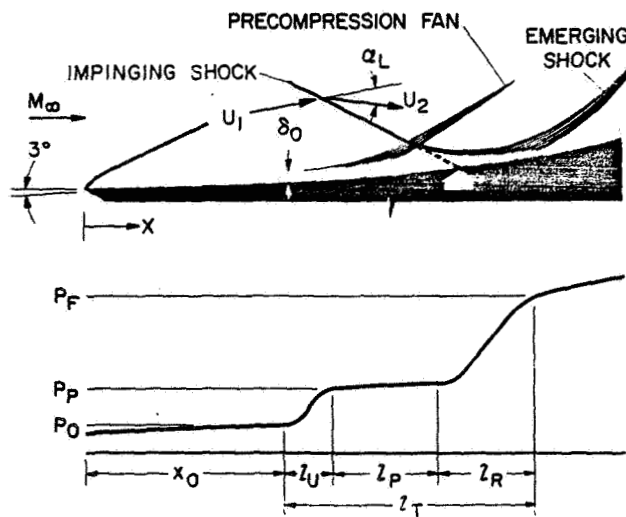


Figure 2

CONFIDENTIAL

INTERACTION OF SHOCK WAVE WITH LAMINAR BOUNDARY LAYER
FLAT PLATE

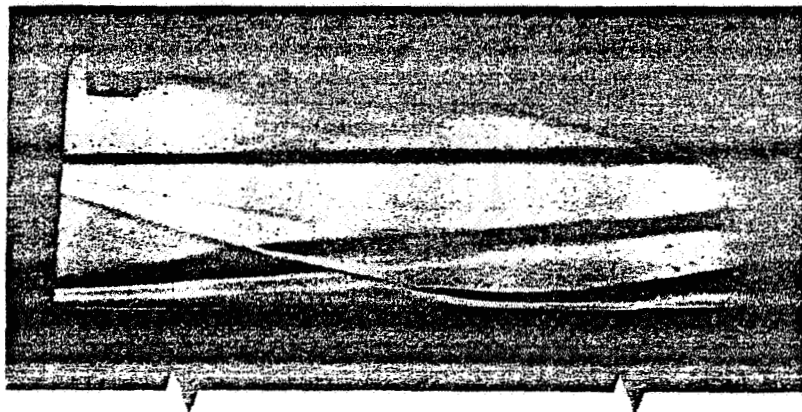


Figure 3(a)

AAA377-3a

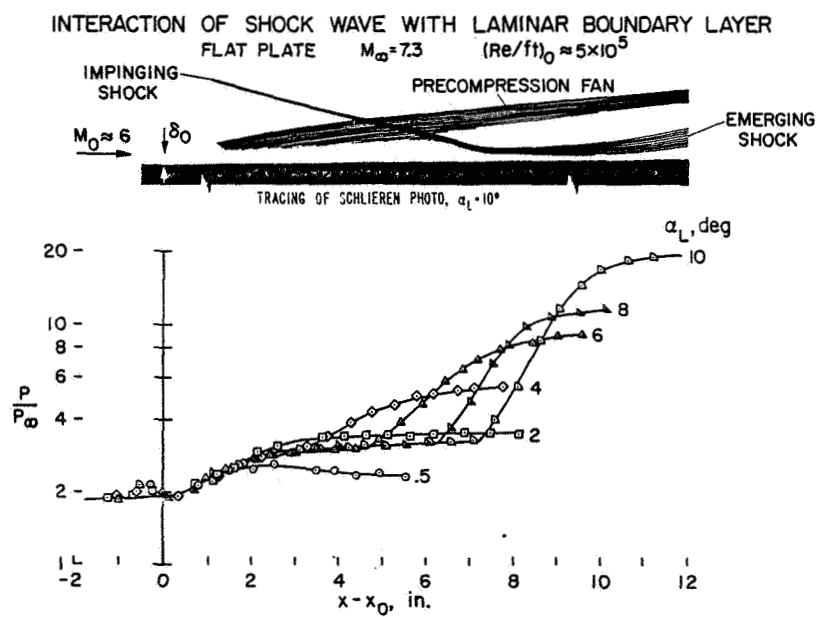


Figure 3(b)

CONFIDENTIAL

~~CONFIDENTIAL~~

INTERACTION OF SHOCK WAVE WITH LAMINAR BOUNDARY LAYER COMPRESSION SURFACE



Figure 4(a)

AAA377-4a

INTERACTION OF SHOCK WAVE WITH LAMINAR BOUNDARY LAYER COMPRESSION SURFACE $M_\infty = 7.3$ $(Re/ft)_0 \approx 2.8 \times 10^5$

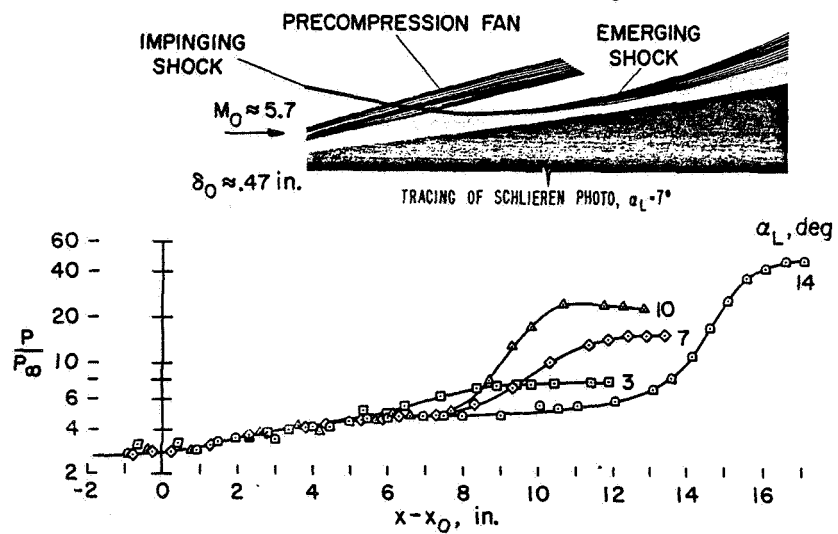


Figure 4(b)

~~CONFIDENTIAL~~

INTERACTION OF SHOCK WAVE WITH TURBULENT BOUNDARY LAYER FLAT PLATE

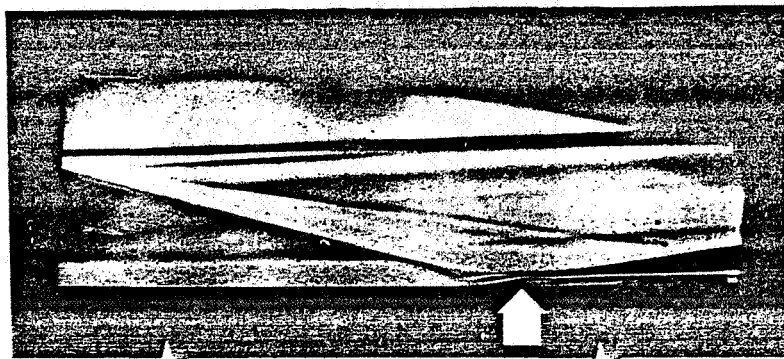


Figure 5(a)

AAA377-5a

INTERACTION OF SHOCK WAVE WITH TURBULENT BOUNDARY LAYER IMPINGING SHOCK FLAT PLATE $M_\infty = 7.3$ $(Re/ft)_1 \approx 3.1 \times 10^6$

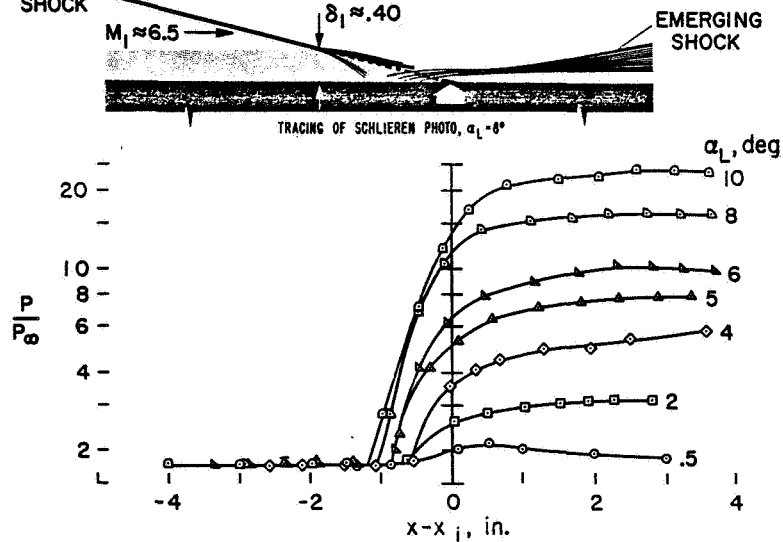


Figure 5(b)

~~CONFIDENTIAL~~

CONFIDENTIAL

INTERACTION OF SHOCK WAVE WITH TURBULENT BOUNDARY LAYER COMPRESSION SURFACE

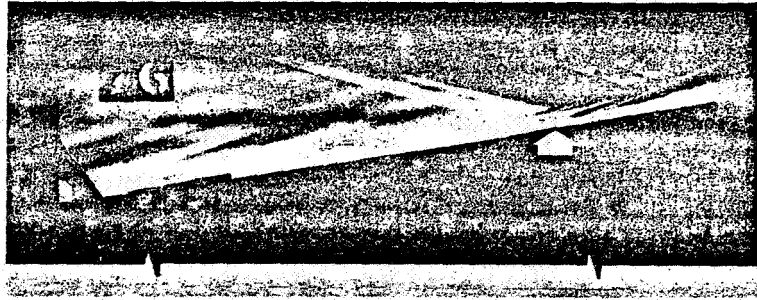


Figure 6(a)

AAA377-6a

INTERACTION OF SHOCK WAVE WITH TURBULENT BOUNDARY LAYER

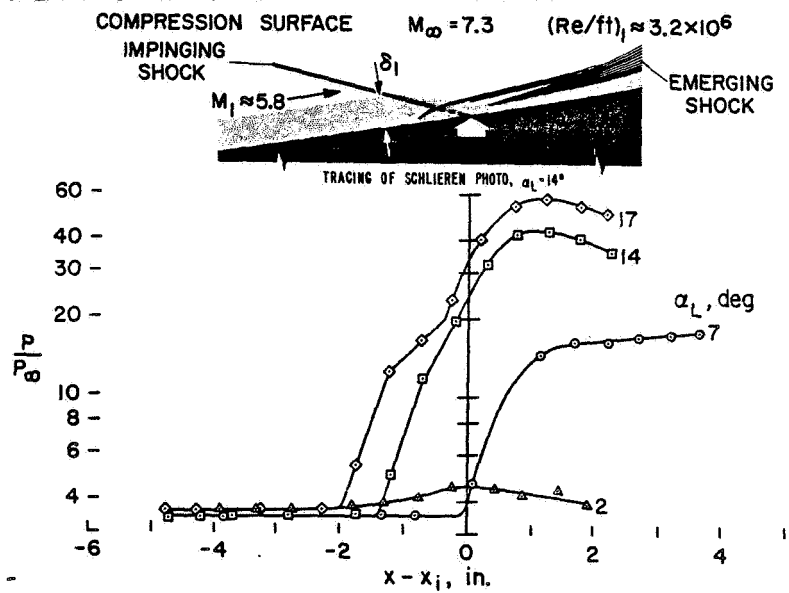


Figure 6(b)

CONFIDENTIAL

~~CONFIDENTIAL~~

CORRELATION OF PRESSURE RATIO FOR INCIPIENT SEPARATION LAMINAR BOUNDARY LAYER

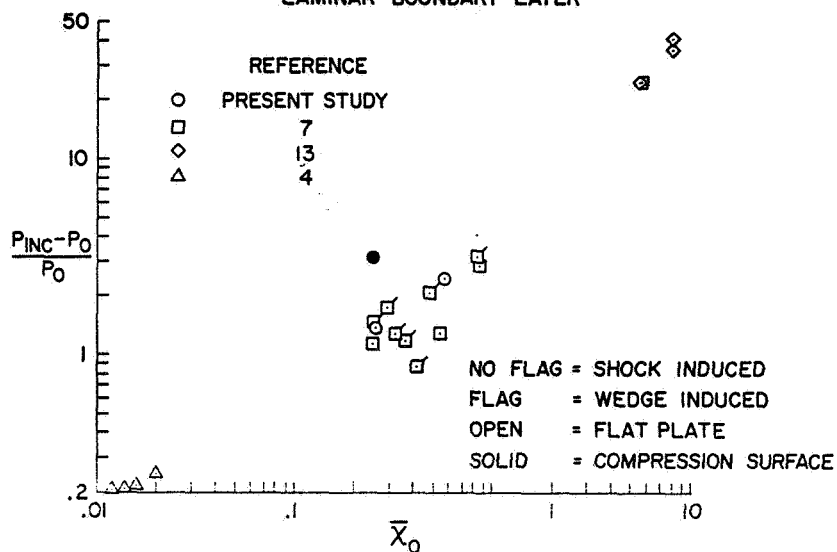


Figure 7(a)

CORRELATION OF PRESSURE COEFFICIENT FOR INCIPIENT SEPARATION TURBULENT BOUNDARY LAYER

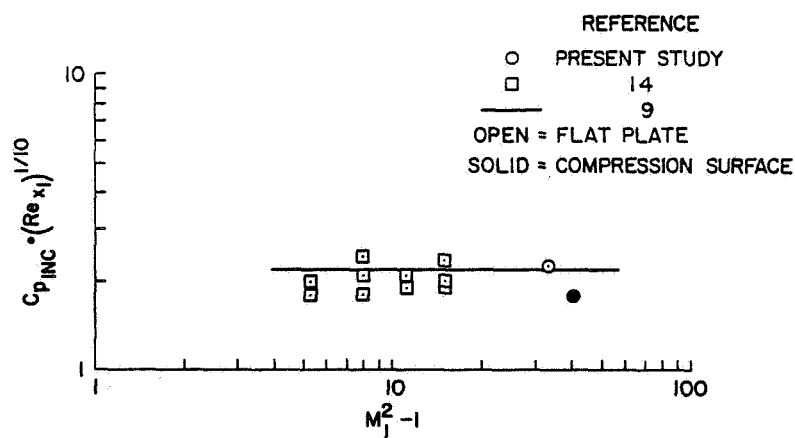


Figure 7(b)

~~CONFIDENTIAL~~

~~CONFIDENTIAL~~

CORRELATION OF PLATEAU PRESSURE RATIO LAMINAR BOUNDARY LAYER

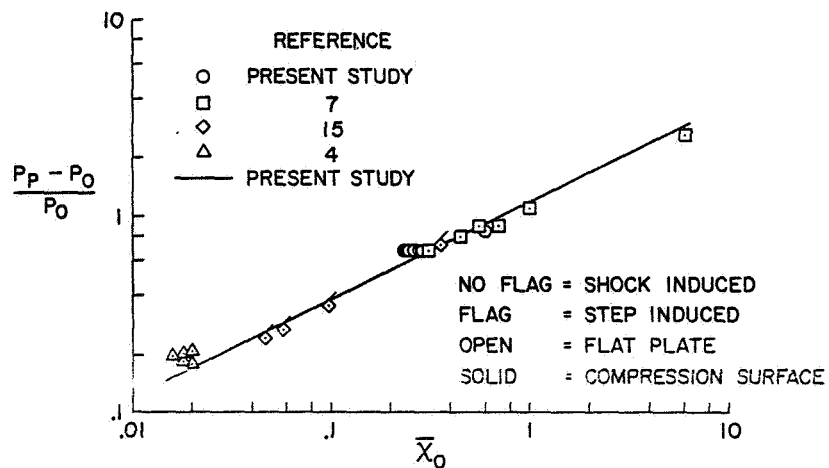


Figure 8(a)

CORRELATION OF PLATEAU PRESSURE COEFFICIENT TURBULENT BOUNDARY LAYER

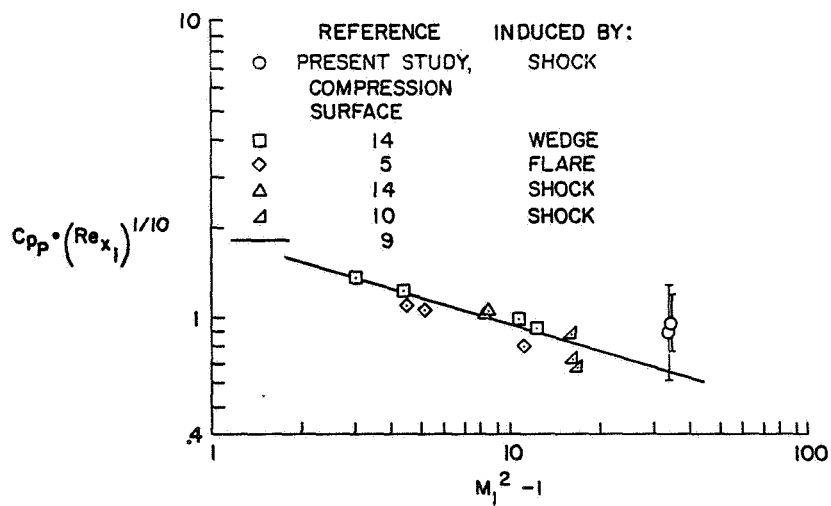


Figure 8(b)

~~CONFIDENTIAL~~

~~CONFIDENTIAL~~

PRESSURE DISTRIBUTION IN FREE-INTERACTION REGION
LAMINAR

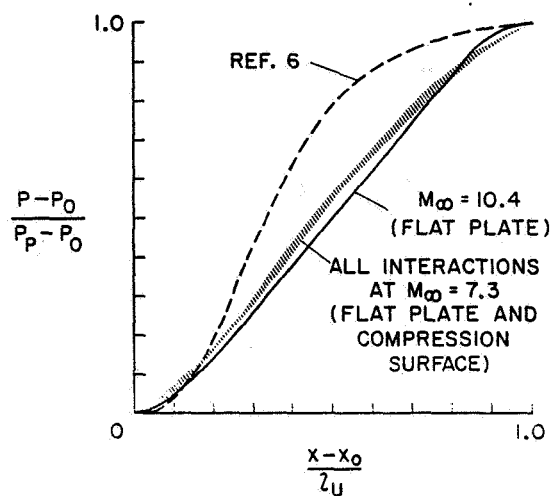


Figure 9(a)

PRESSURE DISTRIBUTION IN REATTACHMENT REGION
LAMINAR

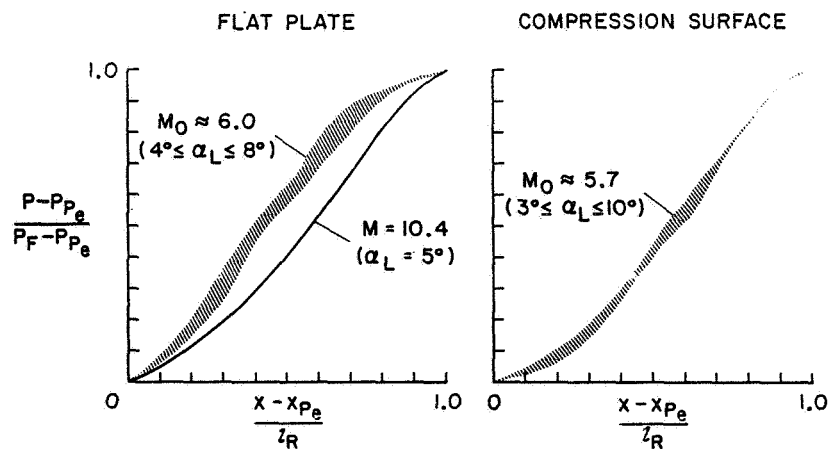


Figure 9(b)

~~CONFIDENTIAL~~

~~CONFIDENTIAL~~

PRESSURE DISTRIBUTION FOR UNSEPARATED INTERACTIONS
LAMINAR

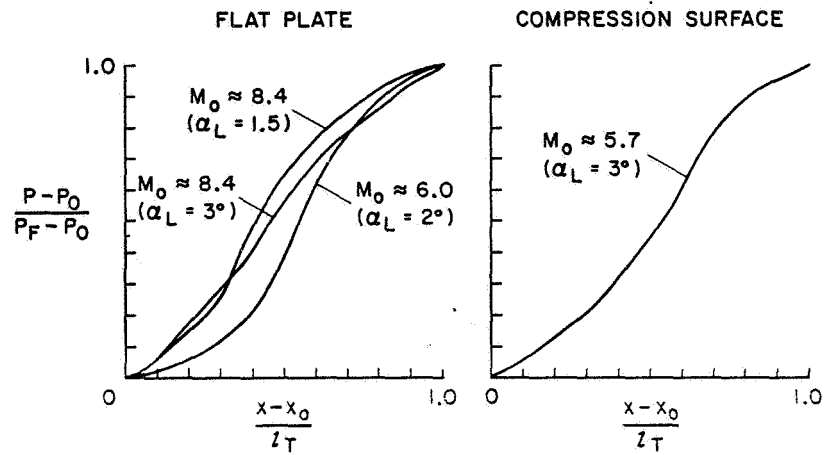


Figure 10(a)

PRESSURE DISTRIBUTION FOR UNSEPARATED INTERACTIONS
TURBULENT

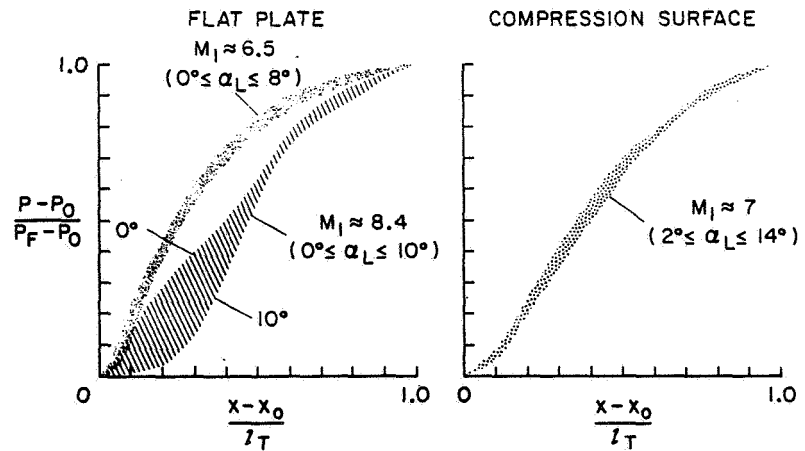


Figure 10(b)

CORRELATION OF FREE-INTERACTION LENGTH LAMINAR BOUNDARY LAYER

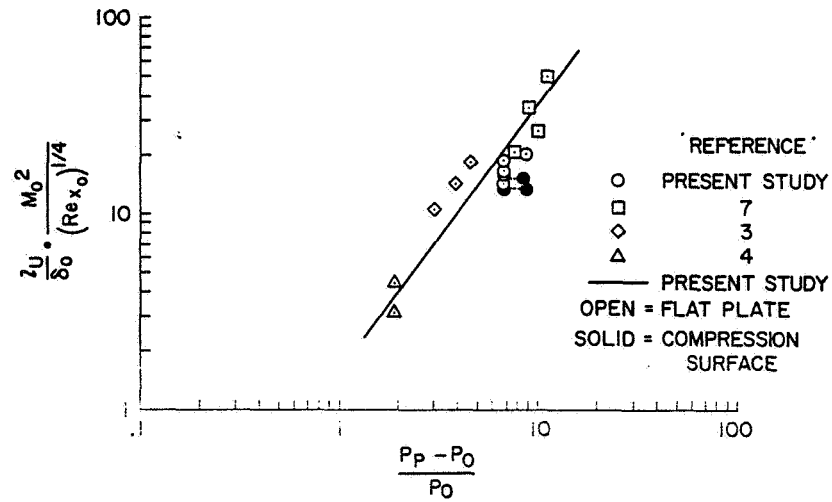


Figure 11(a)

CORRELATION OF FREE-INTERACTION LENGTH TURBULENT BOUNDARY LAYER

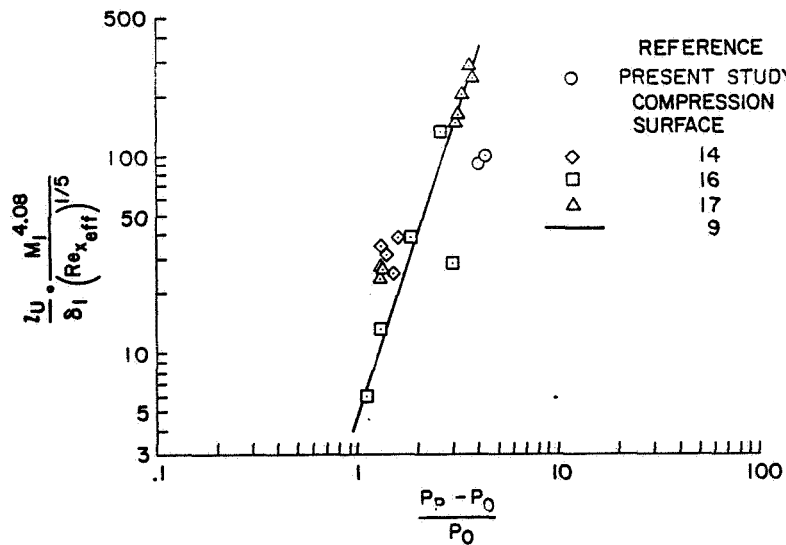


Figure 11(b)

~~CONFIDENTIAL~~

COMPARISON OF PLATEAU LENGTH DATA USING
HAKKINEN PARAMETERS
LAMINAR BOUNDARY LAYER

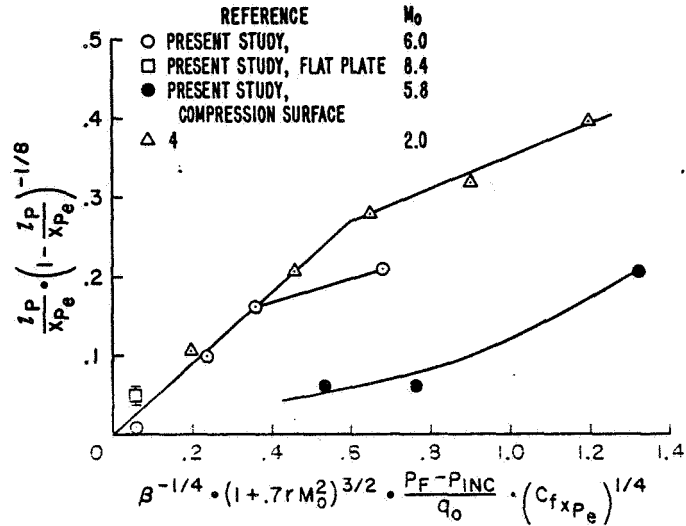


Figure 12

VARIATION OF INTERCEPT OF IMPINGING AND FIRST EMERGING
SHOCKS WITH PRESSURE COEFFICIENT ACROSS THE INTERACTION
TURBULENT BOUNDARY LAYER

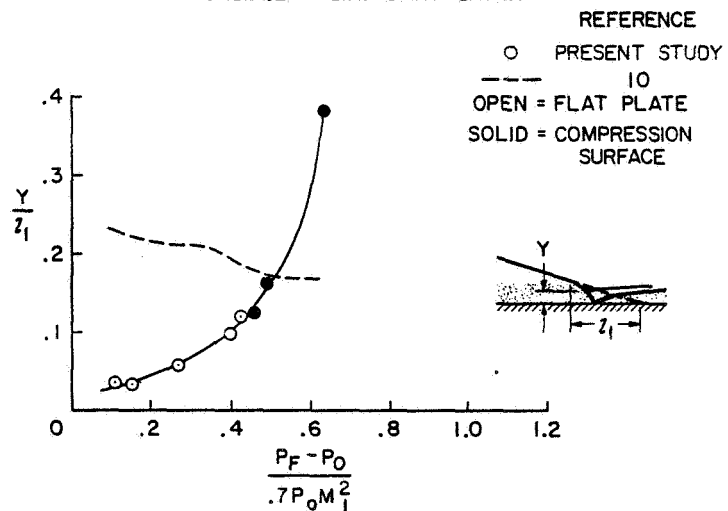


Figure 13

~~CONFIDENTIAL~~

VARIATION OF TOTAL INTERACTION LENGTH WITH STRENGTH
OF IMPINGING SHOCK
TURBULENT BOUNDARY LAYER

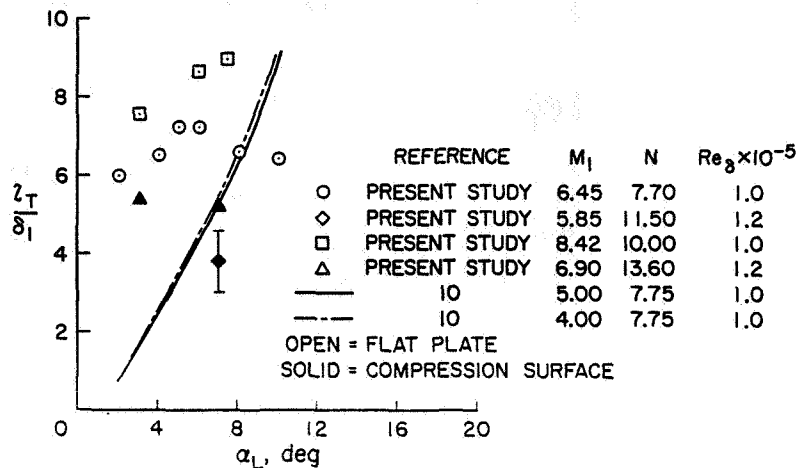


Figure 14

CORRELATION OF TOTAL INTERACTION LENGTH
LAMINAR BOUNDARY LAYER

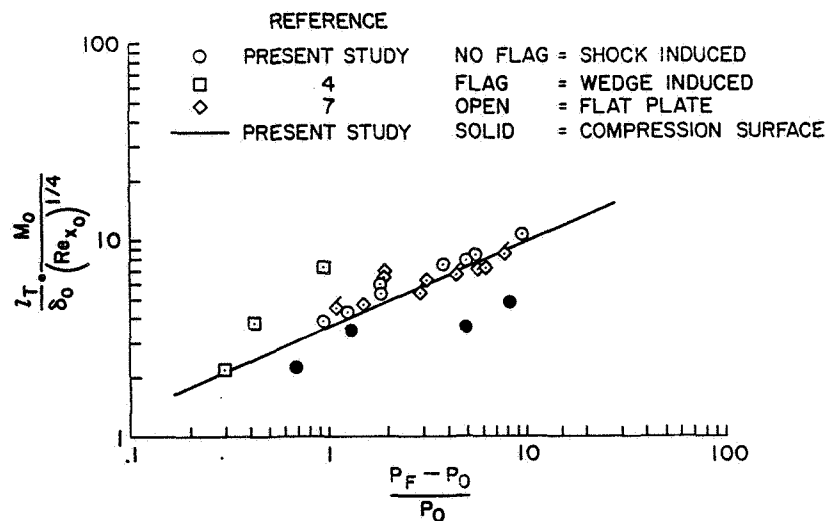


Figure 15

~~CONFIDENTIAL~~

~~CONFIDENTIAL~~

INTERACTION MODEL
LAMINAR BOUNDARY LAYER



Figure 16(a)

AAA377-16a

INTERACTION MODEL
LAMINAR BOUNDARY LAYER

$M_0 = 6.1$ $(Re/ft)_0 = 5.3 \times 10^5$ $\alpha_L = 8^\circ$

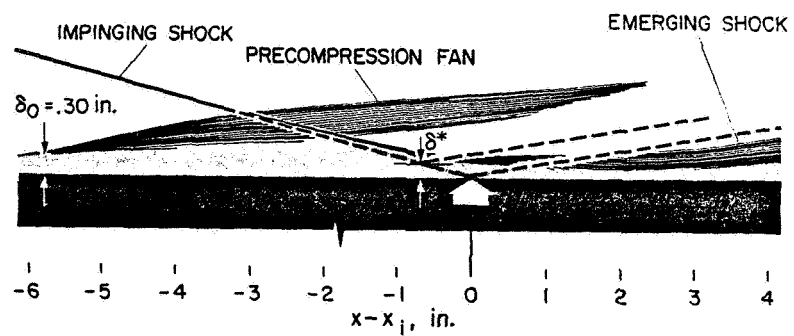


Figure 16(b)

~~CONFIDENTIAL~~

~~CONFIDENTIAL~~

INTERACTION MODEL
TURBULENT BOUNDARY LAYER

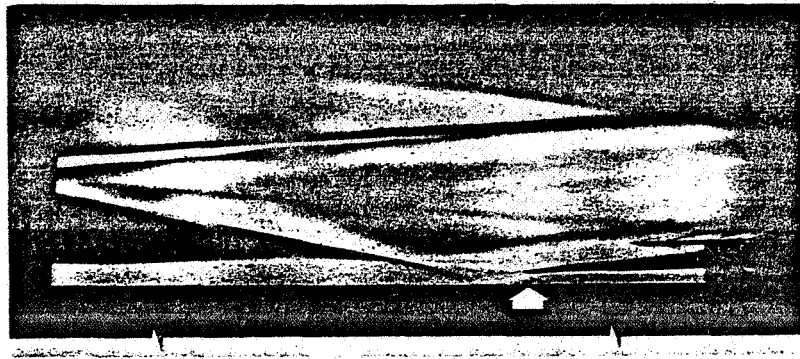


Figure 17(a)

AAA377-17a

INTERACTION MODEL
TURBULENT BOUNDARY LAYER

$M_1 = 6.5$ $(Re/ft)_1 = 3.1 \times 10^6$ $\alpha_L = 5^\circ$

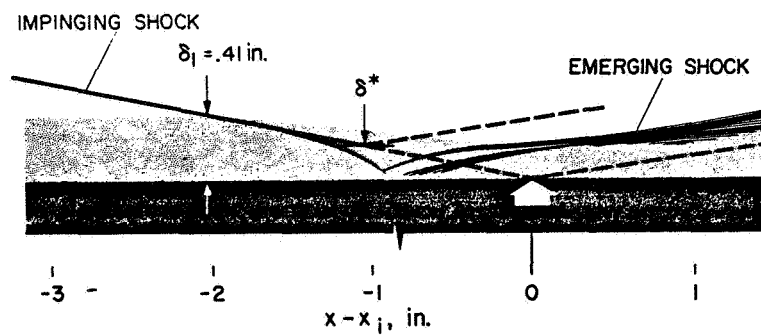


Figure 17(b)

~~CONFIDENTIAL~~

~~CONFIDENTIAL~~

PREDICTION OF SHOCK STRUCTURE BY METHOD
OF CHARACTERISTICS
TURBULENT BOUNDARY LAYER

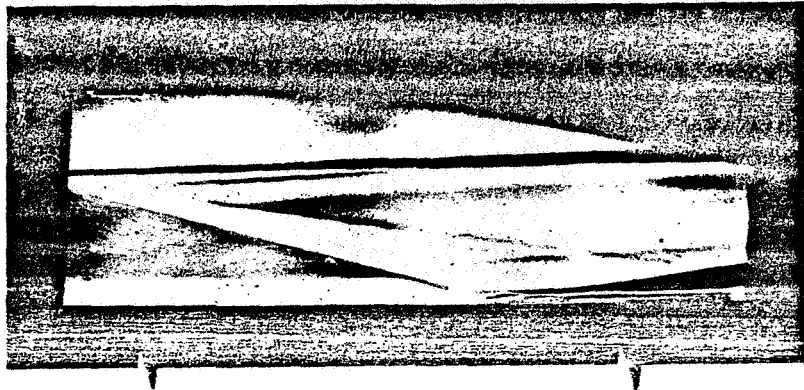


Figure 18(a)

AAA377-18a

PREDICTION OF SHOCK STRUCTURE BY METHOD
OF CHARACTERISTICS
TURBULENT BOUNDARY LAYER

$M_1 = 6.5$ $(Re/ft)_1 = 3.1 \times 10^6$ $\alpha_L = 8^\circ$

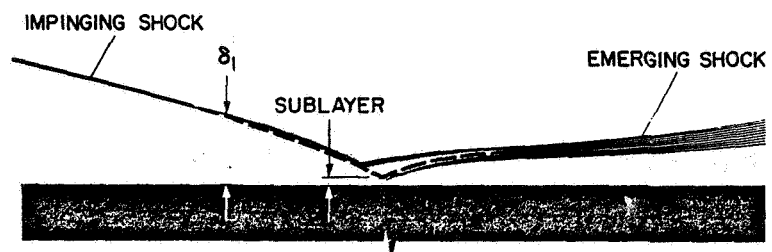


Figure 18(b)

~~CONFIDENTIAL~~

~~CONFIDENTIAL~~

23. FUEL INJECTION AND MIXING IN SCRAMJET COMBUSTORS

By John R. Henry
Langley Research Center

SUMMARY

The technology of fuel injection and mixing in scramjet combustors for both wall injection and stream injection has been examined in the light of new data presented in this paper. A possible approach to designing wall injectors is presented, together with a discussion of data on fuel-air distribution at the exits of several hydrogen-air combustors and some experimental evaluations of the empirical features of one of the parallel-mixing theories.

INTRODUCTION

Air-breathing propulsion systems under study for hypersonic flight generally involve a ramjet thermodynamic cycle utilizing either subsonic or supersonic combustion modes, or a combination of both. The aerothermodynamic problems of subsonic combustion engines from a research point of view have reached an advanced stage. However, there are areas in supersonic combustion technology which are only in early stages; components have been investigated at small scale (refs. 1 to 5) and experiments with small-scale complete engines have just started. This paper discusses recent work in the area of fuel injection and mixing in the scramjet combustor. The general problem is outlined in figure 1.

The sketch of figure 1 represents a combustor in which fuel is injected from both the walls and the stream in order to reduce the length of the combustor. Assume that the combustor has a height at the inlet of 1 foot; if all the fuel were injected from the wall, the combustor would have to be on the order of 10 to 20 feet long. If half of the fuel were injected from struts, then the length might be reduced to as little as 5 to 10 feet. Therefore, a trade-off exists between the cooling requirements and the drag of fuel-injection struts in a short combustor and the wall-cooling requirements and friction of a long combustor with no strut fuel injection. At the present time, there are not enough data in the literature to perform this trade-off study.

Some of the more important injection parameters in the problem are the injector configuration, Mach number M , dynamic pressure q , velocity V , and molecular weight M . Molecular weight depends on the type of fuel; only hydrogen will be considered in this paper. In the airstream, the same

~~CONFIDENTIAL~~

~~CONFIDENTIAL~~

parameters are important in addition to the inlet velocity gradient or profile dV/dy and the longitudinal pressure gradient dp/dx , which affects the mixing length.

A search of the literature has indicated that for wall injection, correlations of downstream measurements exist (ref. 2 and refs. 6 to 9) but no systematic method for designing the injectors is available. For stream injection parallel to the airstream, a number of semiempirical theories are available (refs. 10 to 19); the empirical features in general have not been evaluated fully. In this paper, a possible approach to designing wall injectors will be presented, together with a discussion of some flow studies in hydrogen-air combustion and some evaluations of the empirical features of one of the parallel-mixing theories.

SYMBOLS

A	cross-sectional area of duct, sq ft
C	constant in eddy viscosity relation
D_j	diameter of jet, ft
H	height of duct, ft
h	static enthalpy, Btu/lb
h_t	total enthalpy Btu/lb
K_{max}	maximum mass concentration at a given station, mass of injectant per unit total mass
M	Mach number
$N_{Sc,T}$	turbulent Schmidt number
p	static pressure, atm
p_t	total pressure, atm
q	dynamic pressure, $\frac{1}{2}\rho V^2$, lb/sq ft
r	radius, ft
$r_{1/2}$	term in eddy viscosity relation, jet "half radius" based on mean velocity, ft
S	entropy
T	static temperature, $^{\circ}R$

~~CONFIDENTIAL~~

T_t	total temperature, $^{\circ}\text{R}$
V	velocity, ft/sec
x,y,z	coordinates, ft
x_{mix}	mixing length, ft
β	fuel injection angle measured from the wall, deg
ϵ_T	eddy viscosity, lb-sec/sq ft
ϕ	equivalence ratio, $\frac{\text{Fuel-air ratio}}{0.0293}$
η_{ke}	kinetic energy efficiency
ρ	mass density, lb-sec ² /ft ⁴
M	molecular weight

Subscripts:

∞	free stream in front of vehicle
c	cowl lip station
1	station upstream of injectors at entrance to combustor
2	station downstream of injectors
3	station at exit of combustor
j	jet or injection gas
m	main stream
max	maximum
min	minimum
o	outer wall of annulus or duct wall.
i	inner wall of annulus
N	normal component

A bar over a symbol denotes average value.

~~CONFIDENTIAL~~

WALL INJECTION

The general flow phenomena produced by normal injection from a flat plate in a supersonic stream are illustrated in figure 2. The gas issuing from the orifice produces a complex three-dimensional flow system, as shown, which rapidly turns the jet in a downstream direction (see refs. 6 and 20). After traveling a distance downstream of about 10 jet diameters, the jet flow is essentially parallel to the plate, the penetration has reached a near-maximum value, and most of the disturbances have smoothed out.

The contour of a stream tube is shown by the long-dashed line (fig. 2); all the upstream airflow which becomes mixed with the injected gas by the time it reaches some reference downstream station (station 2) is contained within the stream tube. At the reference station, the penetration is defined as y_2 , the distance from the plate to the point of zero concentration of the injected gas (the dashed-line boundary). A typical cross-sectional shape for the stream tube at station 2 is shown; the cross section of the stream tube at station 1 is assumed to be similar to that at station 2. One approach to the determination of the design of an injector system is to assume that the dimension z_1 represents the required lateral spacing between adjacent injectors and that the dimension y_1 represents the height of a segment of airflow at the combustor entrance for which the orifice can supply fuel; therefore, the dimensions y_1 and z_1 identify the segment of airflow assigned to the single injector and they are the design parameters of interest. A design method has been developed in two steps. First, data in the literature (refs. 6, 7, 21, and 22) on the penetration y_2 have been correlated. Second, the dimensions z_1 and y_1 have been determined by using this correlation in conjunction with the results of reference 6, which permit the determination of the stream-tube area ratio between stations 1 and 2. A summary of the data on penetration at downstream stations used in the first step is presented in figure 3.

Penetration

Penetration is given as a function of downstream distance (fig. 3), both parameters being in terms of the jet diameter. Each curve is for a constant value of the ratio of jet dynamic pressure q_j to airstream dynamic pressure q_1 . All the data correspond to cold mixing and essentially no longitudinal pressure gradient; a wide range of injectant molecular weights is covered and a range of airstream Mach numbers from about 2.5 to 4.0. The data indicate that penetration is not sensitive to changes in injectant molecular weight or airstream Mach number.

For scramjet application, the dynamic-pressure ratios of interest extend up to about 4.0, and for x/D_j values greater than 10 the penetration is nearly constant in this area. In the design method a reference station at an x/D_j value of 30 was selected and the assumption was made that the maximum downstream penetration could be expressed as a unique function of dynamic-pressure ratio by using the values shown in the figure. The existence of this

~~CONFIDENTIAL~~

unique function has been noted by numerous investigators (for instance, see ref. 2). The next step is to use the function to evaluate the dimensions y_1 and z_1 .

The investigation of reference 6 was conducted with air-in-air mixing for the flat-plate case (fig. 2) with a free-stream Mach number of 4.0. A tracer-gas technique was used in conjunction with chromatograph measurements of concentration. Contour maps of parameters bounded by the locus of zero-concentration values, including maps of concentration and mass flow per unit area, were established at several downstream stations. At the selected reference station corresponding to an x/D_j value of 30 the maps were integrated to determine the total mass flow of air which originated at station 1 (fig. 2) upstream of the injector and which was contained within the mixing pattern at station 2 (cross section B-B). From these mass-flow values the stream-tube area at station 1 (cross section A-A) was determined as a function of the dynamic-pressure ratio q_j/q_1 . Assuming that the cross-sectional shape of the stream tube was the same at stations 1 and 2, the following equations were used to determine the three design parameters indicated:

$$\frac{y_1}{D_j} = \frac{\sqrt{\frac{y_1}{D_j} \frac{z_1}{D_j}}}{\sqrt{\frac{y_2}{D_j} \frac{z_2}{D_j}}} \left(\frac{y_2}{D_j} \right)$$

$$\frac{z_1}{D_j} = \frac{\sqrt{\frac{y_1}{D_j} \frac{z_1}{D_j}}}{\sqrt{\frac{y_2}{D_j} \frac{z_2}{D_j}}} \left(\frac{z_2}{D_j} \right)$$

$$\frac{q_j}{q_1} = 0.0293 \frac{4}{\pi} \frac{y_1}{D_j} \frac{z_1}{D_j} \frac{V_j}{V_1} \phi$$

where the square-root quantities in the numerators and denominators represent the square roots of the stream-tube areas at stations 1 and 2, respectively. The values for the parameter y_2/D_j (last term of the first equation) were obtained from figure 3 at an x/D_j value of 30. The values for the parameter z_2/D_j (last term of the second equation) were determined from the following equation:

~~CONFIDENTIAL~~

~~CONFIDENTIAL~~

$$\frac{z_2}{D_j} = \frac{\left(\frac{y_2}{D_j} \frac{z_2}{D_j} \right)}{\frac{y_2}{D_j}}$$

where the numerator on the right side of the equation is the area of the stream tube at station 2. The parameters y_1/D_j , z_1/D_j , and V_j/V_1 are given as a function of the dynamic-pressure ratio in figure 4.

Design Curves

The top set of curves of figure 4 gives the lateral spacing and the center set the penetration parameter at station 1. The bottom set represents a simple continuity relation for hydrogen-air combustion at an equivalence ratio of 1.0, in which the velocity ratio V_j/V_1 is the independent parameter. The solid curves correspond to the data of reference 6 at Mach 4. The dotted and dashed curves for Mach 3 and 5 were estimated by using the following procedure. The area ratios across oblique shocks with flow deflections equal to one-half the maximum value for attached two-dimensional shocks were computed for upstream Mach numbers of 3, 4, and 5. The stream-tube area ratios between stations 2 and 1 determined for Mach 4 were altered to obtain values for Mach 3 and 5 by using the oblique-shock area ratios as a basis for determining proportional factors. The Mach 3 and 5 curves were estimated in order to suggest the probability of a Mach number effect; however, experimental substantiation for the magnitude of the effect is needed.

In using the design curves of figure 4 the first step is to determine for a given set of conditions the value of V_j/V_1 ; the jet velocity can be determined from the jet Mach number and temperature, and the velocity V_1 depends on the conditions at the combustor entrance which are provided by the inlet. From the velocity ratio and M_1 the dynamic-pressure ratio can be determined by using the curves. Having determined the dynamic-pressure ratio, the required fuel pressure can be computed from q_1 and M_j . The penetration parameter y_1/D_j is evaluated next by using the curves and q_j/q_1 and M_1 . The combustor geometry at the entrance specifies the value of y_1 required to mix all the air and fuel; therefore, D_j can be determined directly and thus the injector diameter is found by using an appropriate value for the orifice coefficient. Finally the value of z_1/D_j is determined from the curves and thus the lateral spacing z_1 is found.

Another important parameter which has not been discussed yet is the mixing length required for complete combustion. Cold-mixing data in the literature on the decay of concentration with downstream distance (refs. 6, 7, and 22) were analyzed and the results are presented in figure 5. The data correlation shown in figure 5 is considered to have low accuracy for the following reasons: Data from the various sources did not always exhibit similar trends, the data

~~CONFIDENTIAL~~

had relatively high scatter, the measurements did not extend far enough downstream and did not include low values of q_j/q_1 , and the airstream Mach number and injectant molecular weight appeared to be strong parameters but there were insufficient data to establish these effects accurately. The limited amount of data available indicated the following proportionality:

$$K_{\max} \approx M_1 \mu^{0.39}$$

which was used to normalize the data to hydrogen and a value of M_1 of 2.5 as presented in figure 5. Additional experimental investigations are needed to furnish suitable design data on concentration decay.

Penetration With Combustion

Equivalence-ratio distributions measured at the exits of several circular combustor configurations are presented in references 2 and 3 for hydrogen-air combustion. The fuel-penetration values implied by the data were estimated by constructing step profiles of equivalence ratio which contained approximately the same amount of fuel flow as the experimental profiles. In the step profile the high equivalence-ratio value (near the wall) was fixed at the maximum measured value, and the low value (near the center line) was fixed at zero. The width of the step was considered to be the experimental value of penetration. Comparisons of experimental penetrations with values estimated by the design method of figure 4 are presented in figure 6. In the case of the estimated values for 30° injection, the penetration was assumed to be a function of the normal component of the injectant dynamic pressure.

For all configurations multiple rows of in-line injectors were used. For this type of injector experimental investigations reported in reference 2 show that the penetration of in-line injectors can be correlated by using the equivalent diameter of a single injector with the same mass-flow capacity. Further, correlations in reference 2 indicate that this type of injector configuration provides approximately 62 percent more penetration than a single injector with the equivalent diameter. In estimating the penetration, values determined by using figure 4 were increased by 62 percent.

The data of figure 6 show that the design method of figure 4 overpredicts the penetration for the 30° injectors by amounts ranging from 8 to 17 percent. For the normal-injection data, the method underpredicts by about 5 percent. Although these comparisons between data and analysis are not precise, the design curves appear to be in substantial agreement with the data of references 2 and 3. However, in view of the number of assumptions made in analyzing the data and in establishing the design method, confirmation of these results should be obtained through further research, particularly to investigate such effects as injectant molecular weight, adverse pressure gradient, and reaction.

~~CONFIDENTIAL~~

~~CONFIDENTIAL~~

Equivalence-Ratio Distribution

A typical example of the equivalence-ratio distribution measurements discussed in the preceding section is given in figure 7. The data were taken at the exit of a combustor of circular cross section during operation of the combustor with hydrogen-air combustion. Maximum and minimum values for each equivalence-ratio distribution were selected and distortion coefficients determined which were defined as follows:

$$\frac{\phi_{\max} - \phi_{\min}}{\bar{\phi}}$$

The distortion-coefficient data are summarized in figure 8.

Distortion coefficient is given as a function of the penetration parameter y_1/r_1 estimated by the design method discussed in a previous section. The solid symbols correspond to an injection angle of 30° from the wall, and the open symbols correspond to normal injection. The uniformity of the fuel-air distribution in the combustor has a direct effect on chemical combustion efficiency, particularly for overall equivalence ratios near 1.0. A goal for the distortion factor of about 20 percent has been selected because this would correspond to a combustion efficiency of better than 95 percent based on mixing considerations only, which is recognized as a satisfactory goal in this work. Since the 10 percent of the radius near the center of the duct handles only about 1 percent of the flow, a penetration of 90 percent was considered satisfactory.

The conical-cylindrical combustor (open circles) did not have enough penetration and had correspondingly high distortions. Difficulty was experienced in operating at equivalence ratios near 1.0 because of the interaction of the combustion with the upstream flow, which produced flow separation and instabilities.

The step-cylinder combustor (square symbols) had a downstream-facing step which produced stable flow, and at equivalence ratios near 1.0 the penetration was improved. However, the distortion values are still more than twice the goal value.

For the step-cone combustor (diamond and quarter-circle symbols), the total injector area was reduced by 25 percent compared with the step-cylinder in order to obtain better penetration by operating at higher fuel pressures. All four data points, which are near an equivalence ratio of 1.0, have very high distortion factors. The conical combustor (parachute symbol) with an area ratio of 2.5 had poor equivalence-ratio distribution.

If the data were given as a function of experimental values of penetration (see preceding section) instead of values estimated from the design curves, all the 30° injection data would be moved to lower penetration values by about 15 percent and the maximum penetration for the six data points corresponding to ϕ values ranging from 0.98 to 1.2 would have penetration values ranging

~~CONFIDENTIAL~~

from 0.70 to 0.73. This move would make it more apparent that a mismatch exists between the penetration and continuity in that equivalence ratios near 1.0 are obtained at penetration values which are too low. It appears that this problem could be solved by making appropriate changes to the injector diameters and total injection area, using the design curves as a guide. Furthermore, if the design changes were made, it is probable that the goal values of distortion coefficient and chemical combustion efficiency would be obtained.

Typical Injector Designs for M_∞ From 5 to 12

The design curves of figure 4 were used to compute sonic injector designs for normal wall injection for the flight Mach number range from 5 to 12. The combustor entrance was assumed to be annular in cross-sectional shape with a single row of injectors on both the inner and outer walls. The first step in this problem consisted of surveying the literature on hypersonic inlet experiments to determine the probable inlet performance for purposes of computing flow conditions at the combustor entrance by using the one-dimensional cycle performance program of reference 23. The survey and analysis of data in the literature was performed by Earl H. Andrews, Jr., of the Langley Research Center, and the results are presented in the next section.

Hypersonic Inlet Performance

Hypersonic inlets have high amounts of heat transfer to the walls which affect the inlet performance. Experimental data obtained in wind tunnels with scale inlet models generally correspond to arbitrary values of the wall heat transfer because of model and facility limitations. In comparing experimental performance data, it is desirable to eliminate the wall heat-loss variable entirely; a method suggested in reference 24 for accomplishing this end has been adopted in the study of this paper, and the method is outlined in figure 9.

The inlet thermodynamic cycle is illustrated in figure 9 by means of an enthalpy-entropy diagram. The flow is compressed in the inlet from the free-stream pressure p_∞ to the throat pressure p_1 , with a corresponding loss in energy by heat transfer to the walls and by radiation producing a reduction in stagnation enthalpy from $h_{t,\infty}$ to $h_{t,1}$. The total pressure in the inlet throat is $p_{t,1}$. For purposes of comparing inlet data from several sources, the flow at the throat is corrected to a reference adiabatic condition by using a hypothetical one-dimensional process corresponding to constant-pressure heat addition. The total enthalpy and total pressure in the throat then become $h_{t,\infty}$ and $p'_{t,1}$, respectively. The measure of inlet performance used herein is kinetic-energy efficiency, the definitions of which are given in figure 9 for both the test condition and the corrected reference adiabatic-wall case. The heat losses between stations ∞ and 1 cause large losses in the kinetic-energy efficiency which are nearly completely regained by correcting to the reference adiabatic case. The method of correction has some justification other than analytical convenience in that generally a major portion of the heat loss in the inlet is absorbed by the fuel in regenerative heat exchangers and

~~CONFIDENTIAL~~

reintroduced to the thermodynamic cycle when the fuel is injected near the inlet throat.

Inlet performance data from reference 5 and references 24 to 32 were analyzed, were corrected as described in the preceding paragraph, and are presented in figure 10. All the data were experimental except those from references 5, 25, and 26, which were analytical with some measure of experimental substantiation. In general, the data were presented in the references as mass-weighted averages with the exception of those in references 5 and 26, which were mass-momentum averaged. If velocity distributions for the flow in the throat were available, the mass-weighted averages and continuity were determined independently for this paper as checks on data accuracy. Real-gas procedures were used to make one-dimensional corrections to obtain the values of figure 10.

The increase in kinetic-energy efficiency obtained by correcting from nonadiabatic experimental values to reference adiabatic values is given for two cases in figure 10 (the circular symbols at Mach 15.5). From the size of the corrections, the desirability of correcting to a reference condition is evident. The square symbols (which represent axisymmetric inlets proposed in Phase I of the NASA hypersonic research engine (HRE) project) and the diamond symbols (three-dimensional fixed-geometry inlets) following the same trends as the square symbols correspond to small-scale inlets and relatively low Reynolds number performance. Analyses of Reynolds number effects in reference 33 indicate that if these performances were corrected to Reynolds numbers corresponding to flight dynamic pressures between 1000 and 2000 psf and inlets with diameters of 5 to 10 feet, the performances would lie between the long-dashed lines of figure 10. These lines therefore represent an achievable band of performance representative of large-scale inlets and based on reference adiabatic kinetic-energy efficiency values. The long-dashed lines in addition to a kinetic-energy efficiency of 1.00 (for reference) were used in the injector design problem for M_∞ from 5 to 12.

Engine-Cycle Analysis

The inlet performance predicted for large-scale inlets and described in the preceding section served as input for the engine-cycle computations in addition to the assumptions of a trajectory corresponding to a value of q_∞ of 1800 psf and a fixed inlet contraction ratio of 12.5. This contraction ratio provides a major portion of the thrust that might be obtained by use of variable-geometry inlets with higher contraction-ratio potential; however, a contraction ratio of 12.5 might necessitate some amount of variable geometry for starting purposes at the lower flight Mach numbers. A summary of the input data for the cycle analysis is contained in table I. The schedule for inlet mass-capture ratio A_∞/A_c is typical for a Mach 10 inlet. Results of the cycle calculation which affect the injector designs are given in table II. The cycle calculations were performed for flight Mach numbers from 4 to 12; however, the results indicated that there might be some practical difficulties in obtaining supersonic combustion at Mach 4. Therefore, the injectors were designed for the range from Mach 5 to 12.

~~CONFIDENTIAL~~

Injector Designs

The injector design values determined by using figures 4 and 5 are presented in figures 11 and 12 as a function of flight Mach number. Figure 11 shows that for the curves corresponding to the lowest inlet performance the lateral spacing varies from 6.8 to 6.0 jet diameters, and the jet diameter varies from 0.32 to 0.47 of half of the gap between the inner and outer walls of the annulus at station 1. Figure 12 shows that the corresponding fuel pressures vary from 160 psia at Mach 5 to a maximum of 196 psia at Mach 8 to 114 psia at Mach 12. The mixing-length predictions, which as previously mentioned may be significantly in error, range from 12 to 26 times one-half of the gap between the inner and outer walls. The designs for Mach 8 submitted by the AiResearch Manufacturing Company in Phase I of the NASA-HRE project (ref. 26) correspond to a larger jet diameter at a wider lateral spacing. The AiResearch design should provide fuel penetration beyond the center of the annulus, or overlapping mixing patterns in the radial direction; there is no reason to believe this would be detrimental. According to figure 4, the larger circumferential spacing would be detrimental, although there are no data with combustion to indicate the accuracy of the predictions for z_1/D_j of figure 4.

STREAM INJECTION

The discussion in the introduction in connection with figure 1 indicates that large combustors may require injection from strut-mounted fuel injectors in a direction parallel to the airflow. Recent work at the Langley Research Center has contributed in this area by using new experimental air-in-air, parallel-mixing data to evaluate the empirical constants in the mixing-combustion theory of reference 12.

Theory

The theory of reference 12 was used by the Marquardt Corporation in the preliminary design proposed in Phase I of the NASA-HRE project (ref. 34). There are a number of turbulent mixing theories available in the literature; however, the one of reference 12 was selected for these investigations because combustion equations are included as well as the mixing theory, and it is particularly convenient for scramjet work. The theory employs coordinate transformations, equilibrium chemistry, no considerations of chemical kinetics, and a numerical technique for predicting mixing and combustion in axisymmetric or two-dimensional flow. The theory provides for up to a second-order pressure gradient in the axial direction and employs an eddy viscosity model defined as follows:

$$\epsilon_T = Cr_{1/2}(\rho V)_t$$

The theory also provides for nonunity turbulent Prandtl, Lewis, and Schmidt numbers.

~~CONFIDENTIAL~~

~~CONFIDENTIAL~~

An example of a combined mixing and combustion flow field computed by using the theory is given in figure 13 for typical conditions at the entrance to a combustor for a Mach 8 flight condition. The jet of sonic hydrogen at a stagnation temperature of 1200° R is surrounded by airflow at the indicated conditions. Contour curves of constant equivalence ratio are given. The solid curves were computed for a value of the eddy viscosity constant of 0.065, as recommended in reference 12 for mixing with hydrogen-air combustion. The mixing length is defined as the distance from the injector to the point where the equivalence ratio of 1.0 line crosses the center line, since any point downstream of this location would have an equivalence ratio of less than 1.0 and combustion would have been completed. If the value of the eddy viscosity constant is reduced by a factor of 2 to 0.032, the mixing length is doubled as shown by the dashed curves. Therefore, it is important to select as accurate a value of the constant as possible for a given situation. Experimental evaluations of the eddy viscosity constant are discussed in the following section.

Experimental Evaluation of Theory

Coaxial mixing.- An experimental investigation of coaxial, air-in-air mixing using a tracer-gas technique (ethane) which permitted concentration measurements has been completed at the Langley Research Center by Marvin G. Torrence and James M. Eggers. The basic model consisted of a 0.96-inch-diameter circular jet at a Mach number of 0.90 surrounded by a 7.0-inch-diameter outer stream at Mach 1.3. The total temperature of both streams was near ambient temperature. Radial surveys of total pressure, static pressure, and ethane gas concentration were performed at seven axial stations extending 49 center-jet diameters downstream. Gas samples were withdrawn with a circular probe operating in a near-choked condition and were analyzed with a gas chromatograph. The metered mass-flow rates of the center jet agreed within ± 5 percent with values obtained by integrating pressure and concentration profiles at the several stations.

Analyses of the data performed by James M. Eggers lead to the following observations:

(a) The measured length of the concentration potential core was 87 percent greater than the length predicted by the correlation of reference 14, which expresses concentration potential-core length as a unique function of mass-flux ratio. The 87-percent discrepancy is within the scatter of data used in formulating the correlation of reference 14; data scatter possibly may have been produced by the effects of nozzle-exit lip thickness, initial turbulence levels, and initial profile shapes.

(b) The decay of the center-line concentration downstream of the end of the potential core was inversely proportional to x^2 , in agreement with the correlations of reference 14.

(c) A single value of the constant in the eddy viscosity relation of reference 12 did not correlate the data satisfactorily over the entire mixing field.

In figures 14 and 15 the experimental velocity and concentration distributions, respectively, are compared with the theory of reference 12 using the most favorable values of the empirical constants. Figure 14 shows that a value of the eddy viscosity constant of 0.0025 was required in the near field, which extended 16.2 jet diameters downstream. A value of 0.0060 was required in the far field. The use of these values, however, produced very satisfactory agreement of the theory with the data. The discrepancy of about 100 fps between data and theory at the 49 jet-diameter station was caused by the ambient air mixing with the Mach 1.3 airstream, which is an extraneous effect.

Similar correlations of concentration profiles in figure 15 indicate satisfactory agreement between theory and data. In the case of concentration decay, the value of turbulent Schmidt number exerts an influence. The data correlation was obtained in the near field by assuming a value of 1.0; however, in the far field a value of 0.5 was required to obtain a correlation. The reduced value of Schmidt number in the far field implies a reduced rate of momentum transfer compared with mass transfer.

The eddy viscosity constant of 0.0060 used to correlate the air-in-air mixing data is less than 1/10 of the value recommended in reference 12 for hydrogen-air mixing with combustion. Analyses of the data of reference 14 using the theory of reference 12 suggest that the high value of eddy viscosity constant obtained in reference 12 was primarily a result of not considering the changes in velocity in the mixing region. Correlation of the velocity distributions of the present data resulted in a value of the eddy viscosity constant C of 0.006, and in the case of the reference 14 data, a value on the order of 0.010 was required. In correlating the concentration decay data, the effects of low values of C were offset in both cases by using Schmidt number values less than 1.0. Other variables which may affect the required value of eddy viscosity constant are the injectant molecular weight and Mach number, chemical reaction, and the initial amount of boundary layer in the flow.

Two-dimensional mixing.—Two-dimensional momentum mixing data taken and analyzed by John P. Weidner of the Langley Research Center are summarized in figure 16. The model sketched at the top of the figure consisted of a two-dimensional duct with a width approximately equal to four times the height. The main airstream entered the duct at a Mach number of 4.0 and a total pressure of 150 psia. Three injection nozzles were installed at the bottom of the duct for the purpose of producing the shock system indicated. The first injector nozzle, which furnished all the injection air that became involved in the mixing process within the limits of the measuring stations, was designed to provide an exit Mach number of 4.5 at a total pressure of 500 psia. Static- and pitot-pressure surveys were made at the five indicated stations, three stations in the bay upstream of the intersection of the two 6° shocks and two stations in the downstream bay. The measured Mach numbers at the edge of the mixing region in both streams are listed in table III. Small streamwise pressure gradients are noted in both bays.

The measured velocity distributions are indicated by the data points in figure 16. The faired curve through the data at the station corresponding to an x/H value of 0.77 represents the input for the theory of reference 12. The curves for the other four stations represent results computed by using

~~CONFIDENTIAL~~

the theory. In the two-dimensional flow of this experiment, the values of $r_{1/2}$ and the eddy viscosity constant are arbitrary; however, the product of the two quantities is significant. From station 0.77 to the location of the 6° shocks, accurate data correlation was obtained by using a value of the eddy viscosity constant of 0.0017 in conjunction with an initial value of $r_{1/2}$ at station 0.77 of 0.139H. It is noteworthy that the theory provided the proper mixing rate for the very large wake caused by the boundary layer discharged from the splitter plate. The theoretical calculations through the two 6° shocks were made by using a slab technique; the static pressure and flow direction were assumed to be uniform on the downstream side. From the location of the shocks to station 6 a value of eddy viscosity constant of 0.0085 correlated the data satisfactorily, as shown in figure 16.

However, further analysis of the data indicates that the value of 0.0017 for the eddy viscosity constant could have been continued through to station 6 by assuming that the reduction in the width of the mixing region caused by the 6° shocks was approximately one-half that indicated by the slab calculation. The resulting data correlations are as accurate as those of figure 16. This alternate interpretation of the data is preferred for the following reasons:

(a) There is no known reason for the eddy viscosity between the shocks and station 6 to differ from that between station 0.77 and the shocks; both regions are in the near field.

(b) The slab method is only an approximation.

(c) The mixing region in the vicinity of the 6° shocks might be expected to be subject to high rates of mass influx caused by very high velocity gradients similar to shock—boundary-layer interactions (see ref. 35).

This phenomenon requires further investigation since combustors operating over a range of conditions necessarily will contain shock waves.

CONCLUDING REMARKS

The technology of fuel injection from both the wall and the stream has been examined in the light of new data presented in this paper. With regard to fuel injection from the wall, an approximate injector design method was established by using cold-mixing data. A comparison of the method with combustion data indicates agreement within about 15 percent; however, research is needed to confirm this result, particularly with regard to such effects as injectant molecular weight, adverse pressure gradient, and reaction. Relative to parallel fuel injection in the stream, a theory which computes mixing and combustion simultaneously was investigated. The empirical features required in the turbulent mixing part of the theory were evaluated for coaxial and two-dimensional parallel air-in-air mixing. Further research is required to evaluate the effects of injectant molecular weight, adverse pressure gradient, air-stream Mach number, reaction, and shocks crossing the mixing region.

~~CONFIDENTIAL~~

REFERENCES

1. Yates, C. L.; Billig, F. S.; and Dugger, G. L.: Experimental Results and Data Analysis Techniques of a Hydrogen-Fueled Supersonic Combustor. NASA CR-531, 1966.
 2. Gen. Elec. Co.: Analytical and Experimental Evaluation of the Supersonic Combustion Ramjet Engine. Vol. II - Component Evaluation. AF APL-TR-65-103, Vol. II, U.S. Air Force, Dec. 1, 1965.
 3. Kenworthy, Milton J.; Stanforth, Charles M.; Colley, William C.; et al.: Investigation of Instrumentation and Simulation Techniques for the Supersonic Combustion Process. AFAPL-TR-66-76, U.S. Air Force, Oct. 1966.
 4. Billig, F. S.; and Grenleski, S. E.: Experimental Studies of Hydrogen-Air Ignition in a Supersonic Combustor. TG-848, Appl. Phys. Lab., Johns Hopkins Univ., Aug. 1966.
 5. Anon.: Hypersonic Ramjet Experiment Project - Phase I. Vol. III - Appendix B. AiResearch Rept. No. AP-66-0168-3 (Contract NAS1-5116), Garrett Corp., [1966].
 6. Torrence, Marvin G.: Concentration Measurements of an Injected Gas in a Supersonic Stream. NASA TN D-3860, 1967.
 7. Zukoski, Edward E.; and Spaid, Frank W.: Secondary Injection of Gases Into A Supersonic Flow. Preprint No. 64-110, Am. Inst. Aeron. Astronaut., Jan. 1964.
 8. Anon.: Hypersonic Ramjet Experiment Project - Phase I. Vol. II - Appendix A. AiResearch Rept. No. AP-66-0167-2 (Contract NAS1-5116), Garrett Corp., [1966].
 9. Brown, M. L.: Annual Report, Aerospace Propulsion Program. Vol. VI - Supersonic Combustion Ramjet. Rept. 5883 (Contract AF 33(616)-7046), The Marquardt Corp., Mar. 15, 1962.
 10. Eggers, James M.: Velocity Profiles and Eddy Viscosity Distributions Downstream of a Mach 2.22 Nozzle Exhausting to Quiescent Air. NASA TN D-3601, 1966.
 11. Morgenthaler, John H.: Supersonic Mixing of Hydrogen and Air. NASA CR-747, 1967.
 12. Edelman, R.: Diffusion Controlled Combustion for Scramjet Application. Part I - Analysis & Results of Calculations. Tech. Rept. 569 (Contract NAS1-5117), Gen. Appl. Sci. Lab., Inc., Dec. 1965.
- Hopf, H.; and Fortune, O.: Diffusion Controlled Combustion for Scramjet Application. Part II - Programmer's Manual. Tech. Rept. 569 (Contract NAS1-5117), Gen. Appl. Sci. Lab., Inc., Dec. 1965.

CONFIDENTIAL

~~CONFIDENTIAL~~

13. Schetz, Joseph A.; and Gilreath, Harold E.: Tangential Slot Injection in Supersonic Flow. AIAA Paper No. 67-198, Jan. 1967.
14. Zakkay, Victor; Krause, Egon; and Woo, Stephen D. L.: Turbulent Transport Properties for Axisymmetric Heterogeneous Mixing. ARL 64-103, U.S. Air Force, June 1964. (Available from DDC as AD 604 008.)
15. Zakkay, Victor; and Krause, Egon: The Radial Variation of the Eddy Viscosity in Compressible Turbulent Jet Flows. ARL 65-89, U.S. Air Force, May 1965. (Available from DDC as AD 617 701.)
16. Forstall, Walton, Jr.; and Shapiro, Ascher H.: Momentum and Mass Transfer in Coaxial Gas Jets. J. Appl. Mech., vol. 17, no. 4, Dec. 1950, pp. 399-408.
17. Ragsdale, Robert G.; and Edwards, Oliver J.: Data Comparisons and Photographic Observations of Coaxial Mixing of Dissimilar Gases at Nearly Equal Stream Velocities. NASA TN D-3131, 1965.
18. Weinstein, Herbert; and Todd, Carroll A.: A Numerical Solution of the Problem of Mixing of Laminar Coaxial Streams of Greatly Different Densities - Isothermal Case. NASA TN D-1534, 1963.
19. Channapragada, R. S.; and Woolley, J. P.: Turbulent Mixing of Parallel Compressible Free Jets. AIAA Paper No. 65-606, June 1965.
20. Sterrett, James R.; and Barber, John B.: A Theoretical and Experimental Investigation of Secondary Jets in a Mach 6 Free Stream With Emphasis on the Structure of the Jet and Separation Ahead of the Jet. Presented at the Separated Flows Specialists Meeting, Fluid Dynamics Panel (Brussels, Belgium), AGARD, May 9-11, 1966.
21. Vranos, Alexander; and Nolan, James J.: Supersonic Mixing of Helium and Air. Bumblebee Rept. No. TG 63-53, Appl. Phys. Lab., Johns Hopkins Univ., June 1964, pp. 131-161.
22. Orth, Richard C.; and Funk, John A.: An Experimental and Comparative Study of Jet Penetration in Supersonic Flow. AIAA Paper No. 67-225, Jan. 1967.
23. Jackson, Robert J.; and Wang, Tennyson T.: Computer Program Description - Ramjet and Scramjet Cycle Performance. AiResearch Rept. No. AP-1001-1 (Contract NAS1-5116), Garrett Corp., [1966].
24. Heins, A. E.; and Hartill, W. R.: Shock Tunnel Testing of Scramjet Inlets. Rept. 5991 (Contract AF 33(657)-8491), The Marquardt Corp., May 24, 1963.
25. Anon.: Ramjet Preliminary Design Report. R66FPD70 (Contract NAS1-5115), Advan. Engine Technol. Dept., Gen. Elec. Co., Feb. 28, 1966.
26. Anon.: Hypersonic Ramjet Experiment Project - Phase I. Vol. I. AiResearch Rept. No. AP-66-0168-1 (Contract NAS1-5116), Garrett Corp., [1966].

~~CONFIDENTIAL~~

~~CONFIDENTIAL~~

27. Hartill, W. R.: Analytical and Experimental Investigation of a Scramjet Inlet of Quadriform Shape. AFAPL-TR-65-74, U.S. Air Force, Aug. 1965.
28. Gen. Elec. Co.: Advanced Air-Breathing Engines. Vol. II: Experimental Investigation. APL-TDR-64-21, Vol. II, U.S. Air Force, May 7, 1964.
29. Anon.: Quarterly Review of: Analytical and Experimental Evaluation of the Supersonic Combustion Ramjet Engine. BPSN 4(6399-615E) (Contract AF 33(615)-1586), Advan. Engine Technol. Dept., Gen. Elec. Co., Feb. 10, 1965.
30. Gen. Elec. Co.: Analytical and Experimental Evaluation of the Supersonic Ramjet Engine. Vol. III - Component Evaluation. AF APL-TR-65-103, Vol. III, U.S. Air Force, Dec. 1, 1965.
31. Keirse, J. L.: A Study of the Aerodynamics of Scramjet Engine Inlets. TG-732, Appl. Phys. Lab., Johns Hopkins Univ., Sept. 1965. (Available from DDC as AD 370 936.)
32. Keirse, J. L.; and Snow, M. L.: Modular Inlet Investigation. Quarterly Report, Aeronautics Division, Research and Development. AQR/66-1, Appl. Phys. Lab., Johns Hopkins Univ., Jan.-Mar. 1966.
33. Kepler, C. E.; Clossen, J. W.; and Demarest, P. E.: Hypersonic Inlet Investigations Including Tests to Mach 8.7 and Theoretical Analyses to Mach 15. ASD TR 61-137, U.S. Air Force, June 1961.
34. Bendot, J. G.: Preliminary Design Report - Hypersonic Ramjet Research Engine Project. Vol. I: MA-165 Design Description. Rept. 6102, Vol. I (Contract NAS 1-5117), The Marquardt Corp., Feb. 28, 1966.
35. Pinckney, S. Z.: Semiempirical Method for Predicting Effects of Incident-Reflecting Shocks on the Turbulent Boundary Layer. NASA TN D-3029, 1965.

~~CONFIDENTIAL~~

~~CONFIDENTIAL~~

TABLE I.- INPUT DATA FOR RAMJET CYCLE PROGRAM

M_∞	A_∞/A_c	A_∞/A_1	Alt, ft	p_∞ , atm	T_∞ , °K	T_j , °K	V_j , fps	η_{ke}
4	0.45	5.6	59 400	0.0734	217	165	3040	1.00, 0.98, 0.97
6	.85	10.6	76 400	.0327	220	333	4170	1.00, 0.98, 0.967
8	.98	12.2	88 800	.0184	224	667	5870	1.00, 0.98, 0.965
10	1.0	12.5	98 400	.0118	226	1000	7170	1.00, 0.98, 0.962
12	1.0	12.5	106 400	.00823	229	1000	7170	1.00, 0.98, 0.96

TABLE II.- RESULTS OF RAMJET CYCLE CALCULATIONS

M_∞	η_{ke}	M_1	p_1 , atm	T_1 , °K	V_1 , fps	V_j/V_1
4	1.00	2.16	1.14	473	3070	0.99
	.98	1.91	1.36	528	2870	1.06
	.97	1.78	1.50	558	2740	1.11
6	1.00	3.23	1.07	589	5110	0.81
	.98	2.77	1.38	716	4820	.86
	.967	2.51	1.62	804	4600	.91
8	1.00	4.51	0.667	617	7300	0.80
	.98	3.71	.955	838	6940	.85
	.965	3.25	1.20	1009	6630	.88
10	1.00	5.81	0.426	623	9450	0.76
	.98	4.52	.690	963	9020	.80
	.962	3.76	.959	1273	8570	.84
12	1.00	7.10	0.290	627	11580	0.62
	.98	5.18	.538	1111	11070	.65
	.96	4.15	.813	1592	10500	.68

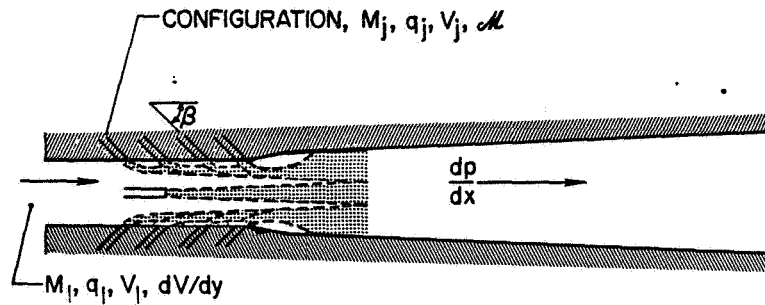
TABLE III.- MACH NUMBERS AT EDGE OF MIXING REGION

FOR TWO-DIMENSIONAL MIXING EXPERIMENT

Station, x/H	M_m	M_j
0.77	3.56	4.47
2.31	3.45	4.33
3.62	3.25	4.12
5.62	2.82	3.62
6.00	2.85	3.68

~~CONFIDENTIAL~~

SCRAMJET FUEL INJECTION FEATURES AND PARAMETERS



STATUS

WALL INJECTION.....DATA CORRELATION
STREAM INJECTION.....SEMIEMPIRICAL THEORIES

Figure 1

SCHEMATIC OF FLOW FIELD WITH WALL INJECTION

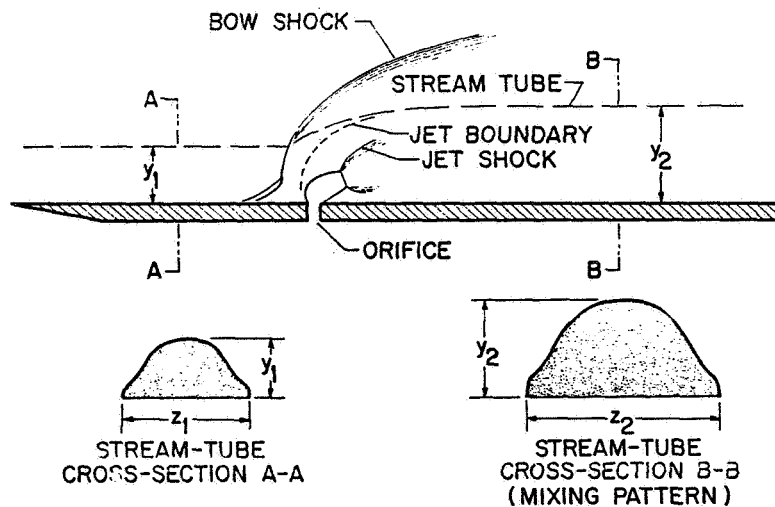


Figure 2

~~CONFIDENTIAL~~

PENETRATION DATA

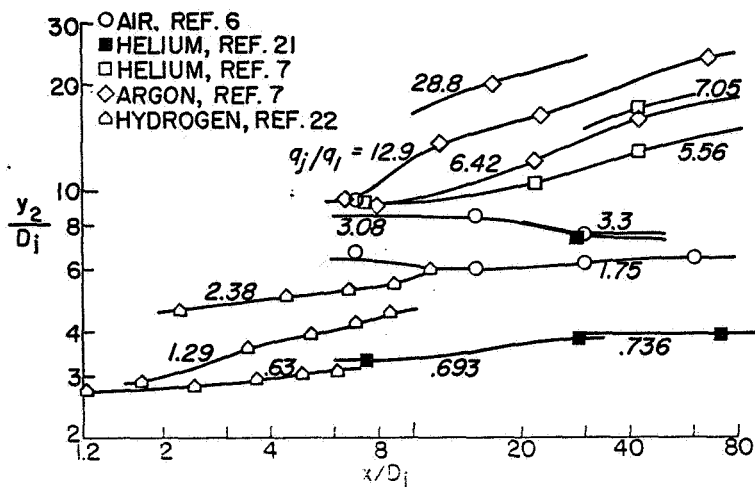


Figure 3

DESIGN DATA FOR NORMAL INJECTION REFERENCE STATION, $x/D_j = 30$

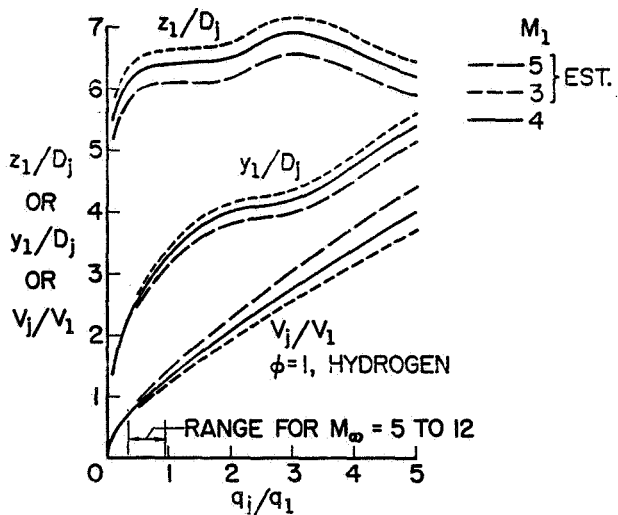


Figure 4

~~CONFIDENTIAL~~

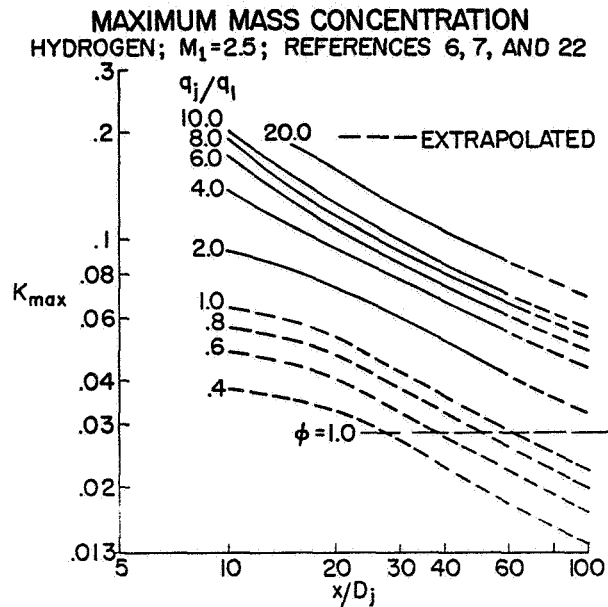


Figure 5

ACCURACY OF PENETRATION ESTIMATES

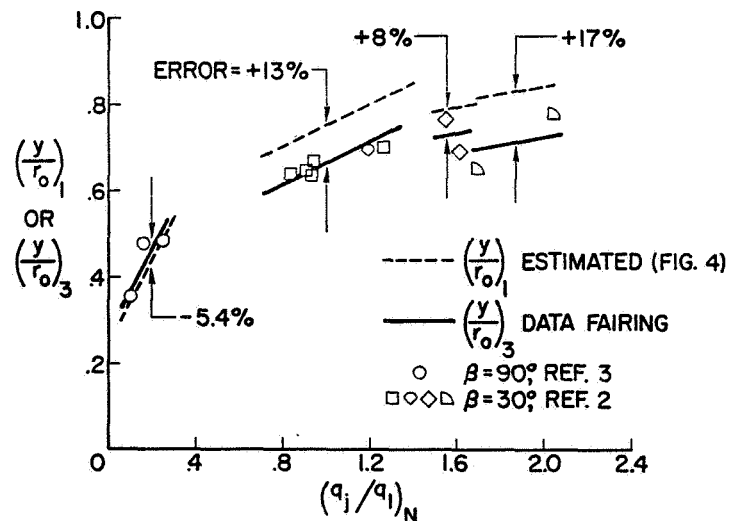


Figure 6

~~CONFIDENTIAL~~

CONFIDENTIAL

EQUIVALENCE-RATIO DISTRIBUTION COMBUSTOR EXIT; REFERENCE 2

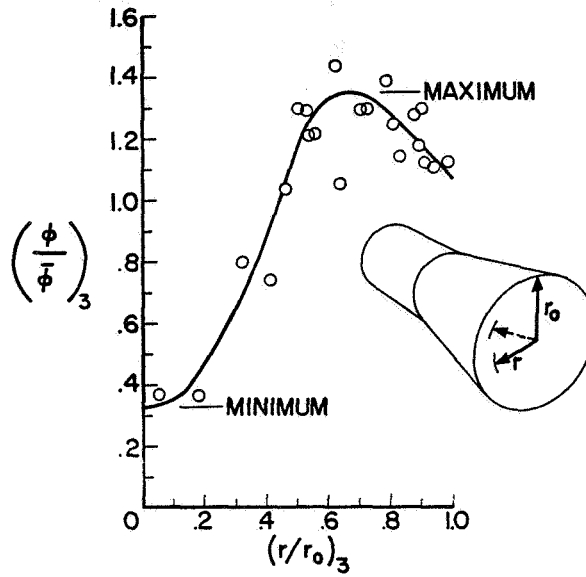


Figure 7

EQUIVALENCE-RATIO DISTORTION AT COMBUSTOR EXIT MULTIPLE INJECTORS IN LINE

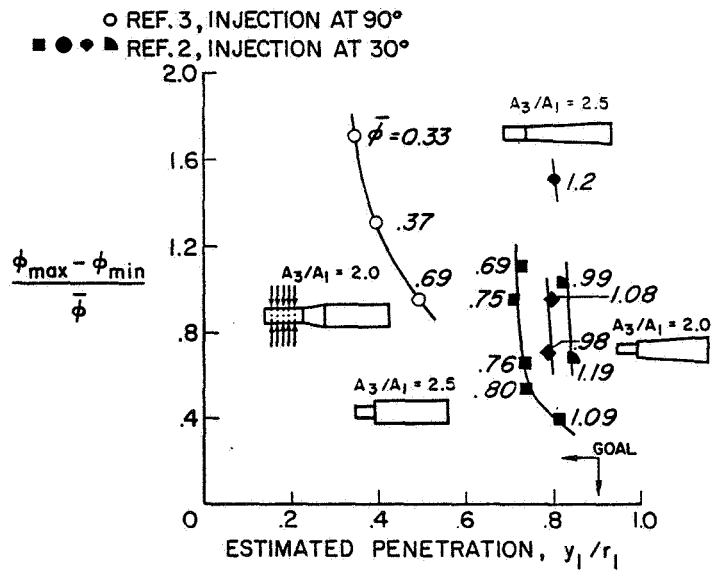


Figure 8

CONFIDENTIAL

~~CONFIDENTIAL~~

INLET CYCLE

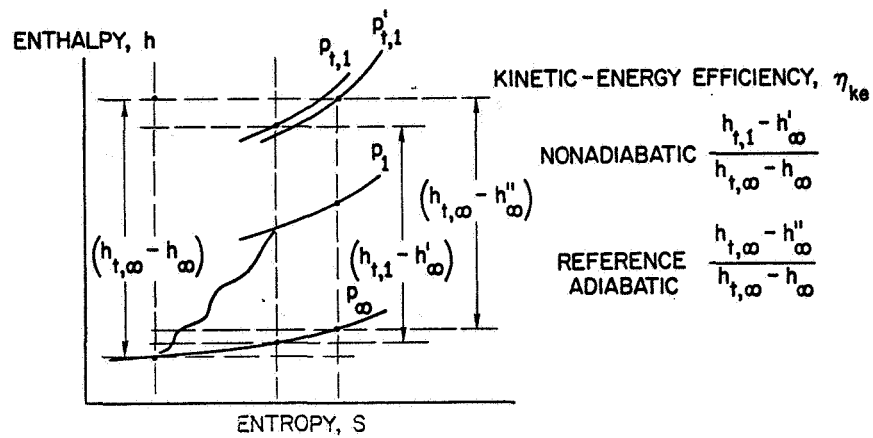


Figure 9

REFERENCE ADIABATIC KINETIC-ENERGY EFFICIENCY

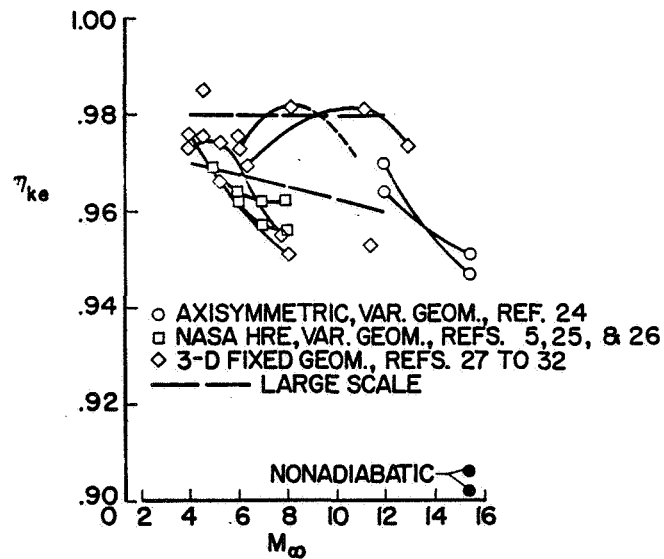


Figure 10

~~CONFIDENTIAL~~

CONFIDENTIAL

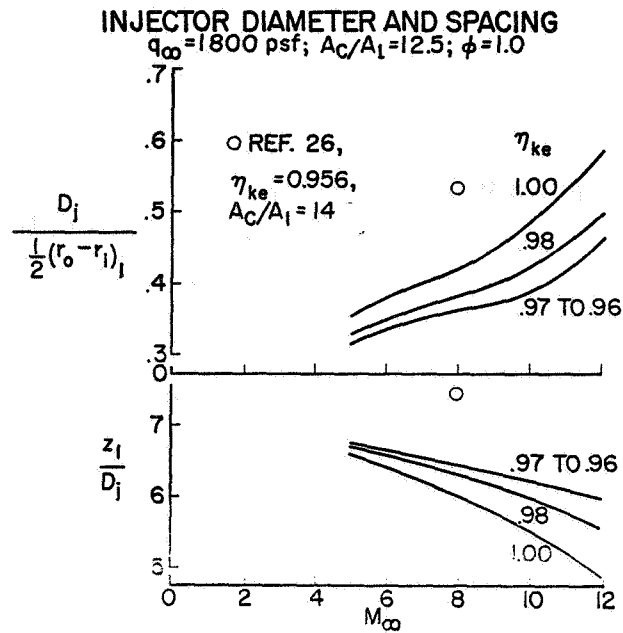


Figure 11

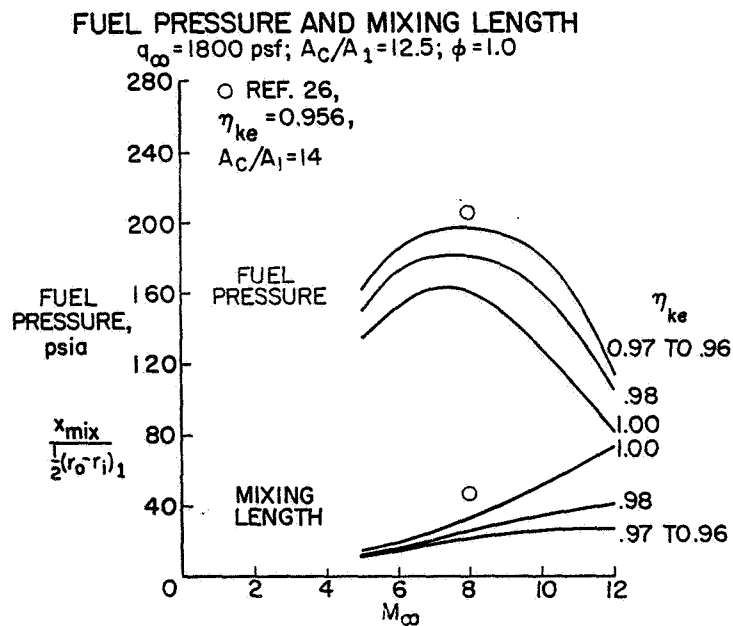


Figure 12

CONFIDENTIAL

LOCAL EQUIVALENCE RATIOS IN SCRAMJET COMBUSTOR

$M_\infty=8$; THEORY FROM REFERENCE 12; $\epsilon_T = Cr_{1/2}(\rho V)_\epsilon$

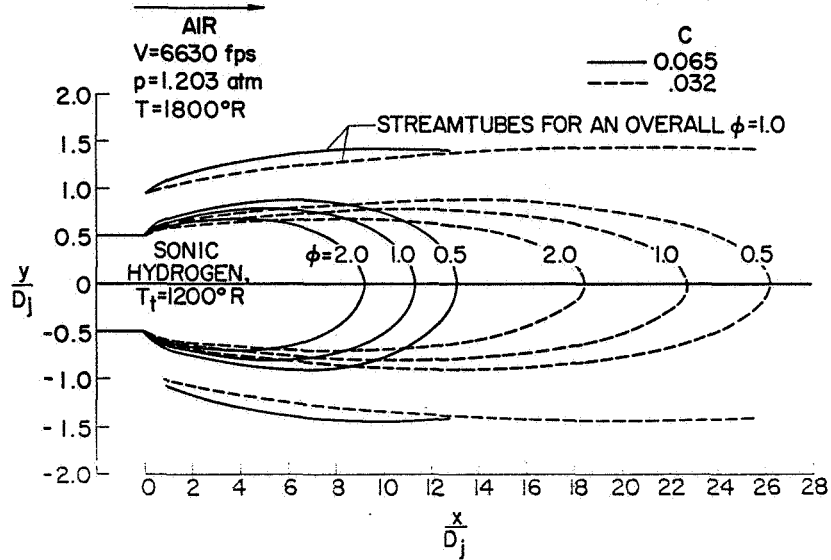


Figure 13

VELOCITY PROFILES

COAXIAL MIXING; THEORY FROM REFERENCE 12

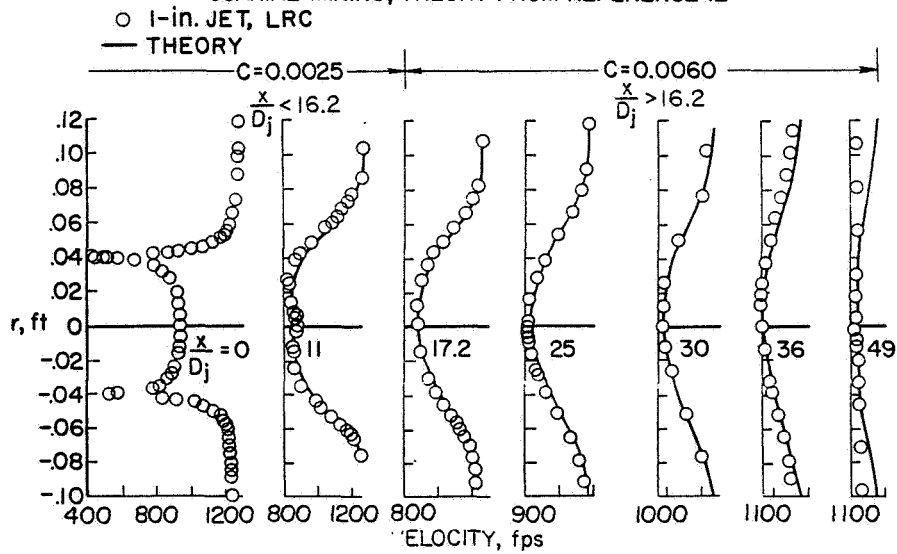


Figure 14

CONFIDENTIAL

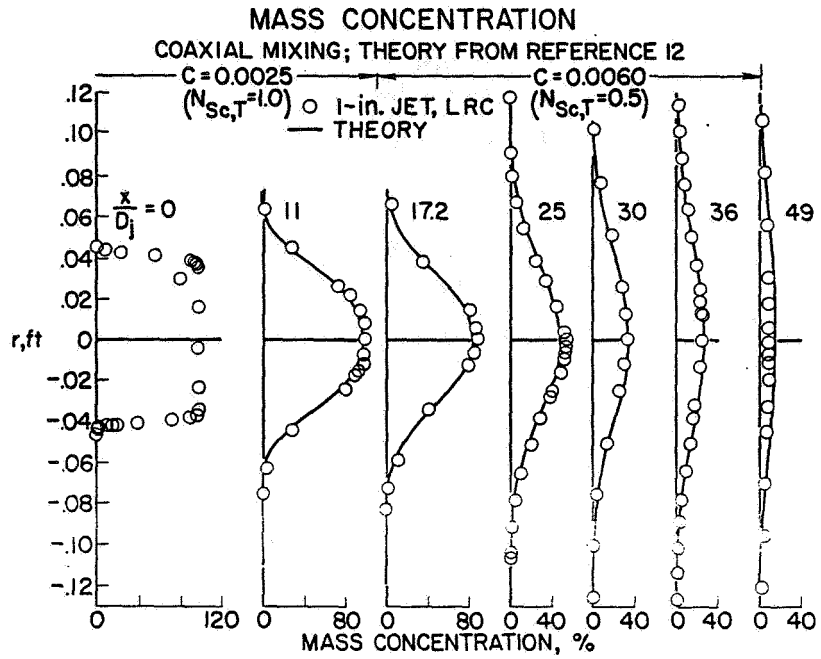


Figure 15

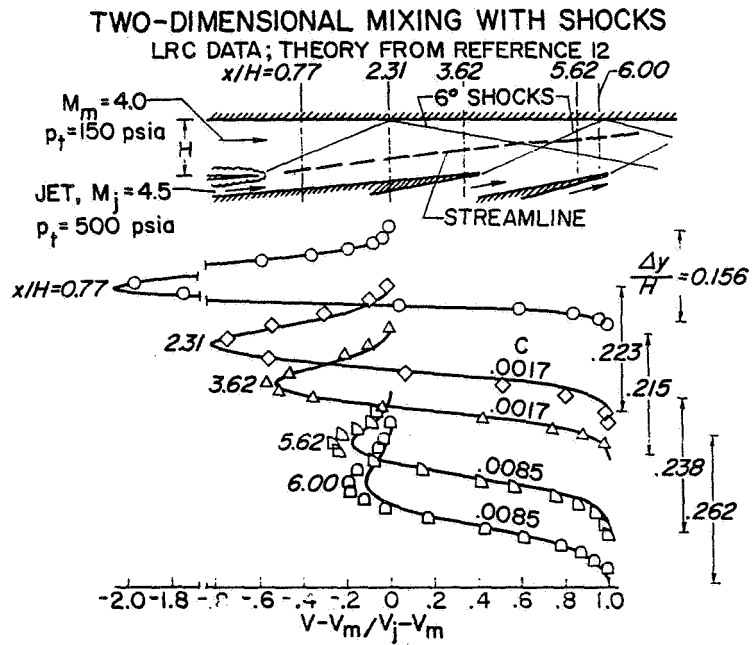


Figure 16

24. IGNITION AND CHEMICAL KINETICS IN HYPERSONIC RAMJETS

By E. A. Lezberg
Lewis Research Center

INTRODUCTION

The calculation of supersonic combustor performance involves determining the limitations that are imposed by the chemical reactions.

The total reaction time in the combustor can be broken up into an ignition delay period in which, superficially, nothing happens and a reaction time in which the hydrogen and oxygen are consumed. A third period which includes part of the gas residence time in the nozzle might be called the recombination period in which some of the atoms and radicals recombine with significant chemical energy release as the gas expands.

A number of computational methods have been developed in the past several years for calculating high temperature gas flows with chemical reactions. Numerical techniques using Runge-Kutta or Predictor-Corrector integration schemes have been in use for a number of years, (refs. 1-3). Generally these techniques require long computing times, especially where the rates of change in major species concentrations are negligible, in the initial delay period and near equilibrium.

These computational difficulties can be avoided by several slightly more approximate techniques. For example, Bray's idea of sudden freezing of the chemistry, reference 4, has worked very well for determining chemical kinetic

losses in nozzles, and can be very useful in parametric engine studies, reference 5.

The ignition delay period can also be calculated in a single step using an analytical solution, (ref. 6). Since the temperature and the concentration of major species remain nearly constant, the reverse reaction rates and temperature dependence of the rate constants can be neglected and the rate equations linearized.

A recently developed technique, (ref. 7), linearizes the entire combustion process, essentially determining analytical solutions in small steps, but with allowable step sizes that are orders of magnitude larger than required by the more conventional integration techniques.

Whatever the calculation procedure, it is important that the proper chemistry and reaction rate data be used. For hydrogen-air, those reactions which are important to the consumption of the major species and the recombination phases have been fairly well understood in previous analytical work while the ignition chemistry has often been oversimplified.

The application of chemical kinetics to supersonic combustion ramjets is discussed in this paper. The Mach number range has been arbitrarily restricted to 8 and below since the application to a hypersonic cruise airplane is more likely in this range and the NASA Hypersonic Ramjet Experiment (HRE) can be used as an example.

Aerodynamic and chemical effects on ignition will be discussed since they are important to design of practical combustors and in ground test simulation.

~~CONFIDENTIAL~~

The chemical kinetic calculations are used to determine areas of the flight trajectory which should be considered to be reaction rate limited.

HYDROGEN-AIR CHEMISTRY AND REACTION RATES

The reactions of hydrogen and air and reaction rate constants are listed in table I. These have been included except as later noted, in the computer programs utilizing the techniques of references 3 and 6.

During the ignition period, small concentrations of atoms and radicals are initially formed by a reaction such as (1). The chain reaction is then propagated and branched by the bimolecular reactions (2) to (4). During most of the induction period, the atom and radical concentrations increase exponentially under nearly isothermal conditions. The induction period is ended when the rates of the energetic three-body recombination reactions (8) to (11) cause the temperature to increase rapidly. At temperatures less than 1100° K and higher pressures, reactions (6) and (7) must be included, (ref. 6). The HO_2 radical will build up in concentration since (7) is slow, and will effectively terminate the branching reactions by removing H atoms. The reactions approach equilibrium through consumption of the reactants (2) to (4) and the recombination reactions (8) to (11), which produce most of the heat release. The reactions of nitrogen with oxygen, (12) to (14) are included in the program of reference 3, but have negligible effect on the kinetics except for possible reactions of the nitric oxide which is formed with species containing hydrogen. These and other reactions of hydrogen and oxygen which may be important at low temperatures have not

~~CONFIDENTIAL~~

been included because of a lack of both rate data and mechanisms. The reverse rates of the reactions listed in table I were determined from a temperature fit of equilibrium constant data (table II).

IGNITION DELAYS FOR HYDROGEN-AIR

Calculations were made using an analytical solution for the delay period, (ref. 6), for a range of pressures and temperatures typical of supersonic combustion ramjet burner entrance conditions below $M = 8$, and stoichiometric premixed combustion. Results of these calculations are shown in figure 1.

The circled points indicate the second explosion limit which is defined by equations (1) and (2) (ref. 6):

$$k_6(M) = 2k_3 \quad (1)$$

$$(M) = (P/RT)W \quad (2)$$

and W is a weighted third-body efficiency as defined in table I. The second limit represents a boundary between short delays at higher temperatures and lower pressures and long delays at lower temperatures and high pressures.

In the vicinity of the second explosion limit, delays increase by two orders or magnitude for a 100° K temperature decrease. The ignition delays are inversely related to pressure in the high temperature region but are changed to a more complicated dependence near the second limit. The existence of the second limit and the change in pressure dependence are directly related to removal of hydrogen atoms from the chain reaction by reaction (6).

Figure 2 shows a comparison of the ignition calculations to experimental data. The high temperature shock tube data reference 8, have been adjusted to the partial pressure of oxygen corresponding to a stoichiometric hydrogen-air mixture at one atmosphere pressure, reference 9. The low temperature shock tube data are taken directly from reference 10.

The end of the delay period can be defined in a number of ways. The calculations indicated by the solid lines represent a 0.1 percent density decrease. The dashed line was computed for a build up of hydroxyl radical concentration to 10^{-6} moles/liter which is the ignition criterion used in reference 8.

The comparison of calculation and experiment is very good in the high temperature region and shows qualitative agreement in the low temperature region.

Additional calculations were made for supersonic combustion ramjet combustor inlet conditions for low altitude (88 000 feet), and high altitude (122 000 feet) trajectories of the NASA Hypersonic Ramjet Experiment Project, (refs. 11 and 12). Ignition delays were calculated as a function of equivalence ratio for premixed hydrogen-air. Initial mixture temperatures were calculated for the nonreacting gases. Results are given in figure 3. The low pressure condition is reaction limited for the Mach 8 staged combustor design, (ref. 11), which is shown in figure 4, since the ignition distance is 8.8 inches compared to 7 inches for the first stage combustor length. Ignition would be further delayed because of the rapid expansion following the first stage com-

bustor. Combustion taking place at larger burner areas and higher Mach numbers would result in additional total pressure loss.

Ignition for the low altitude case could take place in an acceptable flow length of 2.5 inches from the injection point. If mixing time were considered, delays might be considerably longer.

Aerodynamic Effects

Since the HRE combustor design utilizes normal injection of hydrogen from the wall, aerodynamic effects would be expected to increase the local static temperature and pressure and favorably effect ignition delay. Schematic representations of wall slot and jet injection are shown in figure 5.

The case of parallel injection of hydrogen into an air boundary layer with heated walls has been investigated in reference 13. The temperature profile through the boundary layer was calculated by assuming a Crocco relationship between velocity and enthalpy.

Locally higher than free stream temperatures in the boundary layer were found to have a favorable effect on ignition if the delay distance based on the maximum temperature was of the same order as the boundary layer thickness. The maximum boundary layer temperature with no mixing is given as,

$$T_{MAX} = T_w + 1/4 (T_o - T_w)^2 / (T_o - T). \quad (3)$$

A temperature-pressure map, figure 6, gives free-stream burner inlet conditions for a family of supersonic combustion ramjets with simple two-shock inlets. The maximum temperature in the boundary layer is calculated by

~~CONFIDENTIAL~~

equation (3). The line for 100 microsecond delay indicates the approximate boundary between no ignition and probable ignition conditions for injection into the boundary layer of an engine with inlet ramp length of 75 ft. and estimated boundary layer thickness, $\delta = 4$ in. at the inlet throat.

A similar effect of locally high temperatures will occur with normal injection from the wall, figure 5, since some of the air passing through the boundary layer separation shock and bow shock upstream of the jet will be heated nearly to stagnation conditions. The region of influence will be determined by the size of the jet relative to the boundary layer thickness. For $D_j \gg \delta$ the region of heating should be of the order of the jet size because of the rapid expansion of the air downstream of the jet. For $D_j \leq \delta$ boundary layer separation is apt to occur with a more favorable effect on ignition. In experiments with small supersonic combustors utilizing normal jet injection, (ref. 14 and 15), results tended to indicate that ignition did not occur immediately at the injection point, but at a second point of injection, (ref. 14), or by inducing a strong separation, (ref. 15).

Effects on ignition of aerodynamic heating caused by local protuberances and oblique shocks from wedges, were investigated in a Mach 3 stream (ref. 16). Ignition occurred if the air static temperature was greater than 1055°K after passing through the disturbance.

Effects of Vitiation Heating

In ground test facilities, heating of air is often provided by vitiation with hydrogen - using oxygen make up - the justification being that the water is chemically inert. This assumption may be valid in the high temperature

~~CONFIDENTIAL~~

~~CONFIDENTIAL~~

region where delays are short anyway. However, in examining the reaction equations, table I, two possible effects may be inferred: (1) The effects of water vapor as a very efficient third body on the quenching of the chain branching reactions by reaction (6); and (2), the effect of initially high radical concentrations which would be produced by partial chemical freezing of dissociated H_2O during expansion through a supply nozzle. The later effect would be expected to shorten the delays since the delay period is characterized by an exponential build up of radical concentrations to some arbitrary level at which the recombination heat release becomes significant.

Figure 7 shows the effect of the percentage of water vapor on the second explosion limit temperature calculated from equations (1) and (2). Water is seen to have a strong effect on extending the region of long delays to higher temperatures.

Numerical calculations of the ignition delay kinetics were made for vitiated mixtures with initially nonequilibrium free radical concentrations, using the computer program of reference 3, and a weighted third body efficiency for reaction (6). Starting conditions were a temperature of $1121^{\circ} K$ (close to the second limit temperature for pure air) and pressure of 1.7 atmospheres. The stoichiometric mixtures of hydrogen and vitiated air contained 51 percent water and a range of initial OH mole fractions which might result from freezing during a facility nozzle expansion. Other atom and radical mole fractions were set at initially low values. Results are shown in figure 8 as a plot of mixture temperature against time. Ignition cannot be determined by the previously used criteria of a critical OH concentration or small density decrease

because of the complicated behavior of the reaction history. The initial temperature rise is due to the heat release (47 Kcal/mol) from reaction (6) when H atoms recombine with O₂. The removal of H atoms and radicals caused by reaction (6) acting together with reactions (2) to (5) quenches the branching reactions. After additional time the radical concentrations can again build up to produce a true ignition.

The result resembles a two stage ignition process in which mixtures with low initial radical concentrations are quenched and can ignite only after long delays. Higher initial radical concentrations counteract this effect to produce a more normal ignition with short delays. The effect of nonequilibrium free radical concentrations has been discussed theoretically in reference 17, but since reaction (6) was not included in the reaction scheme, the results would not be expected to be meaningful near the second explosion limit.

There is qualitative experimental evidence that water is effective in narrowing the hydrogen-oxygen detonation limits (ref. 18). Shock tube ignition data (ref. 10) show increased ignition delays for stoichiometric mixtures with water below temperatures of about 950° K and shorter delays above this temperature. These results are confusing, however, and indicate a need for further work.

Effects of Nitric Oxide

In ground test facilities in which air is heated to high stagnation temperatures such as arc heaters and ceramic storage heaters, some nitric oxide is formed in equilibrium with the high temperature air. The nitric oxide

does not remain in equilibrium with the expansion through a supply nozzle but freezes chemically near the nozzle throat. These small quantities of nitric oxide can have a profound influence on the ignition behavior in the low temperature region. Data from shock tube experiments with nitric oxide additive, (ref. 10), are shown in figure 9. The data indicate a reduction in the delay of two orders of magnitude below pure hydrogen-air for optimum quantities of nitric oxide. The mechanism is not defined but thought to involve the reaction of NO with the HO_2 radical to regenerate hydrogen atoms.

Since nitric oxide would not be expected to form in these amounts in a supersonic combustion ramjet inlet, care should be exercised in extrapolating ground test ignition behavior to flight.

Ignition Sources

Long ignition delays at Mach numbers below 8 may require ignition aids for supersonic combustors. These may take a number of forms including piloting flames, sparks, flares, strong fuel preheating, chemical additives, or use of aerodynamic effects. The use of a piloting flame has been demonstrated for igniting premixed hydrogen-air at low temperatures (ref. 19).

More recently, results of ignition experiments using a platinum catalyst have been published, (ref. 20). It was possible to reduce the fuel or air temperature in these tests by 600° to 800° R below the temperatures required for noncatalytic ignition.

HEAT RELEASE KINETICS

Comparison of Kinetics- and Mixing-Limited Combustion

The kinetic calculations can be used to predict required combustor

lengths and to arrive at a more nearly optimum combustor geometry for the cases of reaction limited combustion, or to establish whether the process is mixing or reaction limited.

The numerical calculation procedure, (ref. 3), was used to calculate the reaction history for the annular combustor geometry of the NASA HRE engine (fig. 4) at Mach 8. Starting conditions were the inviscid combustor inlet conditions after an initial delay period. The delay period was calculated from the analytical solution (ref. 6), to provide initial radical concentrations for input to the numerical calculations. This procedure was used because it is believed that aerodynamic effects of fuel injection will make the actual ignition delays shorter than shown in figure 3 and to shorten the computation time.

Results of the calculation for an altitude of 88 000 feet are shown compared to a mixing calculation, (ref. 11), in figure 10. Chemical reaction is nearly complete in a distance of 3.3 inches, although some recombination continues in the remaining combustor length. For this low altitude case reaction rates are sufficiently fast so that the process is mixing controlled.

Kinetic calculations for a high altitude trajectory (122 000 feet) were made to illustrate a case where the reaction rates are controlling.

Results are shown in figures 11 and 12 as plots of pressure, temperature and hydrogen mass fraction against combustor length. Combustion is incomplete at the combustor outlet and the recombination reactions are effectively frozen by the more rapid expansion in the second stage combustor. The freezing is illustrated by hydrogen atom mass fraction (fig. 12), which

remains nearly constant from the combustor exit to the nozzle exit. Hydrogen molecule mass fraction continues to decrease slightly because of the faster bimolecular reactions, but little energy is released.

PERFORMANCE PARAMETERS

The performance loss of the combustor or combustor-nozzle combination can be determined for chemical inefficiencies and total pressure losses due to the heat addition process.

A chemical efficiency is defined in terms of hydrogen consumed and includes dissociation losses.

$$\eta_{CH} = \frac{X_{H_2}(1) - (X_{H_2} + 1/2 X_{OH} + 1/2 X_H)(2)}{X_{H_2}(1) - (X_{H_2} + 1/2 X_{OH} + 1/2 X_H)(2)_{EQ.}} \quad (4)$$

A combustor efficiency is defined as:

$$\eta_C = \frac{IVAC (3) - IVAC (1)}{IVAC (3') - IVAC (1)} \quad (5)$$

Where, IVAC (3) = stream thrust expanded isentropically to ambient pressure from the actual conditions at the combustor exit, IVAC (1) = combustor inlet stream thrust, IVAC (3') = stream thrust for an equilibrium combustion process for the actual combustor geometry expanded isentropically to ambient pressure.

Efficiencies were determined for low and high altitude trajectories at Mach 8, and are listed in table III.

For the low altitude case, chemical efficiency is relatively high at the combustor area ratio of 1.1 and 4.0. The drop in η_{CH} at the larger area ratio is due to the equilibrium term in the denominator of equation (4), which decreases as the static temperature falls. A combustor efficiency close to 100 percent indicates the insensitivity of this parameter to small departures from equilibrium. Dissociation losses are not charged against this efficiency because of the equilibrium expansion to ambient pressure in the definition. At an altitude of 122 000 feet the chemical efficiency is under 80 percent with essentially frozen chemistry to the nozzle exit. A combustor efficiency of 64.8 percent was calculated for this altitude.

CONCLUDING REMARKS

Ignition behavior at supersonic combustion ramjet combustor conditions is not as straightforward as previously thought. Conditions for ignition are not favorable over a wide range of conditions below Mach 8. The phenomena governing ignition for the supersonic combustion ramjet in this Mach number range is most often a complex fluid dynamic interaction which produces locally high static temperatures and low velocity or separated regions. Fuel jet-boundary layer interaction or separation regions favor ignition but are not readily amenable to delay calculations or even to analytical description. Ignition delays can be calculated over a wide range of conditions using the proper chemistry with an analytical technique, and these calculations can be useful in predicting marginal spontaneous ignition where positive ignition systems are needed.

Ground testing may not properly simulate supersonic combustion ramjet combustor inlet conditions due to the presence of water and small quantities of free radicals or nitric oxide. Since these can have drastic influences on the ignition kinetics at a temperature near 1000° K, application of such ignition data to design of flight hardware should be viewed with caution. An exception would be data with clean air in which temperatures are not high enough to cause dissociation or nitric oxide formation. Experimental data is needed using carefully chosen experiments to explain the ignition kinetics of hydrogen with vitiated air.

The kinetics of the heat releasing (recombination) reactions are well understood and available calculation methods can be used to predict necessary combustor lengths and to examine combustor geometry for optimum heat release schedules. The a priori conclusion that combustion is mixing limited does not appear to be valid for a range of cruise altitudes and Mach numbers. In these cases the combustion is kinetics limited, or both mixing and kinetics should be considered as interrelated.

For the cases considered in this paper, the nozzle expansion process can be considered frozen at the nozzle inlet. This is a consequence of the rapid expansion in the nozzle compared to the rate in the combustion chamber. This may not be a serious effect for supersonic combustion ramjets, however, since mission studies have indicated that nozzle kinetics losses are of secondary importance to nozzle friction loss (refs. 21 and 22).

SYMBOLS

A.R.	area ratio
D_j	jet diameter
IVAC	stream thrust, seconds
$K_{EQ.}$	equilibrium constant
k	reaction rate constant
M	Mach number
(M)	third body concentration, moles/cc.
P	pressure, atm.
R	gas constant
T	temperature, $^{\circ}K$
T_{MAX}	maximum boundary layer temperature, $^{\circ}K$
U	velocity
W	third body efficiency
X	mole fraction
δ	boundary layer thickness
η	efficiency
ρ	density
τ	ignition delay, microseconds
ϕ	equivalence ratio

Subscripts

C	combustor
CH	chemical
EQ.	equilibrium
i	species, initial

f forward
r reverse
w wall
 ∞ free stream
o stagnation

REFERENCES

1. Libby, P. A.; Pergament, H.; and Bloom, M. H.: A Theoretical Investigation of Hydrogen-Air Reactions. Part 1 - Behavior with Elaborate Chemistry. Tech. Rep. 250 (AFOSR-1378), General Applied Science Labs., Inc., Aug. 1961.
2. Westenberg, A. A.; and Favin, S.: Complex Chemical Kinetics in Supersonic Nozzle Flow. Ninth Symposium (International) on Combustion. W. G. Berl, ed., Academic Press, 1963, pp. 785-798.
3. Zupnick, T. F.; Nilson, E. N.; and Sarli, V. J.: Investigation of Non-equilibrium Flow Effects in High Expansion Ratio Nozzles. Computer Program Manual. Rep. No. UACRL-C910096-11 (NASA CR 54942), United Aircraft Corp., United Aircraft Corp., Sept. 15, 1964.
4. Bray, K. N. C.: Chemical Reactions in Supersonic Nozzle Flows. Ninth Symposium (International) on Combustion. W. G. Berl, ed., Academic Press, 1963, pp. 770-784.
5. Franciscus, Leo C.; and Lezberg, Erwin A.: Effects of Exhaust Nozzle Recombination on Hypersonic Ramjet Performance: II. Analytical Investigation. AIAA J., Vol. 1, No. 9, Sept. 1963, pp. 2077-2083.
6. Brokaw, Richard S.: Analytical Solutions of the Ignition Kinetics of the Hydrogen-Oxygen Reaction. Tenth Symposium (International) on Combustion. The Combustion Institute, 1965, pp. 269-278.

7. Moretti, Gino: A New Technique for the Numerical Analysis of Non-equilibrium Flows. AIAA J., Vol. 3, No. 2, Feb. 1965, pp. 223-229.
8. Schott, G. L.; and Kinsey, J. L.: Kinetic Studies of Hydroxyl Radicals in Shock Waves. II. Induction Times in the Hydrogen-Oxygen Reaction. J. Chem. Phys., Vol. 29, No. 5, Nov. 1958, pp. 1177-1182.
9. Momtchiloff, I. N.; Taback, E. D.; and Buswell, R. F.: Kinetics in Hydrogen-Air Flow Systems. I-Calculation of Ignition Delays for Hypersonic Ramjets. Ninth Symposium (International) on Combustion. W. G. Berl, ed., Academic Press, 1963, pp. 220-230.
10. Snyder, A. D.; Robertson, J.; Zanders, D. L.; and Skinner, G. B.: Shock Tube Studies of Fuel-Air Ignition Characteristics. (AFAPL-TR-65-93, DDC No. AD-470239), Monsanto Research Corp., Aug. 1965.
11. Staff: Preliminary Design Report. Vol. 1. Hypersonic Ramjet Experiment Project, Phase I. Rep. No. AP-66-0168-1 (NASA CR-66224), AiResearch Mfg. Co., Feb. 28, 1966.
12. Dors, J. G.: Engine Performance, Hypersonic Ramjet Experiment Project, Phase I. Rep. No. R66FPD54, General Electric Co., 1966.
13. Schetz, Joseph A.; and Favin, Stanley: The Ignition of Slot-Injection Gaseous Hydrogen in a Supersonic Air Stream. Applied Physics Lab., Johns Hopkins Univ. (NASA CR-344), Jan. 1966. Also presented at the AIAA Second Propulsion Joint Specialist Conference, Colorado Springs, Col., June 13-17, 1966.
14. Staff: Preliminary Design Report. Vol. III. Hypersonic Ramjet Experiment Project, Phase I. Appendix B. Rep. No. AP-66-0168-3 (NASA CR-66226), AiResearch Mfg. Co., Feb. 28, 1966.

~~CONFIDENTIAL~~

15. Staff: Advanced Engine and Technology Department: Analytical and Experimental Evaluation of the Supersonic Combustion Ramjet Engine. Vol. II. Rep. No. R65FPD184, Vol. II (AFAPL-TR-65-103, Vol. II, DDC No. AD-367774L), General Electric Co., Dec. 1, 1965.
16. Dunn, James: Experimental Results for Thermal Ignition of Hydrogen in a Supersonic Viscous Flow. Tech. Rep. 404 (NASA CR-62926), General Applied Science Labs., Inc., Dec. 1963.
17. Rhodes, R. P.: The Effect of Non-Equilibrium Free-Radical Concentration on Ignition Delay in the Hydrogen-Air System. (AEDC TDR-64-241, DDC No. AD-608566), Aro, Inc., Nov. 1964.
18. Kerkam, B. F.; and Dabora, E. K.: The Influence of Water Vapor Addition on Hydrogen-Oxygen Detonations. Rep. No. 06996-1-T (AROD-5209-1, DDC. No. AD-617962), Michigan Univeristy, Apr. 1965.
19. Slutsky, S.; Tamagno, J.; and Trentacoste, N.: Supersonic Combustion in Premixed Hydrogen-Air Flows. AIAA J., Vol. 3, No. 9, Sept. 1965, pp. 1599-1605.
20. Billig, F. S.; and Grenleski, S. E.: Experimental Studies of Hydrogen-Air Ignition in a Supersonic Combustor. Rep. No. TG-848 (NASA CR-81268), Applied Physics Lab., Johns Hopkins Univ., Aug. 1966. Also presented at the AIAA Joint Propulsion Specialists Conference, Colorado Springs, Colorado, June 13-17, 1966.
21. Franciscus, Leo C.: Off-Design Performance of Hypersonic Supersonic Combustion Ramjets. Paper presented at First Annual Meeting and Technical Display of the AIAA, Washington D. C., June 28 - July 2, 1964.

~~CONFIDENTIAL~~

~~CONFIDENTIAL~~

22. Sarli, V. J.; Blackman, A. W.; and Migdal, D.: Exhaust Nozzle Recombination of Dissociated Hydrogen-Air Combustion Products. Paper No. 63120, AIAA, Apr. 1963.
23. Ripley, Dennis L.; and Gardiner, W. C., Jr.: Shock-Tube Study of the Hydrogen-Oxygen Reaction. II. Role of Exchange Initiation. J. Chem. Phys., Vol. 44, No. 6, Mar. 15, 1966, pp. 2285-2296.
24. Dixon-Lewis, G.; Wilson, W. E.; and Westenberg, A. A.: Studies of Hydroxyl Radical Kinetics by Quantitative ESR. J. Chem. Phys., Vol. 44, No. 8, Apr. 15, 1966, pp. 2877-2884.
25. Brokaw, Richard S.: Ignition Kinetics of Carbon Monoxide-Oxygen Reaction. NASA TN D-3664, 1966.
26. Getzinger, R. W.; and Schott, G. L.: Kinetic Studies of Hydroxyl Radicals in Shock Waves. V. Recombination via the $H + O_2 + M \rightarrow HO_2 + M$ Reaction in Lean Hydrogen-Oxygen Mixtures. J. Chem. Phys., Vol. 43, No. 9, Nov. 1, 1965, pp. 3237-3247.
27. Matthews, D. L: Interferometric Measurement in the Shock Tube of the Dissociation Rate of Oxygen. Phys. Fluids, Vol. 2, No. 2, Mar.-Apr. 1959, pp. 170-178.
28. Lewis, Bernard; and Von Elbe, Guenther: Combustion, Flames and Explosions of Gases. Second ed., Academic Press, 1961, p. 29.

~~CONFIDENTIAL~~

TABLE I. - REACTION RATE EQUATIONS

$$k_f = DT^E \text{ EXP. (EA/RT), Concentration } i = \text{moles/cc.}$$

$$k_r = k_f / K_{EQ}.$$

Reaction	D	E	EA	REF
1. $H_2 + O_2 = OH + OH$	2.50×10^{12}	0.	39000.	23
2. $H_2 + OH = H_2O + H$	2.30×10^{13}	0.	5200.	24
3. $H + O_2 = OH + O$	1.00×10^{14}	0.	16000.	(a)
4. $O + H_2 = OH + H$	1.20×10^{13}	0.	9200.	9
5. $O + H_2O = OH + OH$	2.90×10^{14}	0.	18700.	25
6. $H + O_2 + M = HO_2 + M$	8.60×10^{14}	0.	-1280.	26
7. $HO_2 + H_2 = H_2O_2 + H$	5.40×10^{11}	0.	24000.	6
8. $H_2 + M = H + H + M$	1.00×10^{21}	-1.5	103000.	9
9. $O_2 + M = O + O + M$	1.137×10^{25}	-2.5	118000.	27
10. $H + OH + M = H_2O + M$	7.50×10^{19}	-1.0	-0.	5
11. $O + H + M = OH + M$	4.00×10^{18}	-1.0	-0.	5
12. $O + N_2 = NO + N$	1.01×10^{12}	0.5	75500.	9
13. $N + O_2 = NO + O$	1.02×10^{11}	0.5	6200.	9
14. $NO + M = N + O + M$	1.06×10^{25}	-2.5	154000.	9

$${}^b W = 5.0 X_{H_2} + 1.75 X_{O_2} + 2.15 X_{N_2} + 1.00 X_{AR} + {}^c 30.0 X_{H_2O}$$

^a Information received in a private communication with R. S. Brokaw of Lewis.

^b Ref. 28.

^c Ref. 26.

~~CONFIDENTIAL~~

TABLE II. - EQUILIBRIUM CONSTANT CURVE FITS

$$K_{EQ.} = DC T^{EC} \exp(FC/T)$$

Reaction	DC	EC	FC
1. $H_2 + O_2 = OH + OH$	7.64386×10^2	-3.88060×10^{-1}	-9.57746×10^3
2. $H_2 + OH = H_2O + H$	2.15920×10^{-2}	2.84300×10^{-1}	7.92330×10^3
3. $H + O_2 = OH + O$	4.07790×10^2	-4.10380×10^{-1}	-8.66280×10^3
4. $O + H_2 = OH + H$	1.88250	2.18100×10^{-2}	-9.15460×10^2
5. $O + H_2O = OH + OH$	8.71640×10	-2.62470×10^{-1}	-8.83870×10^3
6. $H + O_2 + M = HO_2 + M$	6.99050×10^{-2}	2.80010×10^{-1}	2.38580×10^4
7. $HO_2 + H_2 = H_2O_2 + H$	6.66040×10^{-1}	-4.63830×10^{-2}	-7.63700×10^3
8. $H_2 + M = H + H + M$	3.61600	6.39980×10^{-3}	-5.24210×10^4
9. $O_2 + M = O + O + M$	7.84380×10^2	-4.26200×10^{-1}	-6.01680×10^4
10. $H + OH + M = H_2O + M$	5.95690×10^{-3}	2.78190×10^{-1}	6.03440×10^4
11. $O + H + M = OH + M$	5.18950×10^{-1}	1.57720×10^{-2}	5.15060×10^4
12. $O + N_2 = NO + N$	1.95470	9.83510×10^{-2}	-3.77340×10^4
13. $N + O_2 = NO + O$	1.55910×10	-1.44110×10^{-1}	1.59140×10^4
14. $NO + M = N + O + M$	5.01700×10	-2.81520×10^{-1}	-7.60820×10^4

~~CONFIDENTIAL~~

~~CONFIDENTIAL~~

TABLE III. - PERFORMANCE PARAMETERS
COMPARISON OF LOW AND HIGH ALTITUDE CHEMICAL LOSSES

$$\eta_{CH} = \frac{X_{H_2}(1) - (X_{H_2} + 1/2 X_{OH} + 1/2 X_H)(2)}{X_{H_2}(1) - (X_{H_2} + 1/2 X_{OH} + 1/2 X_H)(2)_{EQ.}}$$

$$\eta_C = \frac{IVAC(3) - IVAC(1)}{IVAC(3') - IVAC(1)}$$

Altitude, feet	Chemical efficiency, η_{CH}			Combustor efficiency η_C
	Combustor exit	Nozzle entrance	Nozzle exit	
	A.R = 1.1	A.R = 4.0	A.R = 23.6	A.R = 1.1
88 000	0.920	0.905	0.905	0.990
122 000	.853	.798	.795	.648

~~CONFIDENTIAL~~

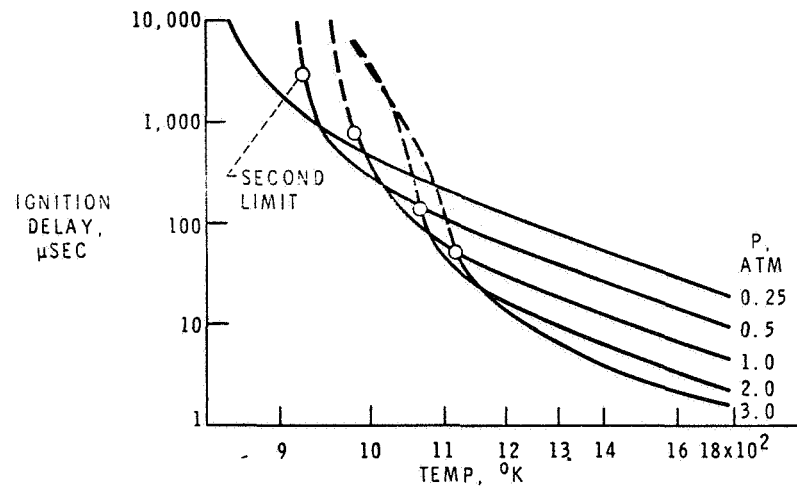


Figure 1. - Ignition delays for hydrogen-air near second limit.

CONFIDENTIAL

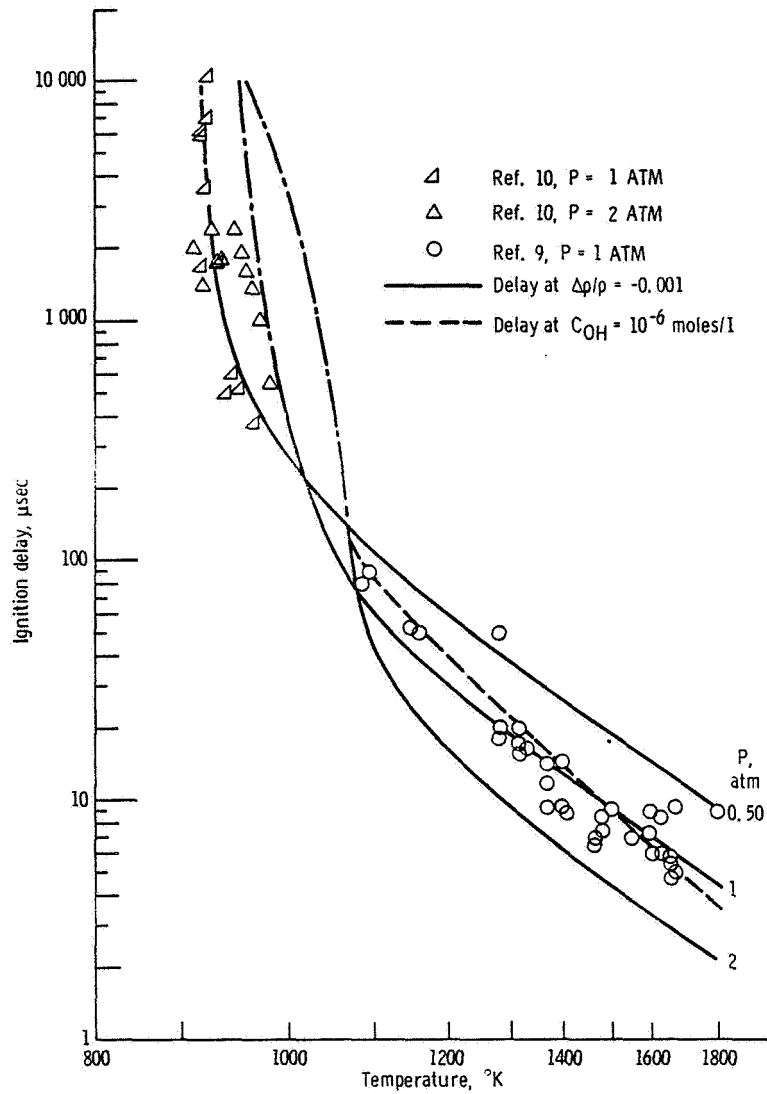


Figure 2. - Ignition delay for H_2 -air, $\phi = 1.0$ comparisons of calculations with shock tube data.

104

CONFIDENTIAL

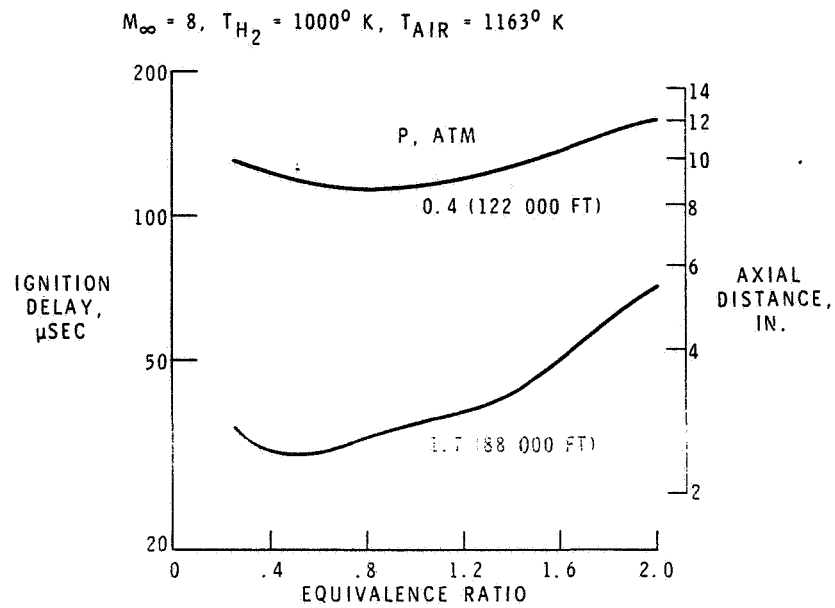


Figure 3. - Ignition delays for hydrogen-air mixtures.

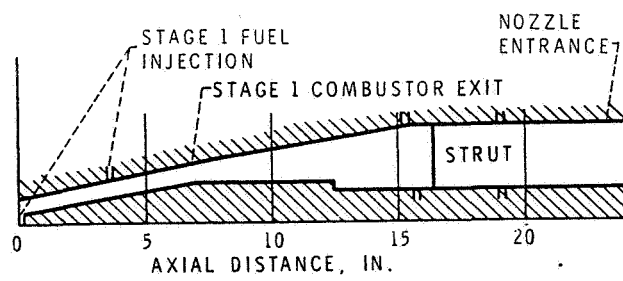


Figure 4. - HRE Mach 8 combustor geometry annular section.

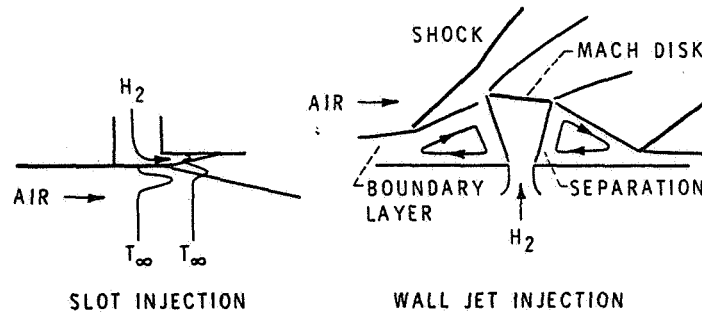


Figure 5. - Aerodynamic effects on ignition.

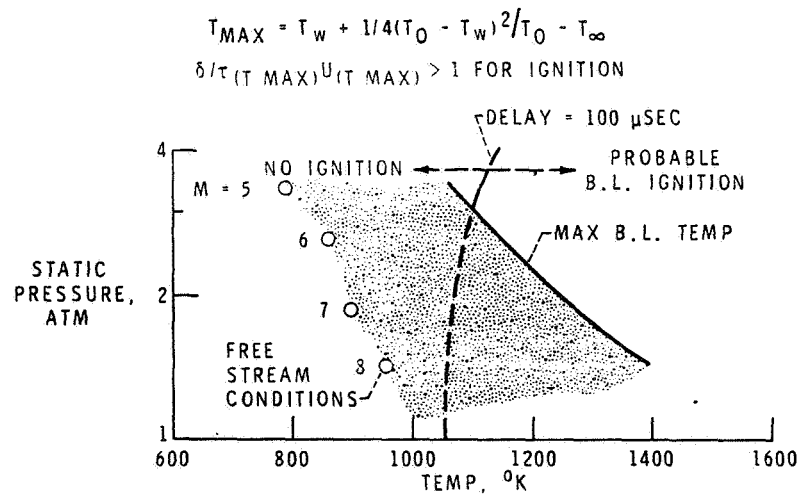


Figure 6. - Effects of boundary layer heating on ignition.

~~CONFIDENTIAL~~

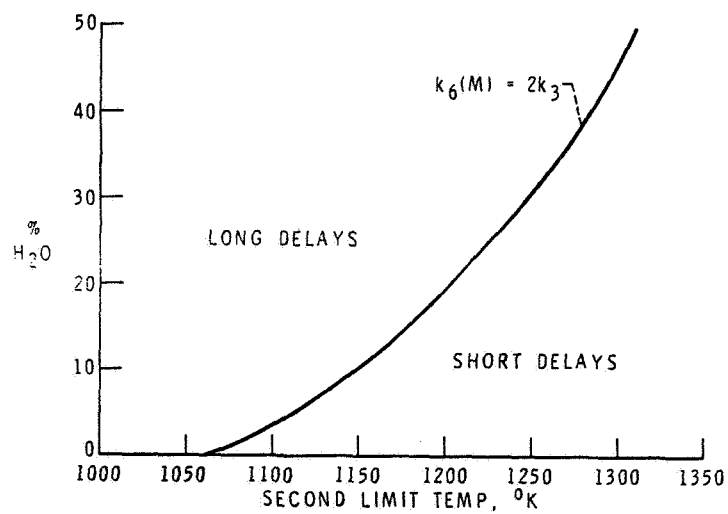


Figure 7. - Effect of water on second explosion limit. Stoichiometric H_2 -air, $P = 2$ atm.

~~CONFIDENTIAL~~

CONFIDENTIAL

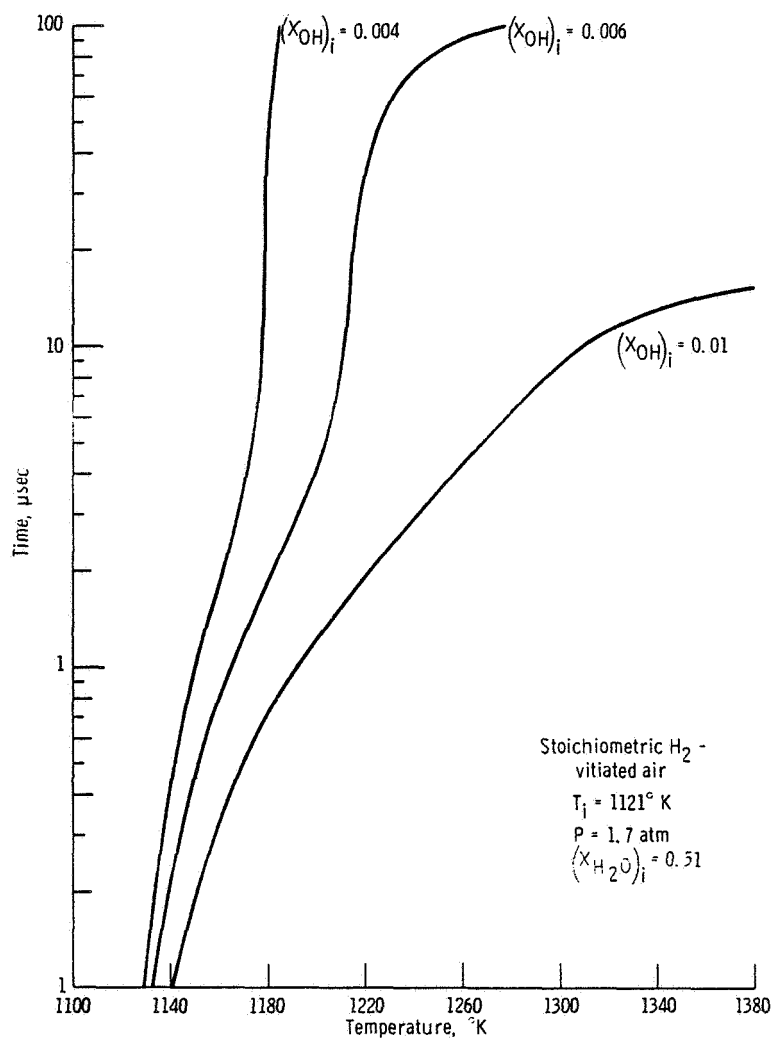


Figure 8. - Effects of initial radical concentrations on ignition of hydrogen and vitiated air (simulation of $M = 8$ flight).

CONFIDENTIAL

~~CONFIDENTIAL~~

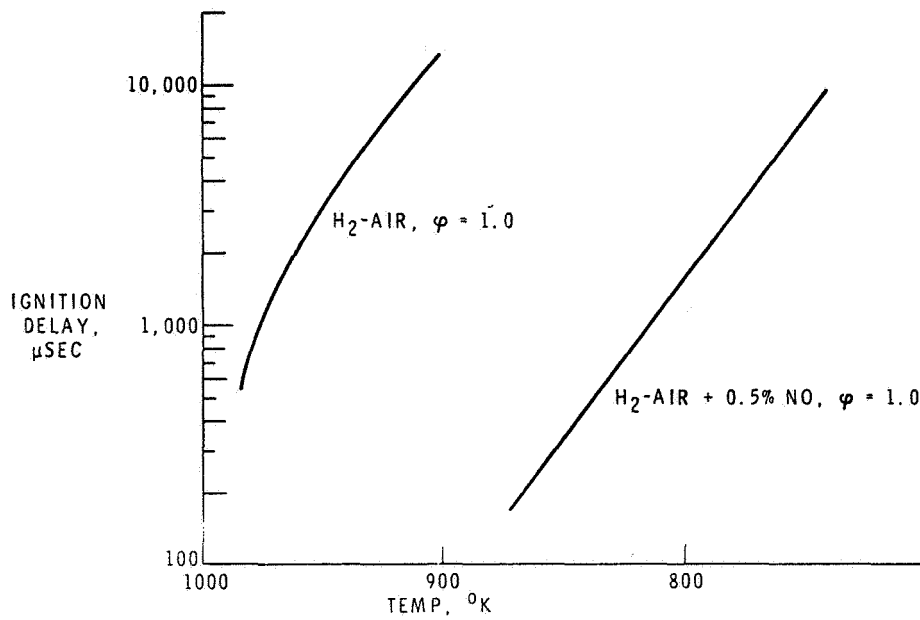


Figure 9. - Effect of nitric oxide on ignition delay. $P = 2 \text{ ATM}$.

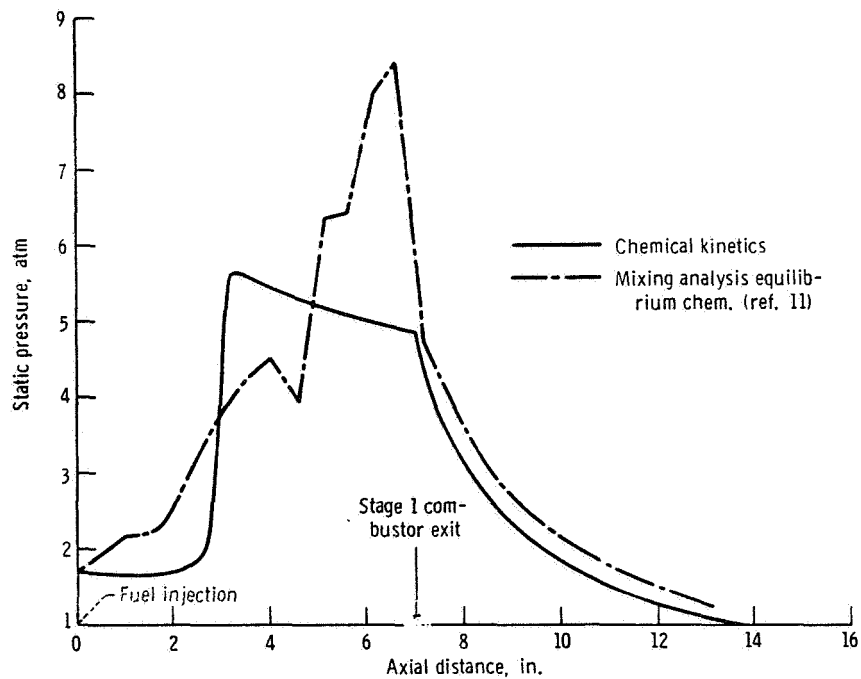


Figure 10. - Comparison of kinetics and mixing limited combustion calculations. Altitude, 88 000 feet; $M_{\infty} = 8$; $\phi = 1.0$, $P = 1.7 \text{ atmospheres}$.

~~CONFIDENTIAL~~

~~CONFIDENTIAL~~

$M_\infty = 8$, ALTITUDE = 122,000 FT, COMB. INLET TEMP = 1121° K,
P = 0.4 ATM, STOICHIOMETRIC H₂-AIR

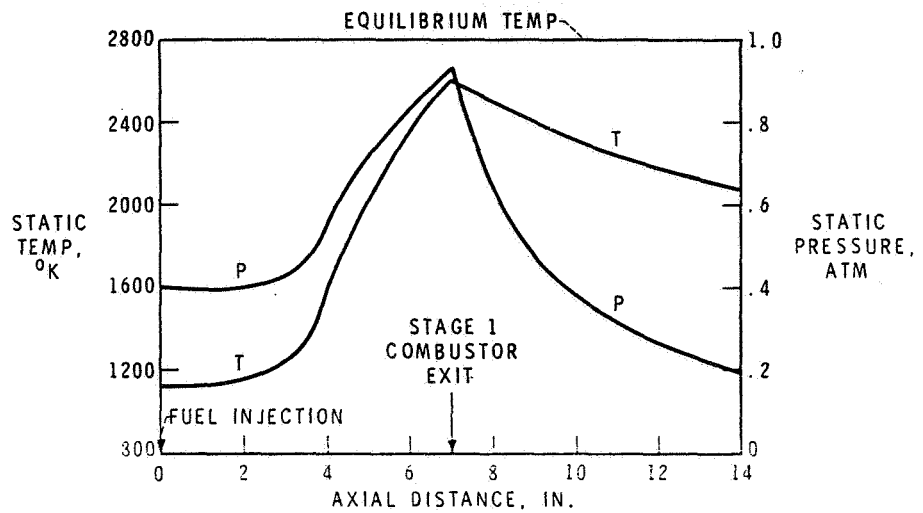


Figure 11. - Kinetic calculations of burner heat release.

$M_\infty = 8$, ALTITUDE = 122,000 FT, COMB. INLET TEMP = 1121° K,
P = 0.4 ATM, STOICHIOMETRIC H₂-AIR

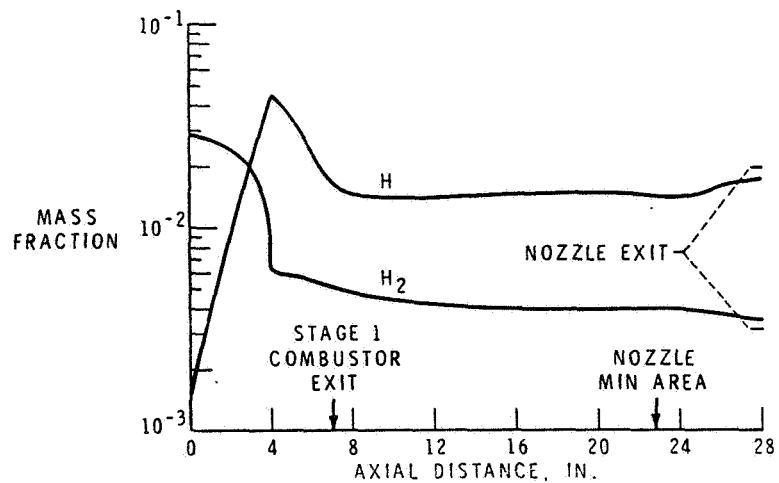


Figure 12. - Kinetic calculations of hydrogen mass fraction.

~~CONFIDENTIAL~~

~~CONFIDENTIAL~~

25. THE VARIABLE-PITCH SUPERSONIC INFLOW COMPRESSOR AND ITS APPLICATION IN A HYPERSONIC ENGINE

By Emanuel Boxer
Langley Research Center

SUMMARY

A unique engine cycle for application to hypersonic cruise vehicles is described in which a variable-pitch supersonic inflow compressor is employed as the fan element of an intercooled afterburning turbofan. The turbofan engine converts to subsonic combustion ramjet operation at high supersonic speeds by stopping the fan rotation and varying the fan blade angle to increase the internal contraction ratio. The results of an experimental study of the cooling, structural, and aerodynamic feasibility of the variable-pitch supersonic inflow compressor are included.

INTRODUCTION

One of the fundamental problems associated with air-breathing propulsion systems for hypersonic flight is the inability of a ramjet to produce static or low speed thrust on the one hand and the inability of a turbine engine to operate at the high inlet temperatures associated with hypersonic flight speeds on the other hand. Therefore, to propel a hypersonic cruise airplane either two separate types of engines must be installed or a composite engine, such as the turboramjet, must be employed with internal valving to direct the flow into the appropriate throughflow channel as a function of flight Mach number.

One potentially attractive means of overcoming the two-engine problem has been proposed by Mr. Edward N. Harris of the AiResearch Manufacturing Company in which an intercooled afterburning turbofan engine is employed incorporating as its fan element a variable-pitch supersonic compressor capable of accepting supersonic axial inflow velocity. The engine which is fueled with a stoichiometric mixture of hydrogen converts to a subsonic combustion ramjet at moderate supersonic speed for acceleration to hypersonic velocity.

SYMBOLS

A	area
A*	critical area
L.E.	leading edge
M	Mach number

~~CONFIDENTIAL~~

~~CONFIDENTIAL~~

p	pressure
Q	heat flux
s	blade spacing
T	temperature
U	rotational speed
β	air inlet angle
σ	solidity
ϕ	equivalence ratio

Subscripts:

A	axial
js	jet stream
l	point of separation
R	relative coordinate system
s	separation region
t	stagnation
∞	free stream
1	station upstream of compressor rotor
2	station downstream of compressor rotor

DISCUSSION

A schematic arrangement of the engine components, a description of its operation, and some of its attractive features are discussed with the aid of figure 1. In the turbofan mode of operation, the fact that the fan can accept supersonic inflow velocity eliminates the need for a variable-geometry inlet for engine-inlet airflow matching purposes and thereby permits the use of a fixed-geometry all-external-compression inlet which, in effect, is part of the engine. In addition, the need for the subsonic diffuser portion of the inlet no longer exists, resulting in a shorter, lighter, less complicated inlet with considerably less surface area to be cooled at hypersonic speeds.

~~CONFIDENTIAL~~

For flight Mach numbers from take-off to approximately 1.5, the inflow velocity to the fan is subsonic and its value is dependent upon blade pitch angle. At higher flight Mach numbers, the inlet geometry predetermines the supersonic inflow velocity to the fan. Under these conditions, the blade pitch angle is adjusted to maximize fan performance and also to ensure compatibility with the existing inlet velocity to prevent subcritical inlet operation with its attendant high spillage drag as may occur with fixed-pitch blading (ref. 1).

The entering flow is decelerated and compressed in the fan stage and enters the fan duct subsonically. A portion of the flow is ducted to the gas generator. Although conventional gas generator components can be used to power the fan turbine, advantage can be taken of the cooling capacity of the hydrogen fuel to provide a unique gas generator with desirable characteristics for application in this engine.

The air which enters the gas generator is precooled by means of a fuel-cooled heat exchanger to maintain approximately constant air discharge temperature. Additional intercooling is employed to obtain high overall compressor pressure ratios near 50. All the engine fuel is injected in a very fuel-rich primary combustor, which results in a low turbine inlet temperature of approximately 1200° F. The combination of high pressure ratio due to intercooling and the fuel-rich combustion process results in bypass ratios approaching 10. The high bypass ratio and high hub-tip-radius ratio of the fan permit the use of centrifugal gas generator compressors for more attractive flow matching and packaging purposes. The fuel-rich mixture is expanded through the fan turbine and into the cooled afterburner where the excess fuel is mixed and burned with the bypassed air. The hot gas then expands through the variable-area nozzle to generate thrust.

At a Mach number of approximately 3.5, the mode of engine operation changes to that of a subsonic combustion ramjet. A brake stops the fan wheel rotation, the gas generator ducts are closed, and the fan-blade pitch angle is positioned in such a manner as to increase the overall contraction ratio of the inlet. The fan blades then form that part of the inlet compression system in which the terminal shock is located. The fuel is injected in the afterburner and burned and the hot gases exhaust through the nozzle. Because the fan blades are exposed to the aerodynamic heating associated with high speed flight, they are fuel cooled in this mode of operation in addition to the remainder of the engine surfaces exposed to the high temperature environment.

To determine the engine performance and the sensitivity of the cycle to variations in component pressure ratio and efficiency, a parametric engine cycle study was performed for an overall equivalence ratio of 1.0. The nominal level of performance of each component is listed in table I. It was found that, over most of the range of flight speeds, the level of combustion efficiency and nozzle discharge coefficient significantly affected engine performance, and to the same degree as for conventional engines. Variations in gas generator element pressure ratio or efficiency do not sensibly affect engine performance; their only effect is to vary the required bypass ratio. The effect of fan performance is illustrated in figure 2. In the left plot, the specific impulse

~~CONFIDENTIAL~~

and corresponding specific thrust are shown as a function of fan total-pressure ratio. At take-off and low flight speeds, the specific impulse is very much a function of fan pressure ratio. A counter-rotating supersonic compressor with a potential pressure ratio near 4 will significantly increase the take-off thrust compared to that of single-stage reaction designs which have consistently demonstrated pressure ratios of approximately 2. At high flight speeds, the engine performance is much less sensitive to the attainable fan pressure ratio for either fan design.

It can be seen that for a given fan pressure ratio and flight condition, the specific impulse is independent of fan efficiency. It should be emphasized that this is true only if the pressure ratio and equivalence ratio are held constant as efficiency varies. The range of low fan efficiencies assumed at supersonic speeds is a result of charging to the fan the terminal shock losses within the blading due to the supersonic axial entry velocity, whereas for conventional compressors these losses are charged to inlet recovery. Although the level of fan efficiency at constant pressure ratio does not affect the specific impulse, the achievement of fan efficiency as high as possible is desirable because of the resulting higher bypass ratio which permits the use of smaller, lighter gas generator elements.

The success of this engine concept is fundamentally dependent upon the achievement of the technology associated with the variable-pitch supersonic inflow compressor, although other serious design problems exist which must be solved. Therefore NASA, with additional funding by the U.S. Air Force, initiated a study with the AiResearch Manufacturing Company to determine the feasibility of such a compressor. This study required the contractor to demonstrate the ability to fabricate a full-scale, flight-weight compressor blade capable of adequately being cooled under conditions simulating supersonic flight, to demonstrate that such a blade and supporting elements would be structurally sound when whirled at high tip speeds, and to demonstrate, through cascade testing, the ability of the compressor to operate with supersonic axial inflow velocity at an acceptable level of performance.

For the cooling and structural tests two identical blades were designed with a 6-inch chord and an aspect ratio of approximately 1.0 and were fabricated of a super alloy (fig. 3). The base of each blade varied in accordance with the type of testing to be done. The blade surfaces were of a double-wall plate-fin-type construction with a representative but arbitrary blade cross-sectional shape. The blade surfaces are supported by being brazed to tip and root manifolds and a corrugated centerbody. Prior cooling and fabrication experience dictated a minimum leading-edge radius of 0.030 inch and a leading-edge wedge angle of 8° . The gaseous hydrogen coolant is routed through the circular blade-root platform and the lower manifold which contains orifices designed in such a manner as to distribute the coolant fluid roughly proportional to the calculated heat flux shown. The coolant is then collected in the tip manifold and routed to the exit down the center of the blade.

Five heating cycle tests were successfully made in a supersonic cascade with a vitiated airstream at a temperature of 3400° F simulating Mach 7 stagnation enthalpy. The average metal temperature as determined by temperature-sensitive paint was approximately 1000° F except along the leading edge where,

~~CONFIDENTIAL~~

due to internal leakage which reduced the coolant flow, the leading-edge metal temperature was estimated to be 1400°F rather than the design value of 1185°F .

The structural strength demonstration was performed with a single blade mounted on a whirl arm in a three-bearing arrangement as shown in figure 4. The center of gravity of the blade was offset from the center of rotation an amount sufficient to approximate the steady-state aerodynamic blade loading. The blade, shank, and bearings successfully demonstrated the structural integrity of the design at a tip speed of 1470 feet/second, which is 10 percent greater than the design operating value.

A more complete description of the blade design and test results is contained in reference 2.

To determine the potential aerodynamic performance of the compressor, supersonic cascade tests were made at conditions simulating three flight Mach numbers. In all, eight blade sections were tested corresponding to two single-stage and counter-rotating fan designs. In the aerodynamic design of the blading, limitations were imposed on the maximum blade camber angle to ensure restart capability of the inlet during the ramjet mode should the terminal shock be inadvertently expelled.

A typical schlieren photograph illustrating the flow within the blades at a simulated flight Mach number of 2.4 is shown in figure 5. The fan inlet flow is diffused to an axial Mach number of 1.62 by passage through an assumed wing leading-edge shock and the inlet conical shock. Test conditions shown represent blades with a solidity of 2.0 operating at a relative inlet Mach number of 1.89.

Only with supersonic axial velocity can an oblique shock be generated by the leading edge of the convex surface and lie within the passage. If the shock falls ahead of the leading edge of the following blade, the fan cannot accept supersonic inflow and the inlet must operate subcritically. Typically, the convex-surface leading-edge shock causes flow separation on the concave surface with rapid reattachment of the flow. For conditions where the shock impinges closer to the leading edge, laminar leading-edge separation takes place in agreement with previous boundary-layer theory (ref. 1) and reattaches to the surface without significantly affecting the flow pattern farther downstream. For conditions for which there are no analytical solutions, a detached bow wave is generated ahead of the leading edge and true infinite cascade entrance conditions are not realized. On the convex surface, the flow separates without reattachment for all tests, so that the flow exits the blade passage as a supersonic stream considerably narrower in width than the blade spacing. The flow then undergoes a dump-mixing diffusion process downstream of the cascade with a rise in static pressure and a significant additional total-pressure loss.

Typical cascade performance measured at the midspan station approximately 1 chord behind the trailing edge is presented in figure 6. The pressure recovery and exit Mach number are shown as a function of the static-pressure ratio across the cascade. The mass averaged data as recorded in the tests are

~~CONFIDENTIAL~~

~~CONFIDENTIAL~~

represented by the open symbols. The solid symbols indicate the result of taking the measured data and correcting to uniform exit conditions by means of a momentum-mixing process. At an inlet Mach number of 1.40, it can be seen that the data as measured are essentially in agreement with that determined for uniform exit conditions. However, at a Mach number of 1.89 the 1-chord distance to the measuring station was insufficient for nearly complete mixing to occur. The measured pressure recovery is low compared with the level of performance of supersonic diffusers, mainly due to the dump diffusion. Based upon data supplied by the contractor, an in-house method of predicting the supersonic cascade performance was developed and is presented in the appendix. The agreement between measured and calculated performance is surprisingly good in view of the unsuccessful past efforts to predict supersonic cascade performance of reaction blading. With this method of performance prediction as a tool, it may be possible to design more efficient blading within the restraints imposed by the aerodynamic and mechanical requirements of this compressor.

The cascade tests demonstrated the ability of the compressor to operate with supersonic axial inflow velocity. To determine whether or not an acceptable level of performance was achieved in view of the high losses, the measured cascade data were used to predict the maximum potential compressor pressure ratio and efficiency of these single-stage and counter-rotating blade designs. With these data and assumed characteristics of the other engine components, the engine specific impulse and thrust were calculated and are presented as a function of flight Mach number in figure 7. Since the results of many cascade tests were utilized, the engine performance is shown as bands. These bands are superimposed upon lines of engine performance for constant nozzle-to-free-stream total-pressure ratio for stoichiometric fuel-air ratio. In this manner the approximate level of the product of inlet recovery and fan pressure ratio is apparent.

At sea-level static conditions, the counter-rotating fan engine produces considerably greater thrust than the single-stage design not only because of its higher fan-pressure-ratio potential but also because of the smaller relative effect upon performance of the 20-percent total-pressure loss associated with a sharp-lip inlet at high inflow velocity (ref. 3). At high flight Mach numbers, the two types of compressors yield almost identical engine performance. Although the counter-rotating design appears to be more desirable for use in an accelerator engine, its estimated low fan efficiency results in bypass ratios of 3 to 5 which preclude the use of centrifugal gas generator compressors, whereas bypass ratios of 10 to 12 for the single-stage design will result in smaller and lighter gas generator elements. Variable-cowl-lip geometry will increase the thrust potential of the single-stage design approximately 15 percent at take-off, so that its specific thrust is comparable to that of current hydrocarbon-fueled afterburning turbofans. It thus appears that either type of fan will operate at an acceptable level of performance.

CONCLUDING REMARKS

The structural and cooling tests have demonstrated the feasibility of the fabrication of the variable-pitch blade; however, the details of the

~~CONFIDENTIAL~~

pitch-change mechanism, coolant routing, and effects of fluctuating air loads have not been investigated. Although adequate compressor performance may be predicted from cascade results, it is necessary to obtain actual compressor data and inlet recovery data in the ramjet mode before the feasibility of the variable-pitch supersonic compressor concept can be assured. In addition, other problem areas, such as the fuel distribution and engine control systems, part power operation, and fuel rich combustion, must be investigated to determine the overall merit of the variable-pitch engine.

~~CONFIDENTIAL~~

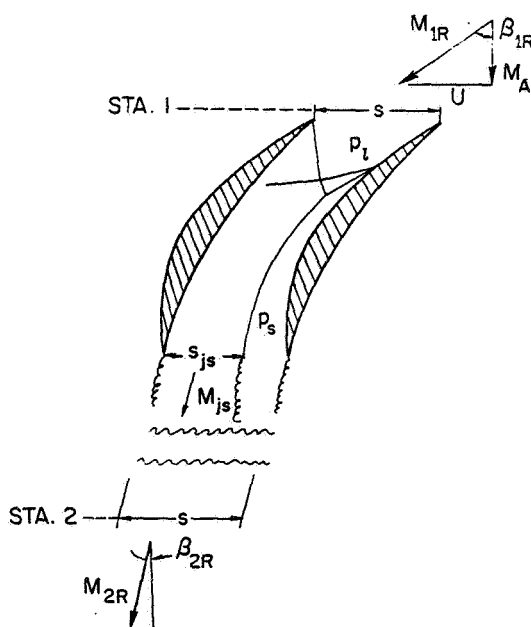
~~CONFIDENTIAL~~

APPENDIX

METHOD OF PREDICTING SUPERSONIC CASCADE PERFORMANCE

A simplified procedure to predict the performance of reaction-type supersonic cascades is herein outlined and is applicable primarily to sections employing large camber angles. For blades of this type, large regions of separated flow exist near the convex surface without flow reattachment to the surface prior to the blade exit. Downstream of the cascade, the flow is diffused by means of a dump-mixing process as the separation bubble collapses. To determine the stagnation-pressure loss and static-pressure rise as the flow is diffused, it is necessary to know the lateral extent of either the separated region or the jet stream and the jet-stream Mach number M_{js} at the trailing edge of the cascade. With these parameters known, the equations of conservation of mass, energy, and momentum are applied as the flow mixes and is assumed to flow uniformly across the downstream boundary of width equal to the blade spacing s .

The static pressure p_s throughout the separated region shown in the sketch is assumed to be constant and is assigned arbitrary values. The maximum limiting value of static pressure is discussed later. In addition, the static pressure is assumed to be uniform across the trailing edge of the cascade. Although this assumption is a gross misrepresentation of the actual flow for blades of large curvature, the variation in the answers is insignificant when compared with the results of calculations assuming linear variation of static pressure from the separation streamline to that corresponding to a Mach number of 1.0 at the concave-surface trailing edge.



The stagnation-pressure recovery at the trailing edge $p_{t,js}/p_{t,1R}$ is assumed to be equal to that for a normal shock corresponding to the inlet Mach number M_{1R} for subsonic axial inlet Mach numbers. For supersonic axial Mach numbers, the stagnation-pressure recovery is calculated to be the product of the recovery across the suction-surface leading-edge oblique shock and the recovery for a normal shock at the Mach number immediately downstream of the oblique shock.

The jet-stream Mach number, assumed to be uniform, is determined from the trailing-edge static-to-stagnation pressure ratio. The exit-jet-stream flow area is then determined from the continuity relationships. With the assumption that for a sharp-trailing-edge blade, the flow leaving the blade as well as that at the downstream boundary is parallel to the concave surface at the trailing edge, the dump-area ratio is obtained from

$$\frac{A_{js}}{A_{2R}} = \frac{s_{js}}{s} = \frac{\left(\frac{A_{js}}{A^*}\right) M_{js} \left(\frac{A^*}{A_{1R}}\right) M_{1R} \cos \beta_{1R}}{\frac{p_{t,js}}{p_{t,1R}} \cos \beta_{2R}}$$

For the calculated dump-area ratio and jet-stream Mach number, the downstream static and stagnation pressures and corresponding Mach number may be obtained by the methods of references 4 and 5, extended to include supersonic jet-stream velocity.

The flow measurements made in the cascade tests indicated that due to side-wall separation and nonidentical flow patterns in the blade passages, the mass flow rate at the midspan measuring station of the central passage exceeded the flow rate entering that passage. The mixing equations were therefore modified to reflect a reduction in downstream flow area proportional to the measured excess flow rate in order to compare the test results with those calculated and presented in figure 6.

The static pressure in the separated flow region, which was assumed to be constant, has indeed been found to be constant in the cascade tests and its value depends upon the chordwise location of the separation point. With increasing downstream throttling, the separation point moves upstream and forward of the point at which the concave-surface leading-edge oblique shock interaction with the boundary layer causes separation to occur at low back pressures. For an arbitrary location of the separation point upstream of the oblique shock interaction, the pressure in the separated flow region may be calculated by determining the local Mach number M_l and static pressure p_l immediately upstream of the separation point by using single-family shock-expansion theory and applying the peak pressure ratio criteria for turbulent-boundary-layer separation of reference 6 to calculate p_s . The applicability of this method to predict the pressure in the separated flow region is indicated in figure 8 in which the calculated values were obtained by the present method

~~CONFIDENTIAL~~

in conjunction with schlieren photographs. The maximum static pressure in the separated region is defined to exist with the separation point at the most forward position for which the oblique shock caused by the flow separating from the surface does not propagate disturbances ahead of the leading edge of the following blade.

.

~~CONFIDENTIAL~~

~~CONFIDENTIAL~~

REFERENCES

1. Boxer, Emanuel: The Flow Induction Process of Compressors Designed To Accept Supersonic Inflow Velocity. AIAA Paper No. 66-615, June 1966.
2. Advan. Propulsion Group Staff: Variable-Pitch Supersonic Inflow Compressor. AiResearch Rept. No. 67-1650 (Contract No. NAS1-4859), Garrett Corp.
3. Fradenburgh, Evan A.; and Wyatt, DeMarquis D.: Theoretical Performance ... Characteristics of Sharp-Lip Inlets at Subsonic Speeds. NACA Rept. 1193, 1954. (Supersedes NACA TN 3004.)
4. Wennerstrom, Arthur J.: Flow Tables for Air ($\gamma = 1.4$) Passing an Abrupt Area Increase Oblique to the Flow Direction. ARL 64-10, U.S. Air Force, Jan. 1964.
5. Joyner, Upshur T.: Charts of Pressure, Density, and Temperature Changes at an Abrupt Increase in Cross-Sectional Area of Flow of Compressible Air. NACA WR L-13, 1945. (Formerly NACA ARR L4L19.)
6. Love, Eugene S.: Pressure Rise Associated With Shock-Induced Boundary-Layer Separation. NACA TN 3601, 1955.

~~CONFIDENTIAL~~

~~CONFIDENTIAL~~

TABLE I.- ASSUMED ENGINE COMPONENT PERFORMANCE VALUES

	Assumed performance value
Inlet:	
Pressure recovery at -	
Sea level at $M_\infty = 0.$	0.80
37 000 ft at $M_\infty = 1.0$	0.97
50 000 ft at $M_\infty = 2.0$	0.95
60 000 ft at $M_\infty = 3.0$	0.90
80 000 ft at $M_\infty = 4.0$	0.83
Fan:	
Pressure ratio	Variable
Efficiency	Variable
Heat exchangers (two):	
Air pressure recovery	0.95
Gas generator compressors (two):	
Pressure ratio	4.0
Efficiency	0.80
Primary burner:	
Pressure recovery	0.95
Efficiency	0.98
High pressure turbine:	
Efficiency	0.85
Inter-turbine duct:	
Pressure recovery	0.95
Low pressure turbine:	
Efficiency	0.85
Fan duct:	
Pressure recovery	0.95
Duct burner:	
Pressure recovery	0.90
Efficiency	0.95
Exhaust nozzle:	
Velocity coefficient	0.98

~~CONFIDENTIAL~~

SCHEMATIC DIAGRAMS OF VARIABLE-PITCH ENGINE

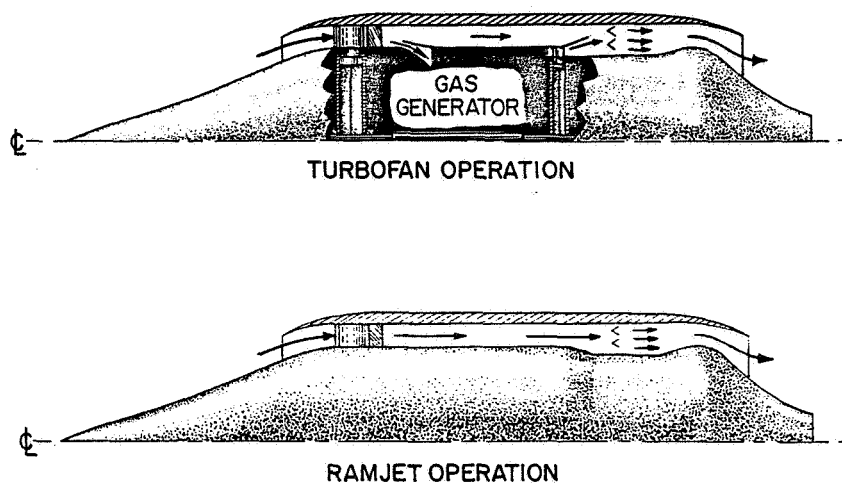


Figure 1

EFFECT OF FAN PERFORMANCE ON ENGINE CYCLE

LH₂ FUEL; $\phi = 1.0$

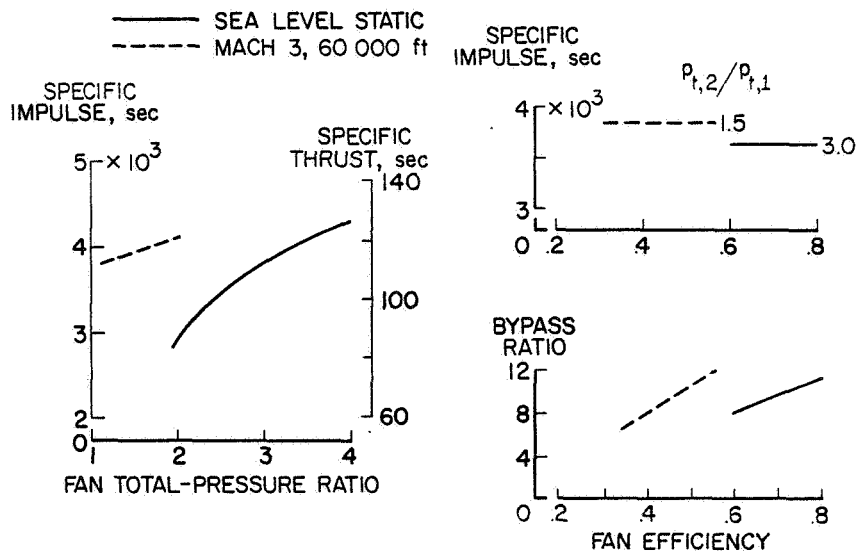
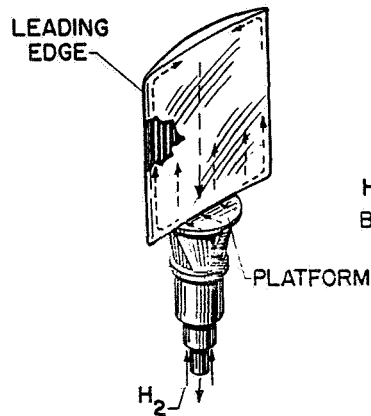


Figure 2

~~CONFIDENTIAL~~

HYDROGEN-COOLED COMPRESSOR BLADE

COOLED-BLADE FLOW ROUTING



ESTIMATED TEST ENVIRONMENT

$T_1 = 3400^\circ \text{F}$; L.E. $Q = 650 \text{ Btu/sec-ft}^2$
AVERAGE $Q = 145 \text{ Btu/sec-ft}^2$

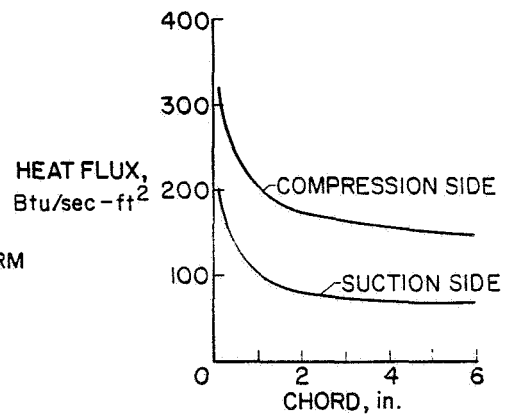


Figure 3

WHIRL-TEST ARRANGEMENT

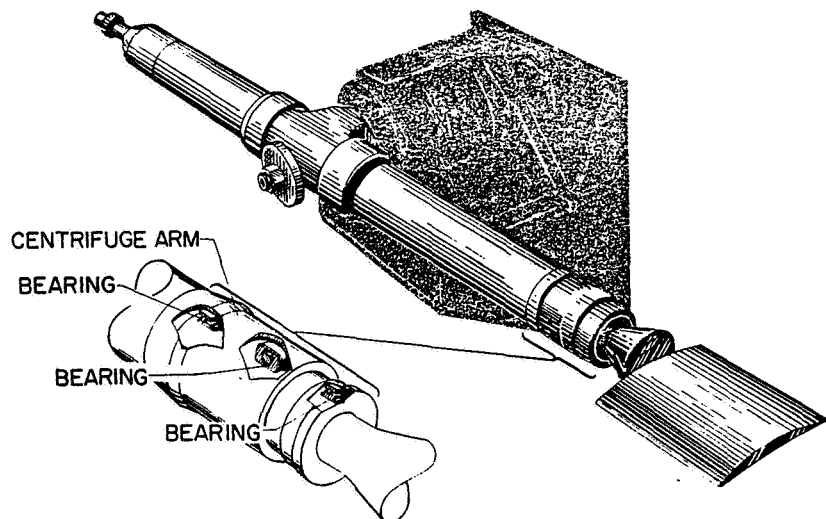


Figure 4

~~CONFIDENTIAL~~

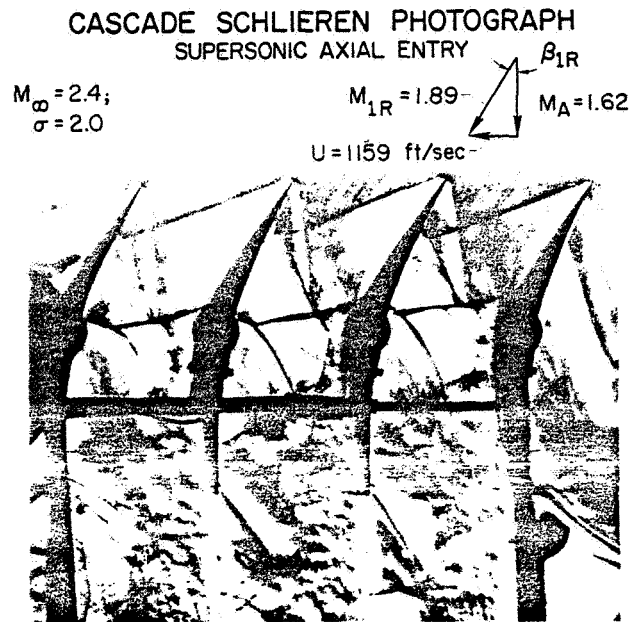


Figure 5

L-2867-5

REPRESENTATIVE CASCADE PERFORMANCE

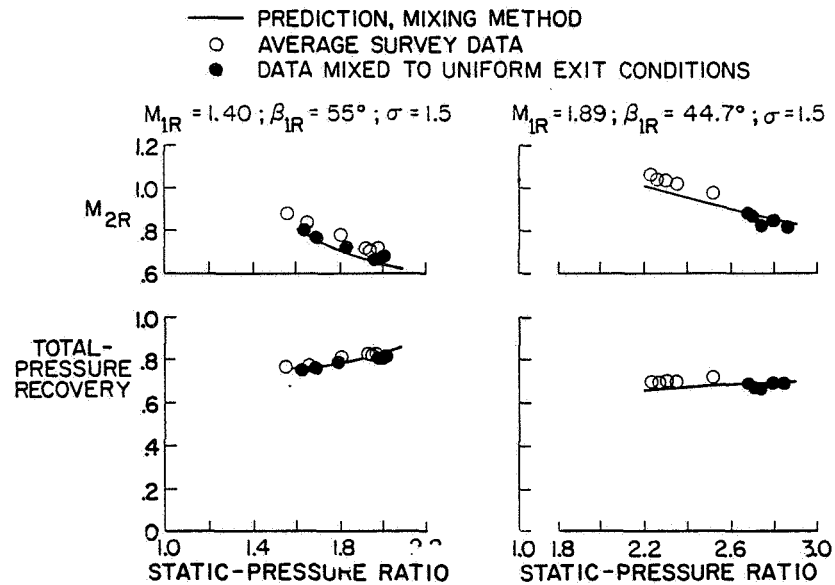


Figure 6

~~CONFIDENTIAL~~

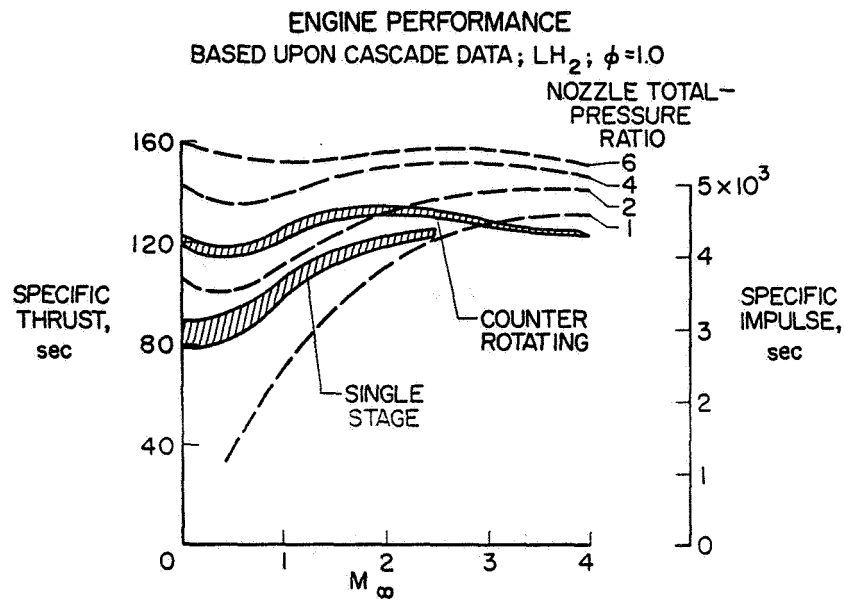


Figure 7

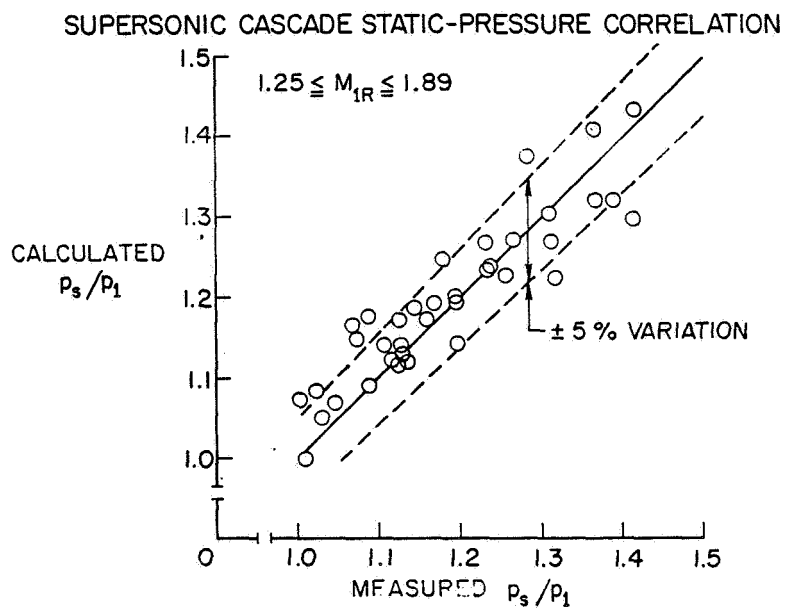


Figure 8

~~CONFIDENTIAL~~

26. MEASUREMENT TECHNIQUES FOR HYPERSONIC PROPULSION

By L. N. Krause, D. R. Buchele, and I. Warshawsky
Lewis Research Center

INTRODUCTION

The engineering development of propulsion systems involves studies of components and tests of the complete engine. During component studies, extensive detailed measurements are required; in testing the complete engine, only certain overall-performance parameters are of main interest.

Examples of some of the quantities of interest during component studies are:

Inlet: efficiency, pressure ratio, skin friction, heat transfer rates, inlet unstart.

Combustor-nozzle: efficiency, initial fuel distribution, local fuel-air ratio, heat transfer rates, skin friction, degree to which equilibrium is reached, detection of ignition point.

Some of the quantities of interest during complete engine testing are: internal thrust, specific impulse, thrust coefficient, and heat transfer rates.

The primary measurements required to obtain the majority of these quantities are: force, pressure, enthalpy or temperature, flow rate, and gas composition. In this report, emphasis will be placed on the

~~CONFIDENTIAL~~

following specific measurements: thrust, total and static pressure, air and fuel flow rate, gas composition, total enthalpy and related quantities, and static temperature and related quantities.

Table I lists some of the conditions throughout a ram jet engine for a Mach 8, 120,000-foot-altitude operation. Figure 1 shows station locations. It is noteworthy that, in front of the engine, the total temperature is above the range of conventional thermocouples, but the static temperature is too low for most optical techniques. Another condition worth noting is the low static pressure encountered in front of the engine. These points will be discussed in the following text.

An important general principle concerning internal measurements is that, if any internal probing is to be done, it should be done during the component-testing phase rather than during complete-engine testing. The problems associated with surveying the internal supersonic passages of a complete engine are too severe, from the standpoints of aerodynamics, heat transfer, and mechanical design, to allow effective solution. However, probe surveys in front of the complete engine and behind its exit plane remain feasible.

In the case of certain variables, a particular measurement technique is clearly to be preferred, and is well established and in routine use, so that a detailed description of its implementation can be furnished. In the case of other variables, a variety of techniques exist that are of comparable merit and that supplement each other in providing useful information; some of these are in early stages of development. These techniques can only be listed and described briefly. The selection of

~~CONFIDENTIAL~~

which are to be used will depend on the particular application and on the instrumentation skills and apparatus available to the experimenter.

Because of the scope of this report, only the main features of the measurements will be discussed, and the reader will be referred to some selected references for more details and more comprehensive bibliographies. This report will be limited also to measurements of slowly varying quantities, and will emphasize those that characterize the performance of a practical engine.

THRUST

Some of the considerations affecting the design of a thrust-measuring system for a complete engine are illustrated in figure 2. Aerodynamic heating, as well as heating due to combustion, may produce slight distortions of the aircraft structure. It is therefore desirable that a single thrust-measuring spring take almost all of the thrust load, because differential thermal expansion might produce non-pertinent loads on springs attached at several locations. However, the use of a single principal spring to constrain thrust is inadequate to fix the position and attitude of the engine; hence auxiliary springs, comparatively weak in the thrust direction, are used to constrain pitch, yaw, and side motion. The pitch-constraining spring is particularly important, because the center line of thrust is removed from the base of the spring, so that there is a large pitching moment.

However well the auxiliary springs are designed to act orthogonally to the thrust direction, they will nevertheless provide some slight thrust constraint. Additional constraints will be provided by piping to the engine,

~~CONFIDENTIAL~~

such as fuel and coolant lines. In order that these additional constraints be minimal, the piping should be hinged by elastic metallic-bellows joints at each end of the pipe, the axis of the piping should be normal to the thrust direction, and the axis should be close to the principal engine support in order to minimize pitching moment. The effect of varying hydraulic pressures upon the thrust indication should be determined in preliminary cold runs; those pressures which prove significant should then be recorded during any actual test run, and appropriate correction made. All-metallic, elastic construction of the piping and its bellows-type hinges is necessary because this piping constitutes an appreciable fraction of the thrust-measuring spring system and the spring constant of the piping will vary least with respect to temperature, internal pressure, time, and installation artifacts if the piping is metallic and elastic.

Detailed consideration of the actual thrust-measuring instrument is not possible here because it depends on details of the actual installation. In general, this instrument will measure the deflection of a spring or the strain in a spring. Particular attention must be paid to preventing stresses in the spring mounting and attachment from influencing the measurement and to preventing transient temperature gradients from affecting the measurement, either through differential thermal expansion or through thermoelectric emf's. (Commercial "load cells" are compensated for steady-state cell-temperature changes but are not ordinarily compensated for temperature gradients.)

The thrust calibration of the entire installation must be established

after all piping is in place and, preferably, when all piping is as near to operating temperature as possible.

The dynamic characteristics of the engine support and constraint system must be known and must be suited to reliable thrust measurement. Any spring-mass system will oscillate in every one of its modes. These natural oscillations will be only slightly damped if the spring system has very low hysteresis, unless deliberate velocity damping is added. There are at least six fundamental modes - more, if the engine structure is not rigid. For this reason, it is desirable that the various points of attachment of restraining springs to the engine be tied together by a comparatively rigid shell, as shown in figure 2.

Pitch, roll, and yaw moments, and side forces, may be induced if fluctuating angles of attack prevent the shock from attaching uniformly around the entire periphery of the inlet lip and remaining attached. However, the predominant oscillations will be in thrust and in pitch. Such oscillations will be induced whenever there is a change in force or moment; for example, when the engine is started, stopped, or accelerated, when the inlet spike position is changed, or when the ambient supersonic flow is initiated or terminated.

The various natural frequencies of oscillation should be kept as high as possible. As a rule of thumb, a longitudinal natural frequency exceeding 50 hertz is desirable. This criterion is tantamount to requiring that the longitudinal deflection of the thrust-measuring system under a force numerically equal to the sea-level weight of the engine shall be less than 0.004 inch.

~~CONFIDENTIAL~~

The oscillation of a 50-hertz system damped only by elastic hysteresis may persist for several tenths of a second after initiation, before the amplitude drops below 10 percent of the initial value. Consequently, additional damping is generally necessary in order to be able to follow thrust fluctuations accurately. Mechanical viscous damping is most desirable, although inconvenient. Electrical damping of the thrust-transducer output may be used, but it cannot prevent the initial mechanical amplification of natural frequencies. (It should be noted that high-order filters with sharp high-frequency cutoff show overshoot in response to impulsive load changes.) Furthermore, if only electrical damping is used, the thrust spring must have an additional design safety factor of 2, because the maximum spring stress and deflection will be twice the steady-state value.

If the shocks of initiating and terminating the supersonic flow may exceed the normal thrust range, additional design safety factors must be applied, or else mechanical locks must be provided to restrain the engine until steady supersonic operation has been reached.

If a sampled-data system of thrust recording is contemplated, it is essential that initial runs be first made with a continuously recorded analog system. These analog runs will show what natural frequencies are appearing in the thrust record. The data sampling rate should then be chosen so that there are at least ten samples per period of the highest natural frequency, of appreciable amplitude, that had appeared in the analog record.

The thrust indicated by the thrust-measuring system must be reduced

by the external drag, to yield the net engine thrust. If the external drag is 5 percent of the net thrust, an error of 5 percent in drag will cause only 1/4 percent error in thrust. Thus, it is sufficient to measure external drag during cold tests in the wind tunnel or in flight, with interference effects from adjacent bodies similar to those found in actual hot runs, and it may even be sufficient to predict the external drag from analytical computations, without recourse to experiment.

However, reproducibility of external drag is achievable only if the springs and piping shown in figure 2 are properly shrouded by telescoping fairings, with the principal fairing attached to the wind tunnel or carrier-plane structure, as suggested in the sketch in the corner of figure 2.

TOTAL PRESSURE

The pitot tube is one of the simplest of all flow measuring instruments. For equilibrium conditions, the total-pressure tube will indicate true total pressure in subsonic flow and will indicate true total pressure behind the normal shock in supersonic flow. Normally, the greatest error encountered is due to misalignment with the flow. Even so, a simple square-ended tube is insensitive to flow angles up to 10° and a 30° internally beveled tube up to 20° (ref. 1).

Figure 3 shows the ratio of indicated total pressure $p_{t,ind}$ to ρv^2 (where ρ and v are density and velocity respectively), and the ratio of indicated total pressure to free-stream total pressure p_t , versus Mach number M . The total-pressure tube actually gives a good indication of ρv^2 at Mach numbers greater than 2 and is fairly insensitive to the ratio of specific heats, increasing only 2 percent for a change in the specific-

heat ratio from 1.4 to 1.3. Because of this specific-heat-ratio insensitivity, similar insensitivity is expected with respect to non-equilibrium flow conditions.

An interesting feature of the total-pressure probe indication ρv^2 is that it is close to the value of stream thrust per unit area. The equation for internal thrust can be written as

$$\frac{T_i}{A} = \frac{A_4}{A} (\rho_4 v_4^2 + p_{s,4}) - (\rho_0 v_0^2 + p_{s,0})$$

where T_i = internal thrust, A = area, p_s = static pressure, and the subscript numbers represent stations in figure 1.

The term $\rho_4 v_4^2$ represents an integration of the total-pressure-probe indication across the exit plane. For hypersonic flow, the difference between the second terms in each of the parentheses may be small compared to the difference between the ρv^2 terms, so that the thrust may be obtained by integrating the total-pressure measurement over the areas and applying only a small correction. For flow regions where the thrust may be represented as a small difference between large values of pressure, the pressure difference should be measured directly. One of the main uncertainties in this method of thrust measurement is the uncertainty in knowledge of the capture area A .

Measurement of thrust of a supersonic turbojet engine in flight using survey probes at the exit is described in reference 2.

If the lower curve in figure 3 is used to obtain free-stream total pressure, the Mach number must be determined accurately by an independent

method. At the higher Mach numbers, a 1-percent error in Mach number will produce a 5-percent error in free-stream total pressure. Furthermore, the curve is quite sensitive to the ratio of specific heats, decreasing 30 percent at a Mach number of 4 as the ratio of specific heats changes from 1.4 to 1.3. Actually, in experiments involving flow nozzles, the lower curve is used to obtain exit Mach number from the ratio of indicated total pressure to nozzle plenum pressure.

STATIC PRESSURE

Conventional wall static taps supply the bulk of static pressure data. The taps should be flush with the surface and free of external burrs. Since error in wall static pressure measurement increases with hole diameter, the hole size should be only large enough to insure adequate time response. Reference 3, chapter 6, lists several articles on dynamic response. For ground testing, static-tap diameter varies from about 0.02 to 0.06 inch.

To check deviations from one-dimensional-flow assumptions, static-pressure profiles are required at the entrance and exit of components or engines under test. Three different body shapes may be used for static-pressure measurement in a supersonic stream: the cylindrical tube, the wedge, and the cone.

The cylindrical tube lends itself to sting-type mounting and has the advantage of not requiring knowledge of any stream parameters for its use. However, the static taps should be about 30 diameters from the nose tip, so that considerable tube length is required, and the tube is sensitive to flow misalignment, having an error of about 5 percent at

a flow angle of 10° (refs. 4 and 5).

Since the wedge and cone are similar in method of use, only the cone will be discussed because it is more commonly used. However, the wedge does find application in situations where the measuring elements must be built into the instrument supporting strut rather than mounted on a sting.

Figure 4 shows a 15° -half-angle cone with a static tap on the conical surface and a total-pressure tap at the nose. The graph shows the ratio of indicated static pressure $p_{s,ind}$ to free-stream static pressure p_s , and the ratio of indicated static pressure to indicated total pressure $p_{t,ind}$, each plotted against Mach number. Because the upper curve is a function of Mach number, the Mach number must be known before the stream static pressure p_s can be determined. The Mach number is first determined from the lower curve and knowledge of the ratio of indicated static pressure to indicated total pressure. Then, the upper curve is used to determine the free-stream static pressure. At a Mach number of 4, changing the ratio of specific heats from 1.4 to 1.3 lowers the upper curve 5 percent and raises the lower curve 1 percent.

The lower curve in figure 4 is for a cone with a sharp nose. Blunting the nose is required to provide adequate heat transfer and to make room for the total-pressure tap. The blunting will change the level of the lower curve about 5 percent (refs. 6 and 7). Because of manufacturing tolerances associated with such a geometry, each probe should be calibrated (ref. 8).

The cone angle should be minimized because decreasing the angle decreases the slope of the upper curve in figure 4 and increases the slope of the lower curve. The 15° conical angle shown is about the smallest angle that will allow use of pressure taps and provide adequate cooling.

The conical probe described in reference 8 has four static taps on the cone surface in addition to the pitot tap at the nose, and is used to obtain indicated total pressure, Mach number, and flow angle in addition to free-stream static pressure. Hence, it can be used as a combination probe to obtain several stream quantities.

As shown in table I, static pressure is small at high altitudes. Accurate measurement can be made with modern capacitance-type differential manometers (refs. 9 and 10) provided there is a means for setting or checking the zero reading shortly before or after the measurement. Figure 5 shows the valving and pumping required for one arrangement that has proved satisfactory. In use, valve V2 is closed and the others left open. The downstream side of the transducer is held continuously at a pressure below 10 millitorr. To check zero, all valve settings are reversed (V2 open, V1 and V3 closed). In transferring to the standby condition, when no measurement is to be made, valve V1 is closed, and the other two valves are open, so that both sides of the manometer are being evacuated by the pump. By never subjecting the manometer to an absolute pressure exceeding in numerical value its differential-pressure range, internal cleanliness and stability of zero and of sensitivity may be maintained. Figure 5 also indicates the time constants obtainable with the type of installation shown.

AIR FLOW RATE

Several methods of air flow rate measurement are shown in figure 6. The methods are listed approximately in order of increasing error.

Connected Pipe With Upstream Orifice (Fig. 6(a))

The most straightforward flow measurement is obtained in experiments where a standard orifice is installed upstream of, and in series with, the system under test. Such a system will yield about 1 percent inaccuracy (refs. 11 and 12).

Flow Nozzle Downstream of Inlet (Fig. 6(b))

To test an inlet or a non-burning engine, a flow measuring nozzle may be located downstream of the section of interest. This arrangement will give uncertainties greater than 1 percent because the nozzle installation is rendered non-standard by proximity of the upstream hardware. A survey of temperature will probably be required to obtain the average gas temperature. For cases where the nozzle can be operated at sonic velocity, the throat pressure tap can be eliminated, thereby simplifying the flow rate measurement (ref. 13).

Shock on Lip Plus Inlet Conditions (Fig. 6(c))

In this method, the position of the inlet shock is observed with a schlieren or shadowgraph. When the shock is on the lip, the stream-tube area is defined and the air flow rate is calculable from known inlet conditions. These inlet conditions are obtained from previous facility calibrations or from a survey in front of the engine made immediately before the test run. Of course, the capture area is not defined for off-design conditions and for operation at non-zero angle of attack, so that this method has limited application.

Probe Survey at Engine Exit (Fig. 6(d))

Mass flow rate may be obtained by surveying across the engine exit

with a mass flow probe. The probe is simply a cooled aspirating tube with a flow-rate-measuring device located where the aspirated gas has cooled sufficiently to be measurable conveniently but not sufficiently to condense any water in the gas. To define the probe capture area, the nose shock must be swallowed.

The main source of error in the mass flow probe is the uncertainty in this capture area, because the lip has to be rounded slightly to allow for adequate cooling. An agreement to within 5 percent with the total flow in a supersonic arc tunnel has been reported in reference 14.

Since the mass flow probe measures exhaust flow rate, the air flow rate would then be determined by the difference between measured exhaust-flow rate, integrated over area at station 4, and fuel-flow rate.

In a previous section it was pointed out that the pitot tube, at Mach numbers greater than 2, does a good job of measuring ρv^2 . Since the mass flow probe measures ρv , a profile of density and velocity across the stream may be computed from the measurements provided by the two instruments.

Use of the mass flow probe has also been reported in references 5, 15, and 16.

Spike Position Correlation

For the case of the burning engine in flight, the flow rate may be obtained from a correlation such as that shown in figure 6(e). The correlation requires knowledge at least of Mach number, pressure, pitch angle, and yaw angle as functions of spike position. This correlation may

be obtained during ground testing or during flight tests of a non-burning engine.

FUEL FLOW RATE

Only hydrogen will be considered as the engine fuel, since the metering of other, less likely fuels poses few special problems. Liquid hydrogen is unique in its low temperature, density, and viscosity. Since continuity of mass exists in the fuel supply system, the flowrate may be measured at a location where the fuel is in a single phase. The flowrate of the liquid can generally be measured more conveniently and accurately than that of the gas. The turbine-type flowmeter is recommended for this purpose, because the simplicity of its installation and use affords highest reliability. Figure 7 shows some of the considerations involved in achieving reliable performance and good accuracy.

Since the flowmeter provides volume-flow-rate indication, density must be determined from pressure and temperature measurements. Little accuracy is required in the pressure measurement, since the density changes on the order of 0.1 percent for a 1-atmosphere pressure change. However, a steady average-pressure indication may not be achieved if there is excessive surging in the pressure-connecting line because the pressure transducer is near room temperature, so that boiling occurs in the line. The surging is minimized if the connecting line is of stainless steel, and is horizontal or slopes upward away from the liquid-hydrogen line (fig. 7(b)).

A density change on the order of 0.1 percent is associated with a 0.3-percent change in temperature. Consequently, a 4-wire platinum

resistance thermometer is recommended for this measurement. NASA Lewis has adopted a 1/16-inch diameter, 0.6-inch long, ceramic-coated element for routine applications, and a 1/4-inch diameter, 1.8-inch long, strain-free element, enclosed in a helium-filled platinum tube, for standards applications. The element must be mounted so that there is minimum conduction of heat along the element support and the connecting wires (fig. 7(c)). These wires are made of manganin, for at least several inches. It may be desirable, for higher accuracy, to measure temperatures upstream and downstream of the flowmeter. Probable errors of less than 0.02°C are generally achieved, if the sensitive element is mounted so that it averages temperature across the pipe diameter.

A turbine-type meter is strongly affected by upstream swirl and is slightly affected by axially symmetric velocity distribution. An upstream swirl eliminator consisting of a honeycomb of square elements or circular tubes is more desirable than one of radial vanes, since the latter arrangement tends to reduce velocity on the pipe axis. The piping lengths recommended in figure 7(a) represent the best guess based on the experience reported in reference 17; no systematic investigation of this subject has yet been reported. The meter may be mounted either vertically, with flow upward, or horizontally, but must be calibrated in the same attitude as that in which it is used. Horizontal installation is more conventional and may increase the linear range. Reference 17 shows that the difference between vertical and horizontal installation is on the order of 1 percent.

Because of the low viscosity of liquid hydrogen, piping, as well

as meters, are sized on the basis of about 100 ft sec^{-1} linear velocity. The resultant high Reynolds number, with its flatter velocity profile, provides several advantages, including a wider linear range for the turbine meter (ref. 17).

For maximum accuracy, the meter must be calibrated in liquid hydrogen (ref. 17), preferably before and after any long period of use. Such calibration must treat the "flowmeter" as consisting of the entire assembly between the flanges shown in figure 7(a). This assembly must remain intact, and never be taken apart, between the times of the "before" and "after" calibrations.

Figure 7(a) also illustrates several means for reducing swirl and ensuring single-phase flow. These include a bell-mouthed exit from the supply tank, radial or honeycombed anti-swirl vanes at this exit, a manifold to distribute pressurizing gas smoothly around the cross-section of the tank, and exit holes in this manifold placed so that pressurizing gas is directed away from the surface of the liquid. If a pump is used, the flowmeter should be well downstream of the pump. The normal venting system, for use after the system has been filled with liquid, and the large vent line required during initial filling and cooldown, are also shown. Additional operational and safety details are described in reference 18.

The most common cause of mechanical failure of turbine-type meters in liquid-hydrogen service has been the overspeeding resulting from passage of hydrogen gas through the flowmeter. This gas is created when liquid hydrogen is first admitted to a warm system. Such overspeeding

must not be permitted. Figure 7(a) illustrates several techniques to prevent overspeeding.

(a) The meter is placed upstream of the shutoff valve that leads to the engine, so that the meter and all piping upstream of it are already cooled before the fuel flow is started.

(b) The filling-line entrance is upstream of the meter, so that the meter is in a blind pocket, and comparatively little filling fluid passes through the meter.

(c) The meter is continuously connected to a ratemeter with overspeed alarm; meter indication is continuously monitored during the filling operation, and filling rate is controlled so that the meter is never overspeeded.

The connection between turbine meter and ratemeter should be by means of a 2-conductor twisted cable with separate shield which is itself covered with insulation. If the ratemeter has a grounded input terminal ("single-ended input"), the shield should be connected to this terminal at the ratemeter end only. If the ratemeter has a floating input, the shield should be connected to one transducer output terminal, at the transducer end only. In either case, the other end of the shield should be carefully insulated.

Sand and dust may enter the system because of a carelessly exposed filling hose. It is therefore desirable, where possible, to install a 25-micron stainless steel filter at the fill-line entrance. If this filter contains cast components, it should first have been checked by thermally shocking it with liquid hydrogen and then inspecting and cleaning it to

~~CONFIDENTIAL~~

remove loose particles. The filling hose should be fitted with a non-separable cap that will ensure internal cleanliness while exposed to the weather.

The entire system, including the portion between fill-line valve and tank-truck valve, must be purged of air before filling. The purging procedure recommended is a cycle of three evacuations with an oil-trapped mechanical pump to a pressure of less than 0.1 torr and two fillings with 99.9 percent pure helium. If the system is to be emptied of hydrogen and prepared to stand by at room temperature, the hydrogen may be allowed to warm up while it vents through the normal venting system, terminating with a positive pressure of about 2 psig of hydrogen in the system. Then a similar sequence of three cycles of evacuation and filling with helium is terminated with a positive pressure of about 2 psig of helium in the system. Additional details of these and related operations are given in reference 18.

The only reports of extensive first-hand experience with liquid-hydrogen flowmeters are contained in references 17, 19, 20, and 21. Reference 17 suggests that probable errors of 0.2 to 0.7 percent are attainable.

If fuel flow rate is to be measured when the fuel is in the completely gaseous condition, commercial turbine-type meters designed for such gas service, or any of the conventional gas flowmeters treated in reference 11, may be used. A critical-flow orifice may be particularly suited to measurement of vented gas.

GAS COMPOSITION

The exhaust gases of interest in the combustion of hydrogen and air are N_2 , H_2O , H_2 , O_2 , OH , H , and O . Corresponding mole fractions for a

~~CONFIDENTIAL~~

stoichiometric Mach 8, 120,000-ft case are 0.62, 0.27, 0.04, 0.02, 0.03, <0.01, and <0.01.

Composition may be measured by sampling with a probe or by optical methods using apparatus outside the gas stream. The latter technique will be treated under Local Static Temperature and Related Quantities.

The simplest type of local gas composition measurement is determination of fuel-air ratio by sampling. A cooled probe such as the mass flow probe, or an aspirated pitot probe which does not swallow the nose shock, may be connected to a gas analyzer. Since there is no rapid quenching, the gas analyzer will receive nitrogen, water, and small amounts of molecular hydrogen and oxygen.

To insure accurate measurement, condensation of water from the sampled gas inside the cooled probe must be prevented by keeping the probe's inside wall temperature above the condensation temperature. If the pressure inside the sampling probe is approximately one atmosphere, condensation can be prevented by using a water cooling system at a line pressure above 25 atmospheres and controlling the flow rate to keep the wall temperature at the exit of the probe above 120° C. The total gas sample flow rate can then be measured. The water can then be condensed and removed to allow analysis of the remaining gas.

A higher degree of sophistication is the determination of composition at the point of sampling, by rapidly quenching the gas with a small cooled probe such as the one shown in figure 8. From the graph in figure 8, it can be seen that the gas must be quenched in a few microseconds. Typical

~~CONFIDENTIAL~~

velocities near the probe are about 0.1 inch per microsecond, which means that the gas must be quenched within a quarter of an inch. To promote rapid quenching, the probe should be small and the pressure downstream of the inlet should be low. Paradoxically, however, it is desirable to swallow the shock in order to prevent composition changes at the nose caused by high gas temperatures that would occur behind any nose shock.

It is doubtful whether true measurements of H_2 and O_2 are obtained even when such a miniature probe is used. Certainly, OH, H, and O cannot be quenched in such sampling probes. Efficiencies determined by this method will be higher than the true efficiency if the reaction continues inside the sampling probe.

Reference 22 reviews the problems associated with gas sampling, primarily in subsonic gas streams. Recently, a sampling system has been developed for flame studies, that consists of a sampling probe using vacuum pumps to obtain rapid expansion. The molecular beam formed as a result of the pumping is passed directly into a mass spectrometer for analysis (refs. 23 and 24). An application of this type of system on a rocket combustion chamber is described in reference 25. Although the sampling probe is quite bulky because of the required sizes of vacuum plumbing, the technique is attractive because it permits study of unstable or reactive species.

The sampled gas may be collected in bottles for later analysis or it may be analyzed continuously, on line. The on-line method should be used whenever possible. A review of recent studies concerning gas analysis is given in reference 26.

LOCAL TOTAL ENTHALPY AND RELATED QUANTITIES

Measurements which provide a map of local enthalpy h_t across the cross-section A of the gas stream can be integrated to yield the average enthalpy H_t of the entire gas stream. We have

$$H_t \cdot \int_A \rho v \cdot dA = \int_A h_t \rho v \cdot dA$$

where ρ and v are local density and linear velocity, respectively.

Practical approximations that yield adequate accuracy are provided by measurement of h_t along two orthogonal diameters; when there is axial symmetry, a single diameter may suffice.

The local measurement is provided by a probe which creates a normal shock in front of its sensitive measuring element. The deliberate use of the normal-shock condition ensures predictability of probe calibration and, generally, reliable correlation between free-stream conditions and the gas conditions actually measured by the probe. The degree to which this correlation may become unreliable will be indicated in the following discussion.

Many probe designs are available. Each type of probe measures a slightly different quantity, so that no distinctive choice may be made. In fact, the simultaneous use of several probe designs often clarifies one's understanding of the physical situation being studied.

Table II lists characteristics of some useful probes. Only the calorimetric probe actually measures enthalpy with minimum dependence on knowledge of gas properties. Intricate and meticulous design and construction are required to prevent heat losses that will prevent an

accurate measurement. Several early designs are described in reference 27; some others are described in references 15, 28, and 29.

Where temperatures are sufficiently low, the noble-metal thermocouple is reliable and relatively easy to use. Designs adaptable to hypersonic applications are described in references 30, 31, and 32. A general discussion of selection principles is contained in reference 33, which also lists some original-source articles. The useful temperature limit can be raised by deliberate, controlled cooling of the junction through radiation, conduction, or both (refs. 33, 34, 35, and 36). The uncertainty in the temperature measurement increases as the correction for cooling becomes larger. Still higher temperature limits may be achievable by using tungsten-rhenium alloy thermocouples, if the thermocouple can reach final temperature (as evidenced by the appearance of the temperature-time curve) before the material is oxidized and destroyed. Preliminary trials of this technique have been reported in reference 37, where 3000° K and a life of 0.2 second were attained in an oxidizing atmosphere. However, the accuracy of the method has not been established because an increasingly larger error is encountered as the free-oxygen content of the gas increases, because the heat of oxidation is added to the heat transported by the gas stream; also, there may be a corresponding alteration of thermoelectric power.

In the range of temperatures measurable with thermocouples, the conversion from translational temperature to enthalpy is straightforward.

Success has also been reported (ref. 38) in using an optical pyrometer

to observe the surface of a graphite hemisphere upon whose surface the gas stagnates; the graphite has sufficiently low thermal conductivity so that the principal cause of heat loss is radiation. A temperature of 2800°K (5000°R) has been measured.

Three devices that depend on reproducible heat transfer rate are the cooled-gas, cooled-tube, and stagnation-point probes. They have been reviewed in reference 39 and are particularly well suited to surveys to determine the shape of the local enthalpy distribution. The cooled-gas probe, originally described in reference 40, resembles the calorimetric probe, is simpler to construct, and involves fewer critical measurements, but requires a calibration at low temperature, and some knowledge of gas transport properties. The cooled-tube design exists in two forms: in one (ref. 41), the temperature rise of the coolant is measured; in the other (ref. 42), the temperature rise of the tube is measured. These designs require more complex construction than the cooled-gas design and some knowledge of free-stream Mach number and gas transport properties, but do not require aspiration, although aspiration is used in one of the designs described in reference 42. The stagnation-point designs require similar knowledge. Reference 43 describes one such design and gives references to many others. The ability of the stagnation-point designs to provide absolute enthalpy measurements is generally limited principally by a large empirical correction for undesired heat loss.

The pneumatic probe is an aspirating device that has been used extensively (ref. 27) so that its characteristics are well understood. It provides

a measure of density if velocity through the entrance orifice is very low and a measure of the product of density and pressure if the velocity is near to sonic. Hence, temperature may be deduced if total pressure is also measured after stopping the aspiration.

The velocity of sound may be used to infer the value of $\gamma T_t / M$, where γ , T , and M are specific-heat ratio, total temperature, and molecular weight, respectively. In a design conceived in references 44 and 45 and now under study by a NASA contractor, sound velocity is measured after the gas has entered an aspirated probe.

The heat-transfer-type devices, the pneumatic probe, and the sound-velocity types have no fundamental upper-temperature limit; the practical limit is imposed by the ability to provide cooling. In some of these devices, gas properties are measured very near to the normal shock front, so that the measurement yielded is influenced by whether or not vibrational modes of the gas are fully relaxed; at very high temperatures, relaxation of dissociation must also be considered. As a rule of thumb, relaxation effects becomes significant when the characteristic relaxation time (time constant) becomes comparable to the time of transit from the shock front to the location where gas property is measured (ref. 46). If transit time is so short that vibrational relaxation cannot occur, the airstream may be treated as having a constant specific-heat ratio of 1.4.

Some of the devices described have been intercompared in the same gas stream (ref. 32), together with a line-reversal pyrometer. The comparison served to increase the understanding of each of the devices and

of their probable accuracies. Under conditions of very careful use, agreements among various devices ranged from 1 to 5 percent, in the range below 2400°K (4400°R) (refs. 32 and 47).

INTEGRATED STATIC TEMPERATURE AND RELATED QUANTITIES

Static temperature, because it is a practically measurable quantity, is used with auxiliary measurements of pressure, composition, or mass velocity, to deduce static or total enthalpy. The temperature itself is an excellent indication of the non-equilibrium conditions of the gas and hence is useful in studying the thermochemistry of gas processes.

Optical-radiation-type thermometers are particularly useful for high-gas-temperature measurements because the radiant fluxes actually measured are several times more sensitive to temperature than to gas density or radiant-emitter concentration. This sensitivity arises from the exponential form of Planck's Law, and is most pronounced when the band or line used lies on the short-wave-length side of the maximum of the Planck radiation curve.

Uncertainty in static temperature deduced by any method that integrates along the path through a gas stream derives principally from the nonlinear nature of the integration. For example, if gas emission is measured, the emission will come principally from the nearer end of the gas column if gas emissivity is high; emission will be averaged linearly over the entire gas column only if gas emissivity is very low (fig. 9(a)), so that the nearer end of the gas column remains transparent to radiation

from the far end. An indication of the quantitative errors obtainable with some integrating devices is presented in reference 48.

Other errors arise because of nonlinear temporal integration (ref. 47), from errors in radiant-flux measurement, and from uncertainty in knowledge of calibrating- or reference-lamp temperature.

Radiation methods of the null-balance type generally provide better accuracy because they do not require accurate flux measurements (only sensitive ones), but are limited to the temperature of available reference lamps.

The line-reversal method was originally conceived by Fery (ref. 49). A modern version, using a stable carbon arc as reference standard, was described in reference 50; the range of this latter instrument has since been extended to 3600°K (6500°R) by use of newly available optical elements with higher transmission factors. References 50 and 51 list other references on line-reversal pyrometry. The technique has been used with radiations from the resonance lines of the alkali elements, the 306.4 nm line of OH, and the $4.4\text{ }\mu\text{m}$ band of CO_2 (ref. 52).

Other null methods that have been used have been adaptations of Kurlbaum's absorption-emission method (refs. 53, 54 and 55). They are potentially capable of the same upper temperature limit as line-reversal instruments, if a carbon arc is used as reference.

Non-null radiation methods do require accurate radiant-intensity measurements. They have no fundamental upper temperature limit, but their inaccuracy rises rapidly as gas temperature rises above reference-

lamp temperature, if one is used; inaccuracy also rises as emissivity drops, because of the reduced sensitivity. The relations between temperature error and flux-measurement error are given in reference 56 for a two-path absorption-emission method using a reference lamp, a two-path method using a reflector, and a "two-color" method. This last method assumes a known ratio of emissivities at the two wavelengths and is sensitive to uncertainty in knowledge of this ratio.

Other optical methods use a high-resolution spectrometer to obtain spectral intensity distributions within a molecular band. These, together with the previously discussed radiation methods, are enumerated and treated very briefly in reference 56, which provides references to more intensive and authoritative treatments. Some other more recent, comprehensive treatments are references 57 and 58. A typical application to temperature measurement is described in reference 59.

Examples of the application of some of these methods to measurement of OH and H₂O concentration are given in references 60 and 61. Concentration determination requires an independent determination of temperature.

A microwave absorption method (ref. 62) requires free electrons, generally produced by seeding with alkali atoms, in an atom-fraction concentration of about one part per million. This method is characterized by very high sensitivity in detecting fluctuations, a limited temperature range of 2000^o to 3000^o K, and comparatively poor absolute accuracy.

Other absorption methods using α , β , γ , or X-rays yield even poorer absolute accuracy because these radiations are attenuated so much more strongly by the high-density low-temperature boundaries of the jet than they

are by the low-density high-temperature central jet that is of primary interest (fig. 9(b)), that the tare corrections that must be applied must be known and must remain stable to a degree that is not practicable in conventional engineering research. The effect of these boundaries is illustrated in reference 48.

Deduction of temperature from sound-velocity measurements is described in reference 63, which also provides good descriptions of other techniques.

The technology involved in measuring sound velocity across a jet, thereby permitting deduction of temperature if specific-heat ratio and molecular weight are known, is illustrated in references 64 and 65. When the effect of the cold boundaries is included, this technique yields a value of 3020° F for the average of the profile shown in figure 10 of reference 48, as compared with the linear average of 3300° F.

As a rule of thumb, the nuclear-radiation and X-ray methods may be considered to yield an average of the reciprocal of temperature, and the sound velocity method to yield an average of the reciprocal of the square root of temperature. The microwave method yields close to a linear average, and the other optical radiation methods mentioned are weighted toward the higher temperatures along the path.

LOCAL STATIC TEMPERATURE AND RELATED QUANTITIES

The uncertainties associated with integration across a jet diameter have prompted the search for a means of combining the advantage of a

local measurement with the advantage of a device that measures static temperature.

An approximation to this combination is use of the line-reversal method with an upstream probe that produces local seeding of the gas stream (ref. 66). This method has proved satisfactory in subsonic streams (ref. 32), but may be limited in hypersonic ramjet application to alkali-metal injection at the fuel-injector strut.

Reference 67 has constructed a U-shaped optical probe that can be moved across a supersonic gas stream. The optical path is thereby brought into a local region of the stream. The probe lasted about 2 minutes in a supersonic stream of hydrogen-air exhaust gas. Although this implies that, for reasons of expense, measurements should be taken by inserting the probe for only a few seconds per run, an advantage of this design is that it may be used with several of the radiation methods. Corrections for the boundary layer attached to each side of the U are less severe than for the cold boundary shown in figure 9(b).

A technique currently receiving consideration by several workers, particularly for studying combustion, is to pass an exciting beam of electrons across one diameter of the gas jet and to observe the excited fluorescence with a spectrometer, in the same transverse plane, but sighting along an orthogonal diameter or chord (fig. 10(a)). A traverse can be made by moving either the exciting beam or the line of sight (refs. 68, 69 and 70). The exciting beam can fully traverse the gas jet only if the gas is sufficiently rarefied (less than 0.001 atmosphere in most reported work).

If the fluorescence is persistent, the above technique may be used to measure linear velocity by locating the spectrometer downstream of the exciter and using a timer. Vibration-rotation lines, with radiative lifetimes on the order of a millisecond, appear to have the greatest promise. A related technique of velocity measurement is to use focused laser light to produce local heating, generally accompanied by ionization and radiation. The passage of the locally excited element of gas volume is then determined by a detector downstream. The method of detection may use a radiation-detector, an electrical conductivity probe, a shadowgraph system, or a photographic system (ref. 71). The accuracy of such velocity measurement would be limited by eddy diffusion and by uncertainty in velocity-vector direction.

When the jet has axial symmetry in local absorption coefficient, a series of scans may be made along successive chords (fig. 10(b)), using a line-reversal or an absorption-emission method. The resulting simultaneous integral equations may then be solved by use of the Abel transform to deduce the radial profile. Uncertainties in this method arise principally from the increasingly weighty effect of cold boundaries as the chord approaches the edge of the jet. The method was used by reference 72 and is discussed also in reference 58.

A related technique that is not limited to symmetric streams and that requires no physical translation of the optical system is often termed "spectral scanning". The temperature distribution along a given line of sight is deduced by measurements made at several wavelengths, chosen

so that the absorption coefficient is distinctly different at each wavelength. The difference between two transmission factors thus determined, as a function of distance along the path, has the appearance of a spatial band-pass filter (fig. 10(c)). With appropriate choice of wavelengths, the peak of this "filter" may be placed at various locations along the path. Solution of the simultaneous integral equations yields the temperature distribution along the line of sight. Uncertainties in this method arise from the fact that "spatial band width" increases in proportion to distance from the gas boundary and that transmission factor-temperature relations must be known in advance for the particular gas, the particular wavelengths used, and the particular acceptance bandwidth of the spectrometer system. This technique is illustrated in reference 73, which also lists further references.

The iterative computational procedures involved in using either spatial or spectral scanning do not always converge. The necessary and sufficient conditions for achieving convergence have not yet been defined by any systematic studies. A favorable case of spectral scanning is shown in figure 11, which shows the approximation to an arbitrarily assumed axisymmetric profile obtained by spectral scanning at three wavelengths; the example might represent a case of stoichiometric combustion of a hydrogen-air mixture at one atmosphere.

PROBE PROTECTION

The various types of probes discussed above must be protected against melting and against effects which would alter the probe calibration. One or more of the following techniques must be used to achieve this protection:

- (a) Momentary exposure to the gas stream
- (b) Cooling
- (c) Back purging of aspirating designs

Whether the probe is cooled or uncooled, it should be exposed to the gas stream only long enough to achieve the desired steady-state reading. At other times it should be shielded by a retractable cover, or it should itself be retracted. In the latter case, the accelerations of retraction and insertion should be sufficiently low to prevent mechanical damage to sensitive probe elements.

The nose of the probe may be cooled by one of the methods shown in figure 12. Thin-walled construction may be used where coolant may be directed at every portion of the wall (fig. 12(a)). If such construction is impractical, so that coolant cannot reach a region of high heat flux, such as a probe nose, the probe may be made of copper in order to provide heat transfer by metallic conduction (fig. 12(b)). When probe size is small, simpler construction is achievable by dumping the coolant into the gas stream (fig. 12(c)); computation will show whether such dumping is practical in many applications. Stagnant pockets of vapor in the cooling system should be avoided; for example, vapor tending to form on the downstream side of an externally cooled horizontal rod will be swept away if the water flows upward. Examples of cooling system design and heat-transfer calculations for probe cooling systems are given in references 5, 15, and 74.

Probes which aspirate the gas must be protected against erosion, oxidation, and dirt accretion that will change critical dimensions or alter

~~CONFIDENTIAL~~

surface heat transfer rates. To this end, aspiration should be maintained only long enough to achieve the desired steady reading. Thereafter, reverse constant-current flow of a clean neutral gas, such as argon or nitrogen, should be maintained to protect internal elements (fig. 13). The constant current of gas is maintained by allowing the gas to flow through an orifice from a source that is at least ten times higher in pressure than the maximum pitot pressure to which the probe may be exposed. The physical location of solenoid- or pneumatically-operated valves should satisfy the conditions specified in figure 13 in order to minimize time delay in obtaining a measurement with the probe.

The internal probe cooling system required to prevent condensation of water from the aspirated gas, as discussed in the Gas Composition section, is also shown in figure 13. Local-total-enthalpy measuring devices that require such precautions are indicated in table II.

A common cause of failure of expensive probes is neglect to provide adequate automatic safety devices to control cooling and purging. There should be no manually operated valves that could prevent flow of coolant or of purge gas. Visual and audible underpressure alarms or low-flow alarms and lockouts should prevent exposure of the probe to the gas streams unless the coolant and purging systems are in operation. Some desirable cooling practices are also shown in figure 13.

CONCLUDING REMARKS

The preceding discussion has sought to highlight those features of instrumentation that appear most important to engineering practice. The

~~CONFIDENTIAL~~

~~CONFIDENTIAL~~

techniques described represent the results of efforts of many workers in the field. The bibliographic references given, directly and indirectly, credit only a few of these workers. Each technique requires a high level of instrument engineering for its successful application. Careful attention to minute detail is required to achieve reliability and the assurance that the measurement obtained actually represents the physical quantity that one intends to measure.

REFERENCES

1. Gracey, William; Coletti, Donald E.; and Russell, Walter R.: Wind-Tunnel Investigation of a Number of Total-Pressure Tubes at High Angles of Attack. Supersonic speeds. NACA TN 2261, 1951.
2. Davidson, Theron W.: Method of Net Thrust Measurement in Supersonic Flight. Aerodynamics of Power Plant Installation, Part I. AGARDograph No. 103, pt. 1, Oct. 1965, pp. 217-244.
3. Doebelin, Ernest O.: Measurement Systems: Application and Design. McGraw-Hill Book Co., Inc., 1966.
4. Hahn, J. F.: The Effect of Mach Number, Incidence and Hole Position on the Static Pressure Measured by a Square Ended Probe. Roy. Aeron. Soc. J., vol. 68, no. 637, Jan. 1964, pp. 54-57.
5. Parobek, Daniel M.: Performance of Free Stream Flow Instrumentation for 9-inch Contoured Nozzle Test in the RTD 4-Megawatt Electro Gasdynamic Facility. Rep. No. AFFDL-TR-65-179, Air Force Flight Dynamics Lab. Wright-Patterson AFB Dec. 1965. (Available from DDC as AD-476608L).

6. Norris, John D.: Calibration of Conical Pressure Probes for Determination of Local Flow Conditions at Mach Numbers from 3 to 6. NASA TN D-3076, 1965.
7. Fox, W. L.; and Blaylock, R. B.: Calibration of a Compact Survey Probe for Pitot Pressure, Mach Number, and Flow Angularity Measurements. Tech. Memo. No. 33-179 (NASA CR-67715), Jet Propulsion Lab., California Institute of Tech., Mar. 15, 1965.
8. Norris, John D.; and Pierpont, P. Kenneth: Experimental Performance of a Conical Pressure Probe at Mach Numbers of 3.0, 4.5, and 6.0. NASA TN D-3719, 1966.
9. Dimeff, John; Lane, James W.; and Coon, Grant W.: New Wide-Range Pressure Transducer. Rev. Sci. Instr., vol. 33, no. 8, Aug. 1962, pp. 804-811.
10. Anon.: Vacuum Technology Directory and Specifications Catalog. F. D. Thompson Publications, Inc., 1967.
11. Anon.: Fluid Meters, Their Theory and Application. American Society of Mechanical Engineers, 1959.
12. Anon.: Flow Measurement, Chapter 4. Part 5 of ASME Power Test Code 19.5; 4-1959.
13. Arnberg, B. T.: Review of Critical Flowmeters For Gas Flow Measurements. J. Basic Eng., vol. 84, no. 4, Dec. 1962, pp. 447-460.
14. Christensen, D.; Chen, Che-Jen; and Price, R.: A Feasibility Study and Preliminary Design of Instrumentation Suitable for Measuring the Gas Flow Parameters of an Arc-Heated Hypersonic Gas Dynamic Facility. (AFASD-TDR-62-154), Plasmadyne Corporation, Oct. 1962.

~~CONFIDENTIAL~~

15. Huber, Franz, J. A.: Probes for Measuring Mass Flux, Stagnation Point Heating, and Total Enthalpy of High Temperature Hypersonic Gas Flows. AIAA Paper No. 66-760, Sept. 21-23, 1966.
16. Stalker, R. J.: A Mass Flow Probe for Use in Short Duration Hypersonic Flows. The High Temperature Aspects of Hypersonic Flow. AGARDograph No. 68. Wilbur C. Nelson, ed., Macmillan Book Co., Inc., 1964, pp. 271-280.
17. Minkin, Herbert L.; Hobart, Howard F.; and Warshawsky, I.: Performance of Turbine-Type Flowmeters in Liquid Hydrogen. NASA TN D-3770, 1966.
18. Minkin, Herbert L.; and Hobart, Howard F.: Liquid-Hydrogen-Flowmeter Calibration Facility; Preliminary Calibrations on Some Head-Type and Turbine-Type Flowmeters. NASA TN D-577, 1961.
19. Bucknell, Richard L.: Liquid Hydrogen Flow Measurement and Calibration. Proceedings of the 8th ISA-National Aero-Space Instrumentation Symposium, 1962, pp. 145-152.
20. Bucknell, R. L.: Calibration Systems and Turbine-Type Flow Transducers for Cryogenic Flow Measurements. Advances in Cryogenic Engineering. Vol. 8, K. D. Timmerhaus, ed., Plenum Press, 1963, pp. 360-370.
21. Bucknell, Richard L.; Lowler, Thomas D.; and Street, Robert L.: Cryogenic Flow Measurement. Standards Laboratories and Measurement Standards. Vol. 19, pt. I of Instrument Society of America 19th Annual Conference, New York, Oct. 12-15, 1964, Paper 12.2-1-64.

22. Howells, T. S.: Sampling of Combustion Gases. Fuel Soc. J. vol. 15, 1964, pp. 15-23.
23. Greene, Frank T.; Brewer, Jerome; and Milne, Thomas A.: Mass Spectrometric Studies of Reactions in Flames. I. Beam formation and mass dependence in sampling 1-atmosphere gases. J. Chem. Phys., vol. 40, no. 6, Mar. 15, 1964, pp. 1488-1495.
24. Milne, Thomas A.; and Greene, Frank T.: Mass-Spectrometric Sampling of 1-atm Flames. Tenth Symposium (International) on Combustion. The Combustion Institute, 1965, pp. 153-159.
25. Netusil, W. F.; Proffit, R. L.; and Enloe, J. D.: Development of a System for the Identification of Rocket Exhaust Products. Rep. No. R-5878 (AFRPL-TR-65-70, DDC No. AD-461444), Rocketdyne Div., North American Aviation, Apr. 1965.
26. Hobbs, A. P.: Gas Analysis. Anal. Chem., vol. 36, no. 5, Apr. 1964, pp. 130 R-139R.
27. Warshawsky, I.; and Kuhns, P. W.: Review of the Pneumatic-Probe Thermometer. Temperature - its Measurement and Control in Science and Industry. Charles M. Herzfeld, ed., Reinhold Publishing Corp., Vol. 3, Part 2, 1962, pp. 573-586.
28. Gregorek, G. M.; and Petrie, S. L.: A Variable Atmosphere Hypersonic Wind Tunnel for Similitude Studies. (AFFDL-TR-66-96), Ohio State University, Sept. 1966.
29. Vassallo, Franklin A.: Miniature Enthalpy Probes for High Temperature Gas Streams. (AFARL 66-0115, DDC No. AD-642280), Cornell Aeronautical Lab., Inc., June 1966. (Also available from CFSTI, Springfield, Va.)

~~CONFIDENTIAL~~

30. Glawe, George E.; Simmons, Frederick S.; and Stickney, Truman M.: Radiation and Recovery Corrections and Time Constants of Several Chromel-Alumel Thermocouple Probes in High-Temperature, High-Velocity Gas Streams. NACA TN 3766, 1956.
31. Glawe, George E.: A High Temperature Combination Sonic Aspirated Thermocouple and Total Pressure Probe. Jet Propulsion, vol. 27, no. 5, May 1957, pp. 543-544.
32. Glawe, George E.; Johnson, Robert C.; and Krause, Lloyd N.: Inter-comparison of Several Pyrometers in a High-Temperature Gas Stream. Temperature - its Measurement and Control in Science and Industry. Charles M. Herzfeld, ed., Reinhold Publishing Corp., Vol. 3, Part 2, 1962, pp. 601-605.
33. Scadron, Marvin D.; Warshawsky, Isidore; and Gettelman, Clarence C.: Thermocouples for Jet-Engine Gas Temperature Measurement. ISA Proceedings, vol. 7, 1952, pp. 142-148.
34. Scadron, Marvin D.; and Warshawsky, Isidore: Experimental Determination of Time Constants and Nusselt Numbers for Bare-Wire Thermocouples in High-Velocity Air Streams and Analytic Approximation of Conduction and Radiation Errors. NACA TN 2599, 1952.
35. Droms, C. R.; and Dahl, A. I.: Iridium Versus Iridium-Rhodium Thermocouples for Gas Temperature Measurements Up to 3500⁰ F. Gas Turbines. Section 5 of ASME and Institute of Mechanical Engineers Joint Conference on Combustion. June 17, 1955, pp. 6-9.

36. Matton, G.; and Foure, C.: Thermoelectric Probes for Measuring High Temperatures in Gas Streams. Sixth Symposium (International) on Combustion. Reinhold Publishing Corp., 1956, pp. 757-763.
37. Burrows, Marshall C.: Mixing and Reaction Studies of Hydrazine and Nitrogen Tetroxide Using Photographic and Spectral Techniques. Paper No. 67-107, AIAA, Jan. 23-26, 1967.
38. Hill, Maynard L.; Akridge, James M.; and Keller, Christian A.: Miniature Recording Optical Pyrometer. Rep. No. TG-825, Applied Physics Lab., Johns Hopkins University, May 1966. (Available from DDC as AD-636101).
39. Krause, Lloyd N.; Glawe, George E.; and Johnson, Robert C.: Heat-Transfer Devices for Determining the Temperature of Flowing Gases. Temperature - its Measurement and Control in Science and Industry. Charles M. Herzfeld, ed., Reinhold Publishing Corp., Vol. 3, Part 2, 1962, pp. 587-593.
40. Krause, Lloyd N.; Johnson, Robert C.; and Glawe, George E.: A Cooled-Gas Pyrometer for Use in High-Temperature Gas Streams. NACA TN 4383, 1958.
41. Glawe, George E.; Johnson, Robert C.; and Krause, Lloyd N.: A Cooled-Tube Pyrometer with Experimental Results Obtained in a High-Temperature Gas Stream. NASA TN D-870, 1961.
42. Fingerson, Leroy M.; and Blackshear, Perry L., Jr.: Heat Flux Probe for Dynamic Measurements in High-Temperature Gases. Temperature - its Measurement and Control in Science and Industry. Charles M. Herzfeld, ed., Reinhold Publishing Corp., Vol. 3, Part 2, 1962, pp. 655-663.

~~CONFIDENTIAL~~

43. Glawe, George E.; Krause, Lloyd N.; and Johnson, Robert C.: A Steady-State, Stagnation-Point, Heat-Transfer-Rate Measuring Device. NASA TN D-1704, 1963.
44. Gottron, Richard; and Gayload, Wilmer: A Temperature-Sensing Pneumatic Oscillator. Rep. No. HDL-TR-1224, Harry Diamond Labs. May 4, 1964. (Available from DDC as AD-351535).
45. Gaylord, Wilmer; and Gottron, Richard N.: Design Considerations of the HDL Pneumatic Temperature Sensor. Rep. No. HDL-TR-1273, Harry Diamond Labs.. Feb. 10, 1965. (Available from DDC as AD-359712).
46. Kuhns, P. W.: Effects of Thermal Relaxation and Specific-Heat Changes on Measurements with a Pneumatic-Probe Pyrometer. NACA TN-4026, 1957.
47. Buchele, Donald R.: Nonlinear-Averaging Errors in Radiation Pyrometry. NASA TN D-2406, 1964.
48. Warshawsky, I.: Pyrometry of High Velocity Gases. Sixth Symposium (International) on Combustion. Reinhold Publishing Corp., 1956, pp. 739-750.
49. Féry, C.: Sur la Temperature des Flammes (Temperature of Flames). Comptes rendus, vol. 137, Nov. 30, 1903, pp. 909-912.
50. Buchele, Donald: A Self-Balancing Line-Reversal Pyrometer. Temperature - its Measurement and Control in Science and Industry. Charles M. Herzfeld, ed., Reinhold Publishing Corp., Vol. 3, Part. 2, 1962, pp. 879-887.

~~CONFIDENTIAL~~

51. Freeze, Paul D.: Bibliography on the Measurement of Gas Temperature. Circ. 513, National Bureau of Standards, Aug. 20, 1951.
52. Gaydon, A. G.; and Wolfhard, H. G.: Flames - Their Structure, Radiation, and Temperature. Chapman and Hall, Ltd. (London), 1953, Ch. X.
53. Kurlbaum, F.: Ueber eine einfache Methode, die Temperature leuchtender Flammen zu bestimmen (Simple Method of Determining the Temperature of Luminous Flames). Phys. Zeit., vol. 3, Feb. 1, 1902, pp. 187-188.
54. Ribaud, G.; Laure, Y.; and Gaudry, H.: Measurement of Flame Temperatures. J. Inst. Fuel, vol. 12, no. 64, Mar. 1939, pp. S18-S30.
55. Buchele, Donald R.: Radiometer-Pyrometer for Analysis of Gaseous Combustion Products. NASA TN D-2405, 1964.
56. Warshawsky, I.: Measurements of Rocket Exhaust-Gas Temperatures. ISA J., vol. 5, no. 11, Nov. 1958, pp. 91-97.
57. Penner, S. S.: Spectroscopic Methods of Temperature Measurements. Temperature - its Measurement and Control in Science and Industry. Charles M. Herzfeld, ed., Reinhold Publishing Corp., Vol. 3, Part 1, pp. 561-574.
58. Simmons, Frederick, S.: Spectroscopic Pyrometry of Gases, Flames, and Plasmas. ISA Trans., vol. 2, no. 2, Apr. 1963, pp. 168-189.
59. Incropera, Frank P.; and Leppert, George: Investigation of Arc Jet Temperature-Measurement Techniques. ISA Trans., vol. 6, no. 1, Jan. 1967, pp. 35-41.

60. Lezberg, Erwin A.; and Buchele, Donald: Some Optical Techniques for Temperature and Concentration Measurements of Combustion in Supersonic Streams. NASA TN D-2441, 1964.
61. Kaskan, W. E.: Hydroxyl Concentrations in Rich Hydrogen-Air Flames Held on Porous Burners. Combustion and Flame vol. 2, no. 3, Sept. 1958, pp. 229-243.
62. Kuhns, Perry W.: Determination of Flame Temperatures from 2000⁰ to 3000⁰ K by Microwave Absorption. NACA TN 3254, 1954.
63. Ladenburg, R. W.; Lewis, B.; Pease, R. N.; and Taylor, H. S., eds.: Physical Measurements in Gas Dynamics and Combustion. Princeton University Press, 1954.
64. Carnevale, E. H.; Lynnworth, L. C.; and Larson, G. S.: High Temperature Measuring Device. Parametrics, Inc. (NASA CR-54339), Feb. 1, 1965.
65. Lynnworth, L. C.; and Carnevale, E. H.: Techniques for Mounting an Ultrasonic Temperature Device. Parametrics, Inc. (NASA CR-54979), Feb. 1966.
66. Buchele, Donald: A Self-Balancing Line-Reversal Pyrometer. NACA TN 3656, 1956.
67. Kenworthy, Milton J.; Stanforth, Charles M.; Colley, William C.; Mossey, Milton J.; and Harsha, P. Thomas.: Investigation of Instrumentation and Simulation Techniques for the Supersonic Combustion Process. (AFAPL-TR-66-76, DDC No. AD-489974L), General Electric Co., Oct. 1966.

~~CONFIDENTIAL~~

68. Muntz, E. P.: Static Temperature Measurements in a Flowing Gas.
Phys. Fluids, vol. 5, no. 1, Jan. 1962, pp. 80-90.
69. Hunter, William W., Jr.: Rotational Temperature Measurements
300^o to 1000^o K with Electron Beam Probe. Paper No. 16.12-4-66,
ISA 21st Annual Conference and Exhibit, New York, Oct. 24-27, 1966.
70. Marrone, Paul V.: Temperature and Density Measurements in Free
Jets and Shock Waves. Phys. Fluids, vol. 10, no. 3, Mar. 1967,
pp. 521-538.
71. Chen, Che Jen: Velocity-Profile Measurement in Plasma Flows Using
Tracers Produced by a Laser Beam. J. Appl., Phys., vol. 37,
no. 8, July 1966, pp. 3092-3095.
72. Elder, P.; Jerrick, T.; and Birkeland, J. W.: Determination of the
Radial Profile of Absorption and Emission Coefficients and Temper-
ature in Cylindrically Symmetric Sources with Self-Absorption.
Appl. Opt., vol. 4, no. 5, May 1965, pp. 589-592.
73. Tourin, Richard H.; and Krakow, Burton: Applicability of Infrared
Emission and Absorption Spectra to Determination of Hot Gas
Temperature Profiles. Appl. Opt., vol. 4, no. 2, Feb. 1965,
pp. 237-242.
74. Simmons, Frederick S.; and Glawe, George E.: Theory and Design
of a Pneumatic Temperature Probe and Experimental Results
Obtained in a High-Temperature Gas Stream. NACA TN 3893, 1957.

~~CONFIDENTIAL~~

~~CONFIDENTIAL~~

TABLE I. - CONDITIONS FOR M8, 120,000-FT ALTITUDE OPERATION

Physical Quantity	Station			
	0	2	3	4
Mach number	8	3	1.5	4
Mach number behind shock	.4	.5	.7	.4
Static pressure, atm	.005	.7	2	.05
Total pressure, atm	80	25	7	7
Total pressure behind shock, atm	.4	8	7	1
Velocity head, atm	.2	.4	3	.5
Static temperature	230 ⁰ K (420 ⁰ R)	1100 ⁰ K (2000 ⁰ R)	2700 ⁰ K (4900 ⁰ R)	950 ⁰ K (1700 ⁰ R)
Total temperature	2800 ⁰ K (5100 ⁰ R)	2800 ⁰ (5100 ⁰ R)	3900 ⁰ K (7000 ⁰ R)	3900 ⁰ K (7000 ⁰ R)

~~CONFIDENTIAL~~

~~CONFIDENTIAL~~

TABLE II. - PRINCIPAL CHARACTERISTICS OF DEVICES FOR MEASURING LOCAL

TOTAL ENTHALPY AND RELATED QUANTITIES

a	velocity of sound	p	pressure	First subscripts:			Second subscripts:		
f	frequency	Pr	Prandtl number	b	base		asp	aspirated	
h	enthalpy	ΔP	pressure drop	c	coolant		t	total	
k	thermal conductivity	Re	Reynolds number	d	duct (ambient)		3	downstream	
\dot{m}	mass flow rate	T	temperature	g	gas				
M	Mach number	ΔT	temperature rise	p	plug				
η	molecular weight	ϵ	emittance	s	surface				
N_λ	monochromatic steradiancy	μ	viscosity	sh	shell				
Nu	Nusselt number	ρ	density	w	wire				
Type	Basic quantity determined	Primary quantities determined	Properties that must be known	Secondary quantities that must be measured or controlled	Aspirated (c)	Condensation must be prevented	Relaxation effects are important	Upper temperature limit	References
Calorimetric probe	$h_{g,t}$	$\dot{m}_g, \dot{m}_c, \Delta T_c$	-----	T_{sh}	x	x		-----	15, 27, 28, 29
Radiation- ^a shielded high-recovery thermocouple	$T_{g,t}$	T_w	-----	$p_{g,asp}$	x		x	Ir-Rh: 2300° K (4200° R)	30, 31, 32
Bare-wire ^a thermocouple	$T_{g,t}$	T_w	ϵ_w, k_w	T_b, T_d			x	Ir-Rh: 2500° K (4600° R) W-Re: 2800° K (5000° R)	33, 34, 35 37
Cooled thermocouple (Fouré)	$T_{g,t}$	T_w	(b)	T_{sh}	x			Ir-Rh: 2700° K (4900° R) (d)	36
Optically-radiating body	$T_{g,t}$	N_λ	ϵ_s	---			x	C: 3500° K (6300° R) (d)	38
Cooled-gas ^a probe	$h_{g,t}$	$T_{g,3}$	Pr, Re, f(Nu, Re)	$p_{g,asp}$	x	x		-----	40
Cooled-tube ^a probe	$h_{g,t}$	$\dot{m}_c, \Delta T_c$	Pr, Re, f(Nu, Re)	-----			x	-----	41, 42
Stagnation-point heat transfer probe	$h_{g,t}$	ΔT_p	Pr, M, $\rho_{g,t}, \mu_{g,t}, \gamma$	-----			x	-----	5, 15, 43
Pneumatic probe ^a	$\rho_{g,t}$ or $\rho_{g,t}^p$	$\dot{m}_g, p_{g,t}, \Delta p_g$	γ, η	$p_{g,asp}$	x	x	x	-----	27, 46
Acoustic probe	$a_{g,t}$	f	γ, η	$p_{g,t}$	x		x	-----	44, 45

^aIntercompared in same gas stream

^bEmpirical calibration

^cVacuum pump not needed if impact pressure is sufficiently high

^dEstimated

~~CONFIDENTIAL~~

-10-

CONFIDENTIAL

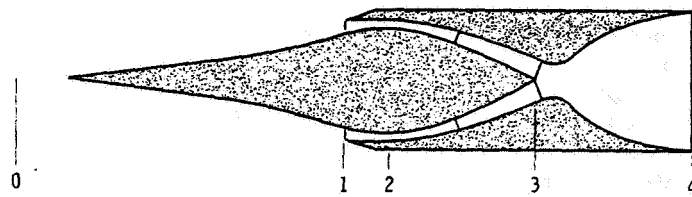


Figure 1. - Station definitions for hypersonic ramjet engine.

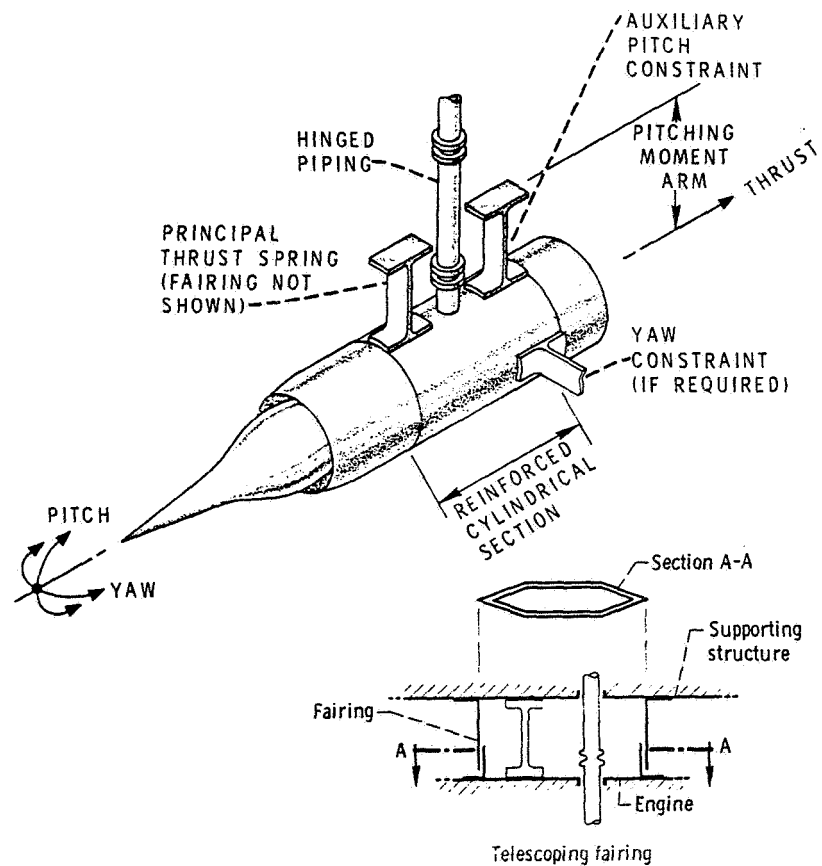


Figure 2. - Illustrative thrust measuring system.

CONFIDENTIAL

CONFIDENTIAL

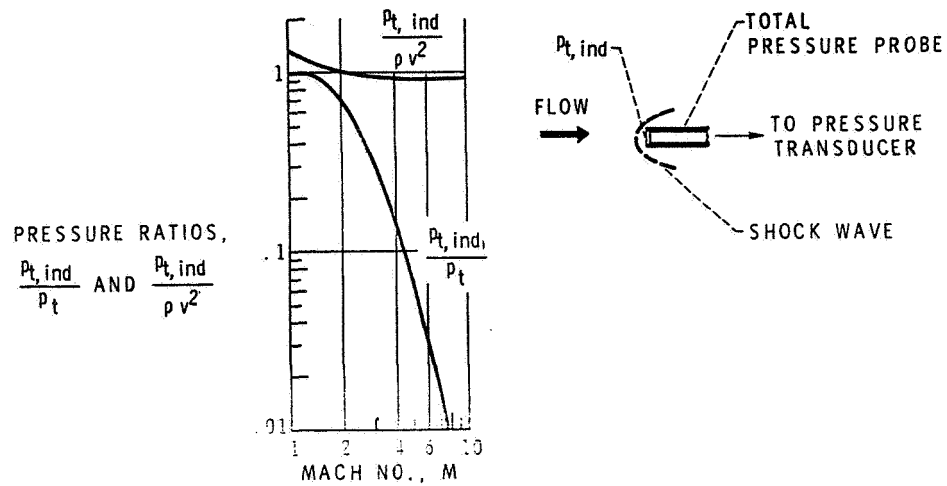


Figure 3. - Total-pressure-probe relations.

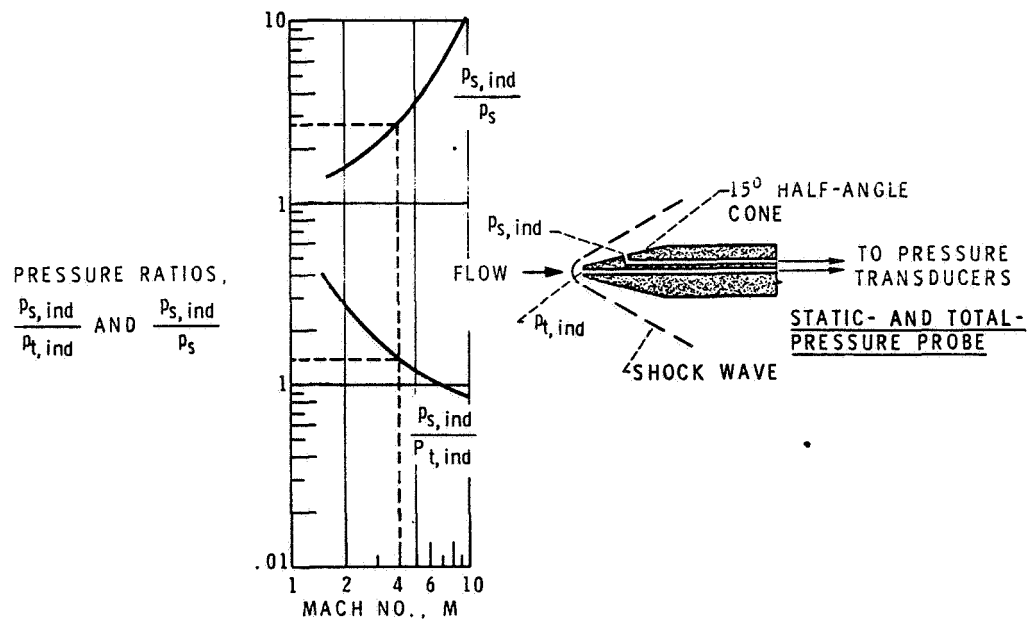


Figure 4. - Conical probe for static pressure and Mach number determination.

CONFIDENTIAL

70

~~CONFIDENTIAL~~

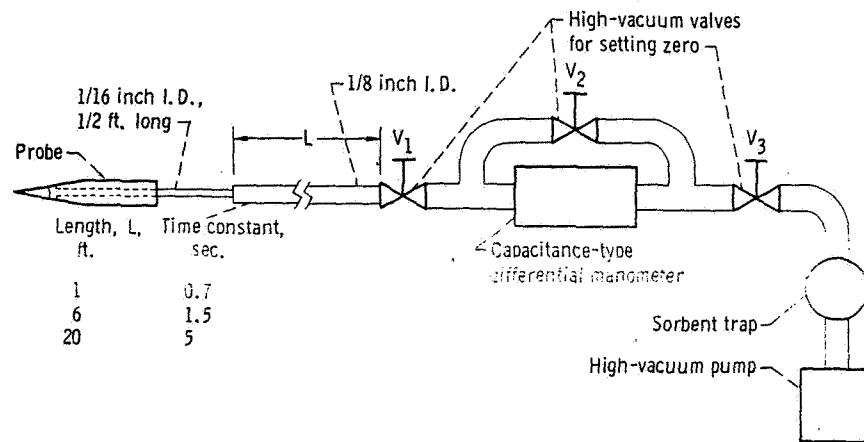


Figure 5. - Typical arrangement for measuring 0.005 atm.

~~CONFIDENTIAL~~

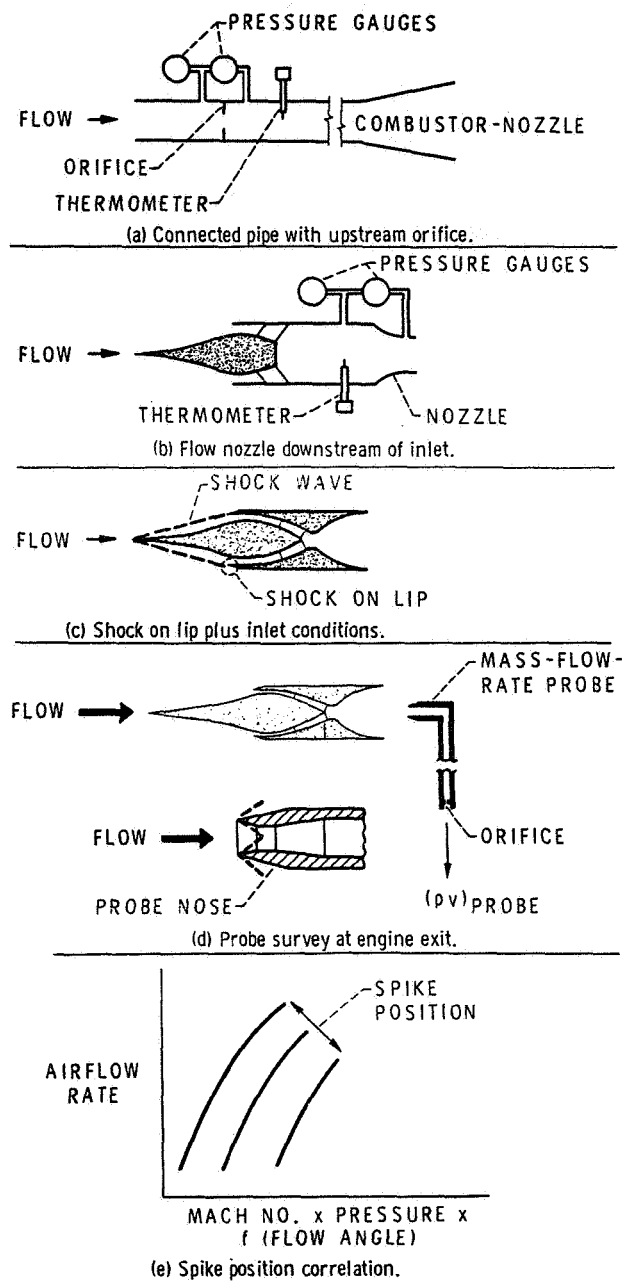
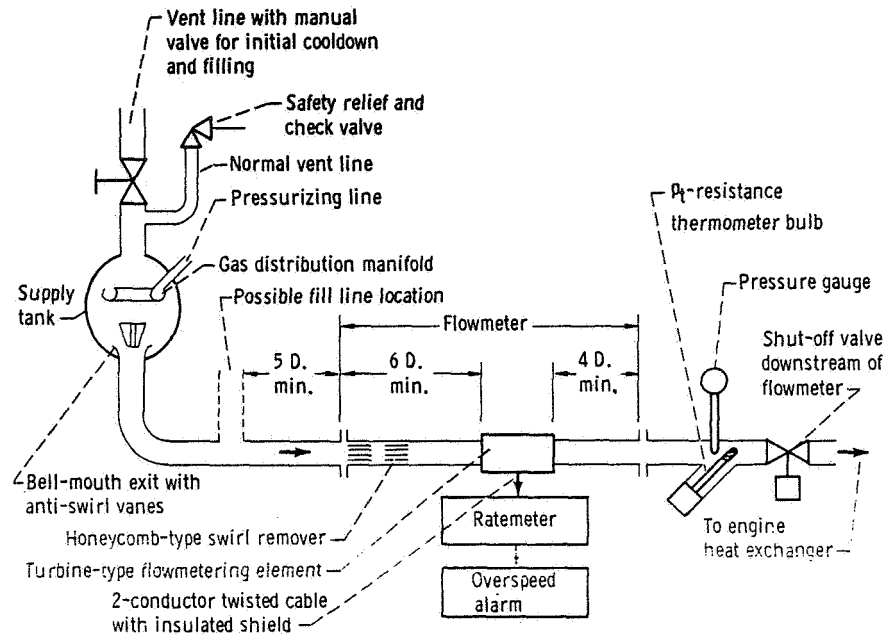
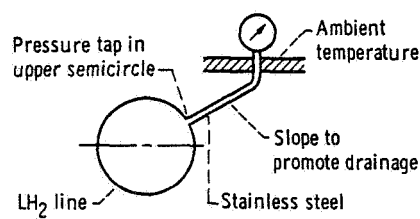


Figure 6. - Methods of airflow rate measurement.

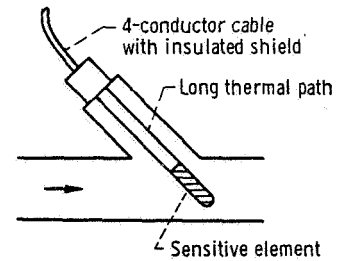
CONFIDENTIAL



(a) Component arrangement.



(b) Detail of pressure connection.



(c) Detail of thermometer-bulb installation.

Figure 7. - Illustrative liquid-hydrogen flow metering installation.

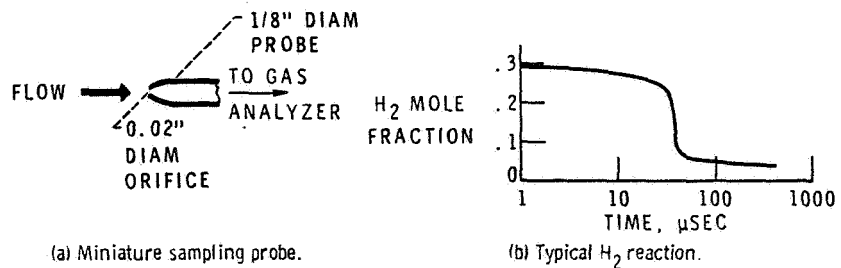


Figure 8. - Gas sampling probe and history of hydrogen concentration.

CONFIDENTIAL

~~CONFIDENTIAL~~

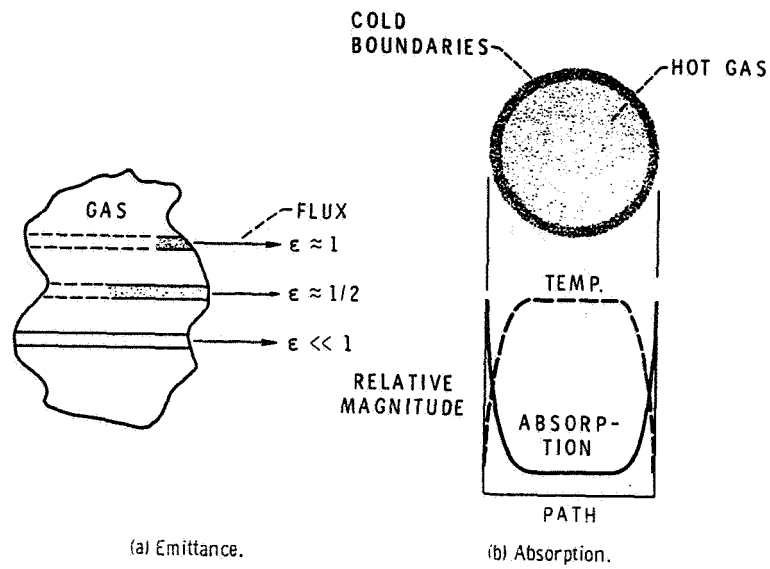


Figure 9. - Nonlinear spatial averaging.

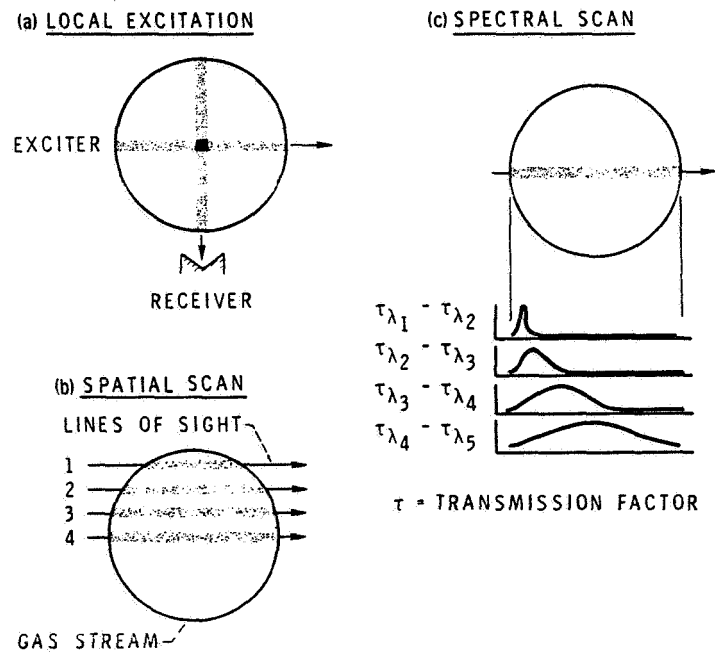


Figure 10. - Optical methods of determining local static temperature.

~~CONFIDENTIAL~~

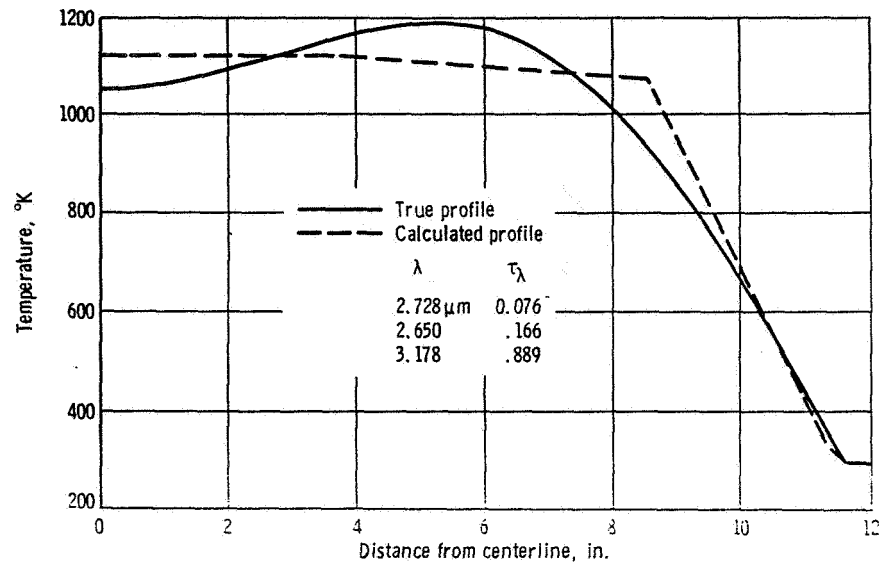
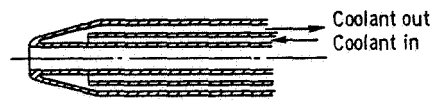
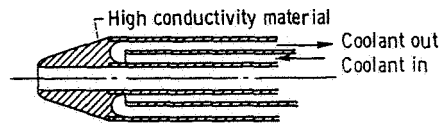


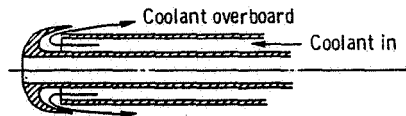
Figure 11. - Example of approximation obtained by spectral scanning.



(a) Conventional cooling.



(b) Conduction cooled tip.



(c) Single-pass cooling.

Figure 12. - Methods of cooling probe tips.

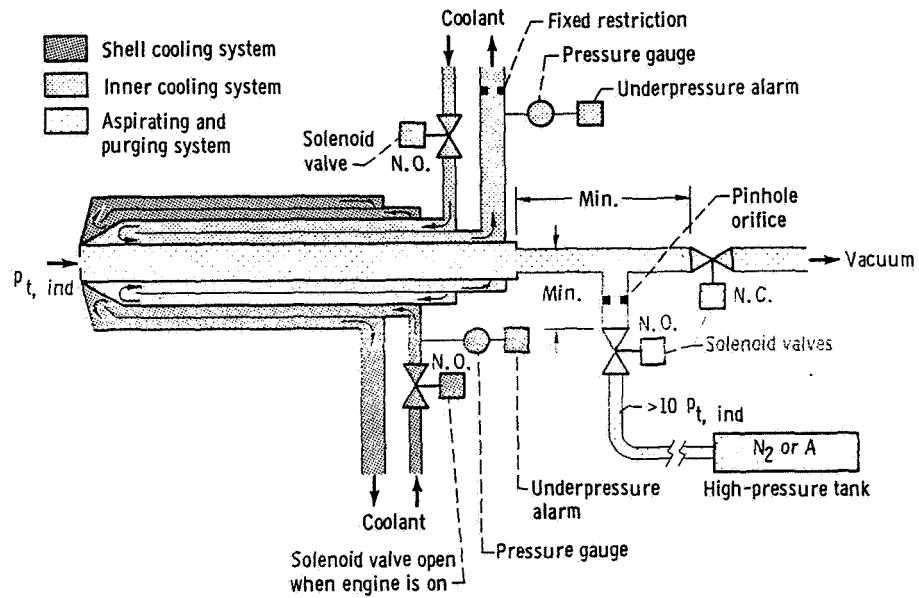


Figure 13. - Probe protection by cooling and purging.

~~CONFIDENTIAL~~

27. INTRODUCTORY REMARKS ON STRUCTURES AND MATERIALS

FOR HYPERSONIC AIRCRAFT

By R. R. Heldenfels
Langley Research Center

INTRODUCTION

The structural designer of a long-range, hypersonic cruise airplane will face one of the great challenges of aeronautics. He will be expected to provide a lightweight structure, with an efficiency approaching that of the best subsonic aircraft, for a very large, low-density vehicle subjected to severe aerodynamic heating (refs. 1 and 2). This paper will review the major structural problems of such vehicles to introduce the technical papers presented in this session.

SYMBOLS

M_{∞}	free-stream Mach number
p	pressure
\dot{Q}	heating rate
q	dynamic pressure
R	radius of curvature
T	temperature
V	velocity
x	streamwise distance from leading edge
α	angle of attack
ϵ	emissivity
Λ	sweep angle

STRUCTURAL WEIGHT RATIOS

Structural information of primary interest to the airplane designer is the fraction of vehicle weight required. In figure 1, the ratio of structural weight to gross weight at take-off for long-range cruise vehicles is plotted as

~~CONFIDENTIAL~~

~~CONFIDENTIAL~~

a function of cruise Mach number. (The gross weight of the vehicle consists of structure, powerplant, fixed equipment, useful load, payload, and fuel.) Shown are data for a number of subsonic commercial air transports that are now operational, the values designers expect to achieve in the Anglo-French and United States supersonic transports, and results from selected studies of hypersonic cruise vehicles. The shaded area is an estimate of the present uncertainty in structural weight ratios in the Mach 4 to 12 range. The width of this shaded band results from the lack of well-established solutions to the three principal structural problems of long-range hypersonic cruise vehicles; namely, (1) the high temperatures produced by aerodynamic heating, (2) the requirement for long service life, and (3) the storage and use of liquid hydrogen fuel.

Subsonic transports have a structural weight ratio of about 25 percent, and the supersonic designs anticipate about the same value despite an expected decrease in structural efficiency due to aerodynamic heating. Some studies of hypersonic airplanes indicate similar values but several studies at Mach 6 show a wide dispersion in the structural weight ratio. The differences result from variations in size and configuration of vehicles and the completeness of the structural and weight analyses. The exact location of these particular points is not a useful measure of current structures technology, because the structural weight ratio is indicative only of the trade-offs made during optimization of the system. A ratio of about 25 percent appears to be desirable throughout the speed range. The goal for structures research and development is to provide materials, concepts, and methods which will decrease this uncertainty and insure the achievement of the optimum structural weight ratio in vehicles with the desired combination of payload, performance, and cost. Accurate structural inputs to integrated airplane design studies are required to determine the feasibility of these vehicles and indicate the problems on which future research should be concentrated.

TEMPERATURES

Figure 2 shows the surface temperature distribution on a representative hypersonic cruise vehicle. The temperatures shown are those at which radiation cooling of the structure is in equilibrium with aerodynamic heating in steady flight. Temperatures are given for the stagnation point on the nose and on the leading edge of the wing, tail, and engine inlet; and isotherms are shown for surface temperatures ranging from 1400° to 2000° F. Temperatures inside the air inlet and propulsion unit are not shown; radiation cooling is not possible on these internal surfaces and active cooling is required for survival. The flight condition that produces these temperatures is Mach number 8 at a dynamic pressure of 2200 psf. This flight condition has been selected as a focus for structures research because it produces difficult problems somewhat beyond the state of the art. When structures and materials technology is adequate for these conditions, it will be good enough to cope with any optimum hypersonic cruise condition the designer may select.

The variation of temperature over the surface indicates that a variety of materials and each of the basic structural approaches (hot, insulated, or cooled

~~CONFIDENTIAL~~

~~CONFIDENTIAL~~

structures) are likely to be used on the vehicle. At the high temperatures shown, metallic materials have lost much of their structural efficiency. However, temperatures can be varied significantly by changing the aircraft configuration and performance. Blunting the nose or leading edges (from the 1/4-inch radius used here) can reduce the highest temperatures several hundred degrees. Reducing the cruising speed or the dynamic pressure will reduce the temperatures significantly and make the structural problems easier to solve, whereas increasing them will make the structural problems extremely formidable. Representative temperatures resulting from such variations are given in table I.

Figure 3, a presentation similar to figure 2, shows surface temperatures at a typical cruising condition, Mach number 6 and a dynamic pressure of 500 psf. The temperatures are substantially lower than in figure 2, with most of the vehicle below 1200° F, so that the most difficult structural problems are eliminated. Blunting the nose and leading edges can provide additional alleviation. The obvious difference between figures 2 and 3 indicates the need for an appropriate relationship between the planned flight trajectories and the structural design conditions. An airplane expected to cruise at the conditions of figure 3 would have a more severe structural design condition, but probably not as stringent as that of figure 2. Establishment of appropriate structural design criteria for hypersonic airplanes is thus an important subject for future research. The structural weight, structural configuration, and structural materials required vary substantially with temperature over the range shown in figures 2 and 3. Consequently, the designer of a hypersonic cruise vehicle must carefully evaluate these important effects on the structural weight along with aerodynamic and propulsion considerations to arrive at a optimum vehicle system.

MATERIALS

The temperatures of figures 2 and 3 are a major factor in the selection of materials for a hypersonic cruise vehicle. However, many material characteristics must be considered when making a selection. The NASA Special Committee on Materials Research for Supersonic Transports used 14 materials rating parameters to screen candidate materials for SST research (ref. 3). These 14 parameters, with appropriate modification and additions, will be required to screen materials for research, development, and construction of hypersonic aircraft. Several such parameters, supplemented by structural design criteria, have been used to determine temperature-time limits for high-temperature structural materials. The results are shown in figure 4. The maximum useful structural temperature of the better candidate materials is shown as a function of total time at temperature for various structural applications. The darker bands are based on existing data; the others are extrapolations. These limits are discussed in more detail by Stein, Illg, and Buckley in reference 4, which is a review of the status of materials for hypersonic aircraft structures. Figure 4 is a highly simplified presentation, but it illustrates the basic characteristics of the materials selection problem.

Time at temperature is used as the abscissa because the hypersonic cruise vehicle must have a structure with a long service life to be economically feasible. High-temperature structures previously developed for vehicles such as

~~CONFIDENTIAL~~

~~CONFIDENTIAL~~

Dyna-Soar and ASSET were designed for a life of 1 to 4 flights, whereas the cruise vehicle structure should be serviceable for 10 000 or more. Each band shows that the temperature limit decreases with increasing service life. These limits are not indicative of relative weights or structural efficiencies of these materials, but are the combinations of temperature and time at which the material will be serviceable in a structure of the type indicated. Ceramic or graphite parts may be useful in the hottest areas but should be designed for periodic replacement. Refractory metal heat shields are useful at temperatures above 2000° F, but the useful life will be short. Long-life heat shields of superalloy appear possible for temperatures to about 1800° F, whereas primary structures may be limited to temperatures of about 1500° F.

Structural materials such as alloys of aluminum and titanium and the stainless steels are not likely to be used on the exterior surface of hypersonic vehicles because their temperature limits fall below 1000° F (being approximately 300°, 600°, and 800° F, respectively, at 10 000 hours). The interesting light alloys of beryllium (temperature limit at about 500° F) will not be considered for similar reasons. Filamentary composites, which have received much attention recently for lightweight aircraft structures, are not expected to have much application to hypersonic aircraft structures because typical capabilities generally lie below 1000° F, too. Ablation materials are unacceptable because they must be replaced after each flight.

STRUCTURAL PROBLEM AREAS

Figure 5 shows some of the structural problem areas of a hypersonic cruise vehicle. The major new aeronautical problem is the storage and use of liquid hydrogen fuel, a low-density, cryogenic liquid that must be stored internally at -423° F. Because of the high thermal-protection weights required to prevent excessive fuel boiloff during flight (which may be 10 to 15 percent of the fuel weight, even with a good design) the liquid hydrogen must be stored in areas where favorable surface-to-volume ratios can be obtained. The fuel tanks, therefore, will be in the fuselage of the vehicle (for a configuration such as this wing-body combination) rather than in the relatively inefficient spaces in the wing. The need to store large volumes of low-density fuel creates interest in configurations in which the wing and body are blended for more efficient volume utilization. Some preliminary studies have indicated that blended-body or all-body configurations may have structural weight advantages, but this subject needs further study. Structural technology for the blended configurations is not well developed and needs additional research. Regardless of the configuration, the body, including the fuel tanks, will be the heaviest structural component of the hypersonic vehicle, whereas the wing is usually the heaviest component of subsonic and supersonic aircraft.

The integration of the cryogenic tank, its thermal protection system, and the body structure presents another new design problem. In addition, should this vehicle have separate tanks suspended within the fuselage structural shell or should integral construction be used, with the tank walls carrying the fuselage bending loads? A proper answer to this question must consider the basic

~~CONFIDENTIAL~~

structural efficiency of prospective concepts plus the interaction between the fuselage and wing structures, which may be at significantly different temperatures. Two of the papers that follow discuss technology for liquid hydrogen tanks in fuselage structures. Jackson and Sharpe (ref. 5) report on a promising thermal-protection system now in the testing phase and Shideler and Jackson (ref. 6) review several concepts for integrating the tanks, thermal protection, and body structure.

The wing, the second heaviest component, will probably be a hot, load-carrying structure. Areas near the leading edge may require insulation covered by heat shields, as indicated in the figure by the checkered area. These heat shields will be divided into small panels to minimize thermal stresses. Both the primary structure and the heat shield may have uneven surfaces and numerous joints which could disturb the air flow over the vehicle. This is another area in which potential reductions in structural weight must be weighed against increased heating or higher drag. Anderson, Robinson, and Klich describe some of the structural design problems of hot wing structures in one of the following papers (ref. 7).

The structure inside the propulsion unit experiences very high heating and loading and requires structural cooling. Hydrogen is an excellent coolant and can be used without a weight penalty if the amount needed for cooling does not exceed that required for propulsion. Extensive structural cooling, however, is another innovation in aircraft design. Some recent developments in regeneratively cooled structures are described in a paper by Kelly and Shideler (ref. 8).

Hypersonic vehicles will have a variety of structural dynamic problems. A preliminary assessment of dynamic problems related to engine and boundary-layer noise, fuel sloshing, wing flutter, and gust response are presented in a paper by Rainey and Martin (ref. 9), and Bohon, Anderson, and Heard (ref. 10) report on flutter design of the types of stiffened-skin panels likely to be used in hypersonic aircraft structures.

Other areas indicated here have not been the subject of recent NASA research and will not be discussed. Thermal protection of the crew, passenger, and cargo compartments should be somewhat less difficult than thermal protection of the liquid hydrogen. Design of tail and control surfaces can be based on wing structures technology. The hottest areas, the nose and leading edges, will require special materials and structural arrangements. Only the material aspects will be considered in this conference, but much applicable technology for these areas has been developed in entry-vehicle programs such as X-15, ASSET, and Dyna-Soar. Therefore, feasible but heavy short-life structures can be built now for noses and leading edges. As these vehicles approach reality, numerous other problems will arise. For example, what type of windshield will the pilot have, will the passengers have windows, what type of landing gear will be required, and where and how should it be stored?

~~CONFIDENTIAL~~

~~CONFIDENTIAL~~

WING RESEARCH

Figure 6 illustrates two wing-structures research programs planned for the near future. The first program involves the analysis and validation of structural design concepts for lightweight wing structures for hypersonic cruise vehicles capable of sustained operation at Mach 8 and a dynamic pressure of 2200 psf. In the first phase of this program, a contractor will conduct analytical and experimental investigations of several structural concepts for the shaded portion of the wing. The better concepts will be validated through component tests to provide a basis for selecting the optimum combination of primary structure, heat shield, leading edge, and wing-fuselage attachment for a representative wing structure. Plans for the second phase call for the contractor to incorporate the selected concepts into the design and fabrication of a wing panel (also shown shaded) that can be flight tested by NASA on the X-15-2 airplane. A second, identical, wing section will be constructed for NASA ground testing in the radiant heating facility at the Flight Research Center and the Langley 8-foot high-temperature structures tunnel. This program will advance wing structures technology by flight verification of a typical structure and comparison of flight and ground test results.

The second program is the proposed delta-wing X-15 hypersonic research airplane. Present plans include a study, by a contractor, to determine the feasibility of constructing such a research vehicle. This study will include an analytical investigation of applicable structures concepts. A NASA analysis of structural arrangements for this wing is described in the paper by Anderson, Robinson, and Klich (ref. 7). If this research airplane is built, the design, manufacture, and flight of the delta wing will provide the first experience with a full-scale, lightweight, delta-wing structure suitable for hypersonic flight.

TEST FACILITIES

Finally, a few words should be said about ground facilities for testing hypersonic structural components. Many high-temperature facilities are available (at the aerospace companies, the Air Force Flight Dynamics Laboratory, and the NASA Flight and Langley Research Centers, for example), and they are capable of performing much of the structures research and development testing needed in the Mach 6 to 8 range. A number of modifications and additions to these facilities will be required, however, and much new small-scale test equipment will be needed, particularly for testing materials.

Most structural testing will be done in furnaces and radiant heating facilities, but some problems require more complete flight simulation which includes airflow. Figure 7 is a photograph of a large, blowdown-type hypersonic wind tunnel constructed for structural testing, the Langley 8-foot high-temperature structures tunnel. Air and methane, stored at high pressure, are burned in a combustion chamber, expanded to a Mach number of about 7 in the test section, and then exhausted to the atmosphere. The design operating conditions of this

~~CONFIDENTIAL~~

~~CONFIDENTIAL~~

facility are shown in figure 8. Stagnation temperature in the test section is plotted as a function of combustion-chamber stagnation pressure. This stagnation pressure is interpreted in terms of test-section pressure altitude by the scale across the top, which indicates that the facility can operate over a range from 80 000 to 140 000 feet. The tunnel is designed to operate within the shaded area, and the darker band defines conditions that simulate Mach 7 flight. Simulation is defined as providing combinations of pressure, temperature, velocity, and heating rate on the structure in the test section that are identical to those encountered in flight at Mach 7. All desired conditions cannot be duplicated simultaneously because this facility uses the combustion products of air and methane as the test medium; this gas mixture has thermodynamic properties different from those of air. Testing in combustion products does not permit investigations of phenomena in which oxidation or combustion are important, but it is adequate for numerous static and dynamic structural studies.

The symbols in figure 8 indicate conditions at which the tunnel has operated to date during its shakedown and calibration runs. When a few modifications are completed in the near future, the tunnel is expected to be operational throughout the design region except in the small area above the Mach 7 simulation band. This facility can be used to test large specimens of all types of structural components that may be used on hypersonic aircraft. Tests of such components (which may include film, transpiration, or regenerative cooling systems) in this facility are expected to provide a valuable link between the usual laboratory tests and flight experience.

CONCLUDING REMARKS

High-temperature structures and materials technology has been accruing for more than a decade from the development of missiles and entry vehicles, but the specific problems of hypersonic aircraft structures are just now beginning to be studied in depth. USAF programs are making substantial contributions in this area. The papers that follow (refs. 4 to 10), which constitute a progress report on NASA research, will present recent research results applicable to hypersonic aircraft structures and will indicate the current state of the art.

~~CONFIDENTIAL~~

~~CONFIDENTIAL~~

REFERENCES

1. Heldenfels, R. R.: Structural Prospects for Hypersonic Air Vehicles. ICAS Paper No. 66-31, Presented at the Fifth Congress of the International Council of the Aeronautical Sciences, Sept. 1966.
2. Fetterman, David E.; McLelland, Charles H.; Jackson, L. Robert; Henry, Beverly Z., Jr.; and Henry, John R.: A Review of Hypersonic Cruise Vehicles. Conference on Aircraft Aerodynamics, NASA SP-124, May 1966, pp. 523-564. (Also available as NASA TM X-1276.)
3. Raring, Richard H.; Freeman, J. W.; Schultz, J. W.; and Voorhees, H. R.: Progress Report of the NASA Special Committee on Materials Research for Supersonic Transports. NASA TN D-1798, 1963.
4. Stein, Bland A.; Illg, Walter; and Buckley, John D.: Structural Materials for Hypersonic Aircraft. Conference on Hypersonic Aircraft Technology, NASA SP-148, 1967. (Paper No. 28 herein.)
5. Jackson, L. Robert; and Sharpe, Ellsworth L.: A Carbon Dioxide Purge and Thermal Protection System for Liquid Hydrogen Tanks. Conference on Hypersonic Aircraft Technology, NASA SP-148, 1967. (Paper No. 29 herein.)
6. Shideler, John L.; and Jackson, L. Robert: Fuselage and Tank Structures for Hypersonic Aircraft. Conference on Hypersonic Aircraft Technology, NASA SP-148, 1967. (Paper No. 30 herein.)
7. Anderson, Melvin S.; Robinson, James C.; and Klich, George F.: Analysis of Wing Structures for Hypersonic Aircraft. Conference on Hypersonic Aircraft Technology, NASA SP-148, 1967. (Paper No. 31 herein.)
8. Kelly, H. Neale; and Shideler, John L.: Regeneratively Cooled Structures for Hypersonic Aircraft. Conference on Hypersonic Aircraft Technology, NASA SP-148, 1967. (Paper No. 32 herein.)
9. Rainey, A. Gerald; and Martin, Dennis J.: Dynamic and Aeroelastic Considerations of Hypersonic Aircraft. Conference on Hypersonic Aircraft Technology, NASA SP-148, 1967. (Paper No. 33 herein.)
10. Bohon, Herman L.; Anderson, Melvin S.; and Heard, Walter L.: Flutter Design of Stiffened Skin Panels for Hypersonic Aircraft. Conference on Hypersonic Aircraft Technology, NASA SP-148, 1967. (Paper No. 34 herein.)

~~CONFIDENTIAL~~

TABLE I.- REPRESENTATIVE SURFACE EQUILIBRIUM TEMPERATURES
ON HYPERSONIC AIRCRAFT

$$[\epsilon = 0.8; \alpha = 4^\circ]$$

Equilibrium temperature, °F, on -								
Mach no.	Nose (q = 2200 psf)		Inlet leading edge (R = 1/4 in.; $\Lambda = 0^\circ$)		Wing and tail leading edge (q = 2200 psf; $\Lambda = 70^\circ$)		Lower wing surface (x = 20 ft)	
	R = 1/4 in.	R = 6 in.	q = 2200 psf	q = 500 psf	R = 1/4 in.	R = 1 in.	q = 2200 psf	q = 500 psf
6	2120	1860	2230	2100	1880	1700	1330	1020
8	3260	2570	3250	2980	2650	2320	1600	1180
10	4000	3050	3990	3560	3200	2790	1700	1230
12	4390	3220	4280	4020	3410	2940	1730	1260

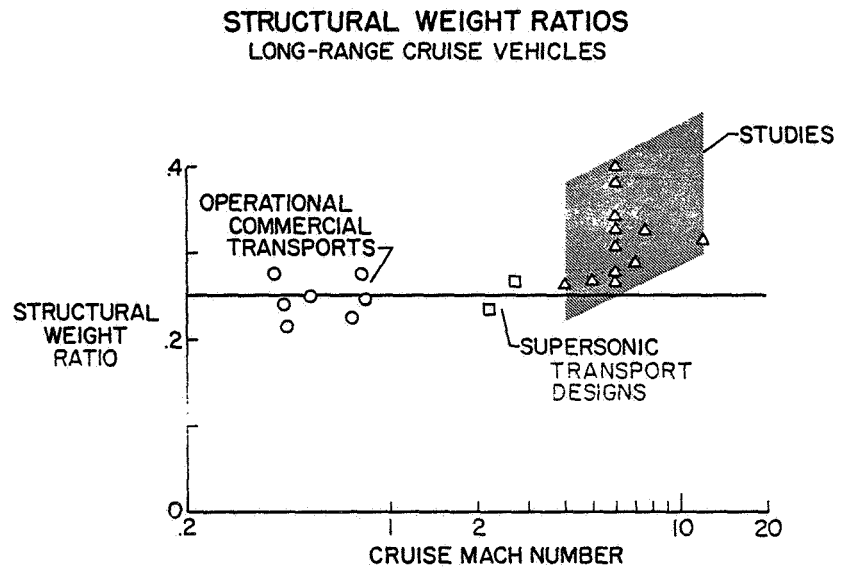


Figure 1

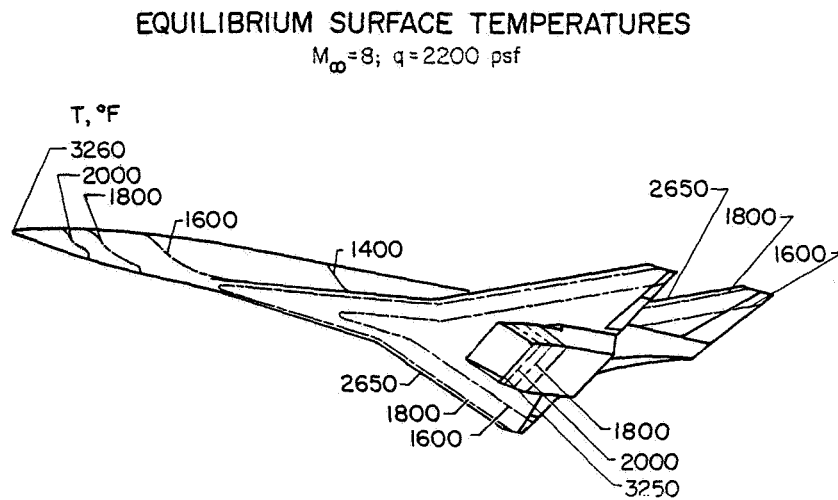


Figure 2

EQUILIBRIUM SURFACE TEMPERATURES

$M_\infty = 6$; $q = 500$ psf

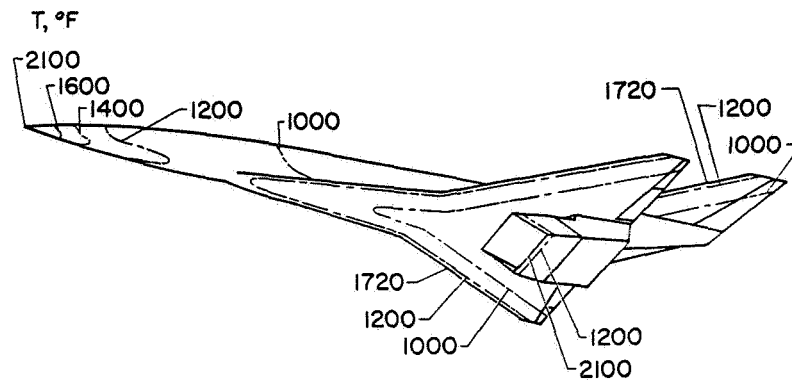


Figure 3

HIGH-TEMPERATURE MATERIAL LIMITATIONS

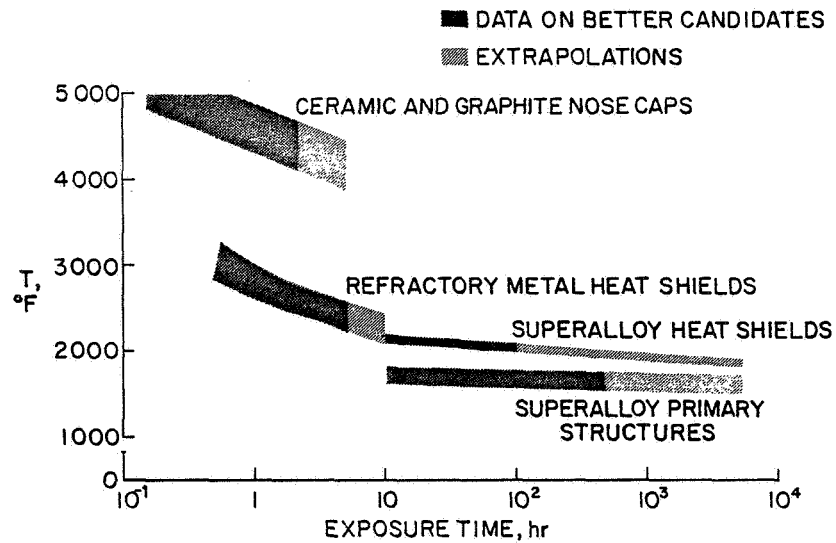


Figure 4

~~CONFIDENTIAL~~

STRUCTURAL PROBLEM AREAS HYPERSONONIC CRUISE VEHICLES

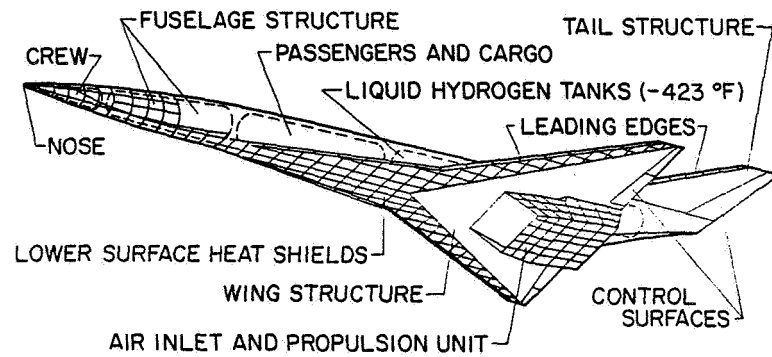


Figure 5

WING STRUCTURES RESEARCH

CONCEPT ANALYSIS AND EVALUATION

DELTA-WING X-15 RESEARCH AIRPLANE

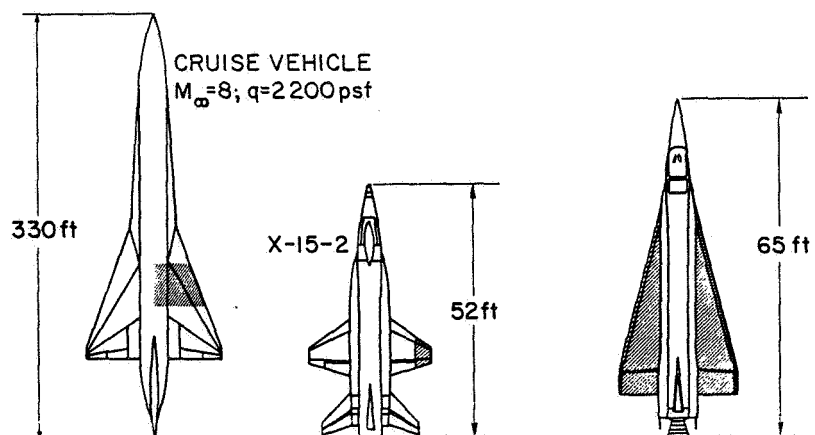


Figure 6

~~CONFIDENTIAL~~

~~CONFIDENTIAL~~

LANGLEY 8-FOOT HIGH-TEMPERATURE STRUCTURES TUNNEL

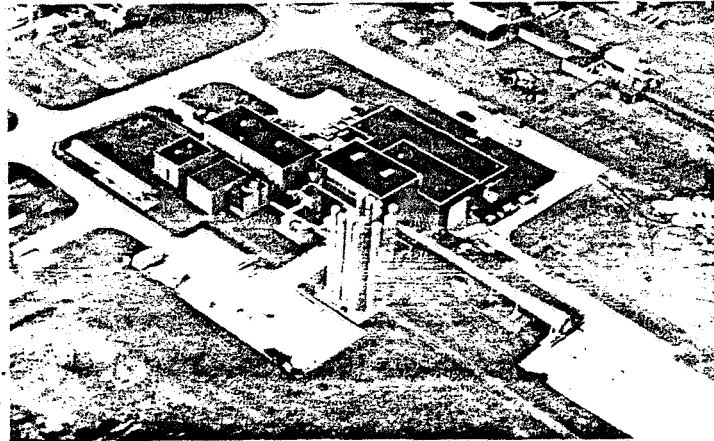


Figure 7

L-64-92

LANGLEY 8-FOOT HIGH-TEMPERATURE STRUCTURES TUNNEL

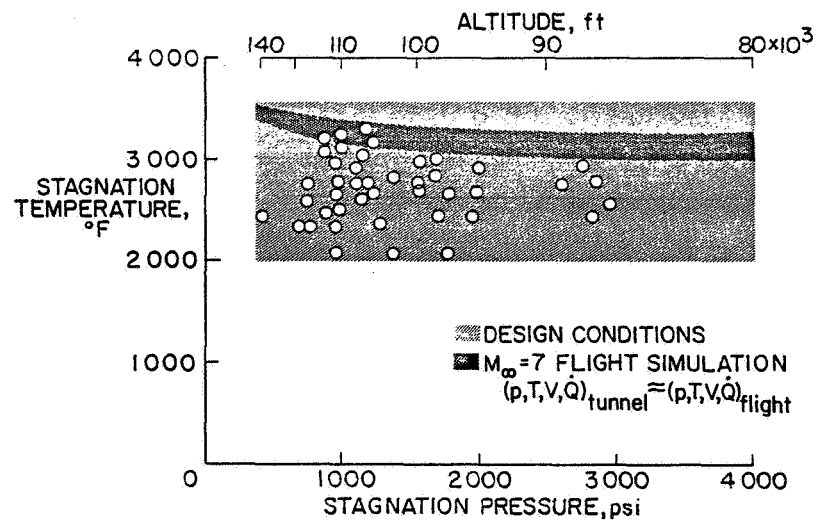


Figure 8

~~CONFIDENTIAL~~

~~CONFIDENTIAL~~

28. STRUCTURAL MATERIALS FOR HYPERSONIC AIRCRAFT

By Bland A. Stein, Walter Illg, and John D. Buckley
Langley Research Center

SUMMARY

The low structural-weight limits and the severe operating environments of hypersonic-cruise-aircraft structures appear to tax existing sheet materials to the limits of their high-temperature capabilities. Requirements for many repeated exposures greatly increase the severity of these problems. This review compares the properties of existing and emerging materials with arbitrary guidelines which appear applicable to structural requirements of these aircraft so as to assess the current state of the art for this application. Five vehicle areas are considered, namely, permanent primary structure and heat shields, replaceable leading edges and nose caps, and liquid hydrogen tankage. Available sheet materials for primary-structure applications may suffice for operation at temperatures of 1400° F for exposures up to 5000 cumulative hours but do not appear adequate for applications at 1600° F. The newly developed dispersion-stabilized sheet alloy, TD NiC, appears promising for permanent heat-shield requirements at temperatures from 1600° to 2000° F. Current refractory materials for leading edges and heat shields operating at temperatures up to 3100° F appear to require replacement after 1 or 2 flight cycles. The JTA graphite composite shows promise for a capability of at least 2 or 3 cycles in nose caps operating at 4000° F. Because of the requirement for cryogenic and elevated temperature operation of hydrogen tankage, stainless steels such as extra-hard type 301 appear most promising for this application.

INTRODUCTION

At previous NASA conferences, consideration has been given to materials for hypersonic applications such as orbital reentry, where one flight (or at most, two or three flights) was required. At this conference, the materials technology for hypersonic cruise vehicles, which must withstand many repeated high-temperature exposures, are considered. Because of the low structural weight limits and the severe operating environment, material requirements for structures of these vehicles are so severe as to tax existing sheet materials to the limits of their high-temperature properties. Earlier reviews (for instance, refs. 1 to 3) touched on deficiencies of materials for this application but did not specifically examine the capabilities of newly developed materials, some of which have emerged in the past year.

In the present review the properties of existing and emerging sheet materials are compared with arbitrary guidelines that appear applicable to structural requirements of certain hypersonic cruise aircraft. These guidelines may be subject to change when results of more studies become available, but they presently provide an assessment of the current status of high-temperature

~~CONFIDENTIAL~~

~~CONFIDENTIAL~~

sheet materials. Because of lack of data, considerable extrapolation was required to compare these materials in the areas of interest.

ENVIRONMENTAL FACTORS AFFECTING STRUCTURAL MATERIALS

The severe factors in the environment of the aircraft include repeated exposures to high temperature in low pressure air with long cumulative exposure times. The ranges of temperatures are indicated in figure 1. The drawing shows the magnitude of equilibrium skin temperatures anticipated during flight Mach number M_∞ of 8 at a dynamic pressure q of 2200 pounds per square foot on a typical hypersonic aircraft configuration. This flight condition is a severe one selected primarily as a focus for research and is not representative of optimum cruise conditions at Mach 8. It is severe enough to provide a strong challenge to current materials technology and includes ranges of temperatures which may be encountered in cruising flight in the range of Mach numbers from 6 to 12.

Materials that meet requirements of operation at the temperatures shown in figure 1 will be adequate to cope with almost all prospective cruise vehicle conditions. Large areas of the surface are primary structures operating at temperatures from 1400° to 1600° F, indicated by the hatched area. It will be shown that structural materials limitations appear to be so severe that heat shields will be required for operation in the 1600° to 2000° F regions of the vehicle, shown cross-hatched. The areas shown in black cover the leading-edge and nose-cap regions of this aircraft, where temperatures range from 2000° to 3300° F. White areas operate at equilibrium temperatures below 1400° F so that existing materials appear to be applicable. Internal engine areas are not considered herein. One other area in this vehicle which may have materials problems is that of liquid hydrogen tankage, indicated by the dotted area.

Arbitrary minimum temperature and time objectives for these vehicle areas are indicated in table I.

TABLE I.- TEMPERATURE-TIME CONDITIONS FOR MATERIALS IN SEVERAL
CRITICAL APPLICATIONS ON HYPERSONIC CRUISE VEHICLES

Application	Temperatures, °F	Exposure time, hr
Primary structure	Below 1600	>5000
Heat shields	1600 to 2000	>5000
Leading edges	2000 to 3100	>50
Nose cap	3100 to 4000	>5
Hydrogen tankage	-423 to 600	>5000

These objectives for the structural components were arrived at through considerations of expected equilibrium skin temperatures for cruise conditions in

~~CONFIDENTIAL~~

the Mach 6 to 12 range, mission requirements, and the capabilities of current and emerging high-temperature materials. However, it should be noted that the data presented in the present review are general and can be used for many temperature-time conditions other than those selected for this particular evaluation.

Periodic replacement of the large areas of primary structures and heat shield which operate at temperatures up to 2000° F (table I) does not appear feasible in a vehicle which may be longer than 300 feet. Therefore, these primary structures and heat shields, probably limited to sheet thicknesses of 0.010 to 0.020 inch, must survive cumulative exposure times on the order of 5000 hours or more in air at free-stream pressures of approximately 8 torr with little degradation of mechanical properties. It should be noted that 5000 hours is a minimum, which should be more than adequate for reusable launch vehicles. Transport requirements may call for 20 000 to 50 000 cumulative hours of exposure. However, extrapolation of currently available data on materials beyond 5000 hours becomes increasingly questionable.

In order to cover materials requirements for vehicles which cruise at speeds up to Mach 12, leading-edge operating temperatures up to 3100° F and nose-cap temperatures up to 4000° F are listed. These leading edges and nose caps cover small areas of the vehicle and may be replaced periodically, but hopefully not sooner than the cumulative exposure times indicated. Of course, the ideal solution would be to have permanent nose caps and leading edges, but this does not appear likely for materials currently under study for the temperatures listed.

Liquid hydrogen tankage may operate over a temperature range from -423° to 600° F. Long-time material stability after repeated thermal cycling in the presence of liquid and gaseous hydrogen is required for this region.

MATERIAL COMPARISONS FOR SPECIFIC AREAS OF VEHICLE STRUCTURE

Table II indicates some specific material guidelines which appear applicable to the five vehicle areas previously discussed. These guidelines were arbitrarily selected for assessment of the present status of materials for the hypersonic cruise aircraft application in the categories noted. Although specific items will not be discussed separately at this point, it should be noted that the guidelines identified with the circular symbols appear to present no problems for existing materials and are not discussed further. The areas marked with triangular symbols do not appear to pose significant problems, but data for long-time environmental exposures are required to confirm this assumption; the areas marked with square symbols appear to be major problem areas in which currently available materials are marginal at best. The remainder of this discussion is largely devoted to these major problem areas.

Very little data are available in the literature for thin sheet at the exposures and environments of interest, and those that exist are from ground tests only, since no significant flight test information has been generated.

~~CONFIDENTIAL~~

~~CONFIDENTIAL~~

TABLE II.- ARBITRARY MATERIAL-PROPERTY GUIDELINES FOR HYPERSONIC-CRUISE-VEHICLE STRUCTURAL APPLICATIONS

■ Major problem area
 ▲ Possible problem area
 ● No apparent problems

Category Application	Oxidation or corrosion	Creep	Ductility	Fatigue	Stiffness	Notch sensitivity	Strength	
	Maximum thickness loss, inch	Maximum creep strain	Minimum tensile elongation in 1 inch, percent	Minimum stress in 10^8 cycles, ksi	Minimum Young's modulus, ksi	$\frac{\sigma_{\text{notched}}}{\sigma_{\text{unnotched}}}$ (a)	Minimum tensile, ksi	Minimum yield, ksi
Primary structure	0.002 ■	0.2% at 10 ksi ■	5 ▲	10 ▲	15×10^3 ●	0.8 ▲	50 ●	40 ●
Heat shield	0.002 ■	0.2% at 5 ksi ■	5 ▲	5 ▲	10×10^3 ●	0.8 ▲	25 ▲	20 ▲
Leading edge	0.1 ■	0.5% at 1 ksi ●	---	1 ▲	5×10^3 ●	0.5 ▲	15 ●	--
Nose cap	0.5 ■	1.0% at 1 ksi ●	---	1 ▲	2×10^3 ●	0.8 ▲	5 ●	--
Tankage	0 ▲	0 ●	5 ●	(b) ▲	10×10^3 ●	0.8 ▲	(c) ▲	(d) ▲

^a σ defined as stress.

^bStress/Density = 0.5×10^6 inches.

^cStress/Density = 0.75×10^6 inches.

^dStress/Density = 0.5×10^6 inches.

The best estimates of the authors were used to account for the effects of sheet thickness, while sea level pressure exposures were considered to give data which would provide conservative estimates of oxidation effects in the lower pressure hypersonic environment. Where exposure data exist, they generally do not cover exposure times of more than 500 hours, extending to 1000 hours in some cases, so that extrapolation was used to predict 5000-hour data.

Primary Structure

The next few figures are concerned with materials for primary structure and heat shields. The two most significant problems in primary-structure applications appear to be oxidation and creep as noted in figure 2. In the graph at the left is plotted the combination of temperature and time, the latter on a logarithmic scale, in which uncoated superalloys and dispersion stabilized materials lose 0.002 inch of sheet thickness by general oxidation or corrosion, or loss by diffusion of strengthening precipitates in bands adjacent to the substrate. This loss may be as much as 20 percent in minimum-gage sheet. That arbitrary guideline is noted at the top while the vertical line from 1400° to 1600° F at 5000 hours gives the desired time-temperature combination. Dashed lines on the figure indicate extrapolations of data.

~~CONFIDENTIAL~~

~~CONFIDENTIAL~~

The available high strength sheet alloy René 41 (ref. 4), which is a nickel-base alloy, and L-605 (ref. 5), which is a cobalt-base alloy, fall in the lower band and seem to meet the guideline at 1400° F. The group in the upper band are all nickel-base alloys. The newer sheet alloy, Inconel 625 (ref. 4), and the lower-strength sheet alloys such as Hastelloy X (ref. 6) and TD Nickel (refs. 5 and 7) fall in this band along with alloys developed for engine applications, such as 713 C (ref. 8) and a newly developed NASA alloy TAZ-8A (ref. 9). As of this date these engine materials have only been used in castings, but if current efforts to fabricate the relatively brittle TAZ-8A alloy into sheet prove successful, structural applications in hypersonic cruise vehicles are possible. A new dispersion-stabilized alloy, TD NiC (refs. 5 and 10), has shown such excellent oxidation resistance in preliminary tests that the projected 20-mil sheet thickness loss lies above the range of this figure, as indicated by the arrow.

The graph on the right in figure 2 shows the combination of temperature and time to produce 0.2-percent creep strain at a tensile stress of 10 ksi. This amount of creep strain has been used as a criterion in some supersonic transport studies. Some of the more promising materials for oxidation resistance fall short of the guidelines here, among them Hastelloy X (ref. 4), Inconel 625 (ref. 4), and the dispersion-stabilized alloys (refs. 4 and 10). René 41 (ref. 4) appears to have the required creep strength but was poor in oxidation resistance. Only the casting alloys (refs. 8 and 9) seem to combine adequate strength plus oxidation resistance. This is also borne out in figure 3 where yield strength is plotted on the graph at the left. The yield strength parameter is 40 ksi. The available sheet alloys are again marginal and the casting alloys the best. The yield strength of the dispersion stabilized alloys and Hastelloy X is so low that they do not appear on the graph.

The drawback of the casting alloys is illustrated in the graph at the right in figure 3 where tensile elongation is plotted as a function of temperature for materials before exposure. Although the significance of tensile elongation as a measure of ductility in structural applications is open to question, a minimum acceptable value is indicated because no better measure of ductility is generally available for sheet materials. An acceptable value for this comparison is arbitrarily considered to be about 5 percent in a 1-inch gage length before exposure, as indicated by the horizontal line on the graph. There appear to be no problems here with available sheet alloys. Furthermore, several of these alloys have been shown to have adequate ductility after exposure. The elongation of the dispersion-stabilized alloys appears adequate but the TAZ-8A alloy exhibits poor elongation below 1500° F. The possibility of further reduction in elongation after exposure must also be expected.

Another class of new materials has been suggested, that of metal matrix filamentary composites. However, it would appear that diffusion reactions between filament and matrix might severely degrade composite properties after long-time, high-temperature exposures so that the outlook for this class of materials cannot be considered promising until long-time stability in a strong composite is proven.

In summary for primary structure materials, available sheet materials do not appear adequate for applications at temperatures of 1600° F, but may suffice

~~CONFIDENTIAL~~

107

~~CONFIDENTIAL~~

for maximum temperatures of 1400° F. The most promising compositions for the temperature requirement of 1600° F appear in the casting alloys and utilization depends upon fabrication into sheet with some ductility. Of course, much more data must be generated for such materials. Joining processes must also be investigated. In many materials, fatigue life or ductility can be significantly degraded by welding processes.

Heat Shields

Materials for permanent heat shields are now discussed. Again, the most significant factors appear to be oxidation and creep, which are shown in figure 4. The oxidation parameter for the graph at the left is again sheet thickness decrease of 0.002 inch and the temperatures of interest are 1600° to 2000° F. Now none of the existing sheet alloys or the casting alloys appear adequate. Included in these is the dispersion-stabilized alloy TD nickel. However, one alloy, the newly developed thoria dispersion-stabilized nickel-20 percent chromium (TD NiC) (ref. 10), appears to be the one sheet material which can meet the oxidation requirement. The graph at the right shows temperature and time to produce 0.2-percent creep strain at a tensile stress of 5 ksi. This lower stress is applicable here since heat shields are not subjected to as high a stress level as is the primary structure. The available sheet and casting alloys show insufficient resistance to creep, but the dispersion-stabilized alloys are promising, the TD NiC being the best of the group. This material appears adequate in other requirements at temperatures up to at least 1800° F, but slightly low in yield strength and elongation at 2000° F. The alloy TD NiC is currently available in sheet as thin as 20 mils. Some joining studies for this material are under way and long-time exposure tests in simulated hypersonic aircraft environments must be made to determine whether the promise of TD NiC as a prime candidate heat-shield material for hypersonic cruise aircraft will be fulfilled.

Leading Edges

Other materials problems for hypersonic cruise vehicles concern areas of the structure where periodic replacement may be permitted. Consider leading edges which encounter temperatures from 2000° to 3100° F during cruise. Two classes of materials are of interest for leading edges; namely, coated refractory metal sheet alloys and coated graphite or graphite composites. Properties of these materials appear adequate for the application except in the area of oxidation resistance. This is indicated in figure 5. Again, temperature is plotted as a function of exposure time, which is on a logarithmic scale. The guidelines are coating failure for coated materials and 0.1-inch substrate thickness decrease for the JTA graphite composite, which forms its own coating. The arbitrary time-temperature requirement is 50 hours at 2000° to 3100° F before replacement.

Protective coatings for refractory metals have been researched extensively for the past decade. Data for the better commercially available aluminide and silicide coatings on molybdenum (refs. 11 and 12), columbium (refs. 13 and 14),

~~CONFIDENTIAL~~

and tantalum alloys (refs. 12, 14, and 15) fall in the upper shaded band for small coupons under cyclic exposure in static air. Both NASA data and that of other researchers are reported here. The top of the upper band in figure 5 has been approached recently with some reliability with the development of fused slurry silicide coatings (ref. 14). The new Hf-Ta alloy coatings for tantalum alloys also fall in this upper band.

It is common knowledge that coatings on large fabricated parts do not have as long lives as coated coupons and that flowing air tests give lower coating lives than static air tests. Limited experience with fabricated parts and with simple specimens in airstreams (refs. 15, 16, and 17) indicate that the actual lives to be expected for existing coatings on refractory alloys in leading edges or heat shields of a hypersonic cruise vehicle lie in the lower shaded band of figure 5. Oxidation failures for siliconized graphite leading edges (ref. 16) also fall in this lower band. JTA graphite composite loses 0.1 inch of substrate in the temperature-time range indicated by the solid line (ref. 18).

An assessment of these data indicates that current candidate materials for leading edges fall short of a 50-flight cycle before replacement requirement at temperatures above 2000° F. Further developments of refractory metal coatings and new materials such as chromium alloys show promise for 50 cycles without replacement at temperatures to perhaps 2600° F. At 3100° F, however, replacement may be necessary after 5 to 10 flights.

Nose Caps

Consider now the parts of the hypersonic cruise vehicle that are exposed to highest temperatures - the nose cap and some leading-edge sections around the engine nacelles. (See fig. 1.) Oxidation or erosion resistance is of prime importance. These properties are shown in figure 6 in a plot of temperature as a function of exposure time with the parameter being either coating failure on coated refractory metal or a material loss of 0.5 inch by erosion or oxidation for the other materials considered. The guideline is an exposure time of 5 hours at temperatures from 3100° to 4000° F before replacement.

Two types of composite nose-cap structures were tested in flowing air for the Air Force ASSET program (ref. 19). Both were ceramic reinforced with tungsten wire mesh. The thorium-oxide (thoria) cap was tested at 4900° F and the hafnium-oxide (hafnia) cap was tested at 4400° F. Both showed good 1-hour performance but data are not yet available on reuse capabilities.

An NASA investigation of JTA graphite composite (ref. 20) in subsonic and supersonic airflow has shown this material to have excellent reuse capability and a much lower oxidation or erosion rate than that of standard graphites. The JTA composite contains zirconium, silicon, and boron in addition to carbon so that it forms a protective coating on outer surfaces as it oxidizes. The standard graphite, ATJ, contains only carbon so that its oxidation rate is relatively high. Data for the Hf-27Ta coating on tantalum alloy are shown in a band for coating thicknesses of 10 mils to 20 mils. Neither the latter nor the ATJ graphite appears suited to the nose-cap requirements.

~~CONFIDENTIAL~~

~~CONFIDENTIAL~~

Another problem area which should be mentioned concerns development of techniques for minimizing thermal stresses in relatively brittle ceramic or graphite nose caps or leading-edge segments at points of attachment to metallic substructures.

In summary, it would appear that the JTA graphite composite is the currently available material which shows most promise for multiple flight capability in nose-cap or leading-edge applications at 4000° F.

Tankage

The last structural application to be considered is the coldest part of the structure, liquid hydrogen tankage. In the previous applications discussed, candidate materials were either similar in density so that weights were comparable or the part of the aircraft in question was not weight critical. For tankage, however, various candidate alloys of wide variation in density are available. In figure 7 one of the more important factors, the tensile strength of specimens with notches which approximate the effects of stress raisers in structural members, is shown for several materials. The stress-concentration factor for these curves is approximately 8. The ratio of the notch tensile strength to the density is plotted as a function of temperature for several materials. The nominal requirement is noted as a notch strength-to-density ratio of 600,000 inches.

The most significant indication from this plot, generated from data in references 6, 21, 22, and 23, is that the titanium alloys, which appear superior at liquid hydrogen temperatures, lose their superiority to extra-hard type 301 stainless steel if high-temperature operation at significant tank stresses is required. It is possible that design of tankage in a hypersonic cruise vehicle may be dictated by a high-temperature operation condition near the end of a flight so that the high material strengths at cryogenic temperatures could not be utilized. In any event, the titanium alloys and stainless steels look best on this plot, whereas the aluminum alloys and the superalloy, René 41, do not appear as promising.

Another important problem which has not received enough research to date is that of possible hydrogen embrittlement of these tankage materials during elevated temperature operation. The notch tensile strength would be most affected by this phenomenon. One result of a study of this effect is noted in figure 7. A specimen of the extra low interstitial content Ti-5Al-2.5Sn alloy was exposed in 0.1 psig hydrogen at 600° F under a stress of 10 ksi (ref. 6). This specimen failed in 50 minutes. Several titanium alloys have been shown to be subject to some degree of hydrogen embrittlement at temperatures above 300° F, so that use of titanium alloys in hydrogen tankage may be limited to operation at that temperature or lower.

Filament-wound tanks of glass-fiber or boron-fiber reinforced resins have been suggested as lightweight tankage materials. For hydrogen tankage, however, a metal inner liner is necessary to prevent diffusion through the wall. The liner weight, plus the considerations of mismatch due to thermal expansion

~~CONFIDENTIAL~~

~~CONFIDENTIAL~~

during cyclic temperature operation, make the combination less attractive at present than conventional metallic construction. A discussion of this problem is given in reference 24.

The stainless steels such as extra-hard type 301 are therefore considered the most promising available materials for liquid hydrogen tankage in the hypersonic cruise vehicle, but more research on hydrogen embrittlement of tankage materials is required for cryogenic/elevated temperature cycling.

CONCLUDING REMARKS

A state-of-the-art review of materials for structural applications in hypersonic cruise aircraft has been presented. The following conclusions are indicated:

1. Available sheet materials for primary structure applications may suffice for operational temperatures of 1400° F for exposures up to 5000 cumulative hours but do not appear adequate for applications at 1600° F. The most promising materials for operation at the latter temperature appear to be the casting alloys developed for engine applications but their utilization depends upon fabrication into sheet with some ductility.

2. The newly developed dispersion-stabilized sheet alloy, TD NiC, appears promising for permanent heat-shield requirements at temperatures from 1600° to 2000° F.

3. Current refractory materials for leading edges and heat shields operating at temperatures up to 3100° F appear to require replacement after 1 or 2 flight cycles. Improved coating reliability might increase this capability to 5 or 10 cycles, but considerable research and development is needed for longer intervals between replacements.

4. The JTA graphite composite shows promise for a capability of at least 2 or 3 cycles in nose caps operating at 4000° F.

5. Because of the requirement for cryogenic and elevated temperature operation of hydrogen tankage, stainless steels such as extra-hard type 301 appear most promising for this application.

~~CONFIDENTIAL~~

~~CONFIDENTIAL~~

REFERENCES

1. Heldenfels, R. R.: Structural Prospects for Hypersonic Air Vehicles. ICAS Paper No. 66-31, 5th Congress Int. Council Aeron. Sci., Sept 12-16, 1966.
2. Childers, Milford G.: Structure and Materials for Hypersonic Vehicles. SAMPE J., vol. 2, no. 6, Oct./Nov. 1966, pp. 21-29.
3. Laidlaw, W. R.; and Johnston, E. W.: Developing HST Structural Technology. Astronaut. Aeron., vol. 4, no. 10, Oct. 1966, pp. 40-43.
4. Weiss, V.; and Sessler, J. G., eds.: Aerospace Structural Metals Handbook, Vol. II A - Non-Ferrous Heat Resistant Alloys. ASD-TDR 63-741, Vol. II A, Suppl. 3., U.S. Air Force, Mar. 1966.
5. Ault, G. Mervin: Current Status and Opportunities for Improved High-Temperature Materials for Advanced Turbojet Engines. AIAA Paper No. 65-741, 1965.
6. Christian, J. L.; and Kerr, J. R.: Selection of Optimum Materials for Use in Liquid-Hydrogen-Fueled Aerospace Vehicles. ASD-TDR-63-798, U.S. Air Force, Oct. 1963.
7. Manning, Charles R., Jr.; Royster, Dick M.; and Braski, David N.: An Investigation of a New Nickel Alloy Strengthened by Dispersed Thorium. NASA TN D-1944, 1963.
8. Anon.: Alloy 713C Technical Data. Intern. Nickel Co., Inc., Aug. 1963.
9. Waters, William J.; and Freche, John C.: Investigation of Columbium-Modified NASA TAZ-8 Superalloy. NASA TN D-3597, 1966.
10. Anon.: TD NiC - A New Dispersion Strengthened Alloy (Nominal Ni-20% Cr-2% ThO₂). Interim Data Sheet. DuPont Metals Products, Aug. 26, 1966.
11. Rummeler, Donald R.; Stein, Bland A.; and Pride, Richard A.: A Study of Several Oxidation-Resistant Coatings on Mo-0.5Ti Alloy Sheet at 2,500° F. NASA TN D-2040, 1964.
12. Wurst, J. C.; Cherry, J. A.; Gerdeman, D. A.; and Hecht, N. L.: The High Temperature Evaluation of Aerospace Materials. AFML-TR-66-308, U.S. Air Force, Oct. 1966.
13. Lisagor, W. Barry; and Stein, Bland A.: A Study of Oxidation-Resistant Coatings on Cb-10Ti-5Zr Alloy Sheet at 2000° F, 2400° F, and 2700° F (1365° K, 1590° K, and 1755° K). NASA TN D-3275, 1966.

~~CONFIDENTIAL~~

~~CONFIDENTIAL~~

14. Priceman, S.; and Sama, L.: Development of Fused Slurry Silicide Coatings for the Elevated-Temperature Oxidation Protection of Columbium and Tantalum Alloys. Annual Summary Report, STR 66-5501.14, U.S. Air Force, Dec. 1966.
15. Stein, Bland A.; and Lisagor, W. Barry: Oxidation and Embrittlement in Silicide-Coated Columbium-Alloy and Aluminide-Coated Tantalum-Alloy Sheet. NASA paper presented at Fourth Symposium on Refractory Metals, Met. Soc., Am. Inst. Mining, Met., Petrol. Engrs., October 3-5, 1965.
16. Anthony, Frank M.; and Mistretta, Andrew L.: Investigation of Feasibility of Utilizing Available Heat Resistant Materials for Hypersonic Leading Edge Applications. WADC Technical Report 59-744, Vol. VIII, U.S. Air Force, June 1961.
17. Wichorek, Gregory R.; and Stein, Bland A.: Experimental Investigation of Insulating Refractory-Metal Heat-Shield Panels. NASA TN D-1861, 1964.
18. Carbon Prod. Div., Union Carbide Corp.: Improved Graphite Materials for High-Temperature Aerospace Use. Vol. II - Development of Graphite Refractory Composites. ML-TDR-64-125, vol. II, U.S. Air Force, Aug. 1964.
19. Anon.: Development of Composite Structures for High Temperature Operation. Rept. ER-1480; ITR-6 (Contract AF 33(615)-1831), Solar, Mar. 1 - June 30, 1966. (Available from DDC as AD-489109.)
20. Buckley, John D.; and Stein, Bland A.: Preliminary Investigation of the Dynamic Oxidation of JT Graphite Composites at Surface Temperatures Between 4000° F and 5000° F. Summary of the Eleventh Refractory Composites Working Group Meeting, Darrell R. James and Elvin H. Beardslee, [compilers], AFML-TR-66-179, U.S. Air Force, July 1966, pp. 595-614.
21. Schwartzberg, F. R.; Osgood, S. H.; Keys, R. D.; and Kiefer, T. F.: Cryogenic Materials Data Handbook. ML-TDR-64-280, U.S. Air Force, Aug. 1964.
22. Figge, I. E.: Residual Static Strength of Several Titanium and Stainless-Steel Alloys and One Superalloy at -109° F, 70° F, and 550° F. NASA TN D-2045, 1963.
23. Weiss, V.; and Sessler, J. G., eds.: Aerospace Structural Metals Handbook. Vol. II - Non-Ferrous Alloys. ASD-TDR-63-741, Vol. II, Suppl. 2, U.S. Air Force, Mar. 1965.
24. Morris, E. E.; Sanger, M. J.; and Darms, F. J.: Filament Wound Structures. Space/Aeron., vol. 47, no. 2, Feb. 1967, pp. 86-92.

~~CONFIDENTIAL~~

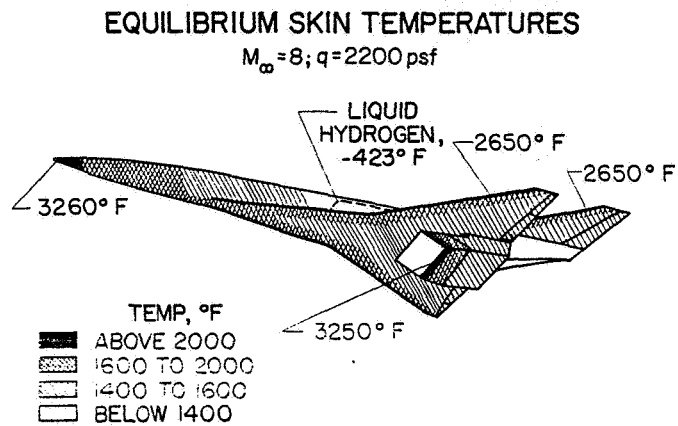


Figure 1

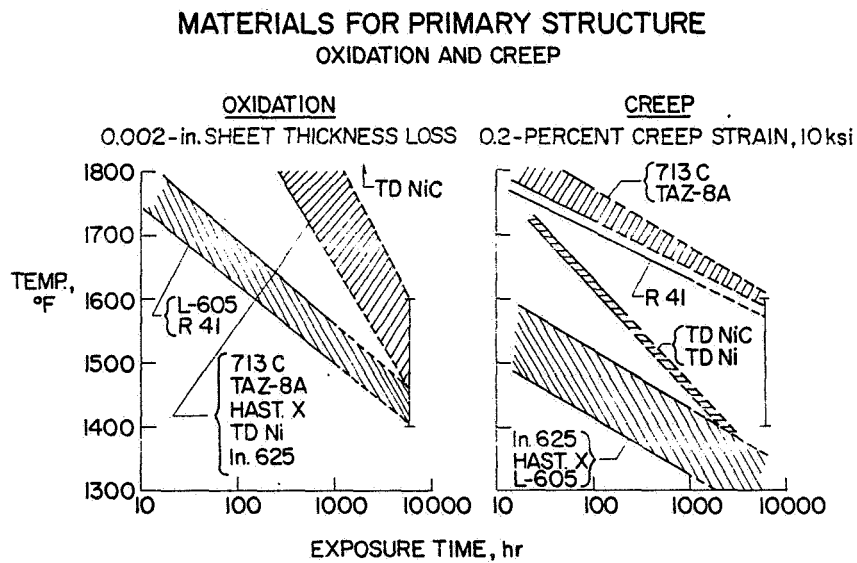


Figure 2

~~CONFIDENTIAL~~

MATERIALS FOR PRIMARY STRUCTURE STRENGTH AND DUCTILITY

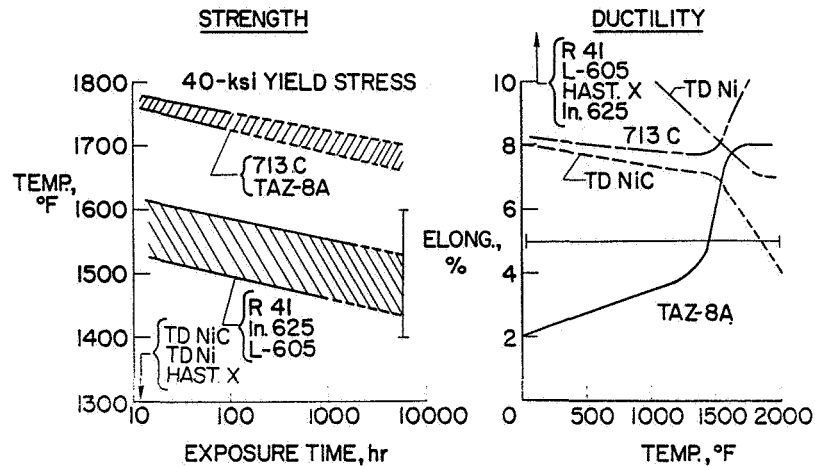


Figure 3

MATERIALS FOR PERMANENT HEAT SHIELDS

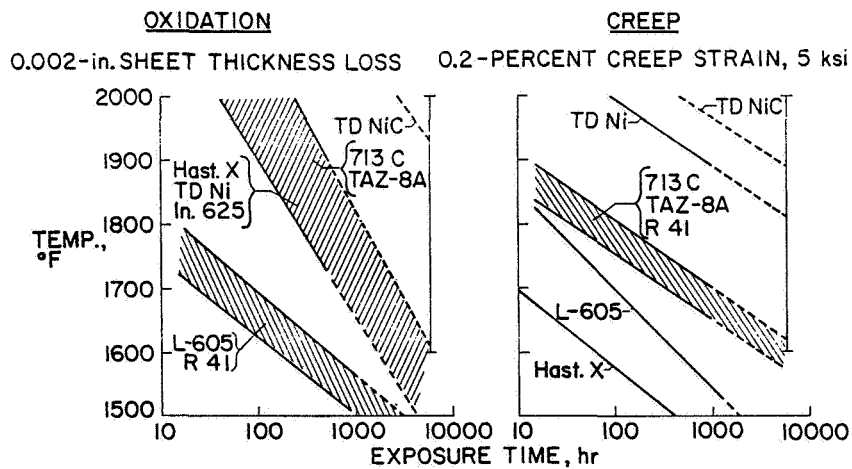


Figure 4

~~CONFIDENTIAL~~

~~CONFIDENTIAL~~

OXIDATION RESISTANCE OF REPLACEABLE LEADING-EDGE MATERIALS

COATING FAILURE FOR COATED MATERIALS;
0.1-in. THICKNESS LOSS FOR GRAPHITE COMPOSITE

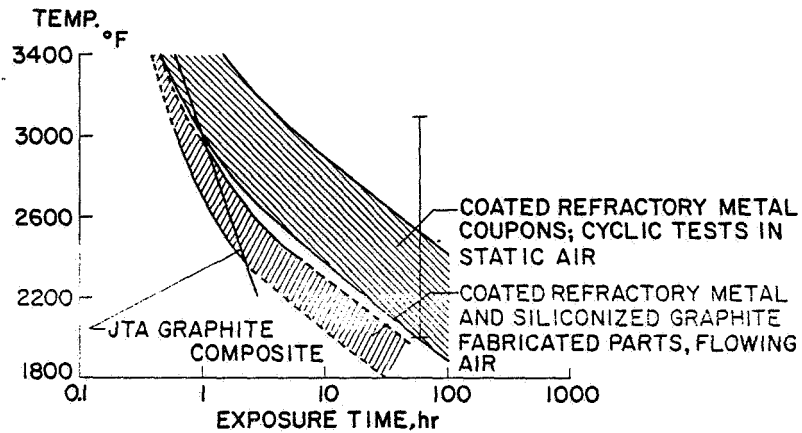


Figure 5

OXIDATION RESISTANCE OF REPLACEABLE NOSE-CAP MATERIALS

COATING FAILURE FOR COATED TANTALUM ALLOY;
0.5-in. THICKNESS LOSS FOR OTHER MATERIALS

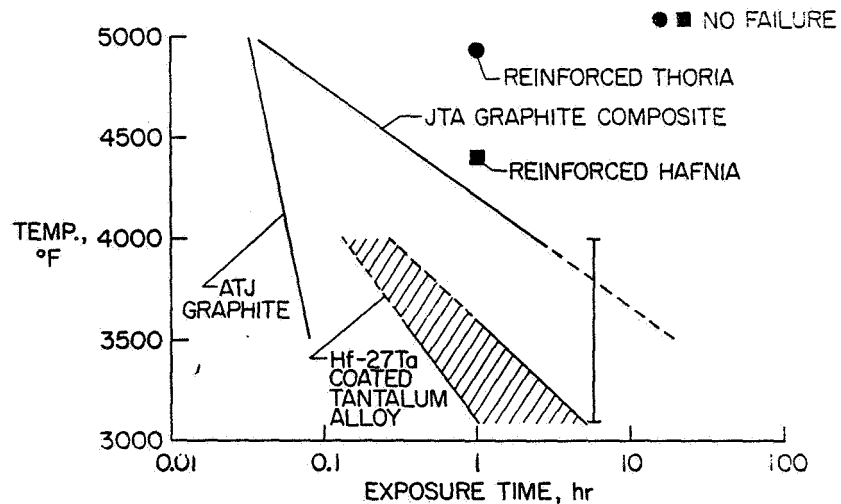


Figure 6

~~CONFIDENTIAL~~

~~CONFIDENTIAL~~

NOTCH TENSILE STRENGTH FOR HYDROGEN-TANKAGE MATERIALS

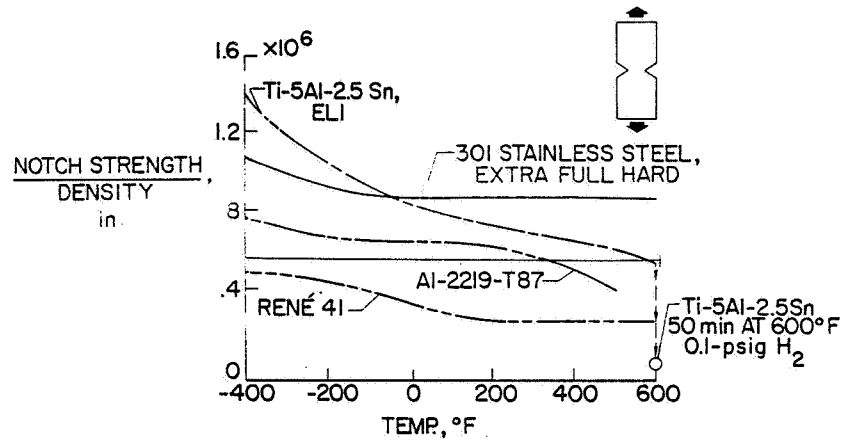


Figure 7

~~CONFIDENTIAL~~

~~CONFIDENTIAL~~

29. A CARBON DIOXIDE PURGE AND THERMAL PROTECTION SYSTEM FOR LIQUID HYDROGEN TANKS

By L. Robert Jackson and Ellsworth L. Sharpe
Langley Research Center

SUMMARY

Hypersonic flight may introduce liquid hydrogen fuel to aircraft. If so, the problem of limiting heat transfer to the fuel will become a principal aircraft design problem. For instance, the low temperature of liquid hydrogen can cause air to liquefy on tank walls and cause a cryopumping action. Should cryopumping be permitted during flight, excessive fuel vaporization could result. Fuselage walls both unsealed (which are gas purged) and sealed (which are evacuated) have been studied to exclude air from the tanks. This paper discusses an unsealed system that offers effective thermal protection through heat absorption by sublimation of CO₂ frost and by transpiration of the resulting gas through the tank insulation. Research to date has established technology for system design and operation. This effort has indicated that the CO₂ system is a workable solution for limiting fuel heat load when used in conjunction with supplemental nitrogen purging for periods of low heating rate. Recent tests with a representative structural model have demonstrated the tank wall temperature control effect of the CO₂ thermal protection system.

INTRODUCTION

Studies (refs. 1 and 2) have shown that liquid hydrogen may be the fuel of hypersonic aircraft. If so, the problem of limiting heat transfer to the fuel will become a principal aircraft design problem. The problem of limiting heat transfer to the fuel is not one of simply insulating the tank because the low temperature of this fuel can cause any gas except helium to condense and cause a cryopumping action (ref. 3). Air must be excluded from tank walls, because its continuous cryopumping can release the heat of condensation at a high rate inside the insulation. Tests (ref. 4) have shown that the resulting heat transfer to the fuel is sufficient to vaporize fuel at a rate of 18 lb/hr-ft² of tank surface area. This rate is not acceptable for a flight vehicle. Furthermore, the accumulations of water and liquefied oxygen from the air can create problems other than the fuel heat load.

In general, only two approaches are possible for preventing flow of air to tank walls. Figure 1 shows several liquid hydrogen tanks in the fuselage of a hypersonic airplane. Enlarged sections of the tank wall illustrate the two systems under consideration. Each section has an unsealed structure, insulation, and a separate suspended tank.

~~CONFIDENTIAL~~

~~CONFIDENTIAL~~

The section on the left shows one of the systems proposed for excluding air from tank walls. The aim of this approach is to seal the insulation space by means of a container. Both thin metals and plastic films have been tried for sealed surfaces. Neither material has been successful to date. However, should an evacuated container be made, air condensation would not occur because the hot face of the container is at a higher temperature than that for the liquefaction of air.

The section on the right shows the other approach under study for the exclusion of air from tank walls. This approach involves a light pressurization with a gas of the purge space between the tank and the structure to prevent air from entering the unsealed structure. Helium has been tested for this purpose (ref. 5), but helium is costly and other systems are possible with less cost and weight.

Recent studies have led to two other gas purge systems. One (described herein and presented in ref. 6) is the CO₂ system that has been under study for about 3 years. The second system (described in ref. 7) is a nitrogen gas purge system that resulted from the CO₂ system studies. Results of the CO₂ purge and thermal protection system study are given and are followed by results of a simulated hypersonic flight with a representative structural model.

SYMBOLS

k	thermal conductivity
L	insulation thickness
\dot{m}	mass-flow rate
P_{CO_2}	CO ₂ partial pressure
P_m	CO ₂ and helium mixture pressure
Q_f	fuel heat load
T	temperature
ΔT	temperature difference over insulation
W_F	frost unit-area weight
ρ	insulation density or insulation-frost composite density
ρ_F	frost density
τ	frost deposition time

~~CONFIDENTIAL~~

~~CONFIDENTIAL~~

CO₂ SYSTEM STUDY

A CO₂ system study has included the experimental determination of thermophysical properties of CO₂ frost and frost deposition data. In addition, analyses of CO₂ system weight and purge requirements were made. Results of these tests and analyses are given after a brief description of the CO₂ thermal protection system.

Description

Figure 2 shows a tank wall section similar to that in figure 1, but the low density-conductivity product ρk insulation on the tank is shown impregnated with CO₂ frost. An insulation with a low density-conductivity product is used because, the lower this product, the more efficient the insulation. At the pressures encountered around the tank, CO₂ has no liquid phase; therefore, when air is purged from around the tank by CO₂ gas during preflight preparation and as the tank is filled with fuel, some of the CO₂ gas condenses directly to a frost within the insulation. The density of this frost is controlled by mixing noncondensable helium with the CO₂ gas around the tank during frost deposition.

Once the required amount of frost has been deposited, take-off results in sublimation of the frost, first by a pressure reduction with altitude, then by aerodynamic heating. Sublimation of the frost provides the purge gas needed to prevent flow of air through the unsealed structure to the tank during hypersonic flight, and supplemental nitrogen purging is provided for subsonic flight. The low conductivity of CO₂ and the heat it absorbs result in an efficient thermal protection system. Therefore, the CO₂ system can limit heat transfer to the fuel at a weight that may be acceptable.

Thermophysical Properties

To assess the performance of the CO₂ system, thermophysical properties for the frost were obtained. These data were obtained under Contract No. NAS1-4017 to Convair Division of General Dynamics, and some results are given in figure 3. This figure shows plots of thermal conductivity of the frost-insulation composite and of ρk for various frost densities. The frost was deposited in a 4.5 lb/ft³ density fibrous insulation.

As shown on the left of the figure, frost conductivity without helium (flight conditions) is less than with helium (preflight conditions) for densities greater than about 10 lb/ft³. During hypersonic flight, the frost is in a pure CO₂ gas environment; whereas, during preflight the frost is in an environment consisting of a mixture of CO₂ and helium. The conductivity of helium is higher than that of CO₂ gas; this fact is in part responsible for the difference in the conductivities at the higher densities. The magnitude of ρk is a measure of insulation efficiency of the frost-insulation composite, and,

~~CONFIDENTIAL~~

~~CONFIDENTIAL~~

as with insulation alone, minimum weight is achieved at minimum ρ_k . This minimum is shown at 20 lb/ft³ frost density. A density of 25 lb/ft³ has been selected for design because the frost is firmer at this density than at lower densities.

CO₂ Frost Deposition

To deposit frost at a given density and unit-area weight, certain variables must be controlled. Variables affecting control of CO₂ frost deposition are shown in figure 4. This figure gives CO₂ frost density as a function of the ratio of CO₂ partial pressure to the pressure of the mixture of CO₂ and helium which surrounds the tank. The constant deposition times are shown by dashed lines, and the constant unit-area frost weights are shown by solid lines. This figure provides the necessary information for frost deposition at the required density and weight for the particular temperature difference and insulation thickness used for these tests ($\Delta T = 390^\circ \text{ F}$; $L = 1.7 \text{ in.}$). Similar data have been obtained for other test conditions.

The principal deposition control variable for frost density is the ratio of CO₂ partial pressure to the gas mixture pressure. That is, the density is increased with increases in this pressure ratio; at a particular pressure ratio, the density is increased with increases in deposition time. The correct CO₂ partial pressure ratio depends on the amount of frost required and the density desired. For example, to deposit 1.0 lb/ft² of frost at a 25 lb/ft³ density requires a pressure ratio of 0.25. The corresponding time for deposition is seen to be just over an hour. This pressure ratio, the deposition time, and the tank-wall cool-down rate are the only variables actually controlled during deposition.

CO₂ System Weight

It is appropriate to consider the manner in which the CO₂ system weight is affected by the selection of a deposition time. Deposition time affects the turnaround time and should not constrain flight operations. The effect of frost deposition time on CO₂ system weight is shown in figure 5. These data are for the lower tank surface and are based on a 1.5-hour flight of a cruise airplane at an average surface temperature of 1500° F. The system weight includes vaporized fuel and insulation as well as the average frost weight carried during the flight. A minimum weight is achieved at a deposition time of about 4 hours. However, deposition for as little as 1 hour results in almost the same CO₂ thermal protection system weight. For other reasons, such as servicing and inspection, a time of 1 hour appears to be a reasonable minimum for airplane turnaround time. Therefore, the CO₂ system deposition time does not constitute a severe operational constraint.

~~CONFIDENTIAL~~

Purge System

Another aspect of any purge system is concerned with the question of how much purge gas is required to overcome the leakage through the structure while maintaining a positive pressure in the purge space. Calculations show that the amount of frost available is adequate for normal cruise flight. However, the critical situation would develop during periods of low heating rate such as could occur in an aborted flight wherein, at the halfway point, the plane must fly one-half the range at subsonic speeds. The absence of aerodynamic heating at subsonic speed greatly reduces the amount of CO₂ gas from frost sublimation which is available for purging. The left side of figure 6 shows the temperature time history of a selected abort mission and the right side shows the gas flow rates during the time of flight.

The aerodynamic surface temperature is shown to rise rapidly during climb, to remain level during cruise, and then to fall rapidly after abort. During abort the Mach number changes from 8.0 to 0.8. To return to base, a $2\frac{1}{2}$ -hour subsonic cruise is assumed. The tank upper surface temperature is increasing during the flight time. The difference in aerodynamic surface and tank wall temperatures is an indication of the heat-transfer rate to the frost on the tank wall.

The heat-transfer rate is high during Mach 8 flight; consequently, the mass-flow rate of CO₂ gas is also high from sublimation of frost (fig. 6, right side). The leakage rate through the unsealed structure is shown by the dash-dot curve, and it varies because of changes in aerodynamic heating and atmospheric pressure. This particular initial leakage rate (0.4 lb/hr-ft²) may be achieved by attention to sealing during construction. Measured leakage from a representative structural model was about twice the sea-level value shown at take-off; however, no attempt was made to minimize leakage with the model.

After abort the sublimation rate drops below the leakage rate; actually, sublimation provides less gas than the amount needed to achieve the indicated redeposition flow. The redeposition-flow rate is the rate at which CO₂ gas would condense on the lower tank surfaces in contact with liquid hydrogen, if sufficient CO₂ gas were available. This analysis indicates that a supplemental purge system is required to prevent cryopumping of air through the structure to the tank during periods of low heating rate. Tests have shown that nitrogen may be used for purging during such periods.

STRUCTURAL MODEL TEST

The first simulated flight test of a representative fuselage structure of a hypersonic airplane has been recently completed. This test was performed with simultaneous loading and heating while the tank contained liquid nitrogen. The model used was designed for Mach 8 flight and incorporated the CO₂ thermal protection system. The model design was based on the first stage of a two-stage-to-orbit airplane.

~~CONFIDENTIAL~~

~~CONFIDENTIAL~~

Model Description

The model is seen in figure 7. The top photograph shows the rear view of the assembled structural model. Under the model are components before final assembly. The hydrogen tank is made of 2219 aluminum alloy and is waffle stiffened. The structure is made of René 41 superalloy and is Z-stiffened. Blankets of fibrous insulation, bonded to the tank, are shown in the final assembly view. The model was designed at the Langley Research Center and fabricated by the Convair Division of General Dynamics (ref. 8). The contractor reported that with an allowance for size difference, the construction shown could be built into a hypersonic airplane without further extensions of the art.

Apparatus

Laboratory experiments with the model were performed with the apparatus shown in figure 8. This apparatus is used at the Langley Research Center to test fuselage structures for hypersonic airplanes. The structural model, supported by a frame as a cantilever, is a calibration model used to check out the components of the apparatus and to serve as a test bed for external heat shields.

A bending moment and a shear force are applied to the front of the model by the hydraulic-load system. Radiant heaters surround the model. For testing, the clam-shell heater frames are rolled in toward the model so that the heaters enclose the model. Five banks of heaters are individually program controlled.

Cryogenics are stored in the Dewar vessels shown behind the model. Liquid nitrogen and liquid helium may be used successively in the tests.

Test Results

Actual test results in which liquid nitrogen was used are shown in figure 9. This figure shows surface temperatures against time for a simulated flight performed in the Langley structures laboratory. Temperatures on the upper and lower aerodynamic surfaces are seen to rise rapidly after take-off; the surfaces then cool gradually before landing some 30 minutes later. Stage separation occurred at about 10 minutes after take-off; a return glide at constant angle of attack, used in the analysis, is responsible for the temperature oscillations shown. The lower tank surface is a nearly constant -323°F for 20 minutes at which time the tank is empty. The temperature starts to rise on the upper surface at take-off since the liquid level begins to recede at take-off and the tank wall absorbs the heat transferring through the thermal protection.

The curves show calculated results, whereas the symbols show measured values obtained during the test. The agreement between these results confirms the correctness of both the thermophysical property data used in the analysis and deposition data used in the experiment.

~~CONFIDENTIAL~~

~~CONFIDENTIAL~~

Both the upper and lower tank surface temperatures level off at about -110° F (the CO₂ frost sublimation temperature) at 12 minutes and 27 minutes, respectively. Then after all frost has sublimed from the upper tank surface, at 15 minutes, the measured temperature rises to a maximum of 45° F at landing. This test clearly demonstrates the tank wall temperature control effect of the CO₂ system.

CONCLUDING REMARKS

The CO₂ purge and thermal protection system for hydrogen tanks of hypersonic airplanes has been summarized. Research to date has established technology for system design and operation and indicates that the CO₂ system is a workable solution to the prevention of cryopumping of air and the limiting of heat transfer to the fuel. During periods of low heating rates, such as occur in an aborted flight, a supplemental nitrogen system supplies the purge gas required. Future effort includes Mach 7 wind-tunnel testing of the CO₂ system structural model.

~~CONFIDENTIAL~~

~~CONFIDENTIAL~~

REFERENCES

1. Gregory, Thomas J.; Petersen, Richard H.; and Wyss, John A.: Performance Tradeoffs and Research Problems for Hypersonic Transports. J. Aircraft, vol. 2, no. 4, July-Aug. 1965, pp. 266-271.
2. Knip, Gerald, Jr.; and Allen, John L.: Analysis of Booster Systems With a Recoverable Hypersonic Airplane First Stage. AIAA Paper No. 64-543, May 1964.
3. Scott, Russell Burton: Cryogenic Engineering. D. Van Nostrand Co., Inc., 1959.
4. McGrew, J. L.: A Comparative Study of Airborne Liquid-Hydrogen Tank Insulation. Advances in Cryogenic Engineering, Vol. 8, Plenum Press, Inc., 1963, pp. 387-392.
5. Heathman, John H.; and Kelly, Larry G.: Hydrogen Tankage for Hypersonic Cruise Vehicles. AIAA/ASME Seventh Structures and Materials Conference, Apr. 1966, pp. 430-438.
6. Jackson, L. R.; and Anderson, M. S.: A Carbon Dioxide Purge and Thermal Protection System for Liquid Hydrogen Tanks of Hypersonic Airplanes. Advances in Cryogenic Engineering, Vol. 12, Plenum Press, Inc., 1967, pp. 146-156.
7. Shideler, John L.; and Jackson, L. Robert: Fuselage and Tank Structures for Hypersonic Aircraft. Conference on Hypersonic Aircraft Technology, NASA SP-148, 1967. (Paper No. 30 herein.)
8. Hopkins, John C.: Fabrication Process Developments of a Structural Model for Research on Hydrogen-Fueled Hypersonic Vehicles. NASA CR-66198, Convair Div., Gen. Dyn., Feb. 1967.

~~CONFIDENTIAL~~

LIQUID HYDROGEN TANKS

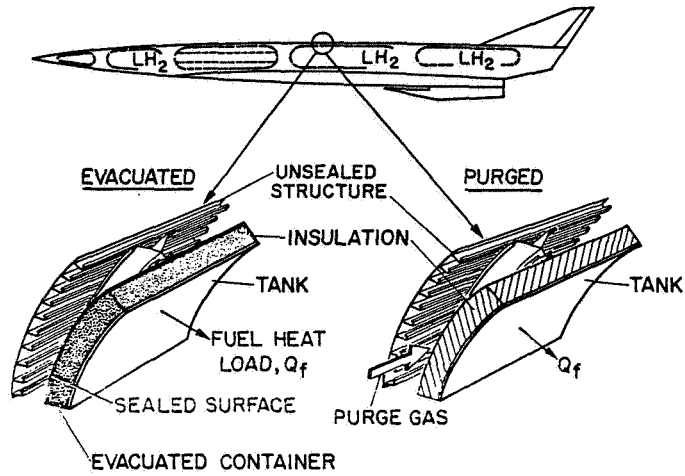


Figure 1

CO₂ PURGE AND FROST SYSTEM

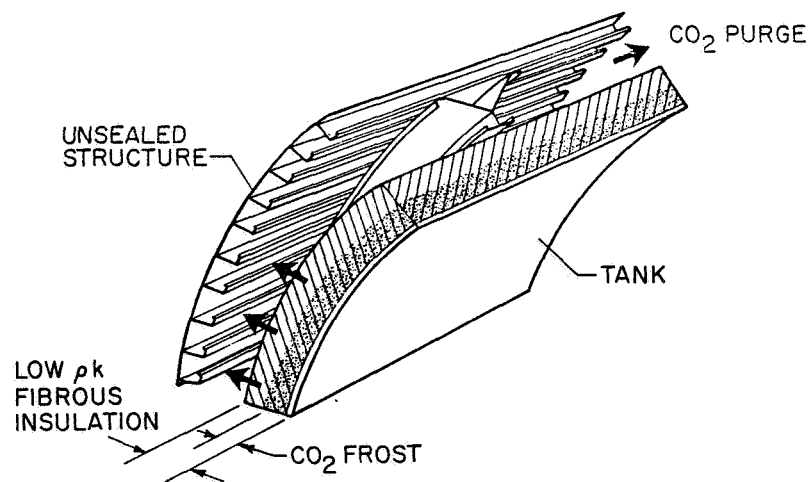


Figure 2

CO₂ FROST THERMOPHYSICAL PROPERTIES

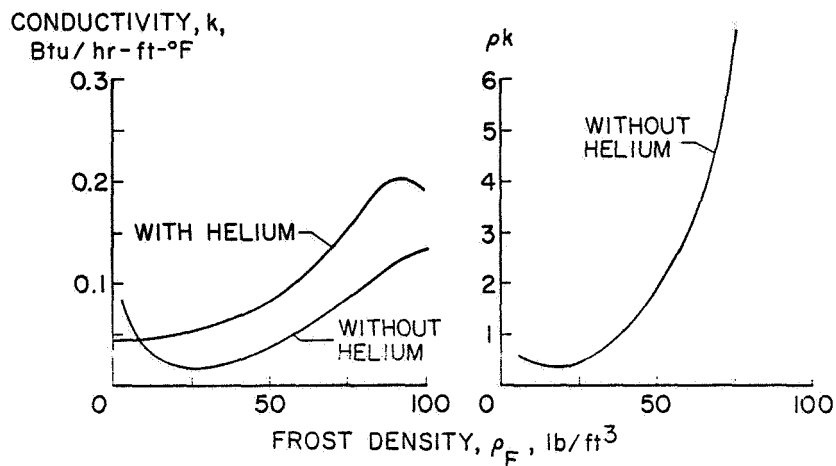


Figure 3

CO₂ FROST-DEPOSITION PARAMETERS $\Delta T = 390^\circ \text{F}$; $L = 1.7 \text{ in.}$

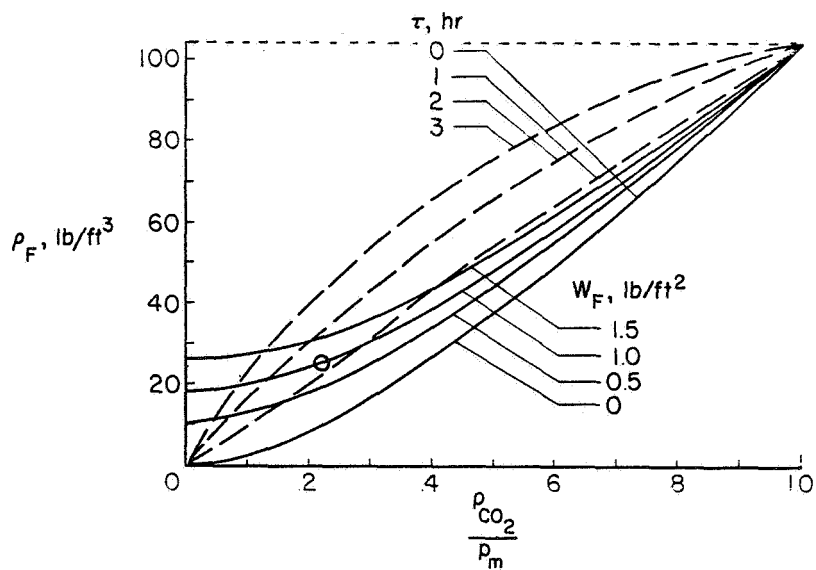


Figure 4

CONFIDENTIAL

EFFECT OF DEPOSITION TIME ON CO₂ SYSTEM WEIGHT

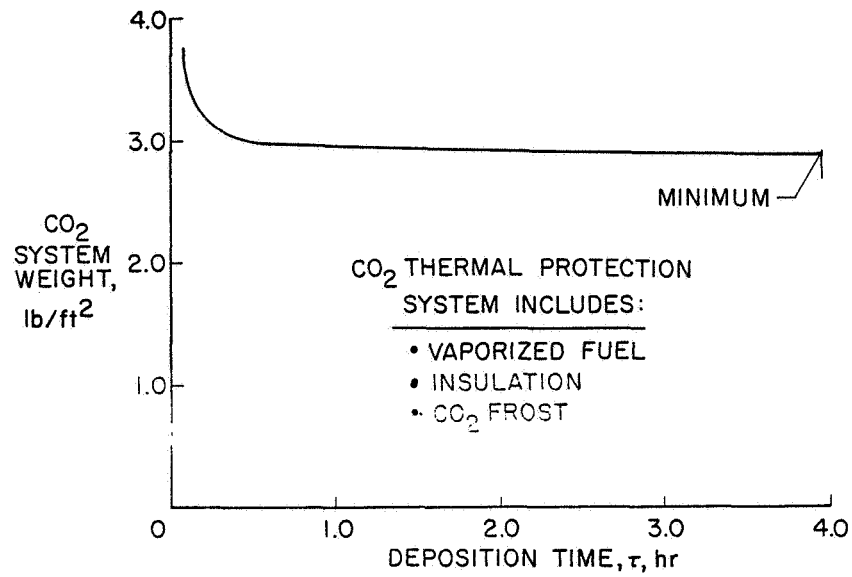


Figure 5

CO₂ PURGE CONDITIONS DURING AN ABORTED FLIGHT

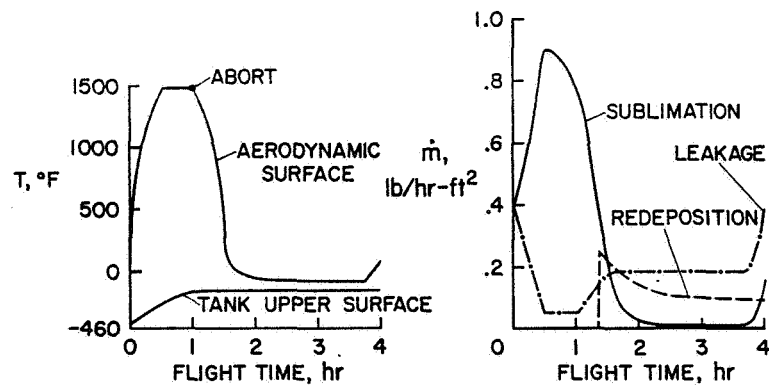
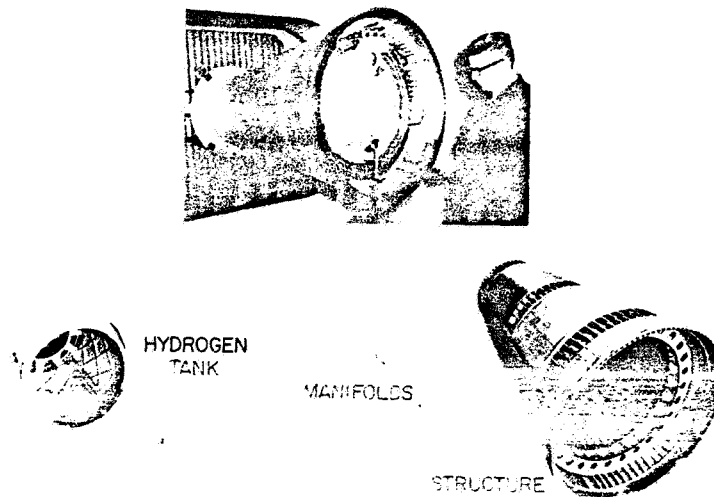


Figure 6

CONFIDENTIAL

~~CONFIDENTIAL~~

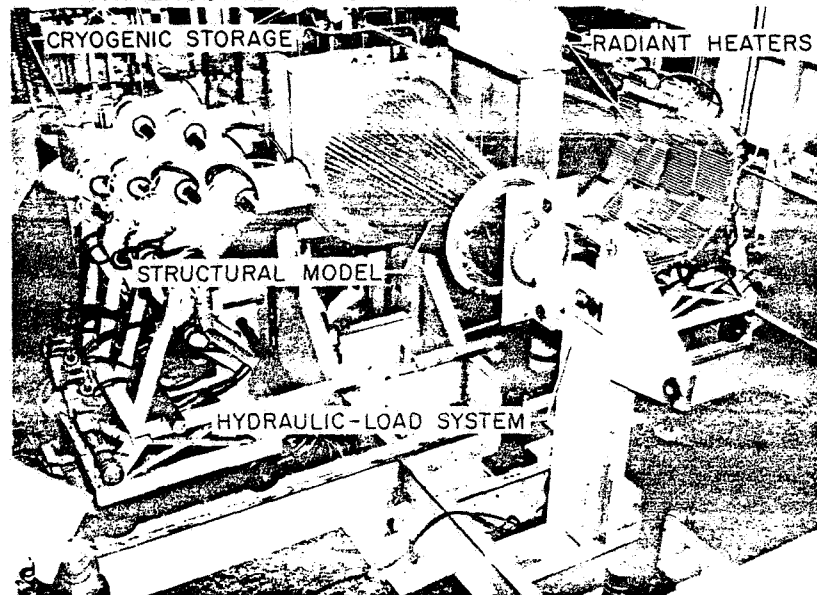
CO₂ SYSTEM STRUCTURAL MODEL



L-2879-7

Figure 7

HYPERSONIC-STRUCTURES TEST APPARATUS



L-2879-8

Figure 8

~~CONFIDENTIAL~~

~~CONFIDENTIAL~~

CO₂ SYSTEM TEST RESULTS

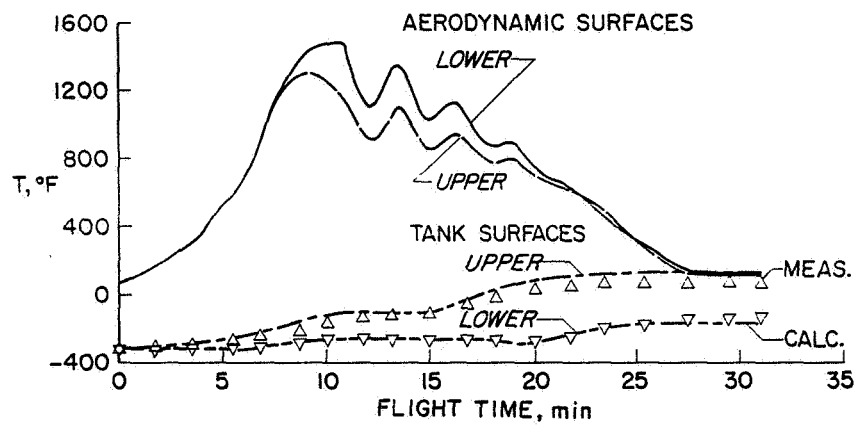


Figure 9

~~CONFIDENTIAL~~

~~CONFIDENTIAL~~

30. FUSELAGE AND TANK STRUCTURES FOR HYPERSONIC AIRCRAFT

By John L. Shideler and L. Robert Jackson
Langley Research Center

SUMMARY

Results of recent analytical studies on primary structure and thermal protection systems for hypersonic airplane fuselages containing hydrogen fuel are reviewed. Weight-strength comparisons of cylindrical fuselage wall structures under axial compression are shown for three new efficient structural concepts. Four thermal protection systems are described ranging from a sealed vacuum system which required further fabrication advances to a new nitrogen purge system. Unit-area weights for total fuselage systems combining load-carrying structures, thermal-protection system, tank, and heat shield are tabulated. The nitrogen system, which has potential cost and operational advantages, compares favorably with other currently feasible concepts.

INTRODUCTION

This report reviews results of recent studies on primary structure and thermal protection systems for hypersonic airplane fuselages containing hydrogen fuel. The use of liquid hydrogen as a fuel and the severe aerodynamic heating environment associated with hypersonic flight impose several new problems on aircraft structure. (See ref. 1.) For example, an exceptionally strong incentive exists to minimize the fuselage weight per unit area because large surface areas will be required to contain the low-density hydrogen. In addition, the fuselage tank structure must prevent undesirable cryopumping and must accommodate a large temperature difference from the aerodynamically heated surface to the liquid-hydrogen tank wall (about 2000° F).

Figure 1 shows schematics of two types of liquid-hydrogen tank-wall configurations which consider these new problems. The nonintegral tank configuration provides separate components to satisfy the primary functions of the fuselage. For instance, an external hot structure, shown as a ring-stiffened truss-core sandwich, is the primary load-bearing structure. An insulated tank is suspended within the hot fuselage structure. To alleviate thermal stress, suspension is such that the tank can contract upon cooling and the structure can expand upon heating. In this configuration the structure may be operating at the upper temperature limit of available materials. In the integral tank-wall configuration, the structure serves as the tank, thereby integrating two functions into one component and limiting the structure to a low operating temperature. Both of these features tend to improve efficiency. Thermal protection is added outside the structure, and heat shields are needed to protect the insulation. The heat shields are attached to the structure with flexible clips that penetrate the insulation and leave each shield free to expand with little restraint as it is heated. Although flexible attachments

CONFIDENTIAL

~~CONFIDENTIAL~~

alleviate thermal stress caused by the temperature difference, they produce heat shorts causing the heat transfer to the fuel to be greater with this configuration than with the nonintegral tank configuration. Probably the most significant problem posed by integral tank construction is the attachment of a nonfueled hot wing to the fuselage tank structure. The solution to this problem affects both the fuselage and the wing structure and will require further research before the merits of the integral tank structure can be properly assessed.

SYMBOLS

E	Young's modulus
k	thermal conductivity
N_x	cylinder buckling load
R	cylinder radius
\bar{t}	effective thickness
ρ	density
σ_y	yield stress

LOAD-CARRYING STRUCTURE

In the past few years several buckling analyses have been developed for cylinders, such as shown in figure 2, which have ring- and stringer-type construction and which are subjected to axial compression. These analyses have included the effects of ring eccentricities and stringer eccentricities, where the eccentricity is the distance from the ring or stringer centroid to the skin centroid. This type of buckling analysis (ref. 2) has been applied herein to a weight-strength evaluation of fuselage structures in bending. In many earlier weight-strength analyses, the effects of rings and ring and stringer eccentricities were either not accounted for or were accounted for in an approximate manner. The present analysis considers internal or external rings, internal or external stringers, and arbitrary skin, stringer, and ring geometries. As the basis for a weight-strength evaluation, this analysis considers local instability of the skin and stringers, panel instability of the skin-stringer combination between rings, and general instability of the total structure including rings. This analysis has been used to calculate weights of three fuselage structures which are shown in figure 3.

The beaded skin structure (upper left in fig. 3) is made of two skins that are joined to one another along seams between beads. Circumferential thermal stress from expansion of the skins relative to the cooler ring is minimized by the beading. However, the outer skin is beaded only slightly so that the

~~CONFIDENTIAL~~

structure provides a relatively smooth outer surface and can serve as the aerodynamic surface of the fuselage.

In the corrugated skin structure (fig. 3, center), the corrugation is made of alternating circular arcs and flats. Because it is a single skin, it has less weight for minimum gage applications than structures made of two or more skins. A rough corrugation of this type cannot serve as the aerodynamic surface, but it may be used as a protected structure where thermal protection is used on the structure to control its temperature. Recent analyses (ref. 2) have shown external ring stiffening to be stronger than internal ring stiffening, and since this structure would not be exposed to the airstream, external rings may be used advantageously.

With the stringer structure (fig. 3, lower right), the load-bearing material near the stringer webs operates at a stress approaching the yield strength at cylinder buckling. Skin material between stringers is permitted to buckle at low axial load; however, these buckled skins do provide shear stiffness. Buckles in the skins may afford too rough a surface for external use, so again external rings are shown. The principle utilized in designing this structure is that it is more efficient to let large surface areas buckle than to provide the material necessary to stabilize these large areas.

Structural efficiencies of each of the structures in figure 3 have been calculated by the analysis previously discussed. The results of this analysis are shown in figure 4 which compares efficiencies of the three structures with that of an efficient honeycomb-core sandwich. Limits in efficiency are indicated by the upper line for an unstiffened skin, which is not very efficient, and by the lower line for the yield strength. The yield strength limit is for structural materials having a ratio of yield stress to Young's modulus of 0.005, which is appropriate for most materials near room temperature. The yield strength limit is not attainable by any known structure in the range of structural index of 10^{-7} to 10^{-6} , which is the range of interest.

Both the beaded and corrugated skin structures are efficient because of the high local buckling strength of their principal load-bearing element - the circular-arc portion of the skin. The stringer structure has high efficiency because of its very low core density of 0.2 percent. This core density is one-tenth that of the 2-percent-density honeycomb-core sandwich shown for comparison. The 2 percent is selected as a minimum practical density. The low density of the stringer structure is possible because the core material is concentrated at the web of spaced stringers; this concentration tends to make the web thicker than that of the honeycomb-core.

The curves shown in figure 4 indicate that for low tank pressures in the structural index range of interest, the stringer structure is nearly as efficient as the very efficient corrugated skin structure. The efficiency of the stringer structure is a function of internal pressure if it is also used as a tank, and the gage of the skins is governed by the internal pressure to be supported. Because the weight-strength analysis is based on the fact that the structure supports bending loads without assistance from the skins which support internal pressure, the weight of the stringer structure increases with an increase in internal pressure from 5 psi to 25 psi.

~~CONFIDENTIAL~~

~~CONFIDENTIAL~~

THERMAL PROTECTION SYSTEMS

There are two general types of thermal protection systems for liquid hydrogen tank walls. They are gas purged and evacuated systems. This study has included each type; two examples are shown in figure 5 as schematics - the helium transpiration purge system, and the evacuated multiwall system.

The helium transpiration system at the upper left in figure 5 employs two improvements over previously studied helium purge systems. With the previously studied systems, the space around the insulation is supplied and lightly pressurized with helium. One improvement is the transpiration of the cold leakage flow of helium through the tank insulation. The purge gas then serves as thermal protection by absorbing heat. In addition, any heat which reaches the tank is absorbed by circulating the fuel on the tank walls through the indicated tubes as the fuel is pumped to the engines. This circulation uses a very small part of the heat absorption capability of the fuel and can prevent fuel boil-off which has been shown to be quite high with helium purge systems previously studied.

In the evacuated multiwall sandwich (lower right in fig. 5), a multiplicity of polished foils are welded to one another at dimpled crests. The resulting voids are evacuated to form efficient insulating layers. Experience obtained while trying to fabricate a structural model based on this concept (ref. 3) has shown that sealing surfaces enclosing the spaces to be evacuated is exceedingly difficult and, in fact, is beyond the present state of the art.

Schematics of two purge-type thermal protection systems are shown in figure 6. The carbon dioxide frost and purge system (upper left) was discussed in reference 4. This system has features, such as tank wall temperature control and low weight, that warrant its consideration.

The nitrogen purge system (lower right in fig. 6) is a newly conceived system which shows promise of being very effective. The entrance of air and water vapor is prevented by lightly pressurizing the purge space with nitrogen gas. Some of the nitrogen does cryopump to the tank wall, but the innermost layer of fibrous insulation on the tank is densified and has a very small mean pore size. Consequently, the liquefied nitrogen does not flow on the tank walls and continuously release its heat of condensation to the tank wall, but instead is trapped and freezes within the densified insulation. The total amount of nitrogen cryopumping diminishes as an equilibrium preflight condition is attained. Tests to date indicate that only a small weight of nitrogen (about $1/4$ lb/ft²) will be deposited. No attempt is made in this concept to use this deposit for thermal protection; consequently, take-off can commence independent of the time of cryopumping or of the amount of nitrogen deposited.

~~CONFIDENTIAL~~

TOTAL FUSELAGE SYSTEM WEIGHT

The four thermal protection systems just described may be combined with the types of structure discussed earlier to form a total fuselage-tank wall. Four such combinations are shown in figures 7 and 8.

Figure 7 displays two integral liquid hydrogen tank structures. The fuselage wall at the left incorporates the helium transpiration thermal protection system and the stringer structure with external rings. The insulation is protected by heat shields that have omega seals to minimize purge gas leakage.

The fuselage wall on the right incorporates the evacuated multiwall thermal protection system. For this configuration, the structure is provided by the use of two thickened inner sheets separated by dimpled core to stabilize the faces and to provide a sandwich structure which is a convenient extension of the thermal protection system itself. The efficiency of this structure is about the same as that of the honeycomb-core sandwich used as a basis for comparison in figure 4.

Figure 8 shows two nonintegral liquid hydrogen tank structures. The carbon dioxide frost and purge system is incorporated with the corrugated skin structure which is stiffened by external rings. The structure is protected by insulation and a heat shield. A separate insulated tank is shown suspended within the structure, and the carbon dioxide frost is shown deposited in the tank insulation.

The nitrogen purge system is incorporated with the beaded skin structure which is stiffened with internal rings. A separate tank is again suspended within the structure and the space between the unsealed structure and tank is nitrogen purged.

The tank wall systems shown in figures 7 and 8 are typical combinations of structure and thermal protection systems. Each of the four thermal protection systems can be applied, with different load carrying structures, to either an integral or a nonintegral fuselage. For simplicity, only these four combinations are considered.

The weight and performance of these systems has been analyzed by using well established equations from literature (refs. 2, 5, and 6). The calculations of thermal protection system weights take into account the time dependent flow of heat by conduction through insulation layers, and heat absorption by sublimation, by purge gases, and by boiling fuel. Tank and heat-shield weights (where needed) are also accounted for. The basis for these weight analyses for a Mach 8 hypersonic cruise airplane are as follows (the values given represent a selected cruise mission). Primary structure weight is affected principally by the bending load which is due to both applied and thermal loads and which is taken to be 1500 lb/in. Joints, reinforcements around openings, bulkheads, and so forth, are estimated to weigh 0.75 lb/ft². Thermal protection weight for each system depends principally on flight time (1.5 hr) and on aerodynamic surface temperature (1500° F). Tank weight is determined either by bending loads (350 lb/in.) or internal pressure (15 psi). For this analysis, the bending

~~CONFIDENTIAL~~

120

~~CONFIDENTIAL~~

loads are supported without dependence on internal pressure. Tank diameter and length were taken to be 20 feet and 50 feet, respectively. Heat shields must sustain transient pressure loads caused by lags in the system controlling pressure in the purge space. An additional 0.25 lb/ft² is allowed for the omega seals used to limit purge gas leakage.

The results are shown in table I where calculated unit-area weights for both integral and nonintegral tank structures are listed for the various thermal protection systems. Other possible combinations of the thermal protection systems and primary structure concepts that have been studied result in no significant reduction in weight.

TABLE I.- STRUCTURAL WEIGHT COMPARISONS

[Based on cruise airplane mission]

Type of thermal protection system	Weight, lb/ft ²				
	Shield	T.P.S.	Tank	Structure	Total
Integral configuration					
Helium transpiration	1.0	3.9	---	2.0	6.9
Evacuated multiwall	0.3	2.0	---	2.0	4.3
Nonintegral configuration					
CO ₂ frost	1.0	2.5	1.2	1.5	6.2
N ₂ purge	---	2.9	1.5	2.4	6.8

Least total weight is shown for the evacuated multiwall sandwich structure. However, sealing of light gage metals for this structure is beyond the state of the art, and the reliability of maintaining vacuum sealing of light-gage metals for the environment has to be established.

The total weights of the three purge systems are between 6 and 7 lb/ft². All three of these thermal protection system weights include the weight of a purge system that can accommodate an aborted mission. (See ref. 4.) Preliminary tests (ref. 7, for example) show that leakage for the helium purge system may require much helium and unacceptable expense. Earlier helium purging systems would have the same helium requirements as the helium transpiration purge system, but would result in a weight increase from 6.9 to about 10.0 lb/ft². Thus, with helium purging, transpiration and fuel circulation are significantly beneficial.

~~CONFIDENTIAL~~

In the CO₂ frost and purge system, helium used during frost deposition time would be considerably less than with helium purging. However, cost for helium will still be significant. Thus, the remaining system - the nitrogen purge system - has a cost advantage not shown here. In spite of the newness of this concept, its weight is comparable to the helium purge and CO₂ systems. Moreover, further research on this system may lead to a significant weight reduction from that shown here.

CONCLUDING REMARKS

Results of recent analytical studies on primary structure and thermal protection systems for hypersonic airplane fuselages containing hydrogen fuel have been reviewed. Weight-strength comparisons of cylindrical fuselage wall structures under axial compression have identified three new efficient structural concepts. Four thermal protection systems have been described ranging from a sealed vacuum system which requires further fabrication advances to a new nitrogen purge system. Unit-area weights for total fuselage systems combining load-carrying structures, thermal protection system, tank, and heat shield have been tabulated. The nitrogen system, which has potential cost and operational advantages, compares favorably with other currently feasible concepts.

~~CONFIDENTIAL~~

~~CONFIDENTIAL~~

REFERENCES

1. Heldenfels, R. R.: Structural Prospects for Hypersonic Air Vehicles. ICAS Paper No. 66-31, 5th Congress Int. Council Aeron. Sci., Sept. 12-16, 1966.
2. Block, David L.; Card, Michael F.; and Mikulas, Martin M., Jr.: Buckling of Eccentrically Stiffened Orthotropic Cylinders. NASA TN D-2960, 1965.
3. Hirsch, Richard A.: Development of Techniques and Fabrication of a Structural Model for Research of Structures for Hypersonic Aircraft. NASA CR-66211, Martin Marietta Corp., [1966].
4. Jackson, L. R.; and Sharpe, E. L.: A Carbon Dioxide Purge and Thermal Protection System for Liquid Hydrogen Tanks. Conference on Hypersonic Aircraft Technology, NASA SP-148, 1967. (Paper No. 29 herein.)
5. Jackson, L. Robert; Davis, John G., Jr.; and Wichorek, Gregory R.: Structural Concepts for Hydrogen-Fueled Hypersonic Airplanes. NASA TN D-3162, 1966.
6. Jackson, L. R.; and Anderson, M. S.: A Carbon Dioxide Purge and Thermal Protection System for Liquid Hydrogen Tanks of Hypersonic Airplanes. Advances in Cryogenic Engineering, Vol. 12, Plenum Press, Inc., 1967, pp. 146-156.
7. Ryan, J. M., et al.: Lightweight Thermal Protection System Development - Volume I. Composite Design and Test Program. AFML-TR-65-26, Vol. I, U.S. Air Force, Jan. 1965.

LH₂ TANK WALL CONFIGURATIONS

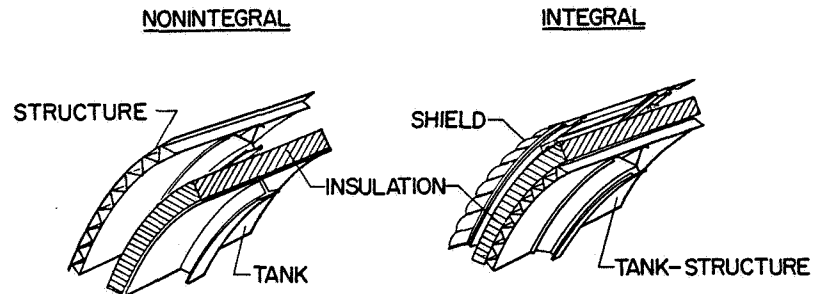
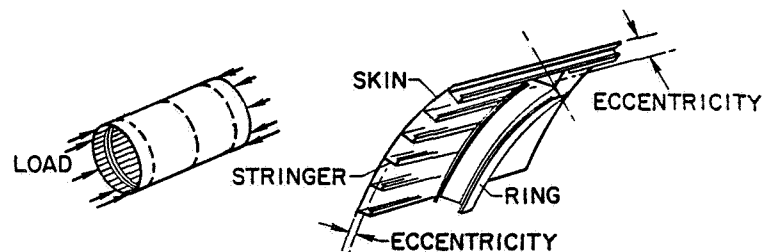


Figure 1

WEIGHT-STRENGTH ANALYSES OF CYLINDERS SUBJECTED TO AXIAL COMPRESSION



CONSIDERATIONS:

- 1-INTERNAL OR EXTERNAL RINGS
- 2-INTERNAL OR EXTERNAL STRINGERS
- 3-ARBITRARY SKIN, STRINGER, AND RING GEOMETRIES
- 4-LOCAL INSTABILITY, PANEL INSTABILITY,
AND GENERAL INSTABILITY

Figure 2

~~CONFIDENTIAL~~

ADVANCED FUSELAGE STRUCTURES

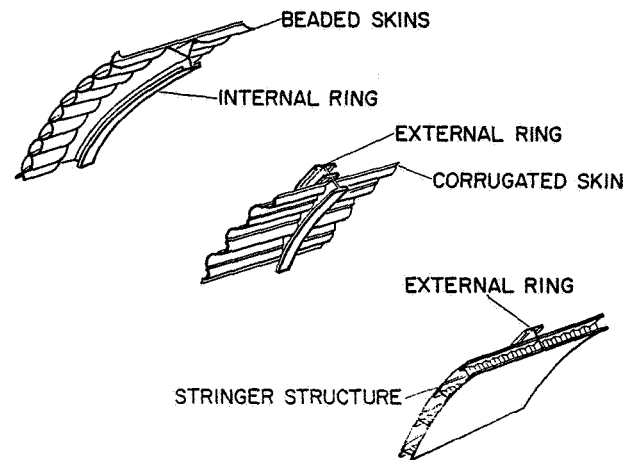


Figure 3

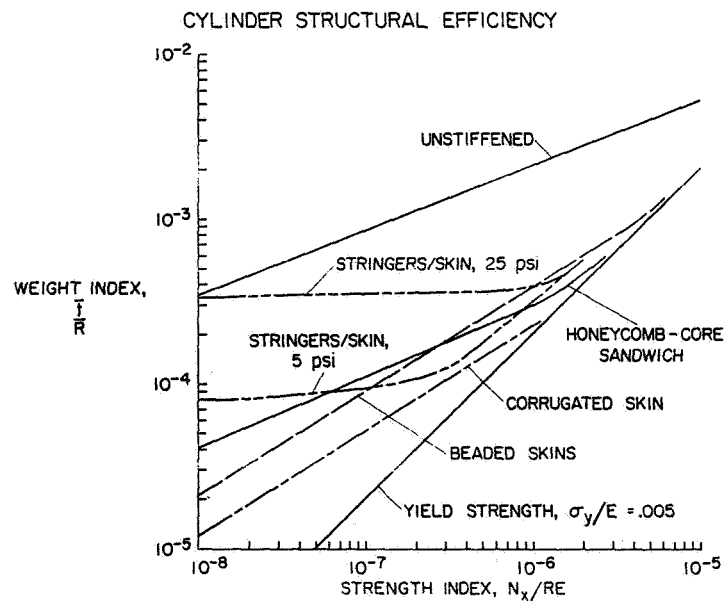


Figure 4

~~CONFIDENTIAL~~

~~CONFIDENTIAL~~

THERMAL PROTECTION SYSTEMS

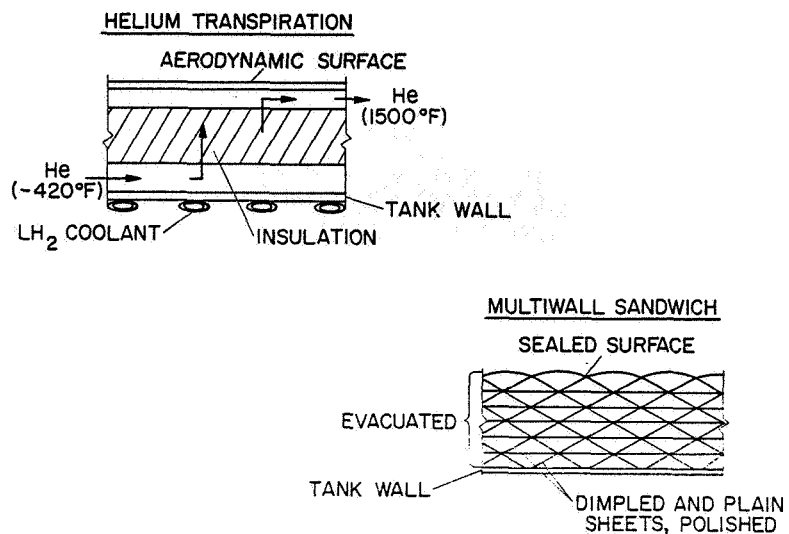


Figure 5

THERMAL PROTECTION SYSTEMS

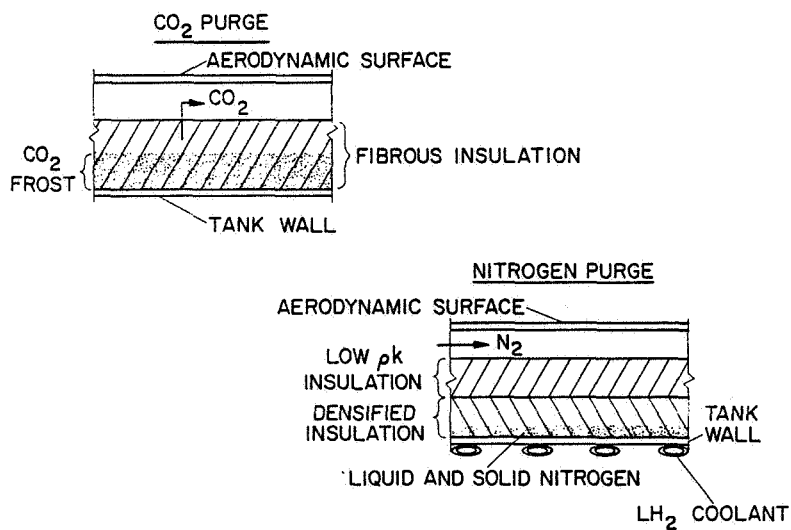


Figure 6

~~CONFIDENTIAL~~

INTEGRAL LH₂ TANK STRUCTURES

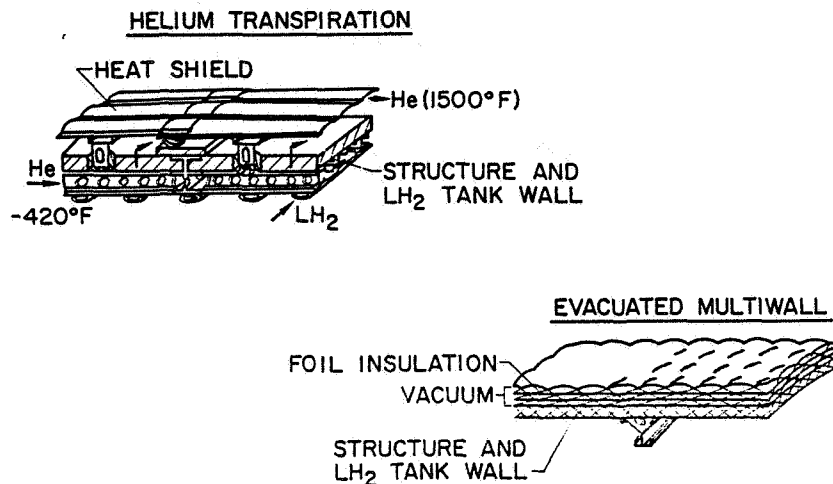


Figure 7

NONINTEGRAL LH₂ TANK STRUCTURES

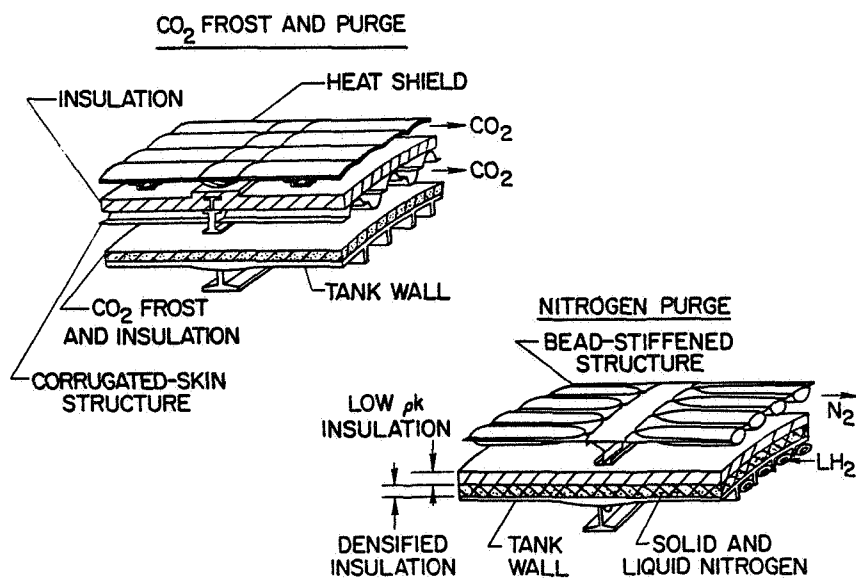


Figure 8

~~CONFIDENTIAL~~

31. ANALYSIS OF WING STRUCTURES FOR HYPERSONIC AIRCRAFT

By Melvin S. Anderson, James C. Robinson,
and George F. Klich
Langley Research Center

SUMMARY

The study considered the effect of air load, temperature distribution, panel concept, and structural arrangement on stresses and deflections. Several wing structural concepts for hypersonic flight were studied for use on the delta-wing X-15. The study indicates that the use of a statically determinate wing-fuselage attachment does not eliminate thermal stress. Spanwise-stiffened wing covers reduce thermal stresses and appear to be an attractive structural concept for delta wings subjected to large temperature differences provided that flutter can be prevented.

INTRODUCTION

A number of wing structural concepts may be found which have the apparent potential to cope with the aerodynamic heating and loading imposed by hypersonic flight. Since economically feasible hypersonic vehicles must have a low structural mass fraction, such concepts incorporate fairly efficient load-carrying structures. They also have provisions to alleviate a large part of the thermal stresses induced by temperature differences throughout the structure. Without relief, these stresses can be a large part of the allowable stress, particularly at the high operating temperature for the cruise vehicle. Proposed concepts, however, must be analyzed in sufficient detail to establish their capability to meet hypersonic-flight requirements.

Several concepts currently being considered for the proposed delta-wing X-15 have been studied in some detail with the aid of a structural analysis computer program. (See refs. 1 and 2.) This paper presents some of these results and a discussion of the performance of some of the concepts.

SYMBOLS

b	panel width
E	Young's modulus
g	acceleration due to gravity
l	wing span (see fig. 9)
N	stress resultant

~~CONFIDENTIAL~~

~~CONFIDENTIAL~~

N_x	chordwise stress resultant
N_y	spanwise stress resultant
T	temperature
ΔT	temperature difference
\bar{t}	equivalent panel thickness
y	spanwise coordinate
z	coordinate normal to wing plane
σ_y	compressive yield stress

DESIGN CONDITIONS

Although the study was specifically for the delta-wing X-15 (hereafter designated Δ X-15), much of the knowledge gained can be applied to the hypersonic cruise vehicle case. The degree to which the wing design of a hypersonic cruise vehicle can be simulated by the Δ X-15 is indicated in figure 1. On the left are indicated possible design conditions for a hypersonic cruise vehicle and on the right are the design conditions for the Δ X-15. Mach number and dynamic pressure can be identical. Design acceleration and "nominal" wing loadings are such as to produce the same maximum air load. The most critical combination of loads and transient temperature differences occurs for both vehicles during a maneuver lasting about 30 seconds or less. Although the Δ X-15 has no time at cruise, only those concepts which could survive in the cruise condition were considered for this study; thus, ablators and heat sinks were not considered. Primary temperature for both is assumed to be limited to the useful value for the superalloys, which is about 1600° F. There will be some areas where the temperature exceeds this value but these areas will have some form of heat protection external to the primary structure.

The Δ X-15 trajectory which produces this environment is indicated in figure 2. Altitude, angle of attack, and velocity are plotted as functions of flight time. Limit loads and heating occur during a $4\frac{1}{2}$ g turn performed at an essentially constant altitude of around 80 000 feet. There is some reduction in velocity from the maximum of Mach 8 as a result of thrust termination which occurs at the initiation of the turn. Such a maneuver also produces the very high local Reynolds numbers which are of interest to the aerodynamicist.

STRUCTURAL CONCEPTS

The Δ X-15 airplane and a possible structural arrangement for the wing are shown in figure 3. The wing consists of surface panels supported by ribs and

~~CONFIDENTIAL~~

spars having corrugated webs. Corrugated webs were chosen for the study because they are structurally efficient, have desirable thermal stress characteristics, and are relatively simple to fabricate. Several alternatives are available, however, for the wing surface panels, and a preliminary screening of these was made with the aid of weight-strength analyses. The panels considered and their relative weights are shown in figures 4 and 5. In figure 4, the values of \bar{t}/b are plotted as a function of structural index N/Eb for square panels of width b subjected to an applied compressive load per unit width N . The equivalent panel thickness \bar{t} is a measure of weight. The structural index is made non-dimensional by dividing by Young's modulus E so that comparisons of different configurations can be made independent of material. The curves are terminated at the yield stress limit which is taken as $\sigma_y/E = 0.005$. This value is typical of superalloy materials in the required temperature range. The dashed portion of the curve for honeycomb represents face yielding which can occur even though the average stress N_x/\bar{t} is below yield, since \bar{t} includes the effective thickness of the nonload-carrying core. The weights of the various configurations referenced to the weight of the honeycomb sandwich are given in figure 5 for a structural index N/Eb of 10^{-6} in order to illustrate the various weight differences. The study considered two types of sandwich panels, a machined panel, and several of sheet-metal construction. The sandwich and the machined waffle grid panel have biaxial load-carrying ability; however, the stiffened sheet-metal panels can carry principal loads in one direction only. The relative weight of the unstiffened skin indicates that significant weight savings result from the use of stiffened panels; however, the differences in weights between various types of stiffened panel construction are much less. These results should be used with caution because relative total wing weights utilizing these same panels with optimum spar and rib spacing will show less of a difference than relative panel weights. However, the trends are generally correct and the numbers do indicate relative merits.

For the present wing study, three different approaches to the design problem were selected by using the panel configurations enclosed by the dashed lines in figure 5. The waffle grid panel is typical of monocoque structure that can carry load in two directions and has a relatively smooth surface. It was selected over the two sandwich panels despite its higher relative weight in order to avoid the more complex fabrication processes of sandwich construction. Moreover, since the waffle has only one skin, it exhibits more favorable radiative heat transfer, and hence less temperature difference, between the upper and lower surfaces as compared with most of the other stiffened panels which have two skins. As a representative of semimonocoque construction having load-carrying ability in one direction only, the beaded skin stiffened by circular-arc corrugations was chosen over the zee- or straight-segment corrugation-stiffened skin because of its structural efficiency. The surfaces of the zee- and corrugation-stiffened skins would probably buckle under thermal stress and thus not remain flat. For such a case it is probably more desirable to provide a controlled regular surface pattern as in the more efficient beaded skin. The single corrugation and tubular panels require the addition of an aerodynamic surface; thus, they have application where external heat shields are required for temperature reasons. The tubular panel was selected for the present study because it offers enough weight-saving potential that it might be considered to compete with these other configurations in all areas even with the addition of

~~CONFIDENTIAL~~

~~CONFIDENTIAL~~

a heat shield. However, for areas of minimum gage construction, the single corrugation would be advantageous.

The application of these panel concepts to wing structure is shown in figure 6. The waffle has a relatively smooth external surface and requires no special orientation. The beaded skin, however, must be aligned with the airstream to minimize the adverse roughness effect on heating and loading. This orientation causes thermal stresses in the chord direction and does not provide load-carrying material for the primary spanwise bending loads. The tubular panel is more favorably oriented, since it is flexible in the chord direction and, as a result, the thermal stresses are reduced. Also it is an efficient structure for carrying spanwise bending loads. Since this configuration has low stiffness in the flow direction, flutter characteristics will have to be examined closely in order to insure adequate flutter margins. The slightly corrugated heat shields are aligned with the airstream presenting a surface very similar to the beaded-skin-panel configuration.

TEMPERATURE DISTRIBUTION

One of the first steps in a detailed analysis of the wing structure is the determination of the temperature distribution throughout the wing. Figure 7 presents typical temperature distributions through the depth of the wing for the critical thermal stress condition and for the three panel concepts of figure 6. For this condition, the lower surface temperature and the temperature difference through the wing approach a maximum simultaneously. Temperatures for various locations through the depth of the wing are plotted on the horizontal scale. The values of ΔT shown are the differences between the average structural panel temperatures of the upper and lower surfaces and are indicative of the relative magnitude of possible thermal stresses due to restraint of chordwise bending. Even though the temperature difference is about the same for the waffle and beaded skins, there is a considerable temperature drop in the beaded-skin panel itself and the surface temperature is almost 100° greater than the surface temperature of the waffle because of the presence of the additional skin.

The presence of the heat shields on the tubular panel significantly reduces the transient structural temperature level; however, the temperature difference and surface temperatures are similar to those of the beaded panel.

Inasmuch as the waffle grid panels and beaded panels have very thin outer skins, they respond rapidly to aerodynamic heating changes and the temperatures indicated are representative of those for the cruise vehicle maneuver. The tubular panel, however, because of the heat shingle will not respond as rapidly and the steady-state temperatures will be higher than those indicated.

The tubular panel has a slight advantage in reduced ΔT . The orientation of this panel, however, effectively eliminates the restraint of the panel to chordwise bending; hence, this temperature difference is not a large factor in establishing the thermal stress level for the wing. For this panel, the chordwise thermal stresses are generated by temperature differences of about 200° F

~~CONFIDENTIAL~~

between the upper and lower rib caps and is not as severe a thermal stress problem.

An indication of the spatial distribution of these maximum primary structure temperatures is shown in figure 8. The shaded areas represent portions of the wing that exceed 1600° F in surface temperature. These areas are considered to be protected with heat shields designed to control the structural temperatures within acceptable values during the design maneuver. Contour lines of constant structural temperatures are shown for the maximum load condition for the upper surface of the wing on the top half of the figure and for the lower surface on the bottom half. The contour lines are panel average structural temperatures, not necessarily surface temperatures. Note that the structural temperatures actually are lower toward the leading edge because of the insulating effect of the heat shield. The results shown are for the waffle or beaded skin; the tubular panel configuration has somewhat lower temperatures.

DEFORMATIONS AND STRESSES

The effects that these temperatures and the associated air loads have on the wing structure are being investigated through the use of a large, finite-element computer program. (See refs. 1 and 2.) The nonlinear thermal gradients in the wing surface and the substantial temperature differences between the two surfaces can produce thermal stresses and deflections. The higher temperature lower surface tends to make the wing bow up as shown by the deflections plotted in figure 9.

The vertical deflection of the wing is plotted as a function of distance along the root chord for various spanwise locations. The solid curves are deflections due to temperature differences and are plotted for the root, one-third, two-thirds, and full-span locations. The total thermal and load deflections for the tip are shown as a dashed curve; note that load deflections are only about one-third of the thermal deflections. In the vicinity of the root, the wing is held relatively flat as it is supported all along its length in this example. This restraint can produce appreciable thermal stress. One proposal to alleviate thermal stress is to provide only two wing-fuselage attachments and let the natural bowing take place. Wing deflections resulting from this support condition are shown in figure 10. There is a significant increase in deflections as would be expected, especially in the forward portion of the wing, and the entire wing is curved rather than just the aft end. The deflection due to load is again about one-third of the thermal deflection. The large thermal deflections indicate the necessity for integration of the structural and aerodynamic design to achieve the desired overall performance.

The effect of changing wing support conditions on the wing-panel stress resultants is shown in figures 11 and 12 where the inplane stress resultants in the lower surface of a monocoque wing are plotted for a section near the root chord. Figure 11 shows the spanwise stress resultant N_y . Tension is positive and each graph shows a curve for air loads and a curve for temperature loading. Figure 12 shows the chordwise stress resultant N_x . For reference it

~~CONFIDENTIAL~~

~~CONFIDENTIAL~~

is noted that a thermal stress resultant of a little over 2000 lb/in. results in an average stress of around 50,000 psi for a minimum gage waffle panel having an equivalent panel thickness \bar{t} of 0.045 inch. From figures 11 and 12 it can be seen that the two-point support results in peak concentrations of load stress which are much higher than those for the fairly smooth results of the full support case. The largest stress resultant by far is the large chordwise thermal stress for the full support case. It should be pointed out that complete freedom of fore-and-aft thermal expansion was permitted; otherwise, the thermal stresses would be much higher. Some alleviation of the thermal stress is obtained by relaxing the support conditions; however, in view of such factors as increased deflection and flexibility, the reduction in thermal loads probably does not warrant the use of a two point support.

Another factor which can affect internal stress distribution, especially that due to temperature differences, is the type of construction used in the wing. Figure 13 presents wing-panel stress resultants for the monocoque or waffle-stiffened construction, the chordwise-stiffened semimonocoque or beaded-panel construction, and the spanwise-stiffened semimonocoque or tubular-panel construction. The upper curves are the chordwise stress resultants N_x , and the lower curves are the spanwise stress resultants N_y . These curves again are for the root chord of the wing. All the curves correspond to a wing fully supported at the root; thus, the waffle panel results are identical to those just shown in figures 11 and 12.

The chordwise thermal stress distribution is similar for the monocoque and chordwise stiffened semimonocoque, the thermal stress resultants being much larger than those due to airloads. However, thermal stress resultants are much smaller for the spanwise-stiffened semimonocoque. Orientation of the weak stiffness in the chord direction greatly reduces the chordwise thermal stress resultant which otherwise would tend to be the predominant one. A comparison of the various forms of construction was obtained by calculating wing weight per unit area for a point toward the aft end of the chord where the stress resultants tend to be the highest. The results of these calculations are shown in figure 14. These weights are based on the stress resultants at a root chord station of 300 inches and are not necessarily representative of the whole wing. The stress resultants do not include the local effects of airload on the panel or thermal gradients within the panel. The weights of ribs, spars, and upper and lower surface panels are included but no provision has been made for production constraints excepting minimum material thickness. All configurations were affected greatly by minimum gage considerations and thus the more lightly loaded areas will not have appreciably lower weights than those shown.

There is not much difference in the weights shown; however, the spanwise-stiffened concept shows a slight advantage even though the weight shown includes the weight of the nonload-carrying shields to provide the aerodynamic surface (approximately 1 lb/ft²). However, the maximum stress level for the spanwise-stiffened concept is only about one-third of that of the other two concepts and the consideration of local stresses should not require a weight increase for this concept. The lower stress level is of prime importance in creep lifetime

~~CONFIDENTIAL~~

which would be severely curtailed in the first two concepts using present-day materials. If a larger wing (such as that for a cruise vehicle where panel stress resultants are larger and require more than minimum gage construction) were being considered, the weight advantage of the spanwise-stiffened concept would probably be greater; therefore, it represents an attractive candidate for a cruise vehicle as well as the Δ X-15.

CONCLUDING REMARKS

In summary, a study including a computer-aided analysis of wing structures for hypersonic flight and, in particular, of the wing of the delta wing X-15 has revealed the following:

First, attempts to eliminate large thermal stresses by supporting the wing at only two points and thus permitting thermal deflections to occur met with only partial success. The thermal stresses were still significant and other disadvantages such as increased flexibility and concentrated loads probably make such an approach undesirable.

Secondly, the results of the structural analysis show that thermal stresses due to temperature differences throughout the wing will have a significant role in design. For concepts which have chordwise panel stiffness, thermal stresses are several times those due to air loads. The spanwise-stiffened semimonocoque greatly reduces thermal stress and appears to be an attractive structural concept for delta wings that have large temperature differences throughout the structure.

REFERENCES

1. Melosh, Robert J.; and Christiansen, Henry N.: Structural Analysis and Matrix Interpretive System (SAMIS) Program: Technical Report. Tech. Mem. No. 33-311 (Contract NAS7-100), Jet Propulsion Lab., California Inst. Technol., Nov. 1, 1966.
2. Melosh, Robert J.; Diether, Philip A.; and Brennan, Mary: Structural Analysis and Matrix Interpretive System (SAMIS) Program Report. Tech. Mem. 33-307, Revision 1 (Contract NAS 7-100), Jet Propulsion Lab., California Inst. Technol., Dec. 15, 1966.

~~CONFIDENTIAL~~

~~CONFIDENTIAL~~

WING STRUCTURE STUDIES DESIGN CONDITIONS



<u>LIMIT CONDITIONS</u>	<u>CRUISE AIRPLANE</u>	<u>DELTA WING X-15</u>
MACH NUMBER	8	8
DYNAMIC PRESSURE, psf	2200	2200
NORMAL ACCELERATION, g	2.0	4.5
WING LOADING, psf	67.5	30
AIR LOAD, psf	135	135
LIMIT-LOAD TIME, sec	30	30
CRUISE TIME, hr	1.5	0
TEMPERATURE, °F	1600	1600

Figure 1

DELTA-WING X-15 DESIGN TRAJECTORY

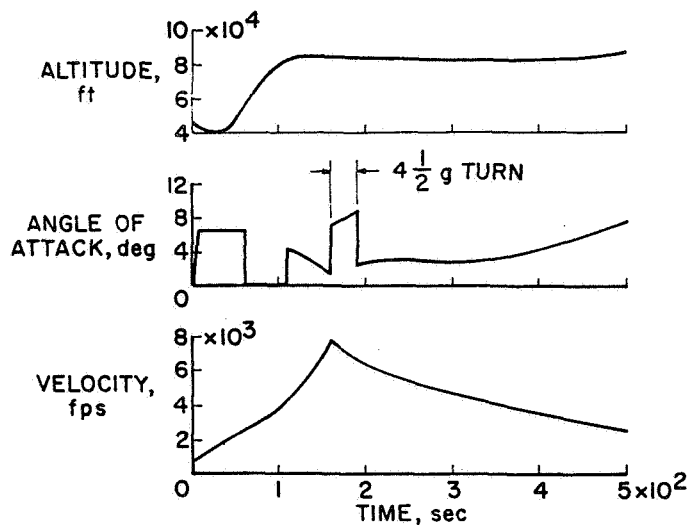


Figure 2

~~CONFIDENTIAL~~

DELTA-WING X-15 RESEARCH AIRPLANE

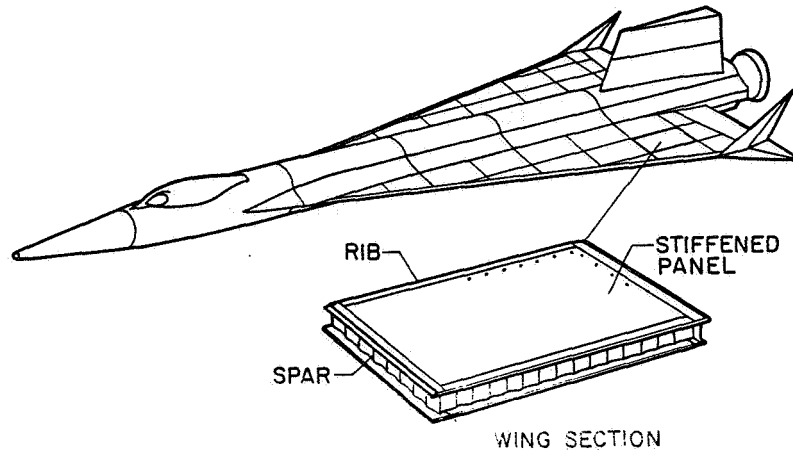


Figure 3

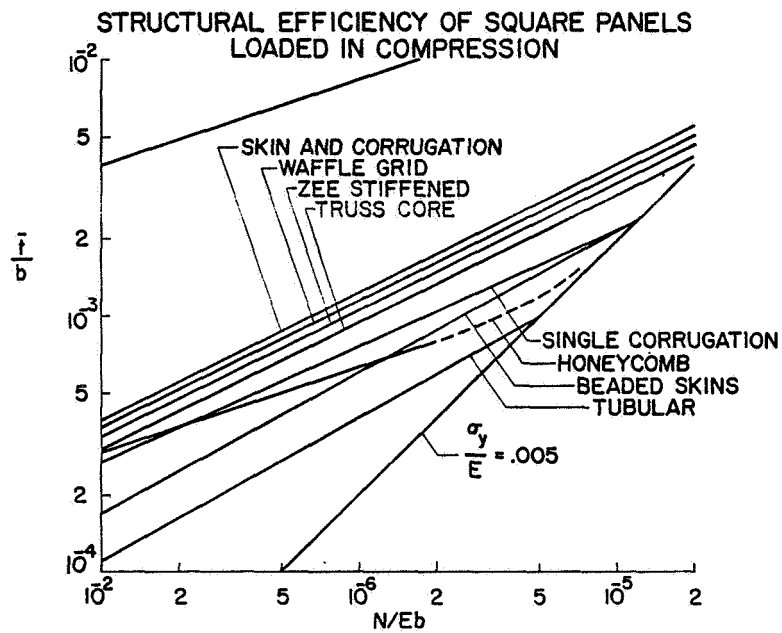


Figure 4

~~CONFIDENTIAL~~

STRUCTURAL-PANEL RELATIVE WEIGHTS SQUARE PANELS AT $N/Eb = 10^{-6}$

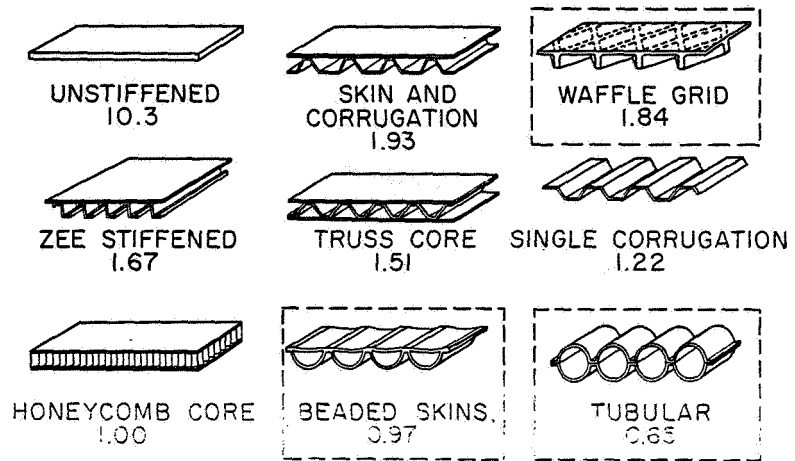


Figure 5

WING STRUCTURES STUDIED

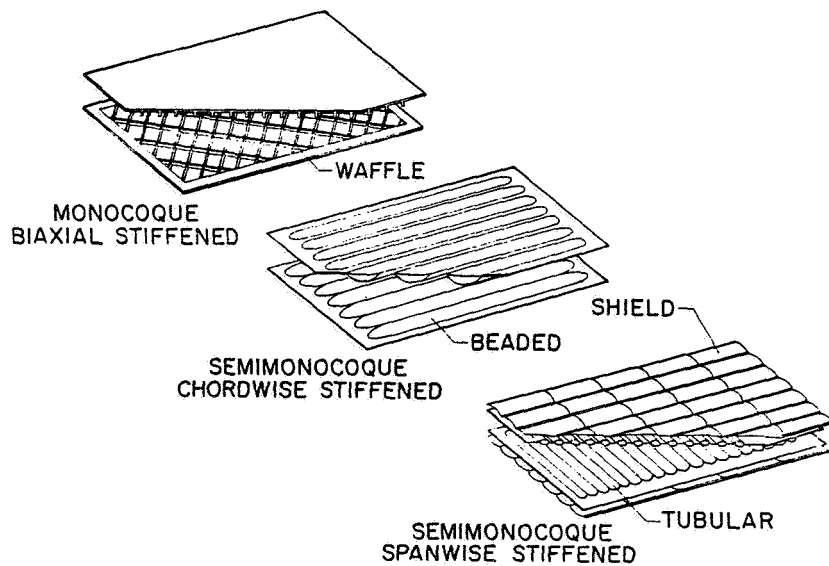


Figure 6

CONFIDENTIAL

TEMPERATURE DISTRIBUTION THROUGH WING MAXIMUM T AND ΔT

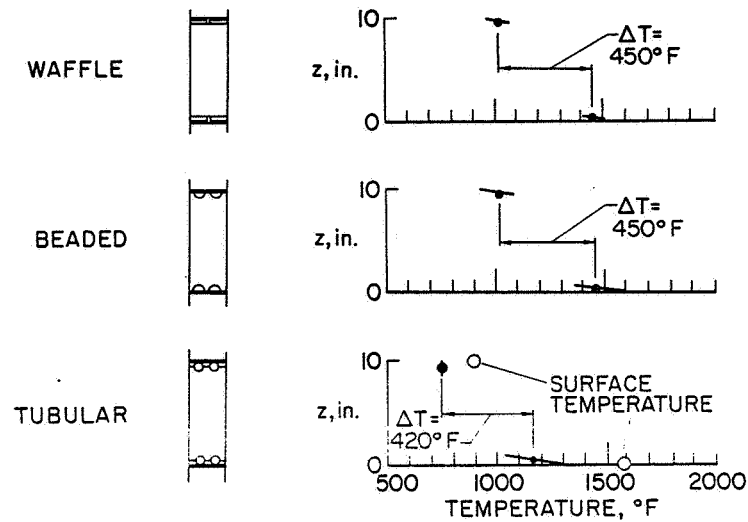


Figure 7

STRUCTURAL-PANEL TEMPERATURES

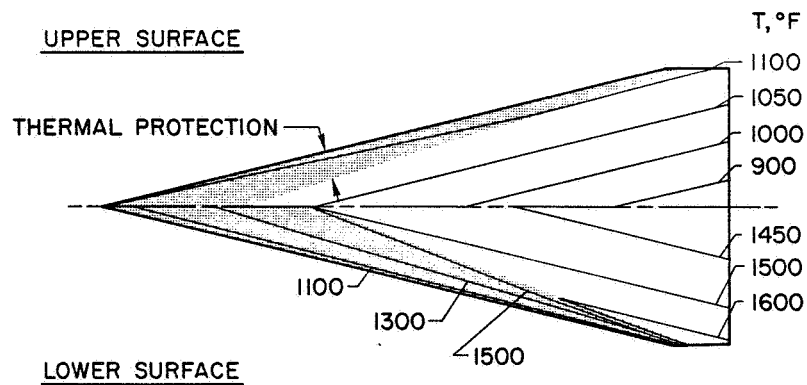


Figure 8

CONFIDENTIAL

~~CONFIDENTIAL~~

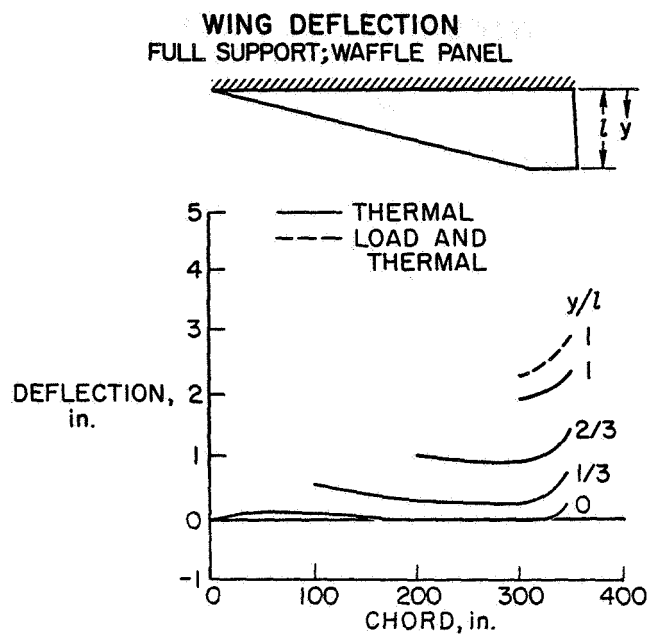


Figure 9

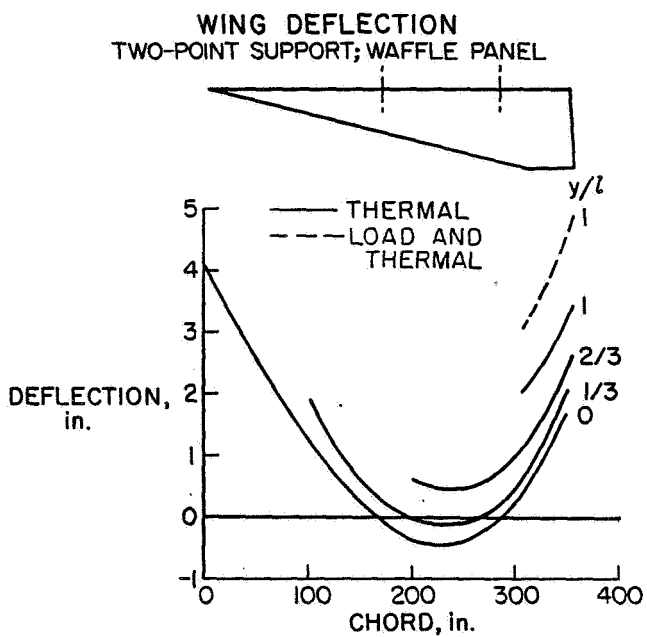


Figure 10

SPANWISE WING PANEL STRESS RESULTANTS WAFFLE PANELS

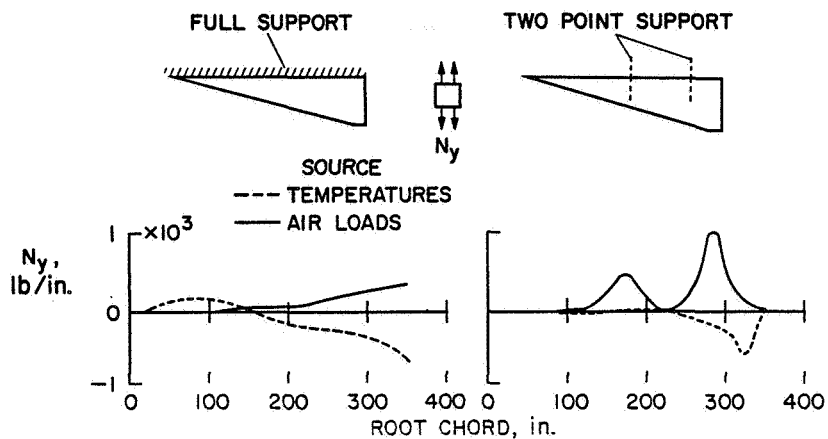


Figure 11

CHORDWISE WING PANEL STRESS RESULTANTS WAFFLE PANELS

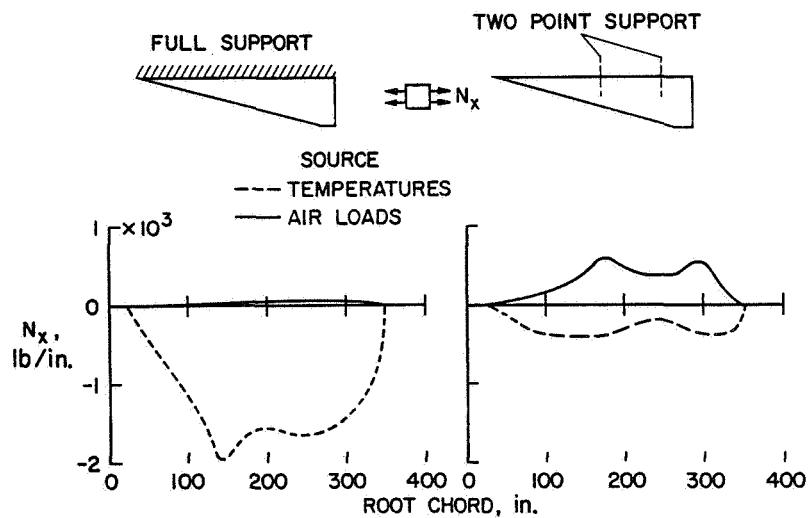


Figure 12

~~CONFIDENTIAL~~

EFFECT OF CONSTRUCTION ON WING PANEL STRESS RESULTANTS

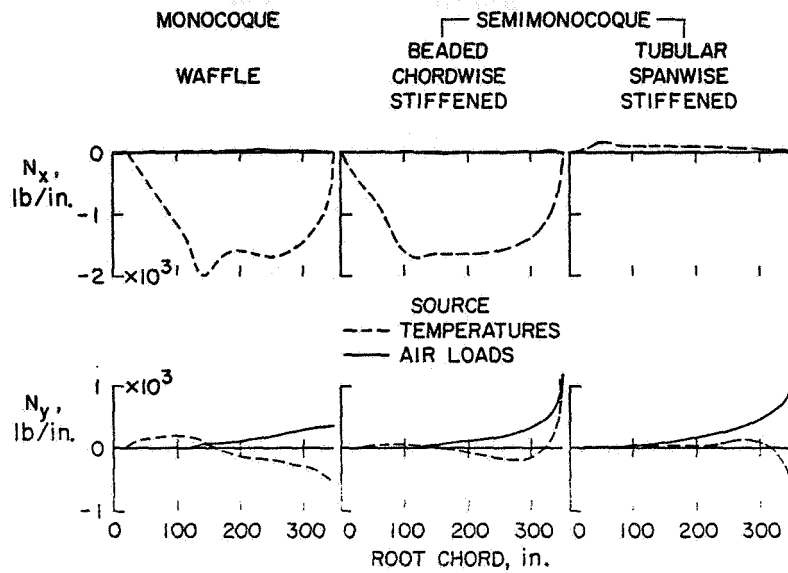


Figure 13

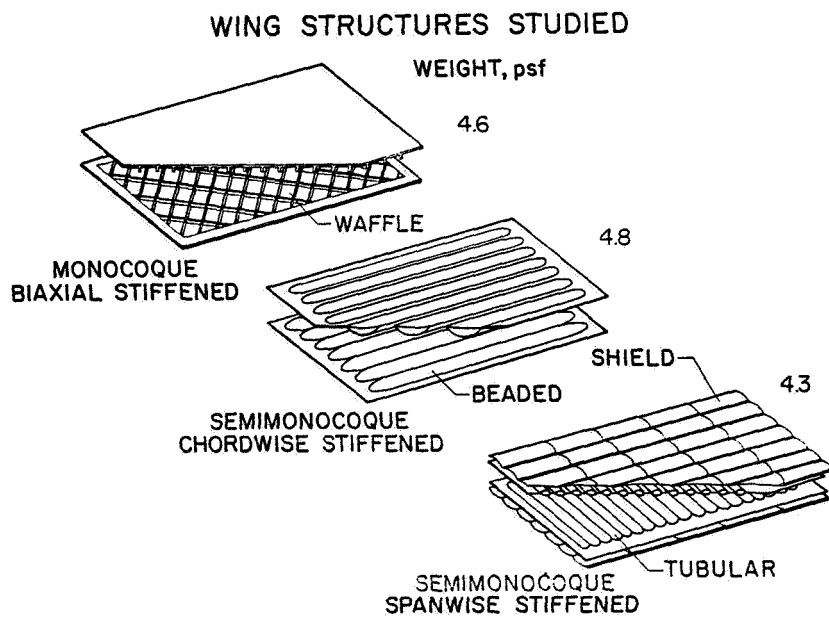


Figure 14

~~CONFIDENTIAL~~

32. REGENERATIVELY COOLED STRUCTURES FOR HYPERSONIC AIRCRAFT

By H. Neale Kelly and John L. Shideler
Langley Research Center

SUMMARY

The results of recently completed analytical studies leading to the design and fabrication of minimum-weight, hydrogen-cooled structures are reviewed. Three basic conceptual designs with varying degrees of integration of the thermal protection and structural functions of the composite structure are examined. Optimized weights for these conceptual designs are presented for wide ranges of heat flux, external pressure loading, and coolant outlet temperature; and the ranges of applicability of the various concepts are delineated. Typical design trade-offs between coolant-flow requirements and configuration weights are indicated for various permutations of one of these basic designs. It is concluded that hydrogen-cooled panels of relatively low weight, which appear practical from an engineering and manufacturing standpoint, can be designed to meet the requirements of hypersonic-cruise aircraft.

INTRODUCTION

It currently appears that major portions of hypersonic-aircraft structure will be radiatively cooled; however, areas exist where radiative cooling is not sufficient and some form of active cooling is required. For the hydrogen-fueled, hypersonic-cruise vehicle, use of the fuel to cool the structure in these areas appears to be the most suitable form of thermal protection.

Under NASA contract NAS1-5002, the AiResearch Manufacturing Company is conducting an analytical and experimental investigation of problems associated with the design and fabrication of hydrogen-cooled structural panels. In the course of the initial analytical studies, procedures for correlating and optimizing the thermal and structural design of such panels have been developed and applied to various conceptual designs. These procedures are based on available experimental heat-transfer data and are tailored to present-day material and fabrication technology. The present paper presents a brief review of some of the results of the initial analytical studies.

SYMBOLS

h_f	fin height, in.
l	flow length, ft
p	external pressure loading, psi

~~CONFIDENTIAL~~

~~CONFIDENTIAL~~

Q heat flux, Btu/sec
 Q/A heat flux per unit surface area, Btu/sec-ft²
 $(Q/A)_{\max}$ maximum heat flux per unit surface area, Btu/sec-ft²
 t_f fin thickness, in.
 $(T_{H_2})_{\text{outlet}}$ temperature of hydrogen coolant at outlet of heat exchanger, °F
 T_r hot-gas recovery temperature, °F
 W weight per unit surface area, lb/ft²
Abbreviation:
 H_2 hydrogen

TYPICAL APPLICATION

Regenerative cooling will probably be used for most of the interior surfaces of hypersonic-aircraft propulsion systems. In a typical propulsion system, such as is depicted in the sketch at the top of figure 1, entering airflow is compressed to high pressures and temperatures, with additional temperature increases occurring in the engine combustor. Pressures as high as 250 psi and heat fluxes on the order of 500 Btu/sec-ft² may be experienced within such propulsion systems.

The interior walls of the propulsion systems will probably consist of a mosaic of hydrogen-cooled panels mounted in such a way as to allow thermal expansion. Functionally, as shown by the sketch at the bottom of figure 1, the panels consist of a thermal protection system and a load-bearing structure. The thermal protection system includes a hydrogen-to-air heat-exchanger surface, a manifold system for distributing the hydrogen to and from the heat exchanger, and possibly (although not shown) a layer of insulation on the surface adjacent to the hot gas. The structure consists of a load-carrying panel supported by a system of beams. (The exterior surface shown in figure 1 is for reference only and is not part of the hydrogen-cooled structure, although in an actual application the heat input from the exterior surface would have to be considered.)

COOLANT-PASSAGE GEOMETRY

A number of coolant-passage geometries were investigated in the course of the study. Sketches of four typical configurations are presented in figure 2. Three of these configurations (the plain-rectangular-fin, rectangular-offset-fin, and pin-fin configurations) may be classed as plate-fin heat exchangers and are fabricated by brazing formed fins between two face sheets. The other

~~CONFIDENTIAL~~

configuration is a tube sheet formed by brazing discrete tubes together. Any of these configurations can be designed to perform satisfactorily as a heat exchanger; however, each has advantages and disadvantages when considered from an overall point of view. For example, coolant-pressure losses are lower for the smooth-passage configurations than for the offset-fin or pin-fin configurations. The latter configurations, however, are capable of maintaining a lower temperature difference across the depth of the passage and of thereby reducing thermal stress and increasing the thermal-fatigue life of the structure. The pin fin, although highly desirable from heat-transfer considerations, is difficult to fabricate. The tube-sheet configuration requires more coolant and is heavier than the plate-fin configurations. The coolant disadvantage is due to the increased surface area exposed to the hot gas; the weight disadvantage arises from minimum-gage restrictions. (For this study, minimum gages were set at 0.010 inch for exposed surfaces and 0.003 inch for interior surfaces. Thus, for the plate-fin configurations, fin thicknesses of 0.003 inch were permissible, whereas a minimum effective fin thickness equal to twice the wall thickness, or 0.020 inch, was required for the tube-sheet heat exchangers.)

As a result of many such considerations the plain fins and the offset fins were chosen for the bulk of the calculations, since they appeared to have the best all-around potential. For designs which required the heat-exchanger panel to support the bending loads due to external pressure loading or which required discrete passageways, the plain fins were used. For designs which required high thermal performance, the offset fins were used.

FIN SELECTION

From a consideration of fabrication limitations and of the heat-transfer and structural properties of the fins, it is possible to define completely the range of fin geometries that will perform acceptably for a given set of operating conditions. Such boundaries for a 2-foot-long panel with 0.003-inch-thick Hasteloy X fins operating at a uniform heat flux of 250 Btu/sec-ft² and a coolant outlet temperature of 1140° F are presented in figure 3.

The right-hand boundary represents the practical limit on the number of fins per inch that can be fabricated for the particular material and material thickness. Past experience indicates that the limiting value of the product of the number of fins per inch and the material gage for superalloys is about 0.12.

The lower boundary is a minimum-fin-height limit which was set to avoid fabrication problems and to avoid the excessively high coolant inlet pressures associated with shorter fins. For this study coolant inlet pressures were not allowed to exceed 1000 psi.

The left-hand boundary is determined from a consideration of the effects of the number of fins per inch and fin height on the coolant inlet pressure and structural capacity of the fins. (Decreasing the number of fins decreases the coolant inlet pressure required to maintain the coolant flow rate, but also decreases the pressure load-carrying capability of the panel. Increasing the

~~CONFIDENTIAL~~

fin height reduces the inlet pressure requirements, but the accompanying increase in metal temperature decreases the strength of the fins.) This boundary represents the point at which the allowable tensile strength of the fins at the maximum temperature for the particular fin geometry and the maximum tensile load due to coolant pressure are equal. It should be noted that this representation is highly conservative since maximum temperature and maximum pressure loading occur at opposite ends of the heat-exchanger panel.

The upper boundary limits the maximum fin temperature. This limit is set in order to avoid excessively high temperatures and temperature differences which would reduce the life of the heat exchanger.

Similar complete boundaries could be constructed for other fin thicknesses and for other operating conditions. The range of usable designs becomes progressively smaller as the heat flux and flow length are increased. At a flow length of 3 feet and a heat flux of 500 Btu/sec-ft², the boundary shrinks to a single point, as indicated by the symbol in figure 3. At higher heat fluxes acceptable designs can be obtained only by reducing the flow length.

It was found necessary to maintain relatively small temperature differences across the depth of the heat-exchanger passages in order to minimize the thermal stress levels. In order to minimize the stresses and to achieve low weight, minimum permissible fin heights were generally used. Minimum fin heights resulted in large coolant-pressure losses and necessitated very high inlet-pressure levels. However, even for minimum-gage configurations, pressure containment was not a problem for the fins or the hot face plate since the fins provided very closely spaced structural support.

The close spacing of the structural support is illustrated by figure 4, which is a photograph of a cutaway sample of a minimum-gage, offset-fin heat exchanger. The heat exchanger has 0.010-inch-thick face plates and 0.003-inch-thick fins. The fins are 0.025 inch high, and there are 20 of them to the inch. (As indicated in figure 3, as many as 40 fins per inch were used for some designs.) The paper clip, which is shown in figure 4 for comparison, was formed from 0.041-inch-diameter wire. The cross-sectional area of the wire is therefore slightly larger than the cross-sectional area of the individual passageways.

Fins, of the geometries considered, have been formed from a variety of materials including the superalloys. At a temperature of 1600° F, burst pressures for small brazed samples fabricated with 0.004-inch-thick Inconel 625 fins were in excess of 2000 psi, the indication being that satisfactory heat-exchanger panels of the design shown in figures 3 and 4 can be fabricated.

COMPOSITE-STRUCTURE DESIGN CONCEPTS

Three basic concepts have evolved from the study of hydrogen-cooled composite structures. These concepts are shown in figure 5.

~~CONFIDENTIAL~~

In the integral concept the webs of the sandwich panel form the passages through which the coolant flows; thus, the sandwich panel serves as both the heat exchanger and the load-carrying panel. Therefore, the panel must withstand both the bending stress due to the external pressure loading and the thermally induced stress. In order to afford the desired load-carrying capability, the temperature differential between the top and bottom plates must be limited to values on the order of 100° , as indicated in the figure.

In the bonded concept the heat-exchanger and structural functions of the composite panel are separated; consequently, the design of the bonded-concept panel is less restrictive. Inasmuch as the heat-exchanger surface is not required to carry any bending load, a larger temperature differential between the top and bottom plates, as shown by the figure, is permissible. The thermal stresses associated with the temperature differences indicated, however, cause plastic strains in the hot face plates. Consequently, thermal fatigue life becomes a critical factor in the design of the bonded-concept panel. For the purposes of this study a minimum acceptable life of 2000 thermal cycles was established. In this concept the bottom plate of the heat exchanger is the top plate of the load-carrying sandwich panel. Therefore, the load-carrying panel operates at a relatively high temperature and must be fabricated of heavy, high-temperature materials.

In the attached concept the heat exchanger and the load-carrying panel are physically separated. As a consequence, advantage can be taken of the higher strength-weight ratios of lower temperature materials. The attached heat-exchanger design features a nonload-bearing, high-temperature heat-exchanger shingle which absorbs the major portion of the thermal load. The shingle is mechanically attached to a low-temperature, load-bearing panel which is protected by a secondary heat exchanger.

PANEL WEIGHTS

The designs of the three basic concepts have been optimized for a wide variety of loading conditions; some of the resulting calculated weights are presented in figure 6. The weight per unit area for each of the concepts is shown as a function of pressure loading for a heat flux of 50 Btu/sec-ft^2 . The data are based on a 2- by 2-foot panel and are for a hydrogen outlet temperature of 1140° F . The weights shown in figure 6 and in subsequent figures include the weight of the heat exchanger, the weight of the structural panel and supporting beams, and allowances for the manifolds, plumbing, and pressure seals between panels. The heat flux and the external pressure loading are assumed to be uniform over the surface of the panel.

It can be seen from figure 6 that the choice of concept for the lightest weight design is dependent upon the particular loading conditions. At the lower pressure loadings, the integral panel design is indicated to be the lightest by a very small margin. At the higher pressure loadings, the optimum panel-web—face-plate material distribution for bending cannot be attained because the fin heights for this concept are limited by heat-transfer considerations. Consequently, the bonded concept, which is not subject to this

~~CONFIDENTIAL~~

restraint, affords the lightest weight over a small intermediate pressure range. As the pressure loading increases, the weight penalty for operating the prime structure of the bonded design at high temperatures becomes more severe. At the highest pressure loadings, this weight penalty more than offsets the weight of the secondary heat exchanger with its additional plumbing, and the attached design becomes the lightest. Although the trends indicated by figure 6 are typical, the regions and magnitude of the superiority of the various designs vary with heat flux and coolant outlet temperature.

INTERRELATED EFFECTS OF HEAT FLUX AND PRESSURE LOADING ON WEIGHT

The interrelated effects of heat flux and external pressure loading on weight are indicated in figure 7. These plots were formed from a series of curves, such as shown in figure 6, for various values of Q/A . The nearly vertical constant-heat-flux lines indicate that the configuration weights are strong functions of the pressure loading, whereas the nearly horizontal constant-pressure-loading lines indicate that the configuration weights are weak functions of heat flux. The sensitivity of the weight to both of these variables varies somewhat from configuration to configuration as indicated by the general slopes of the curves, the integral design being the most sensitive to both variables and the attached design being the least sensitive.

The shaded areas in figure 7 indicate the regions in which a given concept provides the lightest weight design. It can be seen that the region where the integral design is indicated to be lightest is limited to low pressure loadings and low heat fluxes; the bonded design is lightest at moderate pressure loadings over a wide range of heat flux; and the attached design is lightest at the higher pressure loadings regardless of heat flux.

Overall minimum weights for the three configurations range from approximately 2.5 lb/ft^2 to approximately 8 lb/ft^2 at the most severe conditions. The thermal protection system for the bonded design accounts for about 1.5 lb/ft^2 of this weight. For the attached design the thermal protection system weighs approximately 3 lb/ft^2 .

INTERRELATED EFFECTS OF COOLANT OUTLET TEMPERATURE
AND PRESSURE LOADING ON WEIGHT

Plots which illustrate the interrelated effects of coolant outlet temperature and external pressure loading on weight are shown in figure 8 for $Q/A = 10 \text{ Btu/sec-ft}^2$. It can be seen that the integral heat exchanger provides the minimum-weight design at the lower pressure loadings. At pressure loadings between 50 and 100 psi the selection of the minimum-weight design is dependent upon the outlet temperature. The bonded designs are the lightest over a small region at temperatures below about 1280° F , and the attached designs are the lightest at higher temperatures. At the highest pressure loadings, the attached

~~CONFIDENTIAL~~

designs are the lightest regardless of outlet temperature. The insensitivity of the attached designs to outlet temperature might be expected since the heat exchanger and the load-carrying panel are completely separate and the structure, which is the major contributor to the weight, remains at a constant temperature irrespective of the outlet temperature.

The high degree of sensitivity of the bonded design to outlet temperatures compared with the sensitivity of the integral design is due to the higher temperature differentials used for the bonded design. The temperature of the face plate of the bonded design is actually higher than that of the face plate of the integral design operating at the same coolant outlet temperature. Consequently, because of the deterioration of the material properties at the higher temperatures, heavier gage materials are required to contain the coolant and the resulting configuration is heavier.

It should be noted that selection of the proper concept becomes increasingly important at the higher pressure loadings and higher coolant outlet temperatures. At pressure loadings of 250 psi and outlet temperatures of 1440° F, the weight for the bonded design is 12.75 lb/ft² compared with approximately 8 lb/ft² for the attached design. An incorrect choice of concepts would, therefore, result in a weight penalty of almost 60 percent.

DESIGN TRADE-OFFS

The final selection of a cooled-panel concept for an actual application involves trade-offs between panel weight, coolant flow rate, panel life, and other factors which are functions of the specific design mission requirements. The final concept selection is dependent upon the specific details of a particular application and is beyond the scope of the present investigation. However, an attempt has been made to provide some of the tools required to make such selections. In particular, studies have been made which indicate possible trade-offs between configuration weight and coolant requirements. Some typical results of these studies are indicated in figures 9 and 10.

The results shown in figure 9 illustrate the effect of coolant outlet temperature on configuration weight per unit area and coolant flow requirements. These results are for the bonded design with a minimum-fin-height heat exchanger. They are based on a 2- by 2-foot panel operating under an external pressure loading of 100 psi, a maximum heat flux of 250 Btu/sec-ft², and a hot-gas recovery temperature of 4540° F. For the calculations it was assumed that the panel was exposed to a fixed hot-gas environment and that the heat flux varied with the differences between the external-gas recovery temperature and the surface temperature of the heat exchanger. Increasing the coolant outlet temperature from 940° F to 1140° F results in significant savings in coolant with only a small weight penalty. However, as the temperature is increased further, the weight penalty becomes progressively more severe. In addition to the weight penalty, the higher operating temperatures have a detrimental effect on panel life.

~~CONFIDENTIAL~~

~~CONFIDENTIAL~~

Figure 10 illustrates the results of studies of various permutations of the basic bonded design that can be used to effect reductions in coolant requirements. All data indicated by symbols are for a coolant outlet temperature of 1140° F. The results for the basic short-fin configuration are indicated by the symbol on the curve. (The curve for varying outlet temperature has been repeated, for reference, from figure 9.) The results for each permutation should be compared with the results for the basic configuration. By increasing the fin height the temperature of the hot face is increased, with a resulting decrease in coolant requirements for a small weight penalty. However, the panel life is decreased. Flow routing can be used to conserve coolant. One of the best means of flow routing to conserve coolant involves flowing the coolant the length of the panel through one passage and then back through an adjacent passage to the outlet (see folded-flow configuration in fig. 10). Although somewhat complicated manifolding is required, the weight and panel-life penalty associated with this configuration are small. The results for the insulated configuration illustrate the effects of adding insulation to the surface of the heat exchanger next to the hot gases. For this configuration, both the coolant reductions and the weight penalties are relatively large.

CONCLUDING REMARKS

An analytical and experimental investigation of some of the problems associated with the design and fabrication of hydrogen-cooled structural panels is in progress. In the course of the investigation, analytical procedures for analyzing and optimizing the design of such panels have been developed. These procedures have been applied to various conceptual designs, and configuration weights and coolant requirements have been determined. The results indicate that hydrogen-cooled panels of relatively low weight, which appear practical from an engineering and manufacturing standpoint, can be designed to meet the requirements of hypersonic cruise aircraft. Experimental investigations are being continued in an effort to verify the analytical results and confirm the practicality of these designs.

PROPULSION SYSTEM STRUCTURE TWO-DIMENSIONAL AIR INLET

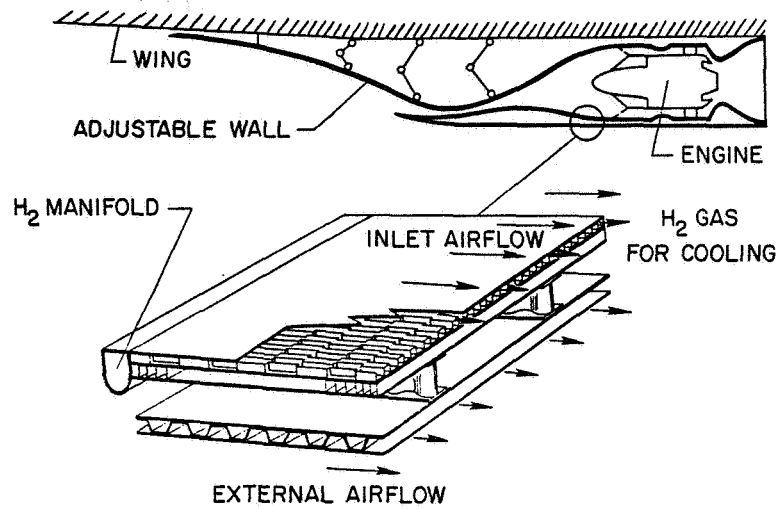
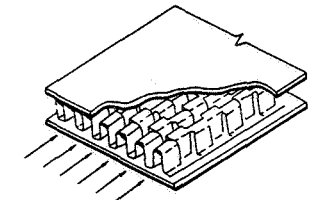
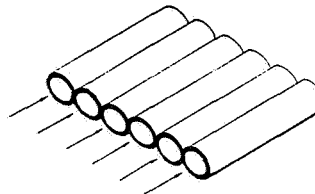
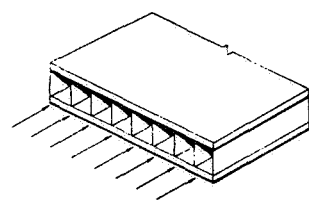


Figure 1

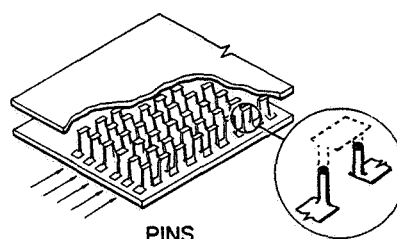
HYDROGEN-PASSAGE GEOMETRY

PLAIN RECTANGULAR FINS

ROUND TUBES



RECTANGULAR OFFSET FINS



PINS

Figure 2

~~CONFIDENTIAL~~

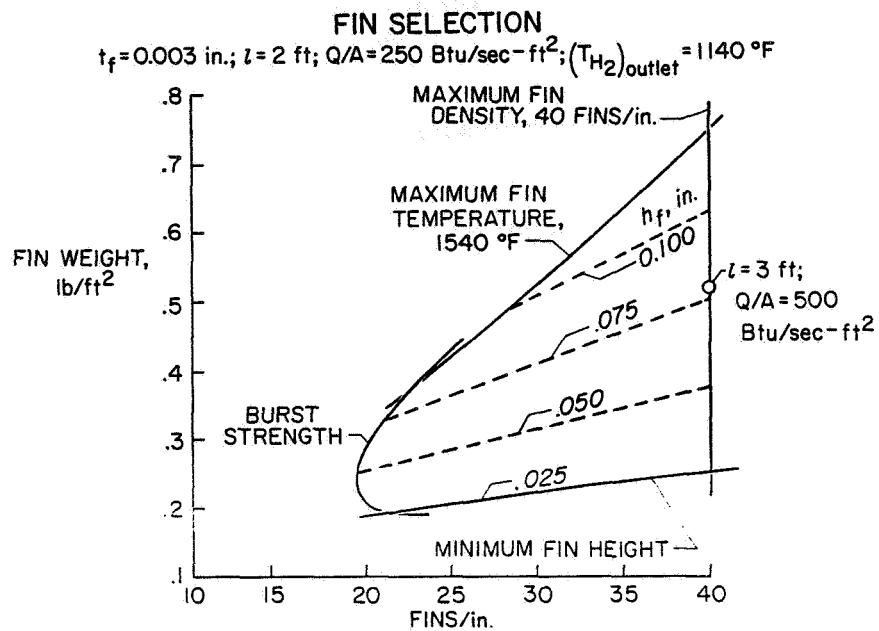
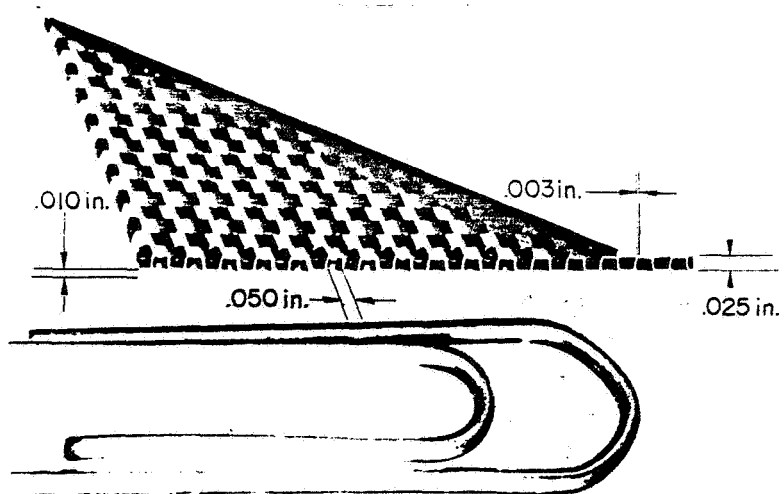


Figure 3

TYPICAL HYDROGEN HEAT EXCHANGER



L-20, 4-4

Figure 4

~~CONFIDENTIAL~~

HYDROGEN-COOLED COMPOSITE-STRUCTURE CONCEPTS

HEAT EXCHANGER

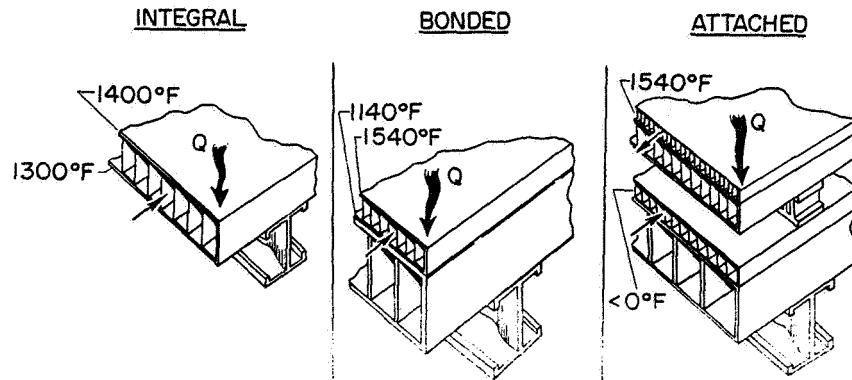


Figure 5

HYDROGEN-COOLED COMPOSITE-STRUCTURE WEIGHTS

2- BY 2-ft PANEL; $Q/A = 50 \text{ Btu/sec-ft}^2$; $(T_{H_2})_{\text{outlet}} = 1140^\circ\text{F}$

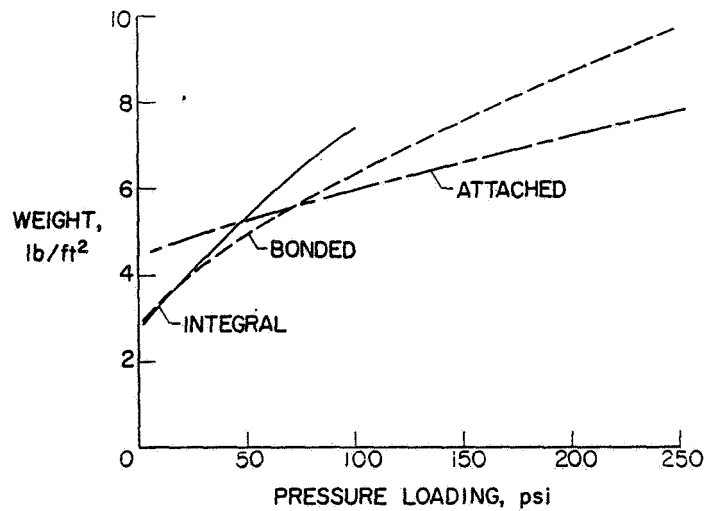


Figure 6

CONFIDENTIAL

HYDROGEN-COOLED COMPOSITE-STRUCTURE WEIGHTS 2-BY 2-ft PANEL; $(T_{H_2})_{outlet} = 1140^\circ F$

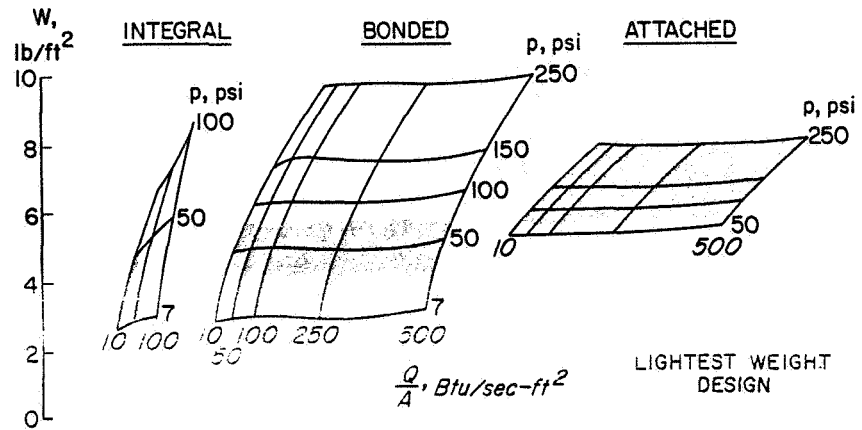


Figure 7

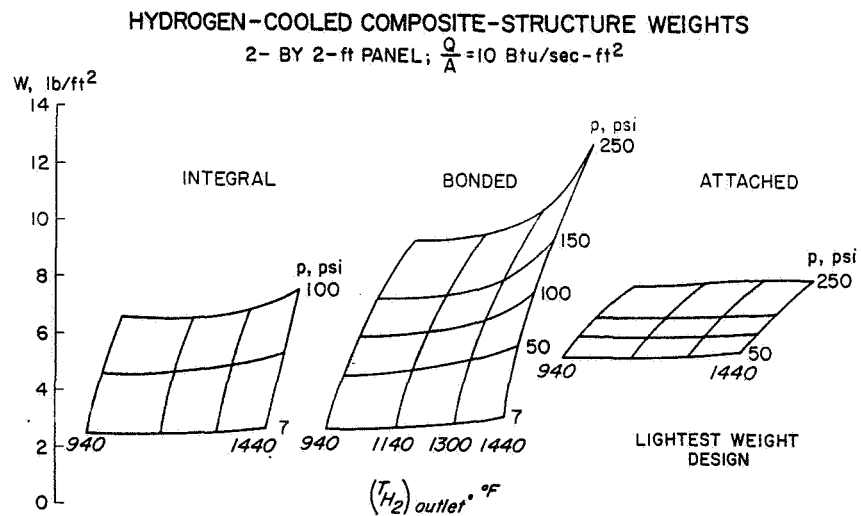


Figure 8

~~CONFIDENTIAL~~

TYPICAL DESIGN TRADE-OFFS
BONDED DESIGN; 2-BY 2-ft PANEL; $p=100\text{ psi}$; $(Q/A)_{\text{max}}=250\text{ Btu/sec-ft}^2$;
 $T_r = 4540^\circ\text{F}$; $h_f = .025\text{ in}$

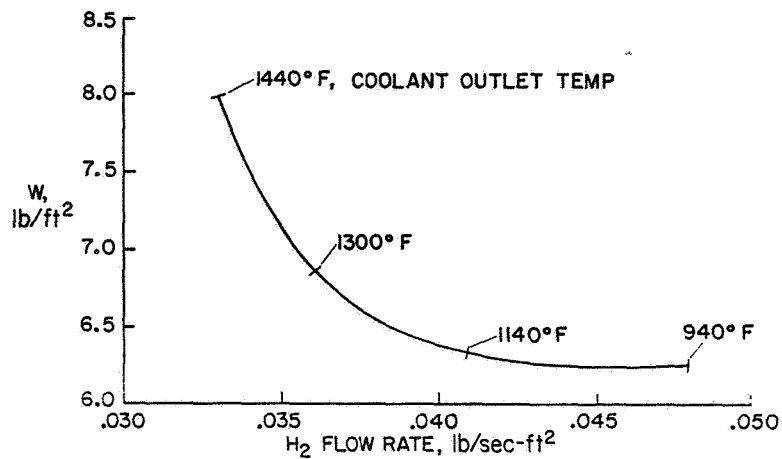


Figure 9

TYPICAL DESIGN TRADE-OFFS
BONDED DESIGN; 2-BY 2-ft PANEL; $p=100\text{ psi}$; $(Q/A)_{\text{max}}=250\text{ Btu/sec-ft}^2$;
 $T_r = 4540^\circ\text{F}$

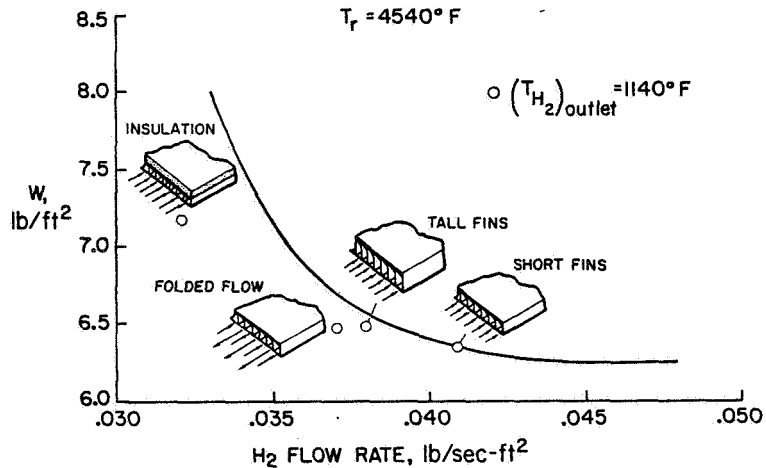


Figure 10

~~CONFIDENTIAL~~

~~CONFIDENTIAL~~

33. DYNAMIC AND AEROELASTIC CONSIDERATIONS OF HYPERSONIC AIRCRAFT

By A. Gerald Rainey and Dennis J. Martin
Langley Research Center

SUMMARY

A review of several dynamic and aeroelastic considerations pertinent to the development of a hypersonic transport has indicated the following preliminary assessments.

Engine noise levels for the hypersonic transport (HST) will be high but probably not as much a problem as indicated by thrust levels alone because of the beneficial effects of low-density exhaust gases. Aerodynamic noise will be similar in intensity and frequency content to boundary-layer noise on previous transports. A recent development of flexible baffles for damping fuel motions may have an application to hydrogen-fueled hypersonic cruise aircraft. No new flutter problems beyond the capabilities of existing flutter technology have been uncovered. Additional information regarding the characteristics of atmospheric turbulence at high altitudes and long wavelengths is needed and careful attention will be required to handle properly the elastic mode contributions to aircraft response to turbulence.

INTRODUCTION

The development of technology for hypersonic cruise aircraft has reached the point where a preliminary assessment of certain dynamic and aeroelastic characteristics of such aircraft might serve a useful function. The purpose of this paper is to review some of these problem areas in relation to the technology requirements for a hypersonic aircraft to point out those areas which will require careful attention in future development work as well as those areas for which current technology appears to be adequate.

There are many dynamic and aeroelastic aspects of importance to hypersonic aircraft; however, this paper will be confined to a discussion of the following:

Engine noise

Boundary-layer noise

Fuel sloshing

Flutter

Gust response

~~CONFIDENTIAL~~

The important related topic of panel flutter is the subject of a separate paper (ref. 1) presented at this conference.

In consideration of these topics a need arose for reference to characteristics of a typical hypersonic transport aircraft. Such properties as engine characteristics and trajectory parameters used in this paper have been taken from the results of the study performed by General Dynamics/Convair for the NASA Mission Analysis Division. (See ref. 2.)

SYMBOLS

AR	aspect ratio
b	semichord
D	width of baffle
E	modulus of elasticity
F	flexibility parameter
f	frequency
M_∞	free-stream Mach number
p	pressure
q	dynamic pressure
R	cylinder radius
T	period of liquid oscillation
t	thickness of baffle
U	velocity of liquid at baffle location
V	velocity
w	vertical velocity fluctuation
μ	mass ratio parameter
ν	Poisson's ratio
ρ	liquid mass density

~~CONFIDENTIAL~~

σ_a	root mean square of vertical acceleration at pilot station
σ_p	root mean square of pressure
σ_u	root mean square of vertical velocity
$\phi_a(f)$	power spectral density of vertical acceleration at pilot station
$\phi_p(f)$	power spectral density of fluctuating pressure
$\phi_w(\Omega)$	power spectral density of vertical velocity
Ω	frequency, ω/V
ω	natural torsional frequency

ENGINE NOISE

One of the most critical problems requiring solution for the continued advancement of aeronautics is the airport community noise problem. It seems appropriate, therefore, to consider at this early date some of the potentialities for engine noise of a typical hypersonic transport. Estimates of the perceived noise level have been made for such a vehicle; these estimates are shown in figure 1 as a function of altitude and are compared with those for a typical subsonic jet transport and a supersonic transport. These estimates were made for engines operating at full thrust by the methods of references 3 and 4. The estimates are applicable to an observer on the ground directly beneath the flight path.

The curve for the hypersonic transport (HST) is shown as dashed to indicate the uncertainty of the estimate since present knowledge concerning the characteristics of engines required for an HST is limited. The interesting result shown in figure 1 is the significantly lower predicted noise level for the HST in relation to the SST. The noise levels for the HST are indicated to be about 3 decibels lower than those of the SST in spite of the fact that the total thrust level for the HST engines is 356 000 pounds as compared with only 232 000 pounds for the SST. This lower noise level is associated with the relatively low density of the exhaust gases for the hydrogen-fueled HST engines.

A curve is shown in figure 1 for the subsonic jet equipped with noise suppressors to indicate the magnitude of noise reduction which is available with present noise suppressor technology. It can be anticipated that continued development of suppressor technology could provide even greater noise reductions by the time period for the advanced aircraft. In addition to the use of suppressors, another effective means of alleviating the annoyance problem is the selection of take-off and climb operating procedures which tend to minimize the problem.

~~CONFIDENTIAL~~

~~CONFIDENTIAL~~

Another aspect of the engine noise problem aside from these considerations of overall noise level is the frequency content of the noise. Predicted spectra of engine noise for the three classes of transports are shown in figure 2. The broad peak in the spectra is seen to shift to lower frequencies for the HST because of the increase in effective diameter of the jet exhaust. Although the overall level is lower, this shift to lower frequencies means that the HST noise might be more effective in producing response in buildings - window rattling, for example.

BOUNDARY-LAYER NOISE

Aerodynamic noise produced by the turbulent boundary layer is of concern in relation to fatigue of skin panels and in relation to passenger comfort. Both of these aspects require a better definition of the structure of the HST than exists at present; however, some estimates can be made of the characteristics of the external boundary-layer noise which serves as the input to both of these problems. Such estimates are shown in figure 3. These results were obtained by use of the methods of references 5 and 6. The overall levels shown on the left of figure 3 in terms of the root-mean-square surface pressure fluctuations indicate that for typical cruise conditions, the HST will have less boundary-layer noise than the SST and only slightly more than the subsonic jet. The relatively low value for the HST is due, primarily, to the decrease in the coefficient of surface pressure fluctuation with increasing Mach number. The cruise dynamic pressure is about the same for the SST and the HST. However, unlike the SST which reaches its maximum dynamic pressure at cruise condition, the HST ascent trajectory produces a maximum dynamic pressure at a Mach number of about 4.5 which is several times higher than that for the typical cruise condition. Although these levels are of relatively short duration, they will exist for several minutes on each flight and will have to be considered.

Estimates of the frequency content of the boundary-layer noise are shown on the right of figure 3 in terms of the power spectral density of surface pressure fluctuations. The curves for the three classes of transports are very similar in shape. Although the boundary-layer thickness is much greater for the HST, which would tend to shift the noise energy to lower frequencies, the counteracting effect of the higher convection velocity of the hypersonic boundary layer tends to keep the spectrum shape unchanged.

FUEL SLOSHING

Although the fuel-weight fraction for a hypersonic transport may not differ greatly from other transports, the use of low-density liquid hydrogen leads to large tanks and the possibility of relatively large fuel motions. Fortunately, fuel-sloshing technology has reached a relatively high level of development because of its importance in the design of launch vehicles which, of course, have a much higher fuel-weight fraction than aircraft. Design procedures and mathematical models for handling fuel sloshing which have been

~~CONFIDENTIAL~~

developed for launch vehicles should be readily adaptable for use in the design of a hypersonic transport when such a vehicle becomes better defined.

A recent development in launch-vehicle fuel-sloshing technology may have an application to the hypersonic transport. It has been found that light-weight flexible baffles are more effective in damping fluid motions in tanks than heavier, rigid baffles (ref. 7). Some results of this work are summarized in figure 4 where the ratio of damping with flexible baffles to damping with rigid baffles is shown as a function of several values of a nondimensional amplitude parameter. The curves indicate that the damping produced by the flexible baffle is always greater than that for the rigid baffle, the amount of increase being a function of the amplitude of the fluid motion and the flexibility of the baffle. It appears that the flexible baffles produce higher damping because they are more effective in producing vorticity in the fluid than the rigid baffle. These results indicate that for a given amount of damping required for a tankage system, flexible baffles would be considerably lighter than rigid baffles.

FLUTTER

Flutter problems on aircraft usually involve specific components of the design such as a control surface; however, occasionally, flutter considerations will dictate structural stiffness requirements for the main lifting surface. The development of hypersonic transport configurations is at too early a stage to assess properly the flutter aspects of its controls. Some observations regarding the state of flutter prediction techniques pertinent to the main lifting surface are in order.

Hypersonic cruise aircraft will require highly swept low-aspect-ratio wings. This requirement leads to configurations which structurally and aerodynamically need to be treated as complete configurations to obtain realistic flutter characteristics. North American Aviation has recently completed a study for the U.S. Air Force Flight Dynamics Laboratory (ref. 8) in which this complete vehicle approach was applied to three configurations somewhat similar to those considered for hypersonic aircraft. This study had the objective of assessing the adequacy of flutter-prediction techniques for configurations of this type in the subsonic speed range. The results of the study are summarized briefly in figure 5 where the measured flutter velocity is plotted as a function of the calculated flutter velocity for the different configurations. The closeness of the points to the line of perfect agreement indicates that the low-aspect-ratio aerodynamic theory used is quite adequate in this subsonic speed range.

Another assessment of aerodynamic theory for use in flutter calculations at hypersonic speeds was presented in reference 9. In this study, structural aspects of the problem were simplified by obtaining flutter of rigid lifting surfaces mounted on springs. The lifting surfaces had delta planforms varying in leading-edge sweepback from 60° to 80° . Some of the results of this study at a Mach number of 7 are shown in figure 6. The measured and calculated

~~CONFIDENTIAL~~

~~CONFIDENTIAL~~

flutter velocity parameters are shown as a function of leading-edge sweepback angle. The flutter velocity parameter, for a given structure, is proportional to equivalent airspeed. The flutter velocity is relatively insensitive to sweepback angle and the piston theory aerodynamics yield calculated flutter velocities in close agreement with measured flutter velocities for these relatively sharp leading-edge airfoils.

Thus, it is seen that two relatively simple aerodynamic theories appear to be adequate for handling the flutter characteristics of lifting surfaces typical of hypersonic transports at the two extremes of operating Mach numbers. These two theories have been used along with the flight profile data of reference 2 to obtain an indication of the main lifting surface flutter trends for an HST which are shown in figure 7. The elongated symbol and the short theory lines in the upper right corner of figure 7 summarize the data of figure 6. Piston theory was used to extend the results down into the supersonic Mach number range and low-aspect-ratio theory was used to obtain a subsonic reference level for a delta wing with a leading-edge sweepback angle of 65° . The two theory lines are connected by a dashed interpolation in the transonic range. The lower solid line represents a typical HST flight envelope taken from the trajectories of reference 2 and adjusted to yield the required 20-percent margin in flutter velocity. These results imply that the hypersonic transport, like many other airplanes, will probably have a minimum flutter margin in the transonic range where flutter theory is not well established. Fortunately, adequate experimental facilities and techniques are available for providing acceptable flutter prevention programs in the transonic region.

GUST RESPONSE

An evaluation of the gust response characteristics of a hypersonic transport would require a level of detailed definition of structural and aerodynamic properties which does not yet exist. However, some observations can be made which point up areas requiring future attention. One of these is the problem of defining the nature of atmospheric turbulence pertinent to HST operations.

Part of this problem is illustrated in figure 8 which shows two properties of atmospheric turbulence (intensity and probability of occurrence) which are needed in performing a "mission profile analysis" of aircraft response to turbulence. (See refs. 10 and 11.) The two properties are shown as functions of altitude and the simple point of the figure is that there are no data for typical HST cruise altitudes. Furthermore, it will be very difficult to obtain data at such high altitudes because of the long flight times required to obtain statistically reliable results.

Another area requiring further definition of properties of atmospheric turbulence is illustrated in figure 9. The normalized power spectral density of vertical velocity fluctuations (the scale of turbulence being taken as 2500 feet for convenience) is shown extrapolated analytically to wavelengths of 100 000 feet. (See refs. 10 and 11.) The validity of this spectrum of turbulence has been established by measurements to wavelengths of only about

~~CONFIDENTIAL~~

5000 feet. The significance of the figure is that both the HST and the SST will have lower limits of response (as determined by the cruise velocity and the frequency of the short-period longitudinal stability mode) well into wavelengths where measurements of turbulence have not been made. Fortunately, programs are underway to obtain turbulence measurements at very long wavelengths at least at modest altitudes.

Although this lack of long, wavelength and high-altitude turbulence information represents a deficiency in hypersonic aircraft technology, the HST will probably encounter most of its significant gust response problems at lower altitudes during climb and descent rather than at cruise conditions. These lower altitude, lower speed conditions will probably lead to response characteristics important to both the structural loads aspects and passenger comfort and crew performance aspects.

On the basis of the assumption that the XB-70 airplane is roughly aerodynamically similar to a hypersonic transport, it might be worthwhile to examine some of the recently measured response characteristics of the XB-70 in comparison with those of a typical subsonic jet transport. Figure 10 shows a comparison of normalized power spectra of vertical acceleration at the pilot station for the XB-70 (unpublished data) and a typical subsonic jet transport (ref. 12). The spectra have been normalized by dividing the power spectral density by the mean-square value such that the area under each curve is equal to 1.0. Thus, comparison of level between the two curves is not particularly meaningful; only the shape or "color."

The striking difference between the two airplanes is the much larger contribution of the two elastic modes for the XB-70 at frequencies of about 4 and 5 cps as compared with the relatively small elastic mode contribution at 4 cps for the subsonic jet. The two modes of large response for the XB-70 correspond to the third and fourth elastic modes whereas the 4-cps mode for the subsonic jet is the fundamental fuselage bending mode.

Moving-base simulator studies reported in reference 12 have indicated that the presence of the relatively small 4-cps motions in simulations of the subsonic jet transport had a large deleterious effect on crew performance. Although simulations of the XB-70 responses have not been made, it is apparent that the relatively large elastic mode response may be responsible for the XB-70 pilots reporting "light to moderate" turbulence whereas chase pilots reported none.

The large elastic mode contribution to response to turbulence shown for the XB-70 is a new feature of aircraft gust response which will require careful attention in the development of both the SST and the HST.

CONCLUDING REMARKS

A review of several dynamic and aeroelastic considerations pertinent to the development of a hypersonic transport has indicated the following preliminary assessments.

~~CONFIDENTIAL~~

~~CONFIDENTIAL~~

Engine noise levels for the HST will be high but probably not as much a problem as indicated by thrust levels alone because of the beneficial effects of low-density exhaust gases. Aerodynamic noise will be similar in intensity and frequency content to boundary-layer noise on previous transports. A recent development of flexible baffles for damping fuel motions may have an application to hydrogen-fueled hypersonic cruise aircraft. No new flutter problems beyond the capabilities of existing flutter technology have been uncovered. Additional information regarding the characteristics of atmospheric turbulence at high altitudes and long wavelengths is needed and careful attention will be required to handle properly the elastic mode contributions to aircraft response to turbulence.

~~CONFIDENTIAL~~

REFERENCES

1. Bohon, Herman L.; Anderson, Melvin S.; and Heard, Walter L., Jr.: Flutter Design of Stiffened-Skin Panels for Hypersonic Aircraft. Conference on Hypersonic Aircraft Technology, NASA SP-148, 1967. (Paper No. 34 herein.)
2. Jarlett, F. E.: Performance Potential of Hydrogen Fueled, Airbreathing Cruise Aircraft. Vols. 1-4, Rept. No. GD/C-DCB66-004/1-4 (Contract NAS 2-3180), Gen. Dyn., Sept. 30, 1966.
3. Anon.: Jet Noise Prediction. AIR 876, Soc. Automotive Engrs., July 10, 1965.
4. Anon.: Definitions and Procedures for Computing the Perceived Noise Level of Aircraft Noise. ARP 865, Soc. Automotive Engrs., Oct. 15, 1964.
5. Houbolt, John C.: On the Estimation of Pressure Fluctuations in Boundary Layers and Wakes. Rept. No. 90, Aeron. Res. Associates of Princeton, Inc., June 1966.
6. Bies, David Alan: A Review of Flight and Wind Tunnel Measurements of Boundary Layer Pressure Fluctuations and Induced Structural Response. NASA CR-626, 1966.
7. Stephens, David G.; and Scholl, Harland F.: Effectiveness of Flexible and Rigid Ring Baffles for Damping Liquid Oscillations in Large-Scale Cylindrical Tanks. NASA TN D-3878, 1967.
8. Hodson, C. H.: Subsonic Flutter Investigations of Aerospace Vehicles With Large Flexible Lifting Fuselages. AFFDL-TR-66-224, U.S. Air Force, 1966.
9. Miller, Robert W.; and Hannah, Margery E.: Flutter Investigation of 60° to 80° Delta-Planform Surfaces at a Mach Number of 7.0. NASA TM X-325, 1960.
10. Hoblit, Frederic M.; Paul, Neil; Shelton, Jerry D.; and Ashford, Francis E.: Development of a Power-Spectral Gust Design Procedure for Civil Aircraft. Tech. Rept. ADS-53, FAA, Jan. 1966.
11. Fuller, J. R.; Richmond, L. D.; Larkins, C. D.; and Russell, S. W.: Contributions to the Development of a Power Spectral Gust Design Procedure for Civil Aircraft. Tech. Rept. ADS-54, FAA, July 1965.
12. Sadoff, Melvin; Bray, Richard S.; and Andrews, William H.: Summary of NASA Research on Jet Transport Control Problems in Severe Turbulence. J. Aircraft, vol. 3, no. 3, May-June 1966, pp. 193-200.

~~CONFIDENTIAL~~

~~CONFIDENTIAL~~

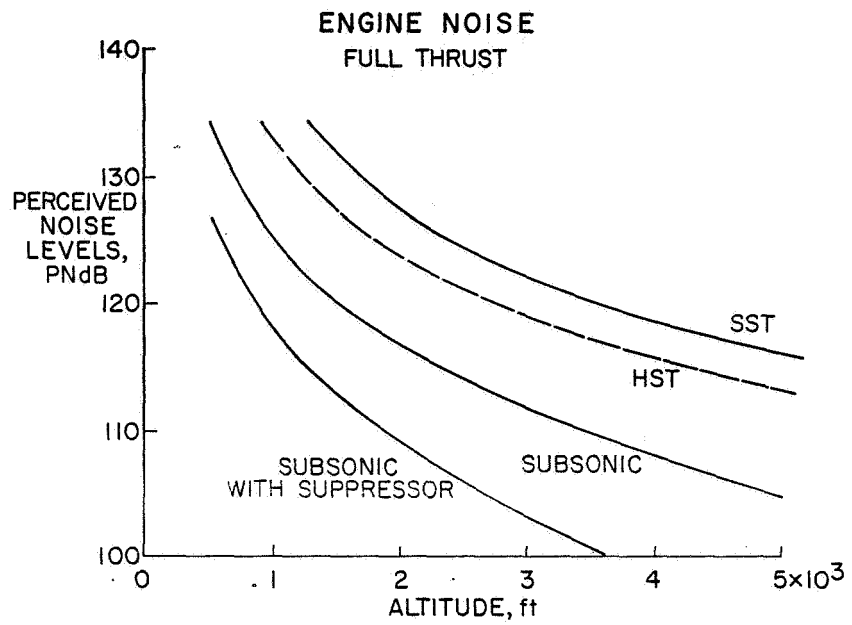


Figure 1

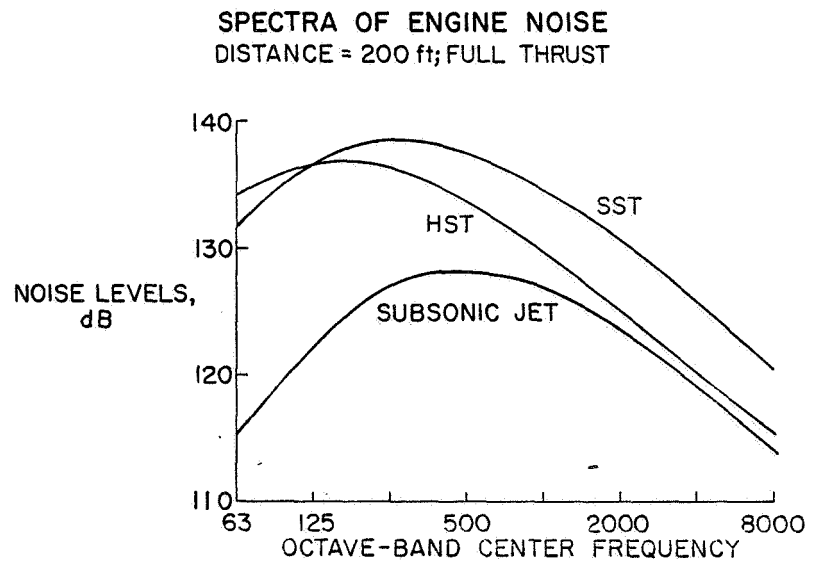


Figure 2

~~CONFIDENTIAL~~

EXTERNAL BOUNDARY-LAYER NOISE

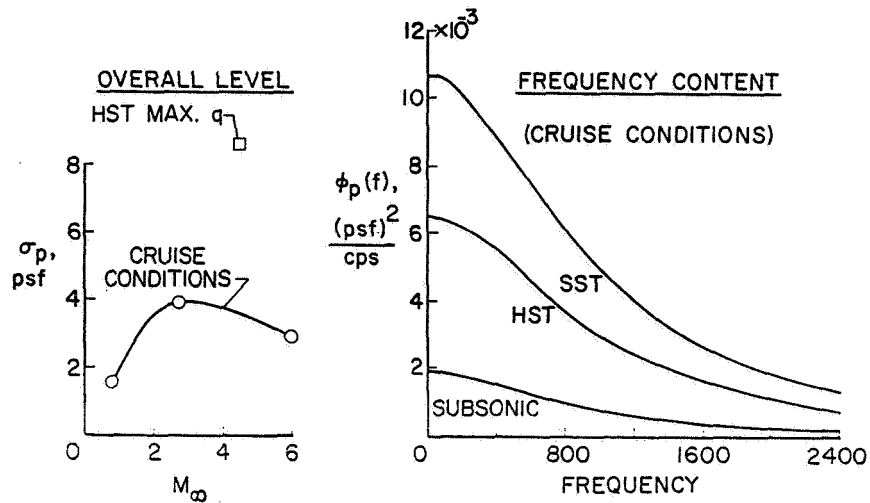


Figure 3

EFFECTS OF FLEXIBILITY ON SLOSH DAMPING OF RING BAFFLES

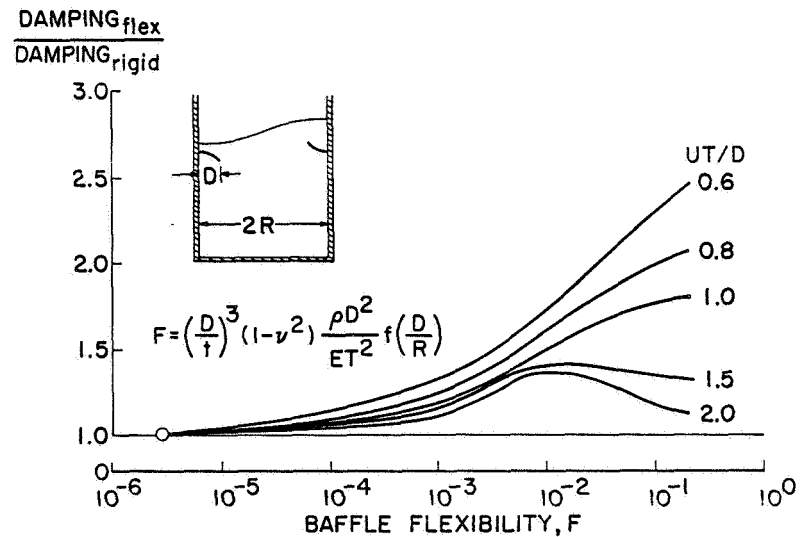


Figure 4

SUBSONIC FLUTTER RESULTS FOR FLEXIBLE WING-BODIES
 $M_\infty \approx 0.2$; HODSON (N.A.A.)

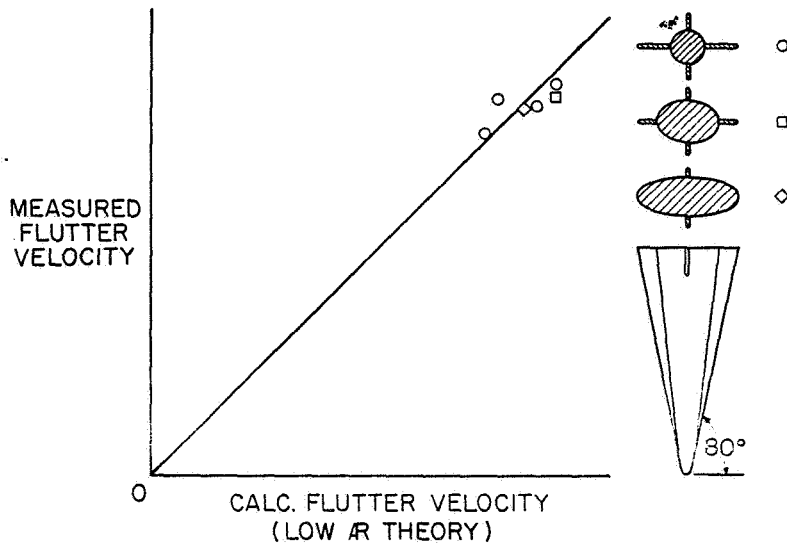


Figure 5

FLUTTER OF SLENDER DELTA WINGS
 $M_\infty = 7$; 5-PERCENT-THICK DOUBLE WEDGE

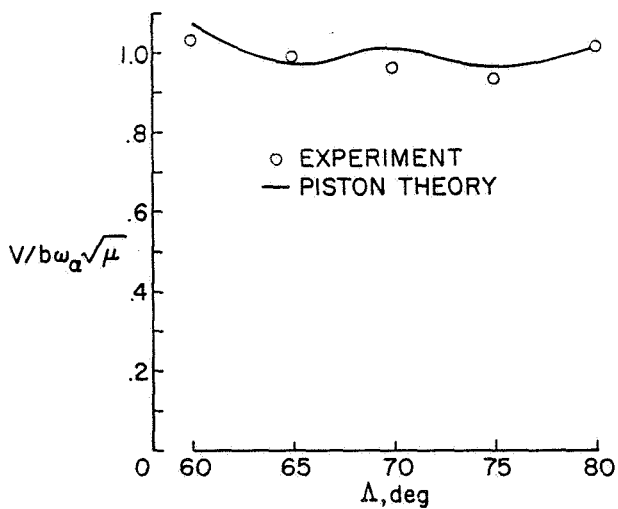


Figure 6

~~CONFIDENTIAL~~

FLUTTER TRENDS WITH MACH NUMBER

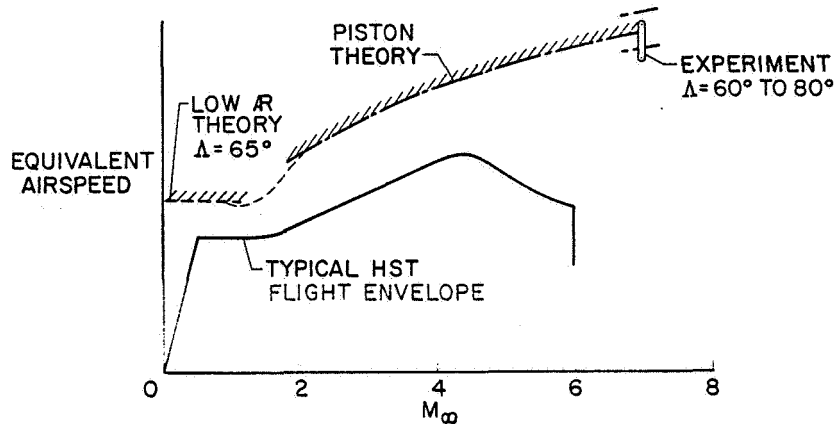


Figure 7

ALTITUDE VARIATIONS OF ATMOSPHERIC TURBULENCE STORM CONDITIONS

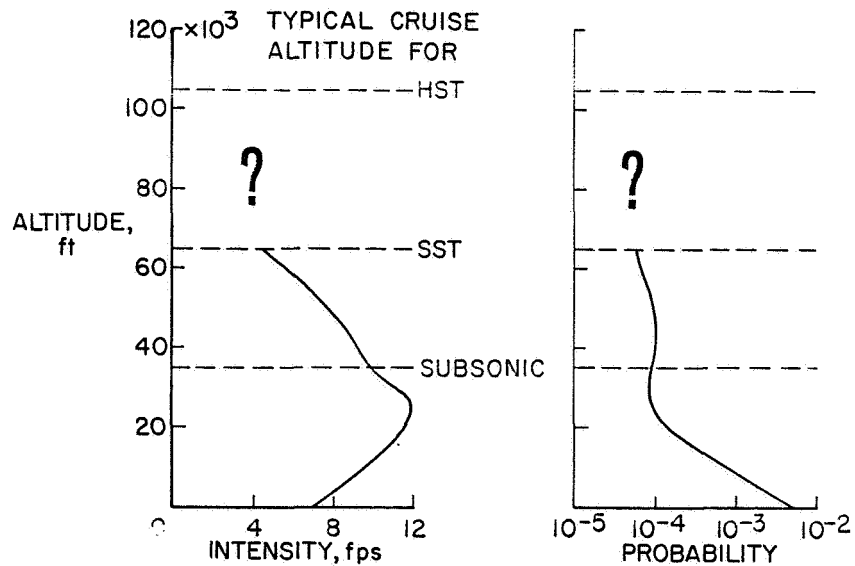


Figure 8

~~CONFIDENTIAL~~

LOWER LIMITS OF LOAD RESPONSE IN RELATION TO SPECTRUM OF ATMOSPHERIC TURBULENCE CRUISE CONDITIONS

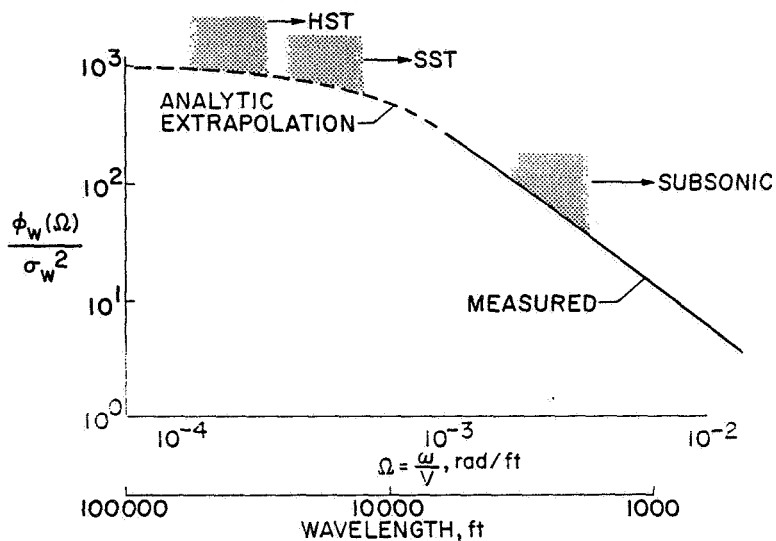


Figure 9

PILOT-STATION VERTICAL-ACCELERATION SPECTRA SHAPES TYPICAL SUBSONIC JET TRANSPORT AND XB-70

$$\int_0^6 \frac{\phi_a(f)}{\sigma_a^2} df = 1.0$$

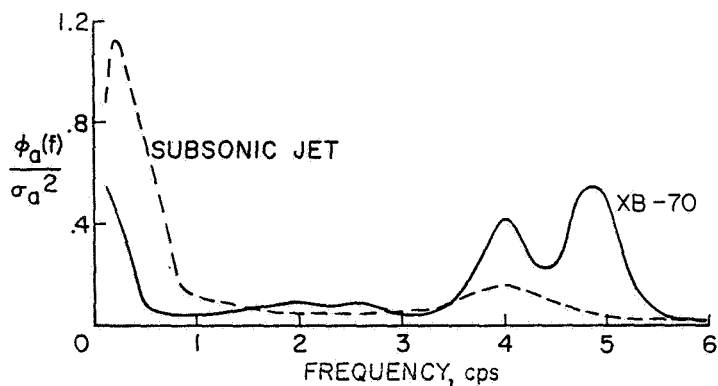


Figure 10

34. FLUTTER DESIGN OF STIFFENED-SKIN PANELS FOR HYPERSONIC AIRCRAFT

By Herman L. Bohon, Melvin S. Anderson,
and Walter L. Heard, Jr.
Langley Research Center

SUMMARY

Experimental and analytical studies have shown that the flutter behavior of panels proposed for hypersonic vehicles is extremely sensitive to support conditions and that support flexibility can seriously reduce the flutter margin. Conservative design curves for such panels have been presented, and means of greatly improving flutter margins by the addition of torsional restraint at the supports are indicated.

INTRODUCTION

Although a wealth of experimental data on the flutter of flat panels has been accumulated over the past few years (see ref. 1), only a small portion of the data was obtained from complex stiffened-skin panels such as are proposed for use on the hypersonic vehicle. Further, only within the past 3 years have flutter data even been generated at Mach numbers higher than Mach 5 (see ref. 2), and nearly all of these data have been obtained from isotropic panels. A notable exception is the orthotropic-panel flutter experiment of Project ASSET, conducted to correlate flight and wind-tunnel flutter data. However, the experimental model was a two-dimensional panel loaded in tension, and the results are not directly applicable to the study of panel flutter on the hypersonic vehicle. Nevertheless, the experimental knowledge accumulated, coupled with numerous explanatory theoretical developments, permit one to make reasonable predictions of the problems associated with the design of exterior panels for hypersonic speeds.

SYMBOLS

\bar{A}_x, \bar{A}_y	stiffness-geometry parameter for airflow in x- and y-direction, respectively
a	length (or width) of panel in x-direction
b	length (or width) of panel in y-direction

$$C = \frac{D_{12}}{\sqrt{D_1 D_2}}$$

D panel bending stiffness

D_1 panel bending stiffness in x-direction

D_2 panel bending stiffness in y-direction

D_{12} panel twisting stiffness

K_D nondimensional deflectional spring constant

K_T nondimensional torsional spring constant

M_l local Mach number

M_∞ free-stream Mach number

q dynamic pressure, psf

x, y coordinates

ω circular frequency

$$\omega_r = \frac{\pi^2}{a^2} \sqrt{\frac{D_1}{\gamma}}$$

α angle of attack

λ_{cr} critical flutter parameter with airflow parallel to corrugations,

$$\frac{2qb^3}{D_2 \sqrt{M_l^2 - 1}}$$

λ_{cr}^* critical flutter parameter with airflow normal to corrugations,

$$\frac{2qb^3}{D_1 \sqrt{M_l^2 - 1}} \left(\frac{D_1}{D_{12}} \right)^{3/2}$$

γ mass per unit area.

PREDICTION OF FLUTTER PROBLEMS

Experimental flutter data generated from flat isotropic panels at high Mach numbers (see ref. 2) have shown no noticeable deviations from trends predicted by using small-deflection plate theory with quasi-static aerodynamics.

~~CONFIDENTIAL~~

This agreement between experiment and theory is illustrated in figure 1, where the parameter $q/D\sqrt{M_\infty^2 - 1}$ is plotted as a function of local Mach number.

The solid line is the flutter boundary, which separates the "flutter" region (above the line) from the "no flutter" region (below the line). This boundary, based on quasi-static aerodynamics, is essentially constant with respect to Mach number; hence, extrapolation into the hypersonic range is relatively simple. The symbols are experimental flutter points from reference 2, obtained from isotropic panels over the range of Mach numbers from 2 to 6. The agreement (considered good for panel flutter) of the experimental data with theory over the entire Mach number range in figure 1 indicates that the flutter boundary may be extended into the hypersonic range with reasonable success. Therefore, a panel on a vehicle traveling over a speed range including hypersonic speeds will be most susceptible to flutter at the maximum encountered value

of $q/\sqrt{M_\infty^2 - 1}$, since for a given configuration the panel bending stiffness D is constant. Thus, trajectories for the hypersonic vehicle need to be examined to determine where the maximum value occurs. Figure 2 shows the variation of the parameter $q/\sqrt{M_\infty^2 - 1}$ with free-stream Mach number for a typical ascent trajectory for a hypersonic cruise vehicle. In the parameter, the dynamic pressure and the Mach number are local conditions. The lower curve represents the local flow conditions over a flat surface at zero angle of attack, whereas the upper curve corresponds to a typical angle of attack of 3° during the early part of the flight and to a typical angle of attack of 5° during the final climb at constant dynamic pressure. The point where a panel is most susceptible to flutter is at the maximum value of $q/\sqrt{M_\infty^2 - 1}$, which occurs on this flight path in the vicinity of Mach 3. Several other advanced vehicle trajectories, examined in reference 3, have led to a similar conclusion - that the low supersonic range is most critical from a flutter standpoint. Thus, panels designed to be free of flutter in the supersonic range, for which a large amount of data is available, will probably have even greater flutter margins in the hypersonic range.

No mention has been made of the transonic range where, as is well known from experimental data, reductions in the critical value of $q/\sqrt{M_\infty^2 - 1}$ occur. (See refs. 4, 5, and 6.) Such losses in flutter margin probably would not be as great as the reduction in $q/\sqrt{M_\infty^2 - 1}$ which occurs in flight in the transonic range (see fig. 2), and in any event the reduced dynamic pressure can be accounted for in the design. Consequently, flutter in the transonic range is not pursued further in this paper.

Most experimental data available on complex panels have been obtained in the supersonic range, and problem areas having special significance with regard to panels proposed for the hypersonic vehicle have come to light. Since existing flutter analyses and experiments are pertinent to the hypersonic range, the effects of these problem areas on panel design are determined.

~~CONFIDENTIAL~~

~~CONFIDENTIAL~~

DESIGN PROBLEMS

Several panel configurations shown and discussed in preceding papers of this conference consist of complex isotropic panels with waffle-grid or honeycomb cores or of corrugation-stiffened panels with either chordwise or spanwise corrugation. One of the primary design problems associated with such panels is the method of attachment of the stiffening structure to the supports. The sensitivity of panel flutter to support conditions is illustrated in figure 3, which shows two typical methods of attaching corrugation-stiffened panels at the ends of the corrugations. The panels were tested at Mach 3 with the corrugations aligned normal to the airflow; thus, the weaker of the panel bending stiffnesses D_1 is in the airflow direction. (Test details are reported in ref. 7.) In one test the corrugations at the edges were attached to an angle clip; the panel fluttered at a dynamic pressure q of 3400 psf. The same panel, when tested with the clip removed (i.e., with the corrugations unsupported), fluttered at a dynamic pressure q of 540 psf. Thus, the flutter margin was reduced by more than a factor of 6 simply by a reduction in the deflectional stiffness of the supports at the ends of the corrugations. In order to determine analytically the flutter mechanism involved in these and other similar tests, the problem has been formulated to account for arbitrary deflectional stiffness at the supports.

Analysis of Panel

An orthotropic panel and the coordinate system are shown in figure 4. The edges at $x = 0$ and $x = a$ are simply supported. The edges at $y = \pm b/2$ are supported by deflectional springs with a spring constant K_D per unit length. These edge conditions may account for flexibility of the supports as well as for local deformations of the cross section at the support. The panel is analyzed for airflow (at Mach number M_1) parallel either to the x -direction or the y -direction; the lateral loading due to the air forces is given by the two-dimensional static approximation. The analytical development is presented in reference 8. Numerical results obtained are applicable to any combination of bending and twisting stiffnesses and panel geometry, but the main part of the discussion applies to orthotropic panels for which D_1 is much less than D_{12} , which is, in turn, less than D_2 .

Spring supports on leading and trailing edges.— When the airflow is parallel to the y -direction, the leading and trailing edges are supported by deflectional springs. Results, obtained from a closed-form solution for zero midplane stress, are shown in figure 5 on a plot of λ_{cr} , the dynamic-pressure parameter at flutter, as a function of $-\bar{A}_y$ for various values of K_D . It should be noted that the panel dimension b is in the airflow direction. Flutter boundaries are shown for finite values of spring constant K_D of 1, 5, and 10. The dashed curve for $K_D = \infty$ is the flutter boundary for the panel with all edges simply supported. Since D_{12}/D_2 is small, for values of b/a

~~CONFIDENTIAL~~

of the order of unity, the region applicable to corrugation-stiffened panels is the left-hand section of the figure. From practical considerations, values of K_D as low as 1 are not unreasonable and the figure shows that support flexibility can reduce the dynamic pressure q by as much as a factor of 10. At low values of $-\bar{A}_y$ the curves become horizontal; hence, the boundaries become independent of the panel width a and of the boundary conditions along the streamwise edges. In fact, the panel behaves as if it were infinitely long in the weak bending direction (i.e., the x -direction).

Spring supports on streamwise edges.— When the airflow is parallel to the x -direction (i.e., normal to the direction of corrugations), the spring supports are at the streamwise edges. A closed-form solution could not be found; instead, a Galerkin solution which used up to 50 natural panel vibration modes to assure convergence was obtained. The analysis is presented in reference 8, and some numerical flutter results are shown in figure 6.

The parameters in figure 6 are slightly modified as a result of the different direction of airflow. The cube root of λ_{cr}^* is plotted as a function of $-\bar{A}_x$ for various values of K_D . However, for this analysis the results are also a function of the parameter C , which is a ratio of panel stiffnesses. A representative value of $C = 7$ was used for these calculations. The curves for finite values of K_D are bounded above by the limiting curve for $K_D = \infty$ (i.e., for simply supported edges), which is obtained from an exact solution, and below by the limiting curve for $K_D = 0$ (i.e., for free edges), which is also obtained from an exact solution. The cusps in the curves are caused by changes in critical modes which coalesce for flutter. The numerals in the regions separated by the dashed curves indicate the modes that coalesce to give the critical flutter boundary.

For corrugation-stiffened panels the ratio D_{12}/D_1 is very large, and therefore the region of primary interest is the far right-hand section of figure 6; the results show that the use of supports which are not infinitely stiff may cause large reductions in λ_{cr}^* . In this region, the flutter boundaries become horizontal and the dynamic pressure q becomes independent of the panel length a ; thus, flutter results are independent of details of the boundary conditions at the leading and trailing edges.

Effect of Orientation of Corrugations

The effect of orientation of the corrugations with respect to the airstream is shown in figure 7 where a direct comparison is made between the modal results and the results from the exact solution. In order to make the comparison, the ratio a/b must be specified; a value of 1 is used. The dashed curves are from the exact analysis made with the corrugations oriented parallel to the airstream; the solid curves are from the modal analysis made with the generators oriented normal to the airstream. As noted previously, the modal results are functions of the stiffness parameter C ; however, for simplicity,

~~CONFIDENTIAL~~

curves are shown only for $C = 7$. For orthotropic panels D_{12}/D_2 is small, and the results show a pronounced adverse effect of weak supports on the streamwise edges, as indicated by the curves for $C = 7$. For example, with $D_{12}/D_2 = 0.02$ and $K_D = 10$, orienting the corrugations in the direction of the airstream provides an increase in λ_{cr} of nearly two orders of magnitude. Whereas the results shown in figure 7 are for spring-supported panels with airflow either parallel to or normal to the corrugations, flutter boundaries for $K_D = \infty$ are presented in reference 9 for arbitrary angles of orientation and for several combinations of panel stiffnesses.

DESIGN BOUNDARIES

As shown in figures 5 and 6, highly orthotropic panels generally fall in the regions where the flutter boundaries become horizontal. These regions may provide good, and often conservative, estimates of the flutter parameter for orthotropic panels and should be very useful as design curves. The plot of minimum values of critical flutter parameter for all values of K_D is shown in figures 8 and 9 where λ_{cr} and λ_{cr}^* , respectively, are plotted as a function of K_D over the range from $K_D = 0$ (free edges) to $K_D = \infty$ (simply supported edges). A family of curves is shown in figure 9 for several values of the stiffness parameter C . These limiting curves show a rapid reduction in λ_{cr}^* for very small reductions in K_D near $K_D = \infty$ and suggest extreme difficulty in fabricating simply supported edges. The application of these curves by the design engineer requires only a knowledge of the panel stiffnesses and geometry and a reliable estimate of the deflectional stiffness at the supports. Good estimates of deflectional stiffness may be obtained experimentally from a thorough vibration survey of the panel.

To date, no experimental flutter data have been obtained on orthotropic panels oriented with the maximum flexural stiffness in the airstream direction to verify or dispute the trends shown in figure 8. On the other hand, all experimental flutter data obtained to date on orthotropic panels have been with the maximum flexural stiffness normal to the airstream, as represented by the theoretical model for the curves in figure 9. A correlation of data from several experimental investigations with the present theory has been made and the results are shown in figure 10. The solid curves are repeated from figure 9 for $C = 7$ and $C = 20$. The experimental data represented by the symbols (taken from refs. 7, 10, and 11) were obtained from corrugation-stiffened panels tested at Mach numbers from 1.2 to 3. The panels have a wide variety of edge-support conditions ranging from very weak supports, with the corrugations unsupported, to the attachment of the corrugations to a rigid substructure. Deflectional stiffnesses at the supports were not measured and were difficult to define. However, an estimate of the stiffness was made in an attempt to account for the flexibility of the corrugations at the supports as well as the flexibility of the attachments.

~~CONFIDENTIAL~~

~~CONFIDENTIAL~~

The diamond symbols in figure 10 are for values of C between 5.5 and 7 and, with the exception of two test points, all lie in the flutter region above the curve for $C = 7$. The square symbols represent panels with intermediate values of C between 9 and 15, and the circular symbols represent panels with high values of C between 19 and 24. All data shown are above the curve for $C = 20$. Although the experimental data appear to verify the theory, the salient fact is that panels tested to date have fluttered at dynamic pressures much less than anticipated and far less than the ultimate value provided by the conditions for all edges simply supported. Also significant is the fact that panel flutter data such as those in figure 10 have resulted in the empirical envelope in reference 12 and other modified envelopes which have become widely used as design curves. As a result, an enormous restriction in critical flutter parameter, of as much as two orders of magnitude, is placed on all panel designs regardless of the method of attachment at the supports.

DESIGN RECOMMENDATIONS

For the purpose of design of stiffened panels for flutter-free operations on the hypersonic vehicle, limiting flutter boundaries have been presented for both chordwise and streamwise orientation of maximum-stiffness corrugations. From each of these conservative boundaries, however, it was noted that initial relaxation at the supports, which provide finite deflectional stiffness, resulted in a rapid reduction in λ_{cr} . It is further believed that some finite deflectional stiffness is inherent in the fabrication of complex stiffened structures and, consequently, some degradation of the flutter boundary must be anticipated.

Recently, a method of support attachment that may provide a sizeable increase in λ_{cr} in the presence of finite deflectional stiffness has become apparent. This method involves the addition of a local torsional stiffness along the boundaries normal to the maximum-stiffness corrugations. For example, a doubler strap along the ends of corrugations provides considerable torsional stiffness at the boundary. In a modal analysis included in a recent investigation of corrugation-stiffened panels at Mach 3 (the results of which are unpublished), this effect has been accounted for by the inclusion of a torsional spring in the boundary conditions. A sample calculation is shown in figure 11 where λ_{cr}^* is plotted as a function of K_T/K_D for $K_D = 10$. For this calculation $a/b = 1$, $C = 7$, and $-\bar{A}_x = 100$; the results plotted are well converged. For $K_T = 0$ the value of λ_{cr}^* represents the value for a deflectional spring constant K_D only. As the ratio of K_T/K_D increases, λ_{cr}^* is seen to increase and the curve for $K_D = 10$ eventually becomes asymptotic to the dashed curve, which is the exact solution for $K_D = \infty$ (i.e., for all edges simply supported) and for $-\bar{A}_x = 100$. Thus, even though $K_D = 10$, the panel flutters as if its edges were simply supported.

~~CONFIDENTIAL~~

The existence of the effect of K_T on flutter has been verified to a degree by experimental data obtained in the recent investigation of corrugation-stiffened panels at Mach 3. The panels were attached at the ends of each of the corrugations to carefully machined cantilevered beams in order to provide for easy calculation of K_D . The panels were constructed with corrugated doublers welded to the panel corrugations at the edges. These doublers provided an unknown value of torsional spring constant K_T . The doubler thickness was only three times the thickness of the corrugated material. The numerical value of K_T was obtained from measured natural frequencies shown in figure 12. The circular symbols are the measured frequencies corresponding to one half-wave in the direction of the corrugations and to the first seven half-waves in the weak bending direction. The dashed curve gives the theoretical frequencies for the calculated value of K_D of 0.64 and zero torsional stiffness. The solid curve yields theoretical frequencies for the same value of K_D , but for the ratio $K_T/K_D = 1.25$, and provides a realistic prediction of the measured frequencies, as can be seen from the figure.

The panel with torsionally stiffened edges was tested at Mach 3, and the flutter point obtained is compared in figure 13 with the experimental data from figure 10. The experimental value of λ_{cr}^* for the torsionally stiffened panel is shown by the solid (diamond) symbol at $K_D = 0.64$. The theoretical prediction of λ_{cr}^* for $K_T/K_D = 1.25$, shown by the solid bar, is within a factor of 2. In the absence of a doubler strap along the corrugated edges (i.e., for $K_T = 0$) the panel would probably flutter at a value of λ_{cr}^* slightly above the theoretical curve for $C = 7$ and at $K_D = 0.64$. Thus, the inclusion of the simple doubler may have increased λ_{cr}^* by as much as a factor of 30. Only a factor of 3 exists between the value of λ_{cr}^* at the test point and the maximum value attainable, which is dictated by the boundary for all edges simply supported. Thus, it is concluded that a simple doubler strap at the supports, or other methods of attachment which provide local torsional rigidity for the stiffening elements, may result in large increases in flutter margin and improved efficiency in panel design.

CONCLUDING REMARKS

Existing flutter analyses and experimental data obtained in the supersonic Mach number range can be applied to the hypersonic speed range with little error. Further, the most critical portion of the hypersonic-vehicle flight trajectory from a flutter standpoint may be in the supersonic speed range. Experimental and analytical studies have shown that the flutter behavior of panels proposed for hypersonic vehicles is extremely sensitive to support conditions and that support flexibility can seriously reduce the flutter margin. Conservative design curves for such panels have been presented, and means of

~~CONFIDENTIAL~~

greatly improving flutter margins by the addition of torsional restraint at the supports are indicated.

REFERENCES

1. Johns, D. J.: A Survey on Panel Flutter. Presented to the Structures and Materials Panel of AGARD (Nancy, France), Nov. 1965.
2. Ketter, D. J.; and Voss, H. M.: Panel Flutter Analyses and Experiments in the Mach Number Range of 5.0 to 10.0. FDL-TDR-64-6, U.S. Air Force, Mar. 1964.
3. Langley, Bobby L.: A Study of Panel Thickness Required To Prevent Flutter in Advanced Performance Vehicles. 11th Annual Air Force Science and Engineering Symposium, U.S. Air Force, Oct. 1964.
4. Dixon, Sidney C.: Comparison of Panel Flutter Results From Approximate Aerodynamic Theory With Results From Exact Inviscid Theory and Experiment. NASA TN D-3649, 1966.
5. Cunningham, H. J.: Flutter Analysis of Flat Rectangular Panels Based on Three-Dimensional Supersonic Potential Flow. AIAA J., vol. 1, no. 8, Aug. 1963, pp. 1795-1801.
6. Dowell, E. H.; and Voss, H. M.: Experimental and Theoretical Panel Flutter Studies in the Mach Number Range 1.0 to 5.0. ASD-TDR-63-449, U.S. Air Force, Dec. 1963.
7. Weidman, Deene J.: Experimental Flutter Results for Corrugation-Stiffened and Unstiffened Panels. NASA TN D-3301, 1966.
8. Bohon, Herman L.; and Anderson, Melvin S.: Role of Boundary Conditions on Flutter of Orthotropic Panels. AIAA J., vol. 4, no. 7, July 1966, pp. 1241-1248.
9. Gaspers, Peter A., Jr.; and Redd, Bass: A Theoretical Analysis of the Flutter of Orthotropic Panels Exposed to a High Supersonic Stream of Arbitrary Direction. NASA TN D-3551, 1966.
10. Bohon, Herman L.: Experimental Flutter Results for Corrugation-Stiffened Panels at a Mach Number of 3. NASA TN D-2293, 1964.
11. Pride, Richard A.; Royster, Dick M.; and Helms, Bobbie F.: Design, Tests, and Analysis of a Hot Structure for Lifting Reentry Vehicles. NASA TN D-2186, 1964.
12. Kordes, Eldon E.; Tuovila, Weimer J.; and Guy, Lawrence D.: Flutter Research on Skin Panels. NASA TN D-451, 1960.

~~CONFIDENTIAL~~

EFFECT OF MACH NUMBER ON FLUTTER BOUNDARY

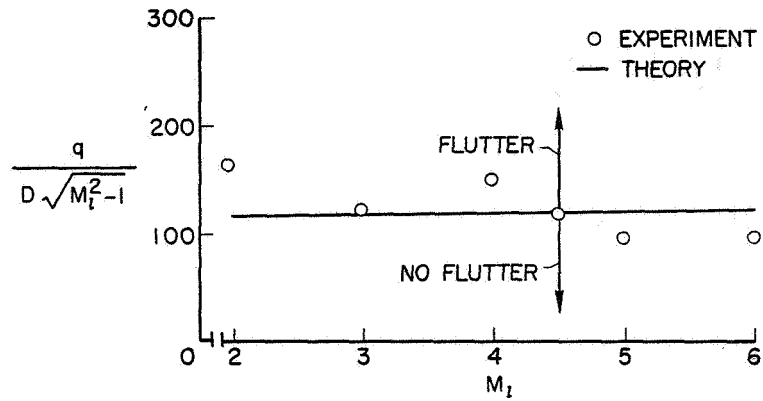


Figure 1

FLUTTER PARAMETER ON ASCENT TRAJECTORY MACH 8 CRUISE VEHICLE

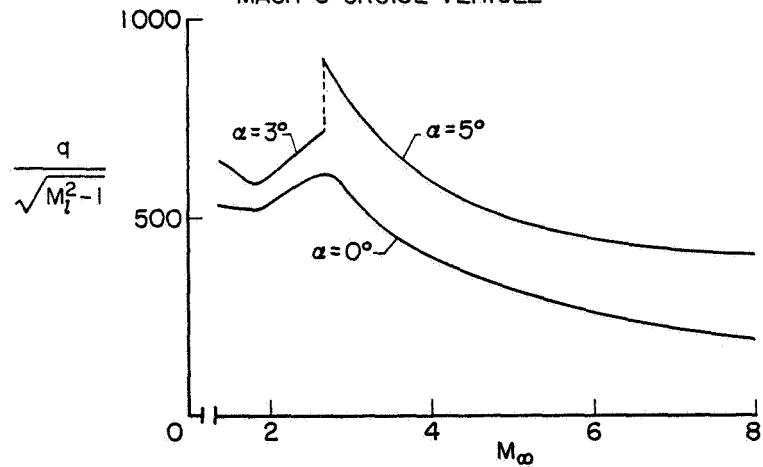


Figure 2

~~CONFIDENTIAL~~

EDGE-SUPPORT EFFECTS ON PANEL FLUTTER $M_1 = 3$

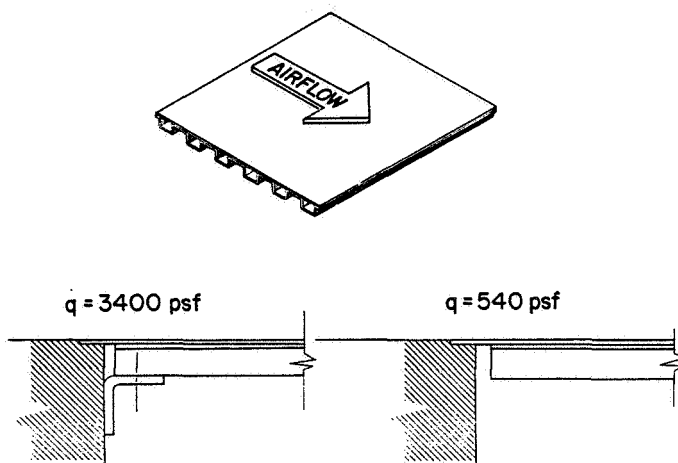
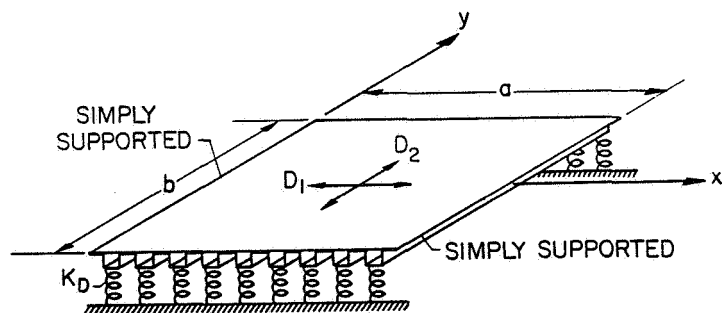


Figure 3

ORTHOTROPIC PANEL AND COORDINATE SYSTEM



D_1 = BENDING STIFFNESS IN x -DIRECTION
 D_2 = BENDING STIFFNESS IN y -DIRECTION
 D_{12} = TWISTING STIFFNESS
 $D_1 \ll D_{12} < D_2$

Figure 4

~~CONFIDENTIAL~~

~~CONFIDENTIAL~~

FLUTTER BOUNDARY FOR FLEXIBLE SUPPORTS FLOW IN STRONG DIRECTION

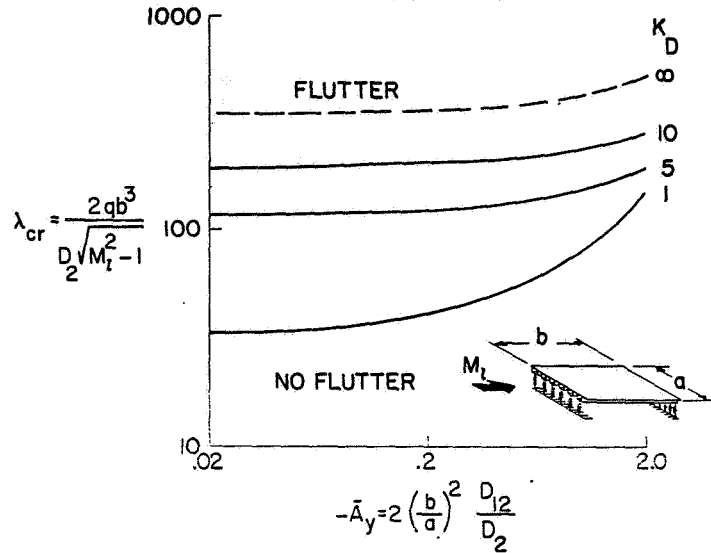


Figure 5

FLUTTER BOUNDARY FOR FLEXIBLE SUPPORTS FLOW IN WEAK DIRECTION

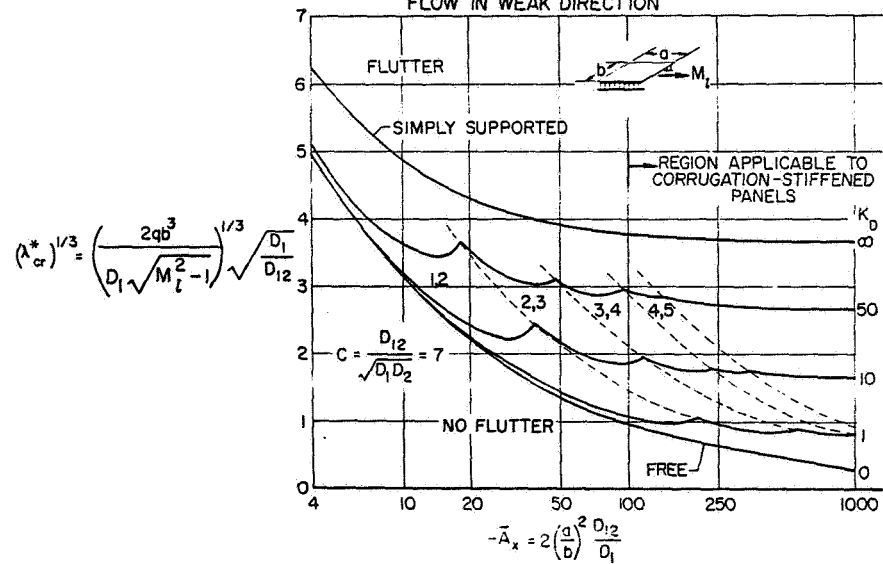


Figure 6

~~CONFIDENTIAL~~

~~CONFIDENTIAL~~

EFFECT OF PANEL ORIENTATION

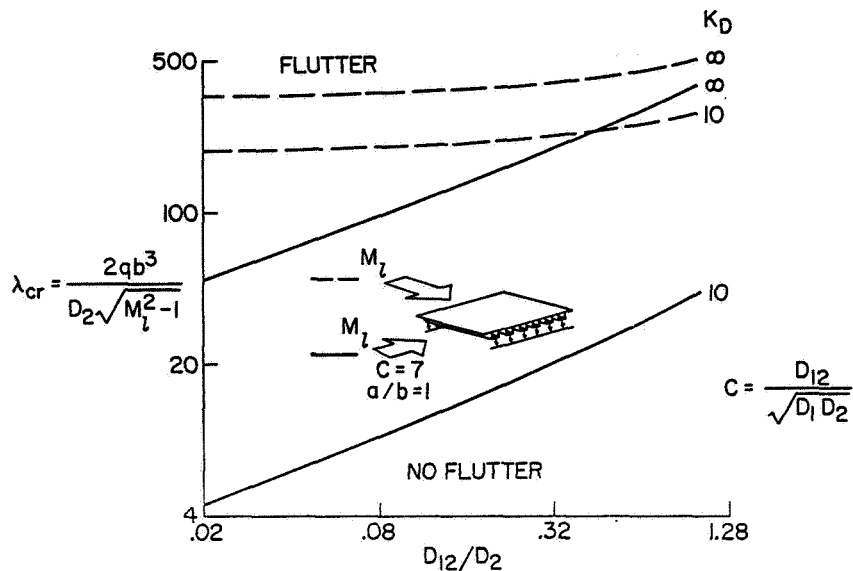


Figure 7

FLUTTER OF HIGHLY ORTHOTROPIC PANELS FLOW IN STRONG DIRECTION

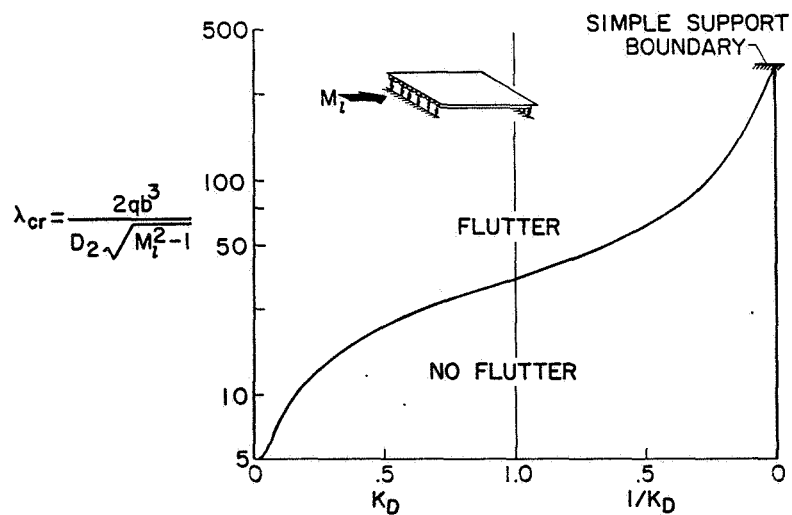


Figure 8

~~CONFIDENTIAL~~

~~CONFIDENTIAL~~

FLUTTER OF HIGHLY ORTHOTROPIC PANELS

FLOW IN WEAK DIRECTION

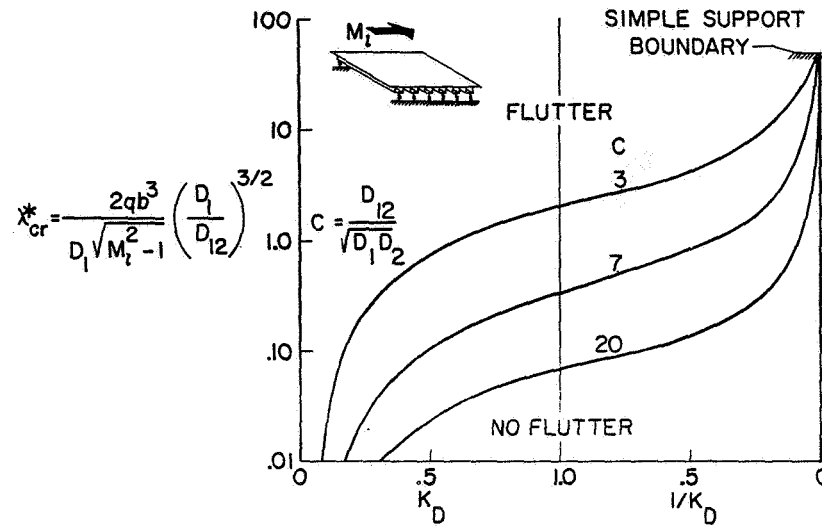


Figure 9

COMPARISON OF THEORY AND EXPERIMENT

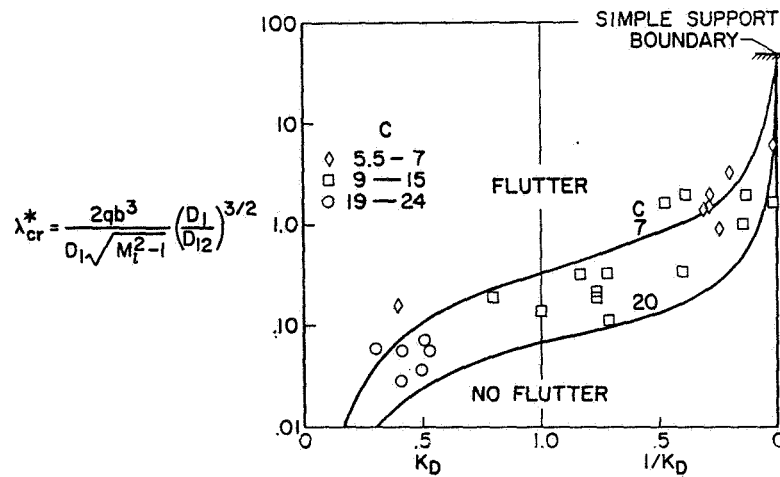


Figure 10

EFFECT OF EDGE TORSIONAL STIFFNESS

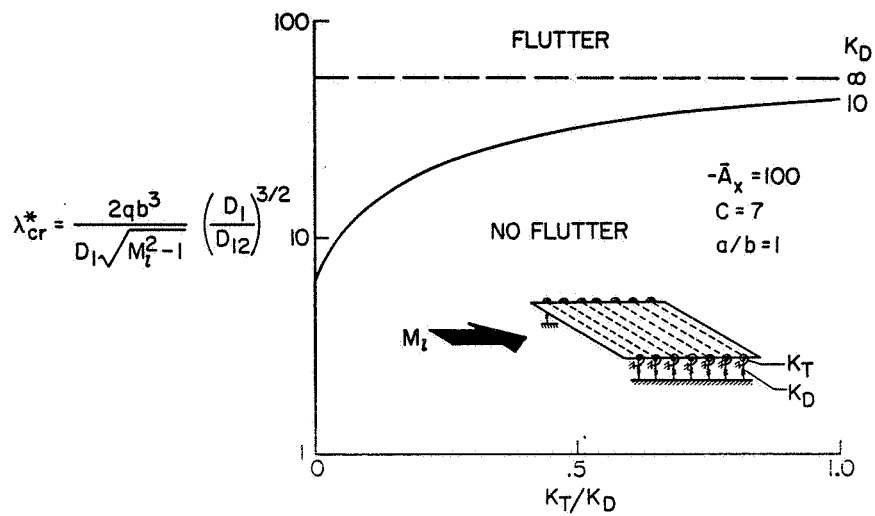


Figure 11

COMPARISON OF EXPERIMENTAL AND THEORETICAL NATURAL FREQUENCIES

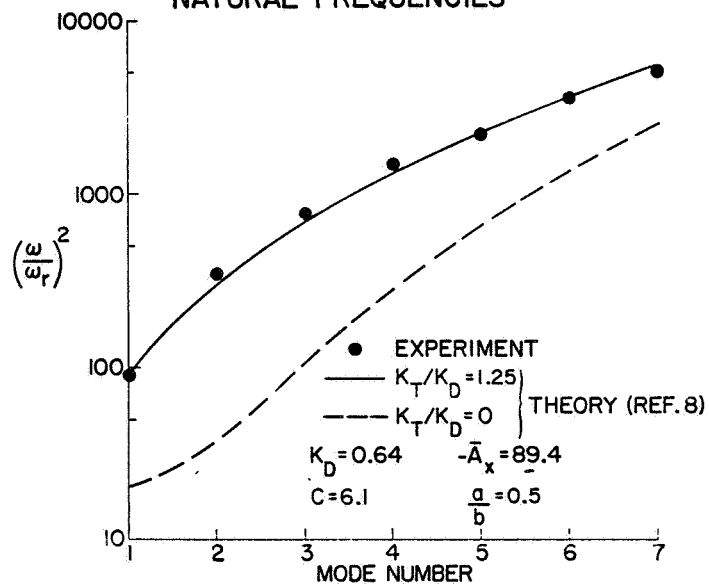


Figure 12

COMPARISON OF THEORY AND EXPERIMENT

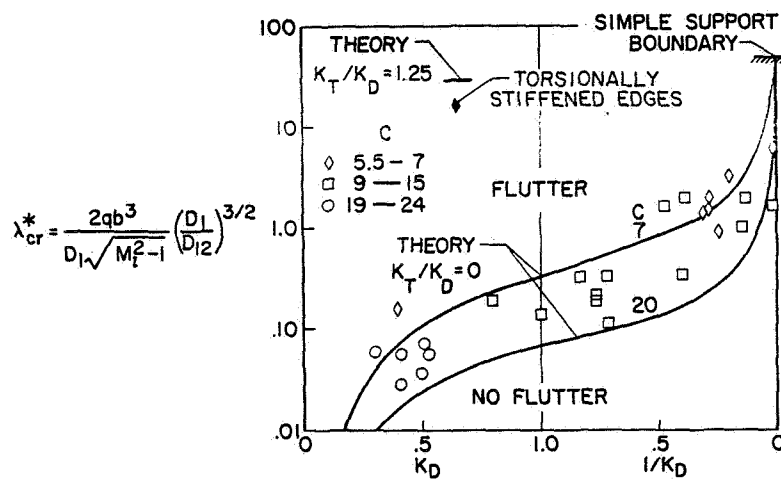


Figure 13